



REFERENCE ONLY

UNIVERSITY OF LONDON THESIS

Degree pho Year 2005 Name of Author ECCLES V.

COPYRIGHT

This is a thesis accepted for a Higher Degree of the University of London. It is an unpublished typescript and the copyright is held by the author. All persons consulting the thesis must read and abide by the Copyright Declaration below.

COPYRIGHT DECLARATION

I recognise that the copyright of the above-described thesis rests with the author and that no quotation from it or information derived from it may be published without the prior written consent of the author.

LOANS

Theses may not be lent to individuals, but the Senate House Library may lend a copy to approved libraries within the United Kingdom, for consultation solely on the premises of those libraries. Application should be made to: Inter-Library Loans, Senate House Library, Senate House, Malet Street, London WC1E 7HU.

REPRODUCTION

University of London theses may not be reproduced without explicit written permission from the Senate House Library. Enquiries should be addressed to the Theses Section of the Library. Regulations concerning reproduction vary according to the date of acceptance of the thesis and are listed below as guidelines.

- A. Before 1962. Permission granted only upon the prior written consent of the author. (The Senate House Library will provide addresses where possible).
- B. 1962 - 1974. In many cases the author has agreed to permit copying upon completion of a Copyright Declaration.
- C. 1975 - 1988. Most theses may be copied upon completion of a Copyright Declaration.
- D. 1989 onwards. Most theses may be copied.

This thesis comes within category D.

This copy has been deposited in the Library of UCL

This copy has been deposited in the Senate House Library, Senate House, Malet Street, London WC1E 7HU.

**Laboratory Electrical Studies on the Thermo-Chemo-Mechanics of
Faults and Fault Slip**

By

David Eccles

A thesis submitted to the University of London
For the degree of Doctor of Philosophy

UMI Number: U591960

All rights reserved

INFORMATION TO ALL USERS

The quality of this reproduction is dependent upon the quality of the copy submitted.

In the unlikely event that the author did not send a complete manuscript and there are missing pages, these will be noted. Also, if material had to be removed, a note will indicate the deletion.



UMI U591960

Published by ProQuest LLC 2013. Copyright in the Dissertation held by the Author.
Microform Edition © ProQuest LLC.

All rights reserved. This work is protected against
unauthorized copying under Title 17, United States Code.



ProQuest LLC
789 East Eisenhower Parkway
P.O. Box 1346
Ann Arbor, MI 48106-1346

Abstract

In nature, electrical signals have been recorded contemporaneously with volcanic and seismic activity, and have been proposed as precursors to earthquakes and volcanic eruptions. In the hydrocarbon industry, streaming potentials are used to investigate steam fronts, thus aiding enhanced oil recovery. There is therefore considerable current interest in electrical signals emanating from the Earth's crust and the mechanisms which give rise to them.

Two of the theories that have been proposed to explain electrical signal generation are:

- The piezoelectric effect, caused by stress changes on piezoelectric minerals, such as quartz, which is found in many crustal rocks.
- The electrokinetic phenomenon, produced at a solid-liquid interface, where an electrokinetic current such as the streaming potential can be induced through a pressure, chemical or temperature gradient, resulting in electrical charge transport within the moving fluid.

In order to investigate the possible mechanisms responsible for the generation of electrical signals in the Earth's crust, carefully controlled laboratory rock deformation and rock physics experiments have been performed under simulated shallow crustal conditions, where both electrical potential signals and acoustic emissions were measured. The deformation strain rate, confining pressure, pore fluid pressure, pore fluid chemistry and temperature were all varied systematically during conventional triaxial rock deformation tests on a range of rock types. Confining pressures were varied from 20 MPa to 100 MPa, pore fluid pressures from 5 MPa to 40 MPa, strain rates from $1.5 \times 10^{-4} \text{ s}^{-1}$ to $1.5 \times 10^{-7} \text{ s}^{-1}$ and temperatures from room temperature (25°C) up to 125°C. Over thirty five experiments were completed at room temperature on rock samples Clashach, Bentheim and Darley Dale sandstones and Portland limestone. More than ten experiments were done at elevated temperature on both dry and saturated samples of Clashach sandstone using a range of pore fluid chemistries. Significant developments in experimental apparatus were necessary for these latter experiments, including the design and construction of an electrical internal heater for the triaxial deformation cell.

I identify that, for the temperature range between 25° and 125°C, that the primary sources of electrical potential signal generation are (i) piezoelectric in dry quartz-rich sandstone and (ii) electrokinetic in saturated samples of both sandstones and limestone. Factors that are found to influence the electrical potential signals during deformation include effective pressure, temperature, strain rate, pore fluid type and fluid flow. As failure is approached, both pre-seismic and co-seismic signals are observed with the magnitude of the signals varying with rock type. These observations can be explained by differences in the rock composition and variation in hydraulic and electrical pathways available for electric current flow during rock deformation.

Variation in electrical potential difference can be seen during both the compactive and dilatant stages of deformation. At slower strain rates, local rock variation can be seen through changes in electrical

potential signals which appear to be obscured at higher strain rates. The change in electrical and streaming potential signals during deformation reflect both the accumulating and accelerating damage identified by acoustic emission prior to fracture and the localisation of damage at dynamic fracture. After failure the potential decreases to a background value where it remains during constant frictional sliding at essentially constant stress. The presence of a crack or fault was identified to affect the electrical and streaming potential signals depending on their relative position with respect to the fault suggesting that electrical potential could be used as a method for fault location.

An increase in temperature was found not to affect the mechanical properties within the range of experimental conditions explored. The effect of increased temperature on the electrical potential signals depends on the conditions applied to the rock such as thermal equilibrium times, deformation and ionic species within the pore fluid. If the rock is allowed to reach thermal equilibrium, the electrokinetic reactions between the solid-liquid interface are increased with an average electrical potential increase of 38 mV per 25°C. However, the new surfaces formed during rapid deformation cannot reach equilibrium, so that temperature has no effect on the electrical potential signals during compaction, dilatancy & failure. With this, the results as a whole suggest that in shallow crustal rocks, the change in electrical potential signal with temperature is below the background electrical noise level.

TABLE OF CONTENTS

SYMBOLS	9
LIST OF FIGURES	12
LIST OF TABLES	22
ACKNOWLEDGEMENTS	24
CHAPTER 1: INTRODUCTION	27
1.1. Introduction	27
1.2. Thesis Description	29
CHAPTER 2: THE DEVELOPMENT OF ROCK PHYSICS AS AN EXPLORATORY TOOL	31
2.1 INTRODUCTION	31
2.2 CRUSTAL CONDITIONS	32
2.3 DEFORMATION OF THE CRUST	35
2.3.1 Statistical Physics Approaches	35
2.4 THE MECHANICS OF ROCK DEFORMATION	36
2.4.1 Isotropic, Deviatoric and Principal Stresses	36
2.4.2 Compressive Failure	38
2.4.3 Brittle Failure	39
2.4.4 Failure Modes During Experimental Triaxial Deformation	43
2.4.5 Acoustic Emissions	44
2.4.6 Elastic Wave Velocity Analysis	46
2.4.7 The Brittle Deformation Cycle	47
2.5 GRIFFITH CRACK ANALYSIS	49
2.5.1 Griffith Crack	49
2.5.2 Linear Elastic Fracture Mechanics	51
2.6 THE DEFORMATION OF FLUID SATURATED ROCKS	54
2.6.1 Application of Pore Pressure	54
2.6.2 Quartz-Water Interaction	55
2.6.4 Permeability	62
2.6.3 Electrical Conductivity and Resistivity of Rocks and Fluids	65
2.6.4 Electrical Conductivity of Rock at Elevated Temperatures	68
2.7 CONCLUSION	68
CHAPTER 3: THE THEORY OF SEISMO ELECTRIC SIGNALS (SES)	69
3.1 INTRODUCTION	69
3.2 ELECTRICAL PHENOMENA IN THE FIELD	69
3.2.1 Electrical Potential Investigation of the Crust	69
3.2.2 Electrical Signals Associated with Geological Hazards	69
3.2.3 Electrical Potential Exploration Methods	71
3.3 LABORATORY INVESTIGATION OF THE ELECTRICAL PHENOMENA	72

Table of Contents

3.4	DEVELOPMENT OF SEISMOELECTRIC THEORY	73
3.4.1	The Piezoelectric effect theory	73
3.4.2	The Theory for the Electrokinetic Phenomenon	75
3.4.3	Electrokinetic Coupled Phenomena	86
3.5	CONCLUSION	88
CHAPTER 4: EXPERIMENTAL EQUIPMENT		90
4.1	INTRODUCTION AND GENERAL DESCRIPTION OF APPARATUS	90
4.2	TRIAxIAL DEFORMATION APPARATUS	93
4.2.1	Introduction	93
4.2.2	Stiffness	93
4.2.3	Actuator	94
4.3	PRESSURE APPLICATION SYSTEMS	95
4.3.1	Hydraulic Oil	95
4.3.2	Piping	95
4.3.3	Intensifiers	96
4.3.4	Control Unit	96
4.3.5	Confining Pressure	97
4.3.6	Pore Pressure	97
4.3.7	Electrical Isolation	97
4.4	MEASUREMENTS AND DATA LOGGING	97
4.4.1	Data Logging	97
4.4.2	Porosity	98
4.4.3	Load Measurements	99
4.4.4	Displacement Measurements	99
4.4.5	Pore Volume and Pore Pressure Measurements	99
4.4.6	Electrical Potential Measurements	99
4.4.7	Acoustic Emission Measurements	100
4.4.8	Angle of Failure	100
4.4.9	Measurement Errors	100
CHAPTER 5: EQUIPMENT DESIGN FOR THERMO-CHEMO-MECHANIC EXPERIMENTS		101
5.1	INTRODUCTION AND GENERAL DETAIL OF CHAPTER	101
5.2	HIGH TEMPERATURE	101
5.2.1	Furnace Calculations	102
5.2.1.1	Energy Required for 320°C Furnace	102
5.2.2	Heating Elements	104
5.2.2.1	Heat Radiated From Coils	104
5.2.2.2	Temperature of Inner Pressure Vessel Wall	105
5.2.3	Furnace Design	105
5.2.4	Stress Analysis	107
5.2.5	Thermal Insulation	109

Table of Contents

5.2.6	Temperature Control	109
5.2.7	Jacketing and Holding Pieces System	110
5.2.8	Piezoelectric Transducers	111
5.2.9	Oil	112
5.2.10	End-caps	112
5.2.11	Lead-throughs	112
5.3	OTHER MODIFICATIONS	112
5.3.1	Pore Fluid Separator	112
5.3.2	Yoke and End-caps	114
5.3.3	Lead-through Design	116
CHAPTER 6: EQUIPMENT SET-UP		118
6.1	ROCK TYPE DESCRIPTION	118
6.1.1	Rock Types Chosen	118
6.1.2	Thin Sections	119
6.1.3	Description of Darley Dale Sandstone	119
6.1.4	Description of Clashach Sandstone	119
6.1.5	Description of Bentheim Sandstone	120
6.1.6	Description of Portland Limestone	120
6.1.7	Description of Seljadur Basalt	120
6.2	ROCK SAMPLE PREPARATION	122
6.2.1	Sample Rock	122
6.2.2	Coring and Grinding	123
6.2.3	Saturation Technique	123
6.2.4	Preparation for Electrical Measurements	125
6.2.5	Preparation of Sample	125
6.3	ROCK SAMPLE ARRANGEMENT	126
6.3.1	Jacket System	126
6.4	EXPERIMENTAL PROCEDURE	128
6.4.1	Experimental Method	128
6.4.2	Calibration and Deformation Correlation	129
6.4.2.1	Linear Variable Differential Transformers	129
6.4.2.2	Pressure Transducers	130
6.4.2.3	Volume Displacement	130
6.4.2.4	Axial Load	130
6.4.2.5	Furnace Calibration	134
6.4.2.6	Error Analysis	138
CHAPTER 7: COMPARISON OF ELECTRICAL POTENTIAL SIGNALS FROM EXPERIMENTAL DEFORMATION OF VARIOUS ROCK TYPES		139
7.1	INTRODUCTION	139
7.2	COMPARISON OF MECHANICAL PROPERTIES	140

Table of Contents

7.3	THE DIFFERENCE BETWEEN DRAINED AND UNDRAINED EXPERIMENTS ON ELECTRICAL SIGNAL GENERATION	145
7.4	THE EFFECT OF DIFFERENTIAL STRESS ON ELECTRICAL POTENTIAL SIGNALS	146
7.5	PRE-SEISMIC AND CO-SEISMIC COMPARISON BETWEEN ROCK TYPES	150
7.6	ELECTRICAL POTENTIAL SIGNALS AFTER DYNAMIC FAILURE	154
7.7	CORRELATING ELECTRICAL POTENTIAL SIGNALS TO THE MEAN CRACK LENGTH	156
7.8	MICROSTRUCTURAL ANALYSIS	158
7.9	CHANGES IN MECHANICAL PROPERTIES DUE TO STRAIN RATE VARIATION	160
7.10	ELECTRICAL POTENTIAL SIGNAL CHANGE DUE TO STRAIN RATE	161
7.11	STRAIN RATE EFFECT ON PRE-SEISMIC AND CO-SEISMIC ELECTRICAL POTENTIAL SIGNALS	169
7.12	STREAMING POTENTIAL AT HIGH PORE FLUID PRESSURES	171
7.13	STREAMING POTENTIAL DURING DEFORMATION	174
7.14	CHAPTER SUMMARY	177
CHAPTER 8: TEMPERATURE EFFECT UP TO 125°C ON THE MECHANICAL AND ELECTRICAL PROPERTIES OF CLASHACH SANDSTONE AND PORTLAND LIMESTONE		179
8.1	INTRODUCTION	179
8.2	INITIAL OBSERVATIONS WITH THE FURNACE	179
8.3	COMPARISON OF PORTLAND LIMESTONE BOTH SATURATED AND IN WATER-FREE CONDITIONS	183
8.4	COMPARISON OF CLASHACH SANDSTONE SATURATED AND IN WATER-FREE CONDITIONS AT 50°C	189
8.5	EFFECT OF ELEVATED TEMPERATURES ON MECHANICAL PROPERTIES OF CLASHACH SANDSTONE	192
8.6	EFFECT OF ELEVATED TEMPERATURES ON ELECTRICAL PROPERTIES	194
	8.6.1 Streaming Potential Measurements at High Pore Pressure Gradients	198
	8.6.2 Cycling Heating Effect	200
8.7	EFFECT OF SIMULATED FORMATION WATER AND RAISED TEMPERATURES ON BOTH MECHANICAL AND ELECTRICAL PROPERTIES	202
	8.7.1 Streaming Potential Generated with Saline Fluid at High Pore Pressures	209
8.8	CHAPTER SUMMARY	212
CHAPTER 9: DISCUSSION		214
9.1	DISCUSSION OF ROOM TEMPERATURE EXPERIMENTS	214
	9.1.1 Discussion of Electrical Potential Signals due to Shear Fracture	124
	9.1.2 The Difference Between Quartz Rich and Quartz Free Rocks on the Electrical Potential Signal	222
	9.1.3 Effect of Strain Rate on Rock Type and Electrical Signals	224
	9.1.4 Discussion of the Effect of Rock Types and Environmental Conditions on Streaming Potential Signals	226
9.2	DISCUSSION OF THE EFFECT OF TEMPERATURE ON THE DEFORMATION OF ROCK SAMPLES	233

Table of Contents

9.2.1 Discussion of the Effect of Temperature on the Mechanical Properties of Sandstone During Shear Failure	233
9.2.2 Effect of Temperature on the Electrical Potential Signals During Shear Failure	233
9.2.3 Discussion of the Effect of Temperature on the Streaming Potential Signal	239
9.2.4 Effect of Temperature and Simulated Formation Waters on Electrical Properties of Clashach Sandstone	240
9.3 APPLICATION TO CRUSTAL CONDITIONS	244
9.3.1 Earthquake Prediction Implications	244
9.3.2 Implications for Shallow Crustal Exploration	246
CHAPTER 10: CONCLUSIONS AND FUTURE WORK	248
10.1 CONCLUSIONS	248
10.2 FUTURE WORK	249
REFERENCES	251
APPENDIX 1	265
APPENDIX 2	314
APPENDIX 3	320
APPENDIX 4	331
APPENDIX 5	351
APPENDIX 6	403
APPENDIX 7	405
APPENDIX 8	413
APPENDIX 9	414
PAPER AND CD	

List of Symbols

g	Gravity acceleration
z	Depth
q_i	Heat flow
K	Thermal conductivity
T	Temperature
V_p	P-wave velocity
V_s	S-wave velocity
M	Earthquake magnitude
b	Seismic b-value
D	Fractal dimension
A	Area
F	Force
δ_{ij}	Kronecker delta
ε_{ij}	Strain tensor
$\dot{\varepsilon}$	Strain rate
σ_{ij}	Stress tensor
$\dot{\sigma}$	Stress rate
σ_{ij}^p	Principal stress
σ_{ij}^e	Effective pressure
θ	Angle
σ_N	Normal stress
$\sigma_S (\tau_s)$	Shear stress
μ'	Coefficient of internal friction
S_c	Cohesive strength
ϕ_f	Angle of friction
S	Specific surface area
W	Work done
U_e	Internal strain energy
U_s	Created surface energy
U_m	Mechanical energy
T_0	Uniaxial tensile strength
K_n	Stress intensity factor
r	Distance from tip
γ	Activity coefficient / Free energy surface
$f_{ij}(\theta), f_i(\theta)$	angular dependence factor
K_c	Fracture toughness
G_c	Fracture energy

List of Symbols

K	Effective bulk modulus
K_s	Grain bulk modulus
P_c	Confining pressure
p_p	Pore fluid pressure
P_e	Effective pressure
n	Stress corrosion index
q_x	Darcy velocity
k	Hydraulic permeability
R_e	Reynolds number
l	Characteristic length of the pore space
r	Radius (grain, pore throat size)
J_i	Electrical current density
ζ	Zeta potential
ϕ	Porosity
E_j	Electric Field
F	Formation Factor
ρ_r	Resistivity of rock
ρ_f	Resistivity of fluid
a	Coefficient of saturation
σ_f	Pore fluid conductivity
σ_B	Bulk conductivity
s	Electric conductivity
S_i	Mechanical strain (Piezoelectric)
T	Mechanical stress (Piezoelectric)
S	Mechanical compliance
d	Piezoelectric strain constant
c_{ijk}	Piezoelectric modulus
C	Elastic constant
$D_p \downarrow$	Electric polarisation
P_{eff}	Effective polarization
$\epsilon_r (\epsilon^T)$	Relative permittivity
(D)	Charge density
τ	Relaxation time
m	Cementation factor
b_v	Quartz volume
r_i	Distance to the measuring point
κ^{-1}	Debye length
φ	Electrical Potential
k_b	Boltzmann's constant
e	Elementary charge of an electron
z	Valence of the ionic species

List of Symbols

q	Total charge
φ	Pore fluid viscosity
I	Electrical current
V	Streaming potential
u_s	Speed of fluid
Σ_s	Specific surface conductance
σ_r	Rock electrical conductivity
L_{ij}	Hydraulic coefficient
S	Electrokinetic source
$\tau_h(T)$	Hydraulic tortuosity
τ_e	Electrical tortuosity
C	Concentration
S_l	Specific internal area

List of Figures

Figure 2.1: Variation of P-wave velocity (V_p) with crustal depth (z) (from Fowler (2001)).	33
Figure 2.2: Variation of electrical conductivity with depth in the continental crust showing three distinct areas of electrical structure (from Shankland and Anders (1983)).	34
Figure 2.3: Seismic moment data from boreholes and earthquakes plotted as a function of the source dimension on a log-log plot. The straight lines represent the scaling laws at different stress drops (in bars) from the dislocation model of the seismic source (from Abercrombie (1995)).	36
Figure 2.4: Schematic diagram showing the nine stress components required to describe the stress at any point	37
Figure 2.5: Principle of a triaxial test.	38
Figure 2.6: Mohr circle and the Coulomb-Navier criterion for shear fracture.	39
Figure 2.7: Mohr-Coulomb failure diagram showing the different types of failure and the brittle-ductile transition (from Murrell, 1965).	40
Figure 2.8: Frictional strength for a wide variety of rocks plotted as a function of normal load at high loads (From Byerlee, 1978).	41
Figure 2.9: Different stress-strain curves and the type of fault associated with them, (a) uniaxial conditions, (b) low confining pressure and low temperature, (c) high pressure (d) and/or high temperature and (e) tension conditions.	43
Figure 2.10: Deformation of Darley Dale sandstone at a strain-rate of 10^{-5} s^{-1} and a confining pressure of 50 MPa. (a) Event rate and (b) b-value during this experiment (taken from Sammonds et al. (1992)).	45
Figure 2.11: Initial nucleation propagation and formation of fault plane from source located AE events during triaxial deformation. Upper and lower row shows evolution in time from two orthogonal directions (from Lockner et al.(1991)).	45
Figure 2.12: Variations in velocities of compressional (V_p) and shear (V_s) waves in a dry sample of Darley Dale sandstone deformed under a confining pressure of 50 MPa at a strain rate of 10^{-5} s^{-1} (from Sammonds et al (1989)).	46
Figure 2.13: Triaxial tests on Solenhofen limestone, at varying temperatures (from Jones (1989)).	47
Figure 2.14: Variation of a number of physical properties with axial strain during a typical deformation cycle (taken from Aves (1995)).	47
Figure 2.15: The Griffith's model for crack propagation in a rod (a), and the energy partition for the process (b) (redrawn from Scholz (2002)).	49
Figure 2.16: (a) The three modes of rock fracture, (b) crack tip stresses. See text for details (taken from Gueguen and Palciauskas (1994)).	52
Figure 2.17: The effects of pore fluid pressure on fracture.	55
Figure 2.18: Influence of pore fluid pressure on the fracture strength of sandstone under triaxial deformation (taken from Murrell (1965)).	55
Figure 2.19: Chemically induced bond rupture. An environmental molecule A reacts with crack tip molecule B to produce terminal bonds A-B (redrawn from Lawn (1993)).	56
Figure 2.20: Michalske and Freiman's model showing (a) the adsorption of a water molecule onto a quartz surface, (b) leading to hydrolysis and (c) rupture of the weak bonds (redrawn from Michalske and Freiman (1982)).	57

- Figure 2.21:** The dependence of crack velocity on the stress intensity (K) between the subcritical crack growth limit (0) and critical rupture (c). The influence of temperature and partial pressure of water is also indicated (from Meredith et al.(1991)). 58
- Figure 2.22:** Stress intensity factor versus crack velocity for Black gabbro cracked at temperatures between 20°C and 300°C under water vapour pressures of 2.5 and 15 kPa. The solid lines represent the least square fits for the data points (from Meredith et al.(1991)). 59
- Figure 2.23:** Schematic illustration of the dissolution process in deionised water (from Dove and Crerar (1990)). 60
- Figure 2.24:** Calculated solubilities of quartz in water as a function of temperature and pressure. The stippled pattern shows a region of retrograde solubility in which the solubility of quartz decreases with increasing temperature at constant pressure (from Fournier (2001)). 61
- Figure 2.25:** Influence of hydrostatic pressure on permeability for (a) isotropic pores and (b) pore and crack porosity of a sandstone (from David and Darot (1989)). 63
- Figure 2.26:** Relationship between permeability and porosity of granites heat treated at temperatures of 500°C and 600°C (from Jones et al.(1997)). 64
- Figure 2.27:** Effect of heat treatment of different granites on their porosity-permeability interrelationship with the lines showing the change porosity and permeability at temperatures of 500°C and 600°C. (from Jones et al. (1997)). 65
- Figure 2.28:** Typical values of conductivity and resistivity for geological materials (from Palacky (1987)). 66
- Figure 2.29:** Conductivity as a function of fluid concentration for (a) different salts at 20°C and (b) for NaCl solution at varying temperatures (from Keller (1987)). 66
- Figure 2.30:** Saturated bulk conductivity as a function of fluid conductivity for a clay bearing sandstone, Darley Dale sandstone and a non-clay-bearing sandstone, Berea sandstone (from Glover et al.(1994)). 68
- Figure 3.1:** Initially stress induced polarisation of quartz crystals is (a) neutralised by mobile bound charges on the charge surface. A rapid stress change (b) induces an effective polarisation in the crystal, which decays (c) through a relaxation process with time constant $\tau=\epsilon/s$ where s is the conductivity (redrawn from Yoshida et al. (1997)). 75
- Figure 3.2:** The Stern layer made up of a solid inner monolayer (S_1), diffuse outer layer (S_2) Bulk fluid phases and the position of the zeta potential in relation to the crystal surface. A decrease in the electrical potential with increasing distance from the crystal surfaces is observed. 76
- Figure 3.3:** Critical distances inside of membrane pore, δ , anion radius; λ , Debye length; a , hydrodynamic radius; r_o , pore radius and r_d external radius of boundary diffusion layer: ϕ_o, ϕ_s and ϕ_d are the electrical potential on the membrane surface, Stern plane and at the limit of the diffuse layer; ζ is the zeta potential (redrawn from Molina et al. (1999)). 77
- Figure 3.4:** Schematic of the electrical potential distribution in the overlapped EDL field between two flat plates, where ψ_o is the electrical potential at the surface, ψ_b is the potential at the middle plane, $2b$ is the separation distance between the two flat plates, and $1/\kappa$ indicates the thickness of the single EDL (redrawn from Qu and Li (2000)). 79
- Figure 3.5:** The effect of an applied pore pressure gradient across a cylinder resulting in the generation of convection (same direction of fluid flow) and conduction (opposite direction to fluid flow) currents required for streaming potential signals.. 80
- Figure 3.6:** How the streaming potential coefficient is linked to different factors (redrawn from Jouniaux and Pozzi (1995)). 83
- Figure 4.1:** Photograph of the laboratory containing the triaxial pressure vessel. 91

Figure 4.2: Diagram of pressure vessel showing seals along with other components. Taken from Clint (1999).	92
Figure 4.3: Details photograph of pressure vessel.	93
Figure 4.4: Photograph of LVDT's attached to top of the pressure vessel.	95
Figure 4.5: Photograph of the pressure intensifier with pressure and displacement transducers.	96
Figure 4.6: Block diagram showing all instrumentation involved in a triaxial deformation experiment together with the data acquisition system.	98
Figure 5.1: Simplified diagram of furnace to calculate the power required to heat the oil, steel and rock sample to 320°C.	103
Figure 5.2: Schematic drawing of furnace assembly, yoke system and bottom inner and outer closures.	106
Figure 5.3: 3D rendering of electric furnace inside the pressure vessel.	107
Figure 5.4(a): Stress analysis of outer bottom closure using Design Space 6	108
Figure 5.4(b): Sliced through stress analysis of the bottom outer closure using Design Space 6	108
Figure 5.5: Circuit diagram of the furnace controller including heating elements, thermocouples and monitors	110
Figure 5.6: Diagram of pore fluid separator design. A moving shuttle plug separates corrosive brine fluids from distilled fluids and is sealed using standard piston and O-ring seals. Pore fluid pressures up to 80MPa can be used in this arrangement. (Taken from Clint (1999))	113
Figure 5.7: Schematic diagram displaying pore fluid system incorporating two separators. The right side of the system is primed with NaCl brine isolated from de-ionised water in the left of the system by the shuttle plug. Pore pressure is applied from the servo-controlled pore fluid intensifier and transmitted to the brines.(Modified from Clint (1999))	114
Figure 5.8: Diagram of sample set-up inside pressure vessel.	116
Figure 5.9: Diagram showing the make-up of lead through design. (Taken from Clint (1999))	117
Figure 6.1: Micrographs of (a) Darley Dale sandstone, (b) Clashach sandstone, (c) Bentheim sandstone, (d) Portland limestone and (e) Seljadur Basalt (thin sections need be further out).	121/122
Figure 6.2a: A 5 x 20mm normalised surface plot of Portland limestone after grinding with tascle bar showing the variation in height.	124
Figure 6.2b: A 5 x 20mm normalised surface plot of Clashach sandstone after grinding with a scale bar showing the variation in height.	124
Figure 6.3: Schematic diagram showing rock sample preparation for electrical measurements.	125
Figure 6.4: Photograph of yoke and set-up	126
Figure 6.5: Diagram showing the metal inserts against the rock surface.	127
Figure 6.6: Diagrams of jackets used in experiments.	128
Figure 6.7a: Calibration curve for LVDT along with σ_x and R^2 .	131
Figure 6.7b: Calibration curve for LVDT along with σ_x and R^2 .	131
Figure 6.8: Calibration curve for the confining pressure along with σ_x and R^2	132

Figure 6.9: Calibration curve for the pore pressure along with σ_x and R^2	132
Figure 6.10: Calibration curve for the load along with σ_x and R^2	133
Figure 6.11: Relationship between confining pressure and furnace temperature.	135
Figure 6.12: Furnace calibration for a sample temperature of 100°C. The furnace thermocouple (L) is at least 25°C warmer than the rock and oil.	135
Figure 6.13: (a) Position of the thermocouples relative to the rock sample and (b) thermal profile along the rock specimen at furnace temperatures of 25, 50, 75, 100 and 125°C.	136
Figure 6.14: Relationship between the master controller temperature and the sample temperature.	137
Figure 6.15a: Comparison of temperature against confining pressure at temperatures up to 125°C showing a similar shape line for both calibrations.	137
Figure 6.15b: Relationship between the temperature of the furnace and the temperature of the oil for both sets of calibrations. The oil is allowed over 1 hr to reach thermal equilibrium before measurements are made.	138
Figure 7.1: Typical stress-strain curve for triaxial deformation of (a) Bentheim sandstone, (b) Clashach sandstone, (c) Darley Dale sandstone and (d) Portland limestone; all experiments had P_c of 40 MPa and P_p of 20 MPa with a strain rate of $1.5 \times 10^{-5} \text{ s}^{-1}$. [Experiment No.:(a) 26, (b) 13, (c) 30, (d) 25]	141
Figure 7.2: Differential stress, pore volume and confining pressure change of drained Darley Dale sandstone against strain. The quasi-elastic linear phase compares well with a pore volume decrease in the rock due to the compaction process. The reduction in rock size also causes a similar reduction in confining pressure; an initial C_p of 40 MPa and P_p of 20 MPa with a strain rate of $1.5 \times 10^{-4} \text{ s}^{-1}$. [Experiment No.: 32]	142
Figure 7.3: Plot showing the link between the change in confining pressure and the change in pore volume during the deformation of drained Darley Dale sandstone; $P_c = 40 \text{ MPa}$, $P_p = 20 \text{ MPa}$ using deionised water and a strain rate of $1.5 \times 10^{-4} \text{ s}^{-1}$. [Experiment No.: 32]	142
Figure 7.4: Stress-strain curves for the deformation of Clashach sandstone under drained conditions with zero pore pressure at confining pressures of 30, 50, 65, 75 and 100 MPa and using a strain rate of $1.5 \times 10^{-5} \text{ s}^{-1}$. [Experiment No.: 1, 2, 3, 4, 5]	143
Figure 7.5: The effect of effective stress on (a) the stress drop and (b) slip displacement during brittle failure of Clashach sandstone under drained conditions using a strain rate of $1.5 \times 10^{-5} \text{ s}^{-1}$. The broken lines shown represent the least squared fit where the accuracy of each point shown given by error bars. [Experiment No.: 1 ($P_c = 30 \text{ MPa}$, $P_p = 0 \text{ MPa}$), 3 ($P_c = 50 \text{ MPa}$, $P_p = 0 \text{ MPa}$), 12 ($P_c = 40 \text{ MPa}$, $P_p = 20 \text{ MPa}$), 16 ($P_c = 60 \text{ MPa}$, $P_p = 20 \text{ MPa}$)]	144
Figure 7.6: Photographs of deformed Clashach sandstone showing the position of the electrodes and where the two dipoles are located. [Experiment No.:17]	145
Figure 7.7: Electrical potential change as a function of time for (a) drained ($P_c = 40 \text{ MPa}$, $P_p = 20 \text{ MPa}$) and (b) undrained ($P_c = 40 \text{ MPa}$, initial $P_p = 15 \text{ MPa}$) experiments. Also shown is the differential stress, pore volume and pore pressure. [Experiment No.: (a) 26 (b) 43]	146
Figure 7.8: The effect of axial loading on Clashach sandstone related to (a) the electrical potential signal produced during deformation and (b) the total number of hits recorded and calculated b-value with a strain rate of $1.5 \times 10^{-5} \text{ s}^{-1}$, P_c of 40 MPa and P_p of 20 MPa. [Experiment No.: 13]	147
Figure 7.9: Change in pore volume with (a) axial differential stress and (b) electric potential during compaction of Clashach sandstone with a confining pressure of 40 MPa, pore pressure of 20 MPa and strain rate of $1.5 \times 10^{-4} \text{ s}^{-1}$. The broken lines shown represent the least squared fit. Each point plotted is given to an accuracy of (a) $\pm 0.01 \text{ cm}^3$ and (b) $\pm 0.2 \text{ mV}$. [Experiment No.: 26]	148

- Figure 7.10:** Change in pore volume with (a) axial differential stress and (b) electric potential change during dilatancy of Clashach sandstone with a confining pressure of 40 MPa, pore pressure of 20 MPa and strain rate of $1.5 \times 10^{-4} \text{ s}^{-1}$. The broken lines shown represent the least squared fit. Each point plotted is given to an accuracy of (a) $\pm 0.01 \text{ cm}^3$ and (b) $\pm 0.2 \text{ mV}$. [Experiment No.: 26] 148
- Figure 7.11:** Variation of electrical potential signals produced during deformation and shear failure of (a) Clashach sandstone, (b) Darley Dale sandstone, (c) Bentheim sandstone and (d) Portland limestone. All experiments had a P_c of 40 MPa, P_p of 20 MPa and strain rate of $1.5 \times 10^{-5} \text{ s}^{-1}$. [Experiment No.: (a) 33, (b) 30, (c) 26, (d) 19] 149
- Figure 7.12:** The electrical potential signals produced during strain softening and shear failure of (a) Darley Dale sandstone, (b) Bentheim sandstone, (c) Clashach sandstone, (d) Icelandic basalt and (e) Portland limestone. All experiments had P_c of 20 MPa with a strain rate of $1.5 \times 10^{-5} \text{ s}^{-1}$. [Experiment No.:(a), (b) and (d) See Clint (1999), (c) 15, (e) 28] 151
- Figure 7.13:** The electrical potential signals produced during strain softening and shear failure of (a) Darley Dale sandstone, (b) Bentheim sandstone, (c) Clashach sandstone, (d) Icelandic basalt and (e) Portland limestone. All experiments had a P_c of 40 MPa, P_p of 20 MPa, distilled water as pore fluid with a strain rate of $1.5 \times 10^{-5} \text{ s}^{-1}$. [Experiment No.:(a) and (d) See Clint (1999), (b) 26, (c) 13, (e) 19] 152
- Figure 7.14:** The deformation of Clashach sandstone showing the effect of a fracture passing through an electrode and (b) photograph and schematic diagram of the deformed sample showing the position of cracks and fault; $P_c = 40 \text{ MPa}$, $P_p = 20 \text{ MPa}$ and strain rate $1.5 \times 10^{-4} \text{ s}^{-1}$. [Experiment No.: 21] 153
- Figure 7.15:** The electrical potential measured during steady-state frictional sliding after dynamic failure of sandstones and limestone. (a) dry Portland limestone with $P_c = 20 \text{ MPa}$ and strain rate $1.5 \times 10^{-4} \text{ s}^{-1}$, (b) Portland limestone with $P_c = 20 \text{ MPa}$, $P_p = 20 \text{ MPa}$ and strain rate $1.5 \times 10^{-7} \text{ s}^{-1}$, (c) dry Clashach sandstone with $P_c = 20 \text{ MPa}$ and strain rate $1.5 \times 10^{-5} \text{ s}^{-1}$, (d) Clashach sandstone with $P_c = 40 \text{ MPa}$, $P_e = 20 \text{ MPa}$ and strain rate $1.5 \times 10^{-5} \text{ s}^{-1}$ and (e) Darley Dale sandstone; $P_c = 40 \text{ MPa}$, $P_p = 20 \text{ MPa}$ and strain rate $1.5 \times 10^{-4} \text{ s}^{-1}$. [Experimental No.: (a) 28, (b) 27, (c) 15, (d) 33, (e) 32] 155
- Figure 7.16:** The variation of normalised mean crack length during the deformation of Clashach; $P_c = 40 \text{ MPa}$, $P_p = 20 \text{ MPa}$ with strain rate of $1.5 \times 10^{-4} \text{ s}^{-1}$. Each point plotted is given to an accuracy of ± 0.01 . [Experiment No.: 21] 157
- Figure 7.17:** Electrical potential change as a function of mean crack length. $P_c = 40 \text{ MPa}$, $P_p = 20 \text{ MPa}$ with a strain rate of $1.5 \times 10^{-4} \text{ s}^{-1}$. The broken black line shown represents the least squared fit. Each point plotted is given to an accuracy of $\pm 0.2 \text{ mV}$. [Experiment No.: 21] 157
- Figure 7.18:** Photomicrographs of Clashach sandstone in cross-polarised light (a) before deformation and (b) after deformation failure showing the presence of grain cracking with axial loadings going into the page; $P_c = 20 \text{ MPa}$ and strain rate of $1.5 \times 10^{-5} \text{ s}^{-1}$. [Experiment No.: 14] 158/159
- Figure 7.19:** SEM images of Portland limestone (PL) and Clashach sandstone (CS). (a) PL at magnification 500, (b) PL at magnification 5000, (c) CS at magnification 500 and (d) CS at magnification 5000. [Experiment No.: (a) 28, (b) 28, (c) 17, (d) 17] 160
- Figure 7.20:** Typical stress-strain diagram at different strain rates for Portland limestone; $P_c = 40 \text{ MPa}$, $P_p = 20 \text{ MPa}$ [Experiment No.: 23, 25, 27] 161
- Figure 7.21:** Electrical potential plotted during the deformation of Portland limestone to show the effect of a (a) strain rate of $1.5 \times 10^{-4} \text{ s}^{-1}$ and (b) $1.5 \times 10^{-6} \text{ s}^{-1}$ on the detail of signal recorded; $P_c = 40 \text{ MPa}$, $P_p = 20 \text{ MPa}$ [Experiment No.: (a) 24, (b) 23] 163
- Figure 7.22:** The electrical potential signal and axial stress measured during the deformation of Portland limestone with a confining pressure of 40 MPa, pore pressure of 20 MPa and a strain rate of $1.5 \times 10^{-6} \text{ s}^{-1}$. The colour sections represent features discussed in the text. [Experiment No.: 23] 164

- Figure 7.23:** Variation of electrical potential difference with strain rate of drained Darley Dale sandstone for (a) compaction and (b) dilatancy (up to failure). The data plotted represents the absolute change in electrical potential difference with no information on polarity of the changes; $P_c = 40$ MPa, $P_p = 20$ MPa. The broken lines represent the least squared fit. The accuracy of each point is shown by error bars. [Experiment No.: see Clint (1999) and 29] 165
- Figure 7.24:** Variation of pore volume change with strain rate during compaction of drained Darley Dale sandstone; $P_c = 40$ MPa, $P_p = 20$ MPa. The broken lines represent the least squared fit. Each point is given to an accuracy of ± 0.01 cm³. [Experiment No.: (a), (b) and (c) See Clint (1999) and (d) 29] 166
- Figure 7.25:** Variation of electrical potential difference with strain rate of drained Clashach sandstone for (a) compaction and (b) dilatancy (up to failure). The data plotted represents the absolute change in electrical potential difference with no information on polarity of the changes; $P_c = 40$ MPa, $P_p = 20$ MPa. The broken lines represent the least squared fit. The accuracy of each point is shown by error bars. [Experiment No.: 21, 22, 33] 167
- Figure 7.26:** Variation of electrical potential difference with strain rate of drained Portland limestone for (a) compaction and (b) dilatancy (up to failure). The data plotted represents the absolute change in electrical potential difference with no information on polarity of the changes; $P_c = 40$ MPa, $P_p = 20$ MPa. The broken lines represent the least squared fit. The accuracy of each point is shown by error bars. [Experiment No.: 23, 24, 27] 168
- Figure 7.27:** Graph showing the effect of varying the strain rate on mechanical strength and electrical potential signal during frictional sliding of drained Portland limestone with a confining pressure of 12 MPa and pore pressure of 7 MPa. [Experiment No.: 18] 169
- Figure 7.28:** Variation of electrical potential (a) prior to failure and (b) during dynamic fracture of drained Clashach sandstone as a function of strain rate; $P_c = 40$ MPa, $P_p = 20$ MPa. The broken lines represent the least squared fit. Each point is given to an accuracy of ± 0.1 mV. [Experiment No.: 21, 22, 33] 170
- Figure 7.29:** Streaming potential signals generated through steady state fluid flow along a pressure gradient in Clashach sandstone, $P_c = 40$ MPa, $P_p = 15$ MPa. [Experiment No.: 20] 171
- Figure 7.30:** Plots showing the streaming potential generated under increasing pore pressure gradients for (a) Darley Dale sandstone, (b) Bentheim sandstone, (c) Clashach sandstone and (d) Portland limestone. Linear relationships were obtained for all samples with regression coefficients ranging between 0.93 and 0.98. Each point is given to an accuracy of ± 0.1 mV. [Experiment No. (a), (b) See Clint (1999), (c) 22, (d) 25] 172
- Figure 7.31:** Plot showing the proportionality between flow rate and applied pore pressure gradient through Clashach, Bentheim and Darley Dale sandstone along with Portland limestone under hydrostatic conditions of 40 MPa. These results suggest laminar flow through the sample with the broken lines representing the least squared fit. Each point is given to an accuracy of ± 0.01 cm³. [Experiment No.: 22, 25, 29, 31] 173
- Figure 7.32:** Streaming potential signals generated through a pressure gradient in Clashach sandstone, of 35 MPa with confining pressure of 40 MPa. The unsteady change in fluid flow and steady-state streaming potential is not obtained, suggesting a turbulent flow regime is present. [Experiment No.: 20] 174
- Figure 7.33:** Variation of streaming potential in Portland limestone before and after fracture with a pressure difference of 10 MPa applied. The magnitudes of the streaming potential results plotted are the values from electrode 3 minus electrode 1. $P_c = 40$ MPa. [Experiment No.: 25] 175
- Figure 7.34:** The variation of streaming potential with pore fluid pressure differences for (a) Darley Dale sandstone, (b) Clashach sandstone and (c) Portland limestone. All experiments had a $P_c = 40$ MPa and $P_p = 20$ MPa. The broken lines represent the least squared fit. Each point is given to an accuracy of 0.2 mV. [Experiment No. (a) See Clint (1999), (b) 20 (c) 25] 176
- Figure 8.1:** Plot showing the effect of heat on the confining pressure, differential stress and the four electrodes (coaxial wires) using a dummy sample (aluminium) to 100°C. [Experiment No. 44] 180

- Figure 8.2:** Plots of temperature profiles at different positions around a dummy sample to show how the oil and rock heats up. The thermocouple located in the rock is positioned in a hole drilled from the lower end of the sample. (See Appendix 7 for more details) [Experiment No.: Cal3] 181
- Figure 8.3:** Acoustic emissions monitored during the use of the furnace at 160°C. This includes switching the furnace on, during the constant strain rate deformation and during cooling down. [Experiment No.: 41] 182
- Figure 8.4:** Electrical potential difference of Portland limestone (a) dry ($P_c = 20$ MPa) and (b) saturated during deformation with $P_c = 40$ MPa, $P_p = 20$ MPa using deionised water as the pore fluid and strain rate of $1.5 \times 10^{-5} \text{ s}^{-1}$ and at 50°C (Electrode 2 is missing due to breakage). [Experiment No.: (a) 39, (b) 36] 184
- Figure 8.5:** Electrical potential during the dynamic failure of Portland limestone deformed (a) dry ($P_c = 20$ MPa) and (b) water saturated ($P_c = 40$ MPa, $P_p = 20$ MPa) using deionised water as the pore fluid with a strain rate of $1.5 \times 10^{-5} \text{ s}^{-1}$ and at 50°C. [Experiment No.: (a) 39, (b) 36] 185
- Figure 8.6:** Streaming potential for Portland limestone at 50°C before fracture. $P_c = 40$ MPa with a 10 MPa applied pore pressure gradient across the sample and a 5 MPa background pore pressure with the change in fluid volume indicating a constant flow rate. [Experiment No.: 36] 186
- Figure 8.7:** Plot showing the streaming potential generated under increasing pore pressure gradients for Portland limestone. A linear relationship was obtained with a regression coefficient of 0.87 with each point plotted accurate to within ± 0.1 mV. [Experiment No.: 36] 187
- Figure 8.8:** Streaming potential and fluid flow rates of Portland limestone at various temperatures with a 10 MPa applied pore pressure gradient prior to fracture with a 5 MPa background pore pressure; $P_c = 40$ MPa with deionised water as pore fluid. The broken line represents the least squared fit of the streaming potential. Each point is given to an accuracy of ± 0.1 mV for streaming potential and $\pm 0.001 \text{ cm}^3/\text{sec}$ for flow rate measurements. [Experiment No. 25, 36, 41] 188
- Figure 8.9:** Electrical potential difference of Clashach sandstone during deformation (a) dry ($P_c = 20$ MPa) and (b) water saturated ($P_c = 40$ MPa, $P_p = 20$ MPa). Deionised water is the pore fluid and a strain rate of $1.5 \times 10^{-5} \text{ s}^{-1}$. [Experiment No.: (a) 34, (b) 35] 190
- Figure 8.10:** Electrical potential during the dynamic failure of Clashach sandstone deformed (a) dry ($P_c = 20$ MPa) and (b) water saturated ($P_c = 40$ MPa, $P_p = 20$ MPa). Deionised water was used as the pore fluid with a strain rate of $1.5 \times 10^{-5} \text{ s}^{-1}$ [Experiment No.: (a) 34, (b) 35] 191
- Figure 8.11:** Plot of stress-strain curves during the triaxial deformation of Clashach sandstone up to temperatures of 125°C. All experiments had $P_c = 40$ MPa, $P_p = 20$ MPa and strain rate of $1.5 \times 10^{-5} \text{ s}^{-1}$. [Experiment No.: 33, 35, 37, 38, 40] 192
- Figure 8.12:** Plot of change in pore volume during the triaxial deformation of Clashach sandstone up to temperatures of 125°C. All experiments had $P_c = 40$ MPa, $P_p = 20$ MPa and strain rate of $1.5 \times 10^{-5} \text{ s}^{-1}$. [Experiment No.: 33, 35, 37, 38, 40] 193
- Figure 8.13:** Time required to achieve steady stress frictional sliding after dynamic failure of Clashach sandstone at various rock temperatures using the triaxial deformation cell. $P_c = 40$ MPa, $P_p = 20$ MPa with a strain rate of $1.5 \times 10^{-5} \text{ s}^{-1}$. The broken line represents the least squared fit. Each point is given to an accuracy of $\pm 0.01\%$. [Experiment No.: 33, 35, 37, 38, 40] 194
- Figure 8.14:** The electrical potential signal produced during the deformation of drained Clashach sandstone at temperatures of (a) 25°C, (b) 50°C, (c) 75°C, (d) 100°C, (e) 125°C; $P_c = 40$ MPa, $P_p = 20$ MPa with deionised water as the pore fluid and a strain rate of $1.5 \times 10^{-5} \text{ s}^{-1}$. [Experiment No.: (a) 33, (b) 35, (c) 37, (d) 38, (e) 40] 195
- Figure 8.15:** The effect of temperature on the average electrical potential signal before deformation begins occurs on Clashach sandstone with a linear coefficient of 0.96. The accuracy of each point is shown by error bars. [Experiment No.: 33, 35, 37, 38, 40] 196

- Figure 8.16:** The electrical potential signal produced during strain softening and shear failure of Clashach sandstone at temperatures of (a) 75°C, (b) 100°C and (c) 125°C; $P_c = 40$ MPa, $P_p = 20$ MPa with a strain rate of $1.5 \times 10^{-5} \text{ s}^{-1}$. [Experiment No.: (a) 27, (b) 28, (c) 40] 196
- Figure 8.17:** Variation of electrical potential (a) prior to failure and (b) during dynamic failure as a function of temperature of Clashach sandstone. $P_c = 40$ MPa, $P_p = 20$ MPa with a strain rate of $1.5 \times 10^{-5} \text{ s}^{-1}$. The broken lines show there is no clear relationship between electrical potential and temperature with each point given to an accuracy of ± 0.1 mV. [Experiment No.: 33, 35, 37, 38, 40] 197
- Figure 8.18:** Streaming potential for Clashach sandstone at 125°C before fracture. $P_c = 40$ MPa with a 20 MPa applied pore pressure gradient across the sample on top of a background 5 MPa pore pressure with the change in fluid volume indicating a constant flow rate. [Experiment No.: 40] 198
- Figure 8.19:** Plot of the average streaming potential generated by an applied pore fluid pressure gradient through Clashach sandstone up to 125°C (a) prior and (b) after brittle deformation failure; $P_c = 40$ MPa with the streaming potentials being the average of all four electrodes. The broken lines represent the least squared fit. Each point is given to an accuracy of ± 3 mV. [Experiment No.: 33, 35, 37, 38, 40] 199
- Figure 8.20:** Plot of fluid flow generated through applied pore pressure gradient through Clashach sandstone up to 125°C (a) prior and (b) after brittle deformation failure; $P_c = 40$ MPa with the streaming potentials being the average of all four electrodes. The broken lines represent the least squared fit. Each point is given to an accuracy of $\pm 0.01 \text{ cm}^3/\text{sec}$. [Experiment No.: 33, 35, 37, 38, 40]] 200
- Figure 8.21:** Plots of (a) streaming potential and (b) fluid flow rates and how they change through successive heating and cooling cycles of pre-fractured Clashach sandstone up to a temperature of 125°C; $P_c = 40$ MPa, $P_p = 20$ MPa. The broken lines represent the least squared fit. Each point is given to an accuracy of (a) ± 0.1 mV and (b) $\pm 0.01 \text{ cm}^3/\text{sec}$ [Experiment No.: 40] 201
- Figure 8.22:** Plot of a stress-strain diagram during the deformation of Clashach sandstone using SFW#1 and SFW#2 as the pore fluids at temperatures up to 75°C. All experiments had $P_c = 40$ MPa, $P_p = 20$ MPa and a strain rate of $1.5 \times 10^{-5} \text{ s}^{-1}$. [Experiment No.: 45, 46, 47, 49, 50, 51] 203
- Figure 8.23:** Plot of change in pore volume during the deformation of Clashach sandstone using SFW#1 and SFW#2 as the pore fluids at temperatures up to 75°C. All experiments had $P_c = 40$ MPa, $P_p = 20$ MPa and a strain rate of $1.5 \times 10^{-5} \text{ s}^{-1}$. [Experiment No.: 45, 46, 47, 49, 50, 51] 204
- Figure 8.24:** Typical electrical potential difference recorded during the brittle deformation of Clashach sandstone at 50°C using SFW#2 as the pore fluid; $P_c = 40$ MPa, $P_p = 20$ MPa with a strain rate of $1.5 \times 10^{-5} \text{ s}^{-1}$. [Experiment No: 50] 205
- Figure 8.25:** The electrical potential signals produced during strain softening and shear failure of Clashach sandstone at temperatures of (a) 25°C, (b) 75°C and (c) 100°C with SFW#1 as the pore fluid. $P_c = 40$ MPa, $P_p = 20$ MPa with a strain rate of $1.5 \times 10^{-5} \text{ s}^{-1}$. [Experiment No.: (a) 47, (b) 45, (c) 46] 206
- Figure 8.26:** Co-seismic signal variation of Clashach sandstone as a function of temperature using (a) SFW#1 and (b) SFW#2 as the pore fluids. $P_c = 40$ MPa, $P_p = 20$ MPa with strain rate $1.5 \times 10^{-5} \text{ s}^{-1}$. The broken lines represent the least squared fit. Each point is given to an accuracy of ± 0.1 mV. [Experiment No.: 45, 46, 47, 49, 50, 51] 208
- Figure 8.27:** Plot of streaming potential against time at (a) 25°C, (b) 50°C and (c) 75°C using SFW#2 as pore fluid; $P_c = 40$ MPa with applied pore pressure gradient of 15 MPa. [Experiment No.: (a) 49, (b) 50, (c) 51] 209

- Figure 8.28:** Streaming potential measurements generated under increasing pore pressure gradients across a Clashach sample (a) before fracture and (b) after fracture. SFW#2 is used as the pore fluid, $P_c = 40$ MPa, $P_p = 20$ MPa. The broken lines show no link between streaming potential and pore pressure gradients at different temperatures. Each point is given to an accuracy of ± 3 mV. [Experiment No.: 49, 50, 51] 210
- Figure 8.29:** Plot of streaming potential against time with SFW#2 as pore fluid with (a) 7 MPa applied pore pressure gradient and (b) -7 MPa applied pore pressure gradient: $P_c = 40$ MPa. $T = 75^\circ\text{C}$ [Experiment No.: 49] 211
- Figure 9.1:** Reproduction of Figure 7.7b showing the electrical potential change, pore fluid pressure and differential stress with cartoons of micromechanics during deformation of Clashach sandstone ($P_c = 40$ MPa, initial $P_p = 15$ MPa). [Experiment No.: 43] 215
- Figure 9.2:** Reproduction of Figure 7.7a showing the electrical potential change, pore fluid volume and differential stress with cartoons of micromechanics during deformation of Bentheim sandstone ($P_c = 40$ MPa, $P_p = 20$ MPa). [Experiment No.: 26] 217
- Figure 9.3:** Schematic diagram showing (a) the distribution of the electrical streaming potential signal with fluid flow and (b) the movement of fluid into the fault region at failure. 218
- Figure 9.4:** Photomicrographs of Clashach sandstone in cross-polarised light after deformation failure showing the presence of grain cracking. [Experiment No.: 14] 218
- Figure 9.5:** Replot of Figure 7.14 showing (a) the deformation of Clashach sandstone showing the effect of a crack fault passing through an electrode and (b) photograph and schematic diagram of the deformed sample showing the position of cracks and fault. $P_c = 20$ MPa and strain rate $1.5 \times 10^{-4} \text{ s}^{-1}$. [Experiment No.: 21] 220
- Figure 9.6:** A schematic diagram illustrating changes in the electrical parameter in relation to strain rate, tectonic stress, seismic activity, permeability, the seismic b-value and electrical potential during earthquake faulting. 221
- Figure 9.7:** The porosity change of Bentheim, Clashach and Darley Dale sandstone and Portland limestone during deformation with an effective pressure of 20 MPa and a strain rate of $1.5 \times 10^{-5} \text{ s}^{-1}$. [Experiment No.: 13, 19, 26, 30] 223
- Figure 9.8:** The elastic modulus of Clashach, Bentheim and Darley Dale sandstone and Portland limestone from experiments at strain rates ranging from $1.5 \times 10^{-4} \text{ s}^{-1}$ to $1.5 \times 10^{-7} \text{ s}^{-1}$. All values given to an accuracy of ± 0.1 GPa with no apparent link between elastic modulus and strain rate [Experiment No.: 21, 22, 23, 25, 26, 27, 29, 30, 31, 32, 33] 225
- Figure 9.9:** Plot of streaming potential and permeability variation during a deformation cycle of Portland Limestone. The stress-strain curve, involving compaction, dilatancy, fracture and stable sliding indicate deformation. A strain rate of $1 \times 10^{-5} \text{ s}^{-1}$ was used and an effective pressure of 20 MPa with deionised water was maintained. Each point is given to an accuracy of ± 0.5 mD for permeability and 0.1 mV for streaming potential measurements. [Experiment No.: 24] 226
- Figure 9.10:** Comparison of streaming potentials measured from sandstones and limestone with values from the literature. Sources of data are given in the legend. 227
- Figure 9.11:** Evolution of electrical and hydraulic flow paths of impure sandstone during (a) compaction, (b) onset of dilatancy, dominated by intergranular cracking and grain rotation (c) between peak stress and immediately after dynamic fracture, dominated by intragranular cracking and (d) during stable sliding on macroscopic fault plane (Modified from Clint (1999)). 232
- Figure 9.12:** Applying a temperature of 160°C to a Clashach sandstone sample and the corresponding effect on the differential stress, confining pressure and electrical potential signals. [Experiment No.: 40] 234

- Figure 9.13:** The effect of temperature on the (a) water permittivity, (b) water conductivity and (c) electrical relaxation constant. Data on permittivity from Hill (1969) and data on water conductivity from Reppert and Morgan (2003b). 235
- Figure 9.14:** Temperature dependence of the streaming potential coupling coefficient ranging between electrolyte conductivity dominant (fluid) and surface conductivity dominant (Taken from Revil et al. (1999a)). 238
- Figure 9.15:** (a) Variation of the zeta-potential of (a) orthoclase, albite and granite as a function of pH in aqueous solution of 10^{-3} N KNO_3 with Q_z representing the data for the quartz and (b) orthoclase as a function of pH. Temperature is set at 45°C with aqueous solutions of 10^{-3} and 10^{-1} N KNO_3 . (After Ishido and Mizutani (1981)) 239
- Figure 9.16:** Variation of the streaming potential coupling coefficient for quartz as a function of temperature in an aqueous solution of 10^{-3} N KNO_3 . The initial value at a temperature is shown by solid circles, and the final value is shown by open circles. The numbers attached to the data points indicate the elapsed time from the beginning of the experiment to each measurement. (After Ishido and Mizutani (1981)) 240
- Figure 9.17:** Schematic plots showing how the increase in pore fluid salinity causes a decrease in pre-seismic and co-seismic signals in relation to elevated temperatures. 242
- Figure 9.18:** Plot of streaming potential against time at (a) 25°C , (b) 50°C and (c) 75°C using SFW#2 as pore fluid; $P_c = 40$ MPa with applied pore pressure gradient of 15 MPa. [Experiment No.: (a) 49, (b) 50, (c) 51] 243
- Figure 9.19:** Streaming potential measurements generates under increasing pore pressure gradients across a Clashach sample before fracture. SFW#2 is used as the pore fluid, $P_c = 20$ MPa. The broken lines show no link between streaming potential and pore pressure gradients at different temperatures. Each point is given to an accuracy of ± 3 mV. [Experiment No.: 49, 50, 51] 244
- Figure 9.20:** The variation of (a) the Mean Crack Length and (b) electrical potential change during the deformation of Clashach; effective pressure of 20 MPa with strain rate of 1.5×10^{-4} s^{-1} . Each point plotted is given to an accuracy of (a) ± 0.01 and (b) ± 0.2 mV. [Experiment No.: 21] 245
- Figure 9.21:** The variation of the self-potential signal across an active geothermal area with regions of upflow and downflow. 247

List of Tables

Table 2.1: The effect of various environmental variables on silica dissolution rate (from Ojala et al.(2003)).	60
Table 3.1: Effect of temperature, valence of the species and concentration of the fluid on the Debye length given in meters.	77
Table 4.1: Physical properties of 100cS silicone oil at room temperature and pressure.	95
Table 5.1: Some properties of BXX-13B-50-4K heating elements from ARi Industries.	104
Table 5.2: Properties of the Alumina spacers and discs used in the furnace assembly.	109
Table 5.3: Results of air aged rubber at 320°C.	111
Table 5.4: Properties of Lithium Niobate transducers purchased from Almaz Optics, Inc, USA.	111
Table 5.5: Physical properties of high temperature silicone oil.	112
Table 5.6: Properties of FV520B steel used in the construction of the ram.	115
Table 5.7: Properties of ULTEM cone.	117
Table 6.1: Summary of rock properties of different rock types.	119
Table 6.2: Properties of fluoroelastomer nitrile jackets.	127
Table 6.3: Showing possible errors in the variables within an individual experiment.	138
Table 7.1: Effect of strain rate on the peak stress and frictional sliding stress of Clashach sandstone, Darley Dale sandstone and Portland limestone; $P_c = 40$ MPa, $P_p = 20$ MPa. The values given are accurate to within ± 0.5 MPa.	161
Table 7.2: Pre and Co-seismic electrical potential signals measured from each electrode during triaxial deformation of Clashach sandstone and Portland limestone at a range of strain rates under drained conditions. Each point is given to an accuracy of 0.1 mV.	169
Table 8.1: Streaming potential of Portland limestone at various temperatures before deformation together with the corresponding fluid flow rate. The applied pore pressure gradient was 10 MPa on top of a 5 MPa background pore pressure. Each value is given to an accuracy of ± 0.1 mV for the electrical potential and ± 0.02 cm ³ /sec for flow rate measurements.	187
Table 8.2: Effect of deformation on the streaming potential of Portland limestone at various applied pore pressure differences. Dipole 1 equals electrode 3 minus 1, dipole 2 is electrode 4 minus 2. Each value is given to an accuracy of ± 0.2 mV.	188
Table 8.3: The effect of temperature on the peak stresses and frictional sliding stresses of Clashach sandstone during triaxial deformation at a constant strain rate of 1.5×10^{-5} s ⁻¹ . Each point is given to an accuracy of ± 1 MPa.	192
Table 8.4: Change in pore volume during the compaction and dilatancy stage of triaxial deformation of drained Clashach sandstone at temperatures up to 125°C. (Values given are absolute, so they do not reflect the direction of fluid loss and are given to an accuracy of ± 0.01 cm ³).	193
Table 8.5: Composition of simulated formation waters SFW #1 & SFW #2 in the form of anions and cations present. Values are given in ppm.	202
Table 8.6: Pre-seismic and co-seismic electrical potential signals measured at each electrode during triaxial deformation of Clashach sandstone at various temperatures using SFW#1 and SFW#2. (Values given to an accuracy of ± 0.1 mV)	207

List of Tables

Table 9.1: Variation of electrical potential pre-seismic and co-seismic of different rocks under dry and saturated conditions. Values given to an accuracy of ± 0.1 mV.	224
Table 9.2: Variation of absolute change in electrical potential signals during compaction and dilatancy stages of deformation at different strain rates for sandstone and limestone samples. The values given to an accuracy of ± 0.2 mV.	226
Table 9.3: Maximum pore pressure gradients used to generate streaming potential signals during previous studies.	228
Table 9.4: The average value of the electrical potential signal prior to deformation of Clashach sandstone between a temperature of 25°C and 125°C under an effective pressure of 20 MPa. Calculated from Figure 8.15. Each value is given to an accuracy of ± 0.1 mV.	236
Table 9.5: Ionic radii of most common species present in SFW's.	242

Acknowledgements

As a member of the Mineral, Ice and Rock Physics Laboratory at University College London, I would like to mention and thank the following people. I give very special thanks to my parents through their endless and unwavering support they provided me and giving me the best opportunities possible. I'd like to express my appreciation and gratitude to my three supervisors. Firstly to my supervisor Prof Peter Sammonds for providing funds for conferences and building equipment and giving me a good kick when needed. Secondly, to Prof Philip Meredith, for endless enthusiasm and advice on every aspect of my work. Thirdly, to Dr Anita Odedra for reading considerable amounts of my research and providing valuable feedback and encouragement throughout.

With the nature of this project, a large amount of design and building was required to complete it. This was only made possible by the patience, hard work and dedication of the senior experimental officers Neil Hughes, John Bowles, Steve Boon and Eddie Benbow. Without the numerous hours they spent with me in the laboratory getting me through demanding times, I would never have completed my work. Special thanks goes to John Bowles for his constant help designing the electric furnace, with good suggestions at every stage, he made this part of my project considerably easier than I believed possible. Also to Neil Hughes who taught me how to use the equipment and helped repair and redesign pieces when they were damaged. And to Eddie Benbow, who built the furnace and made the high temperature experiments possible. I'd also like to thank everybody for making me feel part of the MIRP group and providing me with many memorable moments, inside and outside of working hours.

I would also like to thank Oswald Clint, Melody Tribbeck, Dan Hatton, Dimitri Grigoriev and Rosanna Smith for their thoughts and ideas. To other technical staff, Richard Rabe, Danny Howard and Sean Houlding for their help setting up all the computer equipment, scanning electron microscope instructions and the preparation of thin sections. Thanks also goes to Maria Alfredson for her help in trying to do the computer modelling. For their advice and friendship, I would like to thank Judith Woo, Sudeep Kangungo, Heather Cheshire, Rupert Green, Ian Bailey, Philip Benson, Lena Taylor, Sinead Farrell, Paul Taylor, Sarah White, Ed Townend, Sev Kender and Simon Hunt.

I acknowledge the support given by the National Environmental Research Council through the award of an Industrial CASE studentship. To BG Group, who provided the majority of my laboratory expenses and provided useful industry contacts to aid my research. Also to the UCL Graduate School for providing funds so I could attend conferences and build additional equipment, and the UCL disability unit who helped me purchase a computer and a special needs chair.

Dedicated to my parents

The Truth Will Set You Free.

1 Introduction

1.1. INTRODUCTION

Self-potential anomalies measured geophysically in the field include electric and magnetic telluric signals. These signals can be produced from numerous sources including earthquakes (Varotsos and Alexopoulos 1984a, 1984b, Park et al. 1993), volcanoes (Antraygues and Aubert 1993, Michel and Zlotnicki 1998) and aquifers. Of these different sources, earthquakes are of particular importance due to their destructive force. Debate exists, however, about the exact cause and magnitude of the potential anomalies because knowledge of the earthquake mechanism is incomplete (Geller 1996, Kagan 1997) making hypothesis and modelling difficult without sufficient earthquakes to compare with.

Earthquake prediction can be categorised into two areas, consisting of electrical signals (e.g. self-potential) and seismic activity (e.g. acoustic emissions). For the former, Varotsos and Alexopoulos (1984a, 1984b) claimed to have predicted earthquakes in Greece using 'seismo electrical signals' (SES) and named it the VAN (Varotsos, Alexopoulos and Nomicos) method. However, Kagan and Jackson (1996) note that these predictions are not statistically significant with no prediction of the magnitude or location above those of the null hypothesis. Matsumara (1993) makes the point that this and other models use parameters, post event, which are identified from seismic activity and that using these statistical tests to identify events prior to occurrence makes correlation with subsequent seismicity impossible (Kagan 1997). A severe shortcoming of the VAN method of earthquake prediction is in providing the correct order of magnitude of the earthquake from electric potential signals measured hundreds of kilometres away from the source. This is because the VAN method needs to assume energy conservation and highly conductive layers for the signals to travel such large distances. Also, local signals can easily be misinterpreted as distant sources making the prediction of earthquakes less plausible (Gruszow et al. 1996). With the signals travelling such large distances, it would be difficult to relate the signal directly to an earthquake because other sources, such as aquifers and industrial noise, may be present. With seismic activity as a precursory tool, the precursors are assumed to follow the Gutenberg-Richter relationship with a lower limit of activity related to earthquake magnitude. Under certain conditions, the time and magnitude can be predicted (Shaw et al. 1992), but difficulty exists relating it to a single fault in a fault rich area where seismic activity may be coming from more than one fault. Geller (1996) and Kagan (1997) investigated the predictability of earthquakes, and question if prediction is even possible due to the non-linear dynamics of an earthquake. This makes laboratory experiments important in investigating all possible environmental conditions imposed on crustal rocks so that the data can be modelled and applied to geological situations.

Several mechanisms have been put forward to explain the SES d.c signal observed in the field by authors including Blanpied et al. (1992), Bernard (1992), Fenoglio et al. (1995), Pham et al. (1998) and Fedrov et al. (2001). The most plausible mechanism to explain the electric and magnetic anomalies is the electrokinetic phenomena. Laboratory studies have shown the existence of electrical potential signals under simulated conditions, which depend upon permeability, pressure, pore fluid concentration and porosity (Jouniaux and Pozzi 1995a, Jouniaux and Pozzi 1995b, Lorne et al. 1999a, Lorne et al. 1999b, Revil et al. 1999a, Jouniaux 2000, Eccles et al. 2004). When piezoelectric crystals, such as quartz are

present, an additional signal is recorded due to the piezoelectric effect (Cress et al. 1987). This is explained by the quartz crystal becoming electrically polarized in relation to the applied stress (Yoshida et al. 1994, 1997), which can produce an electromagnetic emission from a crack tip (Yamada et al. 1989).

In a tectonically active region, electrical potential signals have been recorded on the crustal surface. However, since these rocks are heterogeneous and the faults are often non-planar, interpretation of these signals can be highly complex. These factors alter both the fluid and electrical flow within the rock (Brown 1989, David 1993). As faults are in a constant state of charge, the stress imposed on the rock varies regionally. This changes the void aperture, permeability and tortuosity which in turn alters the electrical potentials. Therefore, a thorough understanding is required during all aspects of rock deformation in order to relate the effect of these different variables on the signals generated.

Understanding the relationship between earthquakes and electrical signals is difficult because the start of an earthquake is not easily identifiable. Laboratory experiments have shown that deformation can be divided into compaction, dilatancy and failure phases, and this is also believed to be true for earthquakes. During these phases, the permeability of the rock changes (Zhu and Wong 1996, Keaney 1998), as well as the electrical potential signals (Jouniaux and Pozzi 1995a, Lorne et al. 1999a). Deformation also generates seismic activity. This has been extensively studied in the laboratory (Lockner et al. 1991, Main et al. 1993, Cox and Meredith 1993, Read et al. 1995) and related to the earthquake magnitude (Sammonds et al. 1992). However, Clint (1999) was the first author to extensively examine the link between electric and seismic activity, concentrating mainly on Darley Dale sandstone. These experiments were conducted at room temperature, which is unrealistic when considering that a temperature increase of 30°C/km exists (Fowler 2001).

Temperature and pore fluids vary in the crustal region. The effect of temperature on mechanical and chemical processes has been previously investigated. Seipold (1998) notes that temperature affects transport properties both directly and indirectly, directly by the temperature dependence of the heat transfer mechanism or indirectly by temperature-induced physical and chemical changes in the rock samples. At sufficiently high temperatures, the rock strength decreases (Jaeger and Cook 1979, Cook 1981, Fischer and Paterson 1989, Rocchi et al. 2004, Balme et al. 2004) as chemical processes such as stress corrosion are enhanced (Odedra 1998, Ojala 2003). Chemical reactions such as silica-water interaction (Rimstidt and Barnes 1980, Dove and Rimstidt 1994) have been shown to be temperature dependent. Changes in temperature have also been found to affect chemical reactions which alter the electrical conductivity (Shankland and Anders 1983). Other work on electrical potential signals at elevated temperatures has concentrated on static tests in which the crystal surface is allowed to reach equilibrium (Ishido and Mizutani 1981, Sprunt et al. 1994, Revil et al. 1999a). These show a direct dependence correction between zeta potential and temperature. However, very little work has been conducted on the effect of the mechanical and chemical changes due to temperature on the electrical potential signals generated during deformation. Therefore, the effect of temperature on both the chemical and mechanical processes of the rock during deformation requires investigation.

A major part of this project was to design and build an internal electric furnace capable of heating a rock sample to 320°C. A triaxial deformation cell was used in conjunction with the furnace to more accurately simulate shallow crustal conditions during brittle deformation. I specifically investigated the effect of thermal, chemical and mechanical processes on various rock types to identify the commonality between them. This involved investigating the effect of strain rate, pore fluid chemistry, temperature and composition on the electrical signals and acoustic emissions generated prior, during and after dynamic failure. This was achieved using a specially designed jacketing system allowing for 4 electrodes and 8 acoustic emission transducers. From this work, I hoped to answer the following questions: 1) Does temperature affect the electrical potential signal during any stage of the deformation process? 2) How does the electrical potential signal change during frictional sliding? 3) For brittle failure, how does the location of the fault influence the electrical potential signal? 4) What factors control and change the magnitude of the electrical signals observed?

1.1. THESIS DESCRIPTION

This thesis is divided into ten chapters, which include the description of previous work, present-day theories, equipment design, data collection techniques and the results with interpretation and conclusions.

Chapter 2 describes the present-day understanding of rock mechanics and physics. This includes the effect of various properties such as confining and pore pressures on the mechanical properties of rock. In Chapter 3, the main theories on the generation of electrical potentials are outlined, including the piezoelectric and electrokinetic phenomena.

In Chapter 4, a description of the experimental program and techniques is given. Chapter 5 includes calculations required to heat the rock to 320°C using an internal electric furnace. Following this the design and operation of the furnace is described. The description of modifications to the pore fluid separator follows, made so that brine fluids can be used as the pore fluid in the rock during deformation to simulate shallow crustal conditions and allow streaming potential signals to be measured. Chapter 6 contains rock descriptions, as well as the calibrations and procedures for all the equipment.

In Chapter 7, the experimental testing programme of various crustal rocks at room temperature is described. This includes the effect of composition and strain rate on brittle deformation as well as the effect of fluid flow on the electric signals, the electrical potential difference, electrical potential change and acoustic emissions. In Chapter 8, investigation of the temperature effect on the electrical potential during deformation is described, including the effect of rock composition and pore fluid salinity on the electrical signals generated.

The results from the experimental chapters are discussed in Chapter 9. This includes comparing the data with existing research and applying present-day theories to relate measured electrical potential signals to a wide range of geological conditions. Also discussed in this chapter is the application of the electrical potential techniques to earthquake and volcanic eruption prediction, shallow exploration and the scaling of laboratory results to crustal scales.

Chapter 1: Introduction

A summary of the appendices can be found at the back of this thesis. The appendices are on the accompanying CD, which includes furnace calibration, furnace stress analysis, AutoCAD drawings, operational procedure and experimental summary. The submitted paper, which is based on the work achieved in this thesis, is located with the CD.

2. *The Development of Rock Physics as an Exploratory Tool*

2.1 INTRODUCTION

Rock physics techniques are used to determine the deformation behaviour and physical properties of rocks under simulated in-situ environmental conditions. Rock physics methods are extremely useful for studying rock properties (stress-strain relationship) and for relating the laboratory results to geophysical conditions in the field including borehole physics (Stesky 1986), earthquake source physics (Byerlee and Brace 1968) and fault mechanics (Scholz et al. 1993).

Direct field measurements are very useful but because of the expense of drilling boreholes, the time required and often the limited range of data collected, useful data sets are hard to come by. Due to these problems, laboratory rock physics measurements taken using triaxial deformation testing are essential for an understanding of crustal processes. These controlled and readily repeatable laboratory tests allow the stress-strain conditions to be controlled and physical properties to be measured. The measurements include electrical conductivity and resistivity, pore fluid pressure, volume, and chemistry, permeability, , elastic wave velocities and the acoustic emissions produced during deformation.

Acoustic Emission techniques have been employed by a variety of individuals (Sammonds et al. 1992, Lockner 1993, Ayling et al. 1996, Baud and Meredith 1997) to study the damage occurring during different stages of deformation. During deformation, the Acoustic Emission activity changes according to the stage of deformation with a power-law increase during dilatancy. From this data, the statistical b-value (the slope of the log frequency versus magnitude plot) can be linked to the magnitude of an earthquake (Sammonds et al. 1992) with either a double or single minimum. Plotting the magnitude of acoustic emissions reveals a similar relationship to that found in seismological investigations, namely the decrease of frequency with increasing magnitude. The fractal dimension (D) can then be calculated (Main et al. 1989) from the b-value. Both P-wave and S-wave velocities can also be used (Sammonds et al. 1989, Ayling et al. 1996) to look at the distribution and orientation of the cracks induced by the applied stresses. Results by Sammonds et al. (1989) show that initial closure of pores changes both P and S-waves velocities and depending on the crack orientation, changes one more than the other. It is suggested that this could be an in situ monitor of differential stress (Zatsepin and Crampin 1997, Crampin and Zatsepin 1997). Pore volume changes (Read et al. 1995) measured during deformation show that pore volume decreases initially with loading by closing the pores parallel to loading through compaction and then increases during dilatancy as new micro-channels are formed (Baud and Meredith 1997). The pore volume and permeability are linked through the pore channel development as well as temperature (Darot et al. 1992, Keaney 1998) and show that the crack density increases with increasing permeability (Jones et al. 1997).

Both the fluid and electrical conductivity/resistivity rely on the rock microstructure for transport. Therefore they too are affected by the micro-channel changes during deformation showing complex changes in resistivity (Glover et al. 1996) related to induced damage. This is shown in Walsh and Brace (1984) with closing of the cracks reducing the cross-sectional area of the channels which in turn reduces the conductivity which follows a power-law curve. Jouniaux et al. (1992) found a decrease in resistivity

until fracture with a large change at failure due to coalescence and formation of a new fault plane. Various numerical models have been proposed (Bernabe and Bruderer, 1998) with the Kozeny-Carman model being applied both to permeability and electrical formation factor calculated from macroscopic measurements of porosity and surface area, though it has been proven not to fit all heterogeneous rocks.

This chapter is split into several sections. They are concerned with the conditions associated with particular environmental conditions, lithology and the effect that in-situ conditions have on electrical conductivity. This leads to particular applications such as earthquakes and the mechanics associated with rock deformation including stresses, failure criteria and failure modes which occur in the laboratory. Finally the effect of having water in the rock and how it affects the physical and chemical processes (with particular detail given to the quartz-water interaction) is discussed.

2.2 CRUSTAL CONDITIONS

The crustal surface consists of many different basin depositional environments which include deep water, shallow marine, delta and rift valleys among others. On average, continental crust is 35 km thick, but it may however reach 60 km in places of active tectonics. The crust is composed of a variety of rocks with an average density of 2.7 g/cm³. Oceanic crust is generally 5-7 km thick and is composed of mafic rocks, making it denser than the continental crust. The effect of depth on velocity is shown in Figure 2.1 where the increase in overburden pressure with depth causes the velocity to increase. The overburden pressure P_v is calculated by

$$P_v = \rho \cdot g \cdot z \quad (2.1)$$

where ρ is rock density (kg.m⁻³), g is gravitational acceleration (ms⁻²) and z is the depth (km). The geobaric gradient is 25 MPa/km in the upper crust with typical rock densities of 2.5 x 10³ Kg.m⁻³ (Fowler 2001).

The influence of temperature on the rock and pore fluids plays an important role in the rock mechanics and the processes leading to failure. Fourier's law states that for heat conduction in an isotropic medium, heat flow (q_i) is linearly proportional to temperature gradient ($\partial T / \partial x$)

$$q_i = -K \partial T / \partial x_i \quad (2.2)$$

where K is the thermal conductivity. However, within the shallow crust the conductivity properties of materials differ so that for continental and oceanic crust the heat transfer is different with the geothermal gradient varying greatly depending on the tectonic environment (Fowler 2001). Assuming an average thermal conductivity of 2.1 Wm⁻¹ °C⁻¹ for continental crustal rocks, then the geothermal gradient is approximately 30°C/km (Fowler 2001).

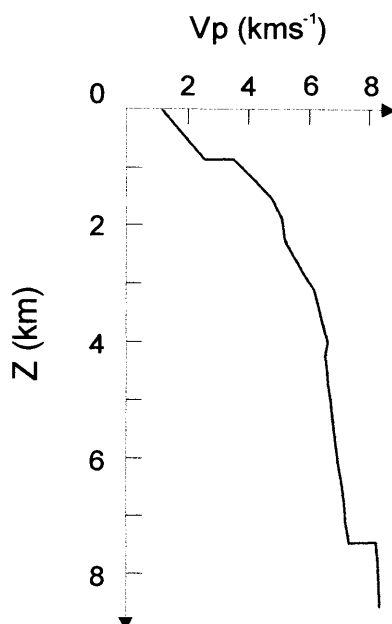


Fig 2.1: Variation of P-wave velocity (V_p) with crustal depth (z) (from Fowler (2001)).

Differential Stress and Pore Pressure

The mechanical behaviour and flow processes of continental rock depends critically on the depth-dependent physical/chemical environment. Within the physical environment, the different types of pressure which influence the rocks are the confining pressure, which is the pressure acting to compress the rock, and the pore pressure which is the pressure within the pore space which acts against the confining pressure. The pore space can be filled with gas and/or liquid. The different stress is discussed in section 2.4.1. The chemical environment includes factors such as pH and ionic species.

Maps of the stress fields generated from studies of borehole and earthquake focal mechanisms (Zoback 1989) show that the differential stresses in the crust can be very small compared to laboratory data. This can be explained by the presence of highly pressurised pore fluids which reduce the effective pressure acting on the medium as was first suggested by Rubey and Hubbert (1959). The amount of fluid depends on the tectonic setting and the depth, with the volume decreasing with depth (Nur and Walder 1990). Brace and Kohlstedt (1980) conclude that there is compelling evidence for pore and/or fracture interconnection to 5 km, good arguments for interconnection to a depth of 8km and a suggestion that transmissivity might be appreciable to approximately 20 km. Geophysical prospecting of boreholes by Nur and Walder (1990) in the Kola Peninsula sampled fluids at a depth of about 11 km.

With the average bulk density of water being above $1.3 \times 10^3 \text{ kg.m}^{-3}$, the pore pressure gradient is 10 MPa/km which is about 40% of the lithostatic pressure (25 MPa/km). In this instance the gradient is said to be hydrostatic (i.e. equal to the pressure of a column of water of height equal to the lithostatic column of rock). However in regions of tectonic activity, superhydrostatic pressure gradients are known to occur. These overpressurised compartments may be fault controlled by sealing faults or stratigraphically-controlled by impremeable rock layering (Nur and Walder 1990). This has been applied by Blanpied et al. (1992) to the San Andreas fault to explain the reduction in shear stress required for sliding by partially “floating” the rock.

Electrical Conductivity

The conductivity of the rock depends on various factors, including the mineral composition, pore water chemistry, effective stresses and fluid flow. Jouniaux and Pozzi (1996a) note that self potential (SP) anomalies are related to streaming potential due to the pressure gradient, thermoelectric potential due to the temperature gradient and chemical potential due to the chemical gradient. In the crust, electromagnetic field techniques are used to measure signals which range from 10^{-4} Sm^{-1} to 10^{-2} Sm^{-1} with laboratory values of 10^{-6} Sm^{-1} obtained by Brace (1971). A possible explanation of the difference between laboratory and field values is given by Shankland and Anders (1983) who suggest the mechanism in the crust is not the same as found in crack closure under drained conditions. In the crust the pathways are influenced by thermal cracking and stress concentrations, where upon new surfaces are formed with the conductivity of the rock and that of the fluids (Dey 1986) affecting the measurements. Another mechanism for the interaction of water is given by Olhoeft (1981) who suggests that volatiles released during outgassing of schists and granite, include water, which could contribute to high conductivities. Other interpretations to explain the high conductivity in the lower crust other than saline fluids include carbon enhanced conduction pathways created during compaction (Glover and Vine 1992). This has been confirmed by experiments on rock recovered from the KBT boreholes (Duba et al. 1994, Shankland et al. 1997). However, since the carbon (here graphite) would form equally on both sides of a fault, it does not explain the difference in signals recorded across the fault (Shankland and Anders 1983).

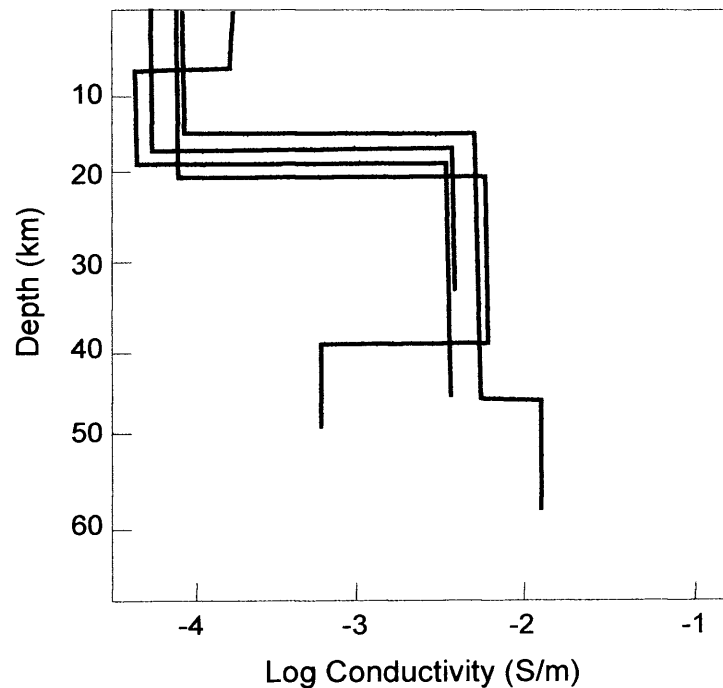


Figure 2.2: Variation of electrical conductivity with depth in the continental crust showing three distinct areas of electrical structure (from Shankland and Anders (1983)).

Strain Rate

A large variety of strain rates have been recorded in the crust. Carter and Tsenn (1987) have compiled data showing strain rates ranging from 10^{-12} to 10^{-17} s^{-1} for a variety of tectonic regimes with the actual rate of deformation depending on the rock type and the environmental conditions (Donath and Fruth 1971). As these strain rates are unrealistic for laboratory based studies (a test taken to 2% strain at

10^{-10} s^{-1} would last approximately 2 months) it is important to relate laboratory experiments to field measurements by scaling the results, assuming that the mechanism of the geological process is the same in both cases (Paterson 2000). Laboratory studies which are generally done at strain rates of 10^{-4} to 10^{-8} s^{-1} have shown that the strength of the rock depends on the loading rate (Paterson 1978, Costin 1987). The effect of strain-rate on the manifestation of electrical properties is investigated in this thesis.

2.3 DEFORMATION OF THE CRUST

2.3.1 Statistical Physics Approaches

Certain features within an earthquake, such as fault length, have been found to have scale invariant properties (Main et al. 1989, Scholz et al. 1993). This has important implications for scaling up from laboratory to field scales. Since fault growth is a self similar process, it follows that it should obey a fractal or a power-law distribution of crack length which is given by Mandelbrot (1982) as

$$N\langle L \rangle = cL^{-D} \quad (2.3)$$

where N is the number of faults/cracks with a discrete length interval $l - \delta l/2 \leq l < l + \delta l/2$ and C and D are constants with D being known as the fractal dimension (Mandelbrot 1982, Turcotte 1989). Mandelbrot (1982) notes that the natural system is fractal. However it has been stated that stress concentrations at the tip affect the surrounding rocks. This stress may be relieved by the fault motion, this complicates the behaviour of the system meaning a simple scaling relationship in the vicinity of the fault cannot always be applied.

The relationship between the number of cracks/faults of a particular size and the magnitude of the event is given by the Gutenberg-Richter relationship expressed in terms of an inverse cumulative frequency $N(M > m)$

$$\log_{10}(N(M > m)) = a - bm \quad (2.4)$$

where M is the earthquake magnitude, a and b are empirical constants and the magnitude range lies between $m - \delta m/2 \leq m < m + \delta m/2$ (Main 1990). Applying this equation to laboratory studies, Aki (1981) showed that the seismic b-value was related to the fractal dimension D by $D = 3b/c$ where c is the slope of the scaling relationship between magnitude m and common logarithm of the seismic moment. Laboratory evidence to support changes in magnitude with changes in fault length was obtained by Sondergeld et al. (1984) who attributed changes in frequency content to a change in the microstructure, with the development of larger cracks after dilatancy giving increasingly low-frequency Acoustic Emission signals (low b-value).

From the results gathered here, theoretical models have been constructed with stress intensity factor, stress, crack length and b-value (Main 1990). Agreement between the different models was investigated using the b-value calculated from laboratory experiments (Sammonds et al. 1992).

The power-law fault model developed by Cowie and Scholz (1992a) is based on an analytical model solution of a homogeneous rock in a tectonic environment with inelastic deformation at the fault tip. Scholz et al (1993) and Schlische et al (1996) found that the amount of displacement depends upon the relative position in the fault zone having a constant value around the central fault region and with values tailing off toward the fault tips. Therefore this needs to be included in the scaling models. However, Cowie and Scholz (1992) note that in all the models, different lithologies and tectonic environments need a different law with no single power distribution fitting all situations, as found by Hatton et al. (1994). A further observation which found that faulting is a scale-invariant process was by Abercrombie (1995) (Figure 2.3) who looked at the relationship between the dimension and seismic moment with a linear fit power-law for a given stress drop. In Figure 2.3, it can be seen that the seismic moments are related to the source dimensions, but the seismic moments can vary substantially making it difficult to model

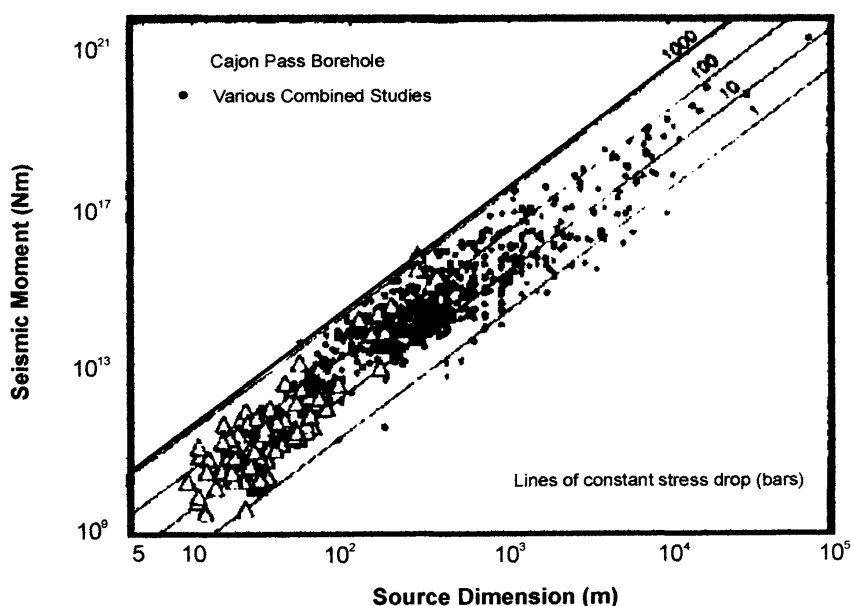


Figure 2.3: Seismic moment data from boreholes and earthquakes plotted as a function of the source dimension on a log-log plot. The straight lines represent the scaling laws at different stress drops (in bars) from the dislocation model of the seismic source (from Abercrombie (1995)).

2.4 THE MECHANICS OF BRITTLE FAILURE

2.4.1 Isotropic, Deviatoric and Principal Stresses

Stresses can be categorised into body forces, caused by acceleration due to gravity and surface forces that act on a particular surface. For surface forces, the stress is related to the ratio of force applied (ΔF) over a given surface area (ΔA). These forces applied at different directions relative to the plane produce both normal and shear stresses as shown in Figure 2.4.

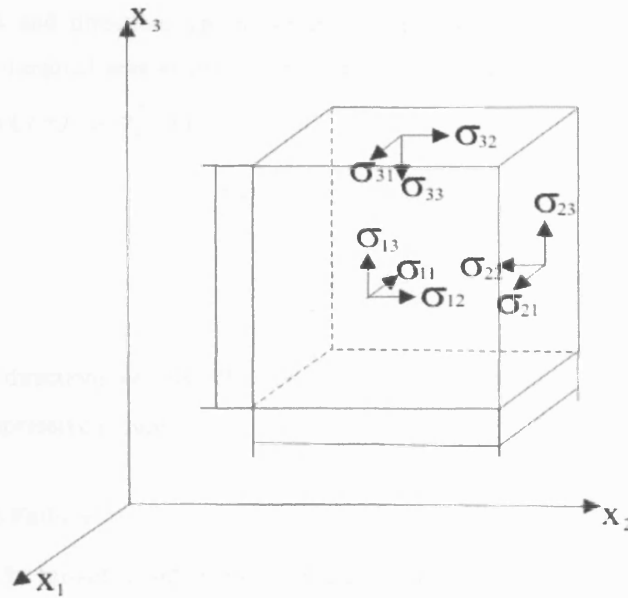


Figure 2.4: Schematic diagram showing the nine stress components required to describe the stress at any point.

Stress is defined by a second-order, symmetric tensor, and is described by the nine stress components shown above (Figure 2.4) in the 3 principal directions X_1 , X_2 and X_3

$$\sigma_{ij} = \begin{pmatrix} \sigma_{11} & \sigma_{12} & \sigma_{13} \\ \sigma_{21} & \sigma_{22} & \sigma_{23} \\ \sigma_{31} & \sigma_{32} & \sigma_{33} \end{pmatrix} \quad (2.5)$$

The stress tensors can be split into (Ranalli 1995) an isotropic stress tensor and a deviatoric stress tensor. The isotropic stress is defined as

$$\sigma_{ij}^0 = (1/3)\sigma_{kk}\delta_{ij} \quad (\delta_{ij} = 1 \text{ for } i = j, \delta_{ij} = 0 \text{ for } i \neq j) \quad (2.6)$$

where σ_{kk} = sum of the on-diagonal components of the stress tensor and δ_{ij} = Kronecker delta, or identity matrix. The deviatoric stress is defined by

$$\sigma'_{ij} = \sigma_{ij} - \sigma_{ij}^0 \quad (2.7)$$

where the deviatoric components are non-zero. The two equations above can be combined to sum up the isotropic and deviatoric parts in the form of

$$\sigma_{ij} = \sigma_0\delta_{ij} + \sigma'_{ij} \quad (2.8)$$

where $(1/3)\sigma_{kk} = \sigma_0$ for the mean normal stress.

The principal stresses and directions are important in structural geology problems. In terms of the principal tensors, the diagonal tensors are the only non-zero components when i is not equal to j the principal tensor is zero ($i \neq j \Rightarrow \sigma_{ij}^0 = 0$).

$$\sigma_{ij}^P = \begin{pmatrix} \sigma_{11}^P & 0 & 0 \\ 0 & \sigma_{22}^P & 0 \\ 0 & 0 & \sigma_{33}^P \end{pmatrix} \quad (2.9)$$

The principal stress directions are usually denoted by σ_1 , σ_2 and σ_3 , by convention in geology $\sigma_1 \geq \sigma_2 \geq \sigma_3$, with compressive failure.

2.4.2 Compressive Failure

Rock deformation can be broadly subdivided into macroscopically brittle (faulting and frictional sliding), macroscopically ductile flow (cataclastic flow through distributed stable micro-fracturing such as grains) and fully plastic deformation where dislocation creep and other crystal plastic mechanisms dominate. Transition between these modes depends upon the pressure, strain rate and temperature (depth).

Conventionally, triaxial testing is achieved with axial compression superimposed on a hydrostatic pressure so that $\sigma_1 > \sigma_2 = \sigma_3$ (Figure 2.5). Macroscopic brittle failure generally occurs on a plane lying at an angle to σ_1 . In *true* triaxial testing all the stresses are different and non-zero.

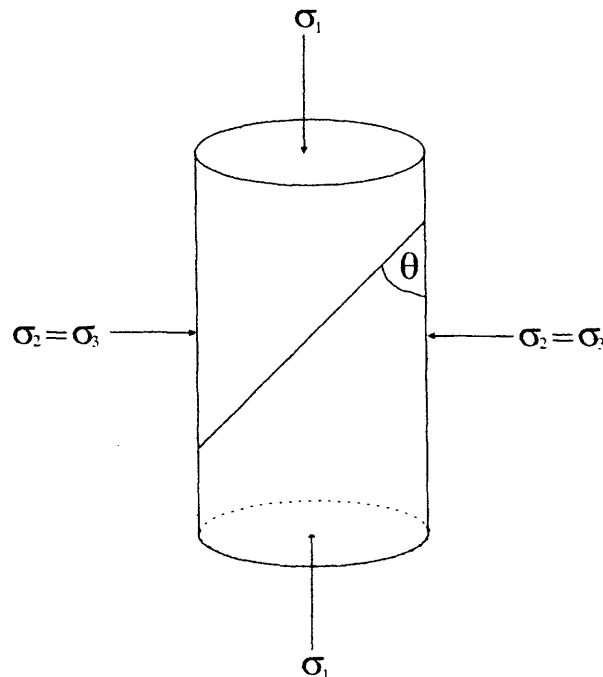


Figure 2.5: Principle of a triaxial test.

2.4.3 Brittle Failure

In order to describe the brittle strength of rock, a failure criterion must be developed. Mohr's criterion states that fracture occurs across a plane when the stress applied to the surface reaches a critical value which depends on the material properties and the orientation of the plane relative to the stress. This is explained by the Griffith crack theory but empirically can be expressed as

$$|\tau| = f(\sigma). \quad (2.10)$$

The Mohr's failure envelope is found empirically to be approximately linear (Figure 2.6), and consequently the equation is written explicitly as

$$|\tau| = S + \mu'\sigma \quad (2.11)$$

where S and μ' are material termed cohesive strength and internal friction, respectively. This is referred to as the Coulomb-failure criterion for the development of new cracks.

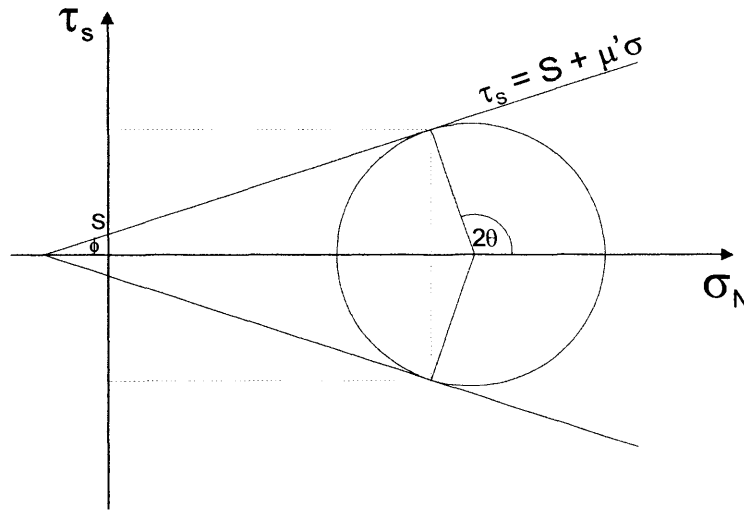


Figure 2.6: Mohr circle and the Coulomb criterion for shear fracture.

The frictional law $\tau = -\mu'\sigma$ (μ' is the coefficient of friction) may also be expressed in terms of the principal stresses. This is achieved by specifying the normal and shear stresses on an arbitrarily orientated in terms of the principal stresses,

$$\sigma_N = \frac{1}{2}(\sigma_1 + \sigma_3) + \frac{1}{2}(\sigma_1 - \sigma_3)\cos 2\theta \quad (2.12)$$

$$\tau_s = -\frac{1}{2}(\sigma_1 - \sigma_3)\sin 2\theta \quad (2.13)$$

where σ_N is the normal stress, τ_s the shear stress with σ_1 and σ_3 the maximum and minimum principal stresses respectively, and θ the angle between σ_1 and the plane.

Mohr-Coulomb diagram

To show the general trend which applies to the majority of rocks, the interaction of friction and the Mohr-circles is shown in Figure 2.7.

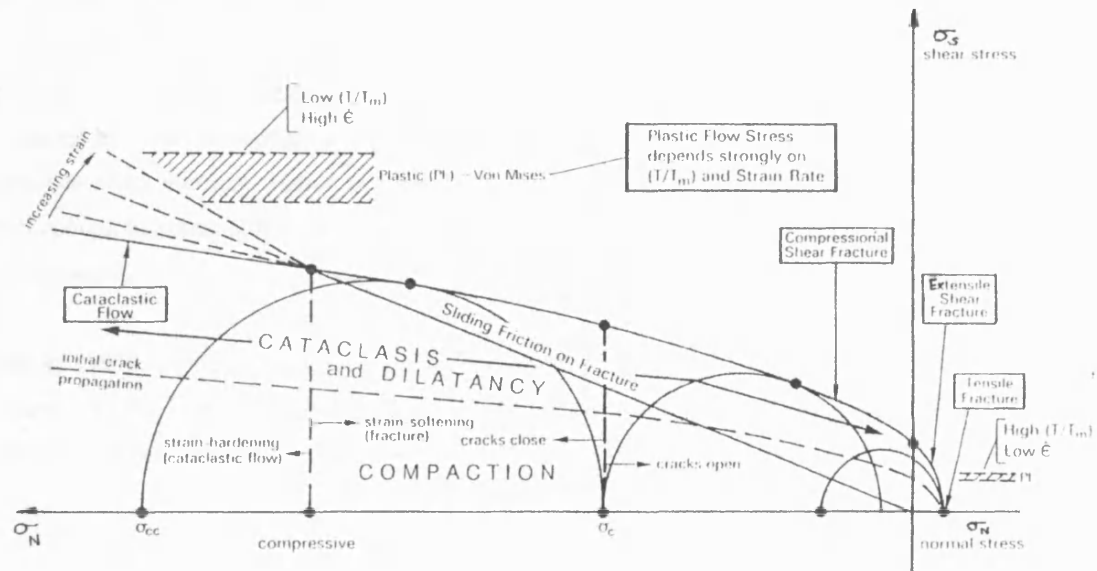


Figure 2.7: Mohr-Coulomb failure diagram showing the different types of failure and the brittle-ductile transition (from Murrell, 1965).

Failure can be described by two different failure criterion consisting of brittle failure and cataclastic flow failure. The first form of brittle deformation is tensile fractures which occur along a plane normal to σ_3 , when σ_3 is tensile and exceeds some critical value (σ_T). Under such conditions the material fails catastrophically in a brittle manner by axial splitting. With a slight increase in normal stress so that σ_3 is zero, shear fracture occurs with some strength in the form of cohesion between individual grains. At intermediate confining stresses the material has a higher strength and fails in a semi-brittle manner by localization of deformation on a shear fault which is known as compressive shear fracture. Compressive failure occurs initially by cracks opening at low stresses. As the stress continues to increase the crack opening is replaced with crack closure and then strain softening which leads to macroscopic failure and a stress drop to steady frictional sliding at some stress which provides a measure of the strength between two surfaces. This frictional strength linearly with confining pressure. The stress drop at failure initially increases at very low confining stresses and then decreases to zero at the transition from localised faulting (brittle) to cataclastic flow

The cataclastic flow represents the second type of failure and occurs at very high confining stresses where the material is even stronger and fails in a pseudo-ductile manner. The term “ductility” is used here to denote the capacity for substantial change of shape without gross fracturing. This is a macroscopic definition and takes no account of the microscopic mechanisms whereby the deformation occurs.

The brittle-ductile transition occurs at the cross-over in the trends of the two types of failure with increasing pressure. Byerlee describes the transition as occurring when the stress required to form a fault surface is equal to the stress required to cause sliding on the fault.

Friction

Due to the complex interactions of two surfaces in contact, which constantly evolve with displacement, no complete description of friction exists that is based on the micromechanical processes. Instead *phenomenological* descriptions of friction behaviour are used which describe the phenomenon of friction, not the processes responsible for the observed behaviour. Friction is controlled by the surface roughness, hardness, temperature, ductility, pore fluid, wear and shear strength of the material with fault gouge produced by wear through shearing of asperities and fracturing of surrounding material. Some of these variables affect the rock friction in such a sensitive way that it is often difficult to duplicate conditions well enough to obtain sufficiently reproducible results to recognise an effect and isolate its causes within the laboratory setting.

Byerlee (1978) plotted a large range of friction coefficients for a wide variety of materials as shown in Figure 2.8. He found that the frictional coefficient is approximately independent of lithology. The usefulness of this empirical observation has led to being referred to as *Byerlee's law*.

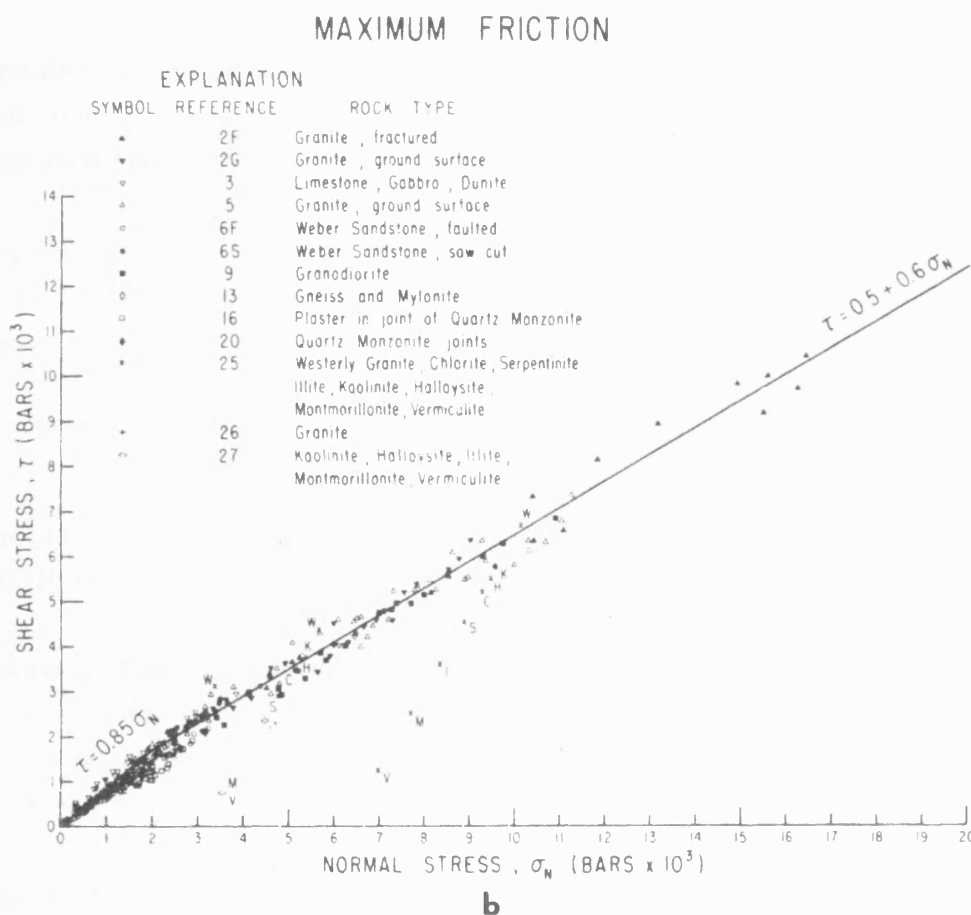


Figure 2.8: Frictional strength for a wide variety of rocks plotted as a function of normal load at high loads (From Byerlee, 1978).

To first order friction is also independent of sliding velocity and surface roughness for silicates up to temperatures of 350°C (Stesky et al. 1974, Blanpied et al. 1995). Byerlee's law does not however indicate the state of sliding. This can be either stable (frictional sliding occurs as a smooth continuous motion) or

unstable (motion is characterised with intervals of rapid sliding and no motion) and which of these depends upon the material, effective pressure and conditions along the frictional surface or gouge layer, the temperature and the rate of sliding (Kohlstedt et al. 1995). The dynamic instability that often occurs during frictional sliding of rock (which is known on the laboratory scale as stick slip and on the geological scale as earthquakes) depends on friction properties that are of only second order.

At low loads, the maximum friction for a given surface will generally follow a linear friction law quite closely, however a great variation can be observed among the surfaces and rock types. This variation is primarily due to the effect of surface roughness, which is dominant at low loads, particularly for joint friction. This is particularly true of some clay minerals which do not obey Byerlee's law, having unusually low friction. With no strong dependence of friction on rock type, and being relatively insensitive to temperature changes, Byerlee's law gives the maximum friction at moderate pressures ($3 < \sigma_n < 200$ MPa) as

$$\tau = 0.85\sigma_n \quad (2.14)$$

where τ is the shear stress necessary to overcome static friction on a surface with a normal stress σ_n . At low loads, sliding of initially mated surfaces up to the maximum friction level is accompanied by riding up of asperities and joint dilatancy.

For friction at higher loads (Figure 2.8), the friction is nonlinear, so Byerlee (1978) fitted the data with a second straight line. For higher pressures ($200 < \sigma_n < 1700$ MPa) the data for maximum friction are well described by

$$\tau = 50 + 0.6\sigma_n \quad (2.15)$$

For plastic strength however a rapid decrease in flow strength with increasing temperature is present but it is relatively insensitive to pressure changes.

The distribution of earthquakes suggests that most faulting takes place at depths of less than 15 km. Below depths of 20 km, the lithosphere deforms slowly in a ductile manner in response to relatively low shear stresses, as opposed to brittle fracture. At approximately 10 km, Byerlee's law suggests that shear stresses of the order of 100 MPa are necessary to cause sliding along unlubricated faults. Much lower stresses are required to cause slip along faults lubricated by high fluid pressures (Sleep and Blanpied, 1992, Woodcock and Middleton, 1994).

2.4.4 Triaxial Deformation Experimental Failure Modes

Room temperature deformation

In triaxial deformation experiments, the type of failure varies depending on the pressure (including confining, pore and effective), stress (on the sample and at a crack tip), temperature, strain rate and the rock type. The rock deforms elastically to stresses of about 50% of their total strength, then crack propagation becomes dominant and eventually the rock fails as cracks coalesce to form a large fracture or failure surface (Jaeger and Cook, 1976). The development and propagation of cracks is discussed in Chapter 2.5.

Under shallow crustal conditions (≤ 0.5 km) where the rock is close to the surface, the effective pressure which supports the rock is negligible. This may be due to the surrounding rock giving little or no confining pressure and/or the pore pressure being high, such as that which occurs in an overpressurised compartment. In such a situation the only significant stress present is from the overlying rock and results in uniaxial loading which produces near vertical cracking, as found in uniaxial laboratory experiments (Figure 2.9a).

At moderate depths (2 – 10 km), the effective pressure on the rock is increased when compared to shallow crustal conditions through higher confining pressure and relatively low pore fluid pressures. This means the surrounding rock is supporting the rock in the centre. Under such conditions brittle-elastic deformation is likely to occur through the coalescing of many microcracks to form a single fault. In the laboratory due to $\sigma_2 = \sigma_3$ the fault which cuts all the way across the sample is formed at approximately 30° to the maximum principal stress (Figure 2.9b).

For the high temperatures and high confining pressures associated with great depths, the development of a single large shear plane does not take place. Rather the rock deforms without localising the cracks into bands (faults) causing it to behave as a plastic material. When this occurs the sample shows continuous deformation with loading, leading into and remaining in the strain hardening regime. This causes the sample to come out barrel shaped (Figure 2.9c). In tensile situations, cracks propagate horizontally as shown in Figure 2.9d.

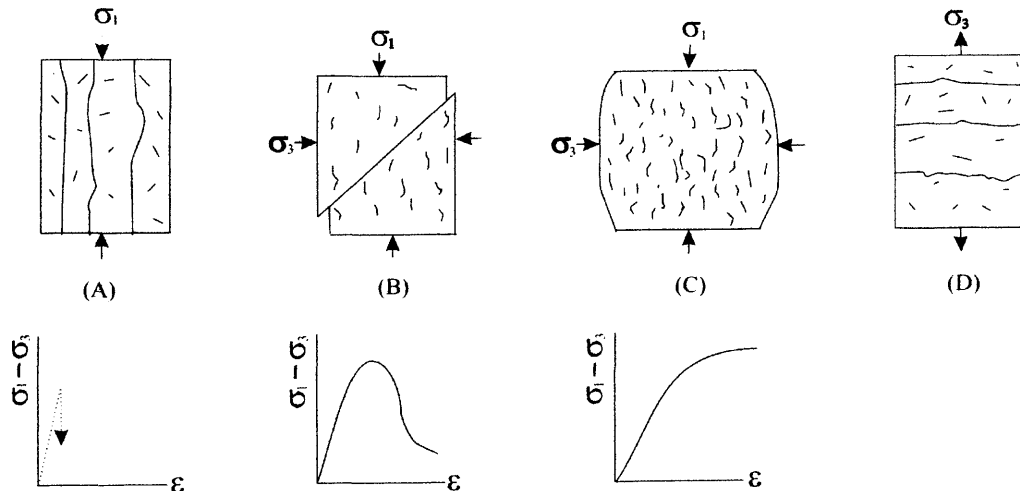


Figure 2.9: Different stress-strain curves and the type of fault associated with them, (a) uniaxial conditions, (b) low confining pressure and low temperature, (c) high pressure and/or high temperature and (d) tension conditions.

2.4.5 Acoustic Emissions

Acoustic Emissions (AE) are elastic waves (usually high-frequency) generated by microfractures and propagating cracks. Each wave packet is regarded as an individual AE 'event', although Byerlee (1993) noted that less than 1% of microcracks generate detectable AE. These microfractures significantly affect many physical properties of rock including strength, transport and elastic properties as well as electric potential signals. Some of the different types of experiments to investigate AE include earthquakes (Scholz 1968), uniaxial (Ohnaka and Mogi 1982), triaxial (Sammonds et al. 1992, Read et al. 1995), tensile (Meredith and Atkinson 1983) and triaxial creep (Baud and Meredith 1997). These studies concur with Brace et al. (1966) that the onset of dilatancy occurs at about two-thirds to seventy-five percent of the peak stress with a corresponding increase in AE activity.

Initial work by Brace et al. (1966) used strain gauges to look at the dilatant volume change during the deformation cycle. Sammonds et al. (1992) and others used pore fluid measurements to look at dilatant changes in volume as well as the stress-strain relationship related to the AE event rates. It was observed that initially the AE event rates were low, which then increased during the dilatant stages (Ohnaka and Mogi 1982, Read et al. 1995) and peaked around dynamic failure as shown in Figure 2.10a. The chemical changes during deformation (Ojala 2003) showed that as the cumulative AE event increased, so did the silica concentration in the exiting pore fluid suggesting a possible link between microcracks formed in the maximum principal direction and the chemical changes in the pore fluid. As well as the number of events, the frequency was studied (Ohnaka and Mogi 1982, Sondergeld et al. 1984). From the analysis of collated waveforms, Ohnaka and Mogi (1982) were able to split them into 5 types of fracture criteria from closure to coalescing of cracks. Lockner et al. (1991) controlled the stress applied to his samples via the AE event rate to slow down the propagation process. From this the coalescing, interaction, growth and formation of cracks occurring around dynamic failure could be better investigated.

AE source location was used by Mogi (1968) in order to build up a 3D map of deformation. The distribution of the AE events has been investigated by several authors since, including Lockner et al. (1991) (see Figure 2.11), Clint (1999) and Jouniaux et al. (2001). Clint (1999) using intact samples of sandstones which were triaxially deformed at an effective pressure of 20 MPa, showed that in a homogeneous rock, the distribution of AE events is fairly homogeneous until failure is approached, when the nucleation and formation of fault planes takes over as shown in Figure 2.11. However, recent work by Jouniaux et al. (2001) on triaxially deformed granite samples with a confining pressure of 40 MPa shows that the final plane of rupture can be clearly identified before dilatancy occurs. In the case of an inhomogeneous sample (such as a sample containing a fault), the distribution of the AE events depends upon any healing which has been applied to the fault, with a non-homogeneously healed fault the distribution of AE events can be predicted (Lei et al. 2004).

Plotting the magnitude of AE occurrences revealed a similar relationship to that found in seismological investigations, namely the decrease of occurrence frequency with increasing magnitude. The slope of the log frequency versus magnitude plot gives the b-value which has been linked to the state of stress (Scholz

et al. 1973) of earthquakes. This model follows time-varying applied stress associated with different experimental types and corrosion-enhanced crack growth under drained and undrained conditions (Sammonds et al., 1992). Figure 2.10b displays the b-value variation during deformation of an air-dried specimen of Darley Dale sandstone. A decrease of the b-value is exhibited during stress-induced dilatancy corresponding to an increasing number of large amplitude events as the rock approaches failure with failure denoted by a minimum b-value (Meredith et al. 1990, Main et al. 1992, Sammonds et al. 1992). Recovery of the b-value occurs post-failure as frictional sliding dominates the deformation sequence.

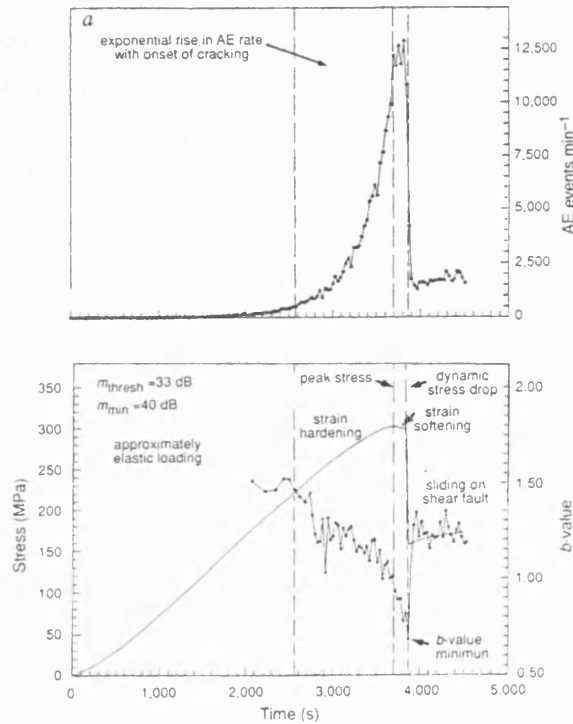


Figure 2.10: Deformation of Darley Dale sandstone at a strain-rate of 10^{-5} s^{-1} and a confining pressure of 50 MPa. (a) Event rate and (b) b-value during this experiment (taken from Sammonds et al. 1992).

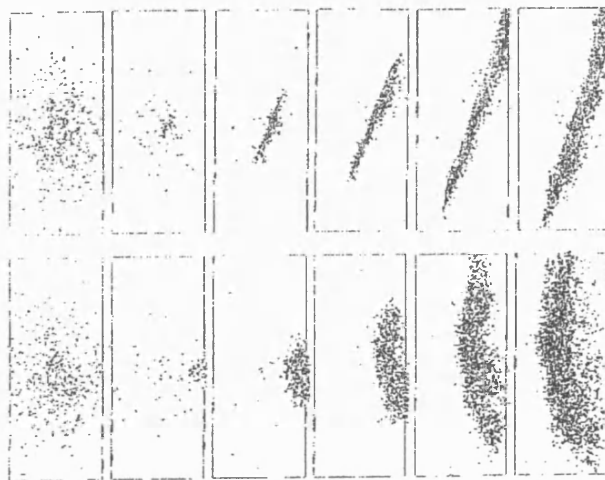


Figure 2.11: Initial nucleation propagation and formation of fault plane from source located AE events during triaxial deformation. Upper and lower row shows evolution in time from two orthogonal directions (from Lockner et al. (1991)).

Two of the main damage models put forward in relation to the paper by Scholz (1968) were by Walsh (1965) and Bruner (1976). Walsh (1965) produced a model for the effect of cracks on the elasticity of the solid, while Bruner (1976) treated the crack interactions. Both predict stress-strain relationships during rock deformation. This was investigated by Cox and Meredith (1993) who found that they both fitted experimental data fairly well. However the self-consistent Bruner method proved superior to the dilute crack approximation model as it dealt with crack interaction occurring around strain softening.

2.4.6 Elastic Wave Velocity Analysis

The effect of triaxial deformation on compressional (V_p) and shear (V_s) waves can be investigated through velocity measurements across the sample. The typical effect on the wave types which are measured in the z-axis (axial) is shown below in Figure 2.12. For both types of waves, an increase is observed during deformation in the linear phase of loading and reaches a maximum at approximately half of the peak differential stress.

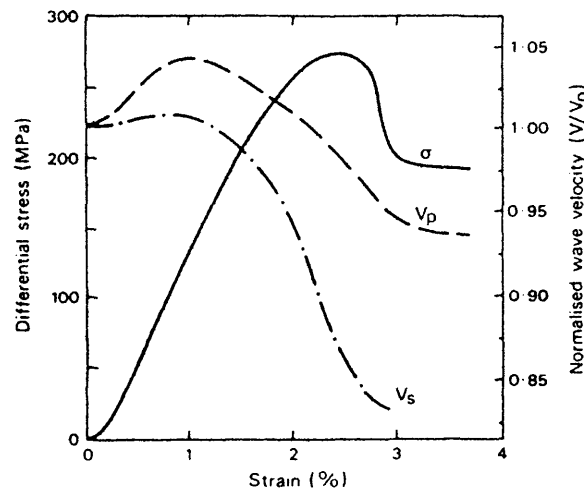


Figure 2.12: Variations in velocities of compressional (V_p) and shear (V_s) waves in a dry sample of Darley Dale sandstone deformed under a confining pressure of 50 MPa at a strain rate of 10^{-5} s^{-1} (from Sammonds et al. (1989))

This is caused by the closure of the pores which are oriented normal or sub-normal to the direction of the maximum principal stress. Initially the open cracks close first with closure becoming progressively more difficult. The velocities then decrease as new cracks are opened (dilatant) and then stabilise during frictional sliding. There is initially a greater effect on V_p than on V_s . But the decrease after failure for V_s is greater than V_p . This is believed to be due to the growth of dilatant cracks with the P-waves more sensitive to the cracks oriented normal to axial stress and the S-waves more sensitive to cracks oriented parallel to axial stress. The results suggest that dilatancy occurs by the growth of tensile cracks along the axis parallel to maximum compression stress. Therefore velocity can be used to conceptualise the development of crack anisotropy during rock deformation.

The effect of temperature on triaxial experiments using Solenhofen limestone has been investigated to temperatures of up to 300°C (Jones 1989) as shown by Figure 2.13.

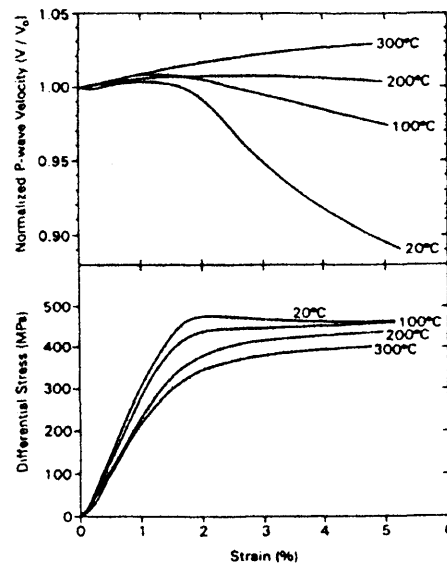


Figure 2.13: Triaxial tests on Solenhofen limestone, at varying temperatures (from Jones (1989)).

For the different temperatures, the stress-strain curves appear fairly similar. Initially all the velocity curves show an initial increase related to crack closure. However, as deformation continues the velocity curves show distinct differences with the cataclastic flow operative at room temperature causing a continuous decrease in the velocity. For the 300°C experiment, the velocities continue to increase with Jones (1989) attributing this to non-dilatant crystal plasticity and plastic pore compaction.

2.4.7 The Brittle Deformation Cycle

Rock deformation during the typical brittle cycle is a result of microscopic to macroscopic processes. In Figure 2.14 the effect of stress on physical properties with increasing strain are shown. Five specific areas can be recognised, first proposed by Brace (1964), and the resulting processes are described below.

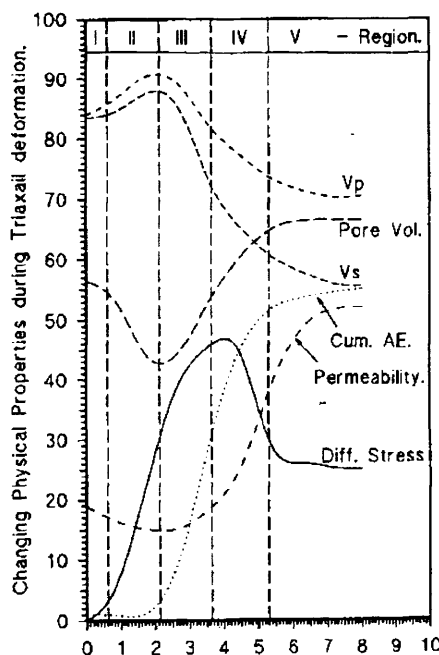


Figure 2.14: Variation of a number of physical properties with axial strain during a typical deformation cycle (taken from Aves (1995)).

Stage 1

In stage 1, a concave upward trend in the stress-strain curve which is caused by compaction. This mechanism is due to the preferential closing of orientated microcracks and pores (i.e. those at high angles to the maximum principal stress direction). This causes both the V_p and V_s velocities to increase whilst the pore volume decreases due to void closure, reducing porosity and permeability. Little or no AE activity can be detected during this stage and the deformation is considered reversible although some hysteresis can occur.

Stage 2

In stage 2, stress is linearly related to the strain, with quasi-linear elastic deformation occurring. Cracks and pores continue to close further reducing the permeability and porosity and V_p and V_s continue to increase. Crack and pore closure also reduces the conductivity of the rock through which the electrical signals must pass (depending on the rock the effects on conductivity may vary).

Stage 3

The stress-strain curve begins to deviate from linearity in stage 3. This corresponds to the formation of microcracks which propagate axially parallel to the direction of the maximum principal stress. AE rate starts to increase exponentially at between 50-75% of peak stress and the sample becomes dilatant. V_p and V_s decrease at different rates. As more crack space is created the pore volume increases as does the permeability as new pathways are created for fluid flow. Electrical resistivity is strongly affected in this region.

Stage 4

In stage 4 the stress-strain curve indicates that the rock sample undergoes strain softening as more cracks and pores are created reducing the stress the rock can support. Both V_p and V_s continue to decrease in all directions at different rates with V_s dropping faster. The AE shows a period of quiescence related to the maximum damage accumulated in the rock sample. The b-value decreases rapidly from a slowly decreasing value in stage 3 of 1.5 to a value of approximately 0.5. This stage therefore represents accelerated crack growth and coalescence to form a macroscopic fault plane. Permeability and electrical conductivity continue to increase during this stage as a linkage of the new microcracks provides fluid, and hence electrical pathways.

Stage 5

Stable sliding occurs on the macroscopic fault plane as stress becomes independent of strain. Many of the physical properties become constant including V_p and V_s velocities, pore volume, and permeability. As the two halves of the rock slide against each other along the macroscopic fault, AE is reduced to a background level with a constant b-value associated with sliding.

2.5 GRIFFITH CRACK ANALYSIS

2.5.1 Griffith Crack

Energy balance concept

Griffith (1920, 1924) proposed the explanation of crack propagation in the form of an energy balance equation based upon the idea of a reversible thermodynamic system, in which absorbing mechanical energy is the only way to break the cohesive bonds and cause systematic failure. This is explained in terms of an elastic body (Figure 2.15) that contains a crack of length $2c$, which is loaded by forces σ on its external boundary.

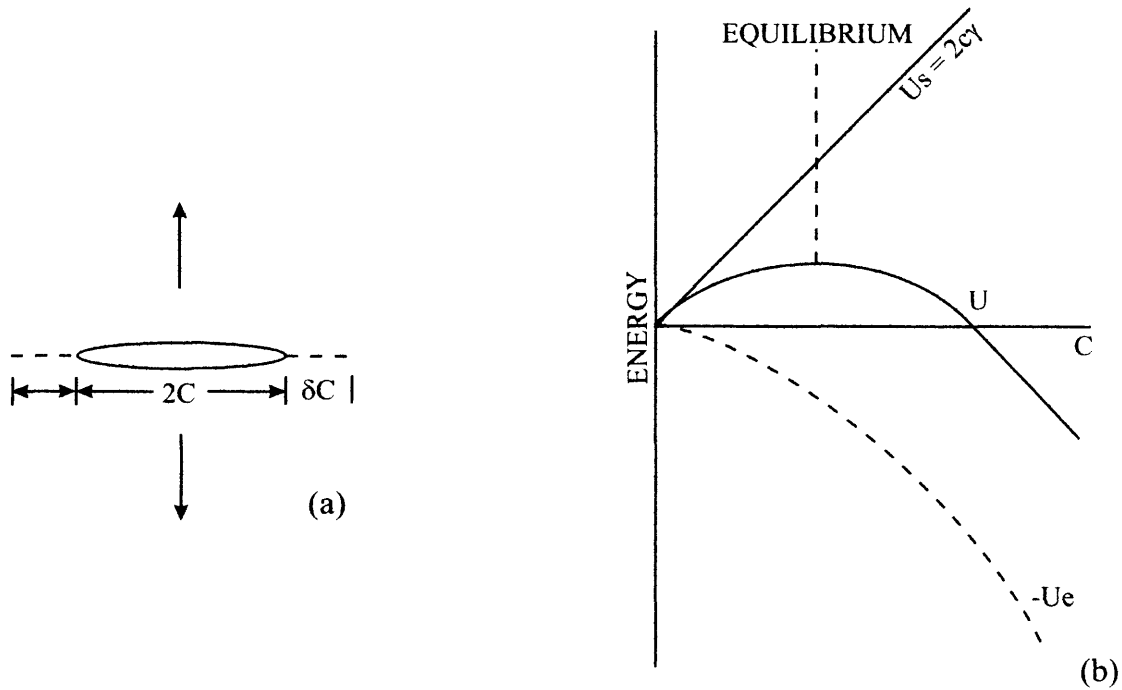


Figure 2.15: The Griffith’s model for crack propagation in a rod (a), and the energy partition for the process (b) (redrawn from Scholz (2002)).

The change in crack length δc requires work W to be done to the external forces changing the internal strain energy U_e . There will also be an expenditure of energy in creating the new surface designated as U_s . The total energy of the system U for a static crack is given by Scholz (2002) as

$$U = (-W + U_e) + U_s = U_m + U_s \tag{2.16}$$

where U_m is referred to as the mechanical energy which must decrease with crack extension otherwise the crack would expand outwards to a lower energy configuration. In contrast U_s increases with crack extension as more energy is required in creating new surface area by overcoming the cohesion forces. These two competing influences for crack extension must be in equilibrium expressed as

$$\frac{dU}{dc} = 0 \tag{2.17}$$

which is the Griffith energy balance with a positive or negative sign denoting crack extension or retraction. Griffith used a rod under tension with a crack present to calculate the energy release. From this, the equation for the rod is given by

$$U = -\left(\frac{\pi c^2 \sigma^2}{E}\right) + 4c\gamma \quad (2.18)$$

where σ is the applied stress, E is the elastic modulus and γ is the free surface energy per unit area. Combining the condition of equilibrium (2.18) with that of total energy (2.17), the critical stress σ_f is given by

$$\sigma_f = \left(\frac{2E\gamma}{\pi c}\right)^{1/2} \quad (2.19)$$

The energies represented in equation (2.19) define a position of metastable equilibrium which is shown in Figure 2.15. When this condition is met, the crack propagates without limit causing macroscopic failure of the body (Lawn 1993, Scholz 2002). This approach is not adequate for the cases of biaxial or triaxial stress with the crack extending out in other planes (Murrell 1964a, Murrell 1964b). Therefore local stresses must be present to cause the rupture of the atomic bonds at the crack edges.

The Plane Griffith criterion

Crack propagation is initiated when the maximum stress near the tip of the most favourably orientated crack reaches a critical value characteristic of the material. This stress concentration at the tip exceeds the stress intensity factor (K_c) (which defines the magnitude of the local stresses around the crack tip) resulting in macroscopic shear failure through the coalescing of cracks. Griffith (1924) developed a biaxial fracture criterion based on his theory of crack propagation around an elliptical crack. Griffith assumed that when the tensile stress around a crack is a constant value related to the tensile strength, the crack would grow until fracture. This was confirmed by Murrell and Digby (1970) who determined that the stress near the crack tip must be equal to the interatomic tensile cohesive strength before fracture initiation occurs. The Griffith criterion in Jaeger and Cook (1976) is written as

$$\begin{aligned} (\sigma_1 - \sigma_3)^2 - 8T_0(\sigma_1 + \sigma_3) &= 0 & \text{if } \sigma_1 > -3\sigma_3 \\ \sigma_3 &= -T_0 & \text{if } \sigma_1 < -3\sigma_3 \end{aligned} \quad (2.20)$$

where T_0 is the uniaxial tensile strength of a material. This produces a parabolic Mohr envelope

$$\tau^2 + 4T_0\sigma - 4T_0^2 = 0 \quad (2.21)$$

For tensile fracture, the most critically orientated crack is normal to σ_3 . In the case of shear failure the crack is orientated to an angle θ from the σ_1 direction given by

$$\cos 2\theta = \frac{1}{2}(\sigma_1 - \sigma_3)(\sigma_1 + \sigma_3) \quad (2.22)$$

This criterion is based on a microscopic failure mechanism and combines both the tensile and shear failure into a single criterion. It predicts that $C_0 = 8T_0$ being in the same order of magnitude as experimental studies (Coulomb).

Modified Griffith criterion

However, the above criterion neglects the fact that certain cracks may close under sufficiently high confining stresses as pointed out by McClintock and Walsh (1962) who formulated a *Modified Griffith criterion*. This modified criterion includes the application of a confining medium, with crack closure occurring and resulting in frictional stress acting on the walls of the closed cracks. This tends to increase the strength of the rock by reducing the stress concentration at the crack tips compared to when the frictional stresses are absent. Scholz (2002) writes this criterion as

$$\left[(1 + \mu^2)^{\frac{1}{2}} - 1 \right] (\sigma_1 - \sigma_3) = 4T_0 (1 + \sigma_c / T_0)^{\frac{1}{2}} + 2\mu(\sigma_3 - \sigma_c) \quad (2.23)$$

which has the corresponding Mohr envelope

$$\tau = 2T_0 (1 + \sigma_c / T_0)^{\frac{1}{2}} + 2\mu(\sigma - \sigma_c) \quad (2.24)$$

Assuming that σ_c is negligible, the simplified forms for fracture at low compressive stresses are created

$$\left[(1 + \mu^2)^{\frac{1}{2}} - \mu \right] (\sigma_1 - \sigma_3) = 4T_0 + 2\mu\sigma_3 \quad (2.25)$$

and

$$\tau = 2T_0 + 2\mu\sigma \quad (2.26)$$

These are identical to the Coulomb criterion with $\tau = 2T_0$ and μ being physically identifiable with the friction acting across the walls of the pre-existing cracks (Scholz 2002).

2.5.2 Linear Elastic Fracture Mechanics

The Griffith crack analysis does not take account of energy dissipation, such as heat and acoustic emissions, which occur during crack development. Irwin addressed this in the 1950's forming the concept of *fracture mechanics* (Lawn 1993). The linear elastic fracture mechanics (LEFM) is a continuum mechanics approach that retains the Griffith energy balance for crack propagation. It is based on an ideal crack in a linear elastic medium with stress fields analysed around the crack.

Modes of crack propagation

There are three basic modes of failure of crack surfaces as shown in Figure 2.16. Mode I (tearing mode) describes normal separation of the crack walls under tensile stresses; Mode II (in-plane shear) describes mutual shearing of the crack walls in a direction normal to the crack front; Mode III (antiplane shear) describes mutual shearing parallel to the crack front (Scholz 2002).

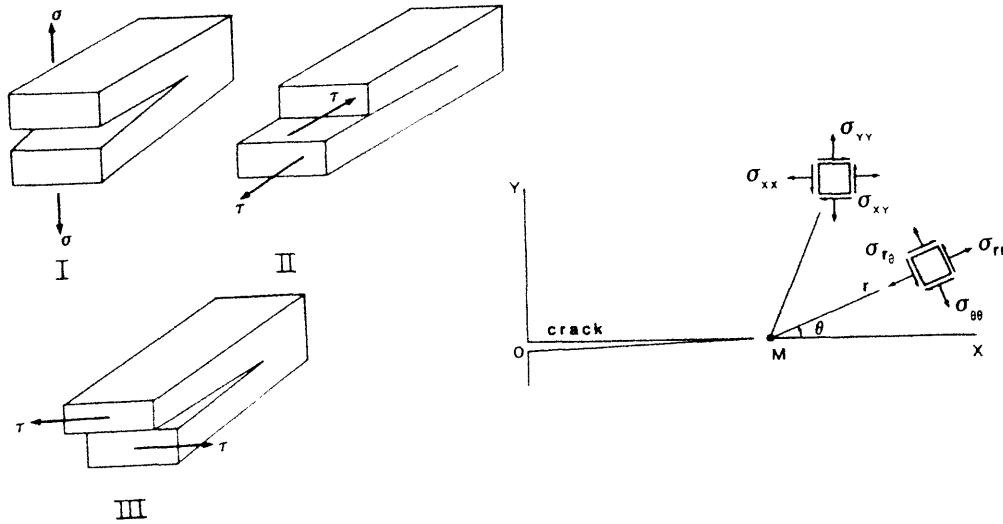


Figure 2.16: (a) The three modes of rock fracture, (b) crack tip stresses. See text for details (taken from Gueguen and Palciauskas (1994)).

If the crack is assumed to be planar and perfectly sharp, with no cohesion between the crack walls, then the near field approximations to the crack tip stress and displacement fields may be reduced to the following analytical expressions (Lawn 1993)

$$\sigma_{ij} = K_n (2\pi r)^{-1/2} f_{ij}(\theta) \quad (2.27)$$

$$u_i = (K_n / 2E) (r / 2\pi)^{-1/2} f_i(\theta) \quad (2.28)$$

where r is the distance from the tip, and θ is the angle measured from the crack plane, shown in Figure 2.16b. K_n is the stress intensity factor and varies depending on the mode of failure so that it is K_I , K_{II} or K_{III} . The functions $f_{ij}(\theta)$ and $f_i(\theta)$ can be found in standard references (e.g. Lawn and Wilshaw 1975) and represents the angular dependence factor which varies with respect to the crack tip.

Crack propagation force

In order to relate the Griffith energy balance to the modes of crack propagation, either the *energy release rate* or *crack extension force* needs to be defined.

$$G = -d(-W + U_e) / dc \quad (2.29)$$

This can be related to the stress intensity factor K by Lawn and Wilshaw (1975) giving

$$G = K^2 / E \quad (2.30)$$

The balance between the driving and resistive forces determines whether the crack will propagate (equations 2.16 and 2.17). This is shown by

$$G_c = K_c^2 / E = 2\gamma \quad (2.31)$$

for plane stress with a related plane strain and γ is the specific surface energy of the solid. Both K_c and G_c depend on the rocks properties. K_c is referred to as the *fracture toughness*, and G_c the *fracture energy*.

Non-linear fracture mechanics

Linear Elastic Fracture Mechanics (LEFM) assumes certain properties which are impractical for real materials. These includes the definition of stress intensity factor (equation 2.27) for a perfectly sharp crack in which there is a stress singularity at the crack tip. However, this is unrealistic as no material can support infinitely large strains. Also, the singularity violates the small strain assumption (Scholz 2002, Lawn 1993), therefore a region of non-linear mechanics at or near the crack tip must exist which relaxes the singularity.

The fracture criteria to address these issues was introduced by Irwin in the 1950s taking into account the nonlinear distribution cracking, plastic flow, and other dissipative processes contributing to crack extension. This is taken into account by rewriting equation (2.31) as

$$G_c = 2\Gamma \quad (2.32)$$

where Γ is a lumped parameter which includes all the dissipation that occurs within the crack tip region. This can be reduced to γ when Γ is equal to zero for an ideally brittle solid.

This model cannot be used as a global criterion for energy balance as it assumes no cohesion behind the crack tip. So it is only valid at very small distances away from the crack tip, thereby reducing equation 2.32 to a local stress fracture criterion.

In recent studies of rock failure under compressional loading, it has been identified that rock fails by organised, unstable coalescence of microcracks which initially grow in tensile mode, and nucleate at the weakest element. Nucleation described by Atkinson (1982, 1984) is affected by the stress intensity factor, subcritical crack influence, temperature, pressure, environmental agents, microstructure and residual strain in the crustal environment. Experiments undertaken by Main et al. (1989) found that the fractal dimension (inferred from the b-value) and the stress intensity have strong correlation with each other. This represents how stress intensity and fracture toughness cause a fractal distribution of damage. Looking directly at the fault tip Lei and Kusunose (2000) found that two different zones exist consisting of the process zone (mutual enhancement of dilatation due to tensile cracking and fault growth) and a damage zone (development of shear fault, linkage between cracks becoming the major mechanism for fault development).

2.6 THE DEFORMATION OF FLUID SATURATED ROCKS

Fluids in the brittle regime of the earth are linked to a variety of faulting processes including fault creep and the long-term structural evolution of fault zones. The effect of water on the physical properties of rock is important for understanding the deformation, failure and slip processes in nature with changes in such properties as permeability and porosity. In terms of rock strength, fluids can affect this through two main mechanisms: mechanical and physico-chemical effects (Scholz 2002). The former is caused by lowering the effective stress reducing the fracture strength with the latter affecting the strength of the rock through time dependent processes.

As well as fluids influencing strength, the fluid is required to generate the electrical signals (discussed in section 3.4.2). These signals may be altered depending on the composition of the fluid and the rock. The effects of fluid on physical properties and changes in electrical conductivity are discussed below.

2.6.1 Application of Pore Pressure

Fluids which vary in salinity, pH, temperature, ions and pressure in the earth's crust have been proved to exist to depths of 15 km. Their presence affects the brittle deformation properties of rock in two different ways, mechanically and chemically.

Depending on the connectivity of the pore space, the pore fluid pressure can reduce the effective pressure (Paterson 1978) which controls the mechanical properties of the rock. Assuming the rock has some connected pore space, the development of a fracture is controlled by the effective stress regardless of the absolute values of total stress or pore pressure, therefore

$$\sigma_1' = \sigma_1 - p, \quad \sigma_2' = \sigma_2 - p, \quad \sigma_3' = \sigma_3 - p \quad (2.33)$$

The effective stress law σ_{ij}^e is expressed by Jaeger and Cook (1979), Nur and Byerlee (1971) as

$$\sigma_{ij}^e = \sigma_{ij} - \alpha p_p \delta_{ij} \quad (2.34)$$

if the rock is fully saturated and where σ_{ij} is the total stress, p_p is the pore pressure, α is a constant and δ_{ij} is the Kronecker delta. If the value of $\delta_{ij} = 1$ an incremental increase in the pore fluid pressure opens pores by the same amount as it would given a decrease in the normal pressure on the fracture by the same amount.

The value of α is not known exactly, but it is known from the theory of elasticity that the strain due to pores is very localised. When the number of cracks approaches zero, the effect of the pores on strain will also approach zero, Nur and Byerlee (1971) showed how α can be determined through the relationship

$$\alpha = 1 - \frac{K}{K_s} \quad (2.35)$$

where K and K_s are the effective and grain bulk modulus of the rock respectively. Purely on a mechanical effect the pore fluid pressure shifts the Mohr stress circle in the direction of increasing tension by the amount P_p shown in Figure 2.17.

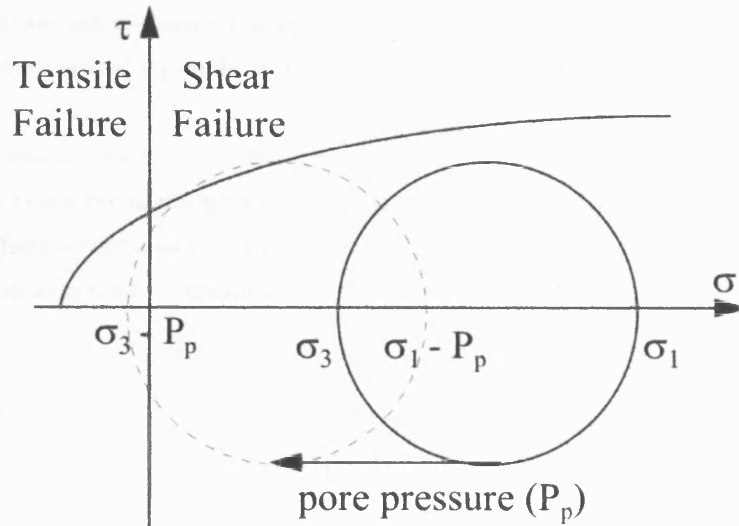


Figure 2.17: The effects of pore fluid pressure on fracture.

A compressive stress system with a small differential stress will actually undergo tensile fracture. The effective stress principle can be shown by the work of Murrell (1965) on Darley Dale sandstone (Figure 2.18).

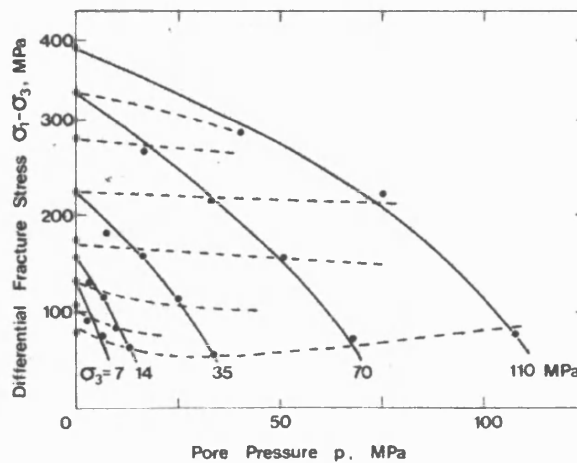


Figure 2.18: Influence of pore fluid pressure on the fracture strength of sandstone under triaxial deformation (taken from Murrell (1965)).

2.6.2 Quartz-Water Interaction

Subcritical crack growth

Experimental work supports the idea that under the influence of temperature and a reactive fluid environment, cracks can propagate in a stable and quasi-static manner at values below G_c or K_{Ic} . At

velocities lower than the dynamic fracture level, this is known as subcritical crack growth and has been observed by many authors (Scholz 1972, Atkinson 1982, 1984, 1987). While dynamic failure is associated with rapid, catastrophic crack propagation leading to dynamic failure, sub-critical crack growth is time sensitive and is characteristically slow in the order nm/s to m/s.

Several different mechanisms contribute towards subcritical crack growth including atomic dislocation, diffusion, dissolution, ion exchange, microplasticity, stress corrosion and cyclic fatigue (Atkinson 1984, 1987). In the shallow crustal region the dominant process is stress corrosion Costing (1987).

Stress corrosion crack growth

In general stress corrosion occurs in rock containing pore fluids where fracturing is slow and attributed to the combined effects of stress and a corrosive agent at the crack tip. However it can occur in the absence of chemical agents as noted by Meredith et al. (1990). The chemically induced rupture is shown in Figure 2.19

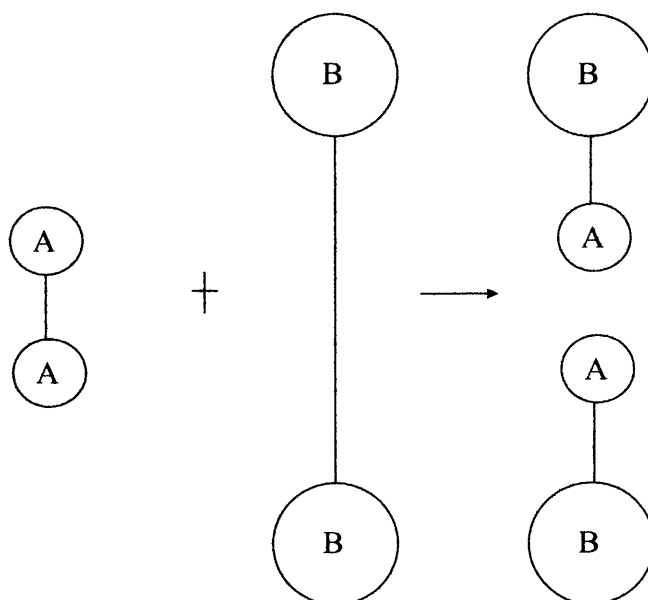


Figure 2.19: Chemically induced bond rupture. An environmental molecule *A* reacts with crack tip molecule *B* to produce terminal bonds *A-B* (redrawn from Lawn (1993)).

Using Figure 2.19 as a simplified basis, the molecule *A* reacts with the crack tip *B* to produce two terminal groups *A-B*. This process breaks the crack tip bond and produces new crack surfaces and newly exposed crack tips which interacts with the next incoming *A* molecule. This can generally be expressed as (Atkinson 1987)



where *X* represents the number of species and *B*⁺ denotes the activated state. This applies to different molecules other than water such as Na⁺ and Cl⁻ which react with rock to different degrees. A more detailed model to show what could occur in my experiments by the interaction of water and quartz is given by Michalske and Freiman (1982) shown below (Figure 2.20).

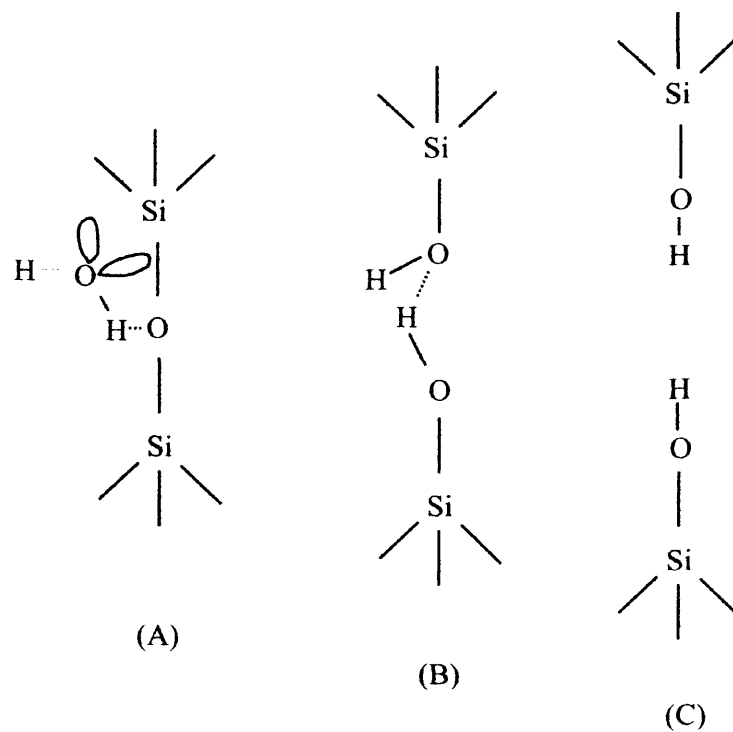


Figure 2.20: Michalske and Freiman's model showing (a) the adsorption of a water molecule onto a quartz surface, (b) leading to hydrolysis and (c) rupture of the weak bonds (redrawn from Michalske and Freiman (1982)).

This model is based on the idea that strained Si-O bonds produce a highly concentrated tensile stress field at the crack tip with strains up to 20%. The water molecule forms four hybrid orbits of which two link the oxygen and hydrogen atoms. The remaining lone pairs are directed away from the hydrogen atoms creating a positive and negative central charge at either end of the molecule with the negative charge at the lone pair end which in all forms a tetrahedral shape. The (Michalske and Freiman 1982) model has three steps: a) The water molecule attaches to a bridging Si-O-Si bond at the crack tip with the water molecule aligned by a hydrogen bond with the O_{br} atom and the interaction of the lone pair of orbitals from O_w with the Si atom, b) Proton transfer to the O_{br} is accompanied simultaneously with electron transfer from the O_w to the Si atom. This results in two new bonds formed (O_w-Si and H-O_{br}) with the original bridging bond (between the O_{br} and Si) destroyed, c) Rupture of the hydrogen bond between the O_w and transferred hydrogen occurs to yield surface Si-O-H groups. Because the hydrogen atom is weak step (c) is thought to occur immediately after the proton transfer. This is similar to a model proposed by Budd (1961) on silica dissolution, the model proposed by Michalske and Freiman does not include the removal of material from the fracture surface.

The majority of the theoretical models on stress corrosion come from empirical fits to laboratory data. These studies generally use a double torsion testing machine. From this data the crack growth v and K can be determined from load-relaxation data of the specimen. Alternatively, G_c may be used (Darot and Gueguen 1986). Since the work by Wiederhorn (1967), stress corrosion has been interpreted in terms of three regions as demonstrated in Figure 2.21.

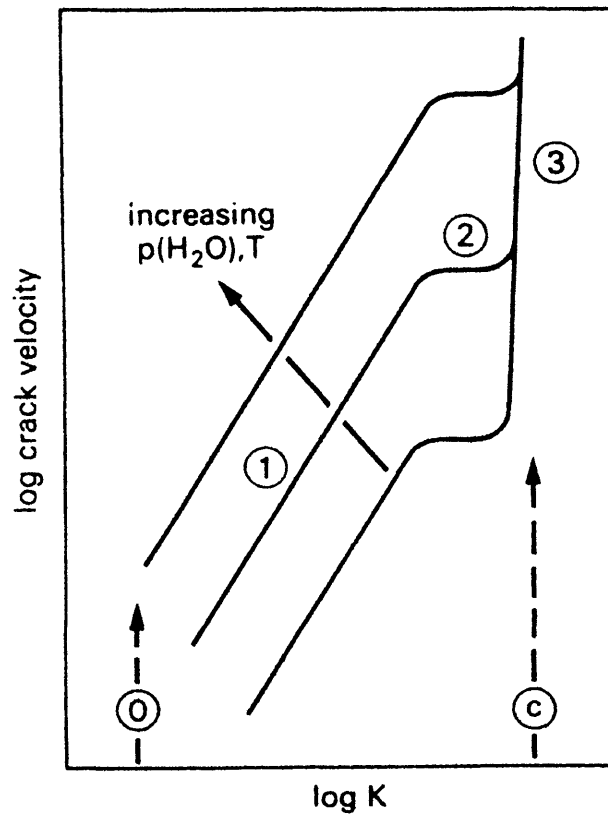


Figure 2.21: The dependence of crack velocity on the stress intensity (K) between the subcritical crack growth limit (0) and critical rupture (c). The influence of temperature and partial pressure of water is also indicated (from Meredith et al. (1991)).

In region I the crack velocity is given by the rate of stress corrosion reaction rate at the crack tip. For region II the crack propagation rate v is controlled by the rate of transport of reactive species (e.g. water) to the crack tip. In region III, v is controlled by the mechanical properties and is relatively insensitive to the chemical environment (Meredith et al. 1991). Atkinson (1982, 1984) note that the fracturing process depends on temperature, pressure and crystal orientation with an increase in crack velocity with increasing temperature, which agrees with the double torsion test of Atkinson (1979). This generally occurs in region I where the corrosive heated fluid gets into the cracks, compared to regions II and III. The effect of temperature on the stress corrosion of region I is shown in Figure 2.22 for Black gabbro under a range of experimental conditions. This data is described by the law

$$V = V_c (K / K_c)^n \quad (2.37)$$

where n is the stress corrosion index.

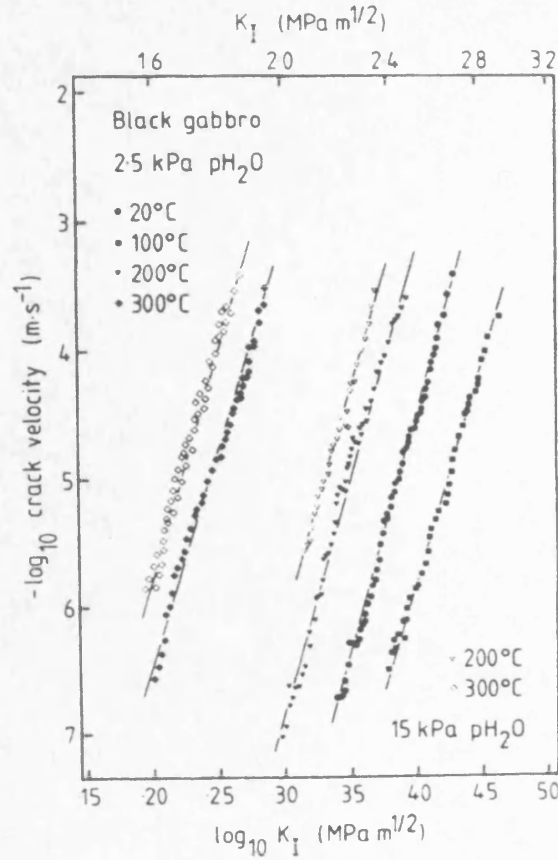
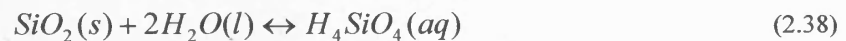


Figure 2.22: Stress intensity factor versus crack velocity for Black gabbro cracked at temperatures between 20°C and 300°C under water vapour pressures of 2.5 and 15 kPa. The solid lines represent the least square fits for the data points (from Meredith et al. (1991)).

Dissolution theory

As well as the stress corrosion that occurs at the crack tip, dissolution and precipitation of quartz crystals with water is a crucial process for mass transport of silicate material. These reactions allow for the chemical healing of faults. The reaction of deionised water with a quartz crystal can be expressed as



where the dissolution and precipitation proceeds by equal rates, with, according to transition state theory (Dove 1999), the dissolution and precipitation given by



where the species marked by a plus represent the intermediate steps (Rimstidt and Barnes 1980). The particular form of the reactive intermediate $(*)^+$ may depend on temperature, pressure or solution composition. A schematic illustration of the dissolution process in deionised water is given by Dove and Crerar (1990) in Figure 2.23.

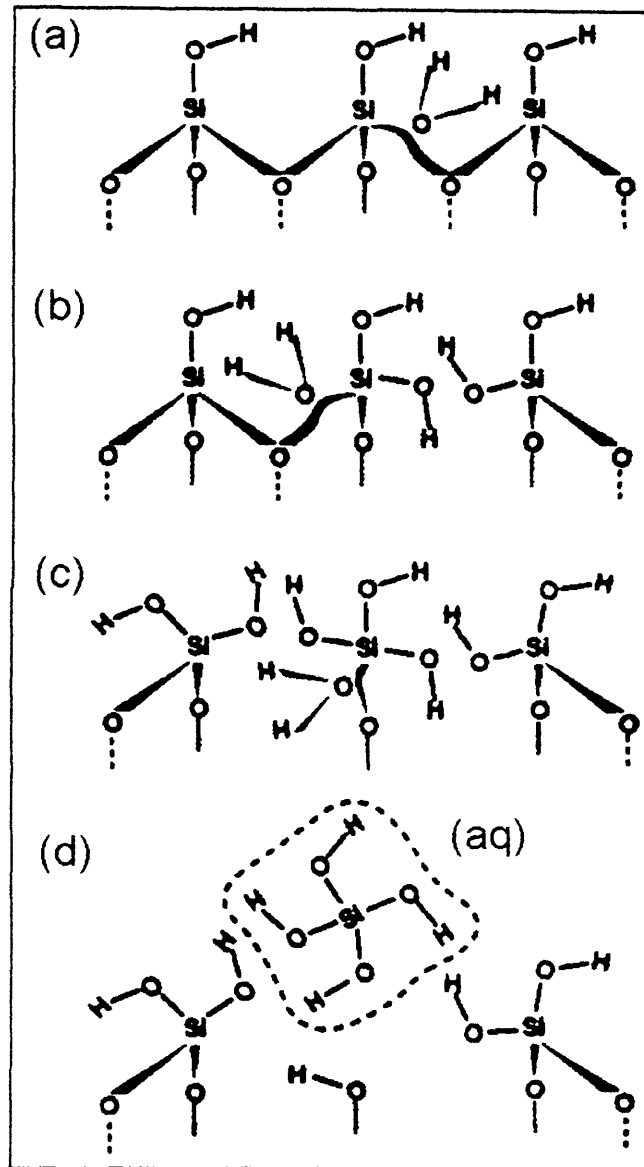


Figure 2.23: Schematic illustration of the dissolution process in deionised water (from Dove and Crerar (1990)).

Laboratory studies have shown that silica-water reaction rates depend upon many factors including temperature (Dove and Crerar 1990, Icenhower and Dove 2000), sample surface area (Rimstidt and Barnes 1980, Gautier et al. 2001), the presence of electrolytes (Dove and Crerar 1990, Carroll et al. 2002) organic acids (Bennett 1991, Franklin et al. 1994) and pH (Schwartzentruber et al. 1987, Carroll et al. 2002). The effect of various environmental factors on dissolution rates are summarised in Table 2.1.

Variables	Effect	Range	Example study
Mechanisms	Breaking of bonds	T<300°C	(Berger et al. 1994)
Temperature	Arrhenius law	T=25-300°C	(Dove and Rimstidt 1994)
Alkali cations	Rate increase	-	(Dove and Crerar 1990)
Trivalent metals	Rate increase	-	(Dove and Rimstidt 1994)
Organic acids	Rate increase	-	(Bennett 1991)
pH	Rate increase	pH > 6	(Brady and Walther 1990)
Particle size	Solubility increase	-	(Rimstidt and Barnes 1980)

Table 2.1: The effect of various environmental variables on silica dissolution rate. (from Ojala (2003)).

Of the factors listed above, the ones which are of most interest in this study are temperature and to a lesser extent the effect of ions. This is due to the majority of the tests being conducted using deionised water as the pore fluid with a comparison study using simulated formation waters to identify differences and relate these to reservoir conditions. A summary of the main variables I am interested in is given below with a comprehensive discussion of all these factors influencing quartz dissolution found in Ojala (2003).

Ions

The composition of natural waters are typically dominated by low concentrations of cations such as sodium, potassium (Dove and Crerar 1990, Bennett 1991, Dove and Rimstidt 1994, Berner and Berner 1996) as well as magnesium and calcium (Dove and Nix 1997) respectively. These enhance chemical rates by a factor of 40 to 1003 in low temperature and hydrothermal solutions. As fluids contain more than one type of ion the effect of this on dissolution was investigated by Dove (1999) who identified that the dissolution rates in solute mixtures have a complex dependence on solution composition and any increase is in direct proportion to the number of Si-O surface structures affected by absorbed cations.

Temperature

The rate of reaction as a function of temperature was investigated by Dove and Rimstidt (1994) who identified that the dissolution rate increased with increasing temperature. The data suggested that for temperatures between 25-300°C the rates can be described by an Arrhenius type equation. The combined effect of temperature and pressure over a much wider range was investigated by Fournier and Potter (1982) and more recently by Fournier (2001) who produced Figure 2.24. Here it can be seen that between 0-350°C a similar trend as found by Dove and Rimstidt (1994) exists, however for higher temperatures a period of retrograde solubility exists between 350-575°C. Above this temperature range the solubility increases to different degrees depending on the pressure. The rise in pressure increases the phase with the lowest volume which enhances quartz solubility.

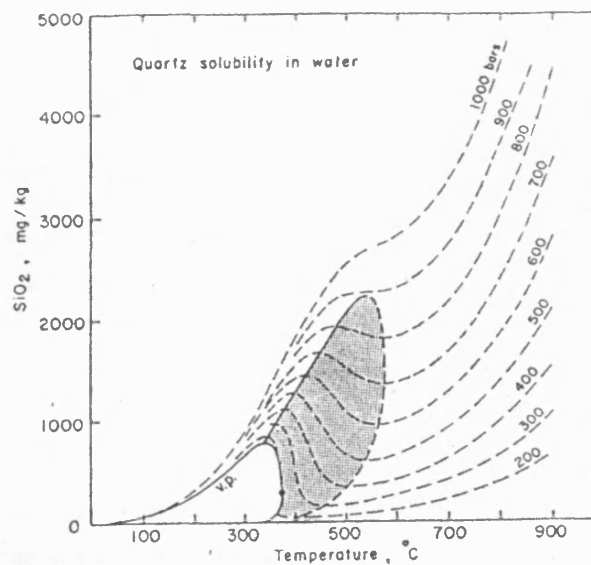


Figure 2.24: Calculated solubilities of quartz in water as a function of temperature and pressure. The stippled pattern shows a region of retrograde solubility in which the solubility of quartz reduces with increasing temperature at constant pressure (from Fournier (2001)).

Pressure solution is generally a temperature driven process which involves the dissolution and recrystallisation of silicate minerals such as quartz. This process can be split into three separate areas of 1) dissolution into a hydrothermal solvent, 2) solute or solution transport and 3) growth from solution with the latter used to chemically heal faults. This is achieved by chemical disequilibrium resulting from an inhomogeneous temperature gradient through the rock medium caused by the movement of pore fluids. When the pore fluid cools, recrystallisation of the quartz crystals from the water located in the void space and faults occurs. This influences the porosity and transport properties including permeability which was found by Meredith (2003 Personal corr) who investigated this healing process on Westerly granite. He found that pore fluid and temperatures of 350°C for over a week healed and strengthened the fault. This is an especially important process in faults located within a reservoir system where this process can both aid and hinder hydrocarbon extraction.

2.6.4 Permeability

Permeability is one of the most important rock characteristics in relation to hydrocarbon production, geothermal recovery rates and radioactive storage procedures. It is especially important in the hydrocarbon industry because a reservoir with a low permeability is not economical. Generally reservoir rock consist of highly porous rocks such as limestone and sandstone, which can have permeabilities varying over several orders of magnitude within a single block (Gueguen and Palciauskas 1994). This makes it difficult to provide reliable permeability values for a given rock type over a large area, especially if environmental conditions are included, such as confining pressure, pore pressure and differential stress.

Fluid flow can be generated by several mechanisms including thermal, chemical and pressure gradients. The coefficient of permeability (k) is defined via Darcy's law

$$q_x = -\frac{k}{\eta} \frac{dP}{dx} \quad (2.41)$$

where q is the Darcy velocity of a fluid and η is the viscosity of the fluid in the x-direction and $\frac{dP}{dx}$ is the fluid pressure gradient. Dimensional analysis reveals k to have units of m^2 , therefore k can be treated as having a cross-sectional area for fluid flow. The unit *Darcy* is often used for the permeability: $k = 1$ Darcy (1 D) when $q = 1$ cm S⁻¹, for a gradient of 1 atmosphere cm⁻¹ and a fluid of viscosity $\eta = 10^{-2}$ poise: thus 1 Darcy = $0.97 \cdot 10^{-12}$ m². A good petroleum reservoir is one whose permeability is equal to or greater than 100 mD.

Darcy's law is only valid for $Re \ll 1$ where Re is the Reynolds number which represents the degree of turbulence occurring in the length of the pathway and is given as

$$Re = \frac{\rho v l}{\eta} \quad (2.42)$$

where ρ is the fluid density and l is a characteristic length of the pore space.

As mentioned previously, environmental conditions can strongly influence permeability. One of the chief factors is the effective stress which depends on the confining and pore pressures. Increasing the confining pressure closes preferentially orientated cracks/pores, whilst increasing the pore pressure opens up pores/cracks which in turn increases the permeability. The combined effect of confining and pore pressure is shown below in Figure 2.25 which agrees with experimental work carried out on microcracks of intact granites (Batzle et al. 1980) and jointed granites (Brown and Scholz 1986). Also axial loading which occurs during brittle-deformation experiments is known to influence permeability. In such tests, both increasing and decreasing (Zhu and Wong 1997) permeabilities have been recorded during the dilatant stage of deformation with certain rock types giving both increasing and decreasing results (Zhu and Wong 1997). It is also possible in rock which is highly porous for dilatancy to be completely absent.

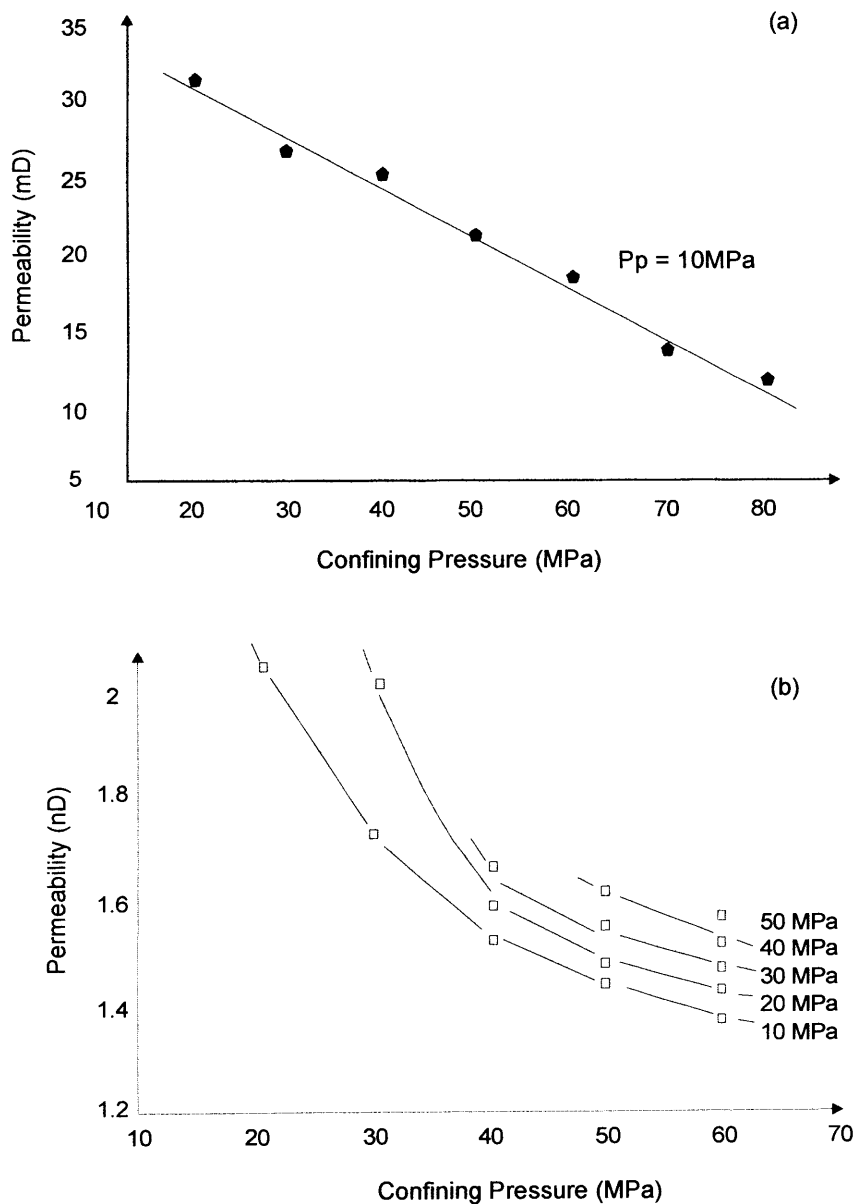


Figure 2.25: Influence of hydrostatic pressure on permeability for (a) isotropic pores and (b) pore and crack porosity of a sandstone (from David and Darot (1989)).

The transport properties in rock at room temperature can be modelled given the pore geometry which includes factors such as porosity, mineral shape and size, connectivity and tortuosity. A link between porosity and permeability is given by Walsh and Brace (1984) by the use of the equivalent channel model

$$k = C \frac{r_h^r \phi_p}{\zeta} \quad (2.43)$$

where K is permeability, ϕ_p is the porosity, r_h is the hydraulic radius, ζ is the tortuosity and C is a constant of 1/3 for cracks. Simulations carried out by Zhu and Wong (1996) using network models consisting of tubular pores suggest that while the accumulation of damage in the form of microcracks may dilate the pore space (increasing the porosity), it causes the flow path to be more tortuous and as a result, the permeability may actually decrease. Therefore, no direct link between porosity and permeability has been established.

Crack healing, plastic compaction and thermal cracking controls fluid transport at elevated temperatures. Experiments by Jones et al. (1997) on Westerly granite, Ailsa Craig microgranite and Icelandic basalt identified three phases of permeability (Figure 2.26). Phase 1) small amounts of cracking and little change in permeability associated with the closure of pre-existing cracks and grain boundaries as the minerals begin to expand. Darot et al. (1992) observed a 2-3 fold reduction in permeability in La Peyratte granite between non-heat treated and those heated to 125°C. Phase 2) permeability increases exponentially by over 2 orders of magnitude being associated with increases in emitted energy and the cumulative number of cracks. Phase 3) increase in permeability by over 3 orders of magnitude by enhancing the crack network with reduced AE due to relatively few new cracks formed. The porosity change from the same experiments is shown in Figure 2.27 where it can be seen that permeability is not solely due to crack density, but is more complex.

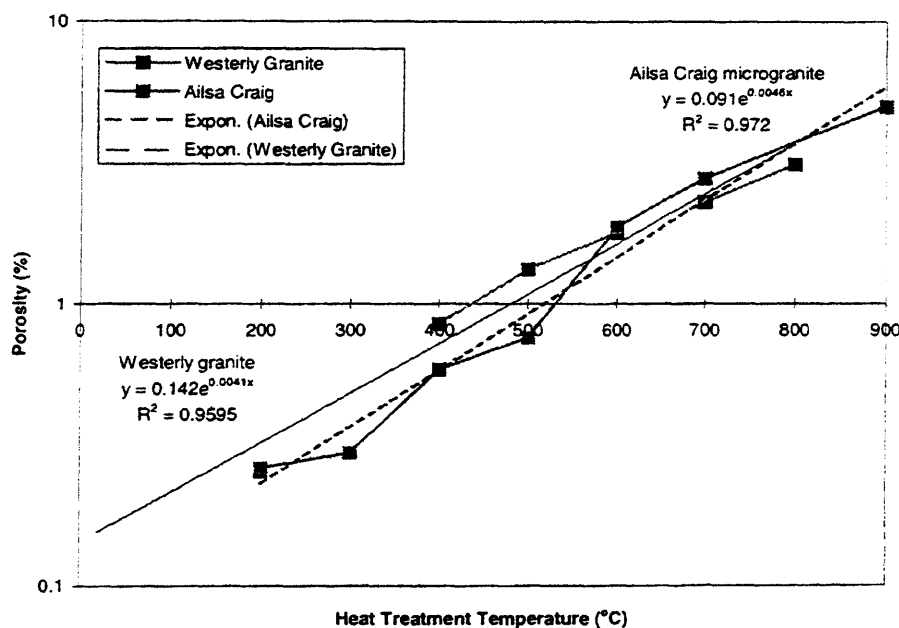


Figure 2.26: Relationship between permeability and porosity of granites heat treated at temperatures of 500°C and 600°C (from Jones et al. (1997)).

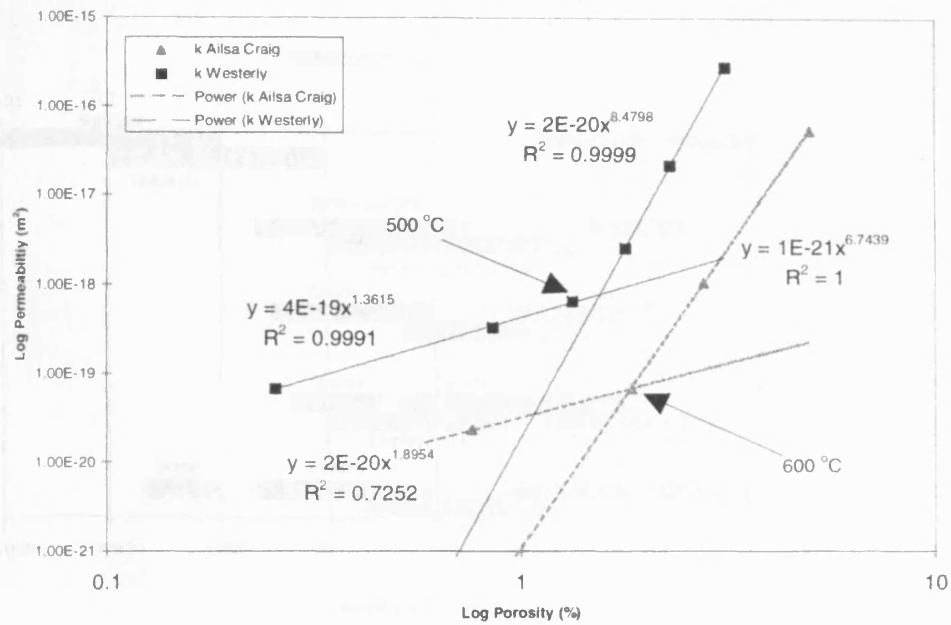


Figure 2.27: Effect of heat treatment of different granites on their porosity-permeability interrelationship with the lines showing the change porosity and permeability at temperatures of 500°C and 600°C. (from Jones et al. (1997)).

2.6.3 Electrical Conductivity and Resistivity of Rocks and Fluids

Conductivity and resistivity are important properties of rock which range by several orders of magnitude from $10^{-2} - 10^5$ in both mS/m and Ωm respectively. Long and Rivers (1975) note that the conductivity is of little importance relative to the porosity, moisture content and fracturing with the matter further complicated by the presence of clays (Dey 1986). Conduction in rock involves mechanical and electrochemical phenomena and can be calculated by

$$J_i = \sigma_{ij} E_j \quad (2.44)$$

where J_i is the electrical current density, σ_{ij} is the conductivity and E_j is the applied electric field.

In geological solids, conduction is mainly through diffusive ionic displacement given by

$$J_i = -D_p \frac{\partial \eta_f}{\partial x} + v n \quad (2.45)$$

where $D_p \frac{\partial \eta_f}{\partial x}$ is a flux due to diffusion (Fick's Law) and $v n$ is a convective transport term involving v the average particle velocity.

Typical values for conduction and resistance are given by Figure 2.28 where the minerals, rocks and fluid formations vary considerably and dramatically affect field measurements with a Wenner array giving values of ± 400 mV (Long and Rivers 1975) through electroseismic response.

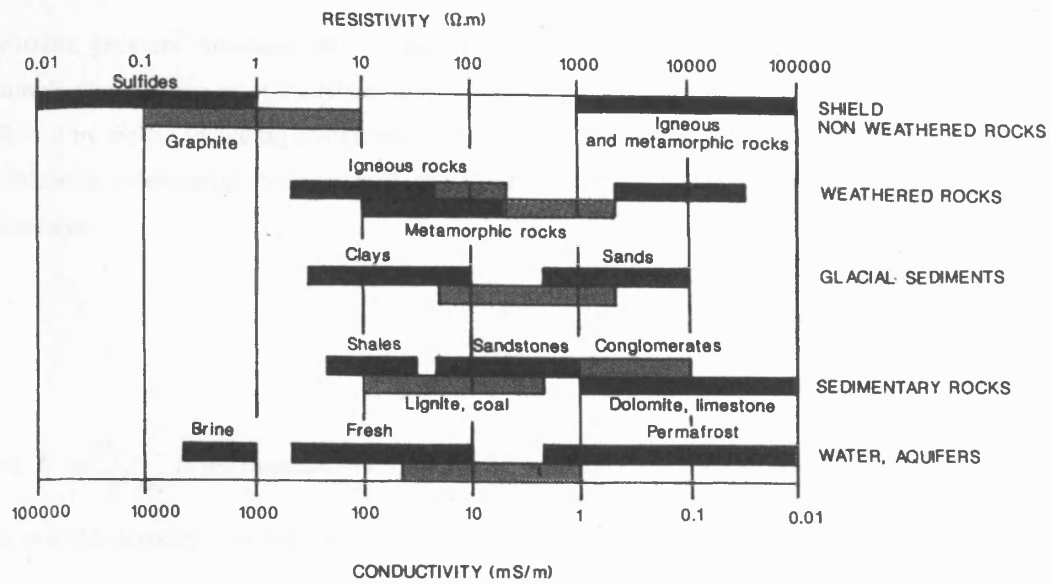


Figure 2.28: Typical values of conductivity and resistivity for geological materials (from Palacky (1987)).

As shown in Figure 2.29a, the properties of waters and aquifers vary considerably due to the presence of a variety of ions that include Na^+ , K^+ and Cl^- which typically move independently under an applied electric field. The effect of these ions on the rock varies by the size and concentration, with the latter occurring on the mineral surface affecting the salinity as shown in Figure 2.29b with more detail given in Chapter 3 on the actual mechanisms.

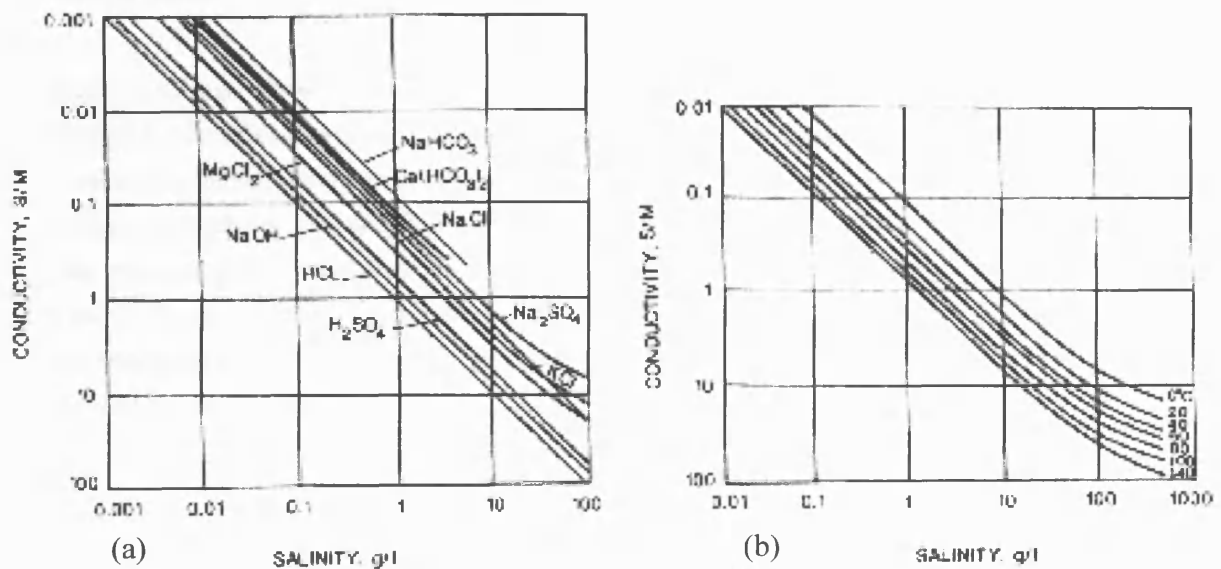


Figure 2.29: Conductivity as a function of fluid concentration for (a) different salts at 20°C and (b) for NaCl solution at varying temperatures (from Keller (1987)).

Hydrostatic Deformation

Hydrostatic pressure increases the d.c resistivity of saturated crystalline rocks by three orders of magnitude over a range of 1GPa (Brace and Orange 1966). This result suggests that electrical resistivity is affected by factors including cracks, pore aspect ratio and porosity of the rock. Archie (1942) proposed the following relationship between bulk and fluid resistivities in the absence of clays which can be expressed as

$$F = \frac{\rho_f}{\rho_r} = a\phi^{-m} \quad (2.46)$$

where $F = \rho_f / \rho_r$ is the formation factor, ρ_r is the resistivity of the rock, ρ_f is the resistivity of the pore fluid, ϕ is the porosity, a is the coefficient of saturation and m is the cementation factor. The formation factor can be related to tortuosity T by $F = T^2 / \phi$ where T describes the scattering of the potential field by the complex random geometry.

Surface Conductivity and the Effect of Clays

In early work it was believed that electrical conductivity and fluid movement occurred using the same transport system of the connected pore spaces. This has proven to be inaccurate through experimental investigation (Glover et al. 1994, Ruffet et al. 1995) and numerical modelling (Brown 1989). The actual process of electrical conduction relies on the development of a charged solid-liquid interface between the rock surface and fluid present known as the Electrical Double Layer (EDL) which is discussed in greater detail in Chapter 3.

Butler and Knight (1998) investigated the effect of clay (Kaolinite and Montmorillonite) on a steam zone formed in hydrocarbon recovery. It was found that clay had two mechanisms for increasing electrical conductivity through forming a highly conductive pathway and changing the water saturation zone. The surface conduction is dominant when low conductivity fluids are used (Bussian 1983, Glover et al. 1994). The mechanism involves conduction in the electrical diffuse layer, conduction in the Stern layer (See Chapter 3) and a fluid independent process operating on the mineral surface (Revil and Glover 1998). It has been shown that the value of surface conductivity extrapolated to low conductivity values is greater for rock containing higher percentages of clay as shown in Figure 2.30.

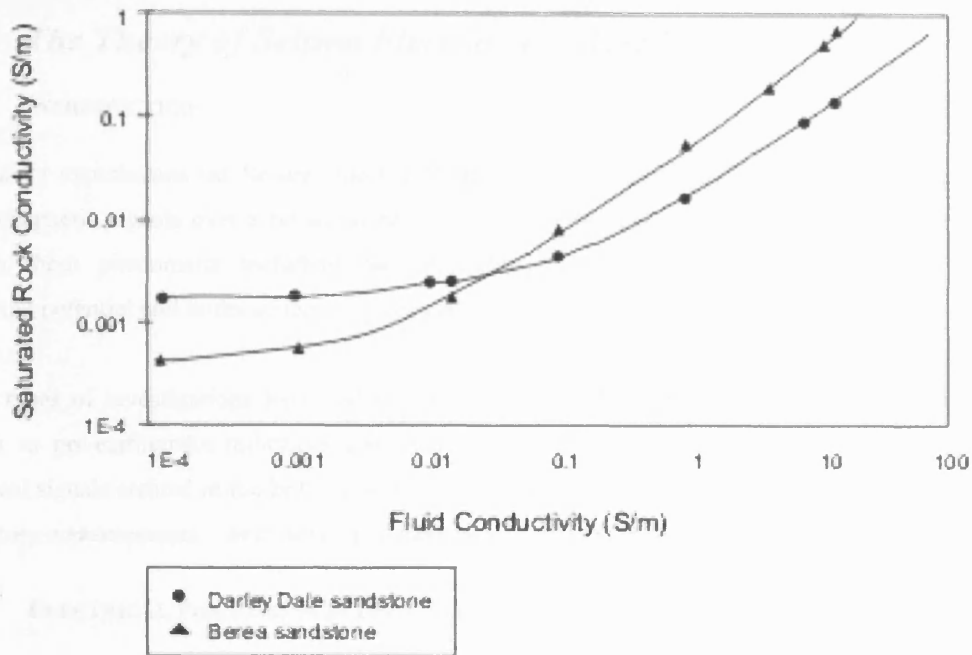


Figure 2.30: Saturated bulk conductivity as a function of fluid conductivity for a clay bearing sandstone, Darley Dale sandstone and a non-clay-bearing sandstone, Berea sandstone (from Glover et al. (1994)).

2.6.4 Electrical Conductivity of Rock at Elevated Temperatures

As well as the mineral composition and pore fluid chemistry, the temperature of the rock and/or pore fluid will also affect its conductivity and resistivity. This has been investigated by several authors including Somasundaran and Kulkarni (1973), Ishido and Mizutani (1981), Morgan et al. (1989), Dunstan (1994), Revil et al. (1999a, 1999b), Reppert and Morgan (2003a, 2003b). The results are inconclusive with the general consensus that the zeta-potential (discussed in Chapter 3) and hence electrical potential and streaming potential increases in magnitude with temperature. The problem in interpreting this experimental work on temperature effects is that the experiments have been done in various ways using differing chemistries and equilibrium conditions, and the significance of experimental problems such as electrical isolation is unclear.

2.7 CONCLUSION

In conclusion, there are several areas within current research that require further examination. At present, a comprehensive understanding of the mechanical conditions that lead to an earthquake is not fully known. This includes predicting earthquakes from precursory seismic, electric and magnetic data. Other issues with earthquake prediction include predicting the magnitude of the earthquake and the location of the event.

Temperature has been shown to affect the mechanical properties of various rock types. However, a thorough understanding of all the processes and their effect on the various electrical potential signals is not well known. This includes the effect of temperature on the EDL due to problems such as equilibration of the EDL. Through this thesis, I intend to address some of these problems, including the effect of deformation and temperature on electrical signals generated during deformation and look at the brittle failure mechanism.

3. The Theory of Seismo Electric Signals (SES)

3.1 INTRODUCTION

Laboratory experiments on Seismo Electric Signals (SES), include studies of electric, magnetic and electromagnetic signals over a broad range of frequencies. Various mechanisms have been proposed to explain these phenomena including piezoelectricity, contact electrification, exoelectron emission, streaming potential and faults acting as electromagnetic (EM) wave guides.

These types of investigations have had renewed interest with the SES forming the basis of electrical signals as pre-earthquake indicators and fluid flow monitors. This current research concentrates on electrical signals created in the brittle upper crust. This chapter discusses the SES by reviewing field and laboratory measurements. These developed theories will be used to interpret later experimental results.

3.2 ELECTRICAL PHENOMENA IN THE FIELD

3.2.1 Electrical Potential Investigation of the Crust

Throughout the Earth a large variety of crustal structures exist, from sedimentary basins, through igneous intrusions and metamorphic features. Geophysical investigations using electrical conductivity measurements can provide useful information about the subsurface, including the evolution of faults. Over a large period of time, the electrical conductivity and associated signals (e.g. magnetic, radio) may be altered by in-situ conditions. These can include changes in fluid concentrations, fluid transport, temperature, strain rate and stresses. All these different factors will affect the conductivity in different ways and by measuring these electrical signals in relation to other geophysical tools, the data can be modelled and used in similar sites. However, the investigation methods must remain constant with an array showing that different mediums produce different electrical potential readings.

In terms of the hydrocarbon industry, electrical conductivity and resistivity techniques are already used. This includes down boreholes, where the resistivity technique is used to analyse the lithology and can also be used to identify the presence of different fluids including oil which has a high resistivity. However, additional knowledge about how different factors found in boreholes can affect the electrical measurements would aid in determining oil reserves.

3.2.2 Electrical Signals Associated with Geological Hazards

Nitsan (1977) first reported that fractured quartz-bearing rocks were accompanied by a simultaneous change in electromagnetic field. These observations were confirmed by Warwick et al. (1982) who investigated stress-induced piezoelectric fields and used this phenomena to explain radio emissions ($2.56 \times 10^{-6} \text{ W Hz}^{-1}$) received shortly before the May 16, 1960, Chilean Earthquake. Derr (1973) reviewed mounting evidence for the phenomena of earthquake light and, luminescent phenomena associated with earthquakes. Within this paper (Derr 1973) are claims that the fluorescent lights were seen above quartz-diorite mountains some distance away from the rupture during the Matsushiro 1965 – 1967 earthquake

swarm. The conclusion was that the electrical disturbance was generated from quartz crystals in the rock formation.

The electrokinetic effect may be produced by fluid percolation in the crust, driven by a pore pressure gradient related to deformation. This model was first proposed by Mizutani et al. (1976) who assumed dilatancy prior to earthquakes (Nur 1972, Scholz et al. 1973) enhancing the permeability and allowing fluid flow to occur in the vicinity of the fault, thereby producing the streaming potential signal. Changes in ground water have been reported with observed increases in water discharge in many areas of an aftershock region. A direct consequence of this unsteady fluid flow may be the associated magnetic signals which may be caused by the electrokinetic, piezomagnetic and magnetohydrodynamic effects. The effect of fluid flow was modelled by Fenoglio et al. (1995) who calculated the magnitudes of the electrical and associated magnetic signals and showed good agreement with the signals recorded prior to the M_s 7.1 Loma Prieta earthquake of October 18, 1989. Fraser-Smith et al. (1990) also comment on the magnetic fluctuations (anomalous feature) increasing in activity which started 3 hours before the earthquake but they note that magnetic signals can only be seen for certain magnitudes. Numerical modelling mostly of the Nankai trough based on the linear relationship between pore pressure and streaming potential signals was done by Jouniaux et al. (1999). They examined fluids expelled from the accretionary prisms by measuring the electric and magnetic fields coupled with studies along the eastern edge of the accretionary prism showing that the fluid circulation is mostly related to the active fault and the near-surface highly permeable zones (Le Pichon et al. 1992). Geothermal activity associated with volcanic events has been investigated by Corwin and Hoover (1979) and Antraygues and Aubert (1993) who compared the self-potential anomalies in the field with laboratory tests and concluded that the self potential (SP) signals were associated with fissures and attributed to the thermal loss and gas release, i.e. indicating thermoelectric and electrokinetic effects may cause the observed signals.

The validity of claims of successful earthquake prediction were based on d.c. electrical potential measurements (Varotsos and Alexopoulos 1984a, 1984b), however, this was called into question by Geller (1996) and Kagan (1997). Gruszow et al. (1996) recorded signals near the VAN station but explained them as artificial (industrial) noise. These included the events of April 18 and 19, 1995 interpreted by the VAN group as SES precursors to the May 13 Kozani earthquake. Another problem with the VAN method is that signals similar to those reported in Greece have not been clearly observed elsewhere (Maron et al. 1993). There has also been no visibly associated magnetic variation (Pham et al. 1998). Also, Varotsos and Alexopoulos (1984a) identify electrical signals several hundred kilometers away from a 10 km source. In order for this to be valid, high dielectric paths and strong local amplification effects (Bernard 1992) must be present. With this discrepancy, a plausible theory is difficult to establish. However, calculations by Bernard (1992) on the evolution of strain perturbation inducing sporadic fluid flow which generates streaming potential signals with low frequency electric and magnetic precursors is plausible.

The main weakness in this area of study is the lack of understanding of the processes involved as self potential signals are influenced by many geophysical factors. In order to predict fault movement, numerous factors such as fluid flow and displacement must be included. Yamashita and Ohnaka (1991)

identified that ruptures do not always occur along pre-existing faults and that some earthquakes may be the result of shear fractures of intact rock masses. One possible solution is to conduct laboratory experiments and scale up the results to field scales. However, scaling issues then arise and the problem of accurately simulating in-situ conditions, given that collecting samples itself alters the conditions applied to the rock specimen.

3.2.3 Electrical Potential Exploration Methods

The 'electroseismic response' has been used to describe the change in electrical current with elastic deformation (Long and Rivers, 1975). Field observations of net potential gradients of 900mV have been recorded over a volcanic basement and explained in terms of electrical streaming potential produced by fluid movement. These results could not be correlated with other geophysical measurements and the magnitudes appear to be of the same order as theoretical electrical potentials calculated for surface measurements from crustal sources. Corwin and Hoover (1979) investigated the generation of a streaming potential through thermoelectric and electrokinetic coupling in laboratory experiments. The thermoelectric effect is due to a constant temperature gradient across the rock. This may cause differential thermal diffusion of ions in the pore fluid and electrons and donor ions in the rock matrix. When comparisons were made with field observation, it was deduced that these signals could be produced by these two phenomena. Recently however, signals observed at a geothermal well have been reproduced using an Gauss-Seidel iteration procedure incorporating pressure, temperature, vapour saturation, flow rate and ionic concentration (Ishido and Pritchett, 1999).

The electroseismic response has been investigated by numerous authors (Long and Rivers 1975, Thompson and Gist 1993, Russell et al. 1997, Mikhailov et al. 1997, Butler and Knight 1998, Zhu et al. 1999, Mikhailov et al. 2000). The generation of the streaming potential signal is most likely due to fluid flow which, in the case of a seismic wave follows Biot's theory, where a wave moves the electric dipoles on the mineral surface. This distortion of the surface produces an electrokinetic field known as streaming potential. This has the same time-dependent behaviour as the incident seismic wave and propagates to the surface of the earth where it can be detected. This electroseismic technique has been employed to investigate boreholes successfully with Zhu et al. (1999) recording an electric pulse induced by a Stonely wave. Other field studies including Long and Rivers (1975) showed that the position of the electrodes within an array affect the electroseismic signal. Thompson and Gist (1993) successfully detected an electromagnetic signal created by a seismic wave to a depth of 300 m and suggested the feasibility of using electrokinetic coupling for near surface measurements such as aquifers. For future studies, improvements suggested include noise reduction techniques (Mikhailov et al., 1997) and enhanced electrode characteristics (Beamish, 1999).

Pride and Haartsen (1996) identified that in a homogeneous porous material, the electrokinetic coupling produces a constant electric field confined to the seismic wave. Therefore, in a region of many layers, an electroseismic response would be associated with every interface. This suggests that all interfaces involve changes in signal and factors including the type of pore fluid (brine, water), rock type and microstructural properties (porosity and permeability) must be considered when interpreting an electroseismic response.

This is especially important with the formation of fractures during rock deformation which is investigated in laboratory experiments here.

3.3 LABORATORY INVESTIGATION OF THE ELECTRICAL PHENOMENA

To understand these field electrical signals and allow quantitative interpretations to be made, laboratory methods must be employed. Early experiments conducted without fluids under uniaxial stress conditions recorded electromagnetic signals due to fracture of piezoelectric minerals (quartz) and rocks (sandstone) (Nitsan 1977). Ogawa et al. (1985) also found that the fracturing of granite through the application of a bending force also produced electromagnetic emissions and Cress et al. (1987) calculated that the electrical dipole moment could be quantitatively explained using contact electrification or piezoelectric models.

Uniaxial deformation experiments have been carried out to look at the piezoelectric effect as a possible mechanism for generating the signals observed in the field. These results showed the electrical signals measured from granite to be approximately eighty times greater than serpentinite. This is confirmed in the dry fracture and slip experiments of Yoshida et al. (1994), where the signals from granite are approximately one hundred times larger than in gabbro. Sasaoka et al. (1998) found electric potential variation due to the piezoelectric effect (bound charges) depends on the magnitude and the sustained time of applied stress. With granite, the piezoelectric coefficient was found to be 3 times smaller than for a single quartz crystal. This was explained by the orientation of the crystals partially cancelling the signals. Yoshida et al. (1997) produced a quantitative model describing the relationship between pre-seismic and co-seismic electrical potential signals observed during stress drops, with and without slip, along a failure plane. Similar uniaxial deformation experiments showed clear electrical precursors seconds before the failure of the rock sample with Enomoto et al. (1992) highlighting the potential use of the signals in earthquake prediction. Several mechanisms were suggested to produce the signals observed, including charged particles and the movement of charged species. A greater understanding of how the rock deforms, especially around failure, is required to determine the mechanism for generating the observed signals.

Several authors (Mizutani et al. 1976, Bernard 1992, Fenoglio et al. 1995) have found electrical signals related to earthquakes. They conclude that the most likely mechanism to generate the electrical variation is the electrokinetic effect which was actually shown by Yoshida et al. (1998). When fluid flow occurs, the streaming potential signal is produced with the most important parameter of this theory being the zeta potential which is part of the Electrical Double Layer (EDL) discussed below in Chapter 3.4.2. The streaming potentials measured in the field correlate with changes in lake water levels, flood steam front displacements and fluid flow rates. Therefore, it can be assumed that a strong controlling factor on electrical potential signal is water movement. Early laboratory tests show the streaming potential varies linearly with applied fluid flow rate up to a pressure gradient across the sample of 9 MPa for porous sandstone and siltstone, after which a non-linear increase with incremental pressure is observed (Tuman 1963). The cause of this non-linearity is thought to be as a result of turbulent flow but it was realised by Tuman that this would be insufficient to explain fully the observed effects.

Ishido and Mizutani (1980) investigated the strength of rock in relation to the zeta potential. They found that the zeta potential which is a controlling parameter of the streaming potential magnitude had a positive correlation with fracture strength of quartz diorites. Temperature and chemistry have been shown to be an important part in the interaction of electric signals. Ishido and Mizutani (1981) demonstrated that the streaming potential coefficients increase with temperature in the range of 30-70 °C and decrease with saturating fluid pH. 2-3 times smaller than that recorded by Lorne et al. (1999b). Later studies on Westerly granite (Morgan et al. 1989) show temperature independence of the streaming potential coefficient for temperatures in the range 5-70 °C. Lorne et al. (1999b) demonstrated the effect of valence and the size of the ions of the zeta potential and noted the importance of additional chemical reactions taking place on the quartz surface. This was in agreement with the findings of Morgan et al. (1989) and Ishido and Mizutani (1981).

One of the key factors investigated is the link between streaming potential and permeability. Overbeek (1960) showed that there is no intrinsic link between the two factors once surface conductivity effects have been taken into account. Using intact samples of Fontainebleau sandstone, Jouniaux and Pozzi (1995a) performed triaxial deformation experiments and obtained a zeta-potential of -97 mV. The authors speculated that the link between permeability and streaming potential coefficient was true up to the onset of dilatant microcracks which occurred at approximately 72-86 % of the sample yield strength. Lorne et al. (1999a) propose a link based on the tortuosity of the hydraulic network increasing faster than the tortuosity of the electrical network during compaction with the increase in streaming potential coefficient up to failure being associated with dilatancy. Lorne et al. (1999b) used crushed Fontainebleau sandstone and obtained a zeta potential of -40 mV. This is less than Ishido and Mizutani (1981) and Morgan et al. (1989) with the difference in results reflecting differences in the processes at the electrolyte-quartz interface. At present no firm relationship has been established between permeability and streaming potential signals.

3.4 DEVELOPMENT OF SEISMOELECTRIC THEORY

3.4.1 The Piezoelectric effect theory

The piezoelectric phenomenon was first observed by Becquerel in 1920 who looked at the charge created by stretching a rubber band and hypothesised that the same effect occurred in crystals. Cady defines a piezoelectric crystal as ‘one that becomes electrified on squeezing; or as one that becomes deformed when in an electric field’. The former effect is known as the direct piezoelectric effect (equation 3.1) whilst the latter is the converse effect (equation 3.2). This interaction has been approximated by static linear relations between two electrical and mechanical variables governed by the following constitutive equations

$$S_i = s_{ij}^E T_j + d_{mi} E_m \quad (3.1)$$

$$D_m = d_{mi} T_i + \epsilon_{mk}^T E_k \quad (3.2)$$

where S_j is the mechanical strain, T is the mechanical stress, E is the electric field, D is the charge density, s is the mechanical compliance, d is the piezoelectric strain constant, ϵ^T is the permittivity, and the subscripts i, j, m and k indicate the direction of stress, strain or electric field. These equations have been

investigated in laboratory studies (Nitsan 1977, Warwick et al. 1982, Ogawa et al. 1985, Yoshida et al. 1994, Yoshida et al. 1998, Takeuchi and Nagahama 2005) in which electric signals associated with rock fracture, including electromagnetic emissions (EME) were measured. Recent work by Yoshida and Ogawa (2004) has shown that the piezoelectric effect is present in both wet and dry piezoelectric rocks such as granite.

A model to describe the generation of the electrical potential signal associated with stick-slip failure (Yoshida et al. 1997) is described below based on the initial model described in Yoshida et al. (1994). When a quartz crystal is electrically polarized in relation to the applied stress the polarization is defined as

$$p_i^0 = c_{ijk} \sigma_{jk}^0 \quad (3.3)$$

where p_i is the i th component of the polarization vector, c_{ijk} is the piezoelectric modulus of the third-order tensor and σ_{jk}^0 is the applied stress tensor. The polarization of the crystal depends on the axis relative to the applied stress. Initially the polarization is neutralised by compensating charges on the quartz surface (Figure 3.1a) stopping a measurable electrical potential signal from outside the rock being detected. When a rapid stress drop occurs ($\Delta\sigma_{jk}$) as with a stick-slip event (Figure 3.1b), the quartz crystal polarization expression is reduced:

$$p_i = c_{ijk} (\sigma_{jk}^0 - \Delta\sigma_{jk}) \quad (3.4)$$

Now, if the stress drop is greater than the relaxation time then the stress-induced polarization appears as an effective polarization P_{eff} given by

$$P_{eff} = p_i - p_i^0 = -c_{ijk} \Delta\sigma_{jk} \quad (3.5)$$

which can be seen outside the rock as an electrical signal with a polarity depending on the electrical axis of the crystal. Mobile bound charges move on the surface to neutralise the effective polarization (Figure 3.1c). This is known as the relaxation time which is defined as

$$\tau = \varepsilon_p / s \quad (3.6)$$

where the permittivity of ε_p and electric conductivity s decays exponentially with a relaxation time τ .

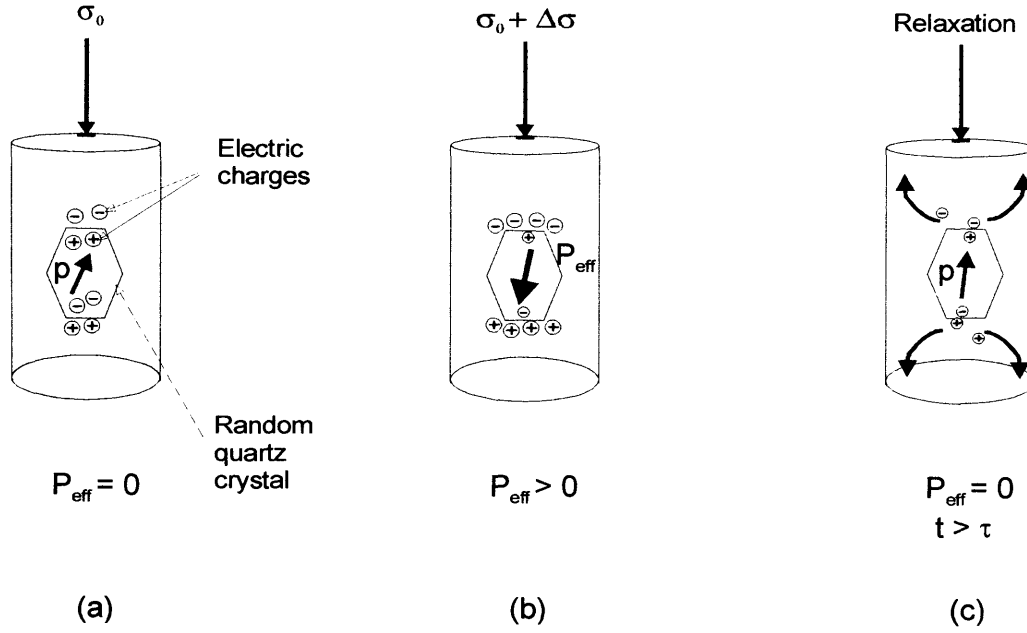


Figure 3.1: Initially stress induced polarisation of quartz crystals is (a) neutralised by mobile bound charges on the charge surface. A rapid stress change (b) induces an effective polarisation in the crystal, which decays (c) through a relaxation process with time constant $\tau = \epsilon/s$ where s is the conductivity (redrawn from Yoshida et al. (1997)).

The electric potential is summed up by the collective effective polarization of the quartz crystals in the rock sample. Equation 3.7 is a proposed theoretical relationship relating electric potential signals to quartz crystals, each of which is subjected to a stress change $\sigma_{jk}^{(m)}(t)$:

$$\varphi(t) = \frac{1}{4\pi\epsilon_p} \sum_m \frac{-b_v^{(m)} r_i^{(m)} c_{ijk}^{(m)} \sigma_{jk}^{(m)}(t) * g(t)}{|r^{(m)}|^3} \quad (3.7)$$

where b_v is the quartz volume, r_i is the distance to the measuring point, c_{ijl} is the piezoelectric modulus of quartz, σ_{jk} is the stress drop, ϵ_p is the permittivity of the medium and $*(g)$ represents the convolution of the inverse Fourier transform $i\omega/(i\omega + 1/\tau)$. From this equation it can be shown that the sign of the electric potential (EP) signal depends on the observational points.

3.4.2 The Theory for the Electrokinetic Phenomenon

Electrokinetic phenomenon involves a coupling between fluid flow and electrical current flow in a solid-liquid system. The theory rests upon the existence of a charged solid-liquid interface, known as an Electrical Double Layer (EDL), between the two phases, which is related to the electrokinetic properties of the dual phase system (Overbeek 1952). In a two-phase system of solid and liquid phases, the main electrokinetic effects involve charged flow. These are electro-osmosis, electrophoresis, and sedimentation potentials.

The Electrical Double Layer (EDL)

The Electrical Double Layer (EDL) is formed by the presence of a two-phase solid, consisting of a fluid and solid phase which interact together. With two phases placed in contact, an electrical potential difference develops with a number of mechanisms assumed to occur including ionisation of surface groups, absorption of species and dipole orientation. In the rock-water system the surface charge of the solid has a charge of one polarity, compensated for by the fluid phase having an excess of oppositely charged ions. These ions are distributed following a Boltzmann distribution pattern. Currently accepted theoretical models of the physical description were first developed by Chapman and further modified by Stern (1924).

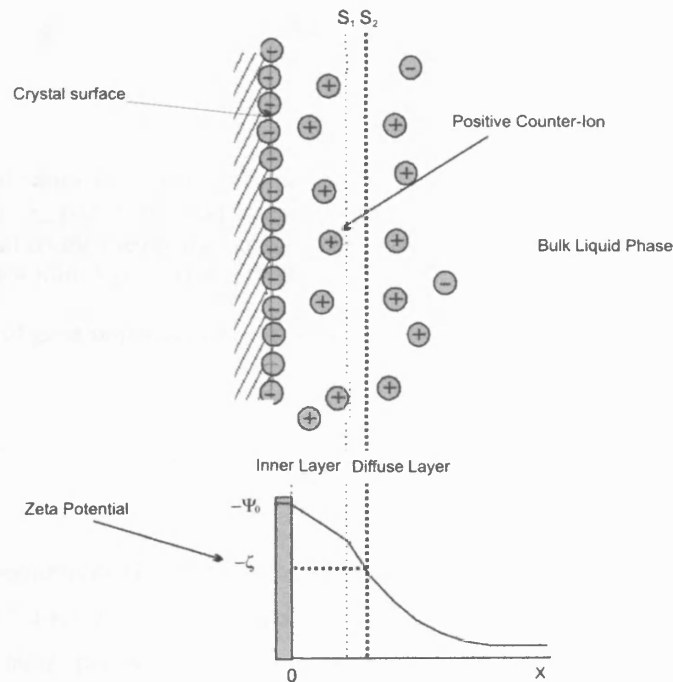


Figure 3.2: The Stern layer made up of a solid inner monolayer (S_1), diffuse outer layer (S_2) Bulk fluid phases and the position of the zeta potential in relation to the crystal surface. A decrease in the electrical potential with increasing distance from the crystal surfaces is observed.

The EDL can be subdivided into different components commonly grouped as the Stern layer shown in Figure 3.2. A more detailed breakdown of the different layers is given in Figure 3.3. The inner most layer is referred to as the solid inner monolayer which consists of a partially hydrated functional group made up mostly of anions (S_1). The outer layer is known as the diffuse outer layer (S_2) which contains hydrated counter-ions compensating the inner plane charge and is weakly held by the solid-liquid interface, being mobile when water flow occurs past the crystal surface. The outer layer extends out of the crystal into the liquid phase with a distance commonly referred to as the Debye length with surface mobilities as well as salinity affecting the proton transfer (Reppert et al. 2001).

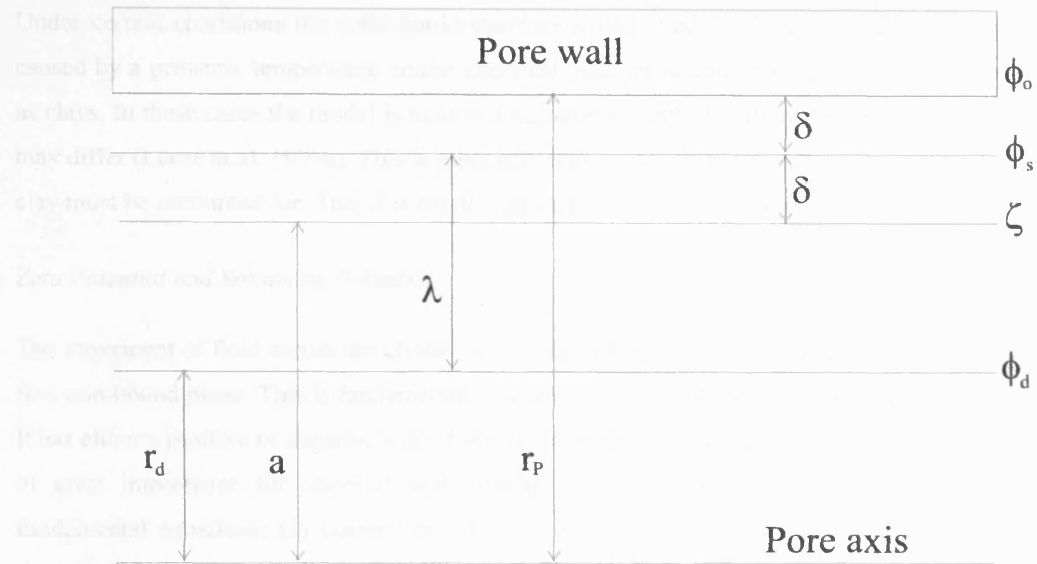


Figure 3.3: Critical distances inside of membrane pore, δ , anion radius; λ , Debye length; a , hydrodynamic radius; r_o , pore radius and r_d external radius of boundary diffusion layer: ϕ_o , ϕ_s and ϕ_d are the electrical potential on the membrane surface, Stern plane and at the limit of the diffuse layer; ζ is the zeta potential (redrawn from Molina et al. (1999)).

The Debye length is of great importance in calculating the extent of the EDL and is given by

$$k^{-1} = \sqrt{\frac{\epsilon_p kT}{e^2 \sum_i C_i z_i^2}} \quad (3.8)$$

where ϵ_p is the permittivity (F/m) of the fluid (7.09×10^{-10} for water), k is the Boltzmann's constant (1.381×10^{-23} J/K), T is the temperature (291 °K), e is the elementary charge of an electron (1.6×10^{-19} moles per m^3), C is the concentration (m^{-3}) and z is the valence of the ionic species. Note that the Debye length is proportional to the square root of the fluid resistivity, also note all the different factors which influence the Debye length including water conductivity (pH) (Jouniaux et al. 2000). Using this equation the Debye length is calculated under different conditions and the results tabulated below. From this table it is shown that an increase in temperature raises the Debye length, while an increase in valance and concentration of the fluid actually decreases the Debye length.

Temperature (K)	Debye length (m)
291	4.21994E-09
491	5.48152E-09

Valence	Debye length (m)
1	4.21994E-09
2	2.98395E-09

Concentration (m^{-3})	Debye length (m)
0.1	4.21994E-09
1	9.43608E-10

Table 3.1: Effect of temperature, valence of the species and concentration of the fluid on the Debye length given in meters.

Under certain conditions the solid-liquid interface is disrupted by fluid flow across the crystal surface caused by a pressure, temperature and/or chemical gradient and the presence of fine mineral grains such as clays. In these cases the model is modified because the paths for fluid flow and electrical conductivity may differ (Lorne et al. 1999a). This is especially true in clay rich rocks where the surface conductivity of clay must be accounted for. This is normally ignored for pure quartz rocks.

Zeta Potential and Streaming Potential

The movement of fluid across the crystal surface strips S_2 and replaces it with the zeta potential (ζ) at the first non-bound plane. This is fundamental to all electrokinetic phenomenon (Mazur and Overbeek 1951). It has either a positive or negative value for earth materials depending on the direction of fluid flow and is of great importance for colloidal and interfacial phenomena, including deposition. There are two fundamental equations: (1) Gauss's law describing the relationship between an electric field and total charge, given by

$$\nabla \cdot E = \frac{d}{dy}(E) + \frac{d}{dx}(E) + \frac{d}{dz}(E) = \frac{\rho}{\epsilon_p} \quad (3.9)$$

(2) The other equation relates the electrical potential and the electrical charge density

$$E = -\nabla \phi \quad (3.10)$$

Combining these equations, the second order partial differential equation known as the Poisson's equation is

$$\nabla \cdot \nabla \phi = \frac{-\rho}{\epsilon_p} \quad (3.11)$$

where ϕ is the electrical potential which has a value of ϕ_0 at the electrical interface, ρ is the charge density with an medium of electric permittivity ϵ_p . This equation describes the charge with the electrical potential spatially determined by the charge density.

The distribution of the ions in the liquid is described through the Boltzmann equation, given as

$$n_i = n_0 \exp\left[\frac{-z_i e \phi}{k_b T}\right] \quad (3.12)$$

where n_i is the concentration of either positive or negative ions of charge e and valence z , electrical potential difference ϕ with n_0 representing the ionic concentration of the bulk solution, T is temperature and k_b is Boltzmann's constant.

The space charge density ρ is given by the algebraic sum of the ionic charge per unit volume

$$\rho = \sum z_i e n_i \quad (3.13)$$

With this, the Poisson's equation can be re-written as

$$\Delta\phi = -\frac{I}{\varepsilon} \sum z_i e n_i \exp\left[\frac{-z_i e \phi}{k_b T}\right] \quad (3.14)$$

However, in the case of an overlapped EDL, the Poisson-Boltzmann equation is inaccurate. Qu and Li (2000) noting that the overlap of the EDL is important for interaction forces between colloidal particles, stability of colloidal systems, electrokinetic flow in fine capillaries plus other electrokinetic phenomena.

The model used to demonstrate the overlapped EDL field is given in Figure 3.4. Qu and Li (2000) identified that the application of the Poisson-Boltzmann equation may cause inaccurate results as such a treatment involves incorrect boundary conditions for a system containing an overlapped EDL field.

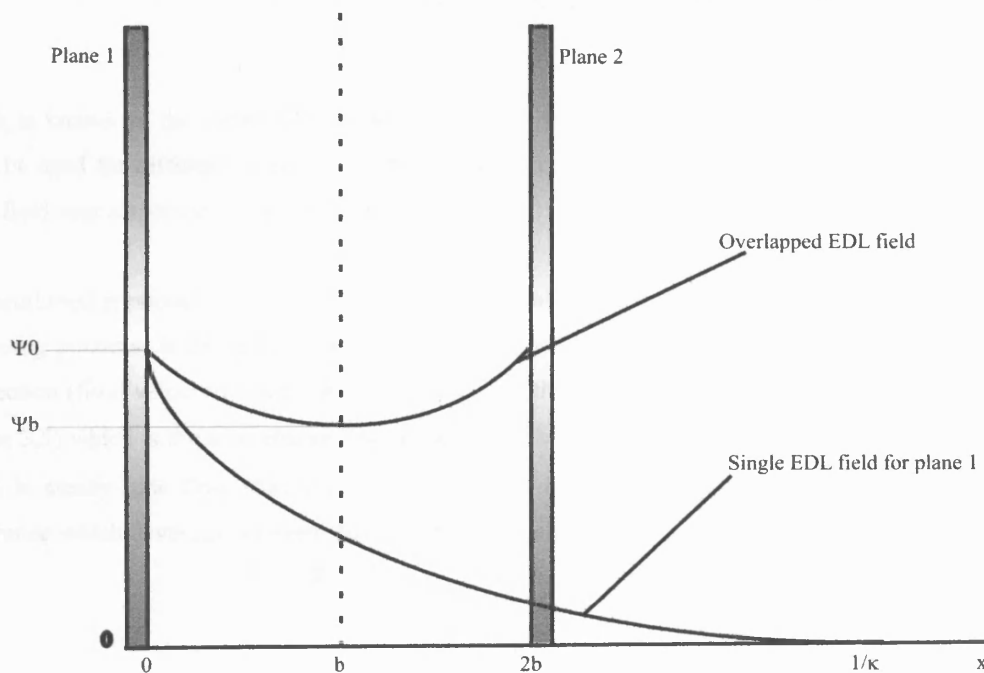


Figure 3.4: Schematic of the electrical potential distribution in the overlapped EDL field between two flat plates, where ψ_0 is the electrical potential at the surface, ψ_b is the potential at the middle plane, $2b$ is the separation distance between the two flat plates, and $1/\kappa$ indicates the thickness of the single EDL (redrawn from Qu and Li (2000)).

The Boltzmann equation requires an infinitely large aqueous phase so that the electrical potential is zero in the liquid at a certain point away from the charged surface. This cannot be so for overlapped EDL fields where the potential in the middle plane is not zero and the ionic concentration in the middle plane is different from the original bulk ionic concentrations.

The Poisson-Boltzmann equation is given by

$$\frac{d^2\phi}{dx^2} = \frac{2en^0}{\epsilon} \sinh\left(\frac{e\phi}{k_bT}\right) \quad (3.15)$$

with this equation being a second-order non-linear, differential equation, whose solution by Overbeek (1952) requires the following boundary conditions

$$\begin{aligned} \phi|_{x=0} &= \phi_0 \\ \frac{d\phi}{dx}|_{x=b} &= 0 \end{aligned} \quad (3.16)$$

Using this, an analytical solution is difficult to obtain. Therefore, an approximate solution is applied which says that if ϕ is small, and $\frac{e\phi}{k_bT} < 1$ then the Poisson-Boltzmann equation can be written as

$$\frac{d^2\psi}{dx^2} = \frac{2e^2n^0}{\epsilon k_bT} \phi \quad (3.17)$$

which is known as the Debye-Hückel approximation. With this, it is noted that the appropriate model must be used for different systems in order to obtain a better description of the surface charge and the EDL field near a specific solid-liquid interface.

As mentioned previously, the streaming potential depends upon the motion of fluid across the EDL. The streaming potential is the result of a balance between the three ion fluxes of electrostatic, chemical and convection (fluid velocity) forces. When movement of the EDL occurs, a current I is produced (shown in Figure 3.5) which is the total charge q with speed u_s . The convection is balanced by a conduction current when in steady-state flow (Reynolds number ≤ 1) is equal in magnitude and opposite. The potential difference which develops between the ends of the sample is referred to as the streaming potential.

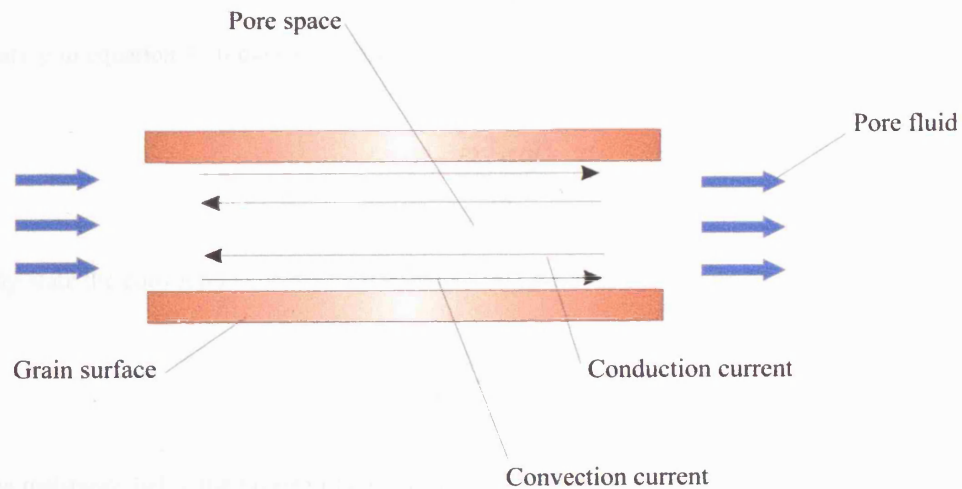


Figure 3.5: The effect of an applied pore pressure gradient across a cylinder resulting in the generation of convection (same direction of fluid flow) and conduction (opposite direction to fluid flow) currents required for streaming potential signals.

To derive the streaming potential, the effect of velocity down a capillary tube must be calculated. Flow within a capillary tube is governed by Poiseuille's equation relating the fluid velocity u as a function of distance x away from the wall, and this is given as

$$u = \frac{P(r^2 - x^2)}{4\eta l} \quad (3.18)$$

where η is the pore fluid viscosity and P/l is the pressure gradient.

The moving part of the EDL has a distance $(r - \delta)$ from the centre of the tube with velocity u_δ , therefore equation 3.18 can be written as

$$\begin{aligned} u_\delta &= \frac{P}{4\eta l} [r^2 - (r - \delta)^2] \\ &= \frac{P}{4\eta l} [2r\delta - \delta^2] \end{aligned} \quad (3.19)$$

As $\delta^2 \ll 2r\delta$ equation 3.19 can be re-written as

$$u_\delta = \frac{rP\delta}{2\eta l} \quad (3.20)$$

The velocity of the moving part of the layer can be stated as

$$I = 2\pi r q u_\delta \quad (3.21)$$

Substituting in equation 3.20 the charge distribution can be expressed as

$$I = \frac{\pi r^2 q \delta P}{\eta l} \quad (3.22)$$

In steady-state the convection current must be balanced by a conduction current which is given by

$$I_{cond} = \frac{\pi r^2 \sigma}{l} \Delta V \quad (3.23)$$

With the resistance being the inverse of conductance ($C=1/R$). Using Ohm's law, the streaming potential can be given as

$$V = \frac{Il}{\pi r^2 \sigma_f} \quad (3.24)$$

Substituting in equation 3.22

$$V = \frac{q\delta P}{\eta \sigma_f} \quad (3.25)$$

The zeta potential ζ can be expressed as

$$\zeta = \frac{q\kappa^{-1}}{\epsilon_p} \quad (3.26)$$

Assuming the Debye length (κ^{-1}) is equal to δ , the distance at which the diffuse layer sharing occurs can be expressed as $q\delta = \zeta\epsilon_p$. Substituting in equation 3.25, the streaming potential which applies in the case of low surface potentials (20 mV), can be expressed as

$$V = \frac{\zeta\epsilon_p}{\eta \sigma_f} P \quad (3.27)$$

With surface conductance mentioned previously in relation to clay minerals, a correction factor is required to account for this high surface charge. This is because the surface conductivity acts to enhance the conductivity of the diffuse zone and provides an alternative route for the potential signal, being more important for low pore fluid salinities. Taking this into account and with the return current being proportional to $\pi r^2 \sigma_f + 2\pi r \sum_s$ where \sum_s is the specific surface conductance Revil (1999) describes the streaming potential as

$$V = \frac{\epsilon_p \zeta}{\eta \left(\sigma_f + \frac{2 \sum_s}{r} \right)} P \quad (3.28)$$

where \sum_s is the specific surface conductance (Overbeek 1952).

Other important factors to be considered include the porosity and the tortuosity of the rock. The porosity represents the fraction of the rock exposed directly to fluid flow; the latter represents the reduction in fluid flow due to the fluid not following a straight path. Tortuosity is defined as $\tau = L'/L$ where L' is the real length and L is the apparent length of the path which the fluid travels along. In the laboratory it can be found as being equal to τ^2 / ϕ where ϕ is porosity. With this the streaming potential can be expressed as

$$V = \frac{\phi \varepsilon_p \zeta}{\tau^2 \eta \sigma_b} P \tag{3.29}$$

Note that C_s is not dependent on the geometrical properties of the rock and has been suggested by Jouniaux et al. (1999) could be used in interpreting field measurements.

In laboratory based experiments, streaming potential can be measured in several ways including using a d.c streaming potential where a constant induced pressure gradient across the sample is used as well as an a.c streaming potential with the voltage varying with time. The different techniques are shown in Reppert and Morgan (2001) with the different methods incorporating the streaming cross-coupling $\frac{\Delta V}{\Delta P}$ with the many factors related to the coefficient are shown in Figure 3.6.

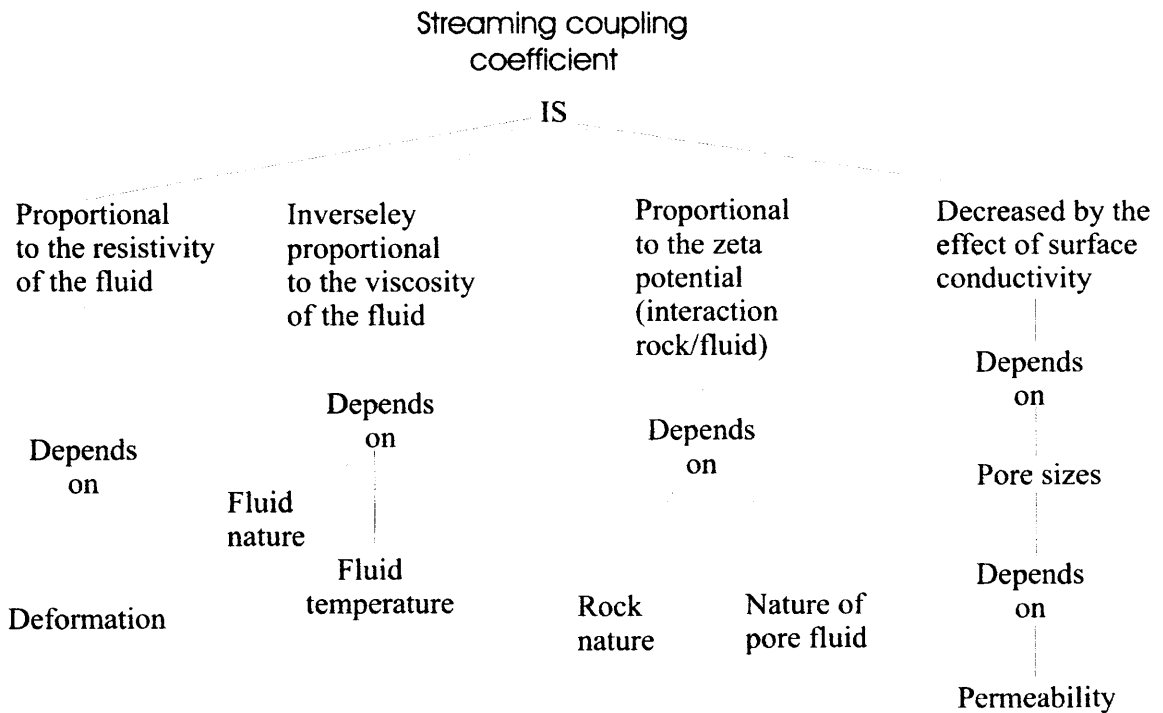


Figure 3.6: How the streaming potential coefficient is linked to different factors (redrawn from Jouniaux and Pozzi (1995a)).

The parameter that quantifies this coupling is the streaming potential coupling coefficient defined by

$$C_s = \frac{\Delta V}{\Delta P} = \frac{\varepsilon \zeta}{\eta \sigma_{eff}} \tag{3.30}$$

where ΔV is the voltage change generated by ΔP pressure gradient, ε is the electrical conductivity with ζ as the zeta-potential and η and σ_{eff} being viscosity and effective conductivity, which is defined by

$$\sigma_{eff} = F \sigma_r \tag{3.31}$$

where F is the formation factor and σ_r is the rock electrical conductivity of the pore fluid used in electrokinetic measurements. If the surface conductivity is negligible as in the case of rocks composed solely of quartz $\sigma_{eff} = \sigma_f$ then equation (3.31) will be written as

$$C_s = \frac{\varepsilon\zeta}{\eta\sigma_f} \quad (3.32)$$

which is the Helmholtz-Smoluchowski equation.

$$C' = \frac{\Delta V}{\Delta P} \sigma_f = \frac{\varepsilon\zeta}{\eta} \quad (3.33)$$

where C' is called the electrokinetic coefficient, ζ is the zeta potential, σ_f is the electric conductivity, ε and η represent the electric permittivity and fluid viscosity respectively. It can be seen from this that the Helmholtz-Smoluchowski equation is dependent on the ζ -potential of the rock.

Laboratory based experiments have been undertaken to look at different aspects of the electrokinetic phenomena, including the zeta potential, streaming potential and fluid flow interaction. Antraygues and Aubert (1993) looked at the properties of the ζ -potential. They found that the major factor governing ζ was the absorption reaction of H^+ ions with other important factors being mineral composition, temperature, pH and fluid conductivity. Jouniaux et al. (1999) mentioned an equation to describe ζ -potential using pH and fluid conductivity (C_f) with certain variables dependent on temperature only.

$$\zeta = c - dpH + b \log_{10} C_f \quad (3.34)$$

Using this equation, the magnitude of ζ -potential and streaming potential can be seen to increase with decreasing electrolyte concentration. Therefore, the largest signals for ζ and streaming potentials are associated with fresh (non-saline) fluid environments. Ishido and Mizutani (1981) also found that the surface electrical conductivity could influence and decrease ζ -potential. As fluid flow is normally required for investigating the streaming potential coefficient, the effect of the EDL on fluid flow was investigated by Liqing et al. (2001). It was found that the solid-liquid interface causes the flow behaviour in the microchannels to frequently deviate from their prediction of the traditional form of the Navier-Stokes equation. This is due to the conduction current, which moves the ions in the fluid, pulling the fluid in the opposite direction to the pressure-driven flow. The result of this is a reduced flow rate. Note that if the reduced flow rate is compared with the flow rate predicted by the conventional fluid mechanics theory without considering the presence of the EDL, it seems that the liquid would have higher viscosity. This is usually referred to as the electro-viscous effect.

The model described above deals with the EDL and the associated signal types and how they are produced, but that model does not take into account the molecular nature of the solvent. In order to address this issue, computational modelling has been used to investigate it in part. Previous calculations on the quartz surface have shown that four crystal surfaces are energetically favourable, namely the

{0001}, {10-10}, {10-11} and {10-1-1} with these surfaces studied in the presence of H₂O, NaOH and Na₂O using inter-atomic based models (de Leeuw et al. 1999). However, the modelling suggested here taken this a stage further to investigate the electrical double layer. The model presented by de Leeuw et al. (1999) was implemented with the computer code 'Metadise' (Watson et al. 1996), while my work used the DL_POLY2 program (Smith et al. 2003). DL_POLY2 allows for both 2D and 3D calculations, so that both the crystal structure and surfaces (and water/mineral interfaces) can be studied at the same computational level. The initial calculations involved investigating the behaviour of the inter-atomic potentials used by de Leeuw et al. (1999) with the DL_POLY2 code. This potential, denoted (1,) was derived by Sanders, and represents the effective inter-atomic forces by ionic, pair-wise potentials of the form:

$$U_{ij} = \frac{(Z_i Z_j)}{r_{ij}} + \phi_{ij} \quad (3.35)$$

where the first term represents the Coulombic (long-range) interactions between each pair of ions in the crystal, and the second term describes the short-range interactions in the Buckingham potential:

$$\phi_{ij}(r_{ij}) = b_{ij} \exp\left(-\frac{r_{ij}}{a_{ij}}\right) - \frac{c_{ij}}{r_{ij}} \quad (3.36)$$

where the fitted values of b , r and c are given in de Leeuw et al. (1999). In this potential formal charges (Si =+4 and O=-2) are used in combination with a shell model on the oxygen atoms to simulate the polarisability of [O]. In addition this model uses a three-body potential to induce directionality on the bonding around [Si]. The second potential (2) is the same as potential (1) but the oxygens are described without the shell model. The third potential (3) investigated is referred to as the Consistent-Valence force field (cvff) potential (Greathouse et al. (2002)). It describes the short-range term in the form of a Lennard-Jones potential:

$$\phi_{ij} = \frac{(A_i A_j)}{r^{12}} - \frac{(B_i B_j)}{r^6} \quad (3.37)$$

where A and B are fitted values for the specific ionic species (see Greathouse et al. (2002)). In the cvff-potential, partial charges are introduced to describe the polarisability of the system (Si = +1.32 and O = -0.66).

Employing the DL_POLY2 code it is found that only potential (2) gives reasonable results for the bulk and surface structures. Employing potential (1) the calculations at zero temperature and pressure give a reasonable structure of the quartz crystal. However, with the increase in temperature on this simulation, the shells “flew off” the oxygen ions. The cvff-potential (3) was investigated next and it was found that

the structural parameters of the surfaces always diverged, i.e. the structure “exploded” irrespective on the conditions applied to the initial surfaces.

At present this is as far as the modelling has reached as a problem exists with the potentials used to describe the water. The existing water potentials derived for the SiO₂-potentials described by (2) are not transferable into the official version of the DL_POLY2-code. The reason being is that the H₂O potential has a Coulombic subtraction term, which has not been implemented in the DLPOLY-code. However, this is being addressed and will be solved in the official version of DLPOLY in the near future.

Furthermore, the potentials have been investigated as a function of pressure to make sure that the calculations on the water/SiO₂ interfaces can be undertaken at elevated pressures.

3.4.3 Electrokinetic Coupled Phenomena

The coupling between electrical charge and the fluid flow can be described by

$$\begin{bmatrix} Q \\ J \end{bmatrix} = \begin{bmatrix} L_{11} & L_{12} \\ L_{21} & L_{22} \end{bmatrix} \begin{bmatrix} \nabla \varphi \\ \nabla P \end{bmatrix} \quad (3.38)$$

given for a capillary tube where Q is the fluid flux, J is the current density, φ is the electrical potential, P represents the fluid pressure and L_{ij} is the hydraulic coefficient, electrokinetic coupling and electrical coefficients. In the case of $i = j$ the equation becomes the generalised relation between flow and the direct forces. When $i \neq j$ the constants are known as the coupling coefficients and relate flow to the indirect driving forces.

These different coefficients represent important physical properties. L_{11} is the hydraulic mobility and L_{22} the electrical conductivity from Ohm’s law. And $L_{21} = L_{12}$ on the basis of the Onsager reciprocity is $-\frac{\varepsilon_p \zeta}{\eta}$ where ε_p is the permittivity, ζ the zeta potential and η is the fluid viscosity.

In a porous medium the electric current density I (A/m²) and the fluid flow J (M/s) are coupled according to the following equations which are directly related to the streaming potential and come from the expanded form of equation 3.38.

$$Q = -\frac{k}{\eta} \nabla P - \frac{\varepsilon_p \zeta}{\eta} \nabla \varphi \quad (3.39)$$

$$J = -\frac{\varepsilon_p \zeta}{\eta} \nabla P - \sigma_f \nabla \varphi \quad (3.40)$$

The properties involved in the streaming coupling coefficient include pore fluid properties and microstructural parameters, such as porosity and permeability. Therefore, it can be assumed that the electrical properties, such as the streaming potential may be sensitive to these changes.

With Sill's approach, it is assumed that the first term of equation 3.39 is the dominant factor controlling fluid flow, with

$$Q = -\frac{k}{\eta} \nabla P \quad (3.41)$$

the total current density (equation 3.40) can be given as

$$J_{total} = J_{convection} + J_{conduction} \quad (3.42)$$

If no external current sources exist and with the system in steady state between the gradients of primary and electric potential (i.e. $\partial/\partial t = 0$) then all the charge in the system is conserved, i.e., $\nabla \cdot J_{total} = 0$, and we can write the equation as

$$\nabla \cdot J_{conduction} = -\nabla \cdot J_{convection} = S \quad (3.43)$$

where S is an electrokinetic source. The significance of this electrokinetic source is that local convective sinks equilibrate the local conductive sources.

Substituting equation 3.40 into equation 3.43 the heterogeneity which causes the electrokinetic source can be found:

$$\nabla \cdot J_{conduction} = \nabla \cdot \left(\frac{\epsilon_p \zeta}{\eta} \nabla P \right) \quad (3.44)$$

$$\nabla \cdot J_{conduction} = \nabla \cdot \frac{\epsilon_p \zeta}{\eta} \cdot \nabla P + \frac{\epsilon_p \zeta}{\eta} \nabla^2 P \quad (3.45)$$

using equation 3.38 and substituting into equation 3.45 then

$$\nabla \cdot J_{conduction} = \nabla \cdot \left(\frac{\epsilon_p \zeta}{\eta} \right) \cdot \nabla P - \frac{\epsilon_p \zeta}{k} \left(\nabla \cdot \frac{k}{\eta} \cdot \nabla P \right) - \frac{\epsilon_p \zeta}{k} (\nabla \cdot Q) \quad (3.46)$$

From this it is possible to identify three sources which induce conduction currents from steady state flow. They are 1) position of a gradient across the cross coupling coefficient L_{21} 2) positions of change in permeability k and 3) source and sinks of fluid flow.

From the above equations there is strong evidence to suggest that the electric current responds to the heterogeneity of the rock. This assumes that the fluid and current flow have similar pathways. But it has been found that surface roughness can create different directions locally for fluid flow and electric current

in a single fracture or joint (Brown 1989, Glover et al. 1997). David (1993) used numerical modelling and found that different spatial patterns may exist for electrical and hydraulic pathways (Thompson and Brown 1991, Brown 1998) giving poor estimates of hydraulic flow in fractures using electrical analogues. It is noted here that all pores contribute to the permeability, however, very tiny pores or conducting mineral phases such as sulfides or carbon may contribute to the electrical conductivity but not to the fluid flow. Lorne et al. (1999a) note that when a pore collapses (i.e. during compaction) a secondary route is used, thereby linking permeability to tortuosity with a conceptual model of tortuosity and streaming potential and showing how they may change. Therefore, caution is required in permeability prediction from electrical current measurements at any stages of deformation. Avellaneda and Torquato (1991) accounted for this by producing a more accurate model involving information about how electrical and momentum transport were derived, which provides a rigorous link between permeability and electrical conductivity.

The effect of temperature on the electrical potential signals such as ζ -potential and the streaming potential coefficient has been investigated by authors including Ishido and Mizutani (1981), Morgan et al. (1989), Revil et al. (1999a,b) and Reppert and Morgan (2003a,b). The results collected from static tests show that the ζ -potential either increases, decreases or remains constant (Reppert and Morgan, 2003a) with increasing temperature which creates a debate as to what actually happens. The absence of a link between the ζ -potential and temperature by Morgan et al. (1989) is explained by the rock not reaching thermal equilibrium (Ishido and Mizutani, 1981). With Revil et al. (1999a), an increase in ζ -potential with temperature is seen where the rock is allowed 48 hours to reach equilibrium. Therefore, thermal equilibrium is an important factor in relation to the ζ -potential signal.

3.5 CONCLUSIONS

In terms of geohazards, earthquake prediction is considered important. With the debate about the viability of the VAN method, further laboratory investigation is required to investigate the limitations of the electrical signals and how the data can be best used. This includes simultaneous measurements of volume change, pore fluid chemistry, temperature and strain rate on both electric and magnetic signals produced during all stages of brittle deformation.

The two main mechanisms believed to be responsible for the generation of electrical signals within the crust and in the laboratory are the piezoelectric and electrokinetic phenomena. Recent evidence shows that the piezoelectric effect occurs in both saturated and dry piezoelectric rocks, but little is known about how this phenomena reacts with the electrokinetic effect. Therefore, further study is required to look into the relationship between these two mechanisms. The effect of crystal size and shape needs to be examined in terms of the piezoelectric effect so that pure sandstones can be modelled. Papers by Ishido and Mizutani (1981), Jouniaux and Pozzi (1995a) and Lorne et al (1999a) have investigated the streaming potential and the zeta potential in relation to pH, size, composition, porosity and permeability. However, further investigation is required to identify how the different parameters interact together during deformation.

At present, existing experimental studies on the effect of temperature on the electrical potential signal have been performed using static tests where no loading of the sample occurs. Therefore, an area which needs investigating is the effect on deformation of the different types of electrical signals produced. Present models which deal with the effect of temperature, pressure, chemistry and fluid flow are based on experimental results and empirical equations. In the current context at present, no existing models have looked at the atomic interactions of the EDL at the molecular level. This needs to be addressed with molecular analysis of the solid-liquid interface and how different factors such as salinity, pressure, temperature and pH affect it. This can then be used as a basis of comparison with existing experimental data to help in our understanding of the thermo-chemo-mechanics of faults, and as a basis for scaling up to investigate aquifers, geothermal reservoirs and earthquakes.

4. Experimental Equipment

4.1 INTRODUCTION AND GENERAL DESCRIPTION OF APPARATUS

The experimental apparatus used for the majority of my experiments is a triaxial rock deformation and rock physics cell (Figure 4.1), which is located in the Mineral, Ice and Rock Physics (M.I.R.P.) laboratory at University College London. The apparatus was specially designed by Peter Sammonds to enable sophisticated rock physics measurements to be made concurrently with rock deformation.

This particular cell has been designed to simulate crustal environmental conditions to depths of around 20 km. The pressure vessel apparatus (Figure 4.2) has been built to contain pressures up to 400 MPa, with a variety of axial stresses up to 1200 MPa. Generally, for the present experiments, strain rates of 1.5×10^{-7} to $1.5 \times 10^{-4} \text{ s}^{-1}$ were used with differential stresses ranging from 30 to 200 MPa. The confining medium used in the cell was hydraulic silicone oil. This oil was chosen for specific reasons: 1) It has a low coefficient of volume expansion (Table 4.1); 2) The flash point is above 150°C; 3) Silicone oil does not conduct an electrical charge which would interfere with electrical investigations. In the region where the confining pressure is located, an electric furnace was established which required electrical connections to a control unit outside. The various components of the furnace, intensifiers and actuator are discussed in more detail in the relevant sections. The actuator is employed to regulate the load applied to a rock specimen, which could be load or displacement controlled. Pore fluid, consisting of deionised water, comes from a pore pressure intensifier similar to the confining intensifier and can produce up to 400 MPa with a volume of 10cm³. Pore fluid is required for the investigation of the electrokinetic phenomenon via the formation of the EDL discussed in Chapter 3.4.2. Intensifiers employ the principle of a moving piston with a large surface area forcing fluid through a small hole, thereby producing a high pressure to displacement ratio. With the rock specimen inside the pressure vessel, a rubber jacket is used to hold it in place. This also prevents confining oil from entering the specimen. Concave inserts, (discussed in detail in Chapter 6.3.1) are required to measure Acoustic Emissions (AE) and electric potential. Holes are present in the jacket wall containing the inserts that when excited, seal the holes and maintain the relevant pressures. The control unit used for monitoring and adjusting all the experimental variables is shown in Figure 4.1. This is located next to the triaxial cell. The axial stress, confining pressure, pore pressure and the strain rate can be independently controlled. All data logging is done by LOCAN AE for acoustic emissions and Labview software for all other data including parametrics and electrical signals.

Additional equipment designed during my research to investigate the effect of temperature on the rock specimens includes an electric furnace and two fluid separators. The development of this equipment is discussed in Chapter 5.

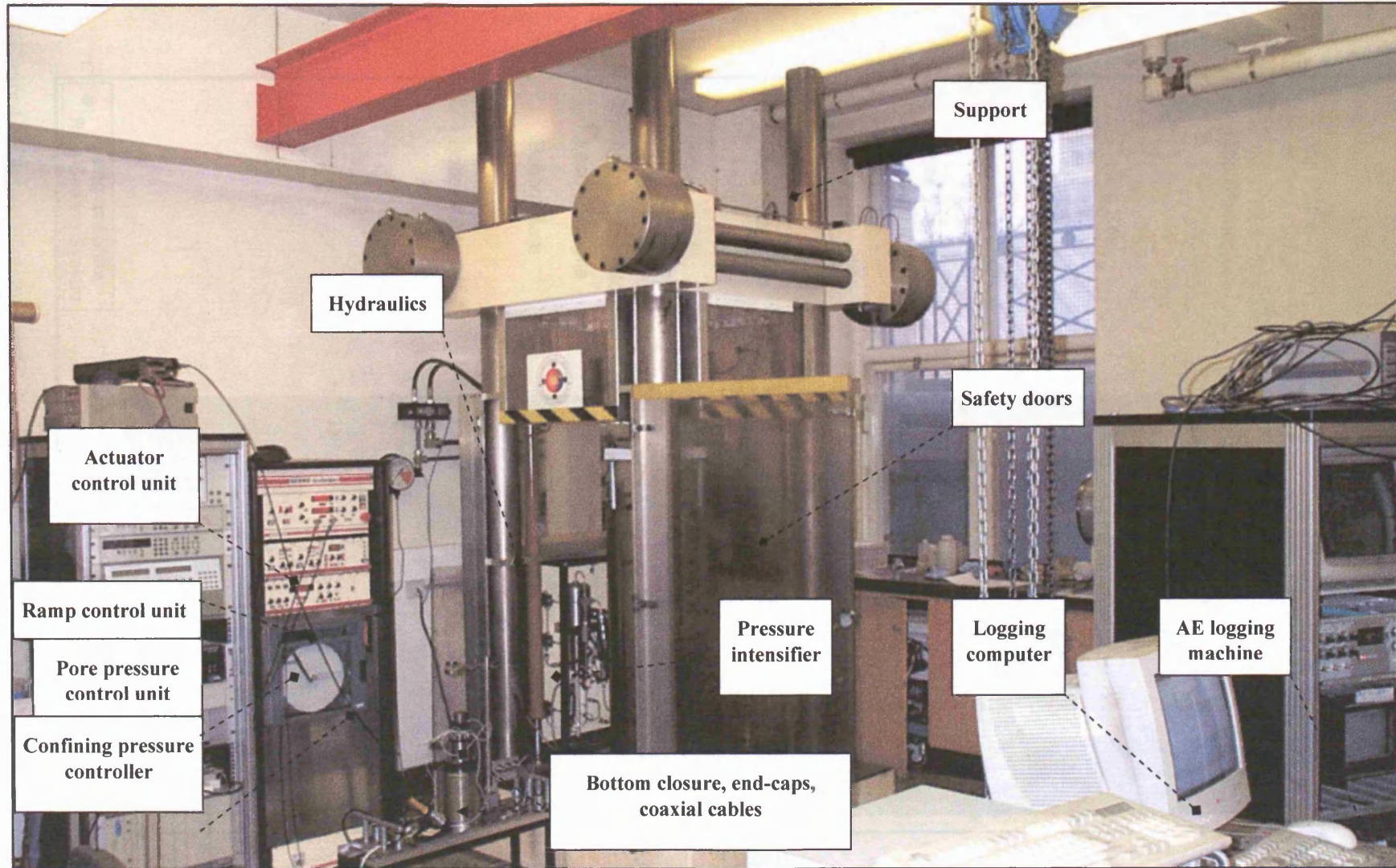


Figure 4.1: Photograph of the laboratory containing the triaxial pressure vessel.

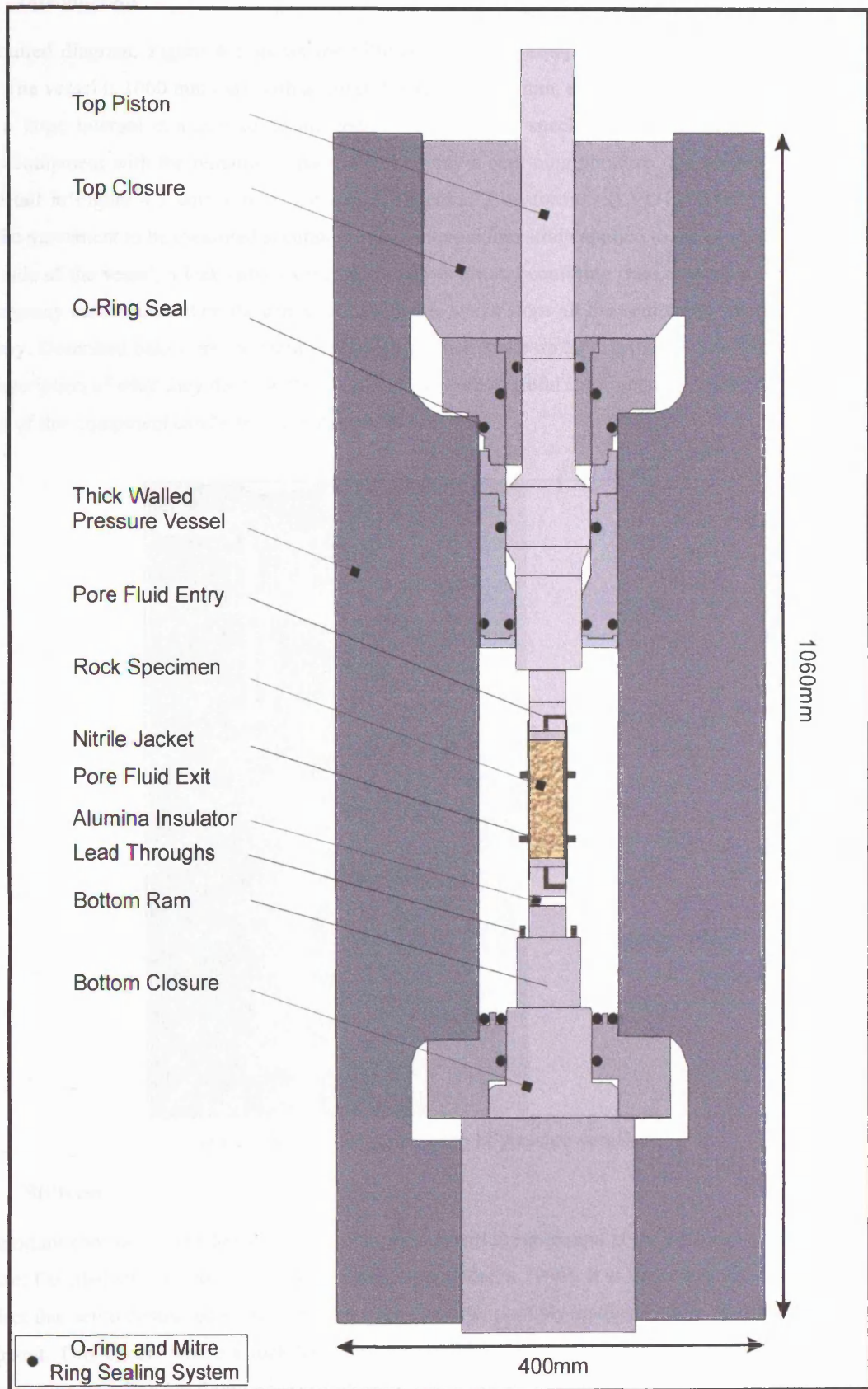


Figure 4.2: Diagram of pressure vessel showing all components and seals. Taken from Clint (1999).

4.2 TRIAXIAL DEFORMATION APPARATUS

4.2.1 Introduction

The detailed diagram, Figure 4.2 shows the different pieces of equipment that make up the pressure vessel. The vessel is 1060 mm long with an outer diameter of 400 mm, and weighs approximately 750 kg. It has a large internal diameter to accommodate various sized specimens, internal furnace and rock physics equipment with the remaining space used to apply a confining pressure. The vessel is shown in more detail in Figure 4.3 with Linear Variable Differential Transformers (LVDTs) fixed to the ram to allow the movement to be measured accurately and converted into strain applied to the sample. Positioned on the side of the vessel, a leak valve exists which allows air and confining fluid to drain away. There is an emergency button located on the central control panel which stops all the equipment should this prove necessary. Described below are the main components which make up the triaxial system, together with a brief description of what they do, how they work and any other useful information. Further details on the running of this equipment can be found in Appendix 1.

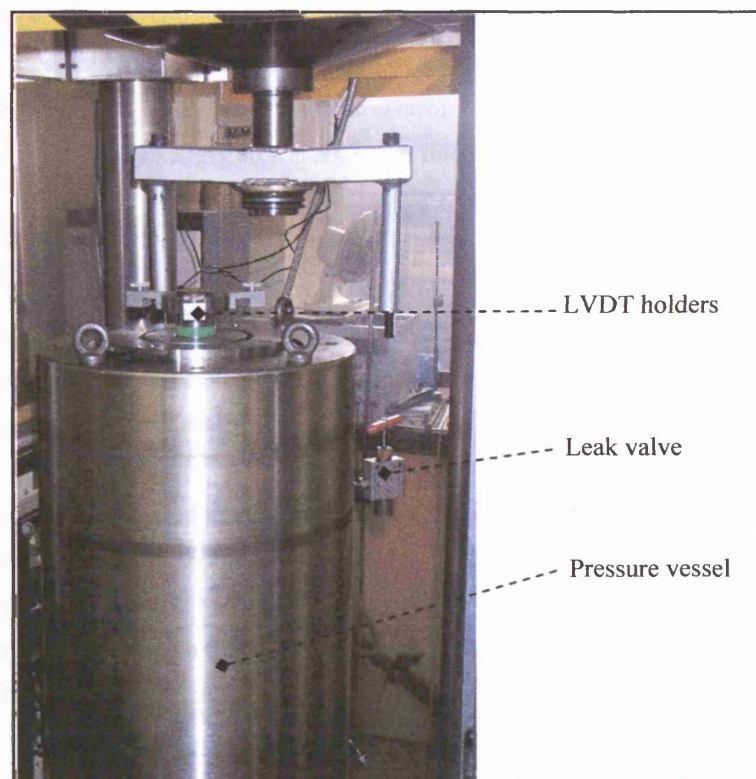


Figure 4.3: Detailed photograph of pressure vessel.

4.2.2 Stiffness

An important consideration when dealing with servo-controlled equipment is the stiffness encountered in their use. Detailed studies have been done on this topic (Odedra 1998). It is important when considering the effect that servo controlled stiffness has on a rock sample, possibly leading to false readings during an experiment. This occurs where a rock has a certain stiffness prior to failure, with the ram containing a different value, at a low confining pressure. Where a failure plane develops, stiffness of the ram becomes larger than the sample. Even though a feedback loop exists within the control unit to respond to changes caused by the effects on the crushing rock, the response is not instantaneous and this is where errors may

occur. If, however, the controls are set correctly there is no release of uncontrolled energy, which in the form of rapid movement along the fault, could cause further errors.

4.2.3 Actuator

The actuator is located directly above the pressure vessel in order to control the ram used to apply the axial stress to the sample inside the vessel when confining pressure ($\sigma_2 = \sigma_3$) is also present. It can be controlled by several different techniques, either load transducers, a large actuator LVDT or smaller more accurate LVDTs.

The maximum load which can be applied during any experiment is 150 tons over the surface area of the 40 mm diameter sample producing, a maximum stress of 1193 MPa and a corresponding voltage of 10 volts. To calculate stress, a calibration (see Chapter 6.4.2.4) is required to convert the data from volts to MPa. Generally, for my series of experiments, the stress applied was lower than 200 MPa converting to less than 2 volts. Such low stresses were used to replicate reservoir conditions discussed in detail in Chapter 2.2. In summary, the reservoir conditions being replicated are for those less than 4 km in depth and having confining pressures of approximately 125 MPa and pore pressure of approximately 50 MPa resulting in an effective pressure of 75 MPa. If load control is used a creep test can be investigated. Usually extension control is used to apply a constant strain rate to fail the sample using LVDT's which are discussed later.

Positioned above the ram, inside the crosshead, a large LVDT accurate to 0.1 volts is present which is used to bring the ram down quickly to an initial position just above the specimen. For more accurate measurements required during experimentation, two LVDTs attached to the ram (Figure 4.4.) are used with an average voltage accurate to 0.01 volts.

In extensional control, LVDTs are used in a feedback loop. The movement of the actuator can be altered to maintain a constant strain rate set by the ramp generator. Feedback control becomes more important around the time of dynamic failure and thereafter as the movement of the fault may vary due to frictional sliding. With the ramp generator set at a low strain rate it becomes more difficult to control due to friction of the seals, ram and the stiffness of the servo-controls.



Figure 4.4: Photograph of LVDT's attached to top of the pressure vessel.

4.3 PRESSURE APPLICATION SYSTEMS

4.3.1 Hydraulic Oil

The silicone oil used as a confining medium was purchased from Dow Corning Ltd. This particular oil (Table 4.1) has a low coefficient of volume expansion, relatively high boiling point and is non-conductive.

Property	100 cS Silicone Oil
Specific Gravity	0.960 (25°C)
Coefficient of Volume Expansion	0.00096
Surface Tension	20.9 (25°C)
Flash Point	150°C

Table 4.1: Physical properties of 100 cS silicone oil at room temperature and pressure.

4.3.2 Piping

To use the intensifiers and pumps, pressure piping was needed to connect the various parts of the rock physics apparatus together. All piping had an internal diameter of $\frac{1}{16}$ in and could maintain a pressure of 400 MPa. As mentioned previously, electrical isolation is required for studying the electrokinetic phenomenon and for this reason the pore pressure piping was covered with non-conductive polyolefin heat shrink.

4.3.3 Intensifiers

To control the pore pressure accurately within the vessel, intensifiers are used in conjunction with the confining pressure pumps. The principle of how they work is a large piston pushing fluid through a small hole, thereby producing a large volume to area ratio. A photograph of one of these intensifiers is given in Figure 4.5 showing the displacement and pressure transducers

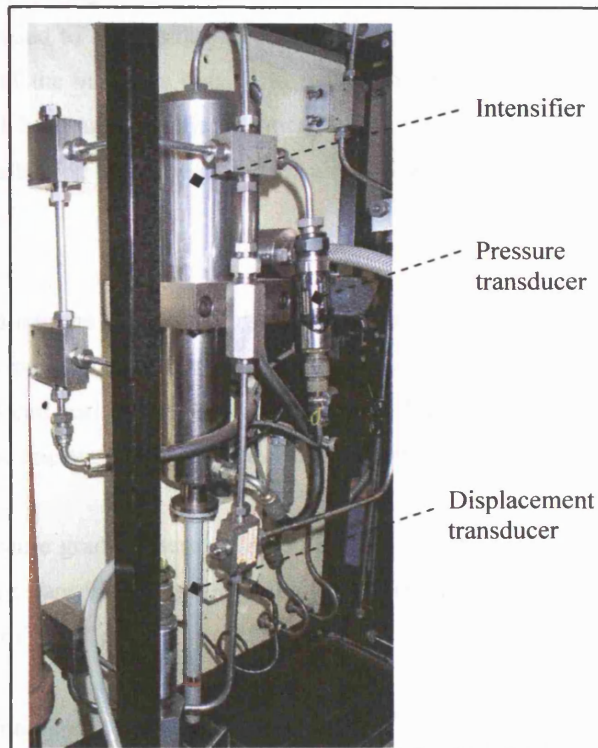


Figure 4.5: Photograph of the pressure intensifier with pressure and displacement transducers.

In order to prime the intensifiers, a priming pump is used to force pore fluid into the intensifier, thereby moving the ram backwards into the initial starting position and allowing the maximum amount of volume to be pushed into the sample. The volume for the intensifiers shown is 10 cm³, and if further fluid is required, it is isolated, re-primed and reconnected back to the sample.

These intensifiers can be controlled by either displacement transducers which hold the piston in place, or pressure transducers which maintain a constant pressure by moving the piston forwards or backwards. The output from both types of transducer is given in voltage ranging from 0-10 V. In order to convert these voltages into S.I. units a calibration is performed prior to testing. This procedure is described in more detail in Chapter 6.4.2.

4.3.4 Control Unit

All controls, including those for the furnace, intensifiers and actuators are located next to the triaxial machine. In most cases, a signal conditioner is located in series between the control unit and the equipment to improve the voltage signal to noise ratio and to smooth out the data. This set-up avoids contamination of the signal by outside electrical interference from nearby industrial equipment. To

maintain control of variables such as pore pressure, load and displacement, feedback loops exist which transmits the relevant signal to the appropriate equipment causing minute adjustments to be made.

4.3.5 Confining Pressure

To pressurise the vessel a two-stage process is used. Initially, the large hydraulic confining pump fills the vessel, expelling all the air through the relief valve. At this stage the relief valve is closed and the confining pressure is increased to the desired level, at which point the isolation valve is closed. If the pressure is too high, one of the valves is opened to reduce the pressure. However, for more accurate confining pressures e.g. 0.1 MPa an intensifier identical to the pore intensifier may be used which has a volume of 20 cm³ thereby allowing it to move forwards and backwards.

4.3.6 Pore Pressure

Pore pressure is introduced into the sample through both end-caps which are attached to two intensifiers. The connecting pipe work passes through the bottom inner closure leading to two termination fittings. The 20° cone shaped ends can seal the pipes to the end-caps. All the pipe work is electrically isolated along with the end-caps, the reason for this is discussed in Chapter 4.3.7.

Applying a pore fluid pressure gradient across the sample allows the permeability to be calculated. For this type of test the pressure transducer attached to the intensifiers needs to be accurate and steady which was achieved with the use of signal conditioners.

4.3.7 Electrical Isolation

Electrical isolation is important in obtaining electrical potential readings because background noise could obliterate any signals present. To achieve the desired goal all metal surfaces are required to be electrically grounded to the cell wall except for the pore pressure piping which needs to be isolated. During the running of normal experiments, the bottom end-cap contains a non-conducting ceramic disc placed between the end-cap and the pressure piping end-cap to prevent electrical leakage, whilst the top of the sample is grounded by the ram. This set-up allows a potential signal gradient across the sample and aids certain forms of investigations. To achieve this, the pore pressure piping must be isolated which is achieved by covering it in heat shrink and having plastic layering between connecting screws.

The electrodes used to measure the electrical charge are located on the steel inserts which are placed around the sample inside the jacket wall. Four electrodes are used with an AE transducer on either side (see Appendix 2) above and below the electrode to relate changes in EP signal to rock properties. The electrodes are 25 mm in from the ends of the jacket.

4.4 MEASUREMENTS AND DATA LOGGING

4.4.1 Data Logging

Two separate programs were used to log the data. The LOCAN program records multi-channel AE data given in voltages, calculating the count, rise, energy, duration, amplitude and frequency of the AE signals

produced by the piezoelectric transducers responding to changes in the rock specimen. Electrical measurements are recorded using Labview. These programs are used simultaneously so that all the data can be compared. The equipment involved in the triaxial experiments e.g. ram, displacement, confining pressure, pore pressure, pore volume, strain rate, temperature and resulting acquisition of data is demonstrated in Figure 4.6.

The parametric data obtained from the apparatus was collected with the use of a National Instrument (NI-6135) Card. It records signal voltages from different channels of the equipment and electrodes attached to the rock sample and together with the calibration data collected, as described in Chapter 6.4.2, the software converts it to S.I. units.

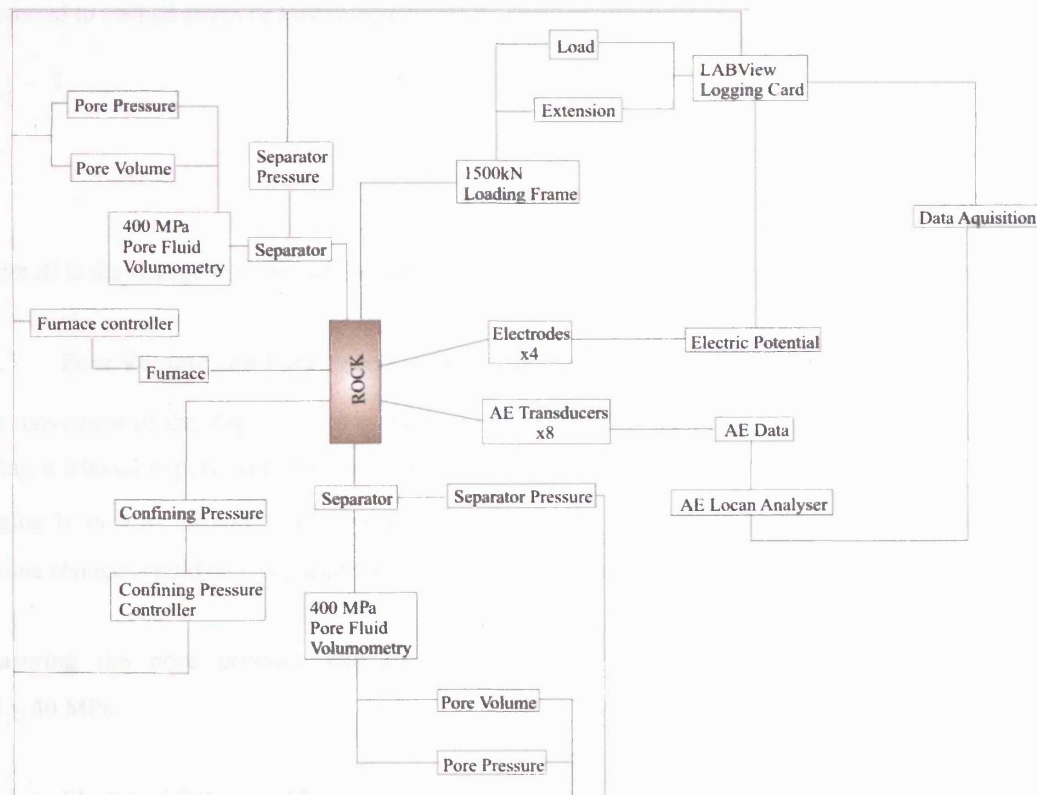


Figure 4.6: Block diagram showing all instrumentation involved in a triaxial deformation experiment together with the data acquisition system.

4.4.2 Porosity

In order to calculate the porosity of a rock specimen, the sample needs to be weighed after being oven dried to remove all moisture and leave only the matrix remaining (M_s). The sample is then placed inside a vacuum and saturated. It is then removed from the vacuum and lightly dried to remove excess water and reweighed (M_{sat}). Finally the rock is placed in a bowl and reweighed whilst being submerged (M_{sub}). Using these weights, equation 4.1 below is used to calculate porosity (ϕ).

$$\Phi = \frac{(M_{sat} - M_s)}{(M_{sat} - M_{sub})} * 100 \tag{4.1}$$

4.4.3 Load Measurements

A servo-controlled actuator applies a compressive force to the end of the sample. The absolute value of the force was obtained using a proving ring to determine the load from accurate resistance changes across a vertical strain gauge. The measurements were given in volts and converted to S.I. units using calibration data.

4.4.4 Displacement Measurements

Displacement changes are recorded using a pair of LVDTs attached to the ram located beneath the actuator. It was necessary to correct the displacement for apparatus distortion, which for the set-up amounted to 0.004 mm/1000 kg of the differential load applied. Using these readings the displacement is converted to normal strain (ε) using equation 4.2.

$$\varepsilon = \frac{\Delta l}{l_0} \quad (4.2)$$

where Δl is the change in length of the original sample length l_0 .

4.4.5 Pore Volume and Pore Pressure Measurements

The movement of the displacement transducer inside the pore intensifier measured pore volume change during a triaxial experiment. The intensifier has a volume of 10 cm³ with the displacement transducer ranging from 0 to 10 volts calibrated as 1V \approx 1cm³. By monitoring changes in piston displacement, volume changes could be calculated and indirect implications identified.

Measuring the pore pressure changes with calibrated pressure transducers it was found that 1 V \approx 40 MPa.

4.4.6 Electrical Potential Measurements

The electrical potential signals measured via the inserts represent the difference between an electrode and usually the ground using an electronic circuit with a high input impedance of 10¹³ Ω . Due to the ionic processes occurring near the contacts on the rock, the electrodes are subject to negligible polarisation when in direct current conditions, and therefore this effect is ignored.

The electrical potential signals during experiment preparation were found to fluctuate. The amount of fluctuation varied with confining pressure, pore pressure and temperature, and so depending on the parameter being changed, time was given for the potentials to stabilise. In certain data plots, the electrical potential change is given between the top and bottom electrodes (dipoles). This is important because increasing the differential stress increases the surface resistance between the rock sample and end-cap assembly. This will undoubtedly increase the measured voltage ($V = IR$) at the electrode and taking the difference between the bottom and top electrodes removes this effect.

In streaming potential measurements a voltage change was produced by a constant pressure gradient initiating fluid flow. The magnitude is given as the difference between the potential under the fluid flow and the base value when a pressure gradient is absent.

4.4.7 Acoustic Emission Measurements

Piezoelectric PZT-5B crystals recorded the acoustic emissions. The transducers used were 3 mm in diameter and attached to the stainless steel insert by conductive epoxy glue. This was to minimise the loss of acoustic energy at the transducer-insert interface. Signals were pre-amplified with a 40 dB gain.

The majority of AE data is within the frequency range 100 to 300 kHz and represents 90% of the data. To record all the signals of interest and reduce noise, 1 MHz transducers were selected and each measurement point was grounded at the source. A description of the frequency response of these transducers can be found in Read et al. (1995).

The emitted signals were amplified, filtered and passed into the LOCAN AT Analyser. This acquisition system, described in Appendix 1, is driven by the number of hits received, storing AE information in grouping bins when an acoustic wave arrives. When the bin is full the data is recorded to disk and the system is reset. This device records the properties of the acoustic waves above a pre-set amplitude, which is set before an experiment to a level which removes the background noise, usually 45-50 dB. The parts of the wave recorded include time, duration, count, amplitude, hits, channel, energy and frequency. With up to eight AE channels recorded, it was noted that a sufficient hit rate could cause the bin to become saturated and the possibility of data loss could occur. For b-value calculations a numerical threshold was chosen to normalise the experimental data to the same amplitude level. The consequence of this is that data at the bottom of the amplitude range is incompletely recorded. Under recording of events is discussed in detail by Cox and Meredith (1993) and taken into account by Sammonds et al. (1995).

4.4.8 Angle of Failure

The angle between the vertical corresponding to the axial compressive stress direction and the fracture plane was measured using a protractor. Two readings were taken, one on each side of the fault with an error of 0.5 degrees. These two results were then averaged.

4.4.9 Measurement Errors

Not all experiments worked due to certain problems in recording. Many of these problems were related to the electrodes which became damaged during deformation, and loose wires attached to the logging card which gave false readings and sometimes became separated, resulting in no reading at all.

5. Equipment Design for Thermo-Chemo-Mechanic Experiments

5.1 INTRODUCTION AND GENERAL DETAIL OF CHAPTER

Over the past decades, advances in technology have allowed detailed experiments to be performed on rocks to investigate different properties (Paterson 1978) and their relationship to most crustal conditions. In the area of triaxial deformation and electrical potential signal generation, most investigations take place at room temperature (Jouniaux and Pozzi 1996b, Revil and Glover 1998) and many use deionised water. However, in the crust, the temperature increases with a geothermal gradient of approximately 30°C/km (Fowler 2001). This will affect the thermo-chemo-mechanics of the rock.

In terms of physical changes within the rock, the effect of temperature on the mechanical properties has been thoroughly investigated. However, the effect of temperature on the electrical potential signals has only been investigated during static tests using different pore fluids and equilibrium conditions by authors including Dunstan (1994), Revil et al. (1999a, 1999b) and Reppert and Morgan (2003a, 2003b). Therefore, the simulation of in situ crustal conditions associated with shallow depths including pressures, strain rate and fluid interaction also needs to include the effect of temperature on the electrical potential signals.

As well as affecting the formation of a crack or fault, temperature also has an affect on post-failure behaviour of the rock. Temperature is known to affect chemical processes such as dissolution and re-precipitation. The solubility of quartz in relation to temperature and pressure is shown in Figure 2.23 and it reaches an initial maximum around 320°C. Therefore, to fully investigate the effect of temperature on electrical potential signals, all stages of deformation need to be examined with the ideal maximum temperature being 320°C (see Chapter 2.6.3 for more details).

In order to investigate the effect of temperature on potential signals during all stages of deformation, and to compare the results with those from room temperature experiments, an internal electric furnace is required. This chapter discusses the design and development of the furnace. Also in this chapter, modifications of existing equipment are discussed including improvements of the lead-through, ends-caps and yoke as well as the design of pore fluid separators to allow the use of different pore fluids.

5.2 HIGH TEMPERATURE

The electric furnace consists of a hollow cylinder which contains the heating elements, thermocouples and insulation beads. Used in conjunction with the furnace are ceramic discs which reduce thermal conductivity. Further details on how the furnace is set-up are discussed in Appendix 1 together with its component parts and associated equipment as shown in Appendix 5.

This internal electric furnace is based on the design implemented by Rocchi (2002) which was used for high temperature fracture toughness and triaxial compression tests. As temperature has different effects on materials such as steel and plastics, modifications were made to the equipment so that experiments could be conducted at confining pressures of up to 400 MPa and temperatures up to 320°C.

The key equipment was designed and consisted of: 1) A bottom outer closure which contains several seals and certain parts of the furnace; 2) a yoke assembly for the sample to reduce convection along the sample; 3) a transducer arrangement capable of high temperatures, which excludes the use of solder; 4) the furnace itself with plugs, heating elements and thermocouples.

5.2.1 Furnace Calculations

In order to achieve the goal of 320°C, calculations were required to investigate convection, conduction, time required to heat the furnace and oil. These calculations are discussed more thoroughly in Appendix 3 with a brief description given below. Figure 5.1 is a schematic diagram of the furnace sizes.

Calculations include:-

- Energy required to heat the oil, rock and steel to 320°C
- Energy loss from the rock surface at 320°C
- Type and properties of heating element

5.2.1.1 Energy Required for 320°C Furnace

The energy required to heat the rock, oil and steel to 320°C is given by:

$$Q = M \times Hc \times T \quad (5.1)$$

where Q is the heat required (kJ), M represents the mass (kg), Hc is the heat capacity (kJ/kg) and T equals temperature (°C). Using this equation the required energy to reach 320°C in 1 hr is ≈ 334 W.

Whilst the whole of the rock sample is heated some heat escapes from its surface through the processes of conduction. To calculate this, the general Fourier Law for 1-dimensional heat conduction (5.2) is used:

$$q = \frac{Ak(T_1 - T_2)}{l} \quad (5.2)$$

where

q = Heat flux (W)

l = Element length (m)

A = Area through which heat is conducted (m²)

k = Coefficient of thermal diffusivity (W/m K)

T_1 and T_2 = High temperature element from which heat is diffused and element diffused to (K)

In calculating the surface area of the rock and with heat dissipating into alumina spacers and silicone oil, the heat loss equals ≈ 2495 W.

Therefore, the minimum energy required to heat the rock to 320°C = 334 W + 2495 W = 2829 W.

Therefore 3 elements of 1000 W each are required.

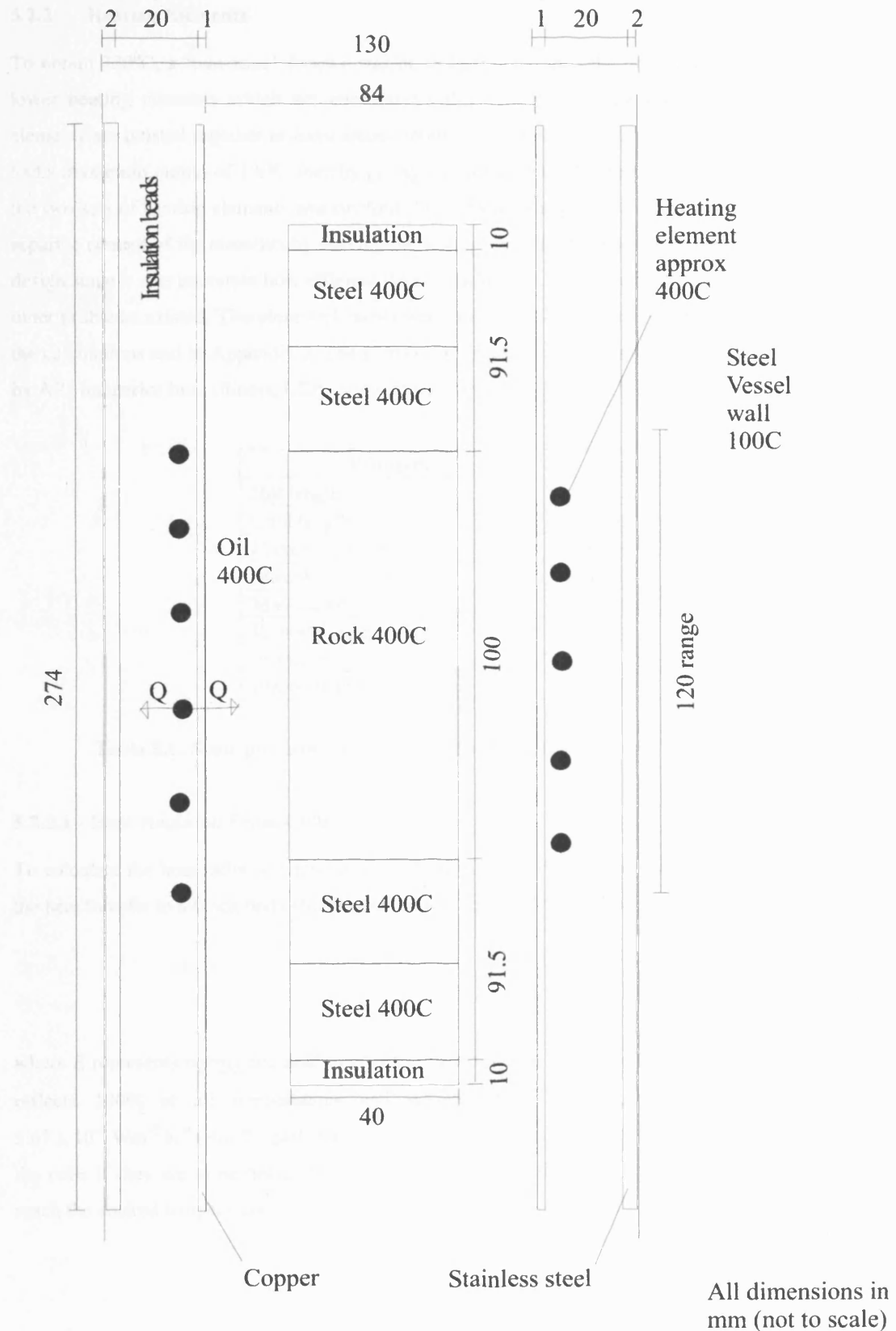


Figure 5.1: Simplified diagram of furnace to calculate the power required to heat the oil, steel and rock sample to 320°C.

5.2.2 Heating Elements

To obtain 320°C, a ‘two-zone’ furnace was built. In this instance the term refers to two upper and two lower heating elements which are concentric rather than to a single vertical heat source. The four elements are twisted together to form a continuous coil around the rock sample. The individual elements had a maximum output of 1 kW, thereby giving the furnace a total output of 4 kW. The reason for having the two sets of heating elements was twofold: 1) To reduce the possible effect of convection by allowing separate control of the elements by varying the wattage to reduce any thermal gradient present; 2) At the design stage it was uncertain how efficient the coils would be, if convection would be a problem or if any other problems existed. Therefore 4 elements were used instead of the minimum 3.5 elements as shown in the calculations and in Appendix 3. The elements themselves were manufactured according to my design by ARi Industries Inc., Illinois, USA. Some of the properties are listed below (Table 5.1).

Property	Value
Hot length	33 in
Cold length	4 in
Maximum Hi-Pot Voltage	1100 V AC
Max Watt Density	116 W/in
Max Current	11 Amps
K-model termination Diameter	1/4 in
Power at 115 Volts	1035 W

Table 5.1: Some properties of BXX-13B-50-4K heating elements from ARi Industries.

5.2.2.1 Heat Radiated From Coils

To calculate the heat radiated from the coils using Kirchhoff’s law for radiated heat and approximating the heat transfer to a black body (Stefan-Boltzmann equation) the following equation is used:

$$E = \epsilon\sigma T^4 \tag{5.3}$$

where E represents energy required to heat the element (Wm^{-2}), ϵ is the emissivity which is ≈ 1 (Surface reflects 100% at all temperatures and wavelengths.), σ is the Stefan-Boltzmann constant of $5.67 \times 10^{-8} \text{ Wm}^{-2} \text{ K}^{-4}$, and T equals temperature (K). From this it is found that 7012 Wm^{-2} is required from the coils if they are to be heated to 320°C. By using this value and the energy required for the rock to reach the desired temperature the surface area required by the coils can be calculated by:

$$A_{\text{coil}} = \frac{Q \text{ (W)}}{E \text{ (Wm}^{-2}\text{)}} \tag{5.4}$$

$$A_{\text{coil}} = 0.40 \text{ m}^2$$

From the heating elements available the surface area was calculated as being 0.013 m^2 , and so 31.5 elements would be needed. However, if the coils are heated to 750°C, only 3.5 elements are required and so that is what I chose to use.

5.2.2.2 Temperature of Inner Pressure Vessel Wall

As well as the furnace and sample assembly, the pressure vessel wall which surrounds the furnace will also be heated. The temperature of this must not go above 200°C or damage will occur. To check that this does not happen, equation (5.5) was used:

$$\text{Heat gradient} = Q = \frac{A.DT.K}{DX} \quad (5.5)$$

Rearranging equation (5.5) becomes

$$\frac{Q.DX}{A.K} = DT \quad (5.6)$$

where $Q = \text{Heat (W)} = 4140 \text{ W}$ $K = \text{Thermal conductivity (W/m K)} = 2 \text{ W/m K}$
 $DT = \text{Temp difference (in K)}$ $DX = \text{Insulation thickness (m)} = 0.02 \text{ m}$
 $A = \text{External surfaces (m}^2\text{)} = \pi \times 0.130 \times 0.274 \text{ m}$

As heat dissipation is extremely high in the coils, heating them to nominally 750°C will locally be nearer 320°C. Assuming this, the inner cell wall reaches 370°K. This value is impractical because the vessel has a large thermal mass and surface area. Also, the insulation is not solid, with oil present between the beads, therefore testing of this is required when at higher temperatures.

5.2.3 Furnace Design

See Appendix 5 for all the drawings.

In order to use the furnace at the desired temperature, the pressure vessel needed to be modified. This was achieved whilst designing the furnace. The main problem with the pressure vessel sealing method was that the O-rings would fail at high temperatures. Therefore, they were replaced with viton O-rings purchased from O-rings Ltd and capable of 260°C. As the O-rings are not close to the furnace they are unlikely to see temperatures above 200°C so are safe. This was checked using thermocouples during thermal calibration.

The main component of the pressure vessel which required re-designing was the bottom outer closure which is situated above the bottom breach and retaining nut and is used to hold the inner closure in-place along with an O-ring to seal the vessel. Using AutoCAD 14, a 3D model of the bottom closure was produced and modified to hold 4 heating elements and 3 thermocouples. Using this drawing the other components used with the furnace were added, including the pressure vessel, ram, seals, ceramic components, end-caps, sealing plug design, transducer fittings, thermal and electrical insulation to produce both a schematic drawing (Figure 5.2) as well as a 3D rendering (Figure 5.3) for stress and other calculations to be performed on later.

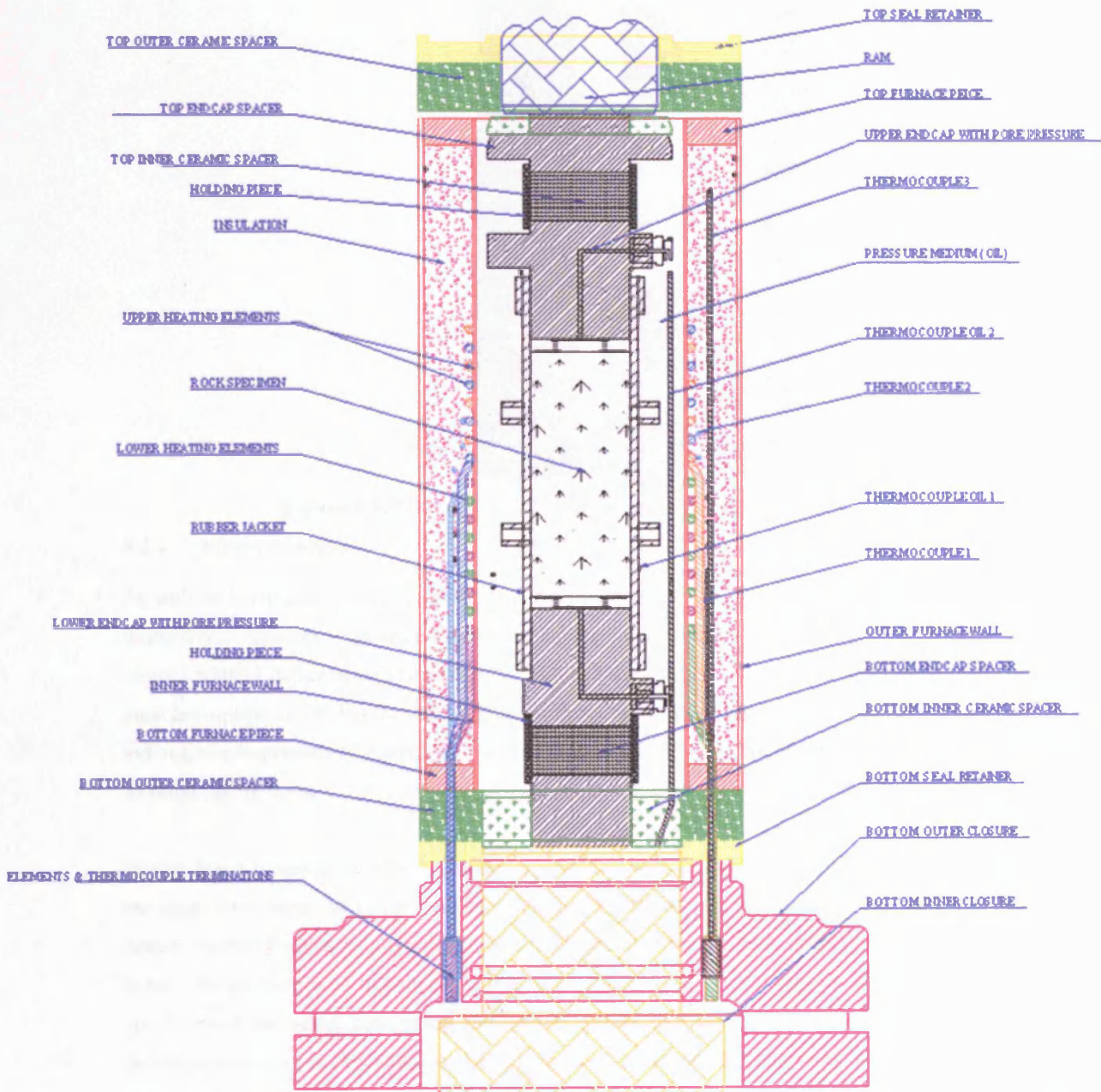


Figure 5.2: Schematic drawing of furnace assembly, yoke system and bottom inner and outer closures.

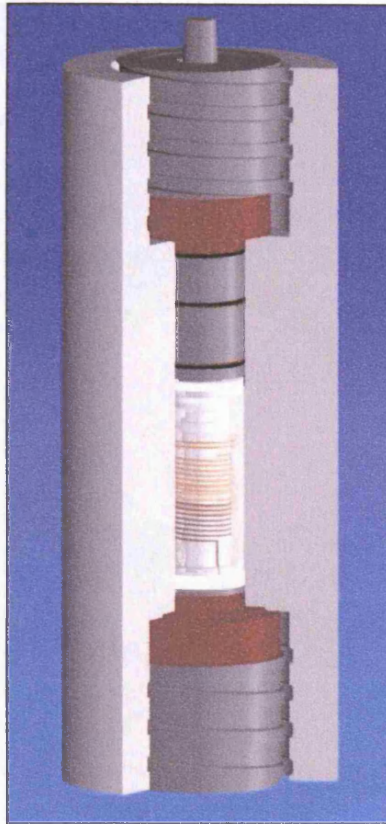


Figure 5.3: 3D rendering of electric furnace inside the pressure vessel.

5.2.4 Stress Analysis

As well as being able to withstand the high temperatures, it was essential that the bottom closure, lead-through and furnace plugs were capable of having large amounts of stress applied to them. The rock physics triaxial deformation cell is capable of 400 MPa confining pressures; therefore all parts designed must be capable of having this load applied without yielding. In order to evaluate the stresses applied to individual components two different types of stress analysis were completed, 1) Using Design Space 6, 2) Hand calculations.

Design Space 6 uses finite element modelling together with an existing 3D AutoCAD drawing to analyse the stress throughout the component and identify what the stress fields are likely to be. Using this on the bottom closure Figures 5.4 (a) and (b) were produced showing the peak stresses located around the screw holes. The problem with this model is that when placing a 3D model into its matrix, certain procedures are followed including converging the data to ensure that the values obtained between altering the numerous variables is as small as possible. On the edge of the 3D component you sometimes get a zero radius which in theory is not possible. The program converges on the highest stress area, which in the case of a corner with a zero radius is impossible, and so instead it diverges and the stress values get higher and higher the more times the program attempts to converge. Therefore, the actual stresses on the component are not exactly as shown in the model here due to the correct maximum stress being around the plug holes rather than the screw holes. However, this model gives a reasonable approximation.

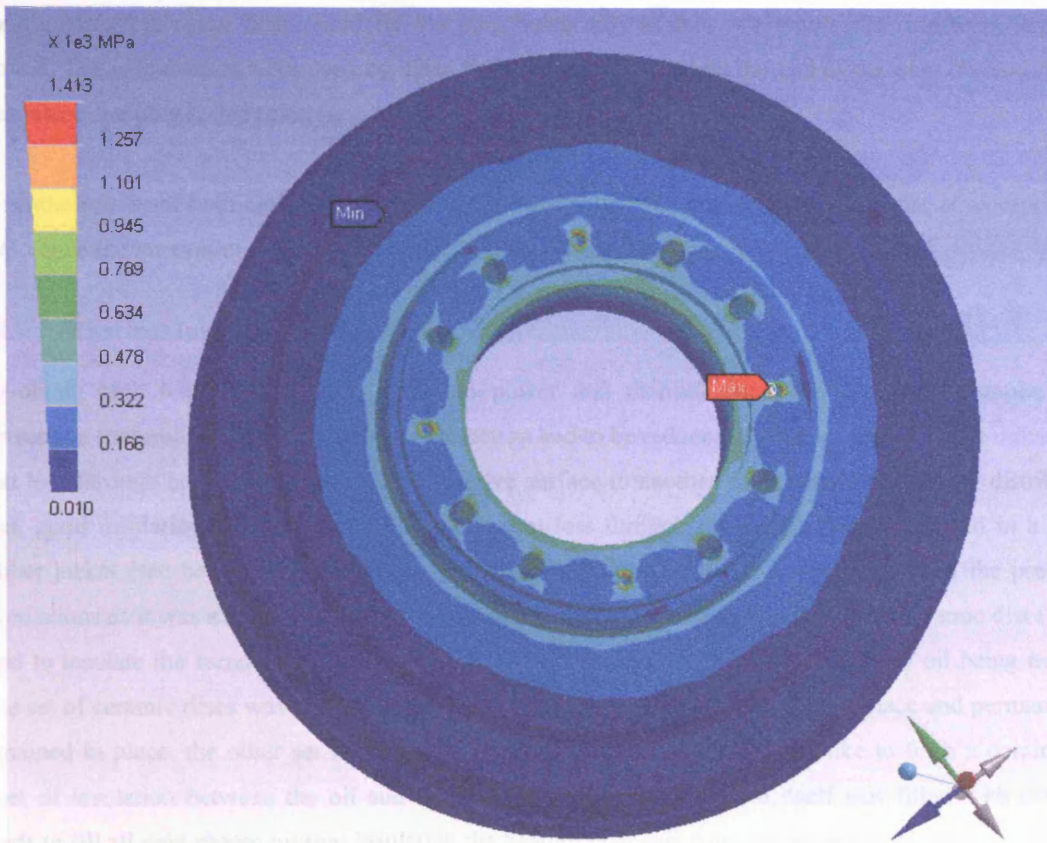


Figure 5.4(a): Stress analysis of outer bottom closure using Design Space 6.

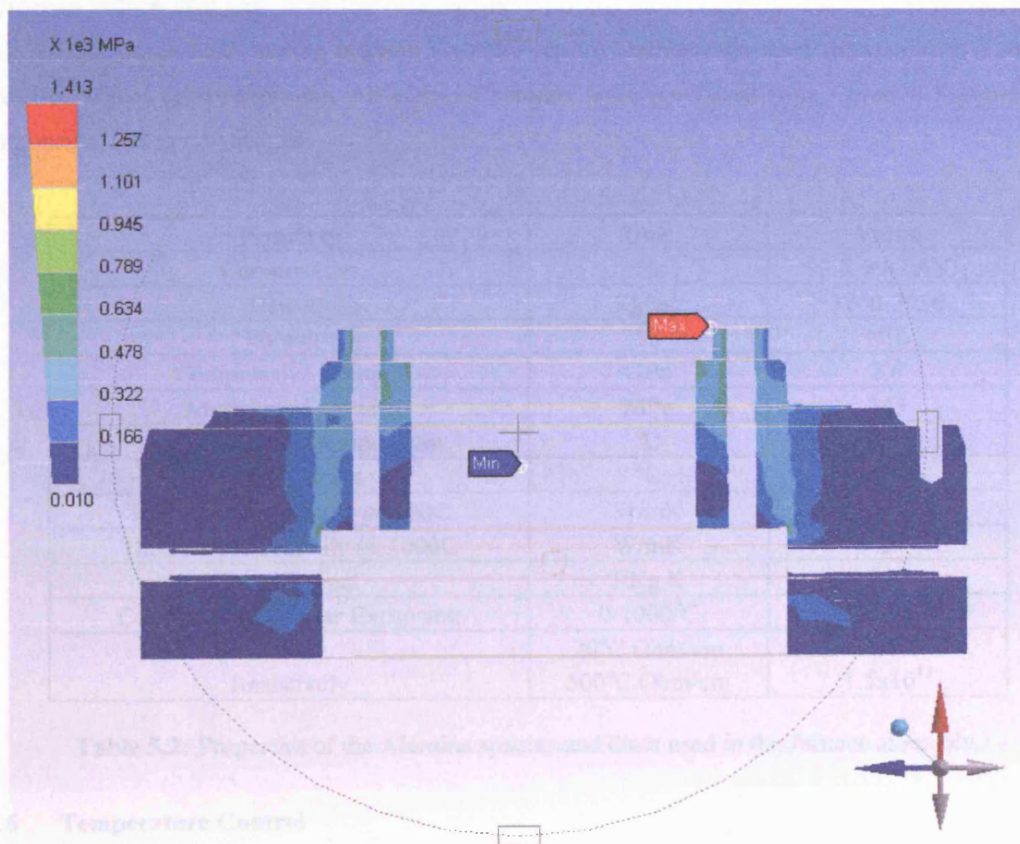


Figure 5.4(b): Sliced through stress analysis of the bottom outer closure using Design Space 6.

Hand calculations were determined for the plug holes only as this was where the maximum stress is located. The calculations were done by using the force acting down on the end of the plug divided by the area which the plug rested upon (see Appendix 4 for more details).

From the results of both Design Space 6 and the hand calculations it was identified that all components could have the maximum stress of 400 MPa applied to them without damage being caused.

5.2.5 Thermal Insulation

To obtain high temperatures with minimum power and thermal gradients across the sample, heat convection (natural convection) and heat conduction had to be reduced as much as possible. To reduce the heat loss through conduction from one conductive surface to another and maintain uniformly distributed heat, good insulation was required. To reduce heat loss through the sample it was encased in a viton rubber jacket (see below) which acted to partially insulate the rock. This was ignored in the previous calculations as it was a simplified model. At the top and base of the furnace assembly, ceramic discs were used to insulate the furnace and also to occupy some volume to reduce the amount of oil being heated. One set of ceramic discs was positioned to rest between the seal retainer and the furnace and permanently remained in place, the other set fit around the lead-throughs, and top of the yoke to form a continuous layer of insulation between the oil and the pressure vessel. The furnace itself was filled with ceramic beads to fill all void spaces present insulating the heating elements from the inner vessel wall.

In order to reduce heat loss from the rock sample ends and stop electrical leaking ceramic discs were used. As this was a load bearing position (in yoke set-up) alumina was used (properties in Table 5.2) instead of Macor (glass ceramic). All types of ceramic were purchased from Ceramic Substrates and Components, UK to my designs.

Property	Unit	Value
Composition	%	99.5-99.7 AlO ₂
Density	kg/m ³	3700-3950
Porosity	%	NIL
Compressive strength	GPa	2.6
Modulus of rupture	MPa	343
Safe Continuous temperature	°C	1650
Melting point	°C	2030
Thermal conductivity @ 100C	W/mK	25-30
Thermal conductivity @ 1000C	W/mK	5
Specific heat	J/Kg K	850
Coefficient of Linear Expansion	0-1000°C	8.1x10 ⁻⁶
Resistively	20°C Ohm/cm	>10 ¹⁴
	500°C Ohm/cm	1.5x10 ¹¹

Table 5.2: Properties of the Alumina spacers and discs used in the furnace assembly.

5.2.6 Temperature Control

Control of the furnace was done using a single control unit as shown in Figure 5.5. Within this unit two temperature controllers regulated the furnace temperature with one being a master and the other the slave.

A K-type thermocouple located next to the lower heating elements was connected to the master input controller with a feedback loop to vary the power output accordingly. As heat rises the slave controller had an approximate 15°C offset compared to the master and was monitored with another K-type thermocouple located next to the upper heating elements. The master controller was programmed for a single heating cycle, subdivided into 4 segments: heating *ramp rate* of 5°C.min⁻¹; *dwelling time* dependent on the exact temperature and on how long the experiment would last; a *cooling segment*; and the *end segment*.

A second controller (Omega), was used as a cut-off for safety reasons. This controller was connected to a thermocouple located against the outer furnace wall with a maximum temperature of 175°C. If this temperature was reached at the thermocouple it would cut all power to the furnace.

Several other K-type thermocouples were located around the furnace to record temperature profiles for calibration data and settings of both the oil and confining pressures.

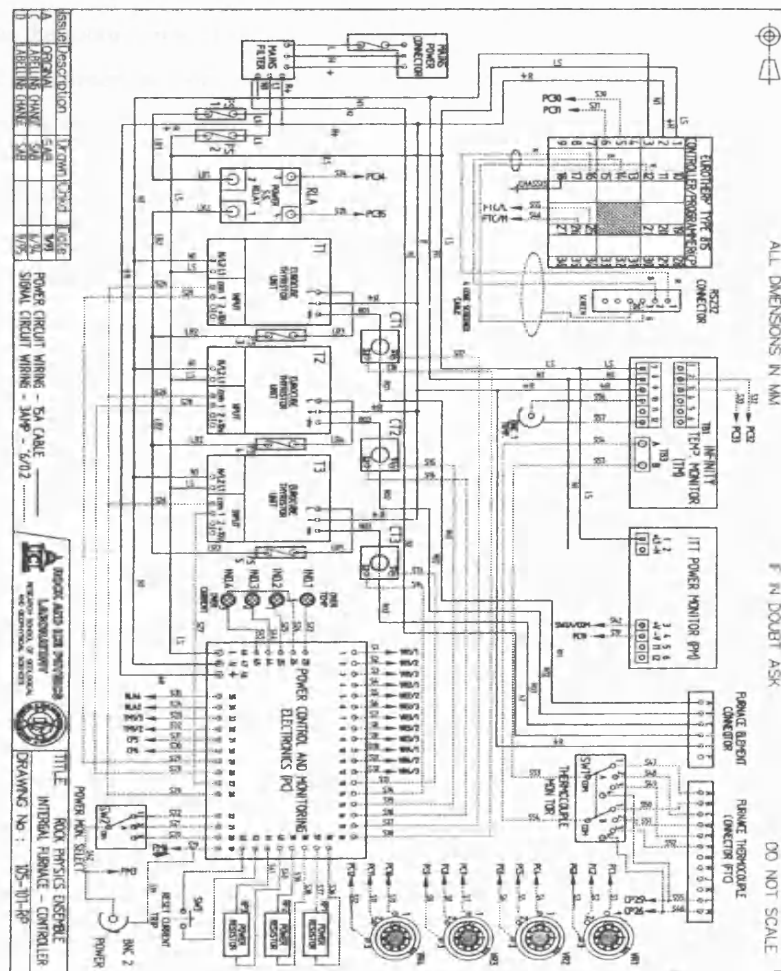


Figure 5.5: Circuit diagram of the furnace controller including heating elements, thermocouples and monitors.

5.2.7 Jacketing and Holding Pieces System

As mentioned previously, the rock sample is encased in a rubber jacket. I was unable to find a material tested to 320°C so I contacted a company called Ergotech, UK who provided me with some viton GF

rubber samples to test. The photos taken of the rubber samples are shown in Appendix 6 with the data summary in Table 5.3.

Exposure time (Hrs)	Change in hardness (IRHD)	Change in tensile strength (%)	Change in elongation @ break (%)
1	+/-0	-26.0	+/-0
2	-1	-32.0	+25.0
4	+/-0	-30.0	+7.1
8	+/-0	-40.0	+35.7
16	+/-0	-41.3	+7.1
42	+/-0	-60.7	+14.3

Table 5.3: Results of air aged rubber at 320°C.

From these results it was determined that I could use this material for the rubber jackets and tests could last for approximately 25 hours at a continuous temperature of 320°C before it would break apart. Therefore, I had viton GF rubber instrumentation jackets made for high temperature tests with identical specifications as the room temperature jackets. Solder is used for the metal inserts which are used to hold the EP and AE transducers at room temperature. However, for high temperature this system could not be employed, therefore transducers with screw fittings were glued to the inserts and used instead.

5.2.8 Piezoelectric Transducers

Due to the temperatures being above the Curie point, PZT-5B piezoelectric transducers cannot be used. For this reason the alternative material of Lithium Niobate was required because it can be used at elevated temperatures ($\leq 600^\circ\text{C}$) and shows good signal amplitude. Some of its properties are listed in Table 5.4.

Chemical Formula	LiNbO ₃
Crystal Class	Trigonal
Lattice Constant, Å	a=5.148 c= 13.863
Density, g/cm ³ at 293 K	4.644
Transmittance Range, μm	0.4-5.0
Dielectric Constant	29
Melting Temperature, K	1530
Thermal Conductivity, W/(m K) at 300 K	5.6
Thermal Expansion, 1/K at 300 K	
α _a (perpendicular)	15 x 10 ⁻⁶
α _c (parallel)	4.1 x 10 ⁻⁶
Specific Heat, cal/(g K)	0.15
Bandgap, eV	4.0
Solubility in water	None
Electro-Optical Coefficients, pm/V	r ₃₃ =30.8 r ₃₁ =8.6 r ₂₂ =3.4 r ₅₁ =28

Table 5.4: Properties of Lithium Niobate transducers purchased from Almaz Optics, Inc, USA.

5.2.9 Oil

For temperature experiments in excess of 200⁰C, the oil used at room temperature would ignite. Therefore, an oil with a low viscosity and higher flash point was purchased from Dow Corning Ltd (Table 5.5) to avoid the problem of igniting and reduce the effect of temperature making the oil more viscous. This is because at very high temperatures, the oil polymerises and lengthens the bonds within the oil and causes it to break down and become a thick black goo. If this was to happen, the triaxial rig and/or furnace could be damaged and they would need to be cleaned after every experiment which would waste time.

Property	Silicone oil
Specific Gravity	0.970 (25 ⁰ C)
Coefficient of Volume Expansion	0.00104
Surface Tension	15.4 (25 ⁰ C)
Flash Point	260 ⁰ C

Table 5.5: Physical properties of high temperature silicone oil.

5.2.10 End-caps

Further details on the end-cap assembly are to be found in Chapter 5.3.3. For high temperature experiments, alumina discs were placed between the pore pressure end-cap and the base end-cap. As a result, the end-cap pieces were shortened where appropriate so that the overall length of the rock assembly remains constant.

5.2.11 Lead-throughs

Further details on lead-through design can to be found in Chapter 5.3.4. Two problems were encountered at high temperatures: 1) The solder became liquefied at 260⁰C and 2) PTFE coated wire broke down into HF acid. To solve these problems high temperature solder was use on the connection and fibre glass tubing was placed over all the wires where possible.

5.3 OTHER MODIFICATIONS

From previous experimental work it was found that improvements were required to several different pieces of equipment to increase the reliability of the rig and to allow the investigation of certain factors including pore fluid effects as mentioned previously. This involved changes to these areas and consisted of designing a new mechanism for introducing brine pore fluid into the sample, designing a structure able to ensure the sample ends are stressed evenly throughout the experiment, and improving the reliability of the lead-throughs so that they last longer.

5.3.1 Pore Fluid Separator

The current pore fluid intensifier cannot operate with salt solutions because this may cause rust and corrode the internal seals and materials causing it to leak. Two separators were therefore designed and used to look at saline fluids and their effect on the failure mechanism and on electrical potential signals.

Figure 5.6 shows how the separator is designed (see Appendix 5 for details). Basically, it is a simplified pressure vessel which contains a central shuttle which is sealed using a central piston GLYD seal with wear rings on the outer ends. A flange is present at each end incorporating mitre rings to seal which are held in position by six screws. The volume of the separator was designed to be 50 cm³ which corresponds with the pore fluid intensifiers. The insertion of the separator into the pore fluid system is shown schematically in Figure 5.7. One of the intensifiers is primed with deionised water and connected to one side of the separator displacing any air present and moving the shuttle. With a manual pump, a brine fluid is introduced to the outlet, pushing the shuttle back. When it is all the way back the void is filled with brine, the outlet is closed. The piping from the separator is connected from the outlet to one end of the rock. Pressure can then be applied to one end of the sample. An identical procedure is applied to the other intensifier at the other end of the sample allowing for fluid flow experiments. In order to monitor the pressure in both separators, a calibrated pressure transducer was positioned on the brine side of the shuttle.

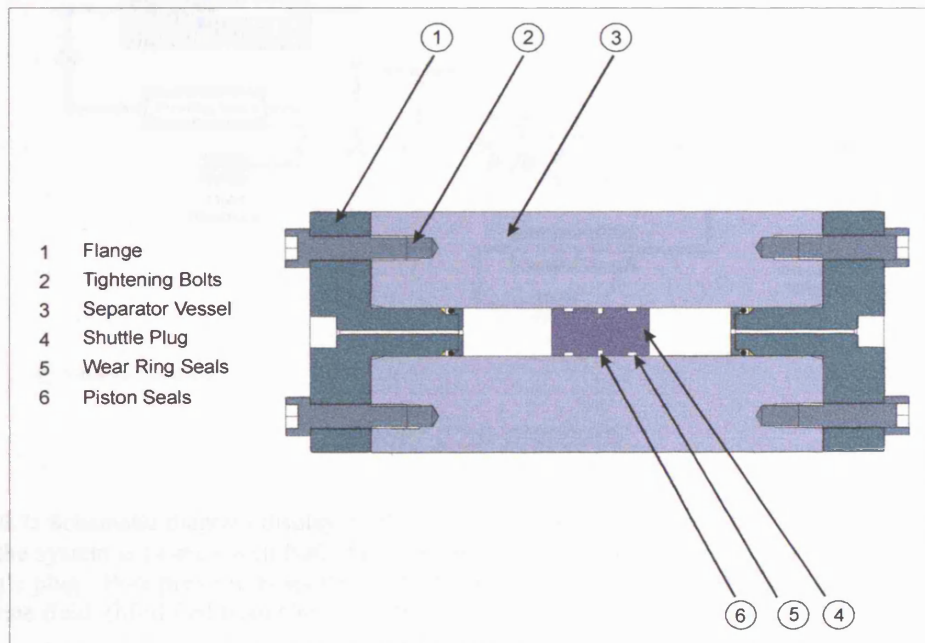


Figure 5.6: Diagram of pore fluid separator design. A moving shuttle plug separates corrosive brine fluids from distilled fluids and is sealed using standard piston and O-ring seals. Pore fluid pressures up to 80MPa can be used in this arrangement. (Taken from Clint (1999))

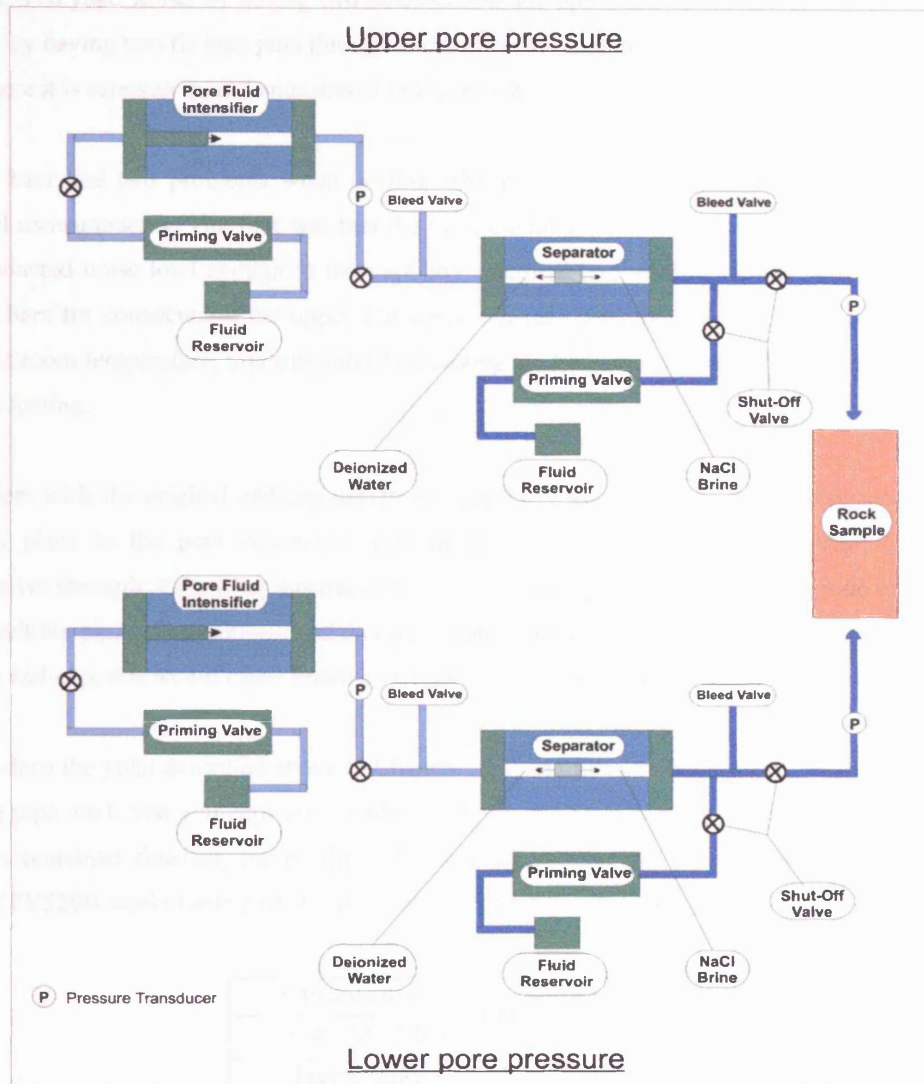


Figure 5.7: Schematic diagram displaying the pore fluid system incorporating two separators. The right side of the system is primed with NaCl brine isolated from de-ionised water in the left of the system by the shuttle plug. Pore pressure is applied from the servo-controlled pore fluid intensifier and transmitted to the brine fluid. (Modified from Clint (1999))

5.3.2 Yoke and End-caps

During any triaxial experiment, the rock specimen is placed inside a pressure field with a relevant confining pressure, which surrounds the whole sample. The upper ram is lowered onto the top of the sample and stress applied. In applying this stress, it is assumed that the ram and the specimen are parallel to each other allowing the load to be distributed evenly over the surface area of the rock from which stress is calculated. Also, in the creation of a fault plane at a given angle, the force applied to the end of the sample is required for calculations of normal and shear stresses. Previously, the rock was held in place by the jacket and the end-caps alone, which, when placed inside the vessel, may have moved due to the effects of gravity and caused uneven loading and miscalculation of properties mentioned previously.

The problem was solved by introducing a yoke instead of a hemispherical seat, as the latter caused potential buckling of the ram if its seating was not accurate. The yoke however, did not present this

problem. The yoke works by having two holes in both the upper and lower end-caps. These are fixed in position by having two tie bars pass through each of the holes along the length of the sample and into the base where it is screwed in as demonstrated in Figure 5.8.

The tie bars had two problems when dealing with the electrical isolation required for the electrical potential measurements. The first was that the bars, composed of stainless steel act as an electric aerial and conducted noise loud enough to interrupt any electrical measurements made. The other problem is that the bars are connected to the upper and lower end-caps directly, allowing electrical leaking to take place. At room temperature, this was solved by having the tie bars made of strong nitrile plastic which is non-conducting.

A problem with the original end-cap design was the method with which the pore pressure piping was fixed in place to the pore connector. This method involved heating the end-cap to improve the compressive strength. Following this treatment, the pore piping was brazed onto the side of the end-caps. As a result the piping is weakened and this significantly increases the chance for deformation to occur to the pore end-cap, this would cause future experiments to load unevenly affecting axial stress.

To introduce the yoke described above in Chapter 5.3.2 and to solve the problem of connecting the pore pressure pipe work new end-caps were made (see Appendix 5). Whilst the overall dimensions of the new end-caps remained constant, the position of individual components changed. The new end-caps were made of FV520B steel (Table 5.6), a summary of its properties is shown below.

Properties	FV520B
Elastic Modulus	210,000 MPa
Temperature	-90/300+

Table 5.6: Properties of FV520B steel used in the construction of the ram.

In order to solve the problem of connecting the pore fluid piping to the end-caps a screw fitting was designed which would not weaken the metal. This connection had to be placed outside the stress field, applied by the upper ram, otherwise when stress is applied to the sample it would be transferred to the end-caps and cause damage to the screw fitting. This was resolved by designing a metal skirt, which extended beyond the 40mm diameter end-caps to where the screw fitting with a 60° pressure fitting were located. The final design, incorporating the end-caps and pore fluid piping is shown in the Appendix 5 with Figure 5.8 below showing the sample set-up including yoke and end-caps.

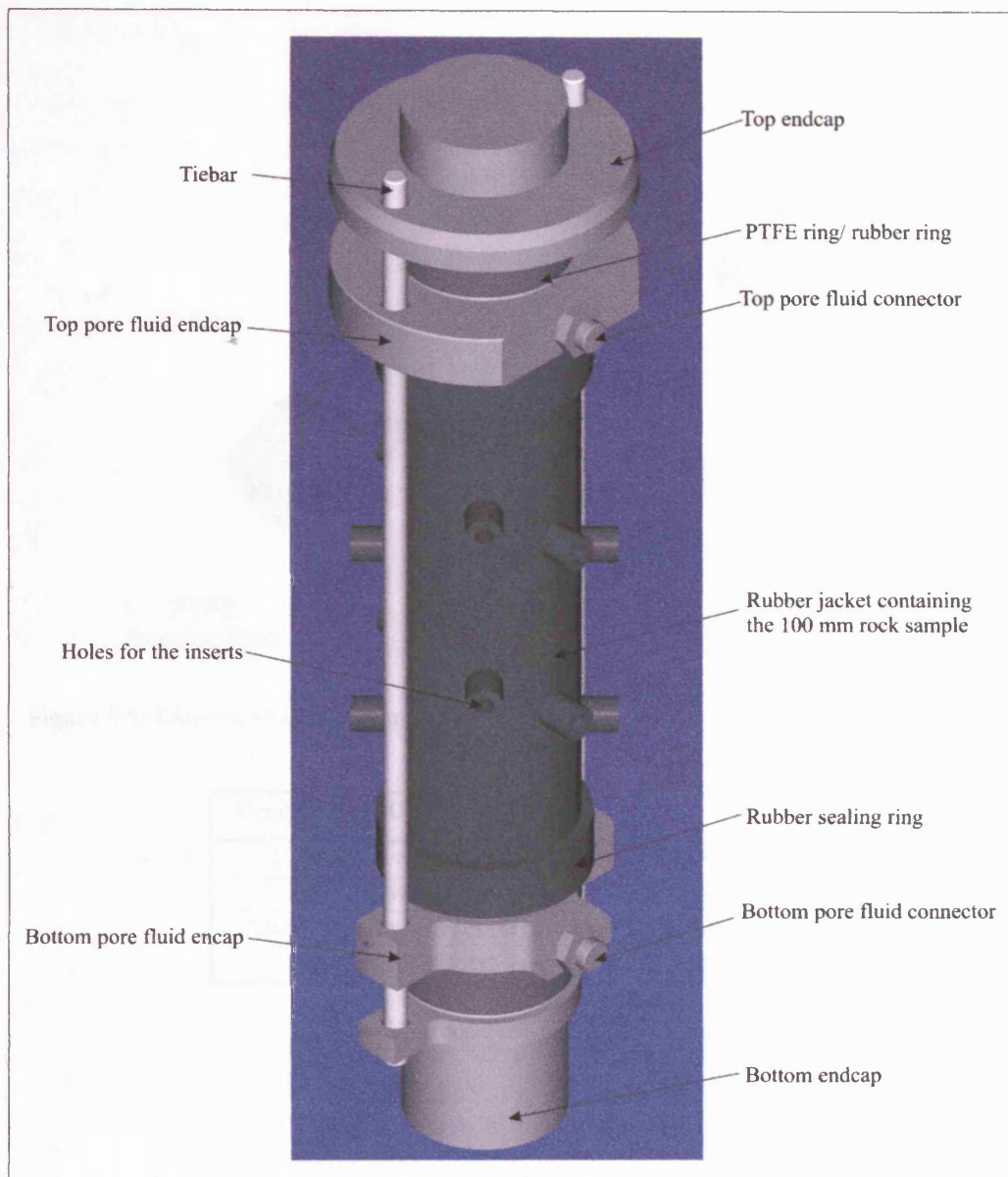


Figure 5.8: Diagram of sample set-up inside pressure vessel.

5.3.3 Lead-through Design

The initial design for the lead-throughs (Figure 5.9) was created by Clint (1999) (see Appendix 5). The coaxial cable is split into an inner core and an outer sheath. The outer sheath is connected to the housing and is earthed together with all the other components whilst the inner core is isolated from the outer sheath by being insulated through the plug where insulator tubes are fitted. This allows a hollow screw to force the insulator and conductor assembly against the 60° ULTEM cone (properties shown in Table 5.7) placed in a 20° cut to prevent the lead-through from leaking. O-rings with PTFE backing rings are used to seal the lead-through assemblies in position within the bottom ram. With this design no strain relief was present on the coaxial cables, which were flimsy and easily damaged causing experimental delays. To improve this, the wires were covered with polyolefin heat shrink film inside the insulator and outside the plug. All three coaxial wires were held together by heat shrink film, thus supporting and protecting the wires from breakages. Also, the earthing wires were cut shorter so that they acted as strain relief and could easily be fixed if damaged rather than having to repair the inner core wire.

6. Experimental Set-up

This chapter describes the experimental apparatus used for the high pressure, high temperature, and high temperature experiments.

In this section, describing the assembly of the samples and the experimental apparatus.

The collection data, which is used to convert the measured data into a form that can be used for analysis.

From the data, the user can determine the physical effects on potential energy and the physical effects on potential energy.

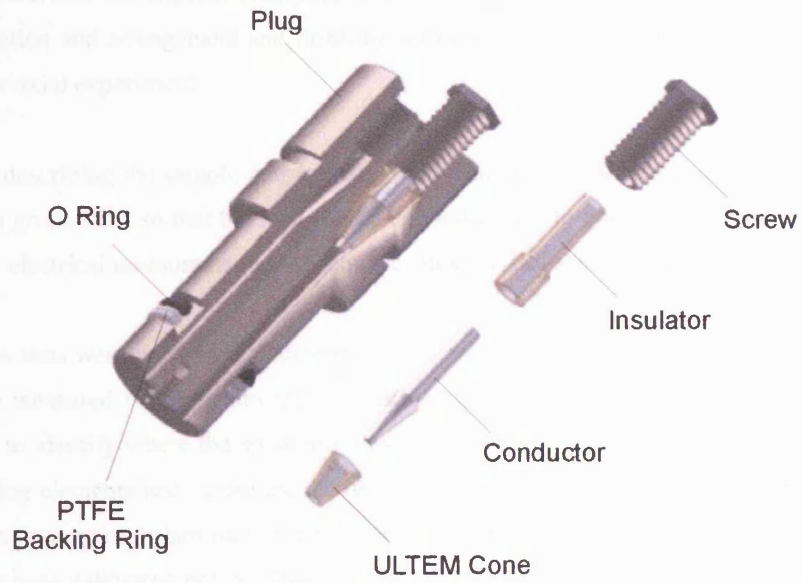


Figure 5.9: Diagram showing the make-up of lead through design. (Taken from Clint (1999))

Properties of ULTEM 1000	
Compressive Modulus	2877 MPa
Tensile Modulus	2945 MPa
Dielectric Strength (in oil)	710 V/mil
Volume Resistivity	6.7 E19 Ω m

Table 5.7: Properties of ULTEM cone.

6. Experimental Set-up

This chapter describes the experimental procedure, starting with the rock description, followed by the sample preparation and arrangement and finishing with the calibration of all the components involved in performing a triaxial experiment.

In the section describing the sample preparation, I will describe how the samples are cored and the ends of the samples ground flat so that the load can be applied evenly to both ends. The method for preparing the sample for electrical measurements and acoustic emission is discussed, followed by the sample set-up.

The calibration tests were performed to determine the corrections which had to be applied to the raw data to convert the measured voltages into the relevant SI units. The calibrations to the new apparatus were done in order to identify where the apparatus was not performing correctly, such as the heat distribution from the heating elements and determine the necessary corrections to be applied to the data. Calibrating the furnace was a very important part of this experimental study, since this apparatus was completely new and had never been calibrated before. This included all the devices used for measurements: the load cell, the displacement transducers, and the pressure transducers.

6.1 ROCK TYPE DESCRIPTION

6.1.1 Rock Types Chosen

The Clashach sandstone was primarily chosen to represent a reservoir rock with similar characteristics to those found in the North Sea. Properties of interest include a porosity of 20%, high permeability in excess of 1 Darcy, mineral composition high in quartz, its homogenous and isotropic microstructure and the fact that it has a compressive strength greater than 130 MPa.

To aid in the understanding of the many physical and chemical factors which influence the electrical signals, two additional sandstones were chosen with slightly different properties. Bentheim sandstone was chosen for its high quartz content and similar permeability and grain size to Clashach sandstone. Darley Dale sandstone was selected because it was anisotropic rock with a varied grain size and reduced quartz content with additional minerals present such as clays. In terms of electrical signals, these rocks allowed the effect of composition on the piezoelectric and electrokinetic phenomena as well as identifying changes in potential signal due to the physical properties of the rocks to be studied.

To investigate the electrokinetic phenomena across different rock types and to determine trends without the presence of the piezoelectric effect, Portland limestone and Seljadur basalt were chosen as neither contain any piezoelectric crystals such as quartz. Portland limestone was used in particular as it represents an alternative reservoir rock with characteristics similar to those found in situ with similar porosity and grain size to Clashach. It is also made of almost pure calcium carbonate so the EDL can be investigated in terms of compositional effects. Seljadur basalt was also chosen due to its low porosity and permeability so the physical effect on potential signals could be investigated.

6.1.2 Thin Sections

To identify the mineral content microscopically and find the porosity of the rock, thin sections were prepared by cutting and gluing the rock to slides and polishing to a thickness of 30 μm . These slides were then studied under the microscope at various magnifications using different light sources (normal and cross-polarized) to recognize the different minerals, compositions, shapes and secondary events that may have occurred after deposition. The porosity measurement technique used is discussed in Chapter 6.2.3 with the permeability measurements calculated from fluid flow experiments through the length of the sample with a confining pressure of 40 MPa and a pore pressure gradient across the sample of 5 MPa. A summary of their main properties collated from these thin sections and experimental data is given in Table 6.1.

Rock Types	Darley Dale Sandstone	Clashach Sandstone	Bentheim Sandstone	Portland Limestone	Seljadur Basalt
Composition	75% Quartz	70% Quartz	95% Quartz	95% Calcium carbonate	60% Plagioclase Felspar
	15% Clay	15% Lithic	5% Lithic	5% Organic	30% Clinopyroxene
	10% Feldspar	15% K- Feldspar			6% Olivine
					4% Magnetite
Grain size	0.008 - 0.8 mm	0.3 - 0.4 mm	0.1 - 0.5 mm	0.25 - 0.50 mm	< 1 mm
Permeability	0.01 D	1.3 D	1.1 D	0.1 D	0.0000001 D
Porosity	13-17%	18-20%	21-24%	19-23%	3%
Triaxial strength ($P_c = 20$ MPa)	85 MPa	120 MPa	110 MPa	70 MPa	500 MPa

Table 6.1: Summary of the properties of different rock types

6.1.3 Description of Darley Dale Sandstone

A micrograph of Darley Dale sandstone under cross-polarised light is shown in Figure 6.1a displaying the mineral content. Darley Dale Sandstone comes from the Millstone Grit of Carboniferous age from England. It is a poorly sorted quartz-feldspathic sandstone bound with siliceous cement. Quartz accounts for approximately 75% of the mineral content, with 10% feldspar (plagioclase and microcline) and 15% clay and other minerals forming the remainder. The grains show angular to sub-angular geometry and ranging between 0.008-0.8 mm with only a small degree of cracking visible in some crystals. The porosity of the rock varies between 13-17% and it has a permeability of about 10^{-15} m^{-2} .

6.1.4 Description of Clashach Sandstone

Clashach sandstone is shown in Figure 6.1b. It is a red sandstone of Permo-Triassic age and comes from Elgin (NE Scotland). The rock is 70% quartz, with feldspars and lithic material and other minerals forming the remainder. On average, the grains are 0.3-0.4 mm long and appear to be well sorted with little preferred orientation and are generally sub rounded to rounded. The porosity ranges between 15-20% and the rock has a permeability of about $1.5 \times 10^{-12} \text{ m}^{-2}$.

6.1.5 Description of Bentheim Sandstone

Bentheim sandstone shown in Figure 6.1c is a well sorted sandstone from Bentheim in Belgium. Quartz accounts for approximately 95% of the rock with other materials (lithic) forming the remainder with little or no clay minerals present. The grain size varies between 0.1 mm and 0.5 mm, and they are sub-rounded. As in the Darley Dale sandstone, the undeformed crystals are relatively homogeneous with little or no cracking evident. The porosity varies between 21 and 24% and the permeability is about 10^{-12} m^{-2} .

6.1.6 Description of Portland Limestone

Portland limestone is a Jurassic oolitic limestone shown in Figure 6.1d from the Portland Formation located in southern England. The stone is formed from micrite (fine grained calcium carbonate) ooids with small quantities of micrite present in the matrix. The shell fragments are typically 5mm across and rounded with high porosity (18-20%) and with interlinking pores giving a permeability of about 10^{-14} m^{-2} . The Ooliths contain a limited amount of organic material with some shell fragments.

6.1.7 Description of Seljadur Basalt

This basalt from Seljadur in south-west Iceland is composed of plagioclase feldspar and pyroxene with accessory minerals as shown in Figure 6.1e. This mineral composition categorises the rock as tholeiitic basalt. Balme et al. (2004) measured the grain size at 100 microns with some variation with the grain being angular. It is a compact, high-density rock with porosity estimated at 3% and a permeability of about 10^{-20} m^{-2} .

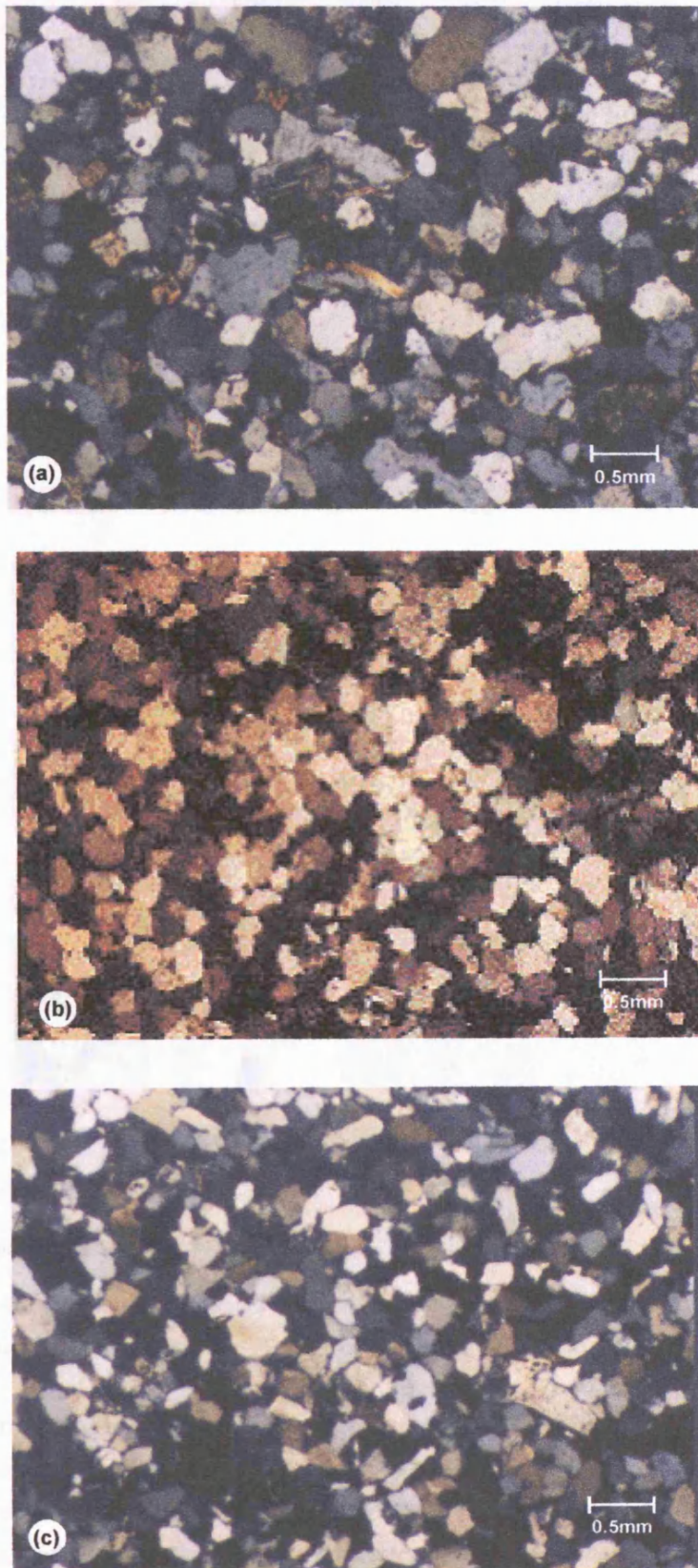


Figure 6.1: Micrographs of (a) Darley Dale sandstone, (b) Clashach sandstone and (c) Bentheim sandstone

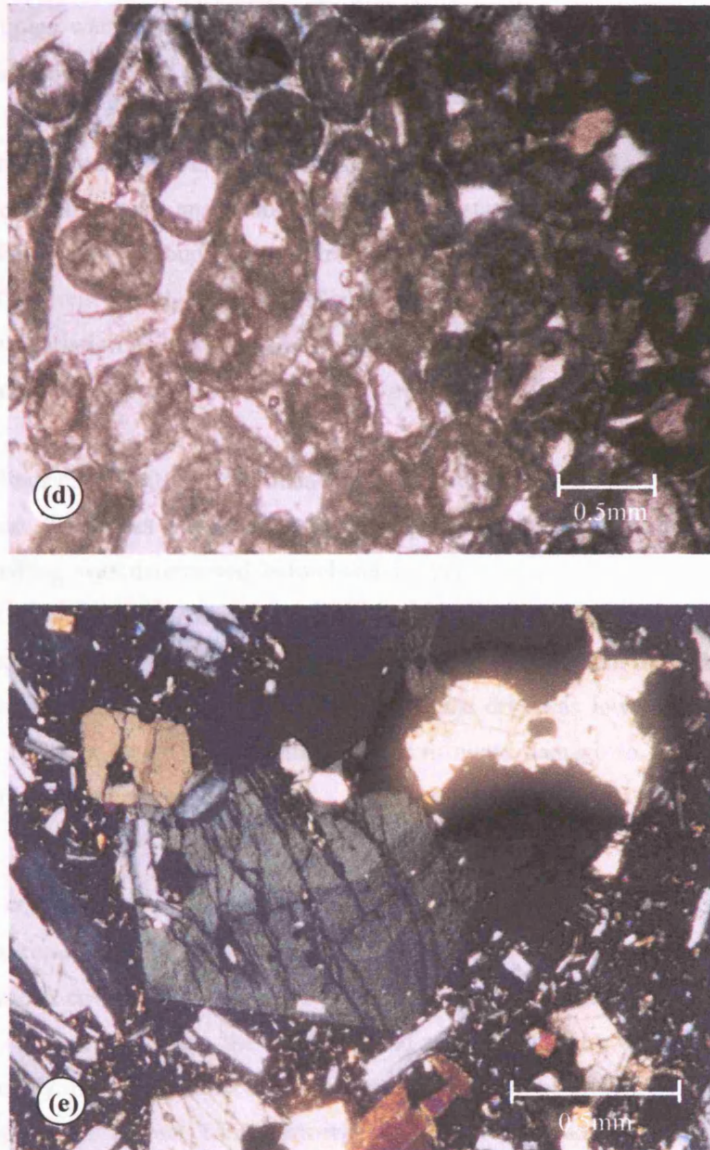


Figure 6.1: Micrographs of (d) Portland limestone and (e) Seljadur Basalt.

6.2 ROCK SAMPLE PREPARATION

6.2.1 Sample Rock

The length of the sample was measured twice at right angles to each other with an average value taken. The diameter was measured at the top, middle and bottom of the sample with an average value taken.

In the preparation of specimens the ideal length for the samples is 100 mm with a diameter of 40 mm. This was chosen because it has an aspect ratio of at least 2.5:1 which is recommended so that faults form in the middle of the sample rather than the ends where stress concentration may occur. Both ends of the sample were smoothed to be parallel to an accuracy of 0.02 mm so that the assumption of load being applied equally to both ends of the sample over the cross-sectional area is valid.

6.2.2 Coring and Grinding

Before the samples were cored, a P-wave velocity analysis was performed on each block of rock to identify the anisotropy and the direction of bedding. Firstly the blocks dimensions were measured to an accuracy of 0.1 mm at several points along each axis (x, y and z) and the results averaged. Then the velocity was calculated by measuring the time for the sound to cross the block of rock at different positions along the three axes and then divided by the distance with average values given for each axis. Clashach and Portland were found to be isotropic with less than a 5% variation in velocity measurement in the three directions. Bentheim and Darley Dale sandstone and Seljudur basalt were found to be anisotropic with variation of more than 14%. All samples were cored parallel to bedding to rule out the effect of bedding planes on the physical properties of the rock.

To produce cylindrical samples with a diameter of 40 mm, a drill bit with an internal diameter of 40 mm was used to core the blocks of sandstone in the appropriate bedding planes to the desired length. The direction of drilling was determined beforehand by performing a velocity analysis on the block and identifying the orientation of bedding. To core all the samples in the same direction the slab was laid flat and held in place by two sets of clamps. The core drill rotated at 960 rpm through a drill chuck with water used for lubrication. To avoid damage to the sample, the drill was lowered at a constant rate with the samples being cut to a length of 130 mm in order to avoid damage to the rock ends. This was later reduced to 110 mm using a saw.

In order for a constant load to be applied to the end surfaces of the sample, the surfaces needed to be parallel to an accuracy of ± 0.02 mm and to a length of 100 mm to aid strain calculations. This involved applying a diamond covered grinding wheel, rotating at 1240 rpm independently to each end of the rock. To remove any fragments present, the rock was held around the centre with the assumption that the core drill went vertically through the rock and this allows the ends to be ground flat using a dial clock checked against each other until correct. Using this wheel removes small amounts of rock during a single pass, avoiding damage to its surface and edges. A water/oil mix was used to lubricate the grinding machine and remove rock fragments, afterwards the samples were washed with water and placed in an oven between 70-90⁰C for two days to evaporate any fluids present. To show how flat the surface of the rock can be Figure 6.2a and b are included which show a 5 x 20 mm section of Portland limestone and Clashach sandstone surface. For the limestone the readings have been normalised with 90% of the rock being one shade of green. However the grinding lines can still be seen running from top left to bottom right. For the sandstone the surface is rougher than the softer limestone with more grains removed from the surface due to the grinding process.

6.2.3 Saturation Technique

If saturated experiments were to be undertaken, the sample needed to be saturated before the experiment could begin. To achieve this, the specimen was placed inside a beaker full of pore water (usually deionised water) with a vacuum pump attached which creates a vacuum of 10^{-4} Tor.

Chapter 6: Experimental Set-up

The time required for a rock to become saturated depends upon its permeability. For example, sandstone rocks were left for 2 days, to be confident of being fully saturated whilst basalt was left in a vacuum for over a week. To confirm the samples are saturated, each was weighed daily until two consecutive readings were identical. From this the porosity was calculated. This is accomplished by measuring the saturated weight of the rock submerge in water and in the air and using the volume of the rock calculated from the length and diameter the porosity is calculated.

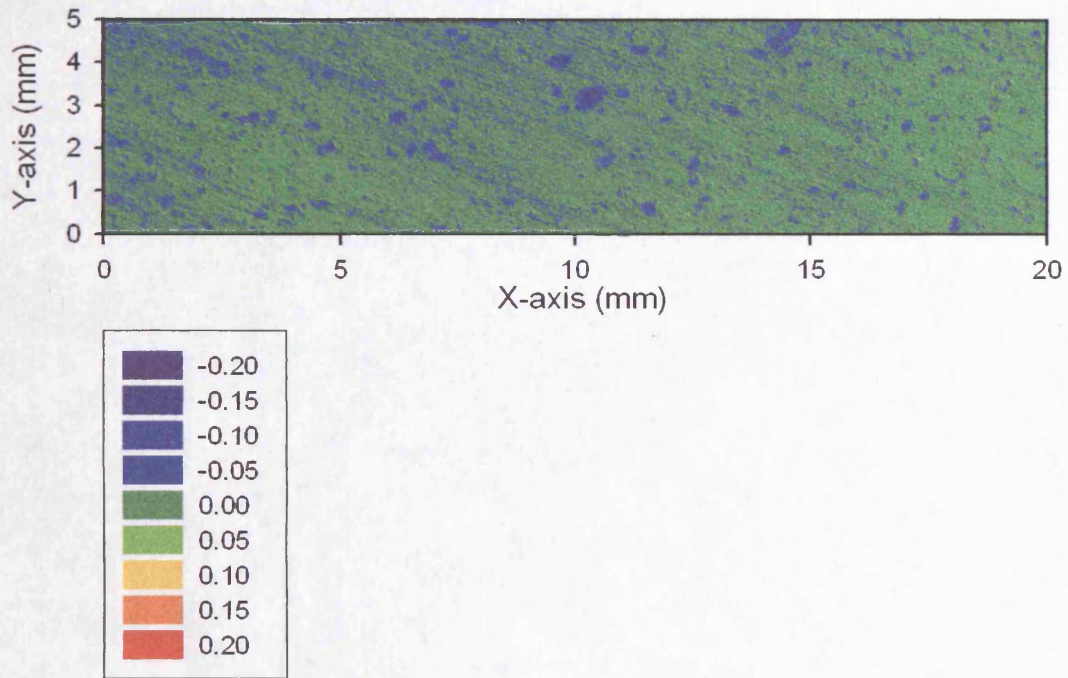


Figure 6.2a: A 5 x 20mm normalised surface plot of Portland limestone after grinding with a scale bar showing the variation in height.

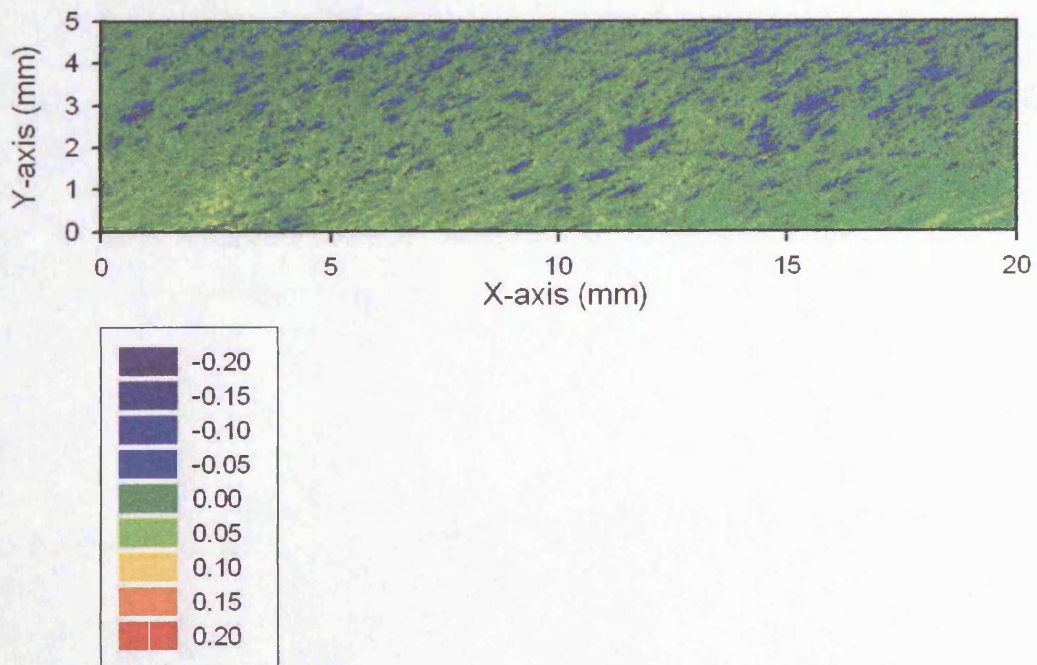


Figure 6.2b: A 5 x 20mm normalised surface plot of Clashach sandstone after grinding with a scale bar showing the variation in height.

6.2.4 Preparation for Electrical Measurements

To improve the electrical contact between the end-caps and the rock necessary to obtain voltage readings, a thin layer of silver conductive paint was applied to the rock ends in the form of a grid pattern. Contact was improved by applying the silver conductive paint to the relevant areas of the inserts and rock surface shown in Figure 6.3. This method of painting allows for improved electrical contact while maintaining unrestricted surface area for fluid percolation.

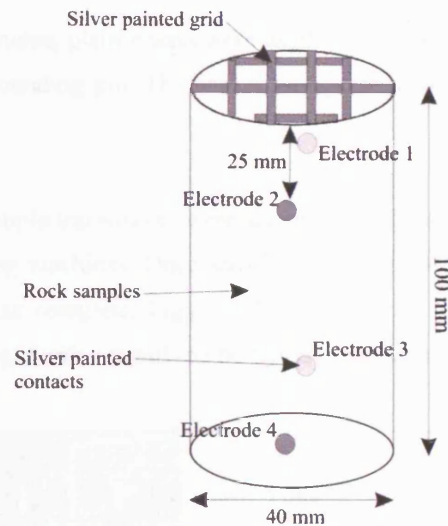


Figure 6.3: Schematic diagram showing rock sample preparation for electrical measurements.

6.2.5 Preparation of Sample

For the preparation of the sample, the rock was covered in silver conductive paint described in Chapter 6.2.4 and saturated in pore fluid if required. Depending on the type of experiment, the lower end-cap may need a ceramic insulating plate for the reason mentioned in Chapter 4.3.7 or stainless steel plates. These plates were held between the pore pressure end-caps and the ram by a nitrile plastic cover and the yoke. The jacket was prepared by the inserting the concave stainless steel inserts into their holes, by pushing and rotating them to rest against the sample. To ensure these inserts were sealed, metal O-rings were placed on top of the nitrile forcing the inserts against the nitrile sleeve.

The sample was then pushed up into the middle of the jacket by the use of a metal cylinder with the same diameter, thereby avoiding possible damage to the rock ends as well as the jacket. A distribution cap was placed at both ends of the rock to allow the spreading of water from the pore pressure piping. The jacket containing the sample was then placed on the bottom end-cap and pushed firmly down to remove any air pockets. A large ring of fluorelastomer nitrile was stretched over the end-caps of the jacket thereby sealing the specimen at the base. To seal the upper surface the upper end-cap was placed on top of the remaining distribution cap and held in place by another ring of nitrile, all of which was held together inside the yoke. The bolts for the tie-bars were screwed down to hold the yoke together which also permitted easier transportation of the sample to the bottom closure. Once in position the pore pressure piping was connected to the end-caps, the shorter pipe for the lower one and long pipe for the upper end-cap.

Chapter 6: Experimental Set-up

For AE measurements the piezoelectric crystal (PZT-5B) was glued to the insert with silver loaded epoxy glue. On the other side of the crystal a copper disc was glued in place. Solder was attached to this disc so that the coaxial wires could be connected. As the inserts needed to be earthed for AE measurements the sheath of the coaxial cable was connected by solder to the grounding pin located next to the transducer. This avoided the crystal shorting. The inner core of the wire was then connected by solder to the copper disc.

For electric potential measurements, plain inserts were used with the inner core of the coaxial wire being connected by solder to the grounding pin. The sheath was positioned so that it did not ground on the insert.

In order to confirm that the sample transducers were set up correctly, a continuity test was completed on every channel up to the logging machines. Once satisfied that this was correct and that the sample was correctly seated, the set-up was complete. Figure 6.4 shows this set-up prior to placement inside the pressure vessel ready for testing. Further detail can be found in Appendix 1.

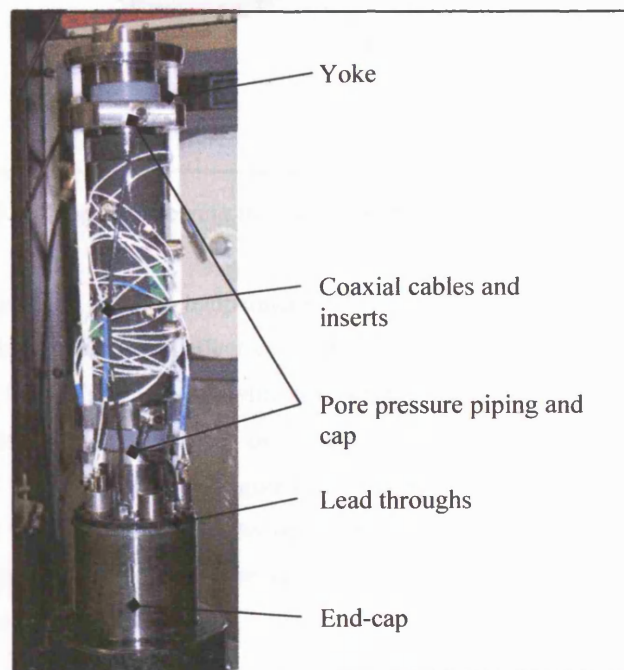


Figure 6.4: Photograph of yoke and set-up

6.3 ROCK SAMPLE ARRANGEMENT

6.3.1 Jacket System

The jacket system was designed and optimised by Peter Sammonds and Laszlo Lombas. This system was used to avoid contamination between the confining oil, which is kept outside the jacket and the pore fluid contained within the specimen. This jacket also allows post-failure experiments to be taken to at least 4mm past dynamic failure due to the flexibility of the rubber moulding.

In the wall of the jacket, holes are arranged in a pattern (see Appendix 2) of 4 sets of 3, which allows source location to be made on the sample during deformation. Into these holes concave inserts are positioned with their shape allowing for a good contact between the rock surface and the insert, which may contain either piezoelectric crystals for AE activity or an electrode for electrical potential investigation. A simplified drawing of the arrangement of a single transducer with the specimen is given in Figure 6.5.

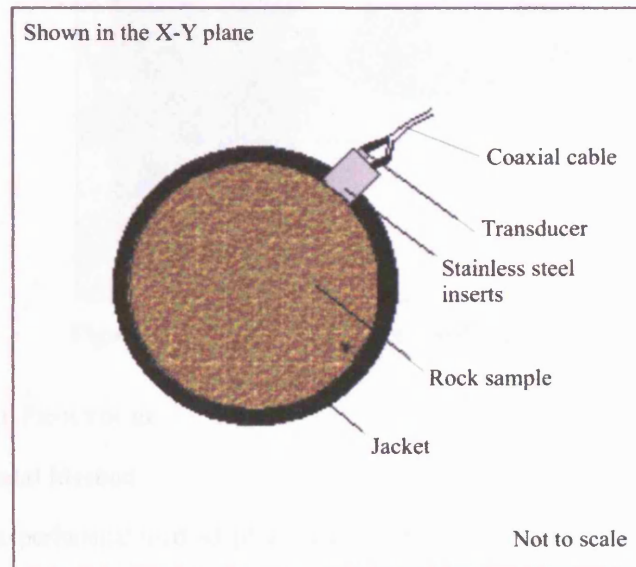


Figure 6.5: Diagram showing the metal inserts against the rock surface.

For the experiments undertaken at room temperature, the jackets were made of fluoroelastomer nitrile (properties shown in Table 6.2) and could effectively withstand confining pressures in excess of 400 MPa at temperatures less than 100°C. The holes, in which the inserts were positioned have ridges, which, with the application of stainless steel O-rings placed over them, excites and seals the jacket. The arrangement of the holes, O-rings and inserts is shown in Figure 6.6. To seal the remaining ends of the jacket against the end-caps, nitrile rings with a reduced diameter of 44.5 mm are stretched over the jacket and end-caps. Depending on the damage inflicted to the inner surface of the jacket during an experiment, the jacket could be used several times.

PROPERTY	Fluoro-el.
Relative Density Mg/m ³	1.85+/-0.02
Tensile Strength MPa	10
Elongation at Break %	250
Compression Set %	30
Tensile Strength Change %	-10
Elongation Change %	-25
Fluid Resistance to	
Weight Change %	8
Volume Change %	15

Table 6.2: Properties of fluoroelastomer nitrile jackets.

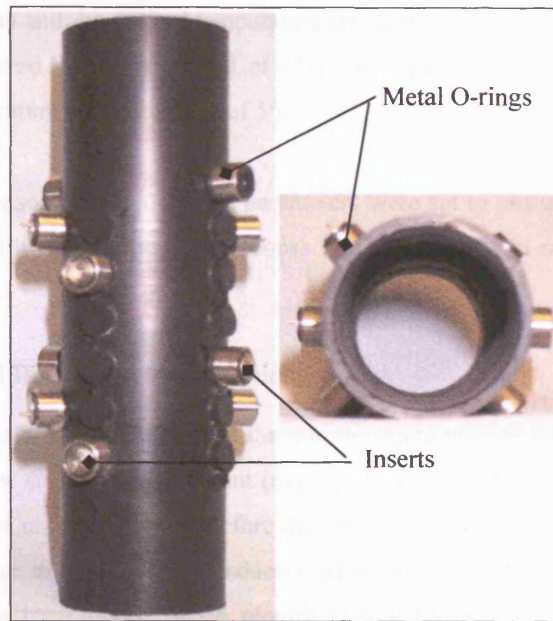


Figure 6.6: Diagrams of jackets used in experiments.

6.4 EXPERIMENTAL PROCEDURE

6.4.1 Experimental Method

For more detail on experimental method, please see Appendix 1 “Operational Procedure”.

In order to put the sample into the triaxial vessel the hydraulics were switched on and the cross-head was raised, lifting the ram and the vessel. The sample assembly was then lifted up and slid into position beneath the vessel using pins to hold it in the correct location. After this, the vessel was lowered down until it was close to resting on the floor, at which point it was adjusted to allow it to rotate in relation to the bottom closure to seal the vessel. For the different pressures, the pore and confining pressures pipes were connected to the appropriate ports and held in place by a cone sealing mechanism using a screw fitting.

Once the confining pressure had been applied to the sample, the position of the ram was adjusted so that its position was known relative to the top of the sample. This was achieved by lowering the actuator under displacement control until the load measured by the actuator was above the seal friction indicating that the ram was pushing on the sample end. The ram was then raised by less than 1 mm so that it was resting close to the top of the sample. The LVDTs which are used for the strain measurements were then attached to the piston.

Depending on the type of experiment being carried out, the pressure and temperature must be set to the desired level. To increase the confining pressure, the isolation valve to the pump was opened together with the valve on the vessel. The pump forces oil into the vessel whilst forcing air out. When this procedure was complete the valve on the vessel was closed allowing the pressure inside the vessel to increase to a pre-determined point at which time the other isolation valve was closed and the pump turned off. For the pore pressure, the appropriate intensifier was primed during isolation, then the pore pressure isolation valve was opened and the pore pressure was set to a given pressure. For temperature, the furnace

controller was switched on and the desired temperature set. The temperature in the furnace increased at a constant rate until the desired limit was reached, at which point the furnace automatically switched on and off to maintain the temperature to an accuracy of 5°C.

On the central control console all the different parameters were set to change where necessary by using the appropriate control unit with the feedback loops. This includes strain rate, pore pressure, confining pressure and temperature.

6.4.2 Calibration and Deformation Correlation

In order to interpret the data which comes from the transducers in voltage format, the data was calibrated into the relevant S.I. units, such as displacement (mm), pressure (MPa) and stress (MPa). Over time, the voltages from a transducer may drift, and therefore the calibrations were repeated every month to identify any changes. The volume displacement transducers were present in both the pore and permeameter intensifiers. The pressure transducers, which require calibration, were inside the pore and confining intensifiers. The displacement transducers, which were used to measure deformation were the two LVDTs which were fixed to the piston. Other calibrations consisted of the ram and the furnace temperature in relation to the oil and rock temperature.

All the calibrations were repeated three times and plotted on a single graph. The least-square fit was calculated along with the correlation coefficient (r^2) using the equation below

$$r^2 = \frac{\left(\sum (x_i - \bar{x})(y_i - \bar{y}) \right)^2}{\sum (x_i - \bar{x})^2 * \sum (y_i - \bar{y})^2} \quad (6.1)$$

where x_i and y_i are readings at particular location.

With the equation of the line, a configuration file in LabView can be created to change voltages in S.I. units such as MPa, cm^3 , °C automatically. A description of the different calibrations is given below.

6.4.2.1 Linear Variable Differential Transformers

Calibration of the LVDTs was undertaken using a LVDT calibration rig. This involved holding the main case of the transducers in a fixed horizontal position with the transducer itself (a metal ball-point) positioned against a metal cylinder with accurate markings of 0.05 mm ranging from 0-25 mm in length. The cylinder was moved to a position where the voltage produced by the transducer was equal to zero. It was then moved forward and backwards at 1mm intervals with voltage readings at every stage. This was repeated several times and the results averaged.

Below in Figures 6.7a and b the calibration for the LVDTs are plotted. On these graphs it is shown that the r^2 value is almost 1 with a calibration of $1 \text{ V} = 2 \text{ mm}$. When two or more transducers are used their voltages were averaged out.

6.4.2.2 Pressure Transducers

For both the confining and pore pressure transducers the same instrument known as the Bundenberg pressure calibration kit is used. The principle of this piece of apparatus is to produce a known pressure using weights which are balanced against the transducer. From the graph shown in Figure 6.8, the link between voltage and confining pressure was identified as $1 \text{ V} \approx 40 \text{ MPa}$. A similar calibration was recorded for pore pressure as shown in Figure 5.9 with both calibrations giving an $r^2 \approx 1$ and linear fit to the data.

6.4.2.3 Volume Displacement

With the displacement transducers, the range of the piston movement from the back position to its forward position was measured, both in voltage form and by measuring the volume of water collected from the full range of movement. From this it was identified that the volume was approximately 10 cm^3 with a voltage range of 0-10 V. Therefore the calibration of $1 \text{ V} = 1 \text{ cm}^3$ was used for volume displacement inside the intensifier with other intensifiers having different volumes and giving different calibrations.

6.4.2.4 Axial Load

In order to measure the load applied by the hydraulic ram to the rock sample, the force needed to be calculated with the use of a 20 tonne proving ring. When this ring was deformed by specified amount the load at that point is known and the voltage recorded. By knowing the area onto which the load was applied (40 mm diameter sample) the stress can be calculated. Repeating this for different angles (hence stresses) and plotting them, Figure 6.10 is produced showing that 1 V equals 246 MPa with a good r^2 correlation.

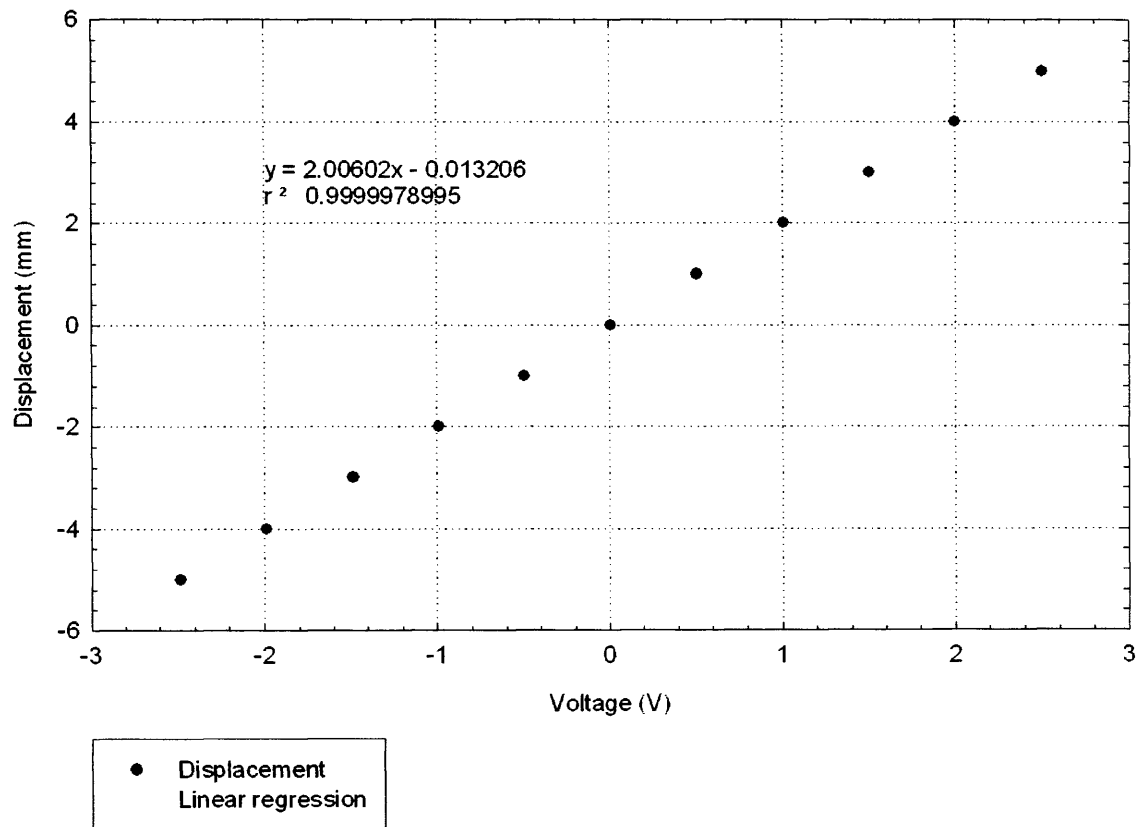


Figure 6.7a: Calibration curve for LVDT along with σ_x and R^2 .

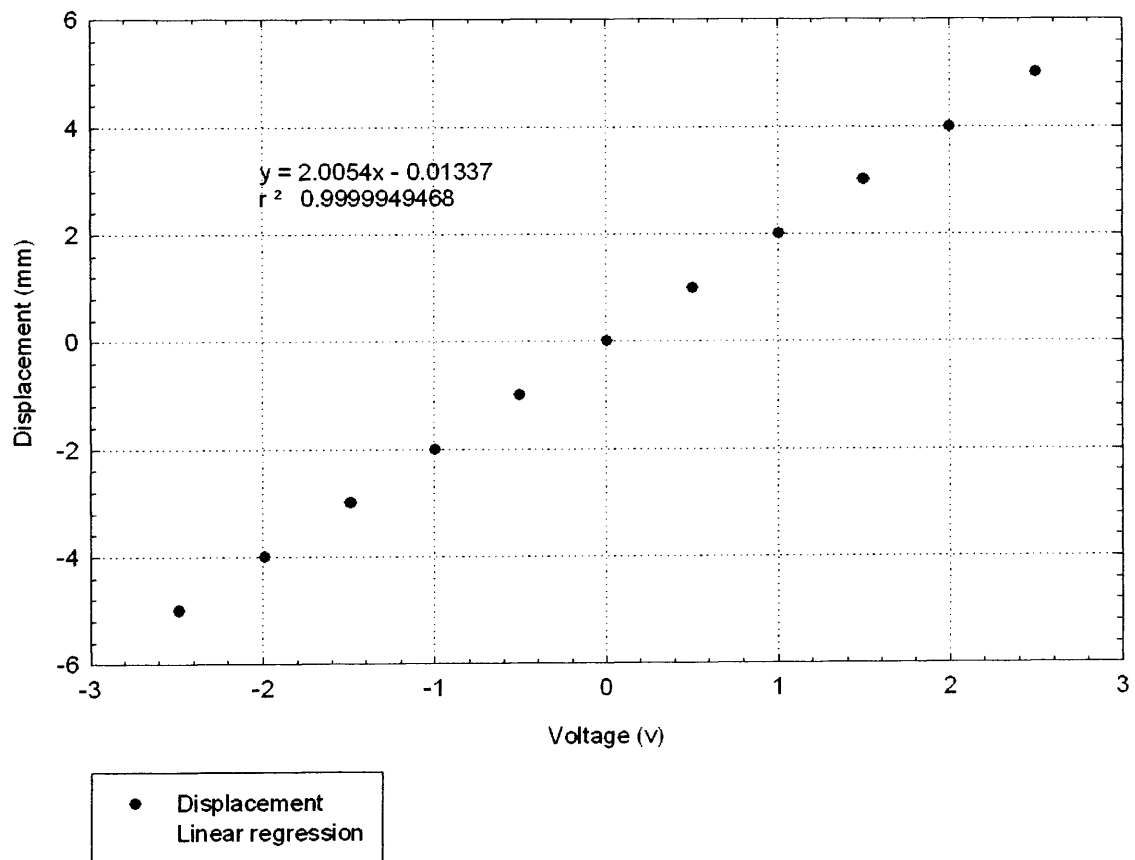


Figure 6.7b: Calibration curve for LVDT along with σ_x and R^2 .

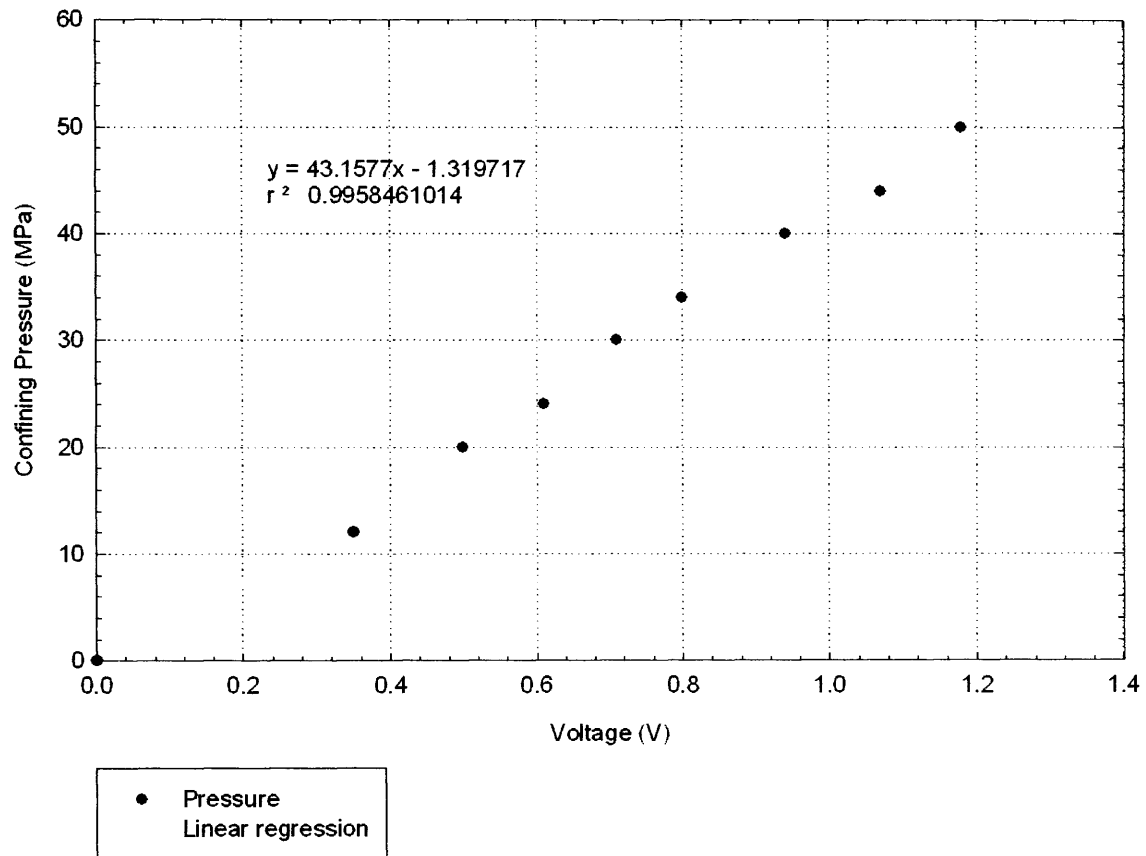


Figure 6.8: Calibration curve for the confining pressure along with σ_x and R^2 .

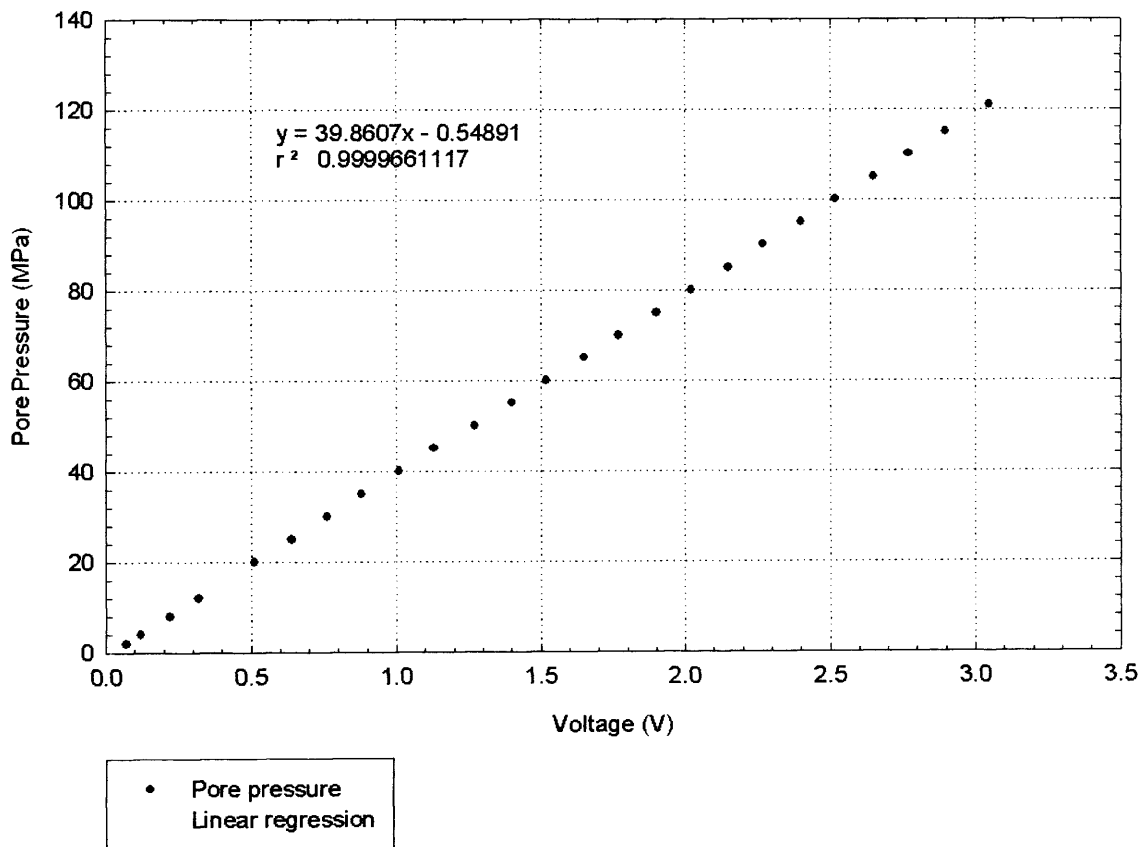


Figure 6.9: Calibration curve for the pore pressure along with σ_x and R^2 .

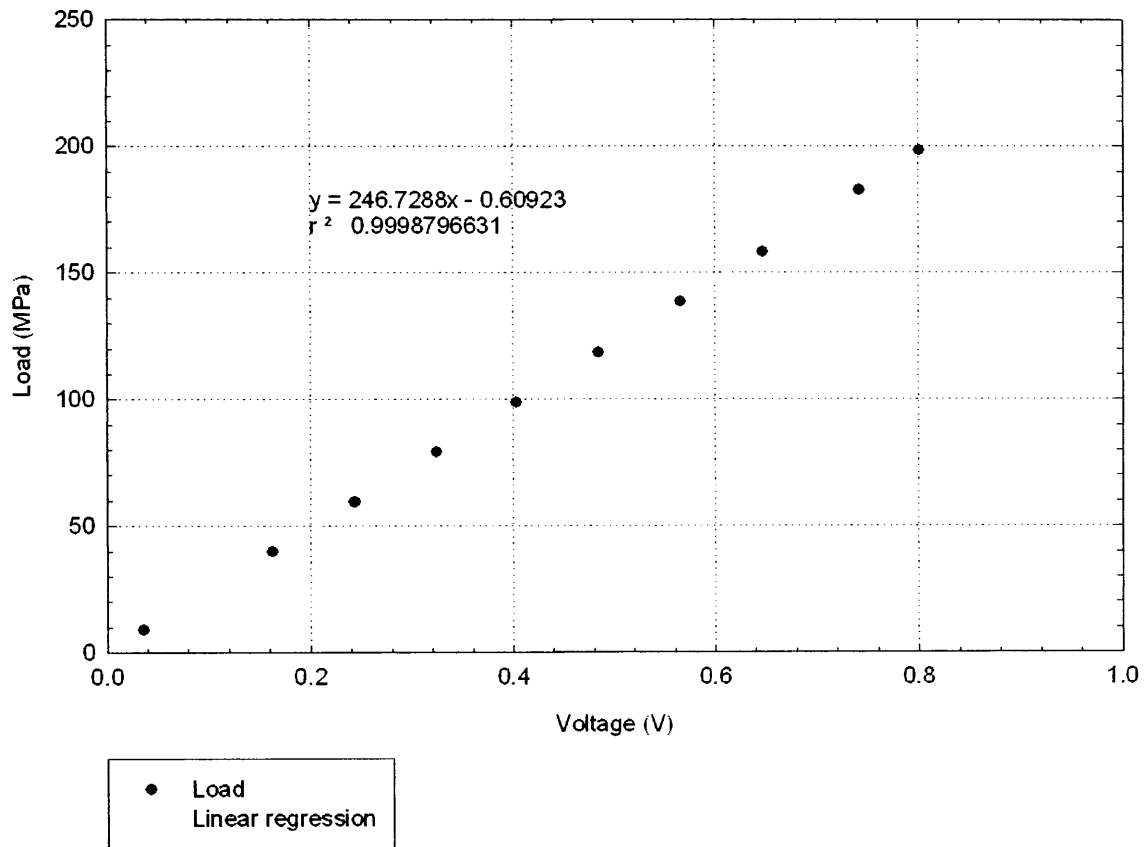


Figure 6.10: Calibration curve for the load along with σ_x and R^2 .

6.4.2.5 Furnace Calibration

As described in Chapter 5, the furnace is controlled with a master, a slave and a cut-out temperature controller, connected via thermocouples to the upper and lower coils, and the inner vessel wall respectively. These thermocouples were calibrated with a known source (oven) and the appropriate gains applied to the individual channels via the LabView software which was used to record the temperature. The other stage of calibration was to apply temperature to the furnace whilst under pressure to look at the problem of convection at the ends of the rock, the effect of temperature on the inner vessel wall and what temperature the rock reached relative to the furnace.

The overall power was set at (10%) with the master at (100%) and slave at (70%). In order to have confidence of the results, the heating cycles were repeated twice at temperatures of 25, 50, 75, 100, 125 and 150°C. With these temperatures it was possible to look at potential damage to the seals, jacket and how the increased temperature affected the jacket-rock interaction with a prediction of what effect increasing the furnace temperature would have upon the rock and seals.

The furnace program was set with a ramping rate of $5^{\circ}\text{C}\cdot\text{min}^{-1}$ with duration at temperature ranging between 2 and 12 hours depending on the experiment. For all the thermocouples, the signals were recorded in differential mode as well as having a running average of the results to remove noise from the data with a calibration table used to convert readings from voltages to degrees Celsius. It was not possible to record the temperature of the rock during a test because the thermocouples act as an aerial and the temperature at the end of the rock may not reflect the temperature in the middle of the sample. Therefore thermocouples were placed at different heights around the dummy sample (see Appendix 7) with one thermocouple placed inside a 5 mm hole in the middle of the dummy sample to monitor the temperature of the rock relative to the other thermocouples.

Using this set-up the link between furnace temperature and confining pressure was established as shown in Figure 6.11. It shows that initially the oil expands rapidly but then the rate of expansion decreases as the furnace reaches the required temperature. The oil continues to expand for several thousand seconds until it reaches the point where all the oil is heated equally. Comparing all the thermocouples against the furnace (Figure 6.12) a difference of at least 25°C exists with the oil reaching a maximum of 75°C around the middle of the sample having the same lag as with confining pressure. Generally all the thermocouples reach a maximum temperature and remain stable until the furnace is turned off and they all decrease at a similar rate to that of the furnace thermocouple. Comparing the furnace temperature with the middle of the dummy sample (Figure 6.12) shows that it takes a couple of hours for the rock to reach equilibrium before a test can begin. This is due to the need to equalise the temperature of the oil, jacket and rock so that any potential convection problem is minimized. To show the thermal profile along the side of the sample, Figure 6.13 shows that the temperature varies by less than 10°C over its length. Therefore, the temperature of the rock will vary by less than 10°C after allowing an additional 30 minutes to reach thermal equilibrium which is after the oil has reached thermal equilibrium.

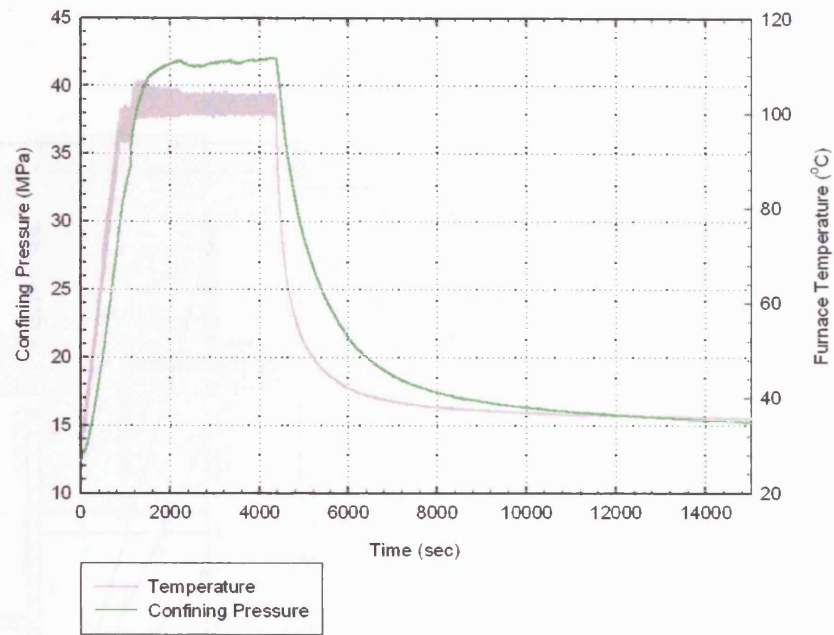


Figure 6.11: Relationship between confining pressure and furnace temperature.

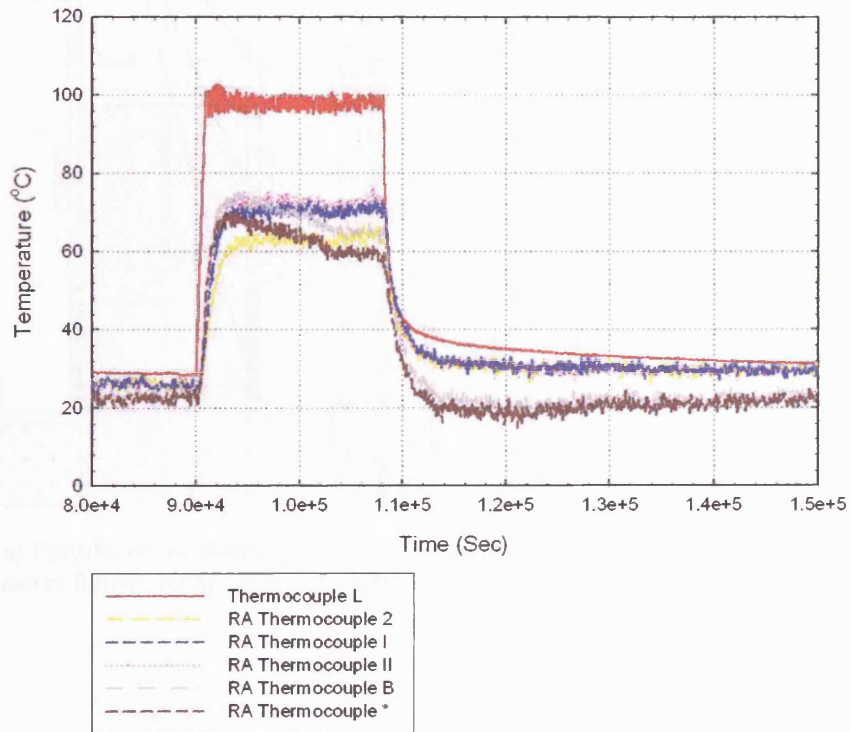


Figure 6.12: Furnace calibration for a sample temperature of 100°C. The furnace thermocouple (L) is at least 25°C warmer than the rock and oil.

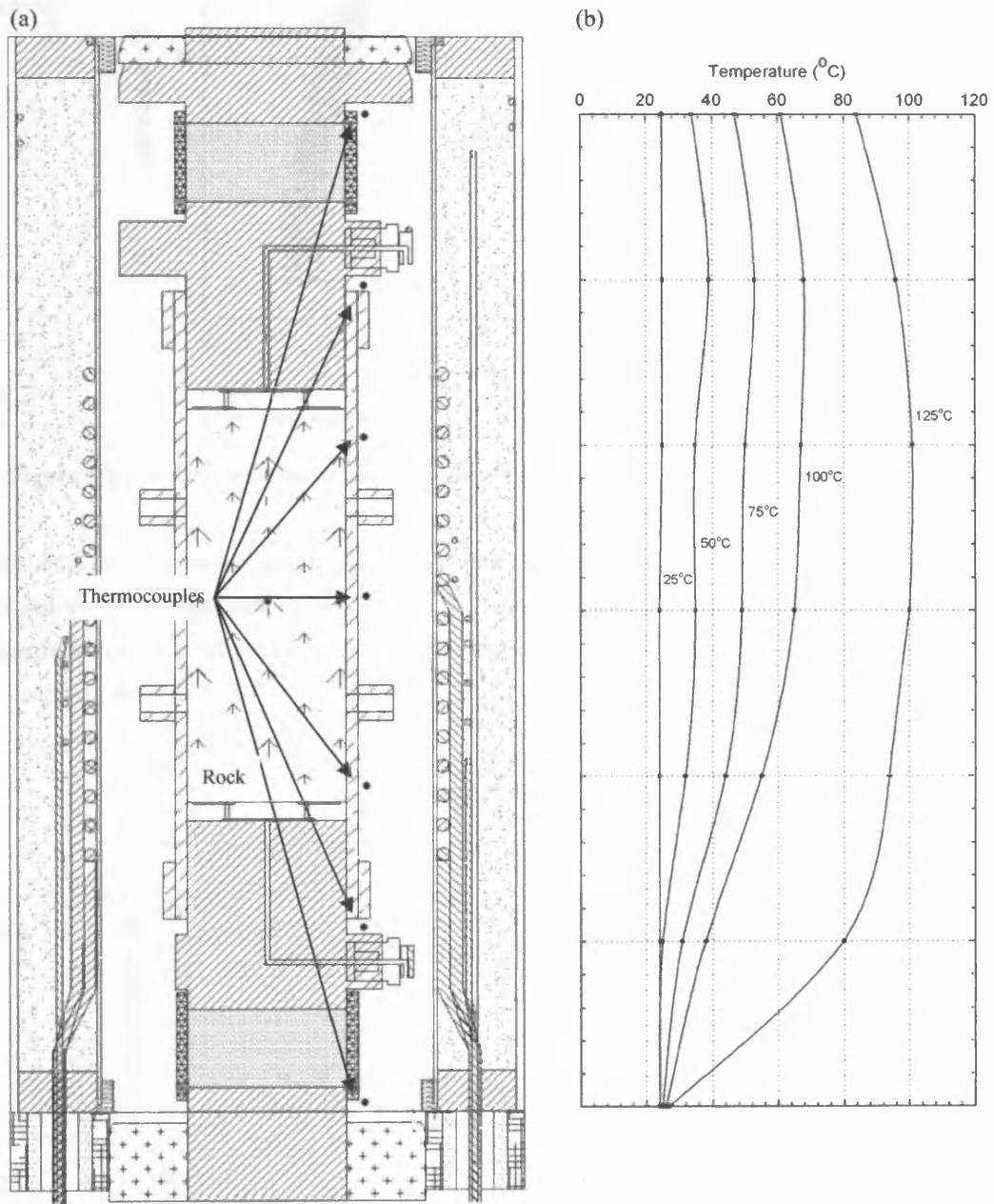


Figure 6.13: (a) Position of the thermocouples relative to the rock sample and (b) thermal profile along the rock specimen at furnace temperatures of 25, 50, 75, 100 and 125°C.

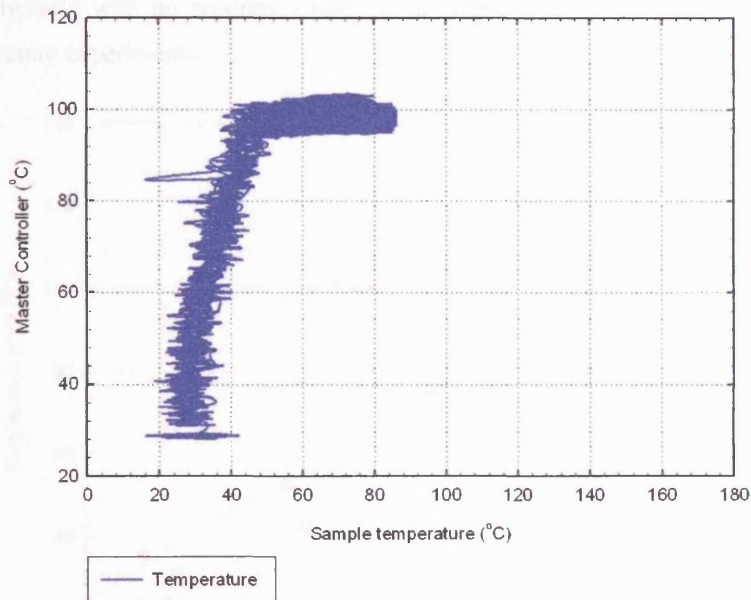


Figure 6.14: Relationship between the master controller temperature and the sample temperature.

Combining the calibration data from the two sets of tests, Figures 6.15a and b show the difference recorded with the temperature of the furnace Vs confining pressure and the temperature of the furnace Vs the temperature of the oil. From these two figures a similar shape is present between furnace temperature and confining pressure.

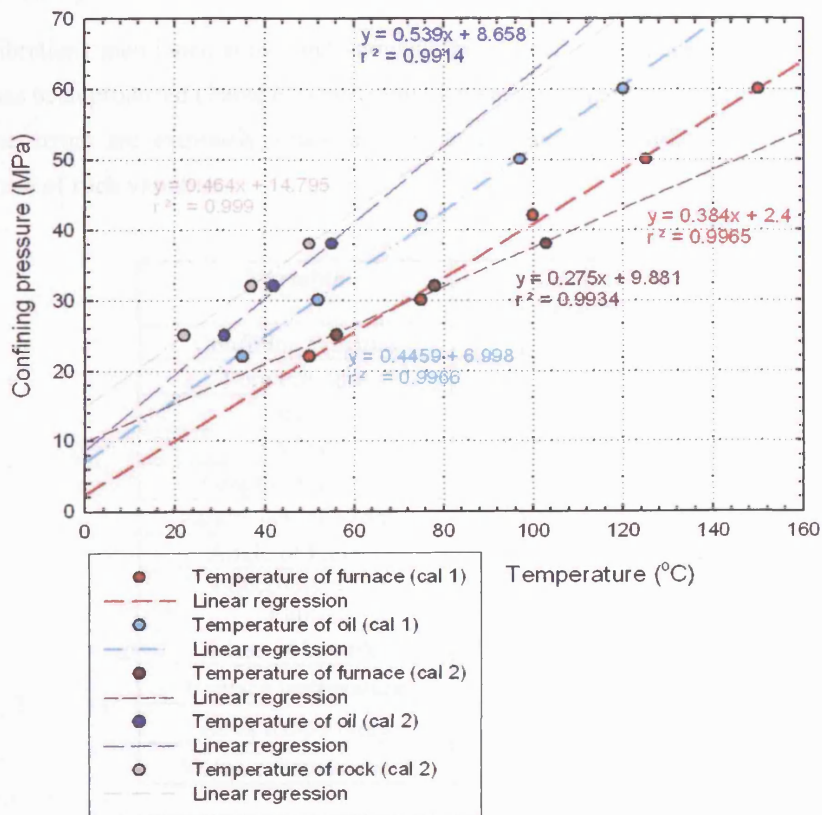


Figure 6.15a: Comparison of temperature against confining pressure at temperatures up to 125°C showing a similar shape line for both calibrations.

However, Figure 6.14b shows that the two calibrations of the temperature of the furnace versus that of the oil differ significantly with no apparent cause. So an average of the two calibrations is used for all elevated temperature experiments.

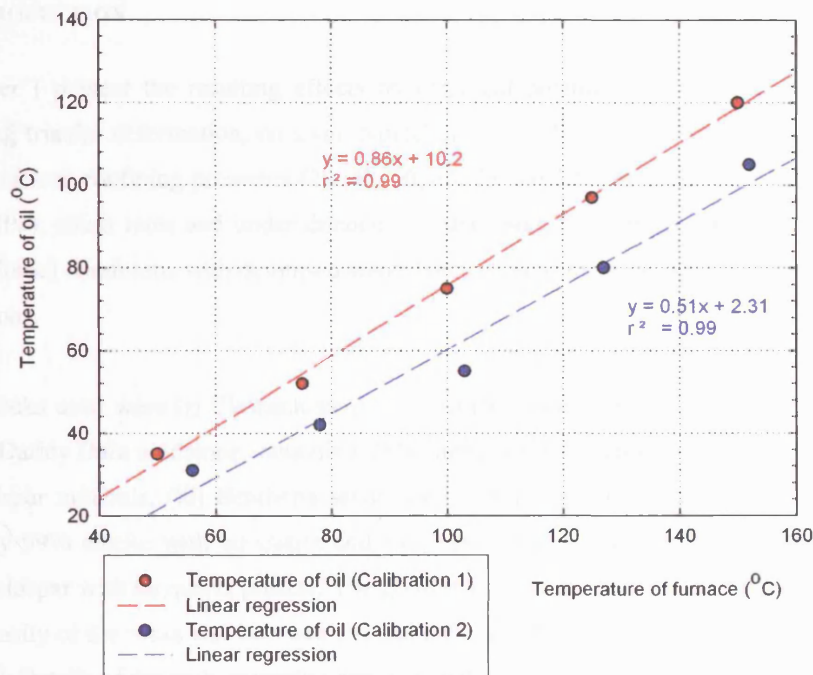


Figure 6.15b: Relationship between the temperature of the furnace and that of the oil for both sets of calibrations. The oil is allowed over 1 hr to reach thermal equilibrium before measurements are made.

6.4.2.6 Error Analysis

Using the calibrations mentioned above and knowing the accuracy of the instruments used to grind the rock, a table has been produced (Table 6.3) that shows how exact an individual reading may be. This table shows that the errors are extremely small and should not have a significant effect on an equation involving the use of such variables.

Variable	Absolute Uncertainty
Confining Pressure	± 0.1 MPa
Pore Pressure	± 0.4 MPa
Stress	± 0.5 MPa
LVDT	± 0.005 mm
Length of Sample	± 0.01 mm
Parallelism of Sample	± 0.01 mm
Angle of Failure	± 0.5°
Conductivity of Pore Fluid	± 1 μS
Mass of Sample	± 0.005 g
Furnace temperature	± 1°C
Rock temperature	± 5°C
Volume displacement	± 0.1 cm ³

Table 6.3: Showing possible errors in the variables within an individual experiment.

7. Comparison of Electrical Potential Signals from Experimental Deformation of Various Rock Types

7.1 INTRODUCTION

In this chapter I present the resulting effects on electrical potential and acoustic emissions of shear fracture during triaxial deformation, on some typical crustal rocks at room temperature. The rocks were deformed at various confining pressures (20, 40, 50, 65, 75 and 100 MPa) and pore pressures (0, 10, 15, 20 and 25 MPa), strain rates and under drained (constant pore fluid pressure) and undrained (constant pore fluid volume) conditions with deionised water being used as the pore fluid because it contained only OH⁻ and H⁺ ions.

The crustal rocks used were (i) Clashach sandstone which is composed of 70% quartz with some lithic material, (ii) Darley Dale sandstone containing 75% quartz, with the remaining volume being occupied by clay and feldspar minerals, (iii) Bentheim sandstone contains over 95% quartz, (iv) Portland limestone, approximately 99% calcite with no quartz and (v) Seljadur basalt made up of 50% pyroxene and 45% plagioclase feldspar with no quartz present. The grain size of these rocks varied from 0.008 mm to over 1 mm. The porosity of the rocks was between 3% and 24% with the permeability ranging between 10^{-17} m^2 up to 10^{-12} m^2 . Details of the rock properties can be found in Chapter 6.1.

The two major mechanisms generating the electrical signals are i) piezoelectric effect (Chapter 3.4.1) and ii) electrokinetic phenomenon (Chapter 3.4.2). The piezoelectric effect was studied using dry, quartz-rich sandstones and compared to the behaviour of quartz-free samples such as limestone. The results were interpreted using the model by Yoshida et al. (1997). The electrical signals of saturated samples of limestone and basalt were also studied as the electrical potential is due solely to the electrokinetic phenomena (Yoshida et al. 1998).

During rock deformation, the microcracking was monitored by acoustic emissions. These can be directly related to changes in the physical properties such as the fractal distribution of cracks (Main 1991). From the number of events and the amplitude of the AE signals, the laboratory results can be related to shear fracture in the crust (Main 1990, Sammonds et al. 1992). Microstructural analysis was also done to see how the AE, due to cracking, could be related to changes in electrical potential signals. The resulting electrical signals recorded during deformation were measured in the form of potential difference and potential change. The former is the difference between the ground and one of the four electrodes, the latter is the variation in potential between two electrodes (dipole).

Strain rate is an important control on frictional strength, shear failure (Odedra 1998) and time-dependent processes (Kato et al. 1993). Strain rates in the crust can vary between 10^{-12} s^{-1} and 10^{-17} s^{-1} . This is difficult to reproduce within a laboratory setting, for example a strain rate of 10^{-10} s^{-1} would take approximately 2 months to reach 2% shortening. Therefore, it is important to investigate strain rate over a

sufficient range that the results can be extrapolated up provided there is no change in deformation mechanism. In this investigation the strain rates were between $1.5 \times 10^{-4} \text{ s}^{-1}$ and $1.5 \times 10^{-7} \text{ s}^{-1}$.

Fluid flow is known to be important in a fault system and it has been suggested as a possible earthquake mechanism (Bernard 1992, Fraser-Smith et al. 1990). Therefore, the influence of fluid flow on the electrical potential signals needs to be considered. This has been investigated previously in relation to pH, conductivity and pore pressure gradients for a few rock types (Morgan et al. 1989, Jouniaux and Pozzi 1996b, Lorne et al. 1999a). Here the effect of rock type is investigated, by comparing sandstones and limestone at elevated pore pressure gradients of up to 30 MPa during different stages of deformation to look at the combined effects.

The main aim of this investigation was to investigate shear fracture under simulated shallow crustal conditions (depth around 2 km) so that the rock properties (Chapter 2) could be related to the electrical signals (Chapter 3). This involved Bentheim, Clashach, Darley Dale sandstones, Portland limestone and Seljadur basalt to identify the commonality and differences between the lithologies. From this I hoped to answer several questions including 1) Does the effective pressure affect the stress drop and slip displacement during failure? 2) How does the magnitude of the electrical potential signal differ between sandstone and limestone rocks? 3) Of the two main mechanisms responsible for the electrical potential signals (electrokinetic and piezoelectric), which is dominant in fluid filled crustal conditions? 4) What electrical signals are present during frictional sliding? The answers to these questions can then be used in conjunction with other data to interpret self-potential signals observed in the field related to fault development and movement. This could perhaps be used for earthquake prediction.

7.2 COMPARISON OF MECHANICAL PROPERTIES

The typical behaviour of the rock during triaxial deformation is shown in Figure 7.1 for drained rocks with a confining pressure of 40 MPa and pore pressure of 20 MPa. Figure 7.1a for Bentheim sandstone the initial application of load causes compaction through the closing of pores up to 0.2% strain. A period of quasi-elastic behaviour follows as cracks and pores are forced closed due to the rock accommodating the strain, with a corresponding reduction in pore volume as shown in Figure 7.2. At the elastic limit of the rock, dilatancy starts to dominate over compaction through the opening of cracks and pores. An increase in pore volume occurs with strain hardening up to a peak stress of 142 MPa, at 1.5% strain. Further loading results in strain softening and dynamic failure through the formation of a macroscopic fault across the sample. At failure the rock can no longer support the load applied to it by the ram, this causes the rock to break and the ram to move downwards towards the sample. At this time the ram is moving at a strain rate in excess of $1 \times 10^{-4} \text{ s}^{-1}$ which is faster than the strain rate set by the servo controls. In response to moving too fast the ram is backed off through the feedback loop system causing a slight decrease in the strain applied to the sample. The ram then moves at the set strain rate and produces the characteristic loop which is seen in Figure 7.1b. Similar trends are also present in other sandstones tested (Figures 7.1b and c), Figure 7.1d, the elastic limit of Portland limestone extends to 0.8% strain with strain hardening up to 120 MPa, with a short strain softening period present before dynamic failure.

The change in pore volume and confining pressure during deformation of Darley Dale sandstone is shown in Figure 7.2 with an initial confining pressure of 40 MPa and constant pore pressure (drained) of 20 MPa. As the stress increases, the resulting compaction causes the rocks pore volume to decrease to -0.23 cm^3 at 1.1% strain. Dilatancy occurs there after, opening pores and cracks and increasing the pore volume after compaction by 0.3 cm^3 . After failure the rocks pore volume continues to increase slowly at a steady rate due to further microcracking during sliding on the failure. This change is also apparent in confining pressure which follows the same trend with a minimum around the compaction-dilatancy transition. This link is emphasised in Figure 7.3 where the change in confining pressure is plotted against the change in pore volume with the different stages of deformation marked.

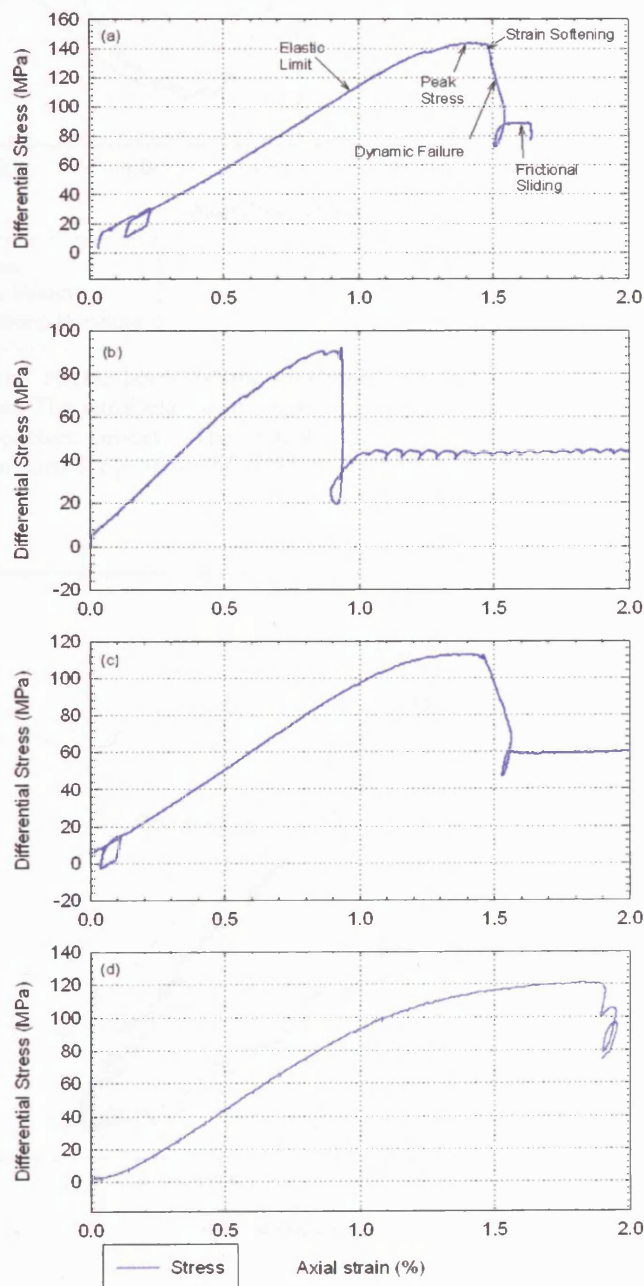


Figure 7.1: Typical stress-strain curve for triaxial deformation of (a) Bentheim sandstone, (b) Clashach sandstone, (c) Darley Dale sandstone and (d) Portland limestone; all experiments had P_c of 40 MPa and P_p of 20 MPa with a strain rate of $1.5 \times 10^{-5} \text{ s}^{-1}$. [Experiment No.:(a) 26, (b) 13, (c) 30, (d) 25]

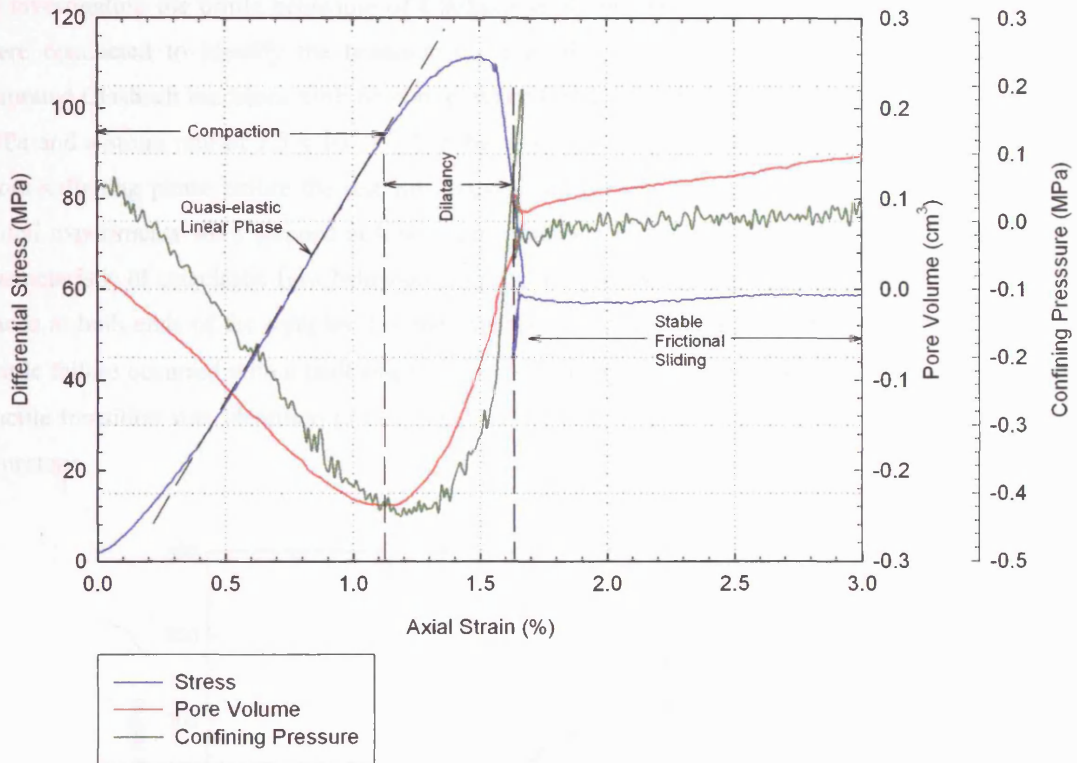


Figure 7.2: Differential stress, pore volume and confining pressure change of drained Darley Dale sandstone against strain. The quasi-elastic linear phase compares well with a pore volume decrease in the rock due to the compaction process. The reduction in rock size also causes a similar reduction in confining pressure; an initial C_p of 40 MPa and P_p of 20 MPa with a strain rate of $1.5 \times 10^{-4} \text{ s}^{-1}$. [Experiment No.: 32]

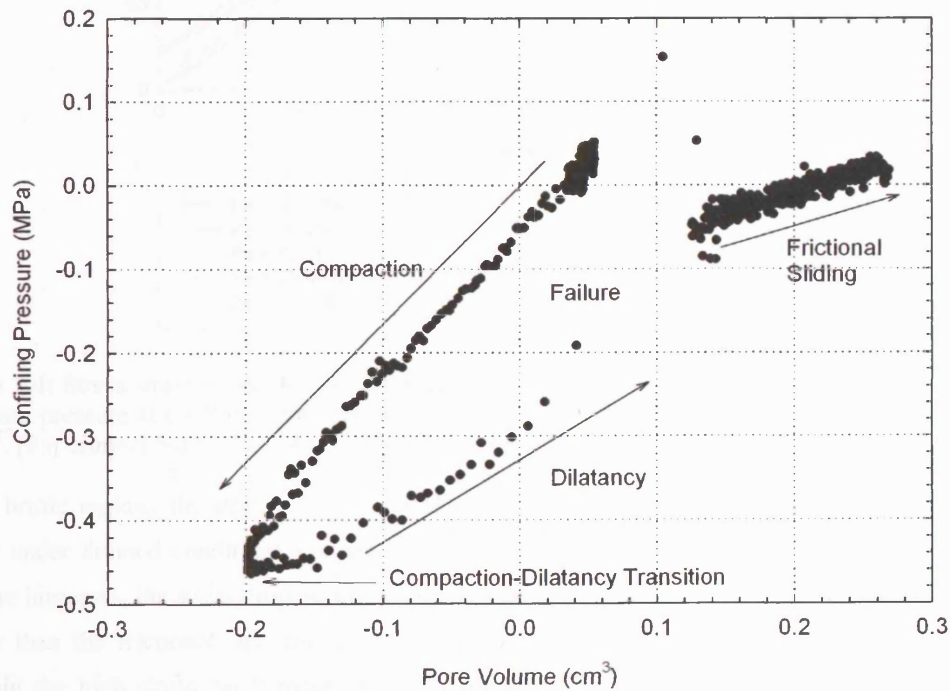


Figure 7.3: Plot showing the link between the change in confining pressure and the change in pore volume during the deformation of drained Darley Dale sandstone; $P_c = 40 \text{ MPa}$, $P_p = 20 \text{ MPa}$ using deionised water and a strain rate of $1.5 \times 10^{-4} \text{ s}^{-1}$. [Experiment No.: 32]

In investigating the brittle behaviour of Clashach sandstone and Portland limestone, initial experiments were conducted to identify the brittle-ductile transition. Figure 7.4 plots the stress-strain curves of saturated Clashach sandstone with no pore pressure but with confining pressure up to a maximum of 100 MPa and a strain rate of $1.5 \times 10^{-5} \text{ s}^{-1}$. For the confining pressures of 65 MPa and above, there was no work-softening phase before the test was stopped. As rupture of the nitrile jackets was to be avoided, initial experiments were stopped at low strains gradually increasing up to 5% strain. These curves are characteristic of cataclastic flow behaviour with the samples being slightly barrel shaped with some shear bands at both ends of the samples. For the experiments at confining pressures of 30 and 50 MPa, brittle failure occurred with a fault angle of $\approx 30^\circ$ to the maximum principal stress. From this, the brittle-ductile transition was identified to be around 60 MPa for Clashach sandstone and 25 MPa for Portland limestone.

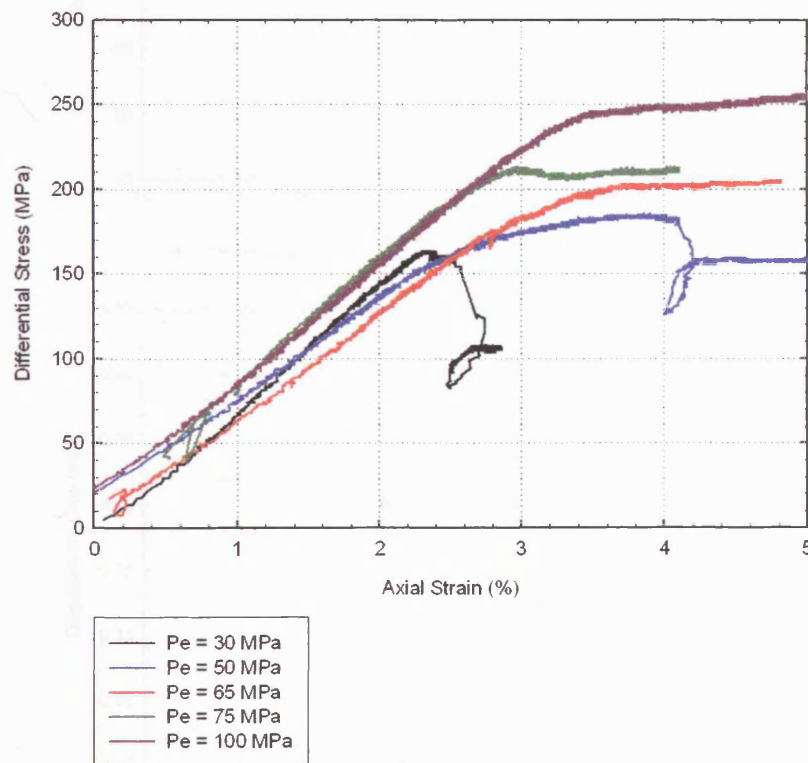


Figure 7.4: Stress-strain curves for the deformation of Clashach sandstone under drained conditions with zero pore pressure at confining pressures of 30, 50, 65, 75 and 100 MPa and using a strain rate of $1.5 \times 10^{-5} \text{ s}^{-1}$. [Experiment No.: 1, 2, 3, 4, 5]

In the brittle regime, the stress drop and displacement changes were also investigated during dynamic failure under drained conditions and are shown in Figure 7.5. Figure 7.5a shows that as the effective pressure increases, the stress drop during failure decreases. This is because the peak strength of the rock is greater than the frictional strength. Therefore, when a fault is formed, the rock is no longer able to maintain the high stress, so it moves in the opposite direction to the applied stress (i.e. downwards) resulting in a decrease in stress applied to the end of the sample. Now the higher the effective pressure the greater the friction on surfaces within the rock. So, at low effective pressures little frictional strength is present so it takes longer for the frictional strength to build up to stop sliding at dynamic failure than at

higher effective pressures where the frictional strength is much greater. The axial component of movement along the fault plane at the instant of dynamic failure is shown in Figure 7.5b where an increase in effective pressure reduces the magnitude of the slip movement which agrees with the observations of Fang and Harrison (2002). These combined results suggest that at the brittle-ductile transition there is no stress drop and no slip movement as cataclastic flow occurs as shown in Figure 7.4.

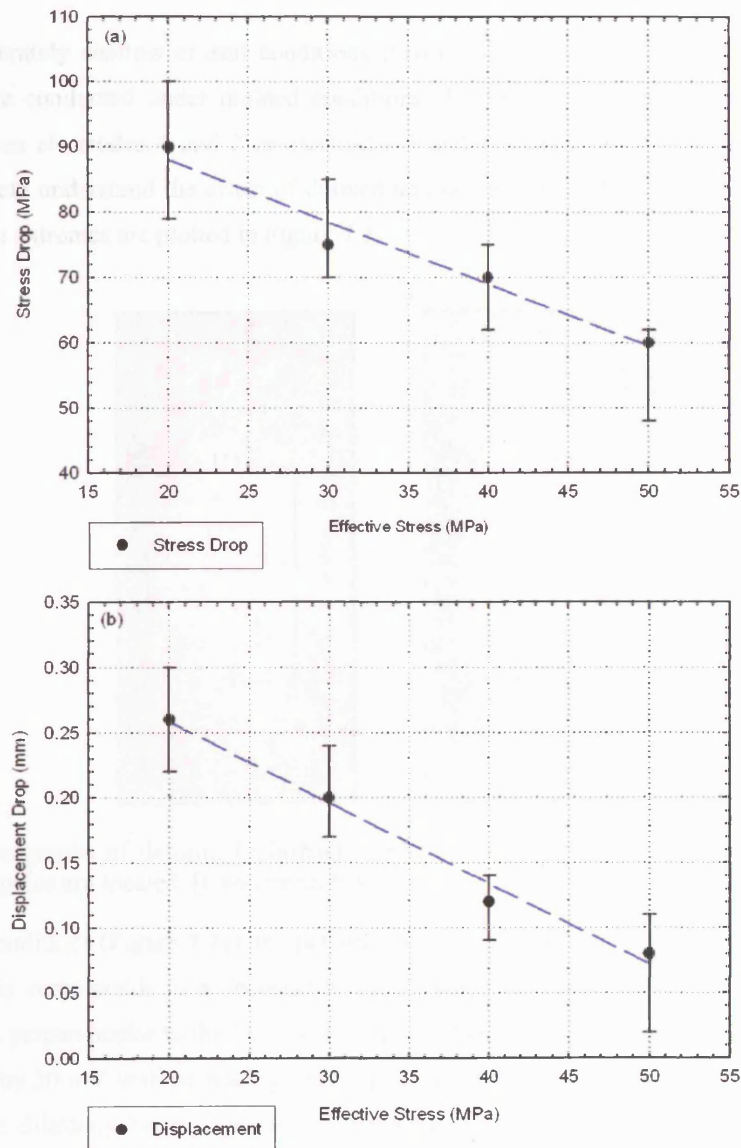


Figure 7.5: The effect of effective stress on (a) the stress drop and (b) slip displacement during brittle failure of Clashach sandstone under drained conditions using a strain rate of $1.5 \times 10^{-5} \text{ s}^{-1}$. The broken lines shown represent the least squared fit where the accuracy of each point shown given by error bars. [Experiment No.: 1 ($P_c = 30 \text{ MPa}$, $P_p = 0 \text{ MPa}$), 3 ($P_c = 50 \text{ MPa}$, $P_p = 0 \text{ MPa}$), 12 ($P_c = 40 \text{ MPa}$, $P_p = 20 \text{ MPa}$), 16 ($P_c = 60 \text{ MPa}$, $P_p = 20 \text{ MPa}$)]

The majority of the remaining experiments were conducted drained with a confining pressure of 40 MPa and a constant pore pressure of 20 MPa, which corresponds to a depth of about 1.6 km and 0.8 km in the Earth's crust respectively.

7.3 THE DIFFERENCE BETWEEN DRAINED AND UNDRAINED EXPERIMENTS ON ELECTRICAL SIGNAL GENERATION

In the drained case the pore fluid pressure is held constant by varying pore fluid volume in response to changes in pore volume during the experiment while in the undrained case pore fluid volume is held constant meaning that there are changes in pore fluid pressure in response to the changes in pore volume.

To simulate accurately shallow crustal conditions involving sandstone and limestone, the majority of experiments were conducted under drained conditions. The electrical potential change represents the difference between electrodes 4 and 2 or electrodes 3 and 1 located on the rock surface as shown in Figure 7.6. To help understand the effect of drained and undrained conditions on the electrical potential signals, these two extremes are plotted in Figure 7.7.

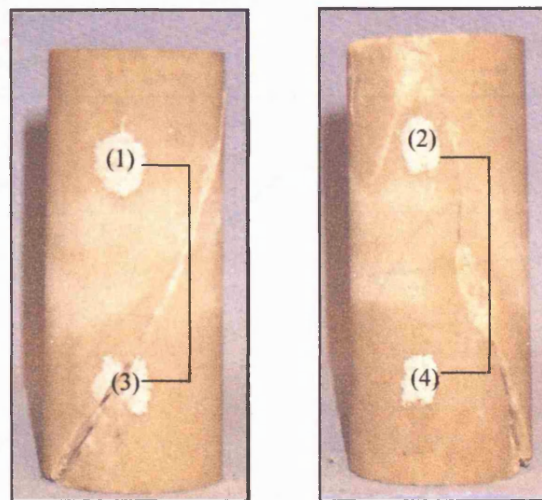


Figure 7.6: Photographs of deformed Clashach sandstone showing the position of the electrodes and where the two dipoles are located. [Experiment No.:17]

Under drained conditions (Figure 7.7a), the potential decreases by 80 mV as the stress increases up to the elastic limit. This corresponds to a decrease in pore volume of 0.2 cm³ caused by the compaction of cracks and pores perpendicular to the loading direction. When dilatancy becomes dominant, the potential signal increases by 30 mV with increasing stress up to failure and a corresponding pore volume increase of 0.1 cm³ since dilatancy began. This increase is caused by the increasing deviatoric stress causing dilatant microcracking, which, under constant pore pressure are filled with pore fluid.

In undrained conditions (Figure 7.7b) the electrical potential change remains constant with an increase in pore pressure of 3 MPa as the cracks and pores close up. When microcracking begins, the pore pressure decreases as the fluid enters the newly formed void space and continues to decrease up to dynamic failure. This decrease occurs at the same time as an increase in electrical potential change following a curve up to failure, with a signal change of over 30 mV as new surfaces are exposed for chemical reaction.

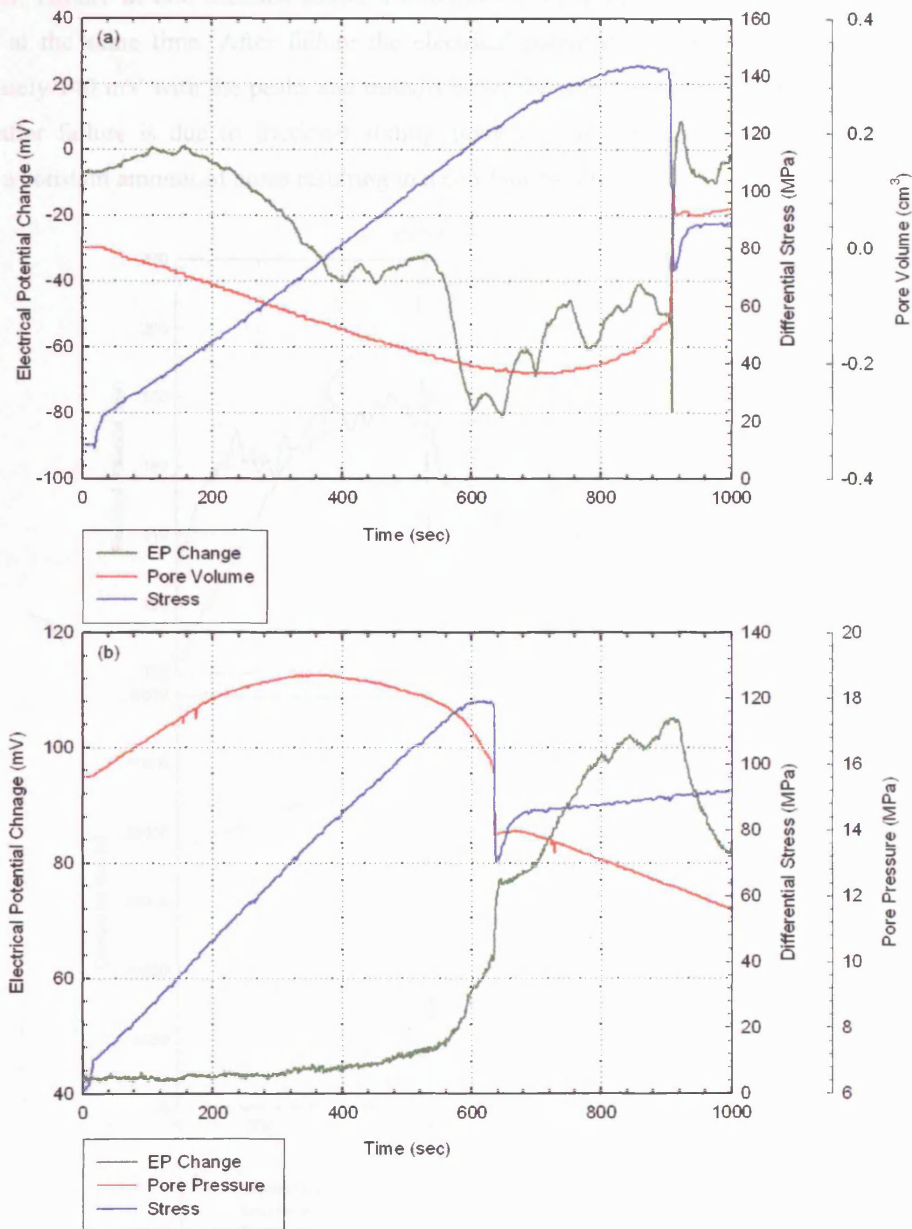


Figure 7.7: Electrical potential change as a function of time for (a) drained ($P_c = 40$ MPa, $P_p = 20$ MPa) and (b) undrained ($P_c = 40$ MPa, initial $P_p = 15$ MPa) experiments. Also shown is the differential stress, pore volume and pore pressure. [Experiment No.: (a) 26 (b) 43]

7.4 THE EFFECT OF DIFFERENTIAL STRESS ON ELECTRICAL POTENTIAL SIGNALS

Changes in a rock's physical properties during deformation can be seen by simultaneously monitoring acoustic emissions and electrical potential signals. In Figure 7.8a, a Clashach sandstone sample is deformed under drained conditions with a strain rate of $1.5 \times 10^{-5} \text{ s}^{-1}$, confining pressure of 40 MPa and pore pressure of 20 MPa with the corresponding changes in electrical potential and acoustic emissions shown. When the load begins to increase, the electrical potential increases at all electrodes (electrode 2 is absent due to breaking before the experiment began), with electrodes 1 and 3 showing similar values, with limited amounts of AE as pores and cracks are closed with little or no noise. As dilatancy occurs, the cumulative number of AE hits increases, due to the creation of new cracks, with the electrical potential

curving off. Failure at 600 seconds shows a minimum b-value of 1.82 with an increase in EP signal occurring at the same time. After failure the electrical potential decreases to a background value of approximately 140 mV with the peaks and troughs being the result of variations in the differential stress. The AE after failure is due to frictional sliding along the fault which occurs at a constant rate and generates a constant amount of noise resulting in a constant b-value.

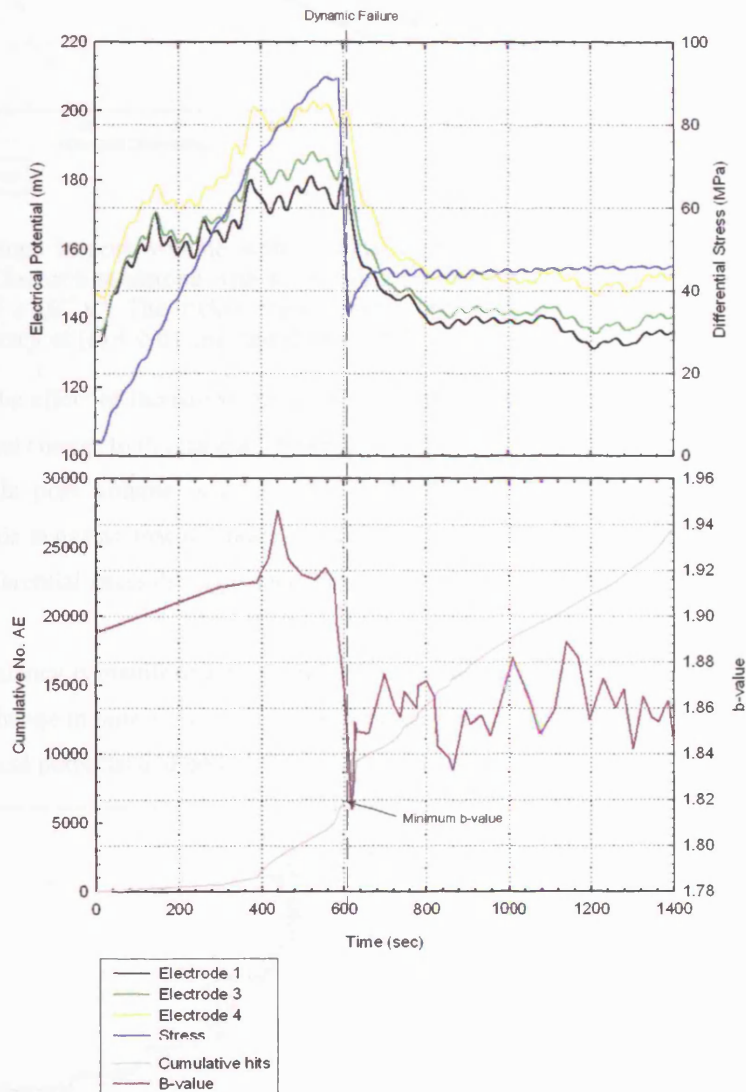


Figure 7.8: The effect of axial loading on Clashach sandstone related to (a) the electrical potential signal produced during deformation and (b) the total number of hits recorded and calculated b-value with a strain rate of $1.5 \times 10^{-5} \text{ s}^{-1}$, P_c of 40 MPa and P_p of 20 MPa. [Experiment No.: 13]

The same type of experiment was attempted on limestone several times. However, as calcite is very weak, the majority of acoustic emissions cannot be detected above background noise of 40 dB, which agrees with other work in this laboratory (Pers. Comm. Meredith 2004). A similar process to that described for sandstone is believed to occur between mechanical and electrical potential signals for Portland limestone. To show the link between differential stress, change in pore volume and electrical potential signals during compaction, Figure 7.9 is produced. This shows the change up to dilatancy, which is regarded as the elastic limit where differential stress and changed in pore volume deviate from a linear fit.

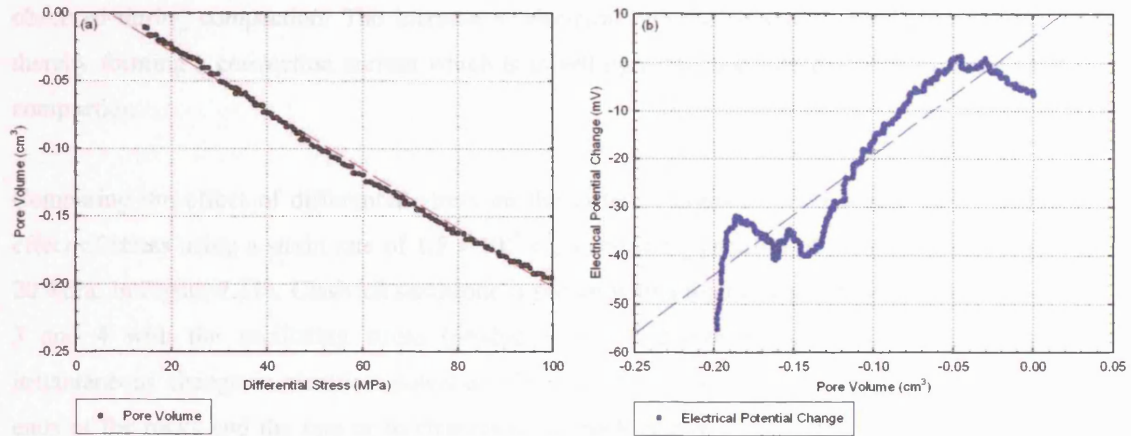


Figure 7.9: Change in pore volume with (a) axial differential stress and (b) electric potential during compaction of Clashach sandstone with a confining pressure of 40 MPa, pore pressure of 20 MPa and strain rate of $1.5 \times 10^{-4} \text{ s}^{-1}$. The broken lines shown represent the least squared fit. Each point plotted is given to an accuracy of (a) $\pm 0.01 \text{ cm}^3$ and (b) $\pm 0.2 \text{ mV}$. [Experiment No.: 26]

In Figure 7.9a, the effect of increasing the differential stress decreases the pore volume which causes the electrical potential change to decrease as shown in Figure 7.9b, where a best fit line has been applied. The rate of change in pore volume is $2.25 \times 10^{-3} \text{ cm}^3/\text{MPa}$ with the electrical potential rate change of $25 \text{ mV}/\text{cm}^3$. This suggests that the potential signal change could be used as an indirect measurement technique of differential stress during compaction.

The onset of dilatancy is manifested as an increase in AE activity brought about by microcracking with a corresponding change in pore volume with fluid entering the rock under a constant pressure gradient. The change in electrical potential and pore volume during this stage is displayed in Figure 7.10.

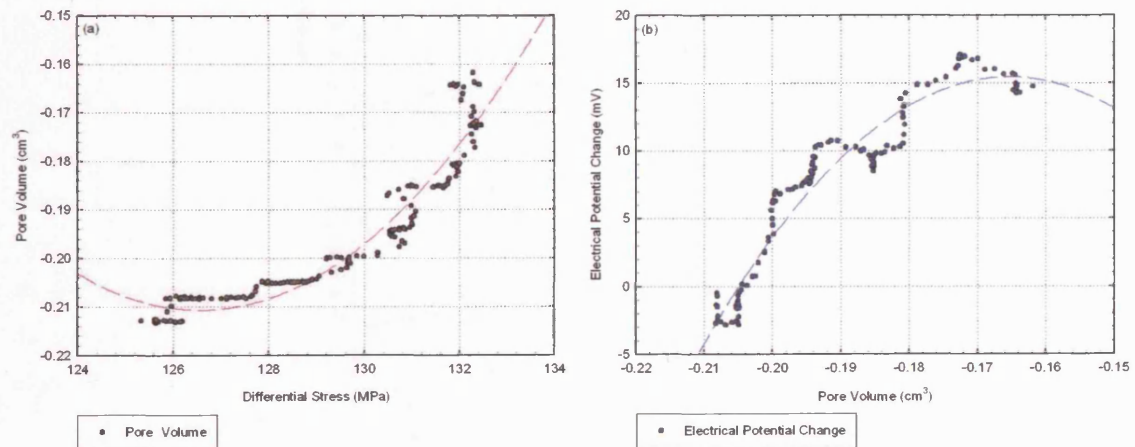


Figure 7.10: Change in pore volume with (a) axial differential stress and (b) electric potential change during dilatancy of Clashach sandstone with a confining pressure of 40 MPa, pore pressure of 20 MPa and strain rate of $1.5 \times 10^{-4} \text{ s}^{-1}$. The broken lines shown represent the least squared fit. Each point plotted is given to an accuracy of (a) $\pm 0.01 \text{ cm}^3$ and (b) $\pm 0.2 \text{ mV}$. [Experiment No.: 26]

The increase in differential stress causes the pore volume to increase as shown in Figure 7.10a where a power law has been fitted to the data. It is also shown that the change in pore volume during dilatancy is less than half that which occurs during compaction. Relating the electrical potential change to a change in pore volume (Figure 7.10b), a linear relationship is not observed. This is significantly different to that

observed during compaction. The increase in electrical potential is due to fluid moving into the rock thereby forming a convection current which is travelling in the opposite direction to that caused during compaction.

Comparing the effect of differential stress on the different drained rock types, Figure 7.11 shows the effect of stress using a strain rate of $1.5 \times 10^{-5} \text{ s}^{-1}$, a confining pressure of 40 MPa and pore pressure of 20 MPa. In Figure 7.11a, Clashach sandstone is shown with a total change of 120 mV on electrodes 1, 2, 3 and 4 with the oscillating stress (produced by the displacement control system) matching an instantaneous change in electrical potential. This may be due to either resistivity changes between the ends of the rocks and the ram or to changes to the rock matrix. The Darley Dale sandstone results are shown in Figure 7.11b with a potential change of 100 mV, and the Bentheim sandstone results in Figure 7.11c with an electrical potential change of 90 mV. For Portland Limestone, in Figure 7.11d, only a change of 80 mV is present. These results show that the same mechanism is present for all rock types investigated here, while the magnitude of the electrical signal depends on rock properties such as composition, porosity, permeability.

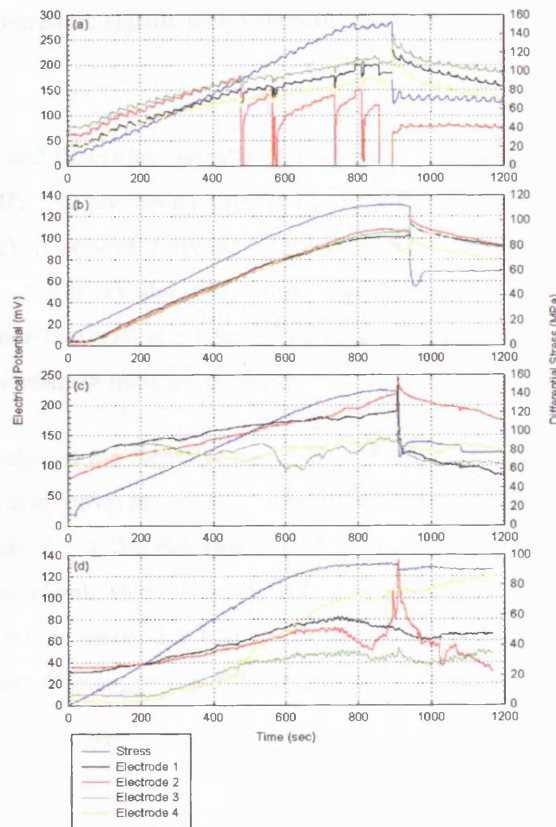


Figure 7.11: Variation of electrical potential signals produced during deformation and shear failure of (a) Clashach sandstone, (b) Darley Dale sandstone, (c) Bentheim sandstone and (d) Portland limestone. All experiments had a P_c of 40 MPa, P_p of 20 MPa and strain rate of $1.5 \times 10^{-5} \text{ s}^{-1}$. [Experiment No.: (a) 33, (b) 30, (c) 26, (d) 19]

7.5 PRE-SEISMIC AND CO-SEISMIC COMPARISON BETWEEN ROCK TYPES

The electrical potential generated around dynamic failure for various rock types is shown in Figure 7.12 for dry specimens with a confining pressure of 20 MPa and Figure 7.13 for water saturated specimens

with a confining pressure of 40 MPa and pore pressure of 20 MPa. Figure 7.12a shows a plot of how all four electrodes and differential stress are affected by dynamic failure of Darley Dale sandstone at a confining pressure of 20 MPa. The differential stress decreases slowly from 108 MPa up to 15 seconds (arbitrary scale), where it drops down to 36 MPa and recovers to steady frictional sliding of 44 MPa. The electrical potential varies by less than 3 mV (background noise) up to 1 second before failure, at which time a 20 mV signal is displayed with both positive and negative polarities. The position of the electrodes was fixed and not responsible for the polarities observed as this feature varied from test to test.

With Figure 7.12b a stress of 50 MPa is present at 21 seconds. The pre-seismic signal has both positive and negative polarities which occur less than 1 second before brittle failure with an average change of 20 mV. Electrode 3 shows the precursory signal slightly earlier than the other electrodes (0.5 seconds) and has a larger co-seismic signal that does not follow the same trend as the rest of the electrodes after failure. This suggests a localised feature is present at electrode 3. In Figure 7.12c the effect of a localised feature can also be seen at electrode 3 with the precursory signal earlier and with a change in magnitude from 110 mV down to 30 mV and then a co-seismic signal change of 120 mV. The remaining electrodes show a similar trend in co-seismic signals with values of 30 mV with all four electrodes decreasing after failure.

Quartz-free rocks (basalt and limestone) are shown in Figure 7.12d and e respectively. With basalt the stress drops below 200 MPa. No precursory signal can be identified above the background level whilst a co-seismic signal of 35 mV is present. Limestone shows a similar trend with no precursory signals but a co-seismic signal change of 100 mV due to a stress drop of 80 MPa. The electrokinetic effect can be excluded due to the absence of water, and with the absence of quartz ruling out the piezoelectric effect, therefore an alternative mechanism must be responsible.

The effect of deionised water on the electrical potential is shown in Figure 7.13. In Figure 7.13a, Darley Dale shows a small stress drop down to 74 MPa before dropping to 62 MPa at failure. Compared with the water free sample in Figure 7.12a, the electrical potential shows a 100 mV signal on all four electrodes two seconds before the co-seismic stress drop. At failure, the potentials in electrodes 1 and 2 change by 40 mV compared to 115 mV in electrodes 3 and 4. However, all electrodes show a similar shape with a decaying signal after failure. This suggests a different mechanism compared to a dry system because a net charge is produced.

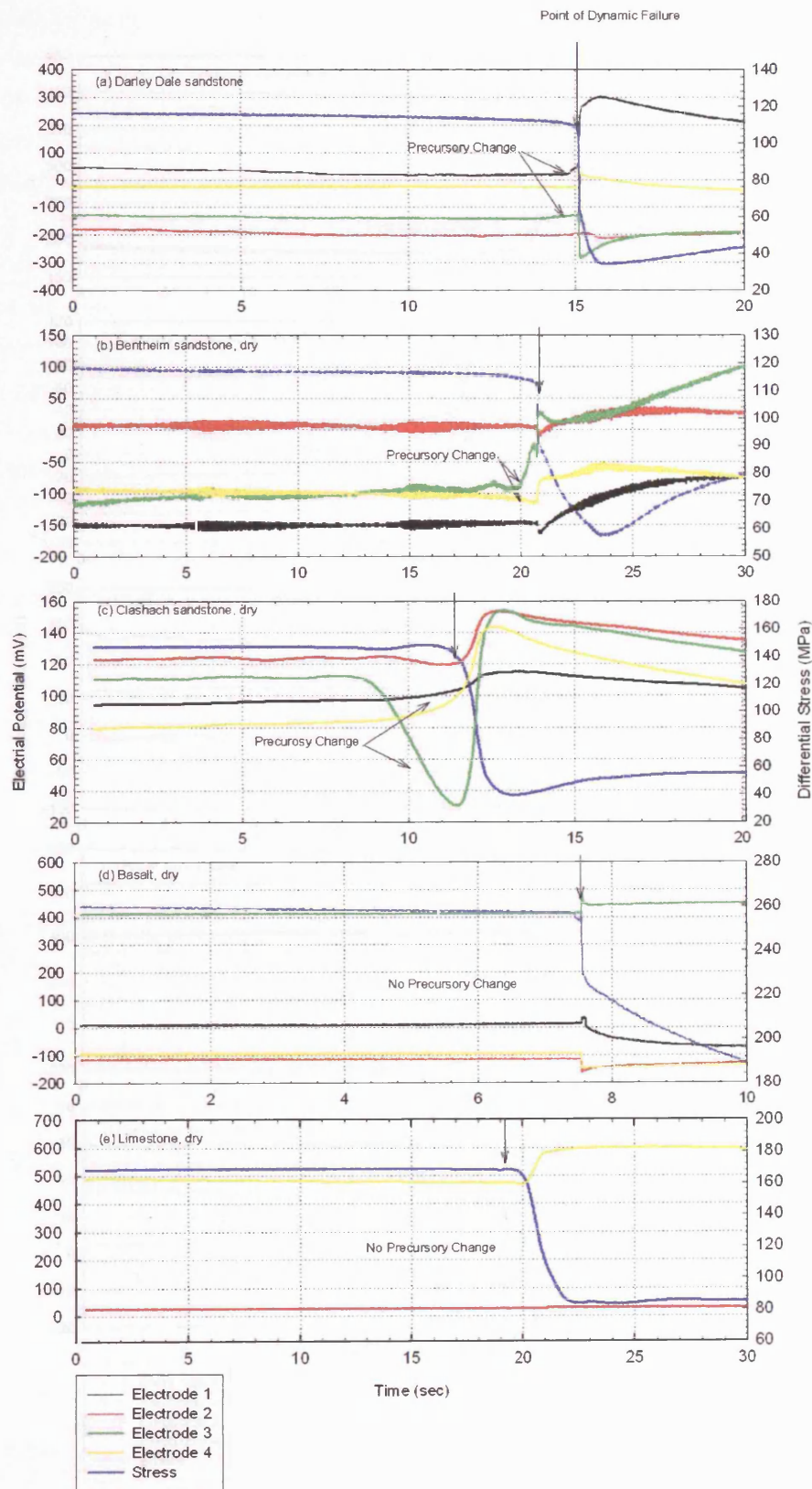


Figure 7.12: The electrical potential signals produced during strain softening and shear failure of (a) Darley Dale sandstone, (b) Bentheim sandstone, (c) Clashach sandstone, (d) Icelandic basalt and (e) Portland limestone. All experiments had P_c of 20 MPa with a strain rate of $1.5 \times 10^{-5} \text{ s}^{-1}$. [Experiment No.:(a), (b) and (d) See Clint (1999), (c) 15, (e) 28]

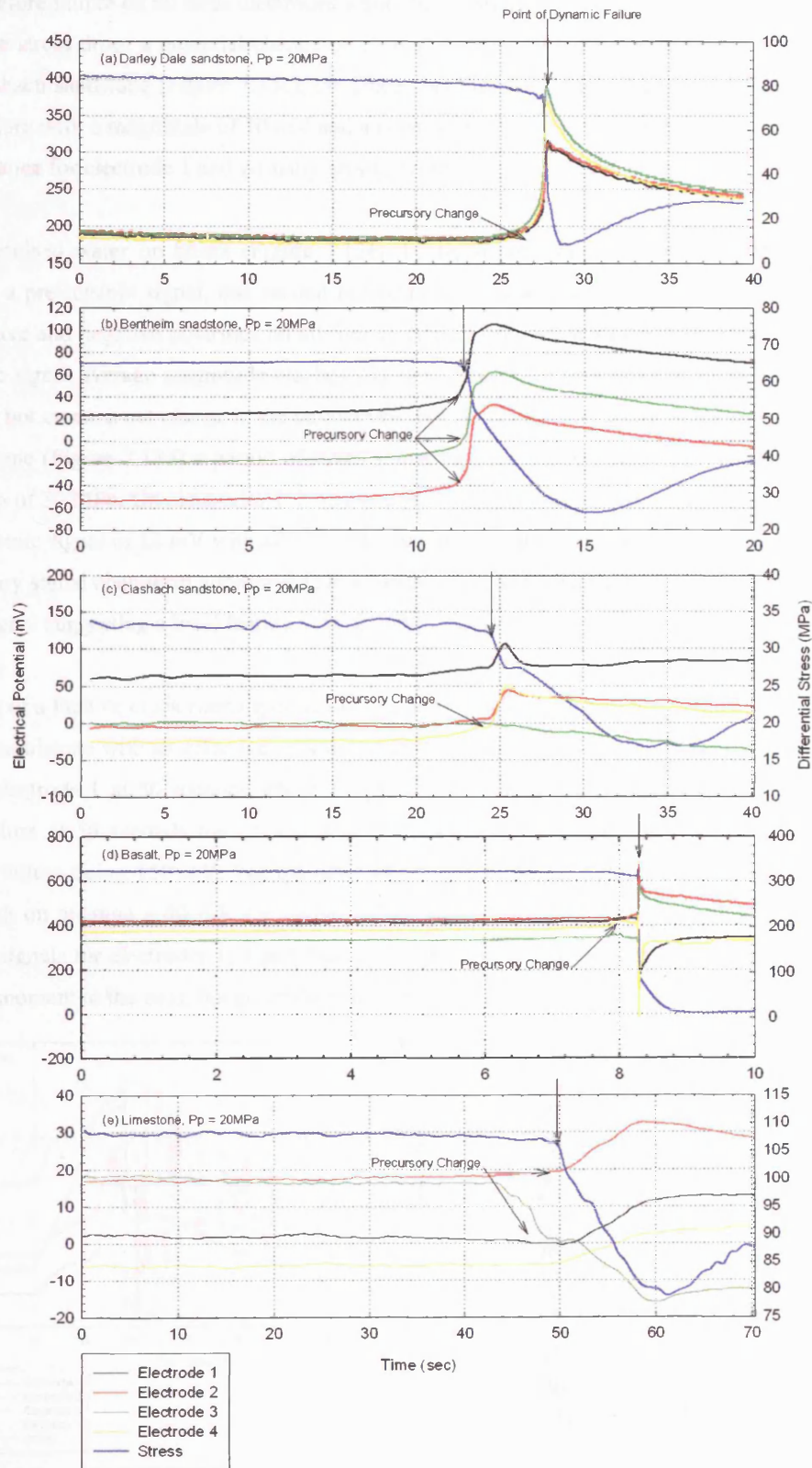


Figure 7.13: The electrical potential signals produced during strain softening and shear failure of (a) Darley Dale sandstone, (b) Bentheim sandstone, (c) Clashach sandstone, (d) Icelandic basalt and (e) Portland limestone. All experiments had a P_c of 40 MPa, P_p of 20 MPa, distilled water as pore fluid with a strain rate of $1.5 \times 10^{-5} \text{ s}^{-1}$. [Experiment No.:(a) and (d) See Clint (1999), (b) 26, (c) 13, (e) 19]

For Bentheim, the co-seismic stress drop of 44 MPa is preceded by a pre-seismic signal of 10 mV two seconds before failure on all three electrodes while the signal base values vary by 40 mV from each other. During the stress drop, a potential change of 70 mV is recorded with a decay type signal after failure. With Clashach sandstone (Figure 7.13c), the precursory signal change occurs approximately one second before failure with a magnitude of 10 mV and a co-seismic magnitude of 40 mV for electrodes 2 and 4, a 30 mV change for electrode 1 and virtually no signal change on electrode 3.

Using deionised water on basalt (Figure 7.13e) the region of strain softening is difficult to identify. However, a pre-seismic signal, one second before failure, shows on average a 20 mV signal which has both positive and negative polarities on all four electrodes present. With the stress drop of 112 MPa, the co-seismic signal average magnitude reaches 232 mV. This result suggests that the introduction of pore fluid does not create a net charge in the basalt even though pre and co-seismic signals were observed. For the limestone (Figure 7.13d) a period of strain softening down to 107 MPa is present before the failure stress drop of 30 MPa. On electrodes 1, 2 and 4, a precursory signal of 3 mV appears two seconds before the co-seismic signal of 12 mV with all electrodes having a positive polarity. Electrode 3, however, shows a precursory signal change an additional few seconds earlier and is negative in polarity along with the co-seismic signal suggesting a local feature near or on this electrode.

The effect of a fault or crack running close to or through an electrode position is shown in Figure 7.14 for Clashach sandstone with an effective pressure of 20 MPa. In Figure 7.14a, electrode 2 deviates from the trend of electrode 1 at 50 seconds where a rapid decrease in magnitude of 35 mV is observed. With partial failure at 56 seconds the co-seismic signal changes by -130 mV with the co-seismic signal at complete failure being 150 mV. For the other electrodes, co-seismic signals are present at both failure points with on average a 40 mV for partial failure and 25 mV for complete failure. After failure, the electrical signals for electrodes 1, 3 and 4 decay at the same rate with electrode 2 changing substantially from one moment to the next, but generally following the same pattern.

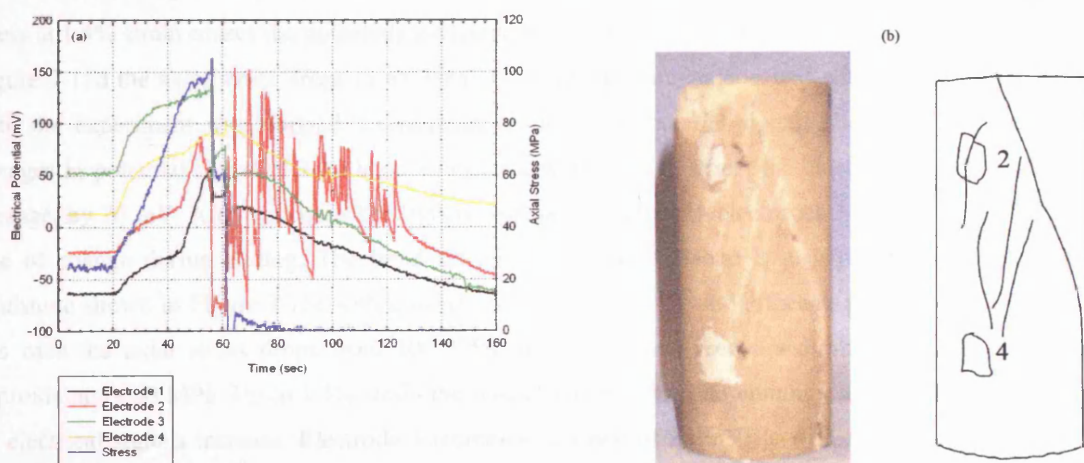


Figure 7.14: (a) The deformation of Clashach sandstone showing the effect of a fracture passing through an electrode and (b) photograph and schematic diagram of the deformed sample showing the position of cracks and fault; $P_c = 40$ MPa, $P_p = 20$ MPa and strain rate $1.5 \times 10^{-4} \text{ s}^{-1}$. [Experiment No.: 21]

After removing the sample from the vessel the photograph in Figure 7.14b was taken with a schematic representation shown next to it. The major fault is indicated by the line running the length of the sample with smaller cracks running off it with one such crack passing across electrode 2. This suggests that this crack may have formed prior to the macroscopic fault because the changes in potential occurred before failure was reached.

7.6 ELECTRICAL POTENTIAL SIGNALS AFTER DYNAMIC FAILURE

As well as the electrical potential signals up to failure, the behaviour of these signals after failure was investigated and results plotted in Figure 7.15. In Figure 7.15a, Portland limestone was deformed with a confining pressure of 20 MPa and at a strain rate of $1.5 \times 10^{-4} \text{ s}^{-1}$ with no pore fluid present. At failure, the axial stress decreases from 120 MPa to 92 MPa and remains constant during frictional sliding up to 2.3% strain past failure, when the stress starts to increase linearly. During this strain period the electrical potential decreases at all four electrodes after the co-seismic spike and decays in electrodes 1 and 3 to 160 mV and 164 mV whilst electrode 1 decreases to 120 mV and electrode 4 to 17 mV. In Figure 7.15b drained Portland limestone was deformed more slowly ($1.5 \times 10^{-7} \text{ s}^{-1}$) with deionised water present and confining pressure of 40 MPa and pore pressure of 20 MPa. After failure, the stress decays slowly down to 52 MPa at 4% after failure. The electrical potential signals after failure decay rapidly and begin to level off at 0.4% strain. At 0.5% strain, the electrical signals begin to increase linearly with a slight decrease around 0.9% strain. After this point the electrical signals increase at a constant rate until the experiment is terminated. Electrodes 1 and 3 are parallel to each other and increase in potential by 25 mV with electrode 2 increasing by 43 mV.

Dry Clashach sandstone is shown in Figure 7.15c with a confining pressure of 20 MPa and strain rate of $1.5 \times 10^{-5} \text{ s}^{-1}$. Here the stress is shown decreasing to 40 MPa after failure and recovering to 50 MPa for frictional sliding. The electrical signal also changes at failure but levels out during sliding with electrodes 1, 2, 3 and 4 having readings of 15 mV, 90 mV, 0 mV and 35 mV respectively. A slight drop in frictional stress at 1.4% strain causes the potentials to change by ± 4 mV. For water saturated Clashach sandstone in Figure 7.15d the axial stress drops to 65 MPa at failure and remains constant with a 5 MPa fluctuation until the experiment was stopped. Corresponding electrical potential signals show this fluctuation by changes in potential signal of 10 mV on all electrodes. Up to 1% strain, the electrical signals decay, on average, by 70 mV. After this point the signals increase linearly with electrodes 3 and 4 having the same rate of change during sliding. The trend seen in Clashach sandstone is also present in Darley Dale sandstone shown in Figure 7.15e with a strain rate of $1.5 \times 10^{-4} \text{ s}^{-1}$ and effective pressure of 20 MPa. In this case the axial stress drops from 100 MPa to 50 MPa and recovers during frictional sliding to approximately 60 MPa. Up to 1.5% strain the four electrodes show no common trend. After 1.5% strain all electrical signals increase. Electrode 3 increases at a rate of 20 mV/%, whilst electrodes 1, 2 and 4 increase at a rate of 30 mV/%.

With the absence of the signal after failure in dry Portland limestone and dry Clashach sandstone, the piezoelectric effect is ruled out as responsible for producing the signal. With water present, the signal

appears at 1.0 - 1.5% strain after failure. The electrokinetic phenomena cannot be ruled out as a possible cause, however an alternative mechanism may be occurring such as polarization of the electrodes.

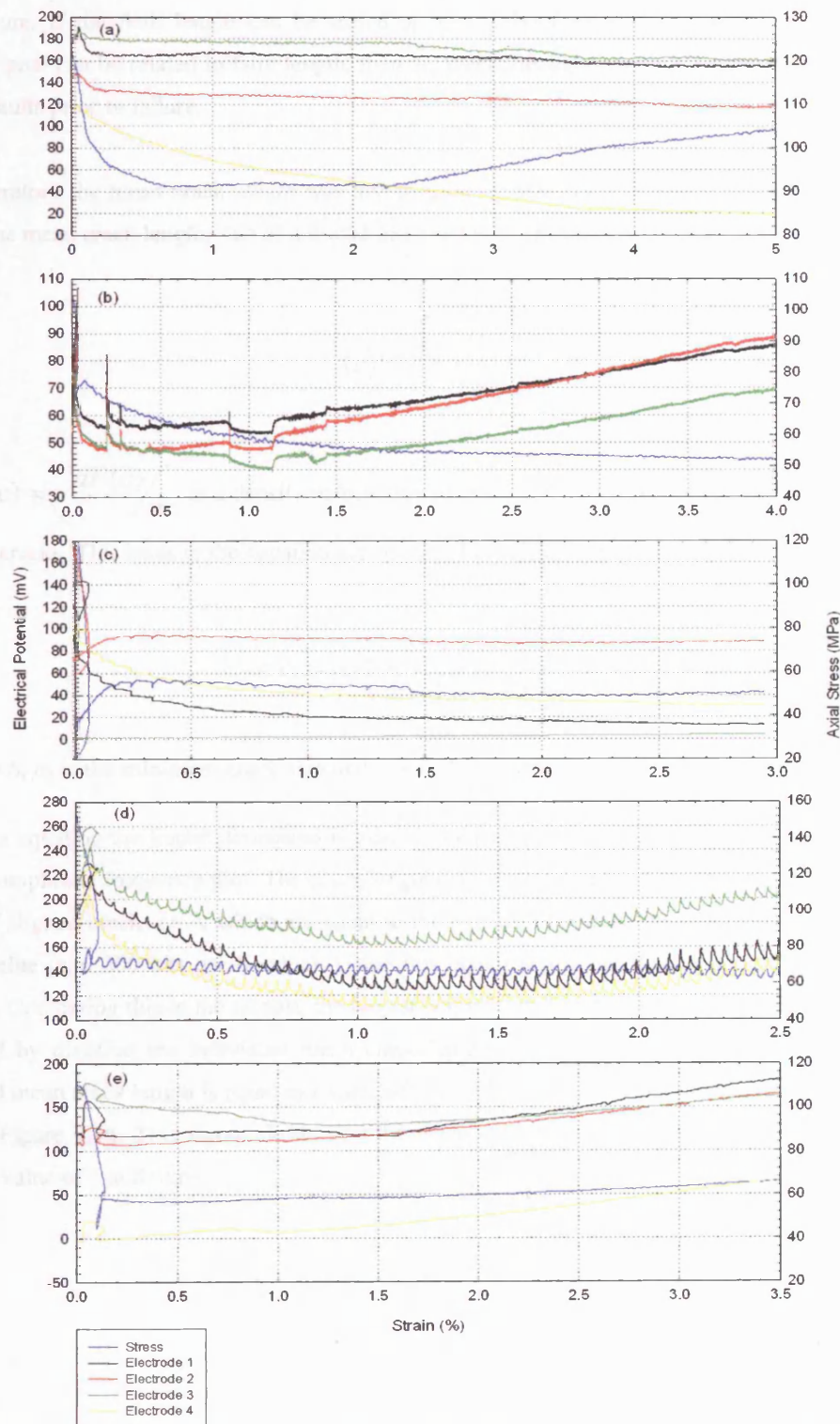


Figure 7.15: The electrical potential measured during steady-state frictional sliding after dynamic failure of sandstones and limestone. (a) dry Portland limestone with $P_c = 20$ MPa and strain rate $1.5 \times 10^{-4} \text{ s}^{-1}$, (b) Portland limestone with $P_c = 20$ MPa, $P_p = 20$ MPa and strain rate $1.5 \times 10^{-7} \text{ s}^{-1}$, (c) dry Clashach sandstone with $P_c = 20$ MPa and strain rate $1.5 \times 10^{-5} \text{ s}^{-1}$, (d) Clashach sandstone with $P_c = 40$ MPa, $P_p = 20$ MPa and strain rate $1.5 \times 10^{-5} \text{ s}^{-1}$ and (e) Darley Dale sandstone; $P_c = 40$ MPa, $P_p = 20$ MPa and strain rate $1.5 \times 10^{-4} \text{ s}^{-1}$. [Experimental No.: (a) 28, (b) 27, (c) 15, (d) 33, (e) 32]

7.7 CORRELATING ELECTRICAL POTENTIAL SIGNALS TO THE MEAN CRACK LENGTH

At present, the magnitude of the fault cannot be predicted from the electrical signals generated prior to or during failure. If the fault length can be scaled up from laboratory scale to crustal scale, and if the electrical signal can be related to fault length, then the electrical signal could be extrapolated and related to crustal faults prior to failure.

In the laboratory the mean crack length was investigated by Main (1991) who produced an equation to calculate the mean crack length, $\langle c \rangle$ of a fractal distribution of cracks by

$$\langle c \rangle = \frac{\int_{c_0}^{c_1} cf(c)dc}{N_T} \tag{7.1}$$

where $f(c) = -dF(c)/dc$ is a density distribution of crack sizes and $N_T = \int_{c_0}^{c_1} f(c)dc$ is the number of aligned cracks. This leads to the equation actually used to calculate the mean crack length of

$$\langle c \rangle = c_0 \left(\frac{D}{D-1} \right) \left(\frac{1-x^{1-D}}{1-x^{-D}} \right) \tag{7.2}$$

where $D = b$, c_0 is the minimum crack size and x is $\left(\frac{c_0}{c_1} \right)$ (maximum crack size over minimum crack size). In this equation the fractal dimension is treated as equal to the b-value which is calculated from the log-linear amplitude frequency plot. The crack length (x) is calculated from the fractal dimension and the number of aligned cracks (N_T), which are equal to the number of cumulative hits required to calculate a single b-value (e.g. 200 hits per b-value). Using this equation and the b-value a mean crack length is calculated. Comparing this to the sample, the largest crack formed is the fault, so the mean crack length is normalised by dividing the individual mean crack lengths by the largest value so that at failure the normalised mean crack length is equal to a value of one with the results from a typical triaxial experiment shown in Figure 7.16. This figure shows that the mean crack length increases near failure reaching a maximum value of 1 at failure.

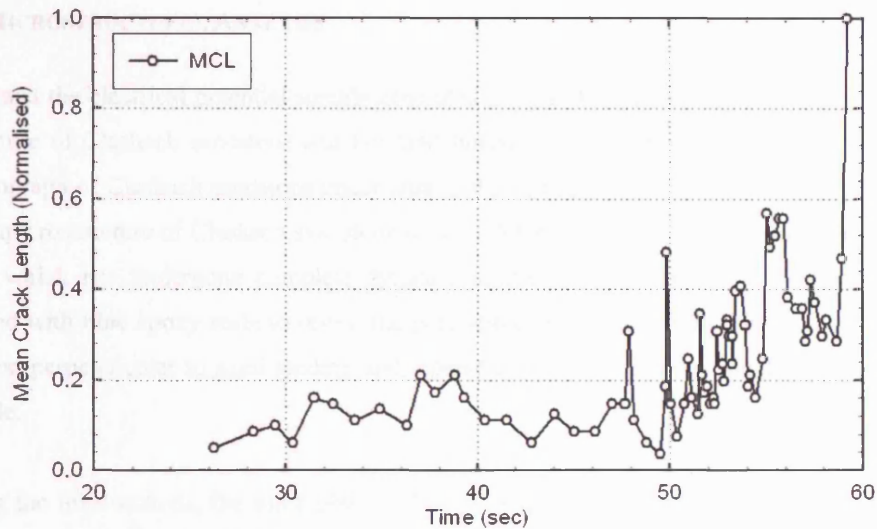


Figure 7.16: The variation of normalised mean crack length during the deformation of Clashach; $P_c = 40$ MPa, $P_p = 20$ MPa with strain rate of $1.5 \times 10^{-4} \text{ s}^{-1}$. Each point plotted is given to an accuracy of ± 0.01 . [Experiment No.: 21]

The corresponding electrical potential change as a function of mean crack length is plotted in Figure 7.17. During compaction (below red line) the potential change is negative with low crack lengths due to a limited amount of AE being generated by closing surfaces. When dilatancy becomes dominant (between red and blue lines), the electrical signal increases linearly with mean crack length right up to failure where the potential increases by 5 mV. After failure, all AE is due to sliding along the fault, and therefore the mean crack length can be calculated.

These results show that the electrical signal at the laboratory scale can be related to the mean crack length through the b-value. As the b-value is related to the Gutenberg-Richter scale, in theory, this can be applied at the crustal scale.

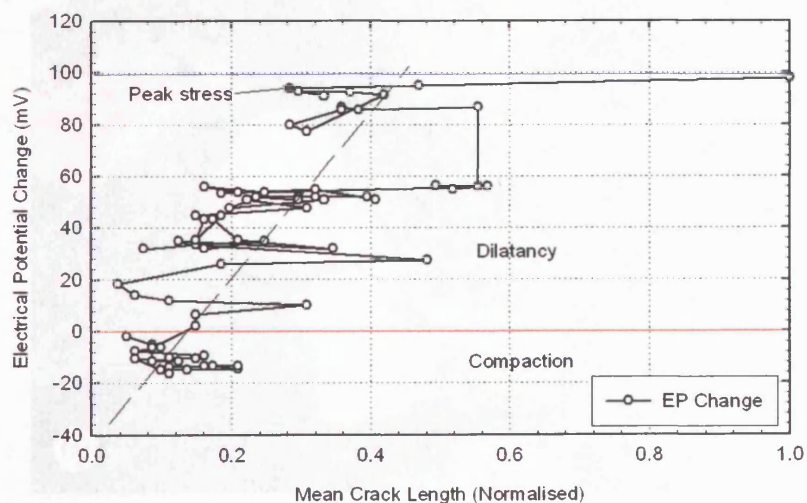


Figure 7.17: Electrical potential change as a function of mean crack length. $P_c = 40$ MPa, $P_p = 20$ MPa with a strain rate of $1.5 \times 10^{-4} \text{ s}^{-1}$. The broken black line shown represents the least squared fit. Each point plotted is given to an accuracy of ± 0.2 mV. [Experiment No.: 21]

7.8 MICROSTRUCTURAL ANALYSIS

To understand the electrical potential signals generated through the deformation of a rock specimen, the microstructure of Clashach sandstone and Portland limestone has been examined. Figure 7.18 shows a photomicrograph of Clashach sandstone under cross-polarised light. In Figure 7.18a the photomicrograph shows the microstructure of Clashach sandstone prior to deformation. The microstructure of dry Clashach sandstone which has undergone complete dynamic failure which is shown in Figure 7.18b. It was impregnated with blue epoxy resin to reveal the pore space and cracks. Both thin sections were taken in the direction perpendicular to axial loading and represent a typical cross-sectional view of the Clashach rock sample.

Comparing the thin sections, the most obvious feature is due to brittle deformation. Before failure the specimen is made up of complete mineral grains which are randomly orientated and approximately equal in size with no apparent cracks present. After failure however, the structure of the sample has changed with the fault present just to the right of this thin section. Generally, for two to three grain widths from the fault the majority of the grains show signs of cracking. These are oblique to the fault, with preferential cracking occurring in the softer minerals with larger gaps between the new crack surfaces than in quartz. These cracks are generally parallel and equally spaced within a single crystal but differ between crystals with some cracks extending through a couple of grains showing that intra-granular and trans-granular cracking occurred during deformation. Mineral grains located further away from the fault do not have cracks running through the centre, but cracking is present around the edges with small sections of crystal breaking off. These pieces vary greatly in size and because of their location they fill up the void space between grains. Therefore, the process of deformation which generates the AE activity comes from increasing the number of crystals to a greater number of smaller crystals; which in turn increases the pore volume of the rock but decreases the permeability by increasing the tortuosity between grains.

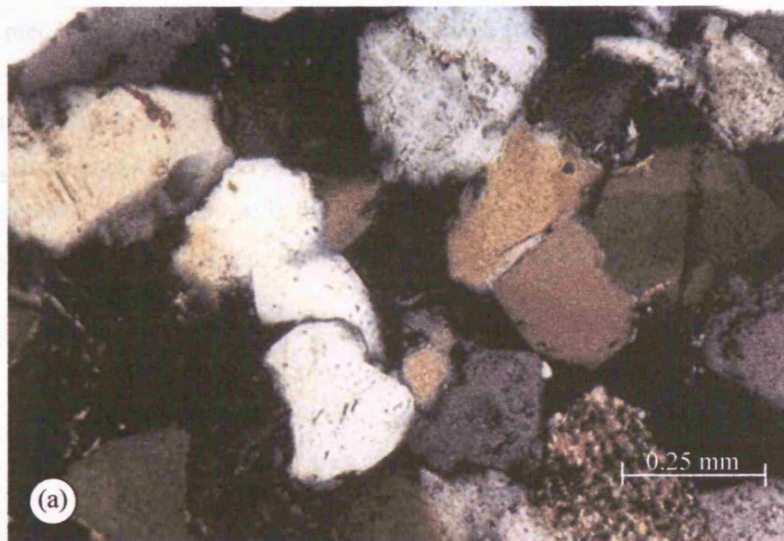


Figure 7.18a: Photomicrographs of Clashach sandstone in cross-polarised light before deformation; $P_c = 20$ MPa and strain rate of $1.5 \times 10^{-5} \text{ s}^{-1}$. [Experiment No.: 14]

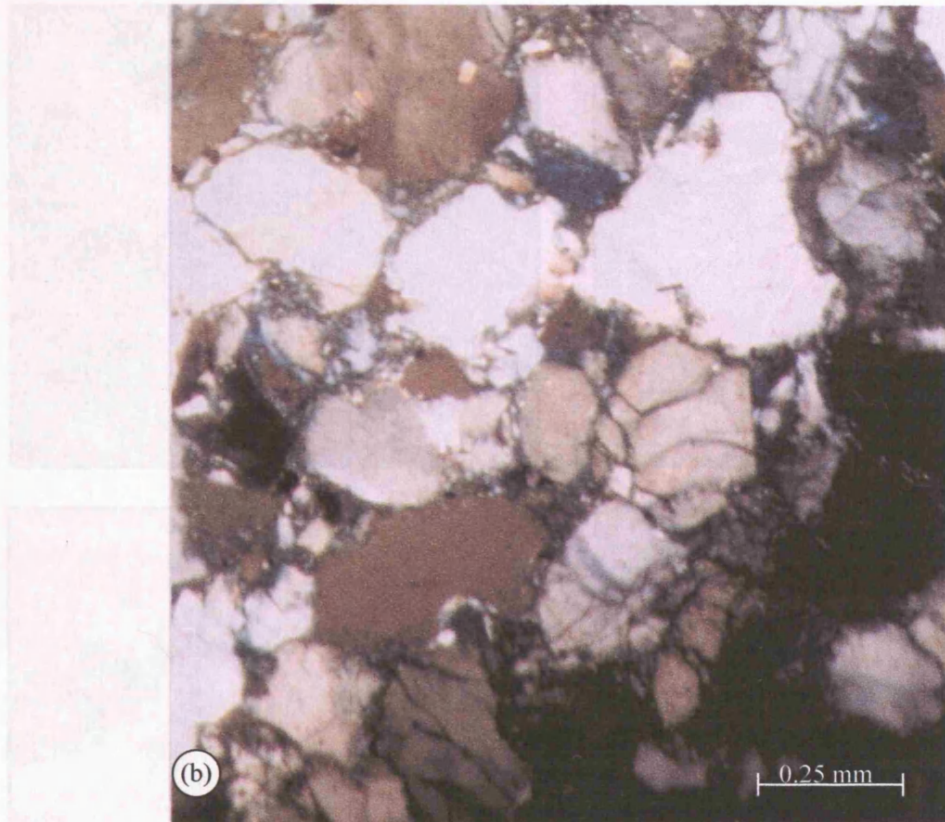


Figure 7.18b: Photomicrographs of Clashach sandstone in cross-polarised light after deformation failure showing the presence of grain cracking with axial loadings going into the page; $P_c = 20$ MPa and strain rate of $1.5 \times 10^{-5} \text{ s}^{-1}$. [Experiment No.: 14]

Scanning Electron Microscope (SEM) images were taken of deformed Clashach sandstone and Portland limestone samples with less than 2% strain sliding after failure. Figure 7.19 shows the SEM images for Clashach and Portland at magnifications of 500 and 5000. In Figure 7.19a, Portland limestone is present with the section in the square magnified into Figure 7.19b. This scan shows the limestone surface consists of various size pieces as small as $0.1 \mu\text{m}$, the surface is rough and broken up with signs of cracking on the feature towards the middle of the photograph. On the right hand side a feature seems to show parallel lines. For the sandstone, at low magnification, (Figure 7.19c), the individual crystals can be seen with a covering over certain grains with all crystals having a rough surface. In Figure 7.19d the surface shows a couple of large cracks, such as the one in the centre of the image, with what appears to be shearing lines intersecting the feature showing crystals smaller than $0.1 \mu\text{m}$ covering much of the larger crystal surfaces.

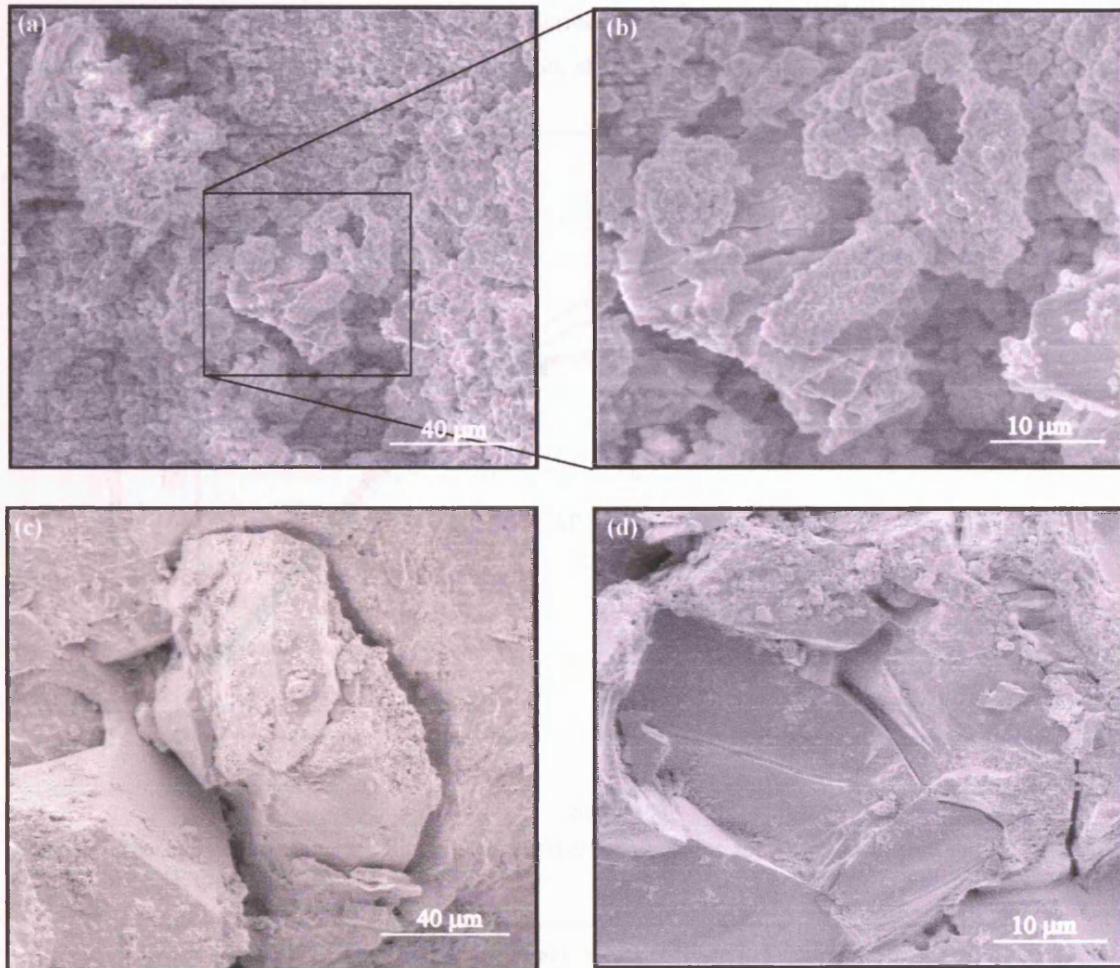


Figure 7.19: SEM images of Portland limestone (PL) ($P_c = 20$ MPa with no pore fluid) and Clashach sandstone (CS) ($P_c = 30$ MPa with no pore fluid). (a) PL at magnification 500, (b) PL at magnification 5000, (c) CS at magnification 500 and (d) CS at magnification 5000. [Experiment No.: (a) 28, (b) 28, (c) 17, (d) 17]

7.9 CHANGES IN MECHANICAL PROPERTIES DUE TO STRAIN RATE VARIATION

Strain rates between $1.5 \times 10^{-4} \text{ s}^{-1}$ and $1.5 \times 10^{-7} \text{ s}^{-1}$ were applied to Clashach and Darley Dale sandstone and Portland limestone to investigate the effect of strain rate on mechanical and electrical properties. Deionised water was used as the pore fluid with a confining pressure of 40 MPa and pore pressure of 20 MPa. The Portland limestone results are shown in Figure 7.20 with the effect of strain rate on peak and frictional stress for all rock types studied given in Table 7.1. For a strain rate of $1.5 \times 10^{-5} \text{ s}^{-1}$ the linear-elastic behaviour of Portland limestone continues up to 0.8% strain which is at 86% of the peak stress with failure at 1% strain. This is different from the values present at slower strain rates of $1.5 \times 10^{-6} \text{ s}^{-1}$ and $1.5 \times 10^{-7} \text{ s}^{-1}$ which reaches only 0.5% strain (78% and 75% of peak stress) before dilatancy begins with macroscopic failure at 1.25% strain. Above the elastic stage the stress shows strain hardening with 'roll-over' to peak stress values of 147, 90 and 99 MPa for the three strain rates with strain softening apparent in 10^{-6} s^{-1} and 10^{-7} s^{-1} followed by dynamic failure causing a sudden stress drop. After failure, the frictional stress drops to 89, 68 and 71 MPa for 10^{-5} s^{-1} , 10^{-6} s^{-1} and 10^{-7} s^{-1} respectively. Table 7.1 shows that the peak stress for sandstone is greater than that of limestone with no significant effect due to

strain rate. The frictional stress on average for Clashach sandstone is 70 MPa compared to Darley Dale sandstone of 53 MPa. Portland limestone has frictional stress at 73 MPa.

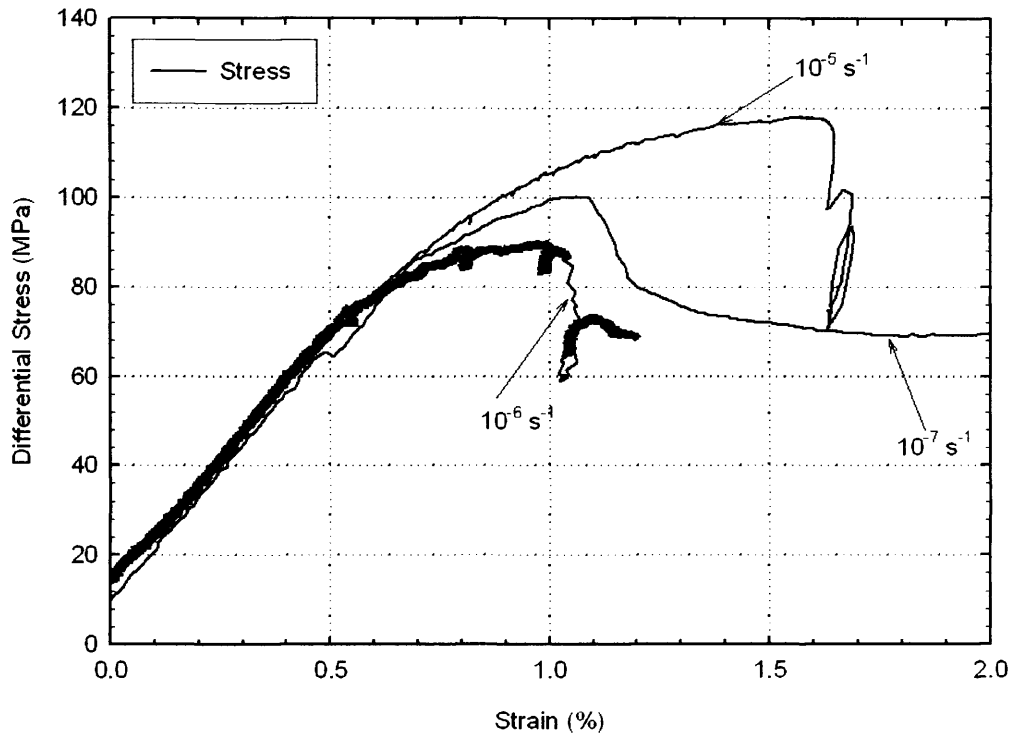


Figure 7.20: Typical stress-strain diagram at different strain rates for Portland limestone; $P_c = 40$ MPa, $P_p = 20$ MPa. [Experiment No.: 23, 25, 27]

Rock Type	Strain Rate (s^{-1})	Peak Stress (MPa)	Frictional Stress (MPa)
Clashach	1.5×10^{-04}	141	70
Clashach	1.5×10^{-05}	150	80
Clashach	1.5×10^{-06}	111	61
Darley Dale	1.5×10^{-04}	111	58
Darley Dale	1.5×10^{-05}	112	59
Darley Dale	1.5×10^{-07}	96	42
Portland	1.5×10^{-05}	118	79
Portland	1.5×10^{-06}	90	68
Portland	1.5×10^{-07}	99	71

Table 7.1: Effect of strain rate on the peak stress and frictional sliding stress of Clashach sandstone, Darley Dale sandstone and Portland limestone; $P_c = 40$ MPa, $P_p = 20$ MPa. The values given are accurate to within ± 0.5 MPa.

7.10 ELECTRICAL POTENTIAL SIGNAL CHANGE DUE TO STRAIN RATE

The effect of two different strain rates on the electrical potential difference of drained Portland limestone is shown in Figure 7.21 with an effective pressure of 20 MPa. In Figure 7.21a, Portland limestone is deformed at a rate of $1.5 \times 10^{-4} s^{-1}$. The onset of deformation is marked by an increase in the electrical potential signal from background values between 40 mV and 100 mV. The electrical signals increases on average by 80 mV up to failure where there is a co-seismic signal change in the range of 20 mV followed by a decaying signal after failure. With a slower strain rate of $1.5 \times 10^{-6} s^{-1}$ as shown in Figure 7.21b, the

electrical potential signals look quite different. During deformation the electrical signals increase by less than 20 mV showing great variability with electrical spikes and troughs and some features only present on an individual channel. At failure a co-seismic signal of the order of 15 mV is present in both positive and negative polarities with a small decay in potential on electrodes 1, 2 and 4 with a small increase on electrode 3. The values in Figure 7.21b are much smaller than those from Figure 7.21a, suggesting that the faster the strain rate the greater the change in potential difference during deformation.

Looking more closely at the difference in the potentials and the time these occur, Figure 7.21b is re-plotted in Figure 7.22 showing several features, highlighted in different colours. Purple represents negative spikes which decrease in magnitude from electrode 1 to 3; blue shows trends which can be seen on all electrodes approximately equal in magnitude; red shows a spike on electrodes 3 and 4 which is absent on electrodes 1 and 2; whilst green represents features which cannot be identified on any other electrode. This suggests that the slower the strain rate, the easier it is to identify features which are localised to an electrode beneath the general trend which occurs during deformation.

The overall change in the electrical potential difference for Darley Dale sandstone during compaction and dilatancy is plotted as a function of strain rate in Figure 7.23. During compaction, the electrical potential change decreases with strain rate. This period is associated with closure of pores and cracks and has the effect of expelling pore fluid from the interior of the rock. This fluid transport creates a convection current by means of the electrical double layer (Chapter 3) and carries away the positive charge causing the electrical potential change to decrease as seen in Figure 7.7.

The amount of change in pore volume during compaction is plotted in Figure 7.24. For the strain rates of $1.5 \times 10^{-6} \text{ s}^{-1}$ to $1.5 \times 10^{-4} \text{ s}^{-1}$ the pore volume is relatively constant at 0.06 cm^3 . For the slowest strain rate, the volume change is greater at 0.19 cm^3 . This may be due to the extra 3% porosity of this sample over the other samples. Taking this into account the volume change is independent of strain rate. This implies that the mechanism for the closure of pores and cracks is the same. As the stress-strain data showed similar behaviour, this electrical change can be attributed to change in pore fluid velocity.

In Figure 7.23b the electrical potential change during dilatancy is shown. As seen with compaction, a decrease in electrical signal occurs at slower strain rates. This is when cracks and pores are opened with an increase in AE activity. With a constant pore pressure, fluid is forced into the newly exposed surface causing a reversal in fluid flow direction and convection current. As the fluid enters the new surfaces, EDLs form with the positive charge carried into the rock causing the electrical potential change to increase as seen in Figure 7.7, with the change during dilatancy being an order of magnitude greater than that during compaction.

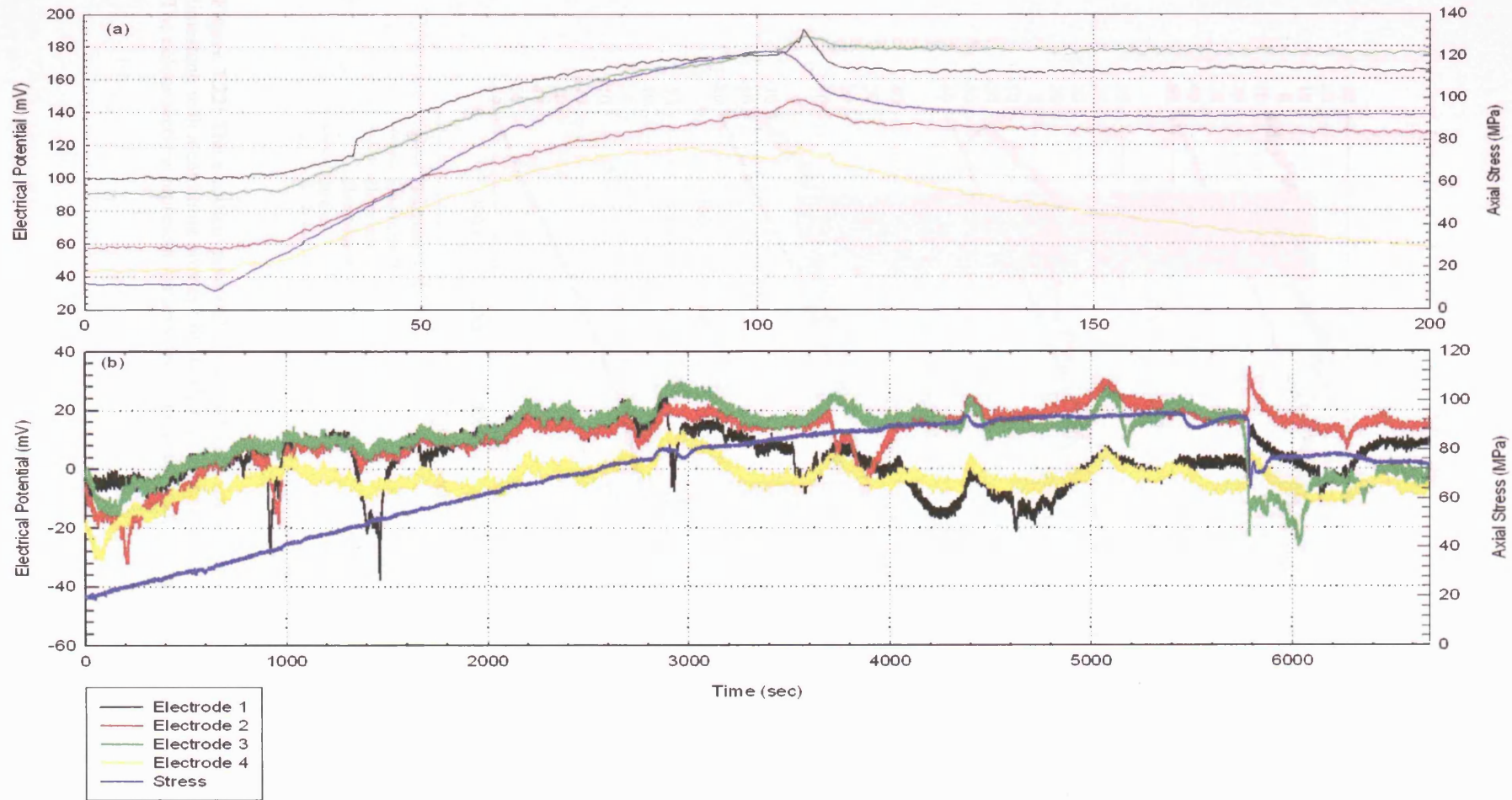


Figure 7.21: Electrical potential plotted during the deformation of Portland limestone to show the effect of a (a) strain rate of $1.5 \times 10^{-4} \text{ s}^{-1}$ and (b) $1.5 \times 10^{-6} \text{ s}^{-1}$ on the detail of signal recorded; $P_c = 40 \text{ MPa}$, $P_p = 20 \text{ MPa}$ [Experiment No.: (a) 24, (b) 23]

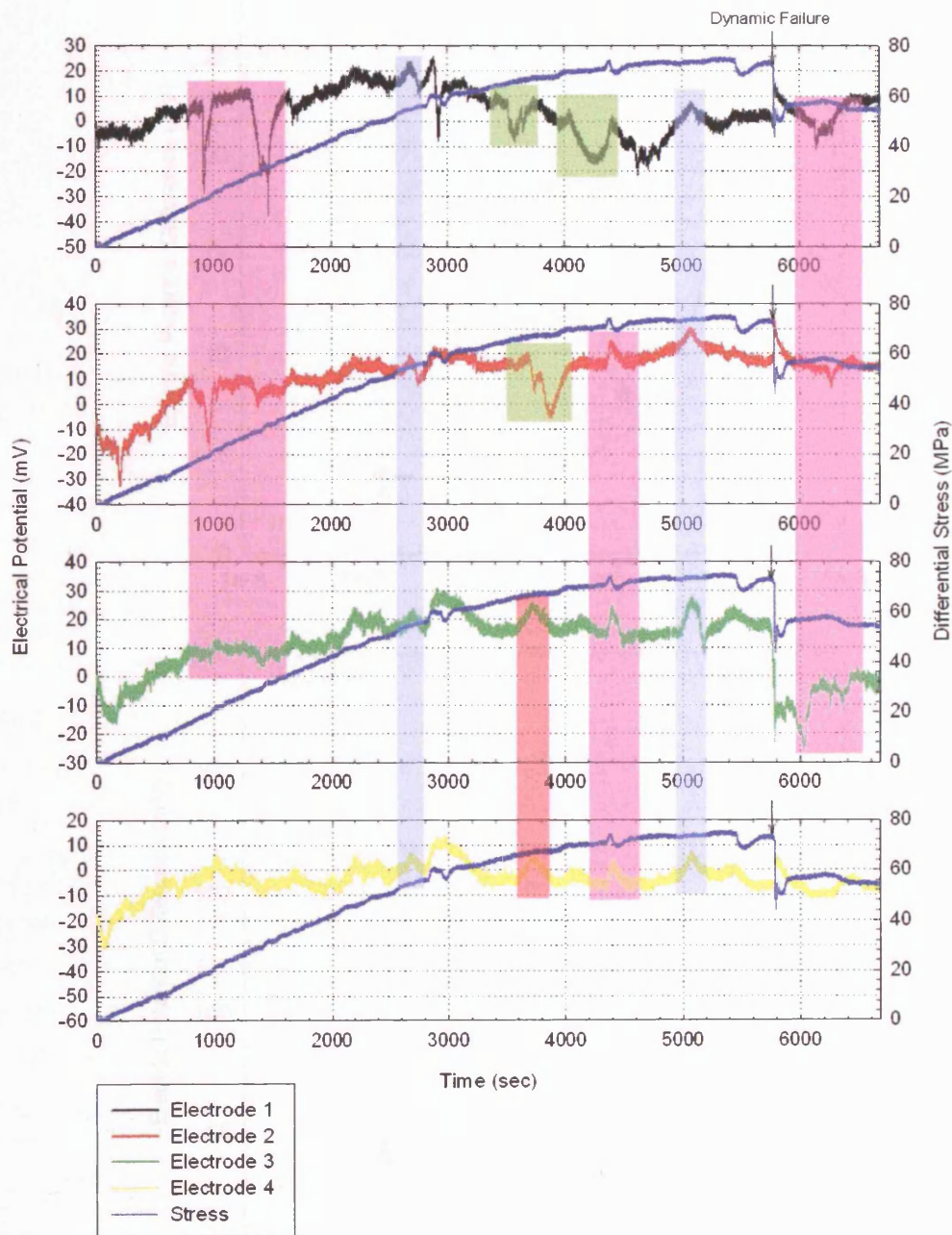


Figure 7.22: The electrical potential signal and axial stress measured during the deformation of Portland limestone with a confining pressure of 40 MPa, pore pressure of 20 MPa and a strain rate of $1.5 \times 10^{-6} \text{ s}^{-1}$. The colour sections represent features discussed in the text. [Experiment No.: 23]

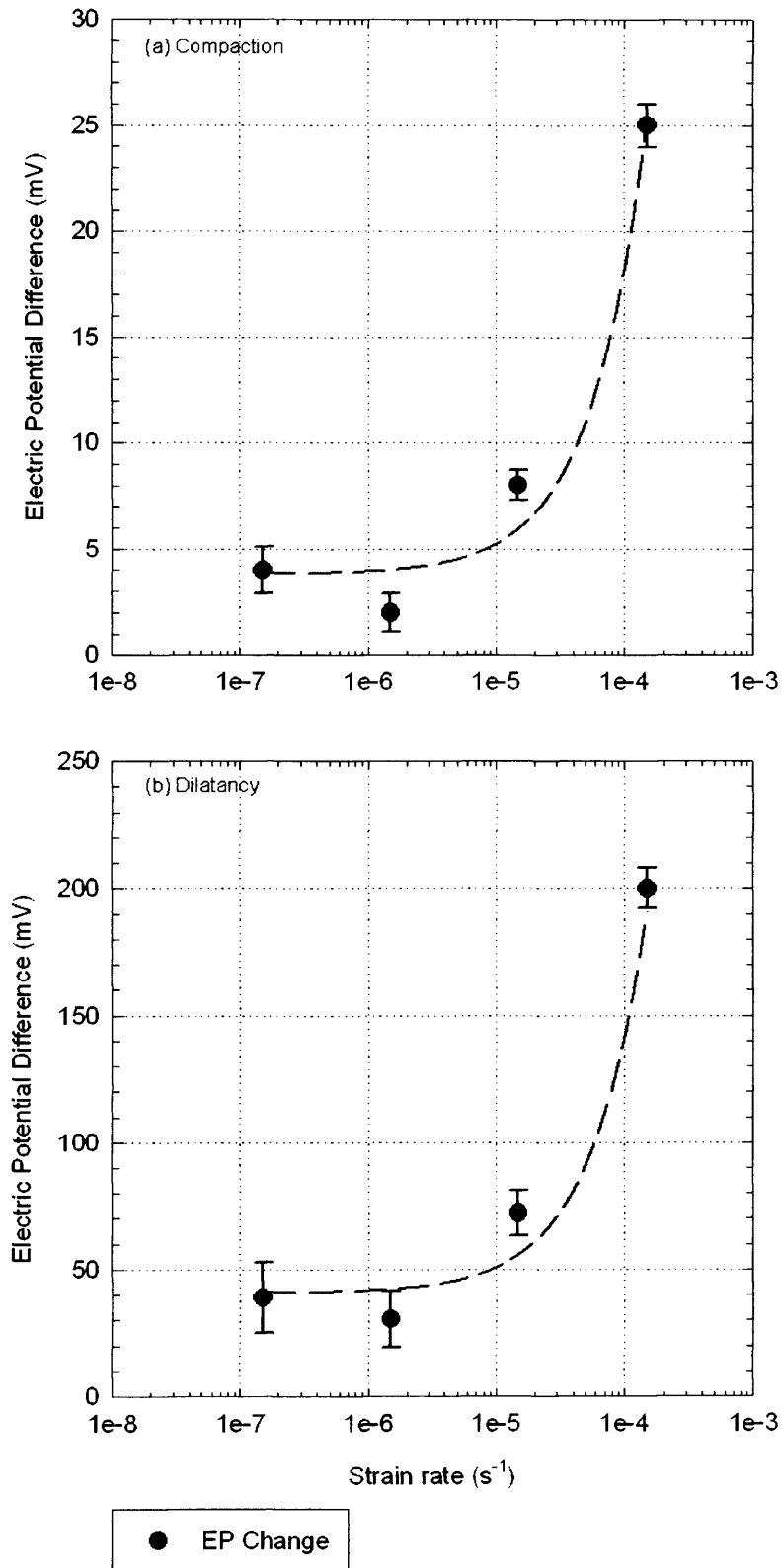


Figure 7.23: Variation of electrical potential difference with strain rate of drained Darley Dale sandstone for (a) compaction and (b) dilatancy (up to failure). The data plotted represents the absolute change in electrical potential difference with no information on polarity of the changes; $P_c = 40$ MPa, $P_p = 20$ MPa. The broken lines represent the least squared fit. The accuracy of each point is shown by error bars. [Experiment No.: see Clint (1999) and 29]

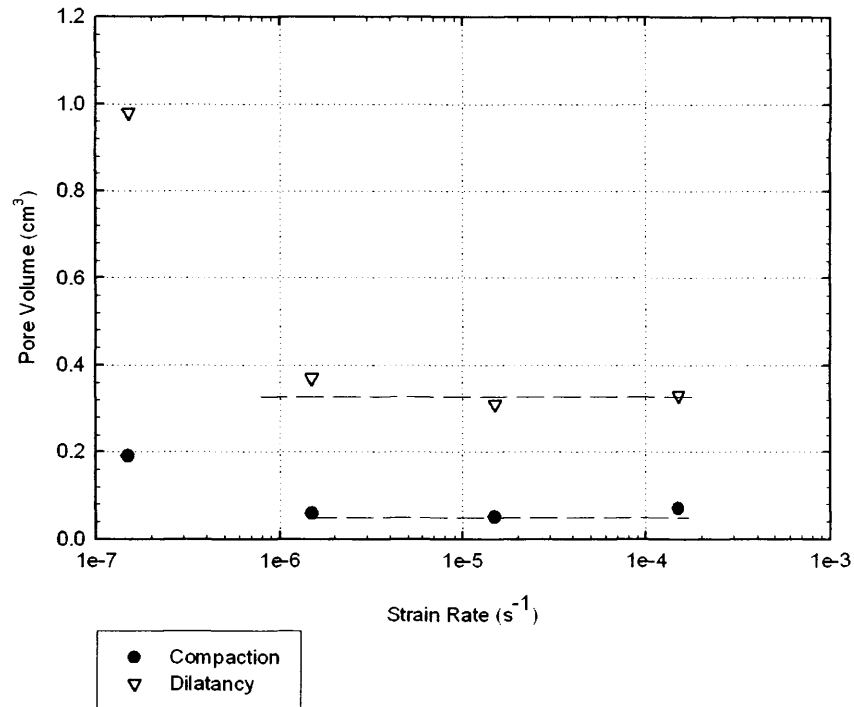


Figure 7.24: Variation of pore volume change with strain rate during compaction of drained Darley Dale sandstone; $P_c = 40$ MPa, $P_p = 20$ MPa. The broken lines represent the least squared fit. Each point is given to an accuracy of ± 0.01 cm³. [Experiment No.: (a), (b) and (c) See Clint (1999) and (d) 29]

With the fluid entering the cracks, the pore fluid volume of the rock increases as more cracks are opened. The change in pore volume during this period up to failure is shown in Figure 7.24. As before, the three fastest strain rates have a constant volume change of 0.34 cm³ compared to 0.93 cm³ for the slowest experiment and may be due to the reason mentioned above.

The same type of plot was applied to Clashach sandstone (Figure 7.25) and Portland limestone (Figure 7.26) with the same trends of decrease in absolute electrical potential change during compaction and dilatancy for slower strain rates. The potential change during dilatancy is always greater than that during compaction with sandstone having larger potentials than limestone.

As well as the strain rate affecting the potential signals during brittle failure, it also affects the electrical signals during frictional sliding as seen in Figure 7.27 using the Portland limestone results. When the strain rate is increased by an order of magnitude from 10⁻⁵ s⁻¹ to 10⁻⁴ s⁻¹ during sliding, the frictional stress increases with a simultaneous change in electrical potential signal. The rise in the electrical potential signal may be due to an increase of fluid flow into the newly exposed crystal surface within the fault region as the slip displacement rate is increased. When the strain rate is reduced, the frictional strength and electrical potential signals decrease to about their original values. This is because the faster the strain rate the quicker new surfaces are formed from the breaking up of mineral grains into smaller pieces. These new surfaces react with the fluid to create additional electric signals.

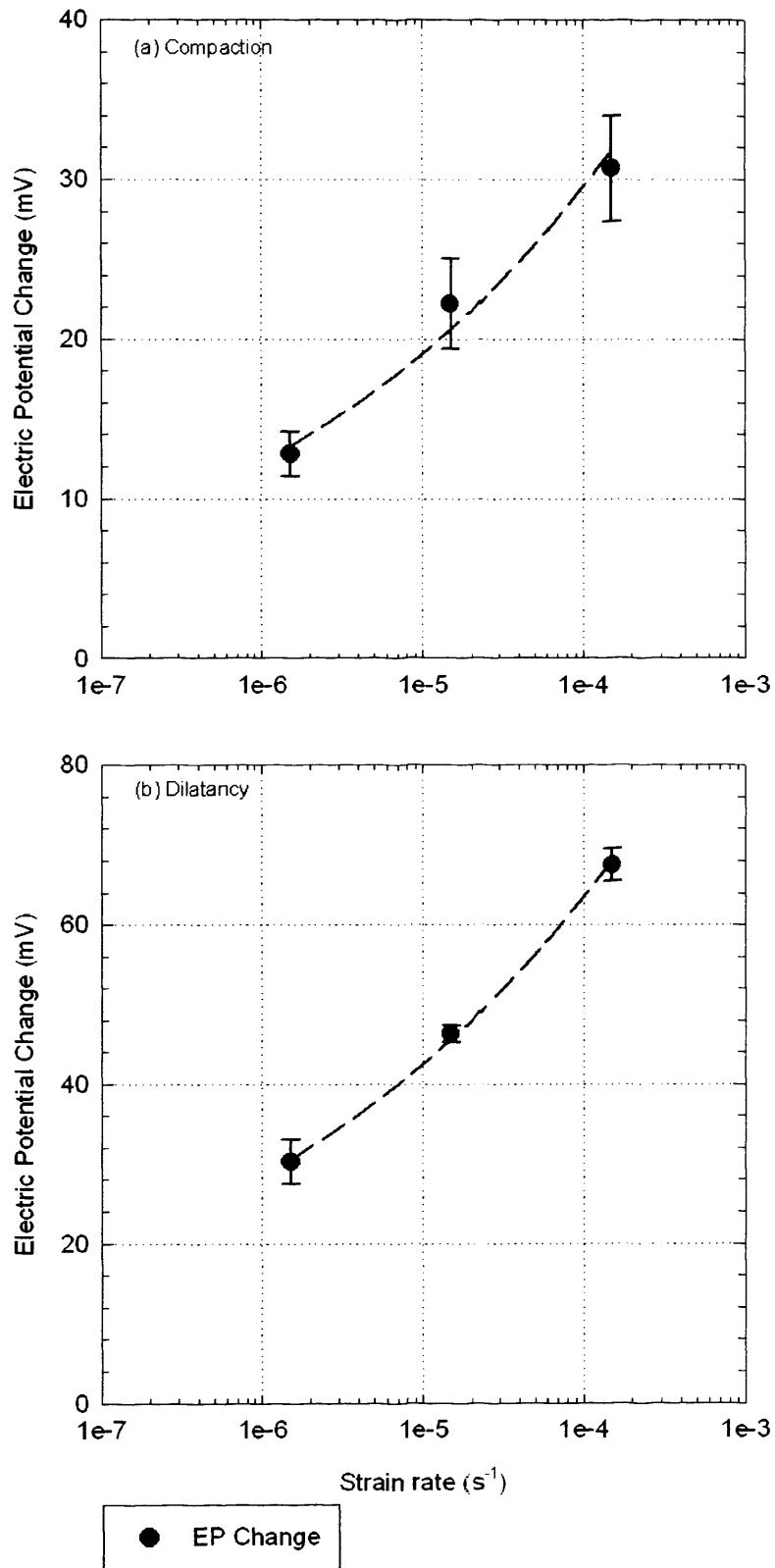


Figure 7.25: Variation of electrical potential difference with strain rate of drained Clashach sandstone for (a) compaction and (b) dilatancy (up to failure). The data plotted represents the absolute change in electrical potential difference with no information on polarity of the changes; $P_c = 40$ MPa, $P_p = 20$ MPa. The broken lines represent the least squared fit. The accuracy of each point is shown by error bars. [Experiment No.:21, 22, 33]

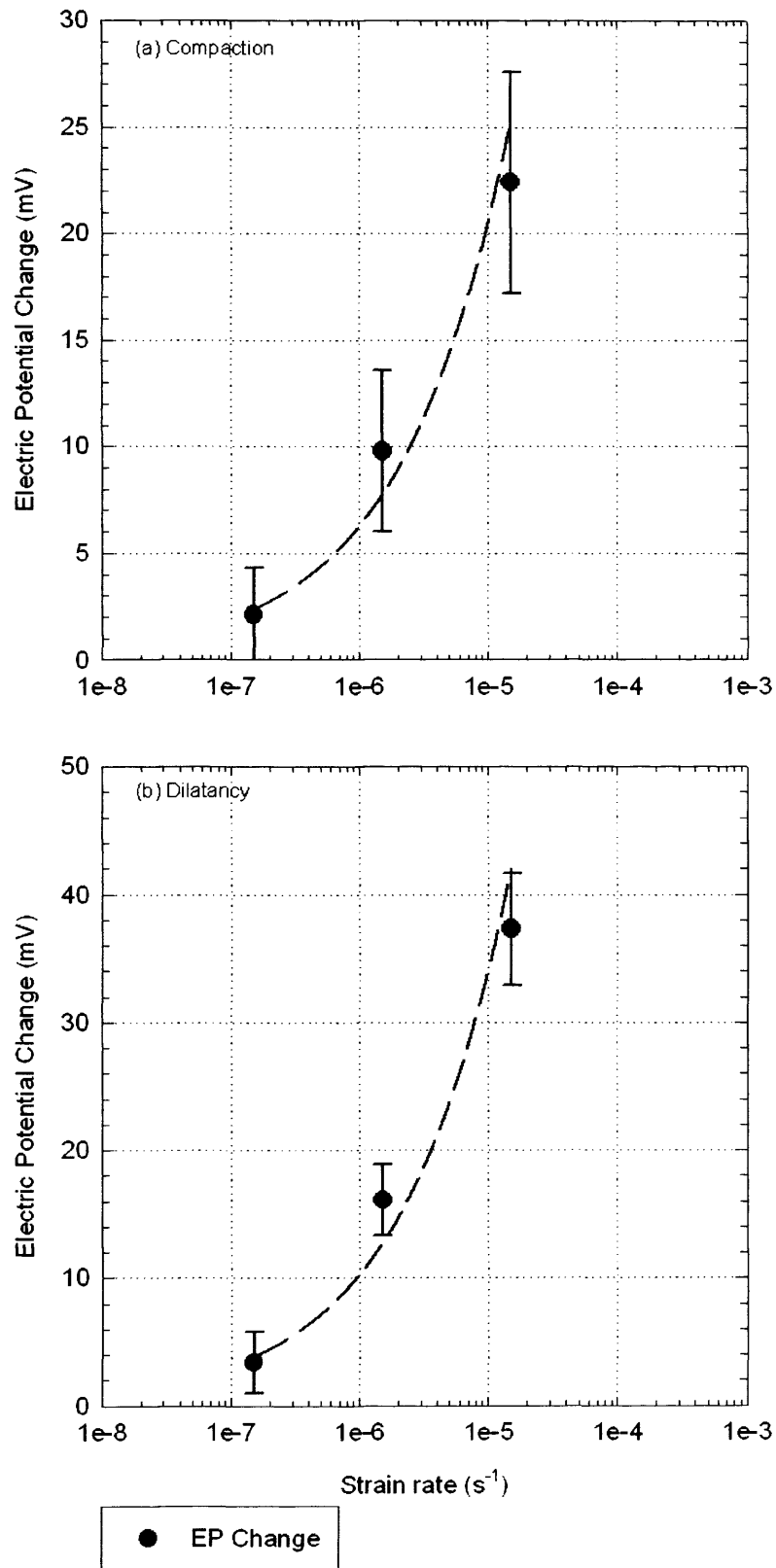


Figure 7.26: Variation of electrical potential difference with strain rate of drained Portland limestone for (a) compaction and (b) dilatancy (up to failure). The data plotted represents the absolute change in electrical potential difference with no information on polarity of the changes; $P_c = 40$ MPa, $P_p = 20$ MPa. The broken lines represent the least squared fit. The accuracy of each point is shown by error bars. [Experiment No.: 23, 24, 27]

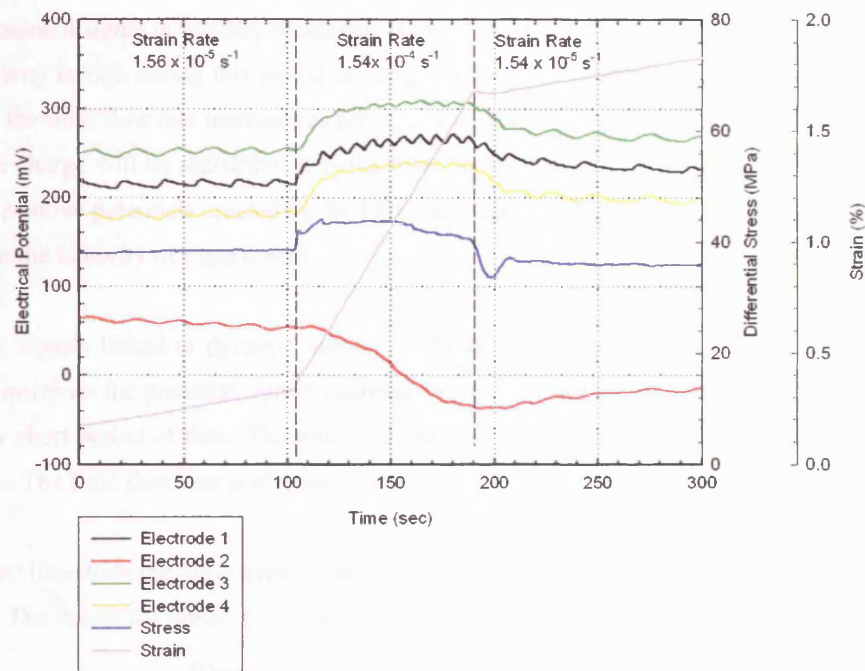


Figure 7.27: Graph showing the effect of varying the strain rate on mechanical strength and electrical potential signal during frictional sliding of drained Portland limestone with a confining pressure of 12 MPa and pore pressure of 7 MPa. [Experiment No: 18]

7.11 STRAIN RATE EFFECT ON PRE-SEISMIC AND CO-SEISMIC ELECTRICAL POTENTIAL SIGNALS

The electrical potential signals have been shown to be affected by rock type and the presence of water (Chapter 7.5). With the strain rate in nature being of the order of 5 times slower than these laboratory based experiments, it is important to look at the effect of strain rate on these signals to quantify them to the field studies. Below in Table 7.2 the electrical potential differences prior to and during dynamic failure is shown for Clashach sandstone and Portland limestone at various strain rates with the Clashach sandstone potentials drawn in Figure 7.28.

Clashach Strain Rate (s ⁻¹)	Pre-seismic				Co-seismic			
	Electrode 1	Electrode 2	Electrode 3	Electrode 4	Electrode 1	Electrode 2	Electrode 3	Electrode 4
1.50E-04	3.9	9.8	8.0	8.5	22.9	35.5	42.8	43.4
1.50E-05	2.5	0.1	5.0	5.3	34.5	52.5	39.1	46.8
1.50E-06	0.5	1.0	0.5	0.5	40.0	43.9	40.0	55.4

Portland Strain Rate (s ⁻¹)	Pre-seismic				Co-seismic			
	Electrode 1	Electrode 2	Electrode 3	Electrode 4	Electrode 1	Electrode 2	Electrode 3	Electrode 4
1.50E-05	2.6	3.1	3.8	4.4	5.1	4.2	6.9	6.6
1.50E-06	3.4	3.0	8.8	3.0	8.3	9.8	4.4	5.4
1.50E-07	3.6	3.3	2.2	1.8	18.5	25.2	19.0	23.9

Table 7.2: Pre and Co-seismic electrical potential signals measured from each electrode during triaxial deformation of Clashach sandstone and Portland limestone at a range of strain rates under drained conditions. Each point is given to an accuracy of 0.1 mV.

In Figure 7.28a, the electrical potential for Clashach sandstone is plotted prior to failure. At slower strain rates the potential signal is smaller, decreasing from an average 7.5 mV down to 0.6 mV. As noted earlier, the AE activity is high during this period creating multiple cracks which may interact. With an increasing strain rate, the fluid flow rate increases as previously mentioned, and therefore the faster the fluid flow the quicker the charge will be redistributed in the rock. As the fluid enters the top of the sample and travels down, the positive potentials created by the EDLs are generally bigger for electrodes 3 and 4 which were observed in the majority of experiments.

Co-seismic signals linked to dynamic failure of Clashach sandstone are plotted in Figure 7.28b. As the strain rate increases the potential signals decrease slightly. At failure the macroscopic fault is formed over a relatively short period of time. The water will be forced into the highly fractured fault zone containing fault gouge. The fluid flow rate is affected in this area and so any current flow will be interrupted.

For Portland limestone the same trend is present for both the pre-seismic and co-seismic signals related to strain rate. The values for limestone are much smaller than those for sandstone.

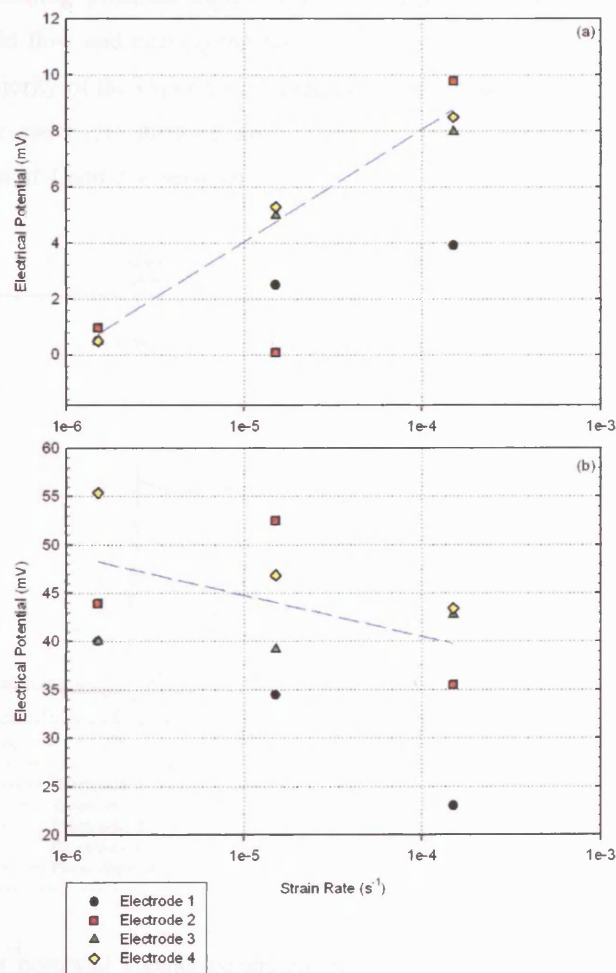


Figure 7.28: Variation of electrical potential (a) prior to failure and (b) during dynamic fracture of drained Clashach sandstone as a function of strain rate; $P_c = 40$ MPa, $P_p = 20$ MPa. The broken lines represent the least squared fit. Each point is given to an accuracy of ± 0.1 mV. [Experiment No.:21, 22, 33]

7.12 STREAMING POTENTIAL AT HIGH PORE FLUID PRESSURES

Pore pressure gradients of up to 30 MPa were applied across the rock sample to investigate the generation of streaming potential signals with a background pore pressure of 5 MPa. A confining pressure of 40 MPa was used with readings taken before and during deformation and again after failure. The differential stress during the measurement of the streaming potential depended on the experiment undertaken and varied from zero (before deformation) to 120 MPa (peak stress) with the typical shape for streaming potential at room temperature shown in Figure 7.29.

Fluid flow strips off the outer diffuse layer of the EDL causing the charges to be transported in the same direction thereby creating a convection current. This potential difference in the sample causes a conduction current to form in the opposite direction. When the two currents are in equilibrium a constant streaming potential signal is produced as shown.

When the valve is opened steady-state flow occurs allowing the currents to reach equilibrium with, ideally, a constant streaming potential signal. When the valve is closed the pore pressure gradient dissipates, stopping fluid flow and causing the potential charges to decay back to their base value. This did not occur in the majority of the experiments undertaken, the reason for this remaining unknown. As electrodes 3 and 4 are twice the distance away from the upper grounded surface, their values are approximately twice that of 1 and 2 as seen here.

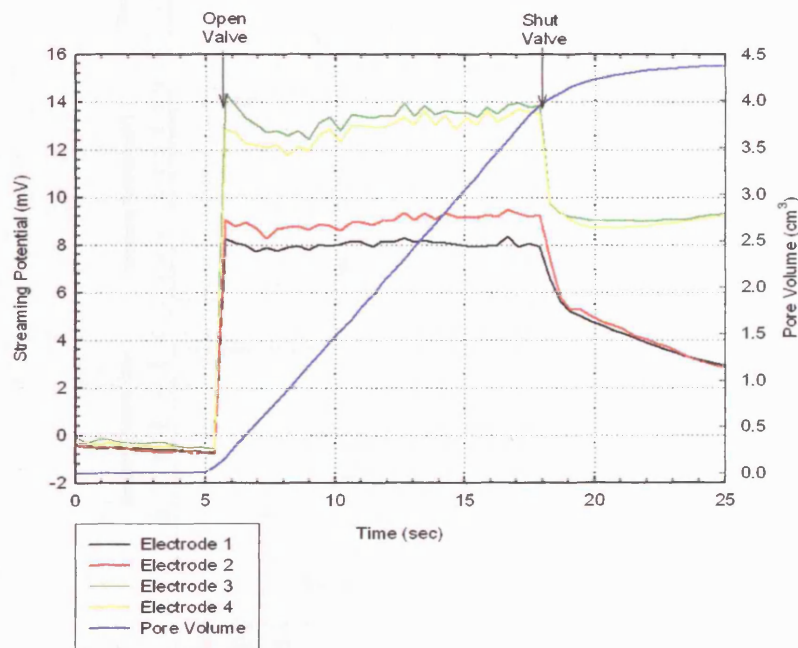


Figure 7.29: Streaming potential signals generated through steady state fluid flow along a pressure gradient in drained Clashach sandstone; $P_c = 40$ MPa, $P_p = 15$ MPa. [Experiment No.: 20]

Using this technique at 5 MPa intervals, the streaming potential for Darley Dale, Clashach and Bentheim sandstones and Portland limestone was produced as shown in Figure 7.30. Linear regression fits to the

upper and lower electrodes giving coefficients ranging from 0.93 to 0.98. The magnitude of the streaming potential signals generated at the maximum pressure gradient for steady state flow for Darley Dale (≈ 325 mV) are an order of magnitude greater than Clashach (≈ 21 mV) which are an order of magnitude greater than Bentheim (≈ 2 mV) and compare with those in Portland limestone of ≈ 600 mV. Looking at the flow rate for a given pressure gradient, Figure 7.31 shows that Clashach sandstone has a faster flow rate than all the other specimens with a flow rate of 0.405 cm³/sec compared to 0.376 cm³/sec, 0.01 cm³/sec and 0.02 cm³/sec for Bentheim, Darley Dale and Portland respectively at a pore fluid pressure gradient of 25 MPa. These flow rates are consistent with the permeabilities given in Table 6.1. Therefore, the streaming potential depends on the rock type more than the fluid flow. With fluid flow increasing linearly with pore pressure gradient, it suggests that fluid flow and streaming potential can be linked for an individual rock type.

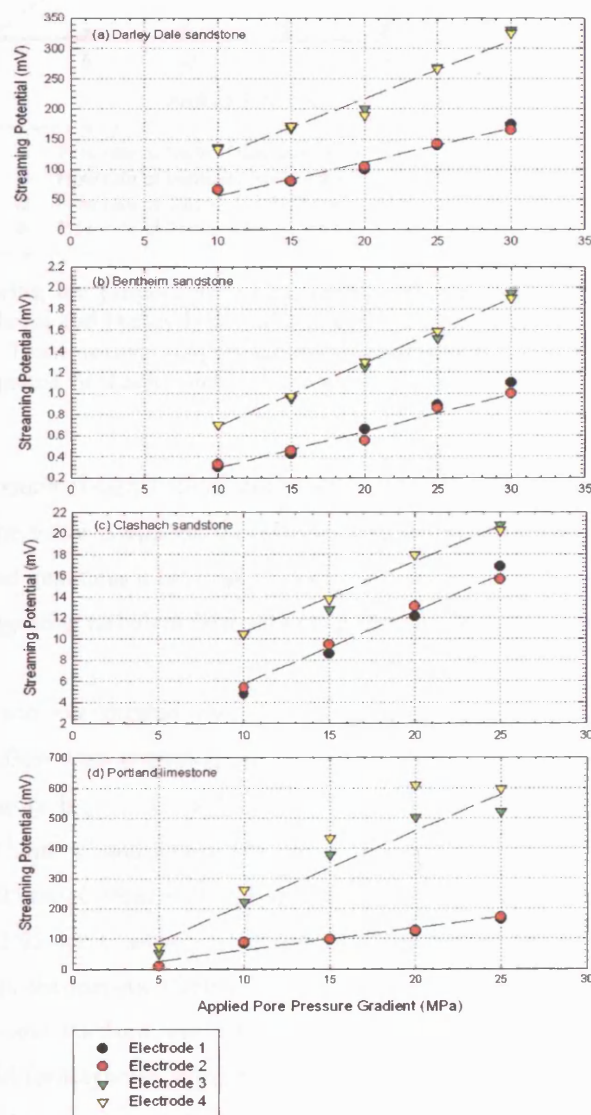


Figure 7.30: Plots showing the streaming potential generated under increasing pore pressure gradients for (a) Darley Dale sandstone, (b) Bentheim sandstone, (c) Clashach sandstone and (d) Portland limestone. Linear relationships were obtained for all samples with regression coefficients ranging between 0.93 and 0.98. Each point is given to an accuracy of ± 0.1 mV. [Experiment No. (a), (b) See Clint (1999), (c) 22, (d) 25]

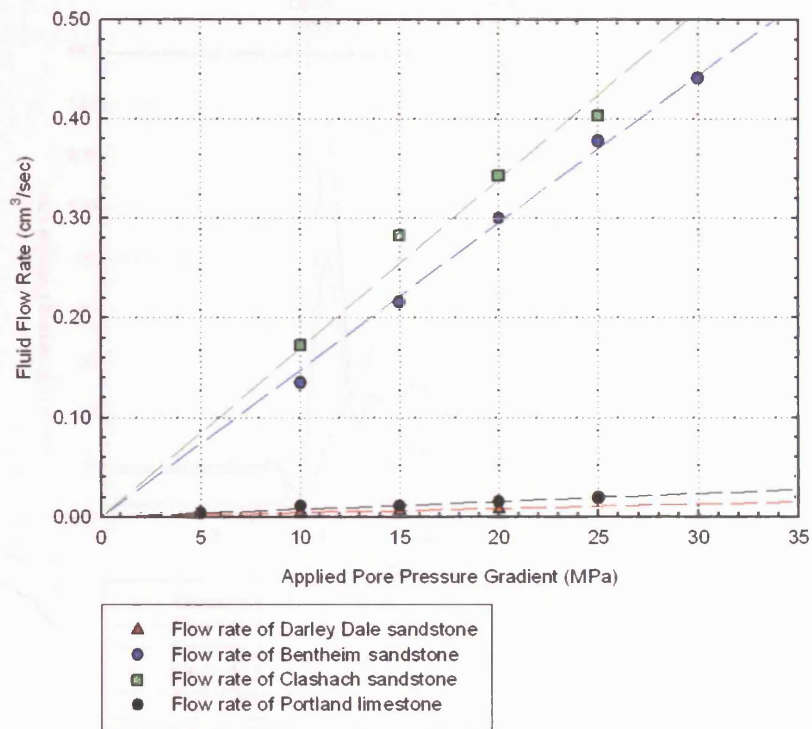


Figure 7.31: Plot showing the proportionality between flow rate and applied pore pressure gradient through Clashach, Bentheim and Darley Dale sandstone along with Portland limestone under hydrostatic conditions of 40 MPa. These results suggest laminar flow through the sample with the broken lines representing the least squared fit. Each point is given to an accuracy of $\pm 0.01 \text{ cm}^3$. [Experiment No.: 22, 25, 29, 31]

Steady-state streaming potential signals could not be achieved for pressure gradients of 30 MPa as shown in Figure 7.32. When the valve is opened, a pressure pulse is forced through the water which interacts with the diffuse layer and generates a large spike. As fluid flow continues the line can be seen to change non-linearly thereby suggesting turbulent flow with the potentials fluctuating until fluid flow ceases.

The state of the fluid was investigated with the use of the Reynolds number (R_e , equation 2.45) to determine if turbulent flow was occurring for Clashach, Bentheim and Darley Dale sandstone and Portland limestone. Density is $\rho = 1.0 \times 10^3 \text{ kg m}^{-3}$, v is the fluid velocity taken to be 0.159 cm s^{-1} , $0.147 \text{ cm}^3 \text{ s}^{-1}$, $5.32 \times 10^{-3} \text{ cm}^3 \text{ s}^{-1}$ and $7.96 \times 10^{-3} \text{ cm}^3 \text{ s}^{-1}$ respectively. l is the characteristic length (pore diameter) taken to be 0.35mm, 0.3mm, 0.4mm and 0.1mm and fluid viscosity $\nu = 0.001 \text{ Pa.s}$. This gives a Reynolds number of 55.65 for Clashach sandstone which is neither truly laminar or truly turbulent. Therefore, Clashach is in the transition between laminar and turbulent flows, which is also the case for Bentheim, Darley Dale and Portland with Reynolds numbers of 44.1, 21.3 and 7.96 respectively. As Darcy's law is only valid for Reynolds numbers less than one, any permeabilities calculated during these experiments are inaccurate.

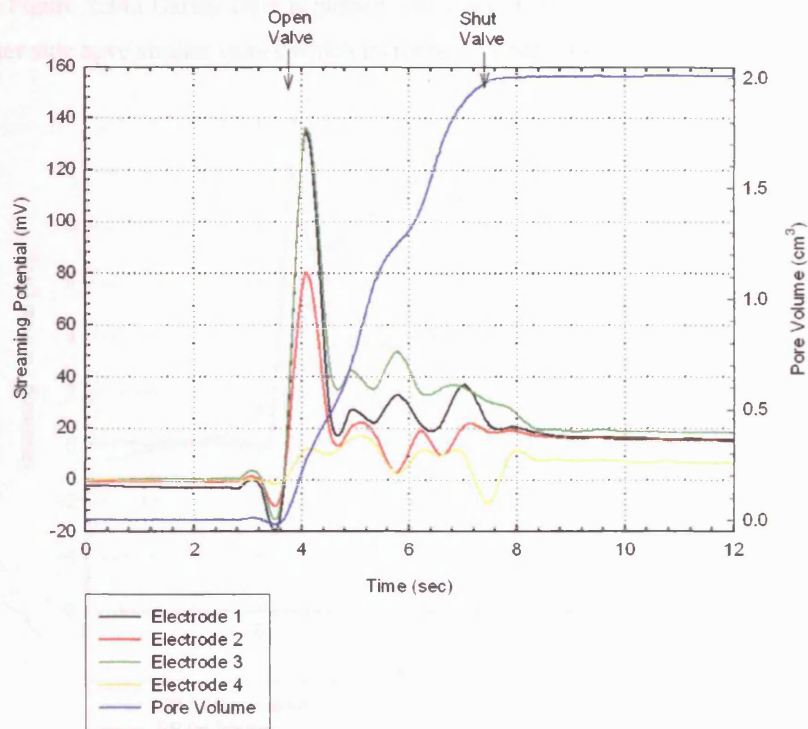


Figure 7.32: Streaming potential signals generated through a pressure gradient in Clashach sandstone, of 35 MPa with confining pressure of 40 MPa. The unsteady change in fluid flow and steady-state streaming potential is not obtained, suggesting a turbulent flow regime is present. [Experiment No.: 20]

7.13 STREAMING POTENTIAL DURING DEFORMATION

A mechanism involving fluid flow has been proposed by Blanpied et al. (1992) involving rapid sealing of faults. Measuring the streaming potential at different stages of deformation could be a useful tool in investigating rock structures. This was examined in one test on Portland limestone with the results shown in Figure 7.33 where electrode 3 minus 1 is plotted to remove end effects. The streaming potential was measured before failure, at failure with residual strength and later after failure using a range of pore pressure gradients up to 30 MPa. Before failure, the typical box shape is present with a value of 4 mV. At failure, where newly formed surfaces are present and with some residual strength, the streaming potential change does not show a recognisable pattern. This may be due to the damage caused by dilatancy enabling the water to go through numerous pathways, and, as a result, stop a steady streaming potential signal. After failure, where the strength is removed, the streaming potential is higher for a shorter period of time, which might suggest that the fault increases fluid flow by by-passing the rock due to the interaction of the rock with the jacket.

As shown in Figure 7.33 the presence of a fault changes the streaming potential signal. This combination of pore pressure gradient and deformation is shown in Figure 7.34 for Darley Dale and Clashach sandstone and Portland limestone. All these experiments were conducted with a confining pressure of 40 MPa, deionised water and at a strain rate of $1.5 \times 10^{-5} \text{ s}^{-1}$. The values plotted are for the two dipoles of dipole 1 (electrode 3 – 1) on one side of the sample and dipole 2 (electrode 4 – 2) on the opposite side of

the sample. In Figure 7.34a Darley Dale is plotted with linear regression lines applied. Before failure the dipoles on either side have similar values which increase with pressure gradient.

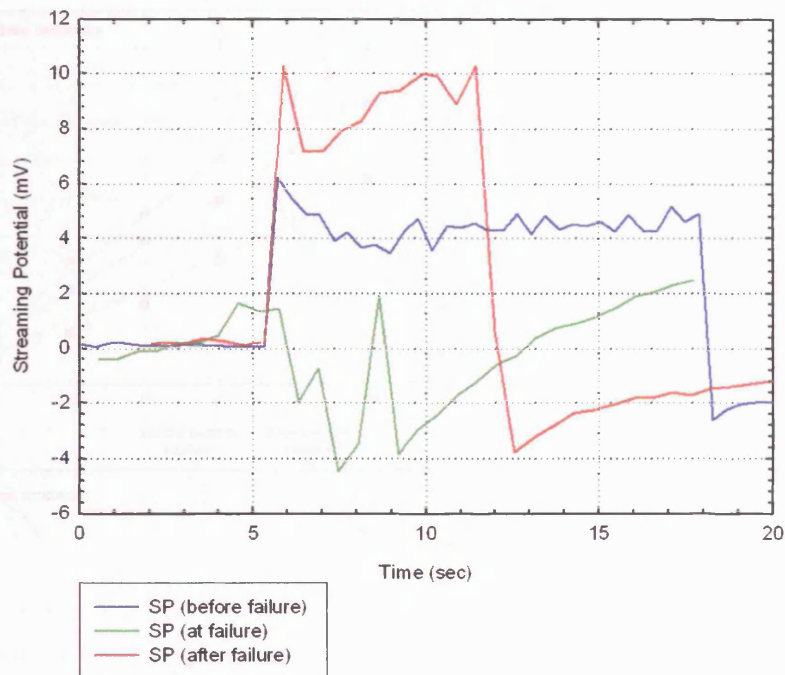


Figure 7.33: Variation of streaming potential in Portland limestone before and after fracture with a pressure difference of 10 MPa applied. The magnitudes of the streaming potential results plotted are the values from electrode 3 minus electrode 1. $P_c = 40$ MPa. [Experiment No.: 25]

This suggests that the rock is fairly homogeneous across the sample. After deformation, the dipoles have a greater magnitude compared to before deformation with dipole 2 increasing in magnitude faster than dipole 1 over the range of pressure gradients. This would be expected because of the increased surface area produced during dilatancy. On the right hand side of the graph is a schematic diagram showing the fault position relative to the four electrodes with dipole 1 on the hanging wall and dipole 2 on the foot wall. For Clashach sandstone in Figure 7.34b the same pattern is observed, before deformation the homogenous nature of the rock is shown with the dipoles having equal magnitudes. After deformation dipole 2 is higher on the footwall compared to dipole 1 on the hanging wall. With Portland limestone the magnitudes of the dipoles are much higher compared with the sandstone. Before failure the dipoles are equal, but after failure dipole 1 is larger in magnitude than dipole 2. This result is opposite to that observed with the sandstones, which may be due to the fault, because electrode 3 on the limestone was on the foot wall and electrodes 1, 2 and 4 were on the hanging wall. This meant that dipole 1 was bisected by the fault. These results suggest that the streaming potential is affected by the position of the electrodes relative to the fault. In the fault region, fault gouge is present which reduces permeability and the number of grain contacts between the two halves of the rock forming a barrier.

Figure 7.34: The variation of streaming potential in (a) Clashach sandstone and (b) Darley Dale limestone. $P_c = 20$ MPa. The broken lines represent linear regression lines. [Experiment No.: 25] (a) See Chm. 11/19/01

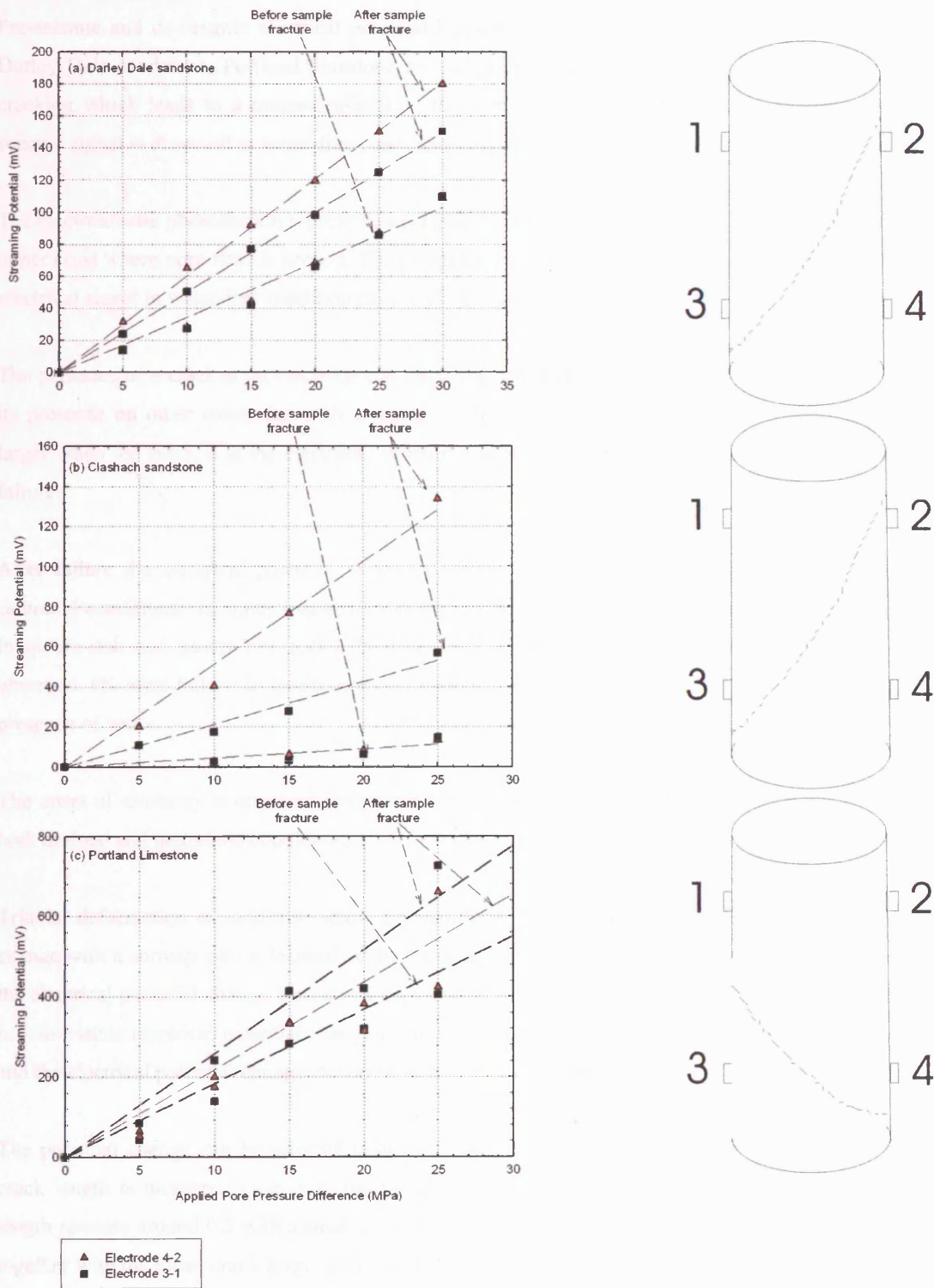


Figure 7.34: The variation of streaming potential with pore fluid pressure differences for (a) Darley Dale sandstone, (b) Clashach sandstone and (c) Portland limestone. All experiments had a $P_c = 40$ MPa and $P_p = 20$ MPa. The broken lines represent the least squared fit. Each point is given to an accuracy of 0.2 mV. [Experiment No. (a) See Clint (1999), (b) 20 (c) 25]

7.14 CHAPTER SUMMARY

Pre-seismic and co-seismic electrical potential signals have been observed in Clashach, Bentheim and Darley Dale sandstone, Portland limestone and Seljadur basalt. These signals occurred during dilatant cracking which leads to a macroscopic fault. In quartz-free rocks such as basalt and limestone a co-seismic signal is observed in water-free conditions suggesting an alternative mechanism is present.

The electrokinetic phenomenon represents a plausible mechanism for generating an electrical signal in the upper crust where pore fluid is present. The piezoelectric effect is the dominant mechanism generating an electrical signal in water-free conditions as found by Yoshida et al. (1998).

The presence of a crack at an electrode can cause the pre-seismic signal to occur several seconds before its presence on other electrodes with a negative polarity. The magnitude of the co-seismic signals is larger when the crack is at the electrode. When this occurs it can rule out identification of features after failure.

After failure the electrical potential signals decrease to a lower level in both water-free and water-saturated conditions. In water-free conditions an increase in potential signal is not observed after failure in quartz-rich and quartz-free rocks. In water-saturated conditions an increase in potential signal is observed 1% after failure in quartz-rich and quartz-free rocks showing this signal to be related to the presence of water.

The onset of dilatancy is observed with an increase in AE activity and electrical potential difference in both drained and undrained conditions.

Triaxial deformation of sandstone under drained conditions produces a decrease in electrical potential change with a corresponding decrease in the rocks pore volume throughout compaction. During dilatancy the electrical potential change increases with a similar increase in pore volume. For undrained conditions no observable electrical potential change is noted, because as the pore pressure increases with dilatancy and the electrical potential change increases with a decrease in pore pressure.

The potential change can be inferred from the mean crack length calculated from the AE. Each mean crack length is measured relative to the largest crack formed at failure. During compaction the crack length remains around 0.2 with a small change in electrical signal. At dilatancy the AE activity increases together with the mean crack length to 0.4 as well as the electrical potential change. Fracture is associated with the largest potential increase and a crack length of 1.0, with both decreasing after failure. The results suggest that this could, in theory, be applied at a crustal scale.

Microstructural analysis of Clashach sandstone prior to deformation shows no cracking in any grains of quartz and feldspar. After deformation, a large number of intergranular and transgranular cracks are present with a wide distribution of broken mineral fragments.

Chapter 7: Comparison of Electrical Potential Signals from Experimental Deformation of Various Rock Types

The amount of roll-over varies with strain rate. The strength changes slightly with strain rate while the frictional strength does not vary significantly.

Electrical potential difference decreases with reducing strain rate during compaction and dilatancy. The slower the strain rate the easier it is to pin point localised features to an electrode which are obscured at higher strain rates. A fluid mechanism is suggested as producing the potential difference because the change in pore volume during deformation is independent of strain rate.

Pre-seismic electrical potential difference signal increases with increasing strain rate during drained triaxial deformation of Clashach sandstone and Portland limestone. The co-seismic signal shows a slight decrease in potential with increasing strain rate.

Streaming potential increases linearly with applied pore fluid pressures for Clashach, Bentheim and Darley Dale sandstones and Portland limestone with values in the range of 600 - 2 mV. The linearity with pressure gradients and streaming potentials is valid up to 25-30 MPa with values above this not giving constant streaming potential signals. The fluid flow increases linearly with the greatest fluid flow in Clashach sandstone, followed by Bentheim sandstone then Portland limestone and finally Darley Dale sandstone with a flow rate of at least 4 times less than the other sandstones.

The streaming potential varies during deformation with the magnitude of the signal affected by the presence of the fault. Prior to deformation the rock is approximately homogeneous with readings on both sides of the rock being equal. After deformation the presence of the fault causes the electrodes on the foot wall and hanging wall to diverge up to a 30 MPa pressure gradient. Depending on the position of the fault, the electrode values may be altered. This suggests that the streaming potential signals could be used to recognise the fracture position relative to the electrodes.

8. Temperature Effect up to 125°C on the Mechanical and Electrical Properties on Clashach sandstone and Portland limestone

8.1 INTRODUCTION

The effect of temperature and pore fluid chemistry on electrical potential signals needs be investigated to form accurate conclusions in relation to the crustal scale environment as well as to produce base values for models of the electrokinetic and piezoelectric phenomenon. The effect of temperature on the potential signals during deformation is investigated here using a range from 25°C to 125°C under drained conditions with an effective pressure of 20 MPa and a constant strain rate of $1.5 \times 10^{-5} \text{ s}^{-1}$. From these experiments I hope to address the following questions for Clashach sandstone and Portland limestone: 1) How do the mechanical properties of the rock change with temperature (e.g. peak stress, friction, pore volume)? 2) Do the rock samples have to be left for prolonged periods of time to reach thermal equilibrium? 3) How are the electrokinetic and piezoelectric phenomena affected by temperature? 4) How does simulated formation water combined with elevated temperature affect the electrical potential signals during all aspects of deformation? These questions will be answered in the following sections.

8.2 INITIAL OBSERVATIONS WITH THE FURNACE

I conducted trial tests on the furnace to identify how the heat is distributed within the triaxial pressure vessel and how it affects electrical potential signals. An example of how the confining pressure, differential stress and electrical potential are affected by temperature is shown in Figure 8.1. With the confining pressure at 3 MPa, the furnace is turned on and the temperature increases at 5°C/min until the set controlled temperature is reached, which in this example is 100°C. As the furnace begins to heat up the confining pressure increases due to fluid expansion. Once the desired temperature is reached after 1000 seconds, the control unit switches the furnace power on and off to maintain that temperature to an accuracy of $\pm 5^\circ\text{C}$. Therefore, when the furnace is switched off, heat is lost through the thermal conductivity of the oil and pressure vessel. The controller is switched on when the temperature is 5°C less than the desired value and because it takes several seconds for the heat to dissipate from the heating elements the furnace temperature overshoots the desired temperature by approximately 5°C. At this point the furnace switches off and the temperature falls again. With the increase in temperature, the confining pressure is raised causing the pressure on the balanced ram to increase simultaneously; this causes the differential stress to follow the same trend as the confining pressure. After about 30 minutes, the oil and rock inside the pressure vessel reach thermal equilibrium (i.e. all the rock is at the same temperature) and the experiment is started.

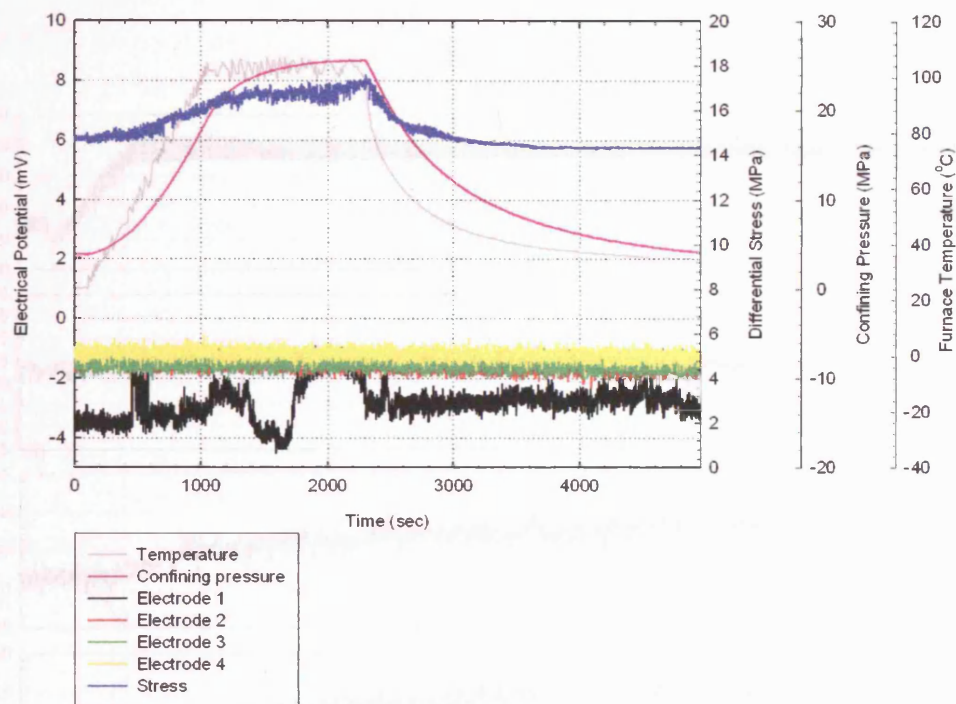


Figure 8.1: Plot showing the effect of heat on the confining pressure, differential stress and the four electrodes (coaxial wires) using a dummy sample (aluminium) to 100°C. [Experiment No. 44]

After the experiment has been completed the furnace is switched off, in this case at 2300 seconds. The furnace temperature, confining pressure and differential stress all decrease until they reach the values present before heating began, which, depending on the temperature, may take several hours. Once the furnace and oil have cooled the sample is removed.

During the heating cycle the electrical potential is measured at all four electrodes to investigate the effect of temperature on the electrical signal. Electrodes 2, 3 and 4 remain constant throughout the heating cycle varying by less than 1 mV. For electrode 1, slight variation is present but it remains less than 3 mV. This shows that the electrodes and the coaxial wires are unaffected by temperature up to 100°C at least.

As discussed in Chapter 5.2, the temperature of the furnace does not reflect the temperature of the oil or the rock due to thermal convection. This is demonstrated by the furnace calibration which is re-plotted in Figure 8.2. The temperature of the furnace is shown in the top box with various thermocouples positioned around the sample assembly and in the centre of the rock. From this plot the temperature at the base of the sample changes least (25°C) with the temperature at the top of the sample (70°C) changing the most. For all thermocouples around the sample, a time lag is present between turning the furnace on and an increase in temperature within the rock, generally of the range of 500 seconds. Once the furnace has reached its desired temperature the temperature around the rock continues to increase and reaches a constant approximately 30 minutes after that of the furnace.

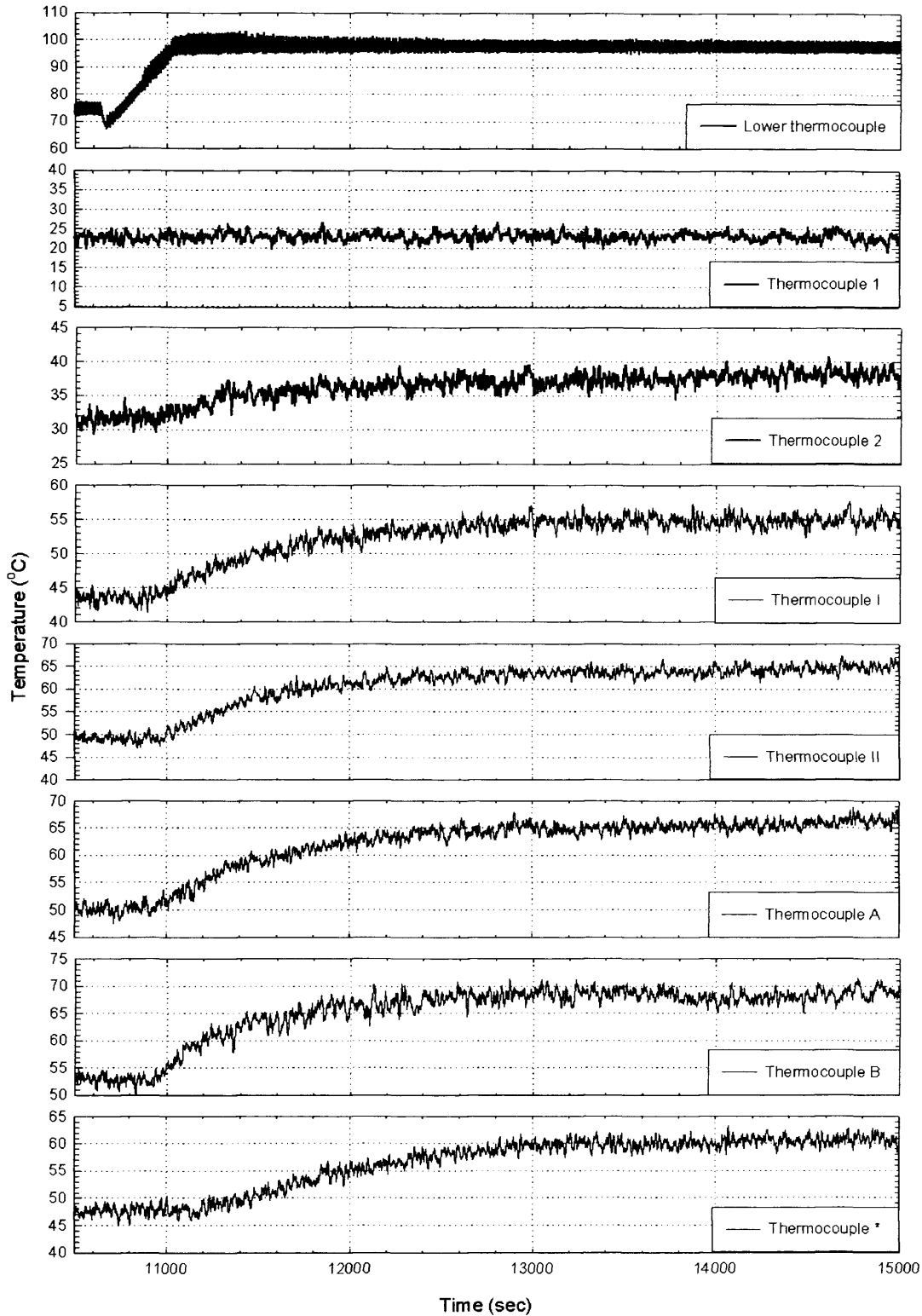


Figure 8.2: Plots of temperature profiles at different positions around a dummy sample to show how the oil and rock heats up. The thermocouple located in the rock is positioned in a hole drilled from the lower end of the sample. (See Appendix 7 for more details) [Experiment No.: Cal3]

During the investigation of rock deformation at elevated temperatures, the mechanical properties of the rock including changes in pore volume, ultimate and frictional strength were measured in conjunction with acoustic emissions. The typical AE values recorded are shown in Figure 8.3. When the furnace reaches the required temperature, the amount of AE on channels 1 and 2 increases from 54 dB at 1000 seconds to 70 dB at 3800 seconds. The AE is then split into two amplitude regions of 55-60 dB and 62-70 dB. These zones remain constant during deformation which is shown at 8200 seconds, with a decrease in confining pressure and a peak in channel 4. After deformation the AE on channels 1 and 2 varies between 65 dB and 88 dB until the furnace is switched off, at which point channels 1 and 2 become quiet with a limited number of hits on channels 3 and 4. This suggests that the furnace generates electrical noise by constantly turning on and off to maintain a temperature which is then picked up by the AE transducer as acoustic noise, agreeing with other work done in these laboratories (Pers. Comm. Meredith 2004). As the electrical potential signals were the main interest in this study, the AE data collected was disregarded because it was not possible, in the scope of this investigation to identify real features from artificial ones.

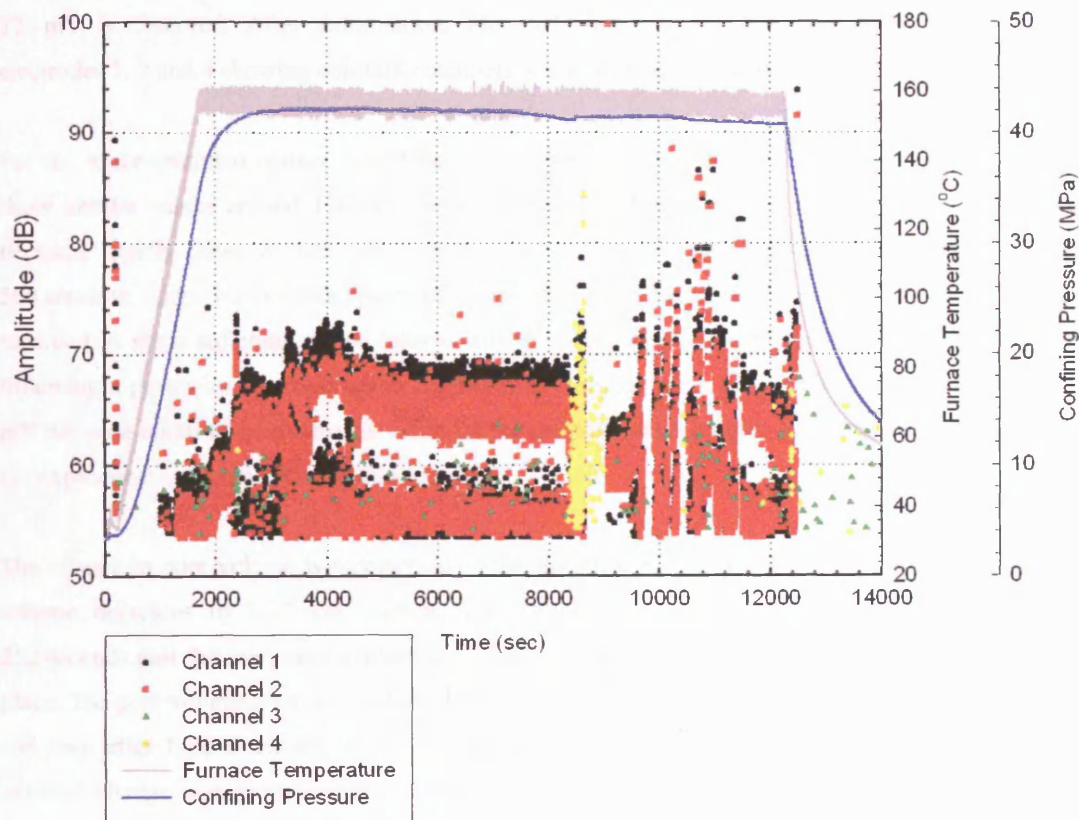


Figure 8.3: Acoustic emissions monitored during the use of the furnace at 160°C. This includes switching the furnace on, during the constant strain rate deformation and during cooling down. [Experiment No.: 41]

8.3 COMPARISON OF PORTLAND LIMESTONE BOTH SATURATED AND IN WATER-FREE CONDITIONS

In this section I investigate the effect of temperature on the electrokinetic phenomena during all stages of deformation in quartz-free Portland limestone rock at temperatures up to 125°C under dry and saturated conditions. This includes investigating how temperature influences the pre-seismic and co-seismic electrical signals during deformation as well as the streaming potential signals generated by applied pore pressure gradients.

In Figure 8.4a the dry limestone results are shown with the electrical potentials varying from -800 mV up to 1700 mV. When deformation begins, the potentials at all four electrodes show no significant change. Peak stress is reached at 490 seconds, where partial failure occurs with a stress drop from 153 MPa to 130 MPa. This is seen on electrode 1 by a signal increase of 58 mV and on electrode 2 with an increase of 20 mV. At 571 seconds, failure occurs showing a stress drop of 54 MPa with electrodes 1, 2 and 4 increasing in potential by 176 mV, 17 mV and 24 mV respectively. With electrode 3 a decrease on 326 mV is observed. After deformation, frictional sliding occurs having a stress of 85 MPa with electrodes 1, 2 and 4 showing constant potentials while electrode 3 fluctuates slightly.

For the water-saturated drained limestone Figure 8.4b is shown. Before deformation all three electrodes show similar values around 170 mV. When deformation begins at 100 seconds, the electrical signals decrease rapidly down to 110 mV, 106 mV and 120 mV for electrodes 1, 2 and 3 respectively at 500 seconds. After this point the potentials increase steadily up to 800 seconds where the peak stress is recorded. A strain softening period follows with the opening of new surfaces and the electrical potentials following a power-law increase up to failure at 894 seconds when co-seismic signals in the range of 30 mV are seen on all three electrodes. After failure the potentials continue to increase at a steady rate until the experiment is terminated at 2500 seconds.

The change in pore volume is represented by the grey line in Figure 8.4b. During compaction, the pore volume decreases by 0.23 cm³ through the closure of pores and cracks by deformation. This is 252 seconds past the minimum in electrical signals and past the elastic limit with strain hardening taking place. The pore volume after compaction then increases by 0.14 cm³ up to failure as new surfaces open up and then after failure remains approximately constant. These results show that a similar relationship between change in pore volume and electrical potential signal exists to that at room temperature. When the pore volume increases due to dilatancy, the electrical signal also increases as it flows into the newly formed void spaces. However, this increase in pore volume does not occur at the elastic limit as observed at room temperature, suggesting a different mechanism. A possible explanation is that with the higher temperature chemical dissolution is increased which significantly reduces the permeability of the rock. Alternatively, the effect may be due to the influence of temperature on the maturation/dehydration of all the non-calcitic material present in the limestone. In either case it results in the pressure in the centre of the sample being different from the outside of the rock causing a pressure gradient through it. At the elastic limit, cracks begin to open and fluid enters them. However, the excess water which cannot fill the

newly formed cracks is forced down the pressure gradient out of the rock which further reducing the pore volume. At a particular point, the pressure gradient dissipates and fluid from the intensifier enters the newly formed cracks thus increasing the pore volume of the rock. At failure, the sample is displaced altering the shape of the jacket and creating additional void space along the fault, which reduces the pore pressure. In response to this the intensifier rushes forward by 0.15 cm³ to maintain the desired pressure.

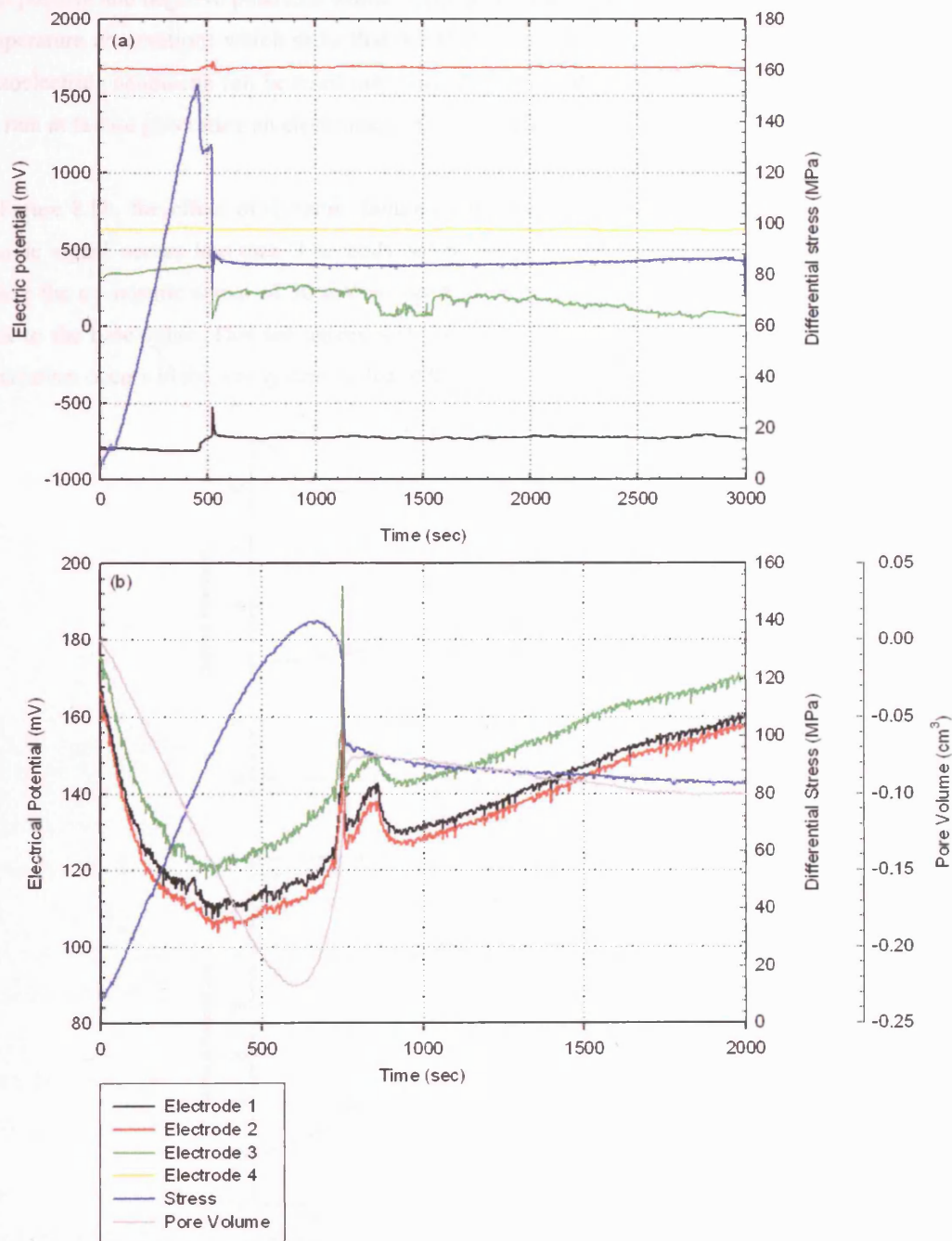


Figure 8.4: Electrical potential difference of Portland limestone (a) dry ($P_c = 20$ MPa) and (b) saturated during deformation with $P_c = 40$ MPa, $P_p = 20$ MPa using deionised water as the pore fluid and strain rate of $1.5 \times 10^{-5} \text{ s}^{-1}$ and at 50°C (Electrode 2 is missing due to breakage). [Experiment No.: (a) 39, (b) 36]

Pre-seismic and Co-seismic signals

The electrical potential generated around failure for Portland limestone is shown in Figure 8.5 with the values normalised to a base value. For the dry condition in Figure 8.5a there seems to be no pre-seismic signals at any of the four electrodes. As the stress decreases, electrode 1 increases slightly and at failure electrode 1 potential reaches 58 mV. On electrodes 2 and 3, a co-seismic signal of 4 mV is present with both positive and negative polarities whilst electrode 4 shows no signal change. This agrees with the room temperature observations which show that due to the absence of water and quartz, the electrokinetic and piezoelectric phenomena can be ruled out. This suggests an alternative mechanism such as movement of the ram at failure generating an electromagnetic signal at the electrodes.

In Figure 8.5b, the effect of dynamic failure on water-saturated drained limestone is shown. The pre-seismic signal occurs less than 3 seconds before brittle failure with an average change of 10 mV. At failure the co-seismic signal of 30 mV is observed on all three channels followed by a signal decaying back to the base value. This too agrees with room temperature observations suggesting that a different mechanism occurs in the wet system to that of the dry, as a net charge is produced.

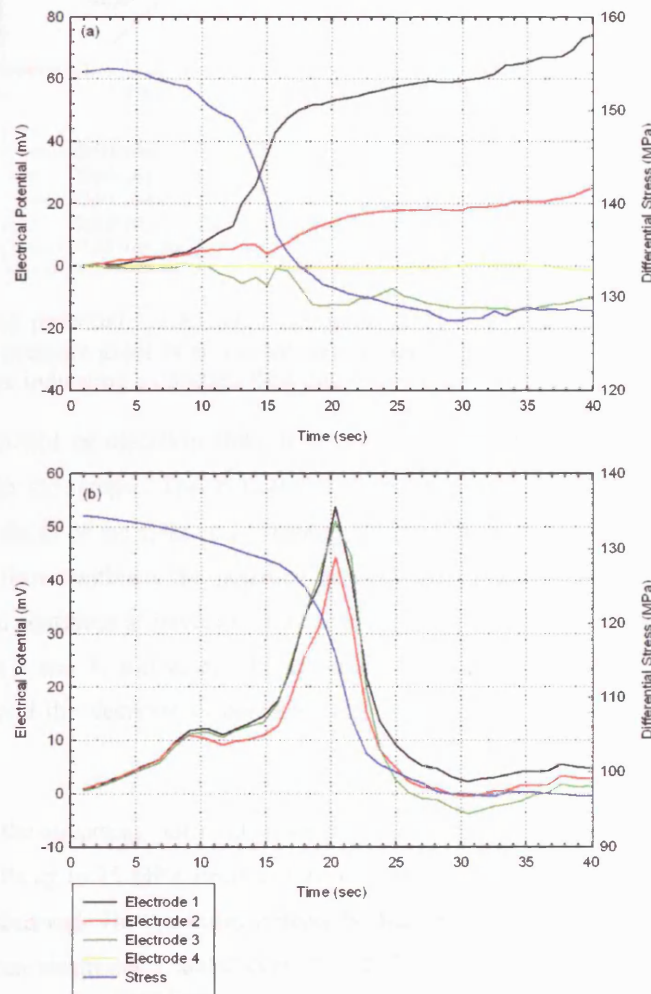


Figure 8.5: Electrical potential during the dynamic failure of Portland limestone deformed (a) dry ($P_c = 20$ MPa) and (b) water saturated ($P_c = 40$ MPa, $P_p = 20$ MPa) using deionised water as the pore fluid with a strain rate of $1.5 \times 10^{-5} \text{ s}^{-1}$ and at 50°C. [Experiment No.: (a) 39, (b) 36]

Streaming potential at high pore pressures

With limestone, pore pressure gradients of 10, 15, 20 and 25 MPa were applied across the rock sample to investigate the generation of streaming potential signals at 50°C. A confining pressure around 40 MPa was used and the typical shape produced is shown in Figure 8.6.

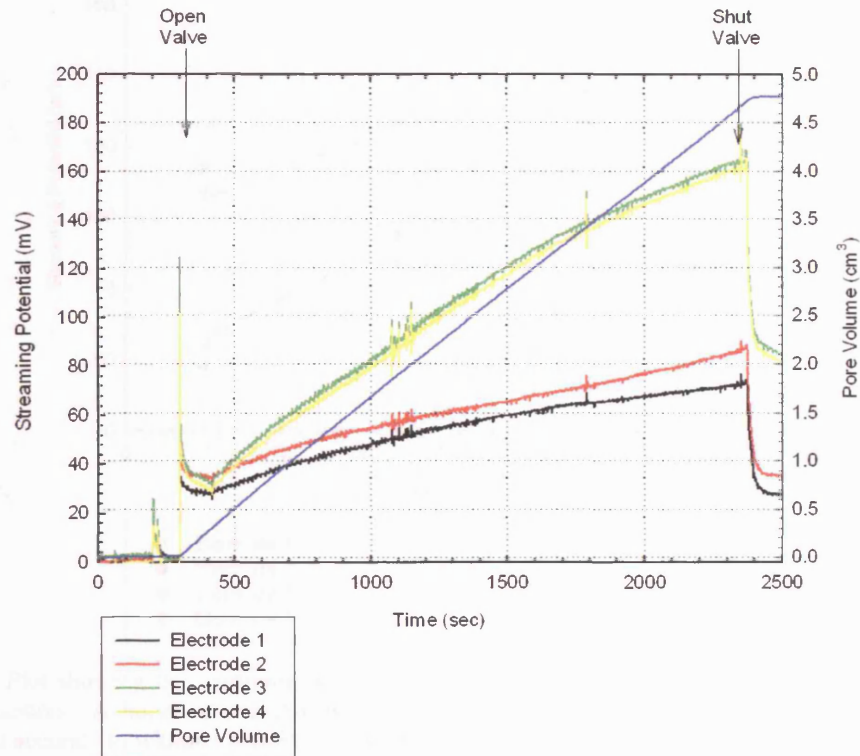


Figure 8.6: Streaming potential for Portland limestone at 50°C before fracture. $P_c = 40$ MPa with a 10 MPa applied pore pressure gradient across the sample and a 5 MPa background pore pressure with the change in fluid volume indicating a constant flow rate.[Experiment No.: 36]

When the valve is opened an electrical spike is observed which is thought to be caused by sending a pressure wave through the sample. This is treated as an artefact of the method used. When steady-state flow occurs after the decay of the spike, the streaming potential reaches equilibrium of 35 mV on all four electrodes. As fluid flow continues the potential at electrodes 3 and 4 increases at a faster rate than electrodes 1 and 2 and continues to increase until the valve is shut. At this point the potentials decrease by 75 mV for electrodes 3 and 4, and 40 mV for electrodes 1 and 2. The average reading of the increase excluding the spike and the decrease in potentials with opening and closing the valve is taken as the streaming potential.

Using this technique the streaming potential was obtained at 5 MPa pore pressure gradients for Portland limestone from 10 MPa up to 25 MPa. From Figure 8.7 a linear increase in streaming potential with pore pressure increase is observed. The streaming potentials obtained from electrodes 3 and 4 are significantly greater than those from electrodes 1 and 2 even though the bottom of the sample is not isolated. This suggests that the same mechanism whereby the magnitude of the streaming potential signals is correlated with fluid flow rates noted at room temperatures also occurs at temperatures up to 125°C. The heat has

some additional effect causing the values at the top of the sample to have lower potentials than those at the bottom.

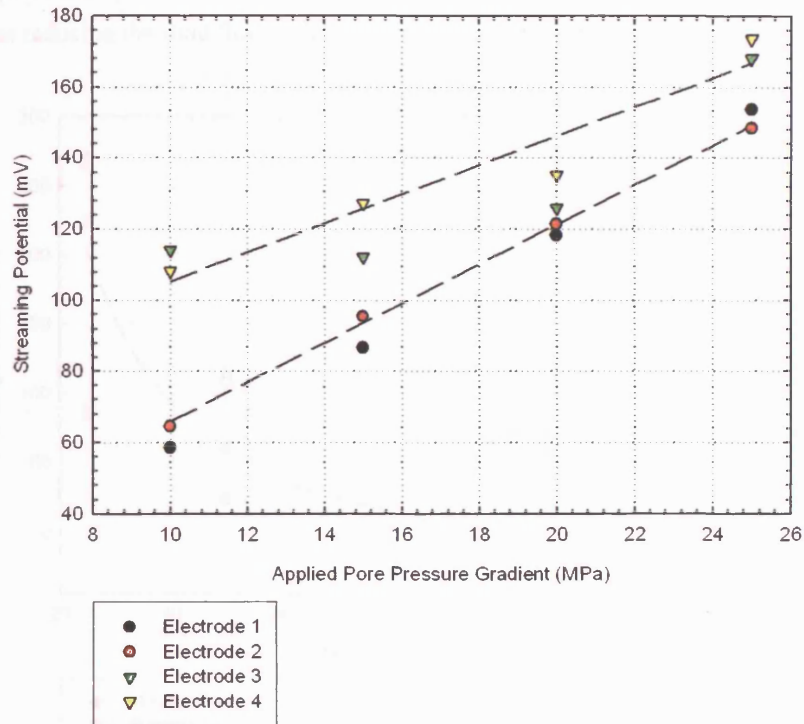


Figure 8.7: Plot showing the streaming potential generated under increasing pore pressure gradients for Portland limestone. A linear relationship was obtained with a regression coefficient of 0.87 with each point plotted accurate to within ± 0.1 mV. [Experiment No.: 36]

To identify if the streaming potential of limestone is affected by temperature, it was measured at 50°C and 125°C and compared with the room temperature results. These are tabulated into Table 8.1 and plotted in Figure 8.8.

Temperature (°C)	Electrode 1	Electrode 2	Electrode 3	Electrode 4	Flow Rate (cm ³ /s)
25	83.1	89.2	224.7	264.1	0.011
50	58.8	64.8	114.3	108.0	0.0024
125	8.5	24.4	56.5	51.9	0.0014

Table 8.1: Streaming potential of Portland limestone at various temperatures before deformation together with the corresponding fluid flow rate. The applied pore pressure gradient was 10 MPa on top of a 5 MPa background pore pressure. Each value is given to an accuracy of ± 0.1 mV for the electrical potential and ± 0.02 cm³/sec for flow rate measurements.

At room temperature, a volume fluid flow rate of 0.011 cm³/s was observed with the streaming potential at electrodes 3 and 4 being 224 and 264 mV which is approximately 3 times the readings at electrodes 1 and 2 of 83 and 89 mV respectively. At 50°C the fluid flow rate drops to 0.0024 cm³/s, which is 5 times slower than at room temperature. Also, the streaming potential values are halved with this 25°C increase. Experiments conducted at elevated temperatures did not have the bottom of the sample assembly isolated due to heating problems connected to the pore pressure piping. Therefore it would be expected that the potential readings at all four electrodes would be similar. However the potentials at electrodes 3 and 4 are

approximately double those at electrodes 1 and 2. Heating the rock to 125°C shows a further reduction in fluid flow rate down to 0.0014 cm³/s with the streaming potential decreasing by half and with electrodes 3 and 4 being approximately double those of electrodes 1 and 2. This suggests that the limestone is affected by the heat, thus reducing the fluid flow which, in turn, affects the streaming potential.

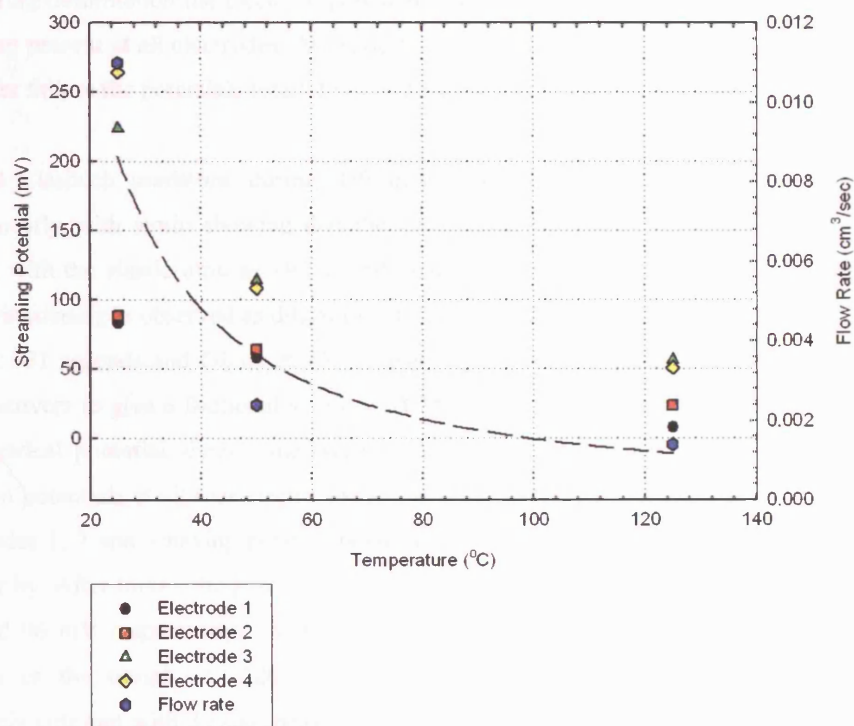


Figure 8.8: Streaming potential and fluid flow rates of Portland limestone at various temperatures with a 10 MPa applied pore pressure gradient prior to fracture with a 5 MPa background pore pressure; $P_c = 40$ MPa with deionised water as pore fluid. The broken line represents the least squared fit of the streaming potential. Each point is given to an accuracy of ± 0.1 mV for streaming potential and ± 0.001 cm³/sec for flow rate measurements. [Experiment No. 25, 36, 41]

To look at the effect of deformation on the streaming potential signals, dipoles on both sides of the sample were taken (dipole 1 = electrode 3 – 1, dipole 2 = electrode 4 – 2) and the results tabulated in Table 8.2. This table shows that there is no discernable pattern between the streaming potentials before and after failure. As the bottom of the sample is not isolated, electrical leakage may take place, thereby reducing the potential, and as the distance to the grounding point is the same for all electrodes the difference between the ends of the sample is negligible.

Applied Pressure Gradient (MPa)	Before Dipole 1	Before Dipole 2	After Dipole 1	After Dipole 2
10	55.3	44.4	-66.9	-60.1
15	-32.4	-45.2	-57.4	-51.2
20	-53.3	-56.7	-71.8	-70.4
25	-66.8	-100.3	-51.0	-83.1

Table 8.2: Effect of deformation on the streaming potential of Portland limestone at various applied pore pressure differences. Dipole 1 equals electrode 3 minus 1, dipole 2 is electrode 4 minus 2. Each value is given to an accuracy of ± 0.2 mV.

8.4 COMPARISON OF CLASHACH SANDSTONE SATURATED AND IN WATER-FREE CONDITIONS AT 50°C

The effect of triaxial deformation on dry and water saturated Clashach sandstone at 50°C is shown in Figure 8.9. In Figure 8.9a the piezoelectric effect is believed to be the dominant mechanism with no water present. During deformation the electrical potential signals remain fairly constant with certain peaks and troughs being present at all electrodes. At brittle failure, co-seismic signals are observed on electrodes 2, 3 and 4. After failure the potentials return to their base values until the experiment is stopped.

For drained Clashach sandstone during deformation, Figure 8.9b is shown. The differential stress increases linearly with strain showing that the quasi-static behaviour of the rock occurs above room temperature with the elastic limit at 540 seconds and a change in pore volume of -0.28 cm^3 . Above this point strain hardening is observed as dilatant microcracking occurs with a 'roll-over' to the peak stress of 159 MPa at 731 seconds and failure at 751 seconds with a corresponding stress drop of 120 MPa. The rock then recovers to give a frictional stress of 58 MPa until the experiment is stopped at 3500 seconds. For the electrical potential signals, the onset of deformation is accompanied by an increase of equal magnitude in potentials at all four electrodes. At failure a co-seismic signal is observed at each electrode with electrodes 1, 2 and 3 having positive polarities and electrode 4 a negative polarity due to the fault passing near by. After failure the potentials for electrodes 1, 2 and 3 decay away and level off at 118 mV, 154 mV and 96 mV respectively. Electrode 4 follows the same general trend with an additional few spikes such as the trough at 1320 seconds. As the deformation continues the potentials remain approximately constant with 3 small peaks around 3000 seconds present on all electrodes. This suggests that the same mechanism of electrokinetic effect at room temperature can be applied to elevated temperatures with the same link between differential stress and change in pore volume along with electrical potential change. However, with the signal after failure being absent at 50°C it suggests that this signal is related to electrical reaction rather than a reaction at the fault surface.

Pre-seismic and Co-seismic signals

The electrical potential generated around failure for Clashach sandstone is shown in Figure 8.10 with the values normalised to a base value. In Figure 8.10a the deformation of the dry sandstone is shown. The pre-seismic signal is negligible, but a co-seismic signal of 140 mV is picked up on electrode 3 with electrodes 1 and 4 having values of 10 mV and -9 mV respectively. The co-seismic signal for electrode 3 lasts 3 seconds before it decays slowly over the next 15 seconds before reaching its base value.

For the deformation of water saturated sandstone in Figure 8.10b a pre-seismic signal is difficult to identify above the background electrical noise of 2 mV. At failure the stress drop produces co-seismic signals of 19 mV, 25 mV, 23 mV and -81 mV for electrodes 1 through 4. These peaks decay after failure with electrode 4 increasing slowly up to -48 mV and the other electrodes decreasing down to less than 12 mV. These results agree broadly with the room temperature results suggesting the same mechanism occurs at highly temperature.

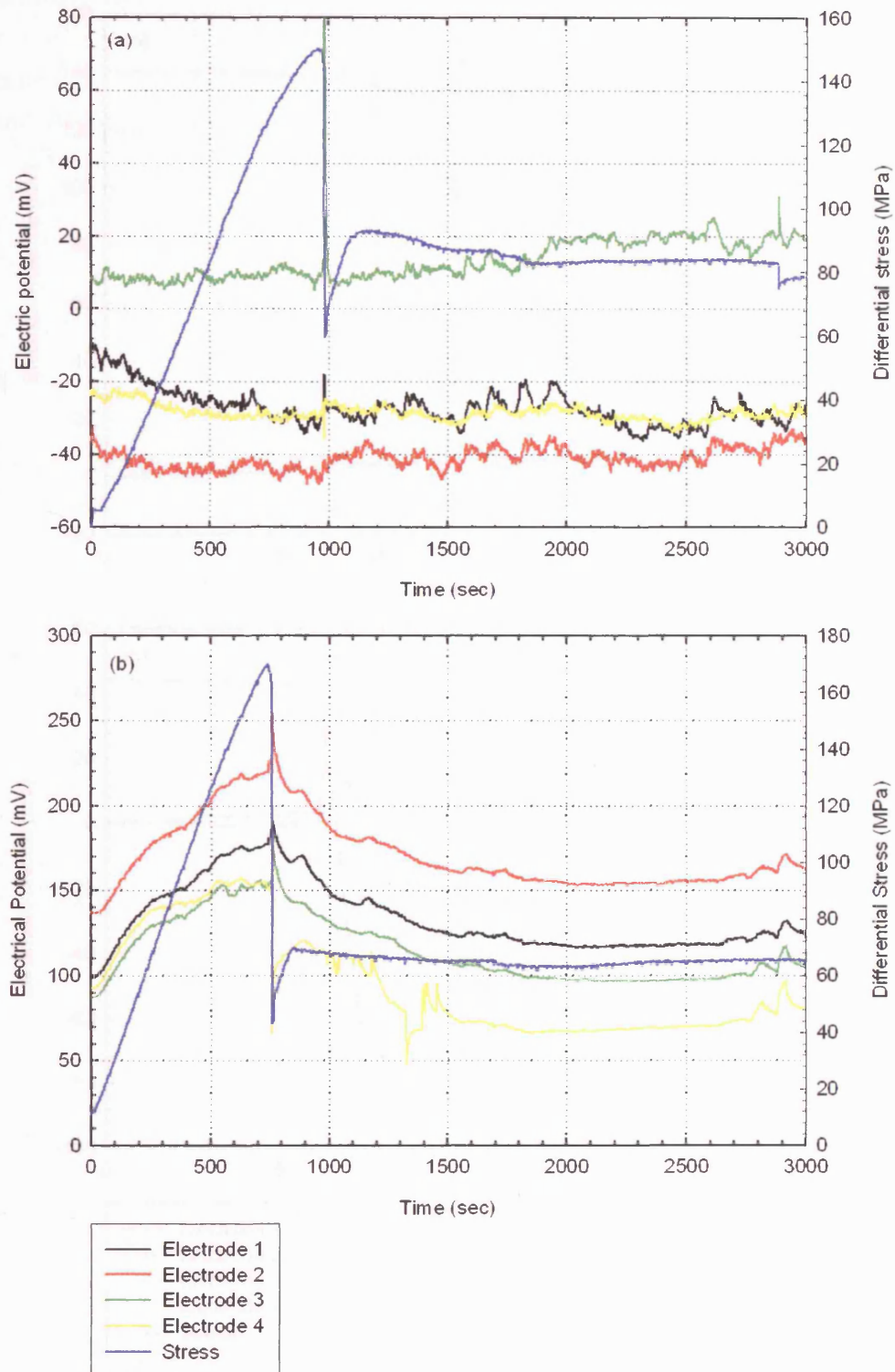


Figure 8.9: Electrical potential difference of Clashach sandstone during deformation (a) dry ($P_c = 20$ MPa) and (b) water saturated ($P_c = 40$ MPa, $P_p = 20$ MPa). Deionised water is the pore fluid and a strain rate of $1.5 \times 10^{-5} \text{ s}^{-1}$. [Experiment No.: (a) 34, (b) 35]

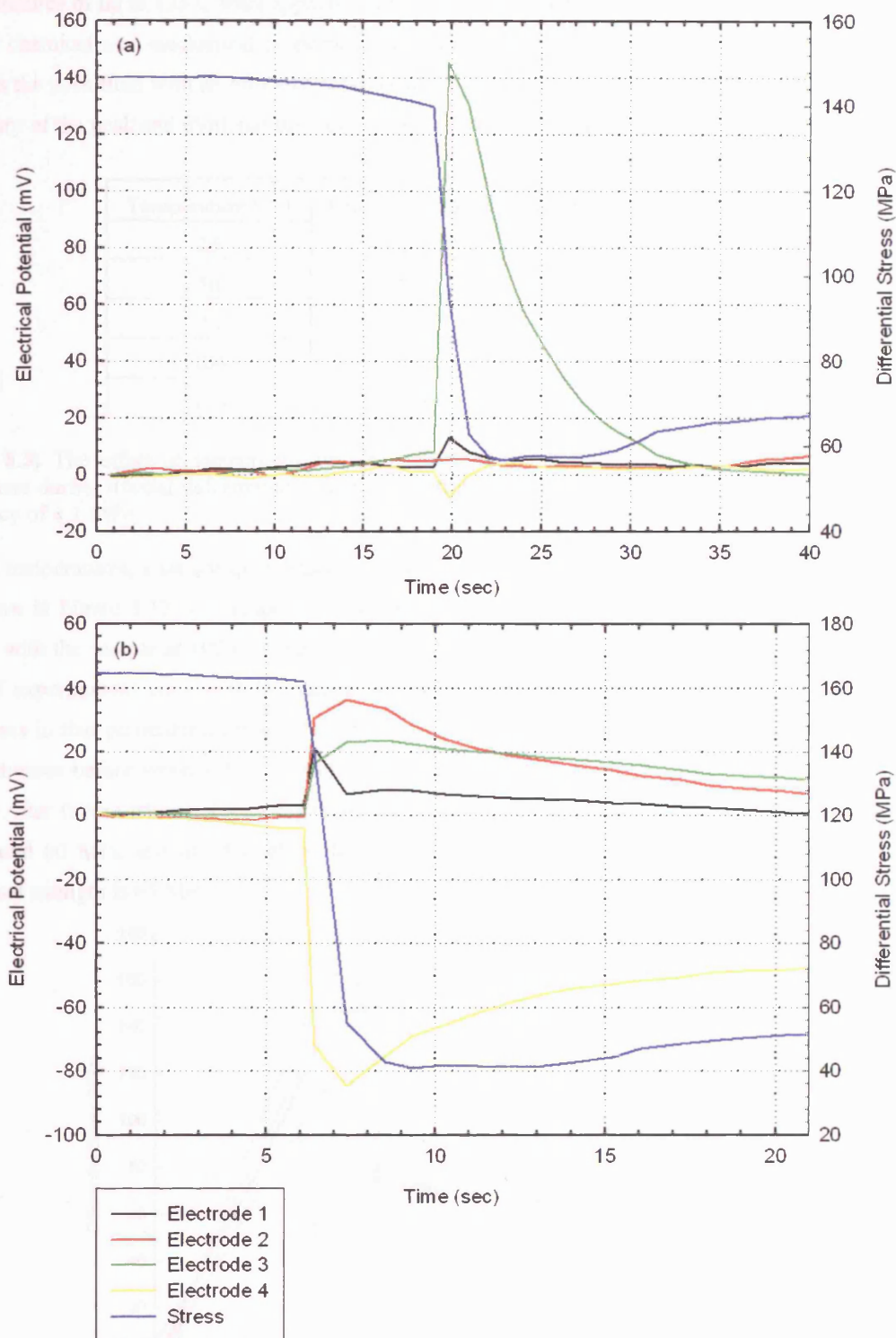


Figure 8.10: Electrical potential during the dynamic failure of Clashach sandstone deformed (a) dry ($P_c = 20$ MPa) and (b) water saturated ($P_c = 40$ MPa, $P_p = 20$ MPa). Deionised water was used as the pore fluid with a strain rate of $1.5 \times 10^{-5} \text{ s}^{-1}$ [Experiment No.: (a) 34, (b) 35]

8.5 EFFECT OF ELEVATED TEMPERATURES ON MECHANICAL PROPERTIES OF CLASHACH SANDSTONE

Temperatures of up to 125°C were applied to Clashach sandstone to look at the effect of thermal changes on the chemical and mechanical properties during drained deformation. Deionised water was initially used as the pore fluid with an effective pressure of 20 MPa and a constant strain rate of $1.5 \times 10^{-5} \text{ s}^{-1}$. A summary of the peak and frictional stresses is given in Table 8.3, and shown graphically in Figure 8.11.

Temperature (°C)	Peak Stress (MPa)	Frictional Stress (MPa)
25	151	69
50	164	60
75	158	95
100	87	39
125	116	60

Table 8.3: The effect of temperature on the peak stresses and frictional sliding stresses of Clashach sandstone during triaxial deformation at a constant strain rate of $1.5 \times 10^{-5} \text{ s}^{-1}$. Each point is given to an accuracy of $\pm 1 \text{ MPa}$.

For all temperatures, a similar quasi-static behaviour exists. The change in pore volume with deformation is shown in Figure 8.12. All temperatures show a similar elastic limit around 0.8% for 25, 50, 75 and 125°C with the sample at 100°C being lower at 0.7%. The peak stresses do not vary significantly above that of experimental error with the sample at 100°C failing early, which may be due to an inherent weakness in that particular sample. All curves have a strain hardening period with the ‘roll-over’ to the peak stresses before strain softening and dynamic failure which normally occurred around 1.1 – 1.3% strain. After failure frictional recovery takes place with stable sliding at 3 of the temperatures at stresses of around 60 MPa and of 75°C of 95 MPa and 100°C of 39 MPa. Taking an average of these, the frictional strength is 65 MPa.

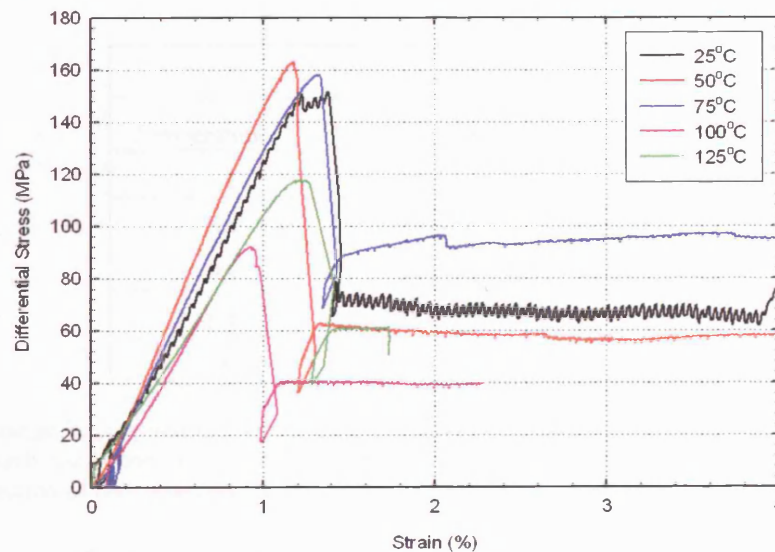


Figure 8.11: Plot of stress-strain curves during the triaxial deformation of Clashach sandstone up to temperatures of 125°C. All experiments had $P_c = 40 \text{ MPa}$, $P_p = 20 \text{ MPa}$ and strain rate of $1.5 \times 10^{-5} \text{ s}^{-1}$. [Experiment No.: 33, 35, 37, 38, 40]

The change in pore volume during these drained experiments is shown in Figure 8.12 with the absolute changes during compaction and dilatancy tabulated in Table 8.4.

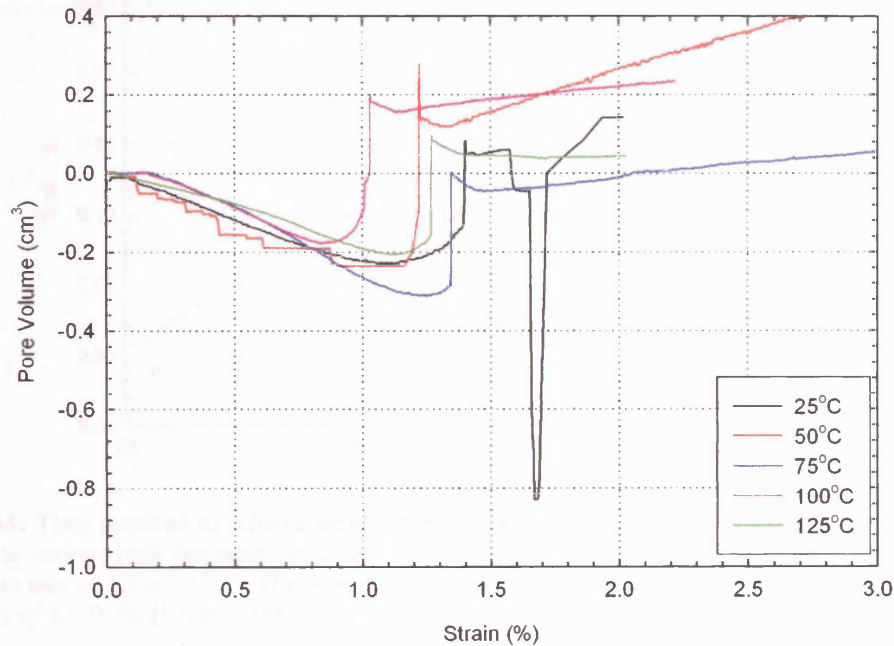


Figure 8.12: Plot of change in pore volume during the triaxial deformation of Clashach sandstone up to temperatures of 125°C. All experiments had $P_c = 40$ MPa, $P_p = 20$ MPa and strain rate of $1.5 \times 10^{-5} \text{ s}^{-1}$. [Experiment No.: 33, 35, 37, 38, 40]

All the temperatures investigated show a similar rate of change in pore volume during compaction decreasing on average by 0.23 cm^3 at 1.1% strain. With dilatant microcracking occurring, the pore volume after compaction increases by 0.12 cm^3 up to failure when 0.2 cm^3 goes into the macroscopic fault region. These results imply that the mechanism for the closure and opening of cracks and pores is the same up to 125°C.

Temperature (°C)	Change in Pore Volume (cm ³)	
	Compaction	Dilatancy
25	0.22	0.11
50	0.24	0.12
75	0.31	0.10
100	0.18	0.18
125	0.21	0.07

Table 8.4: Change in pore volume during the compaction and dilatancy stage of triaxial deformation of drained Clashach sandstone at temperatures up to 125°C. (Values given are absolute, so they do not reflect the direction of fluid loss and are given to an accuracy of $\pm 0.01 \text{ cm}^3$).

With the only variable being temperature, the time to reach stable frictional sliding was investigated and the results plotted in Figure 8.13. This shows that the higher the temperature the longer it takes to reach this state suggesting that the temperature is affecting the state of the fault surface.

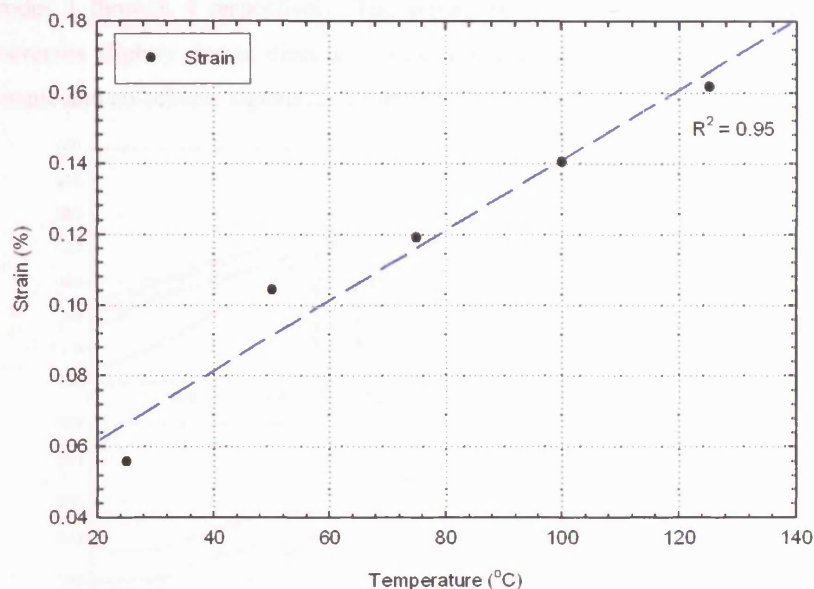


Figure 8.13: Time required to achieve steady stress frictional sliding after dynamic failure of Clashach sandstone at various rock temperatures using the triaxial deformation cell. $P_c = 40$ MPa, $P_p = 20$ MPa with a strain rate of $1.5 \times 10^{-5} \text{ s}^{-1}$. The broken line represents the least squared fit. Each point is given to an accuracy of $\pm 0.01\%$. [Experiment No.: 33, 35, 37, 38, 40]

8.6 EFFECT OF ELEVATED TEMPERATURES ON ELECTRICAL PROPERTIES

The effect of triaxial deformation on the electrical signals of drained Clashach sandstone at temperatures up to 125°C is shown in Figure 8.14. As the temperature increases, the electrical potential signal before deformation, increases from approximately 60 mV at 25°C up to 210 mV at 125°C. This is shown graphically in Figure 8.15 where a linear fit has been applied to the data. With an r^2 value of 0.96, it suggests the electrical potential signal is directly related to temperature.

When deformation starts the potentials increase steadily until the elastic limit is reached and then the rate of change of the electrical signal rate increases up to failure. The change in potential up to failure, including compaction and dilatancy for the different temperatures remains constant at around 75 mV. At failure pre-seismic and co-seismic signals are observed (see Figure 8.16) with the co-seismic signal decaying after failure when the potentials generally level off until the experiment is stopped. In Figure 8.14a the stress increases causing the potentials to follow suit with the cracks and the fault forming close to electrode 2 causing drops in potential at various times. In Figure 8.14c, electrode 4 has a bad contact causing electrical noise, but the same trend seen in the other electrodes remains present. For Figure 8.14d the edges of the fault occur close to electrodes 3 and 4 which may cause the potential changes observed. These results suggest that the temperature increases the potential gradient at the rock surface thereby increasing the electrical signal before deformation.

Pre-seismic and Co-seismic signals

Figure 8.16 shows the electrical potential signals produced around dynamic failure of drained Clashach sandstone at 75°C, 100°C and 125°C. In Figure 8.16a, a pre-seismic signal is observed on electrodes 2 and 3 two seconds before brittle failure. At failure a co-seismic signal of -32 mV, 40 mV, 33 mV and 9 mV is

seen at electrodes 1 through 4 respectively. The signals on electrodes 1, 2 and 3 decay away while electrode 4 increases slightly due to electrical noise. For the other temperatures of 100°C and 125°C similar pre-seismic and co-seismic signals are observed a summary of which are shown in Figure 8.17.

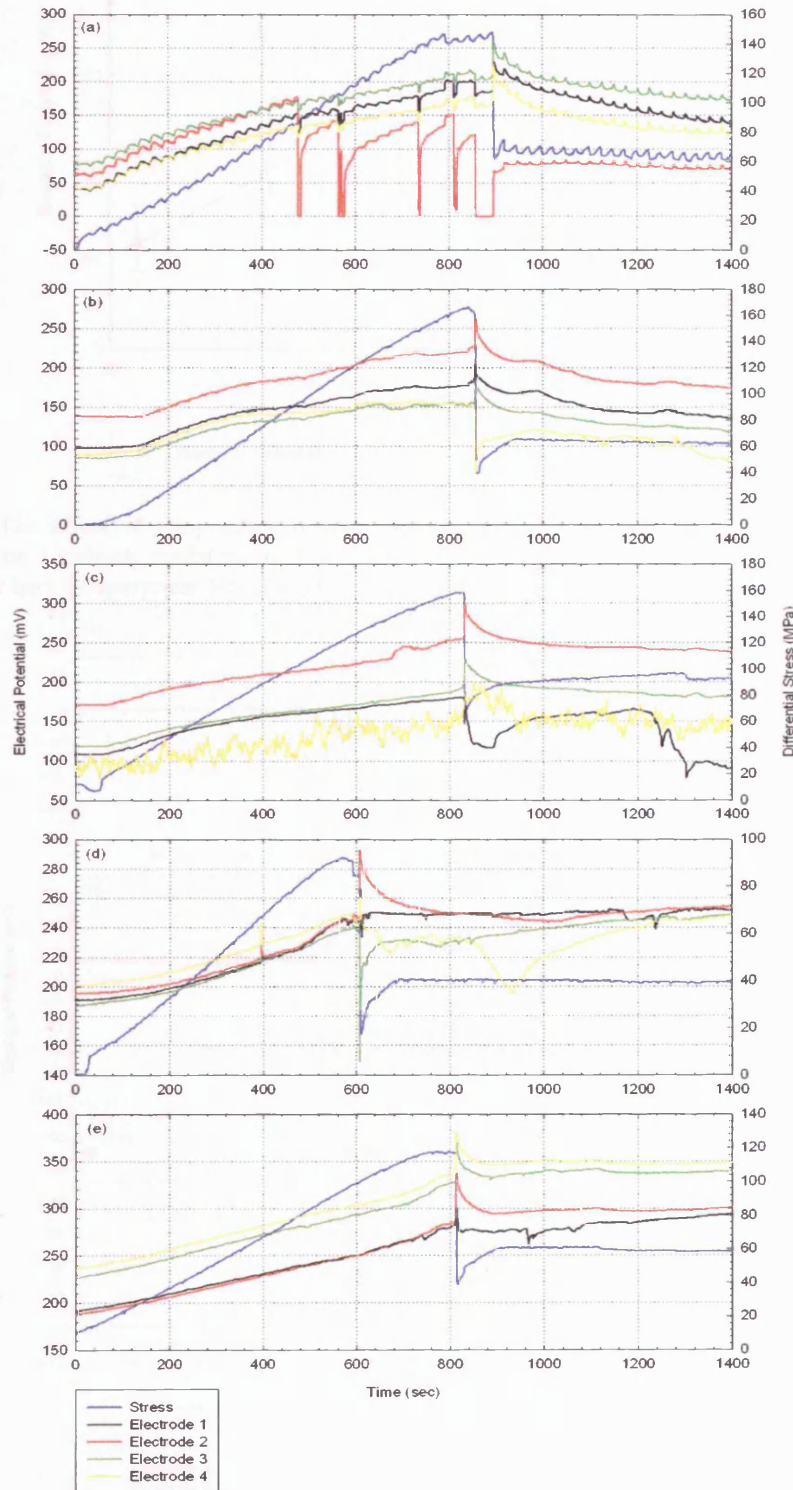


Figure 8.14: The electrical potential signal produced during the deformation of drained Clashach sandstone at temperatures of (a) 25°C, (b) 50°C, (c) 75°C, (d) 100°C, (e) 125°C; $P_c = 40$ MPa, $P_p = 20$ MPa with deionised water as the pore fluid and a strain rate of $1.5 \times 10^{-3} \text{ s}^{-1}$. [Experiment No.: (a) 33, (b) 35, (c) 37, (d) 38, (e) 40]

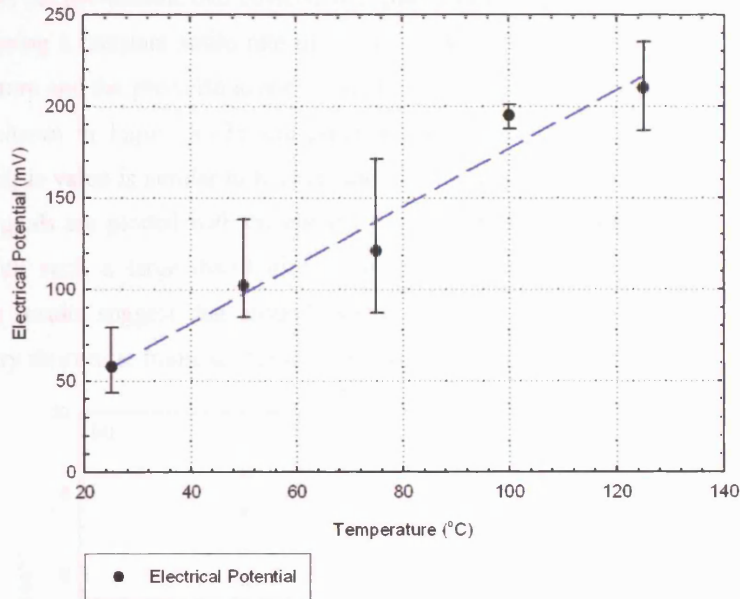


Figure 8.15: The effect of temperature on the average electrical potential signal before deformation begins occurs on Clashach sandstone with a linear coefficient of 0.96. The accuracy of each point is shown by error bars. [Experiment No.: 33, 35, 37, 38, 40]

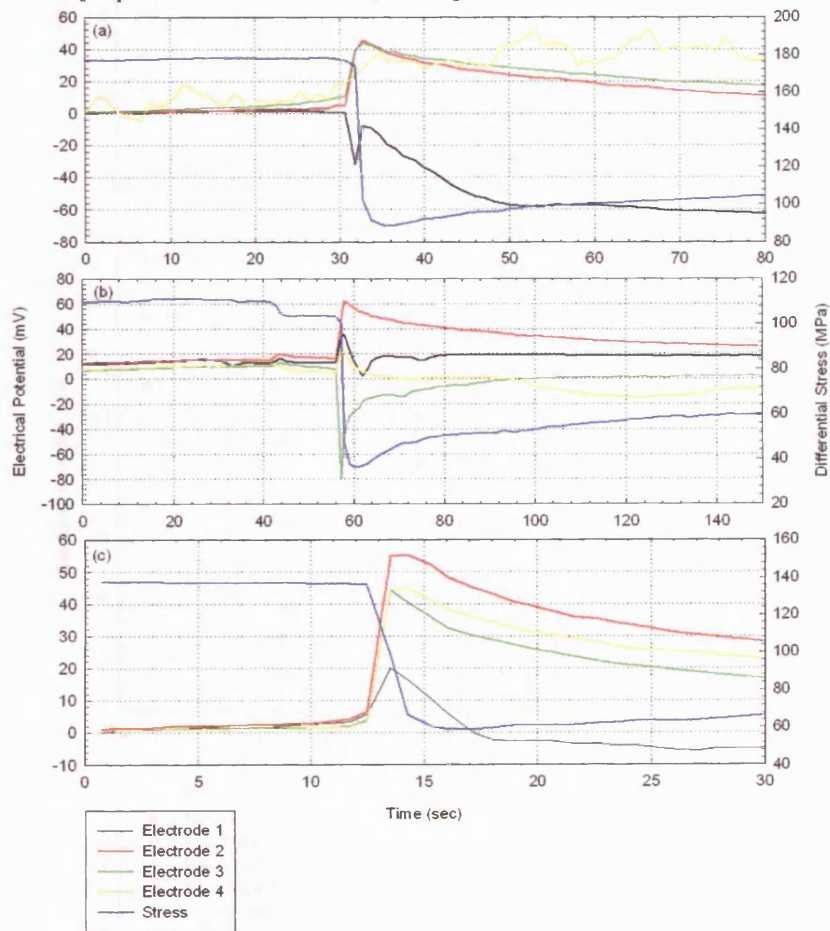


Figure 8.16: The electrical potential signal produced during strain softening and shear failure of Clashach sandstone at temperatures of (a) 75°C, (b) 100°C and (c) 125°C; $P_c = 40$ MPa, $P_p = 20$ MPa with a strain rate of $1.5 \times 10^{-5} \text{ s}^{-1}$. [Experiment No.: (a) 27, (b) 28, (c) 40]

Figure 8.17 shows the pre-seismic and co-seismic signals of drained Clashach sandstone at temperatures of up to 125°C using a constant strain rate of $1.5 \times 10^{-5} \text{ s}^{-1}$. Over this range 25°C to 125°C, no trends between temperature and the pre-seismic and co-seismic electrical signals could be observed. For the pre-seismic signals shown in Figure 8.17a, the potentials vary by approximately 4 mV on an individual experiment; which is value is similar to background electrical noise noted in Chapter 6. In Figure 8.17b the co-seismic signals are plotted with the electrical potentials at any particular temperature varying by over 30 mV. With such a large distribution of potentials, no relationship with temperature can be identified. These results suggest that around failure, changes in mechanical and electrical properties happen over a very short time frame so that temperature effects cannot be identified.

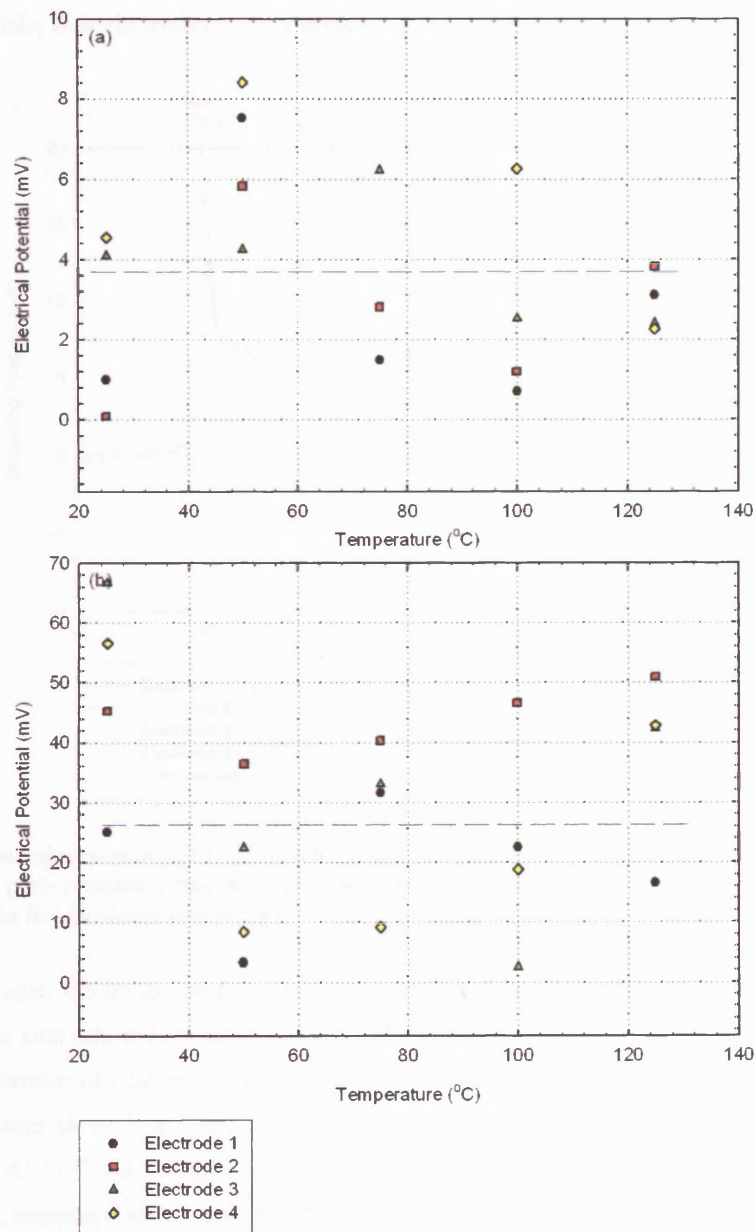


Figure 8.17: Variation of electrical potential (a) prior to failure and (b) during dynamic failure as a function of temperature of Clashach sandstone. $P_c = 40 \text{ MPa}$, $P_p = 20 \text{ MPa}$ with a strain rate of $1.5 \times 10^{-5} \text{ s}^{-1}$. The broken lines show there is no clear relationship between electrical potential and temperature with each point given to an accuracy of $\pm 0.1 \text{ mV}$. [Experiment No.: 33, 35, 37, 38, 40]

Microstructural analysis of the rock after deformation at all the different temperatures showed no significant difference from the room temperature experiments.

8.6.1 Streaming Potential Measurements at High Pore Pressure Gradients

The typical streaming potential signal recorded on Clashach sandstone at an elevated temperature prior to deformation is shown in Figure 8.18 with all potentials normalised to a base value. A similar pattern is observed in the room temperature experiments with the opening of the valve causing an initial potential spike which decays away during steady-state flow where the currents reach equilibrium resulting in a constant streaming potential of around 6 mV. When the valve is shut the currents dissipate reducing the streaming potentials, with electrodes 3 and 4 decreasing by 10 mV and electrodes 1 and 2 by 6 mV.

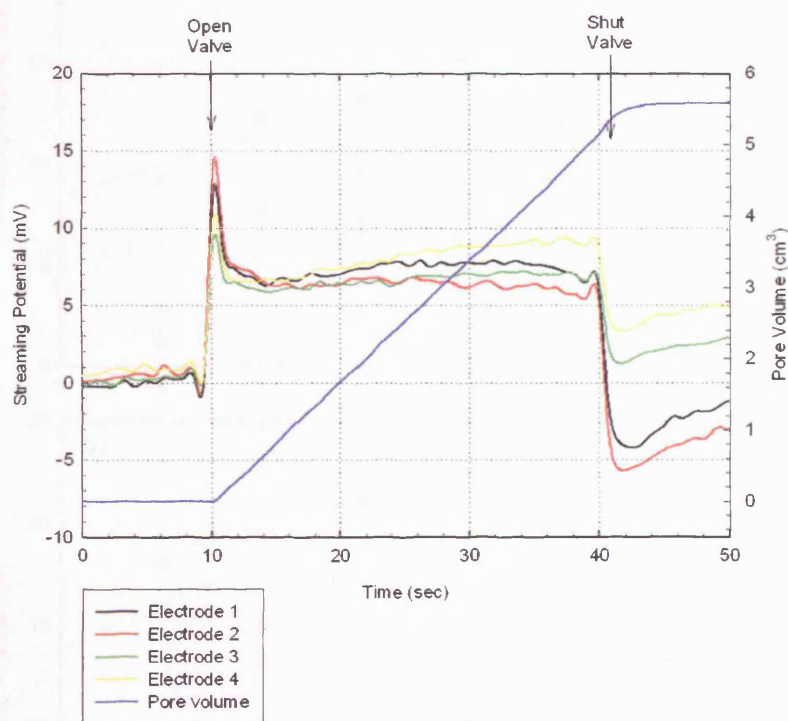


Figure 8.18: Streaming potential for Clashach sandstone at 125°C before fracture. $P_c = 40$ MPa with a 20 MPa applied pore pressure gradient across the sample on top of a background 5 MPa pore pressure with the change in fluid volume indicating a constant flow rate. [Experiment No.: 40]

Using this technique, the streaming potential was investigated up to applied pore pressure gradients of 30 MPa at 5 MPa intervals and the results before and after failure plotted in Figure 8.19. In Figure 8.19a the streaming potential of Clashach sandstone is shown for temperatures of 25, 50, 75, 100 and 125°C. For all temperatures there is a linear relationship between pore pressure gradient and the streaming potential signal. At 25°C the potential changes from 9 mV with a 5 MPa gradient up to 14 mV with a 20 MPa gradient, compared with 3 mV at 15 MPa and 12 mV at 30 MPa for the rock at 125°C. The rocks at 20, 100 and 125°C have similar linear relationships, with the high temperatures having lower values. For 50 and 75°C the streaming potential slopes are steeper. The fluid flow rate for this series of experiments is shown in Figure 8.20, showing that the maximum fluid flow at any pressure gradient occurs in the rock at 25°C, then 50, 125, 75 and the lowest flow rate for the rock at 100°C. After

deformation the streaming potentials are shown in Figure 8.19b. On average the potentials for 25°C have increased by 5 mV, those for 100 and 125°C have decreased by 2 mV with the potential slope at 75°C decreasing to match the other 4 temperatures. The fluid flow rates for these series of experiments are shown in Figure 8.20b. They follow the same order as the streaming potentials, highest values for any particular pressure gradient occurs in the rock at 25°C, followed by 50, 125, 75 and finally 100°C. These results suggest that increasing the temperature reduces the fluid flow which in turn reduces the streaming potential signals.

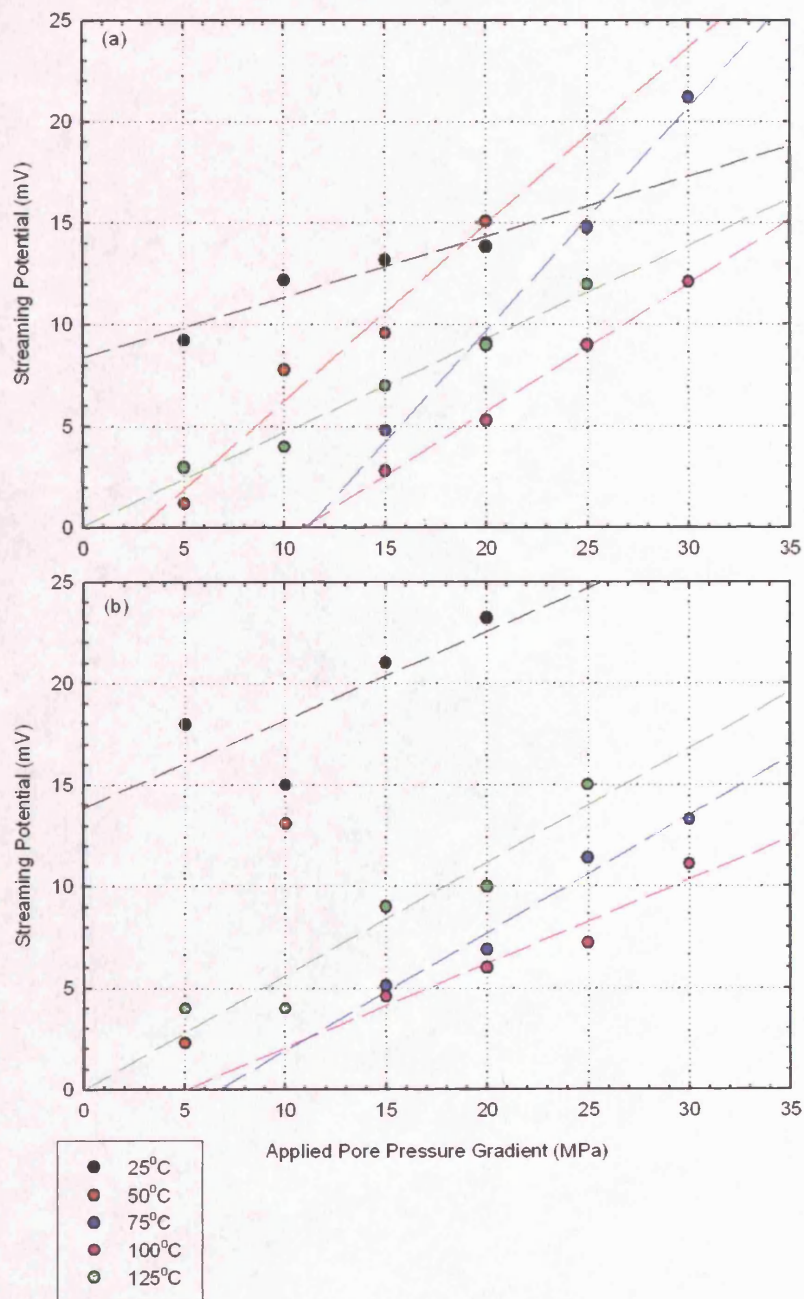


Figure 8.19: Plot of the average streaming potential generated by an applied pore fluid pressure gradient through Clashach sandstone up to 125°C (a) prior and (b) after brittle deformation failure; $P_c = 40$ MPa with the streaming potentials being the average of all four electrodes. The broken lines represent the least squared fit. Each point is given to an accuracy of ± 3 mV. [Experiment No.: 33, 35, 37, 38, 40]

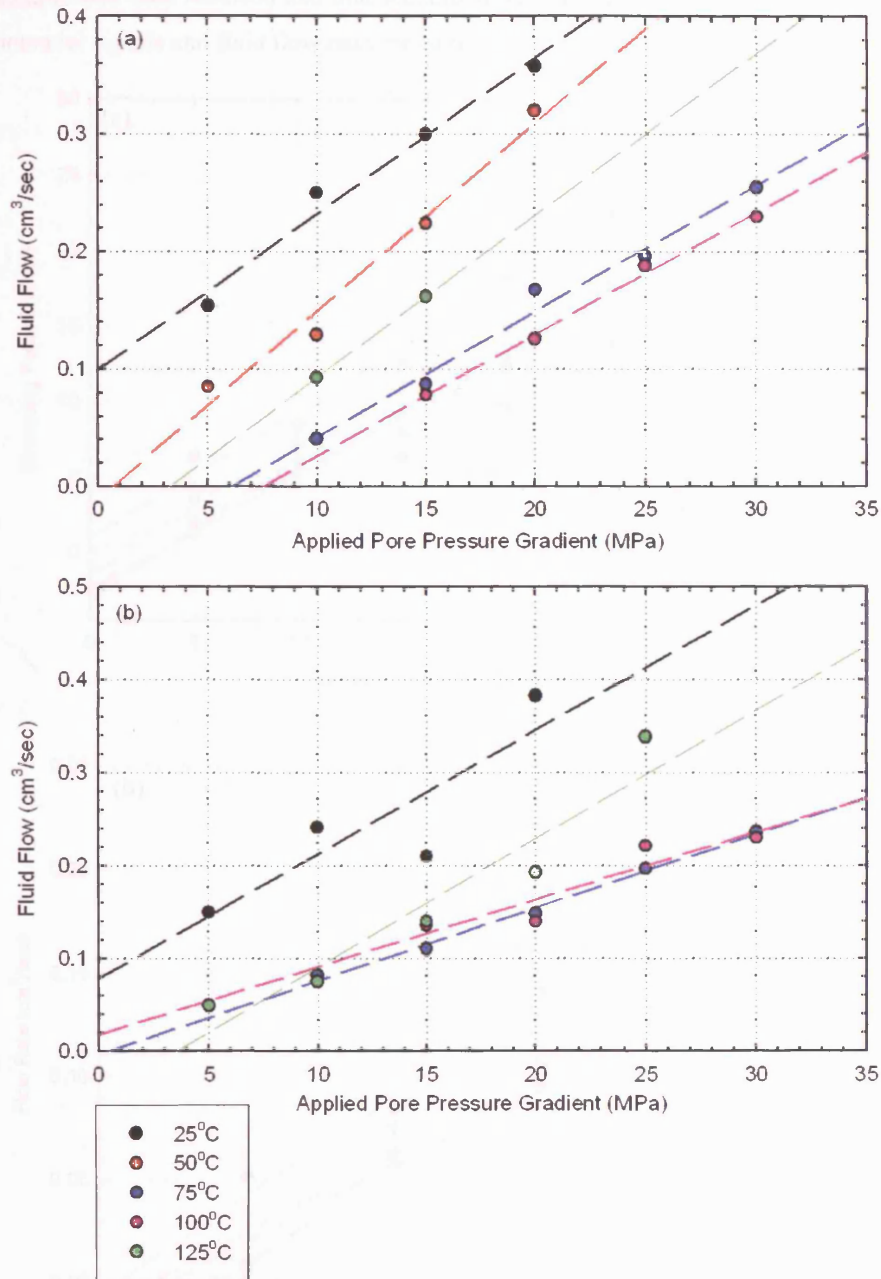


Figure 8.20: Plot of fluid flow generated through applied pore pressure gradient through Clashach sandstone up to 125°C (a) prior and (b) after brittle deformation failure; $P_c = 40$ MPa with the streaming potentials being the average of all four electrodes. The broken lines represent the least squared fit. Each point is given to an accuracy of ± 0.01 cm³/sec. [Experiment No.: 33, 35, 37, 38, 40]

8.6.2 Cycling Heating Effect

As rocks are heated for prolonged periods of time in the Earth's crust, the effect of this heating was investigated by applying heating cycles to Clashach sandstone. This can then be applied to molecular dynamical modelling as a base value in order to further investigate the EDL. These cycles consisted of heating the rock up to 125°C where the streaming potential was measured at 5 MPa intervals up to 30 MPa. Afterwards the rock was left at an effective pressure of 20 MPa with no load for 8-10 hours. Then the furnace was turned off and the rock allowed to cool overnight. This was repeated a further four

times, the sample was then removed and thin sections were made across the fault. The summary of the streaming potential signals and fluid flow rates measured are given in Figure 8.21.

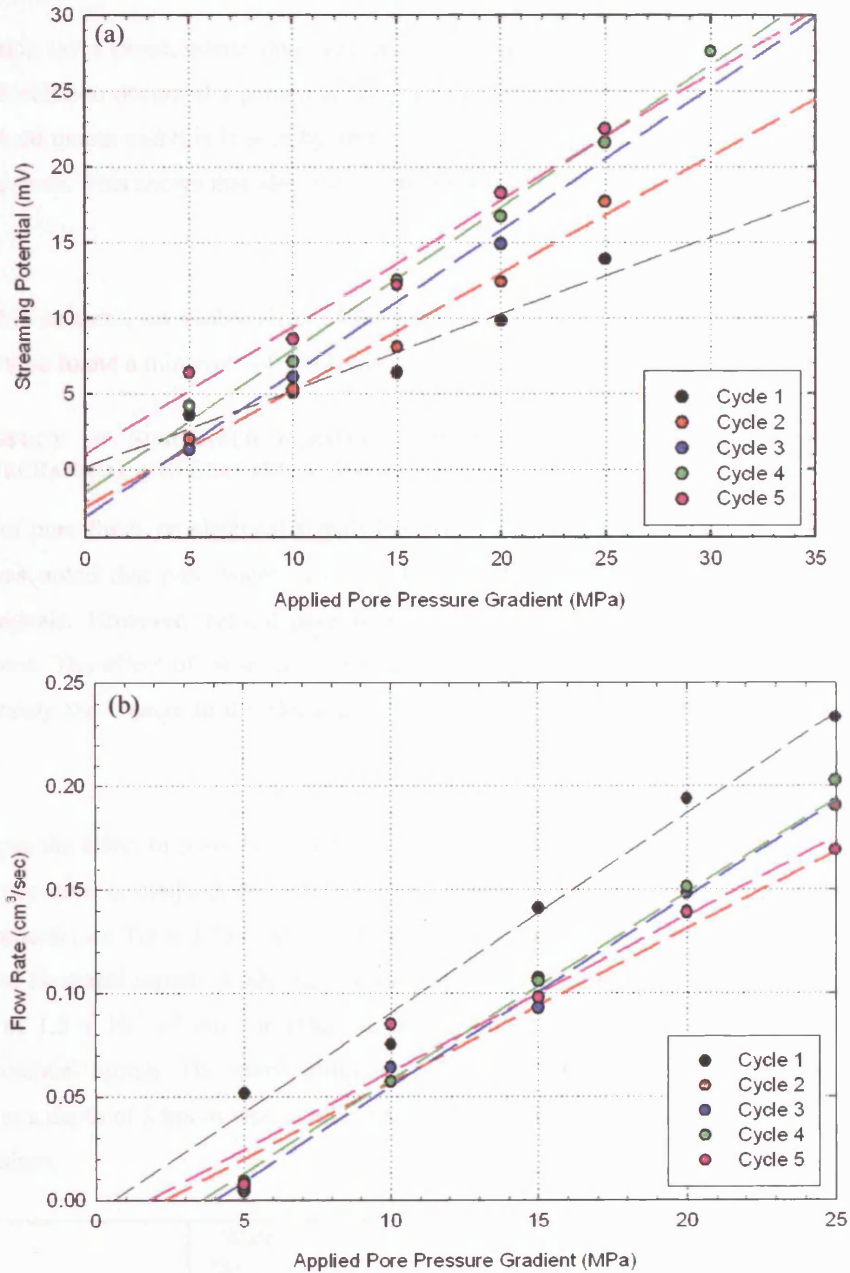


Figure 8.21: Plots of (a) streaming potential and (b) fluid flow rates and how they change through successive heating and cooling cycles of pre-fractured Clashach sandstone up to a temperature of 125°C; $P_c = 40$ MPa, $P_p = 20$ MPa. The broken lines represent the least squared fit. Each point is given to an accuracy of (a) ± 0.1 mV and (b) ± 0.01 cm³/sec [Experiment No.: 40]

In Figure 8.21a the change in streaming potential is shown. For the first cycle the streaming potential starts at 4 mV at 5 MPa and linearly increases up to 14 mV at 25 MPa, a linear regression was fitted giving a value of 0.94. The fluid flow rate for cycle 1 is shown in Figure 8.21b and shows that the fluid flow increases linearly with pore pressure gradients from 0.05 cm³/s to 0.23 cm³/s over a 20 MPa range. During the next cycle, the streaming potential increases on average by 1 mV over the pressure range

while the flow rate decreases by about 0.03 cm³/s. The following cycles show a steady increase in streaming potential of, on average, 1 mV per cycle while the flow rate remains approximately constant.

As the heating takes place, quartz dissolves into the water in small quantities. The purer the water the faster the dissolution occurs at a particular temperature. With successive heating, the water will contain more dissolved quartz and this is seen by an increase in streaming potential signals while the fluid flow remains the same. This shows that after the second cycle the purity of the water does affect the potential signals.

From the thin sections, no visible signs of healing can be observed which agrees with Meredith (pers. corr. 2004) who found a minimum of 100 hours were required before healing could be observed.

8.7 EFFECT OF SIMULATED FORMATION WATER AND RAISED TEMPERATURES ON BOTH MECHANICAL AND ELECTRICAL PROPERTIES

The effect of pure fluids on electrical signals has been investigated thoroughly by Yoshida et al. (1994) where it was noted that pure water gives the highest electrical potential gradient and hence highest electrical signals. However, natural pore fluids in the crust contain a variety of salts of differing concentrations. The effect of these salts with varying conductivities must be investigated to understand more accurately the change to the electrokinetic mechanisms where fluid conductivity is an important parameter.

To investigate the effect of pore fluid conductivity, two simulated formation waters were purchased from Corelabs to be used in conjunction with Clashach sandstone during deformation. These fluids contain a variety of anions (see Table 8.5) instead of a single type to more accurately investigate the link between the fluid and electrical signals produced. The drained samples were deformed at 25, 50 and 75°C, at a strain rate of 1.5 x 10⁻⁵ s⁻¹ with an effective pressure of 20 MPa and simultaneous measurements of electrical potential signals. The temperatures and pressures used were chosen to simulate shallow crustal conditions to a depth of 2 km as well as allowing for the possibility of extending the effect of temperature to higher values.

Anions (ppm)	Water Samples		Cations (ppm)	Water Samples	
	SFW#1	SFW#2		SFW#1	SFW#2
F ⁻	-	999	Na ⁺	76962	15348
Cl ⁻	95095	37800	K ⁺	15397	20462
NO ³⁻	187	3026	Mg ²⁺	-	135
SO ⁴⁻	-	2132	Ca ²⁺	546	-

Table 8.5: Composition of simulated formation waters SFW #1 and SFW #2 in the form of anions and cations present. (Values are given in ppm)

Mechanical properties

The stress-strain curves using the two formation waters in drained Clashach sandstone at temperatures of 25, 50 and 75°C are shown in Figure 8.22. A similar quasi-elastic behaviour is observed for all temperatures and fluids with an elastic limit of 0.9%. This is followed by a period of strain hardening lasting over 0.3% which leads to the peak stress and a small amount of strain softening before failure. The strength of samples using SFW#1 appear to show an increase in peak stress, while SFW#2 samples have similar values. At failure a stress drop of 60 MPa occurs for both fluids with the steady frictional sliding stress ranging between 52 MPa to 104 MPa with three samples having the same stress of 64 MPa, which is virtually the same as that of deionised water. The effect of pH is ignored due to it being a narrow range 6.3 and 7.0, but it has been reported elsewhere to have a less important effect on mechanical properties (Revil 1999b).

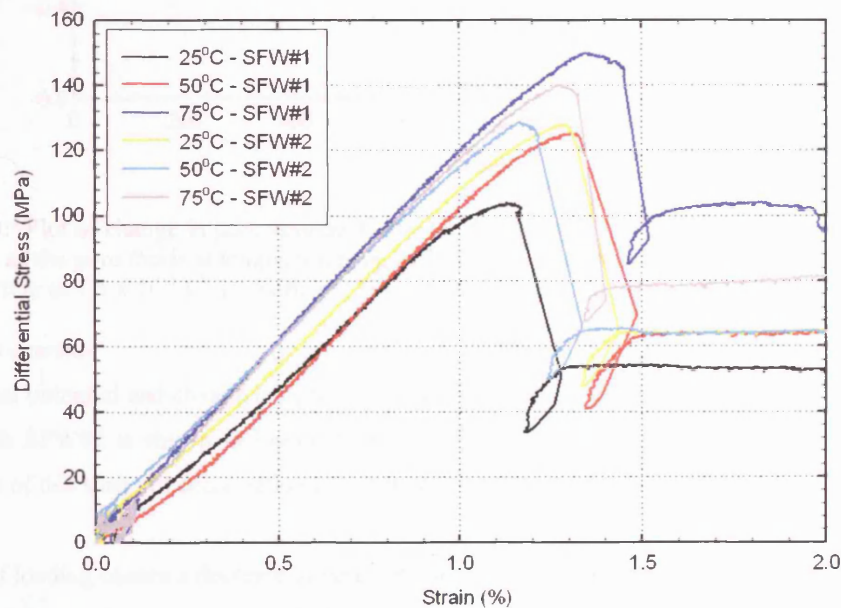


Figure 8.22: Plot of a stress-strain diagram during the deformation of Clashach sandstone using SFW#1 and SFW#2 as the pore fluids at temperatures up to 75°C. All experiments had $P_c = 40$ MPa, $P_p = 20$ MPa and a strain rate of $1.5 \times 10^{-5} \text{ s}^{-1}$. [Experiment No.: 45, 46, 47, 49, 50, 51]

Looking at the normalised (zeroed) change in pore volume shown in Figure 8.23, all the experiments show the same general trend. During compaction, the pore fluid is forced out of the rock giving a volume change of -0.28 cm^3 for four of the six experiments with the remaining two having a change of -0.4 cm^3 . When dilatant microcracking becomes dominant the water is forced back into the rock to maintain the desired pressure resulting in a volume change of $+0.12 \text{ cm}^3$ for all experiments. At failure, the volume of the rock increases by 0.4 cm^3 and when steady frictional sliding occurs the pore volume increases linearly with time due to the generation of fault gouge.

These results suggest that the same physical mechanism takes place with both fluids and for elevated temperatures up to 75°C and that the amount of compaction may be aided by the presence of the saline fluid.

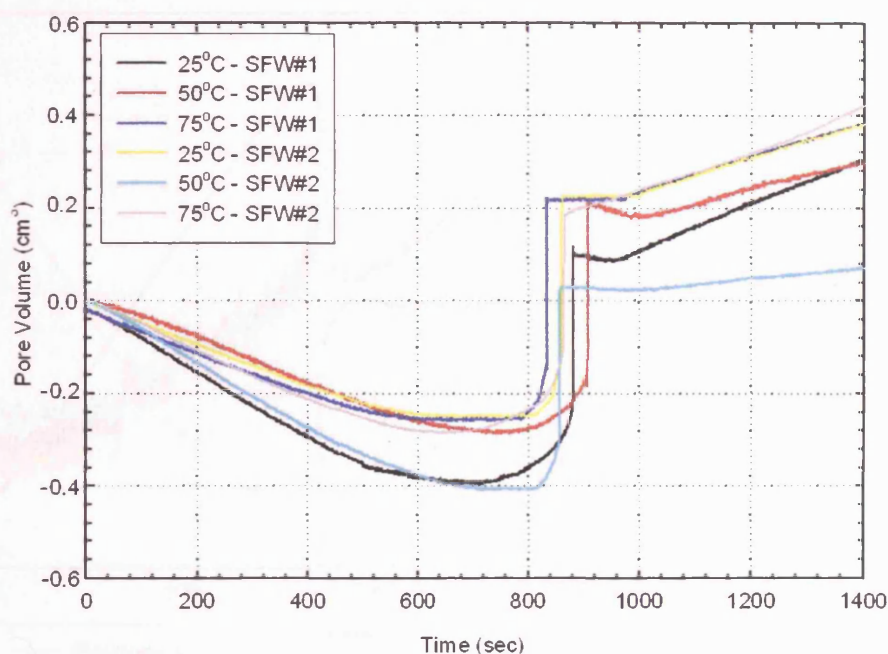


Figure 8.23: Plot of change in pore volume during the deformation of Clashach sandstone using SFW#1 and SFW#2 as the pore fluids at temperatures up to 75°C. All experiments had $P_c = 40$ MPa, $P_p = 20$ MPa and a strain rate of $1.5 \times 10^{-5} \text{ s}^{-1}$. [Experiment No.: 45, 46, 47, 49, 50, 51]

Electrical properties

The electrical potential and change in pore volume during the triaxial deformation of Clashach sandstone at 50°C with SFW#2 is shown in Figure 8.24. This figure is typical of the changes seen in the other experiments of this series of deformation experiments.

The onset of loading causes a decrease in pore volume as the water is force out of the rock matrix. This is accompanied by an increase in electrical potential for all four electrodes, fluctuating by 2 mV. At 700 seconds the number of cracks and pores closed by compaction is balanced by the number of cracks and pores opened by dilatant microcracking, which can be seen at the electrodes by an increase in potential. Up to failure the potential changes by less than 15 mV. After the peak stress strain softening takes place and the pore volume increasing together with the electrical signals as fluid flows into the newly formed cracks to maintain a constant pore pressure. At 850 seconds brittle failure takes place with electrodes 2, 3 and 4 showing a co-seismic signal of the order of 10 mV while electrode 1 has a co-seismic signal drop of 1000 mV due to the fault passing near to the electrode. After failure the co-seismic signals dissipate over a time scale of 50 seconds and once steady frictional sliding occurs at 1000 seconds the pore volume increases linearly with time, and there is a steady increase in potential for electrodes 2, 3 and 4.

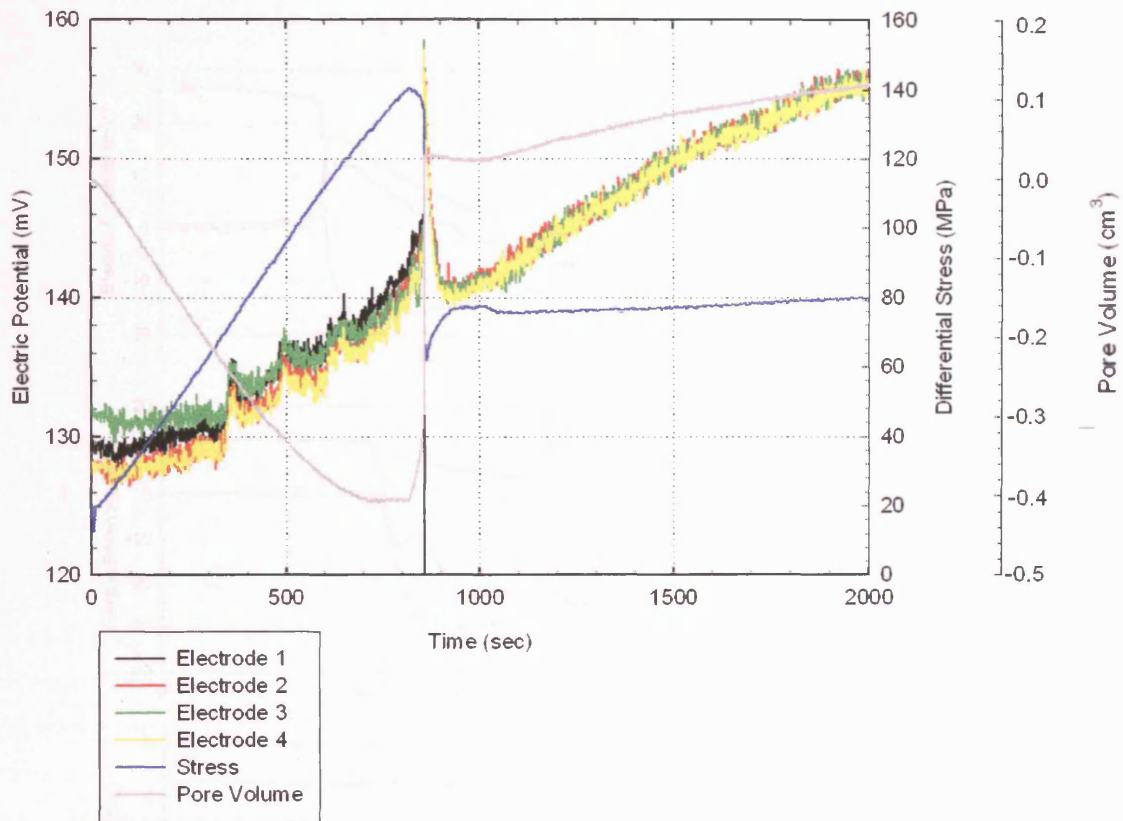


Figure 8.24: Typical electrical potential difference recorded during the brittle deformation of Clashach sandstone at 50°C using SFW#2 as the pore fluid; $P_c = 40$ MPa, $P_p = 20$ MPa with a strain rate of $1.5 \times 10^{-5} \text{ s}^{-1}$. [Experiment No: 50]

Pre-seismic and Co-seismic signals

The pre-seismic and co-seismic signals for SFW#1 at 25, 50 and 75°C showing strain softening and brittle failure are displayed in Figure 8.25 for Clashach sandstone under drained conditions. In Figure 8.25a strain softening occurs with the potentials at all four electrodes increasing slightly until 2 seconds before failure, at which time a 4 mV signal is displayed with a positive polarity. At failure, with a stress drop of 60 MPa, a 14 mV co-seismic signal is observed for all four electrodes. These signals then dissipate over the next 45 seconds as steady frictional sliding is reached.

For the rock at 50°C shown in Figure 8.25b, the co-seismic signal occurs with dynamic failure at 11 seconds, having a value of 6 mV, being half the value for the rock at 25°C. Continuing this to 75°C shown in Figure 8.25c the co-seismic signal is reduced still further, on average, to 3 mV which is only 1 mV above the electrical noise. Comparing this with the deionised water experiments over the same temperature range (see Figure 8.16), the saline fluid has reduced the potentials by over 1 order of magnitude. The additional heating of the samples to 75°C reduces the potentials so much that pre-seismic signals cannot be seen and the co-seismic signal is only just visible above the background noise at this temperature. This suggests that a combination of a conductive fluid and temperatures in excess of 100°C would make the pre-seismic and co-seismic signals so small that they could not be seen above the background noise of around 2mV.

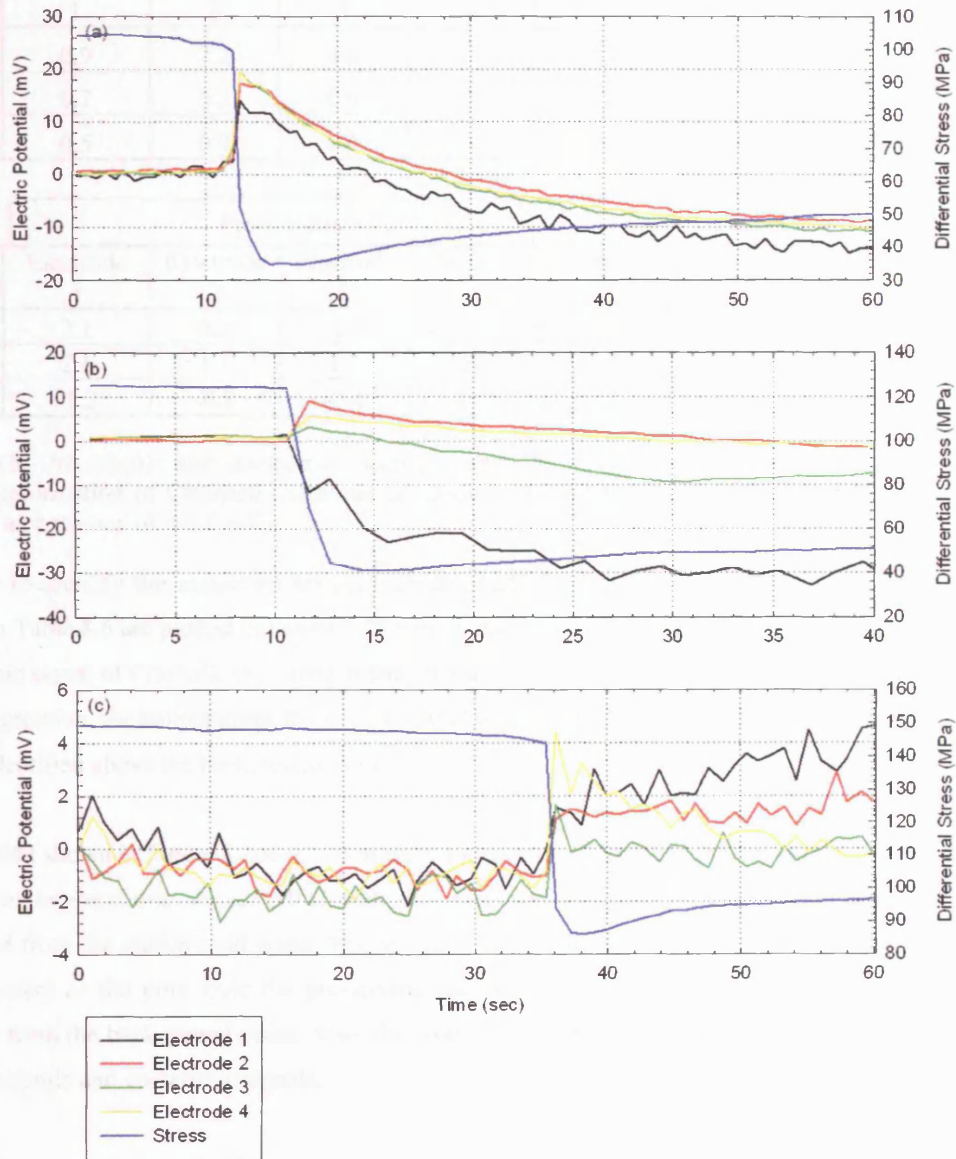


Figure 8.25: The electrical potential signals produced during strain softening and shear failure of Clashach sandstone at temperatures of (a) 25°C, (b) 75°C and (c) 100°C with SFW#1 as the pore fluid. $P_c = 40$ MPa, $P_p = 20$ MPa with a strain rate of $1.5 \times 10^{-5} \text{ s}^{-1}$. [Experiment No.: (a) 47, (b) 45, (c) 46]

The pre-seismic and co-seismic signals for SFW#1 and SFW#2 at the temperatures investigated are shown in Table 8.6. For both fluids a decrease in pre-seismic signals is observed with SFW#1 having values equal to or below the background noise and SFW#2 having minus readings at 75°C. For the co-seismic signals SFW#1 decreases from 14 mV to 3 mV with SFW#2 changing from 16 mV to 10 mV over a 50°C temperature increase. This suggests that at temperatures in excess of 75°C, with formation waters, which are highly conductive, the pre-seismic signals cannot be distinguished from background electrical noise.

Chapter 8: Temperature Effect up to 125°C on the Mechanical and Electrical Properties of Clashach sandstone and Portland limestone

SFW#1	Pre-seismic				Co-seismic			
Temperature (°C)	Electrode 1	Electrode 2	Electrode 3	Electrode 4	Electrode 1	Electrode 2	Electrode 3	Electrode 4
25	0.9	2.2	4.5	5.3	11.6	14.1	14.5	13.7
50	0.7	0.2	0.0	-0.2		9.1	3.2	5.7
75	0.5	0.0	0.6	-0.2	1.6	2.1	3.7	4.4

SFW#2	Pre-seismic				Co-seismic			
Temperature (°C)	Electrode 1	Electrode 2	Electrode 3	Electrode 4	Electrode 1	Electrode 2	Electrode 3	Electrode 4
25	2.1	0.3	-1.5	-1.1	14.6	18.7	-1.9	-
50	2.1	1.1	1.3	2.0	11.6	10.4	12.4	13.3
75	-1.2	-0.8	-0.4	-0.2	10.0	9.5	7.8	10.2

Table 8.6: Pre-seismic and co-seismic electrical potential signals measured at each electrode during triaxial deformation of Clashach sandstone at various temperatures using SFW#1 and SFW#2. (Values given to an accuracy of ± 0.1 mV)

In order to identify the maximum temperature at which the co-seismic signal could be identified, the values in Table 8.6 are plotted in Figure 8.26 with linear regressions fitted to the data. In Figure 8.26a the co-seismic signal of Clashach sandstone at temperature using SFW#1 as the pore fluid is shown. From the linear regression, for temperatures in excess of 80°C with this rock and fluid the co-seismic signals could not be identified above the background noise.

For SFW#2 shown in Figure 8.26b the co-seismic signals also decrease with temperature. Using the linear regression temperatures above 110°C with this rock and fluid the co-seismic signals could not be separated from the background noise. This suggests that for in-situ rocks at shallow crustal depths with saline waters as the pore fluid the pre-seismic and co-seismic electrical signals would be difficult to separate from the background noise. Also, the types of ions present in the fluid have different effects on the pre-seismic and co-seismic signals.

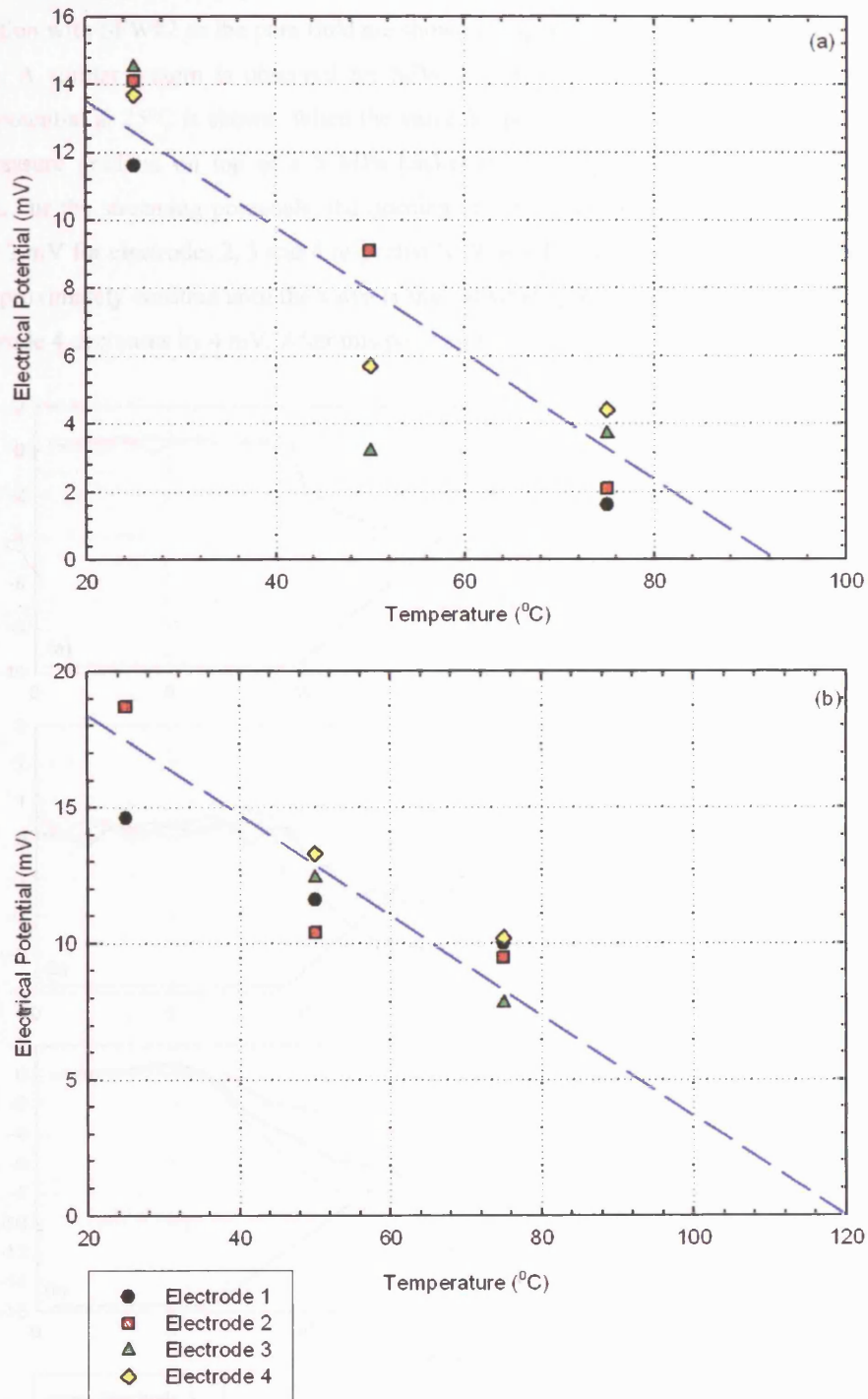


Figure 8.26: Co-seismic signal variation of Clashach sandstone as a function of temperature using (a) SFW#1 and (b) SFW#2 as the pore fluids. $P_c = 40$ MPa, $P_p = 20$ MPa with strain rate $1.5 \times 10^{-5} \text{ s}^{-1}$. The broken lines represent the least squared fit. Each point is given to an accuracy of ± 0.1 mV. [Experiment No.: 45, 46, 47, 49, 50, 51]

8.7.1 Streaming Potential Generated with Saline Fluid at high pore pressures

The typical streaming potential signals recorded on Clashach sandstone at an elevated temperature, prior to deformation with SFW#2 as the pore fluid are shown in Figure 8.27 with all potentials normalised to a base value. A similar pattern is observed for SFW#1 which is not shown here. In Figure 8.27a the streaming potential at 25°C is shown. When the valve is opened at 10 seconds the fluid flows down the 10 MPa pressure gradient on top of a 5 MPa background pore pressure until the valve is closed at 20 seconds. For the streaming potentials, the opening of the valve causes the potential to change by -2, -2.2 and -5.2 mV for electrodes 2, 3 and 4 respectively. When the currents reach equilibrium the potential remains approximately constant until the valve is shut, at which point electrodes 2 and 3 increase slightly while electrode 4 decreases by 4 mV. After this point all the potentials increase at similar rates.

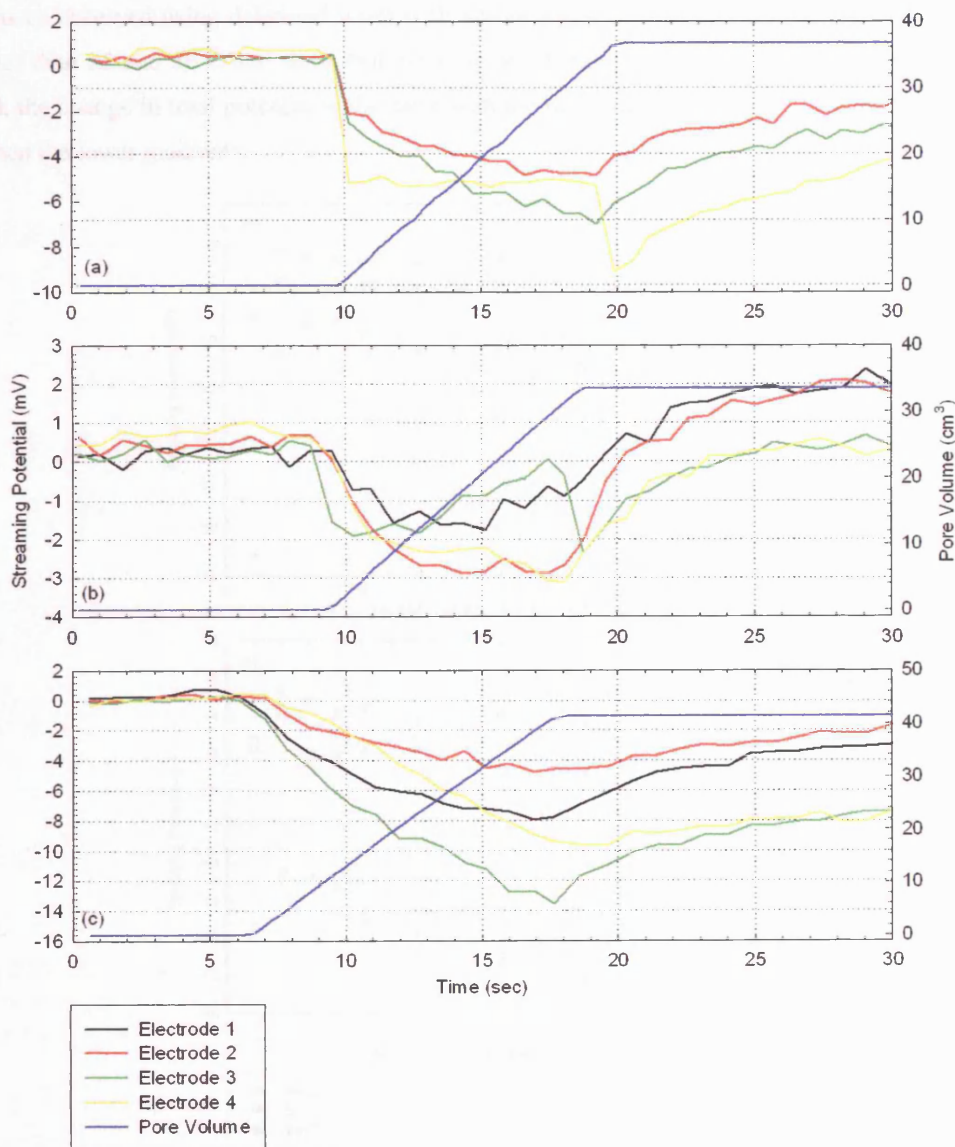


Figure 8.27: Plot of streaming potential against time at (a) 25°C, (b) 50°C and (c) 75°C using SFW#2 as pore fluid; $P_c = 40$ MPa with applied pore pressure gradient of 15 MPa. [Experiment No.: (a) 49, (b) 50, (c) 51]

For 50°C shown in Figure 8.27b a similar pattern is observed as in Figure 8.27a. Opening the valve causes the potentials to drop by around 2 mV and closing the valve causes the potentials to increase with electrodes 1 and 2 and electrodes 3 and 4 staying together. At 75°C the typical box shape is not observed as in Figure 8.27c. Opening the valve causes the potential to decrease and continue its decline at a steady rate until the fluid flow is stopped, at which point potentials 1 and 2 increase at a different rate to those of 3 and 4. As the fluid flow at 75°C is comparable to 25 and 50°C with laminar flow taking place, the currents should reach equilibrium, but this does not appear to happen.

Assuming the total change in potential at 75°C represents the streaming potential signal, the potentials for pore pressure gradients ranging from 1-20 MPa and temperatures 25-75°C are shown in Figure 8.28. This figure shows that the streaming potential does not significantly change with applied pore pressure gradients as observed using deionised water with all the potentials being negative. The values for 75°C are lower than 25 and 50°C and show that even though steady-state equilibrium does not appear to be reached, the change in total potential is the same with the higher gradients causing the potentials to drop faster than the lower gradients.

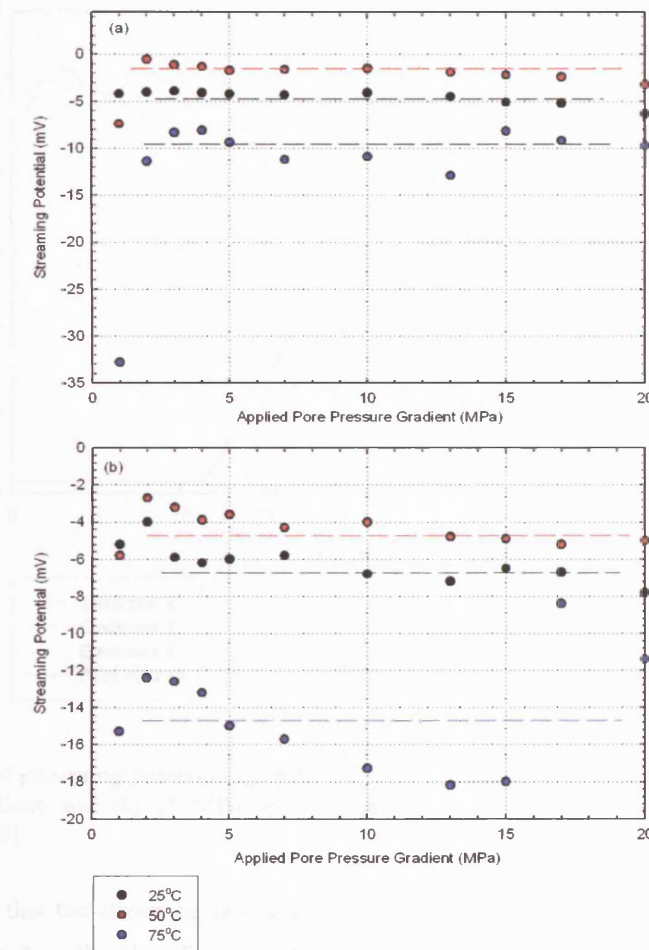


Figure 8.28: Streaming potential measurements generated under increasing pore pressure gradients across a Clashach sample (a) before fracture and (b) after fracture. SFW#2 is used as the pore fluid, $P_c = 40$ MPa, $P_p = 20$ MPa. The broken lines show no link between streaming potential and pore pressure gradients at different temperatures. Each point is given to an accuracy of ± 3 mV. [Experiment No.: 49, 50, 51]

Looking at the effect of fluid flow direction on streaming potential signal generation, Figure 8.29 shows the potentials generated during the same test with the fluid flow direction reversed.

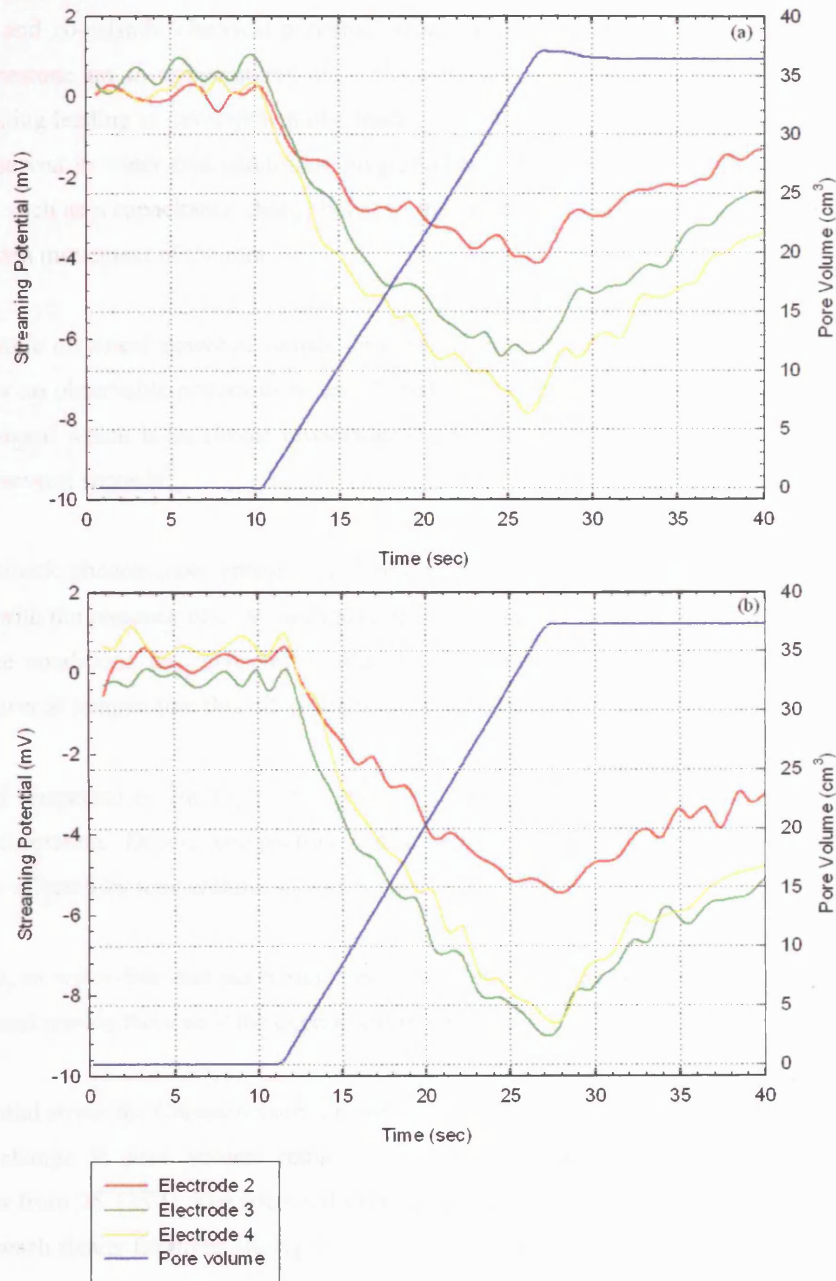


Figure 8.29: Plot of streaming potential against time using SFW#2 as pore fluid with (a) 7 MPa applied pore pressure gradient and (b) -7 MPa applied pore pressure gradient: $P_c = 40$ MPa. $T = 75^\circ\text{C}$ [Experiment No.: 49]

Figure 8.29 shows that the streaming potential is always negative when fluid flow takes place and is independent of fluid flow direction. These results on streaming potential with saline fluid suggest that the reaction between the pore fluid and the crystal surface has been affected by the ions in the fluid.

8.8 CHAPTER SUMMARY

Deionised Water

Pre-seismic and co-seismic electrical potential signals have been observed in Clashach sandstone and Portland limestone up to temperatures of 125°C with deionised water. These signals occurred with dilatant cracking leading to development of a macroscopic fault. In the quartz-free limestone a co-seismic signal is observed in water-free conditions suggesting that the presence of an alternative mechanism is taking place such as a capacitance charge between the ram and the sample or an electromagnetic change through sudden movement of the ram.

The pre-seismic electrical potential signals decrease as the temperature increases while the co-seismic signals allow no observable pattern to be established suggesting that the temperature does not affect the co-seismic signal which is an almost instantaneous potential compared to the pre-seismic signal which occurs over several seconds.

The electrokinetic phenomenon represents a plausible mechanism for generating an electrical signal in the upper crust with the presence of pore fluids at temperatures up to 125°C for both sandstone and limestone. In water-free conditions the piezoelectric effect is the dominant mechanism generating the electrical signal; however at temperature this effect seems to be reduced.

For elevated temperatures, the higher the temperature the higher the initial electrical potential signals prior to deformation. During compaction and dilatancy the electrical potential difference was not significantly affected by temperature, staying around 70 mV.

After failure, in water-free and water-saturated conditions, the electrical potential signals decrease to a lower level and remain there until the experiment was stopped.

The differential stress for Clashach sandstone up to 125°C appears to decrease slightly with temperature, whilst the change in pore volume remains constant, suggesting the same mechanism is valid for temperatures from 25-125°C. The frictional strength is independent of temperature, around 65 MPa, with the time to reach steady frictional sliding increasing linearly with temperature.

Cyclic heating of Clashach sandstone causes the streaming potential signals to increase on average 1 mV per heating-cooling cycle. Successive heating causes the water to obtain more ions and dissolved quartz with the fluid flow rate remaining approximately constant.

Microstructural analysis of Clashach sandstone and Portland limestone shows no observable effect due to temperature increase.

The streaming potential increases linearly with applied pore fluid pressure gradients for Clashach sandstone and Portland limestone up to 125°C. The linearity with pressure and potential signals is valid

Chapter 8: Temperature Effect up to 125°C on the Mechanical and Electrical Properties of Clashach sandstone and Portland limestone

up to 30 MPa with the fluid flow rate also increasing linearly with pressure gradient. For limestone the streaming potential decreases from, on average, 165 mV at 25°C to 35 mV at 125°C with a fluid flow rate decreasing from 0.011 to 0.0014 cm³/s. For sandstone, an increase in temperature generally causes a decrease in the streaming potential signal. However the streaming potential seems more linked to fluid flow than temperature.

Saline Fluid

Pre-seismic and co-seismic electrical potential signals have been observed in Clashach sandstone with SFW#1 and SFW#2 up to a temperature of 75°C. These signals occurred with dilatant cracking leading to development of a macroscopic fault.

The pre-seismic and co-seismic electrical potential signals decrease with a temperature increase. For temperatures above 75°C no observable pre-seismic signal is present above the background noise. For the co-seismic signals, there is no observable co-seismic signal for SFW#1 above 80°C and SFW#2 above 110°C.

The electrical potential signal change during deformation is reduced considerably by the saline fluids over that of deionised water showing a total electrical potential difference during deformation of 20 mV up to dynamic failure compared to 70 mV with pure water.

The electrokinetic phenomenon represents a plausible mechanism for generating an electrical signal in the upper crust with the presence of pore fluids at temperatures up to 75°C for sandstone with saline pore fluid. The presence of saline fluid reduced the potentials, due to the high conductivity of the fluid.

Streaming potential signals remain constant for applied pore fluid pressures up to 20 MPa for SFW#1 and SFW#2 up to 75°C. The potential is always negative irrespective of the direction of fluid flow and at 75°C the streaming potential does not reach equilibrium even though laminar flow is present.

9. Discussion

This section discusses the effect of thermo-chemo-mechanics of faults during the deformation cycle and the corresponding changes in electrical potential signals in relation to my experimental procedure. The deformation of various rock types including Clashach, Bentheim and Darley Dale sandstone, Seljadur basalt and Portland limestone was seen to produce observable seismo electric signals (SES) and acoustic emissions (AE) (see Chapter 7). Throughout this study the physical properties such as permeability, strain rate, pressure, pore fluid chemistry and temperature are shown to play an important role in the generation of different types of electrical signals. During triaxial rock deformation, the rock samples undergo compression loading which causes pre-existing flaws or pores to close, then open, and grow to induce new fractures which in turn can change the structure of the rock and alter the fluid flow properties. The closure of pores forces fluid out, which generates a change in electrical potential signals. Around failure, an increase in microcracking leads to changes in mechanical properties such as permeability, tortuosity and porosity with corresponding changes to electrical potential signals. At failure, a macroscopic fault is formed which alters the mechanical and electrical properties of the rock.

As the temperature of the rock increases with depth in the crust, the effect of temperature on its physical and chemical properties is important. The temperature dependence of the electrical properties has not been studied in detail prior to this work. This study shows that temperature affects the observed electrical potential signals at all stages of deformation particularly pre-failure and post-failure. In my experiments, where simulated formation fluids were studied, real in-situ conditions are more accurately represented for the first time during deformation. My results show that the combined effects of temperature and pore fluid chemistry during deformation strongly influence the electrical potential signals.

9.1 DISCUSSION OF ROOM TEMPERATURE EXPERIMENTS

9.1.1 Discussion of Electrical Potential Signals due to Shear Fracture

Sandstones which are deformed under air-dry conditions produce a measurable electrical signal during compaction and dilatancy. From my experiments it can be seen that during dilatancy, a small pre-seismic signal is followed by a larger co-seismic signal at macroscopic failure. With no fluids present, the electrokinetic effect can be ruled out as a possible cause of the signals, therefore other mechanisms such as piezoelectricity or charge separation are responsible for their existence. Moreover, because my experiment tests showed an increase in SES (seismo electric signals) with samples of increasing quartz content, this suggests the piezoelectric phenomenon is the dominant mechanism. The change in potential can be explained by a model described in chapter 3.4.1 by Yoshida et al. (1997) through the stress induced effective polarisation of quartz crystals. Where the stress at failure, causes charge separation across the crystal surface, and if it takes longer for the charge to dissipate rather than the relaxation time then the stress-induced polarization appears as an effective polarization and is recorded on the rock surface. The pre-seismic signals are related to the growth of cracks by stress changes. When the crack growth reaches a critical point, a large instantaneous stress drop occurs with the failure of many quartz crystals and cementation resulting in dynamic failure with slip along the fault plane. An earlier study by Yoshida et al. (1994) showed the change in electrical potential signal which accompanies failure is due to

the rapid change in stress and not the frictional slip along the fault plane. This result agrees with similar experiments on granite by Sasaoka et al. (1998) and basalt by Clint (1999) and with my experiments.

In the model of SES by Yoshida et al. (1997), it was deduced that the rapid stress drop is required to release the effective polarisation built up across the crystal. This does not explain the pre-seismic signals observed in experiments. However, a similar mechanism can be assumed to occur here where strain softening is treated as small decreases in stress, caused by localised microcracking. If this is considered as a series of discrete stress drops, then it can be seen that a similar mechanism is occurring but on a smaller scale and hence resulting in lower magnitude electrical signals.

In nature, crustal rocks can be both drained and/or undrained; these conditions have different effects on the pore fluid flow and the resulting change in electrical signals. With the flow of pore fluid into a rock space void, the mechanical properties of rock are affected by both instantaneous changes in effective stress and time-dependent processes such as stress corrosion. The effect on the strength is observed in this study with a decrease in strength of 25% for water-saturated samples as opposed to air-dried. Previous studies by Sammonds et al. (1992) and Read et al. (1995) show similar results. Along with the changes in mechanical properties, the electrical and hydraulic pathways within the rock are altered during deformation.

In deformation experiments performed under undrained conditions the electrical potential signal remains constant during loading because there is limited movement of fluid. This is shown in Figure 9.1

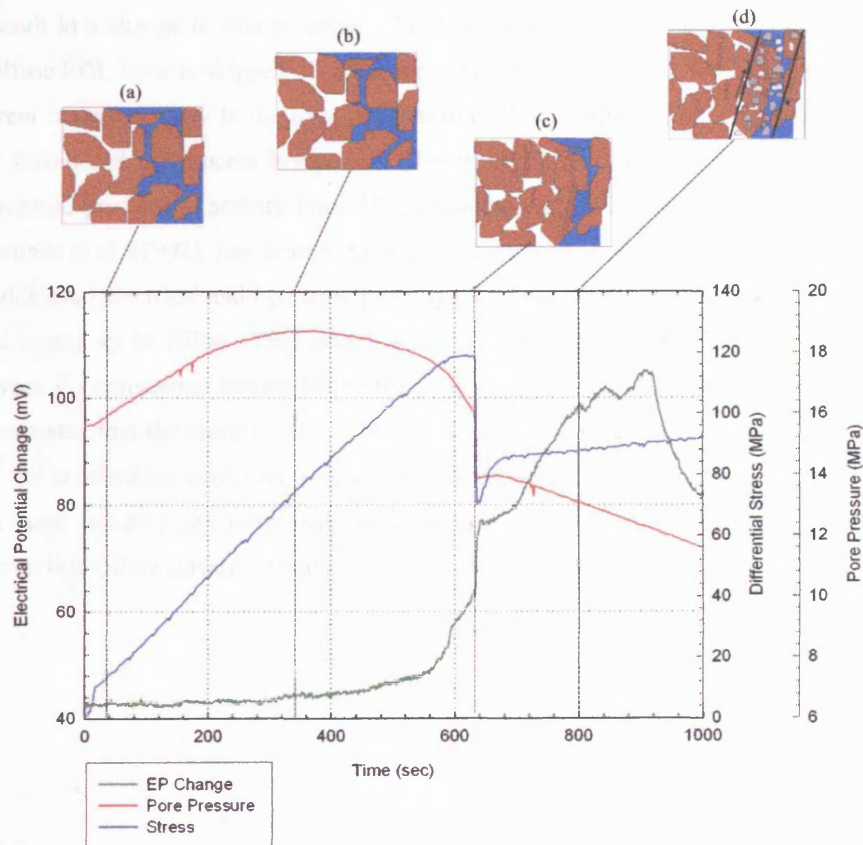


Figure 9.1: Reproduction of Figure 7.7b showing the electrical potential change, pore fluid pressure and differential stress with cartoons of micromechanics during deformation of Clashach sandstone ($P_c = 40$ MPa, initial $P_p = 15$ MPa). [Experiment No.: 43]

In Figure 9.1 with the cartoons (A) and (B) having the same grain positions, but where (B) has a higher pore fluid pressure until dilatant microcracking being at 70-80% of the peak stress. During this stage of microcracking, water contacts the newly formed crystal surfaces resulting in an increase in electrical potential up to failure. At failure, marked by cartoon (C), a fault is formed together with a corresponding dynamic stress drop and peak in electrical signal. After failure, there is sliding along the fault plane which increases the fault gouge material as shown in cartoon (D). This increase in material, increases the porosity and causes the pore fluid pressure to decrease by entering the newly formed void space.

In experiments performed under drained conditions (Figure 9.2) when the load is first applied to the rock sample, the pores in the rock close. This forces fluid out of the rock to maintain a constant pore fluid pressure and causes the electrical potential to increase. During the elastic regime, the rock continues to compact to accommodate the strain, closing pores, cracks and hydraulic pathways and forcing fluid out of the rock. The maximum compaction is shown in cartoon (B) with the grains being closely packed. The tortuosity increases while the permeability of the rock decreases. A similar effect on permeability has been observed by Keaney (1998) and Zhu and Wong (1996). However, from my experiments this could be deduced not only from the permeability measurements, but also from the electrical potential measurements. At around 70% of peak stress, the compaction-dilatancy transition takes place where acting to close surfaces, is balanced by dilatant microcracking which opens them. The type of crack varies (Lei and Kusunose 2000) and includes tensile, shear and tensile shear (wing crack) cracks. After this transition, microcracking dominates, which, under a constant pore pressure forces fluid into contact with the new surfaces. These surfaces are chemically different from the pre-existing pore surfaces (Jouniaux et al. 2000) and result in a change in zeta potential. The fluid flow induced the transport of the electrical charge as the diffuse EDL layer is stripped off, generating a convection current, which in turn, produces a conduction current instantaneously in the opposite direction. Before equilibrium is reached new cracks are opened and linked and the process is repeated. This theory is embedded in the dilatancy-diffusion hypothesis of seismic precursory activity (Nur 1972, Scholz et al. 1973) with comparable laboratory results by Sammonds et al. (1992). Just prior to failure, the coalescence of cracks causes strain softening, which creates additional electrical and hydraulic pathways for fluid flow, and so increases the amplitude of the electrical signal up to failure. This agrees with the work by Yoshida (2001) who found good correlation between the convection current before the main failure and the dilatancy rate and water flow rate. This demonstrates that the electric current is caused by an electrokinetic effect due to water flow associated with the accelerating evolution of dilatancy before the main fault forms at failure. At failure (cartoon (C)) a large failure plane is formed producing a big increase in electrical potential. This is followed by slip on this failure surface, creating fault gouge as shown in cartoon (D).

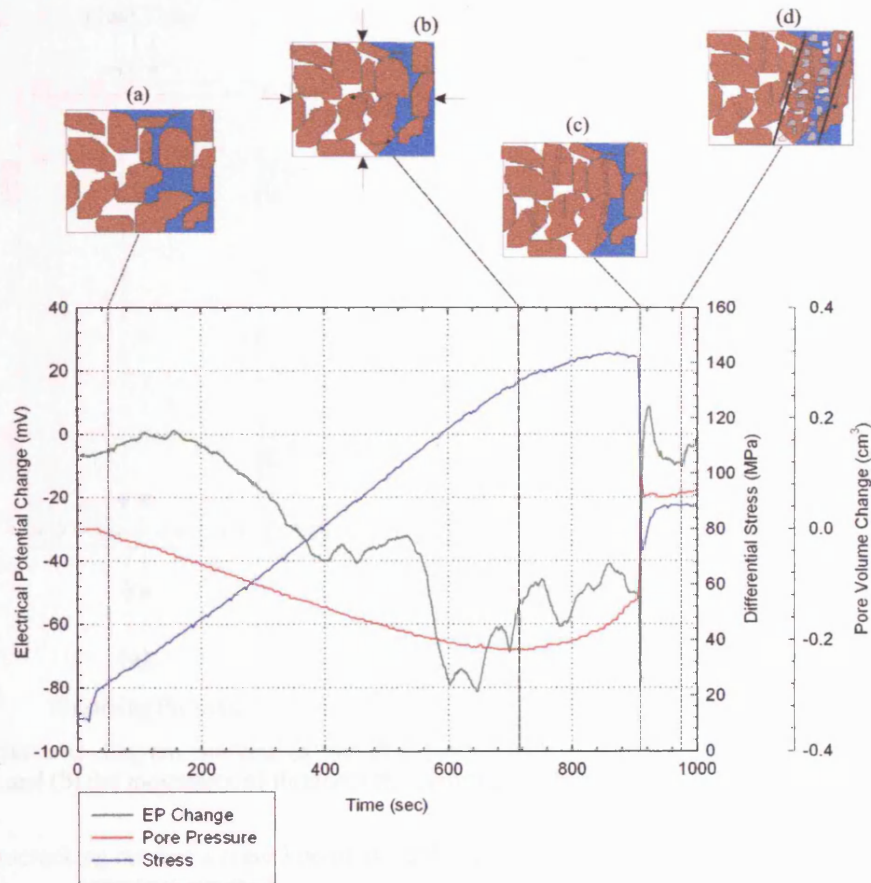


Figure 9.2: Reproduction of Figure 7.7a showing the electrical potential change, pore fluid volume and differential stress with cartoons of micromechanics during deformation of Bentheim sandstone ($P_c = 40$ MPa, $P_p = 20$ MPa). [Experiment No.: 26]

The convection current can be written as

$$I_{convection} = \phi \tau^{-2} \frac{\epsilon_p \zeta}{\eta} \nabla P \quad (3.29)$$

The zeta potential is normally negative in a quartz-water (deionised water) system (Ishido and Mizutani 1981). This means the diffuse layer is composed of a greater proportion of positive ions within the diffuse layer of the EDL. In a laboratory test, with a pore pressure gradient across the rock sample, the fluid flows in the same direction as the convection current causing the charge to be redistributed between the sample ends with a resulting increase in potential at all electrodes (Figure 9.3a). When a sample fractures and a fault forms with the same signal at all electrodes, it means therefore that the same signal exists around the fault. This shows that the source mechanism in the fault zone is microcracking with fluid movement (Figure 9.3b). We can see this is supported by my experiments.

Figure 9.4: Photographs of Chalkos with the fault showing the presence of grain crushing. [Experiment No.: 26]

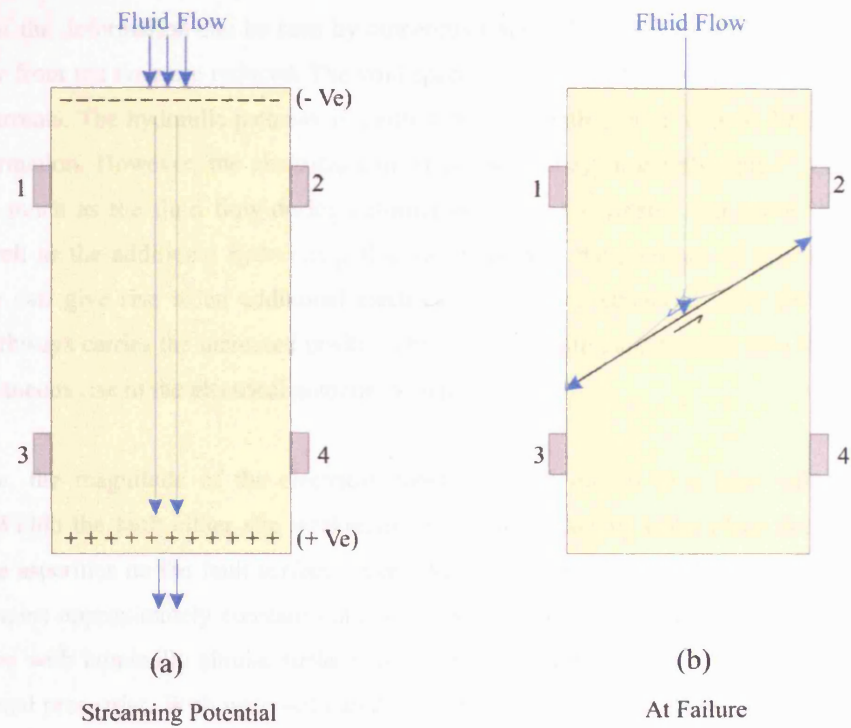


Figure 9.3: Schematic diagram showing (a) the distribution of the electrical streaming potential signal with fluid flow and (b) the movement of fluid into the fault region at failure.

At failure, microcracking reaches a critical point along the fault plane (Lockner et al. 1991) with a peak in AE activity and in the amplitude of electric potential signals. In Figure 9.4 a thin section of a rock fault from a deformation experiment on Clashach sandstone is shown.

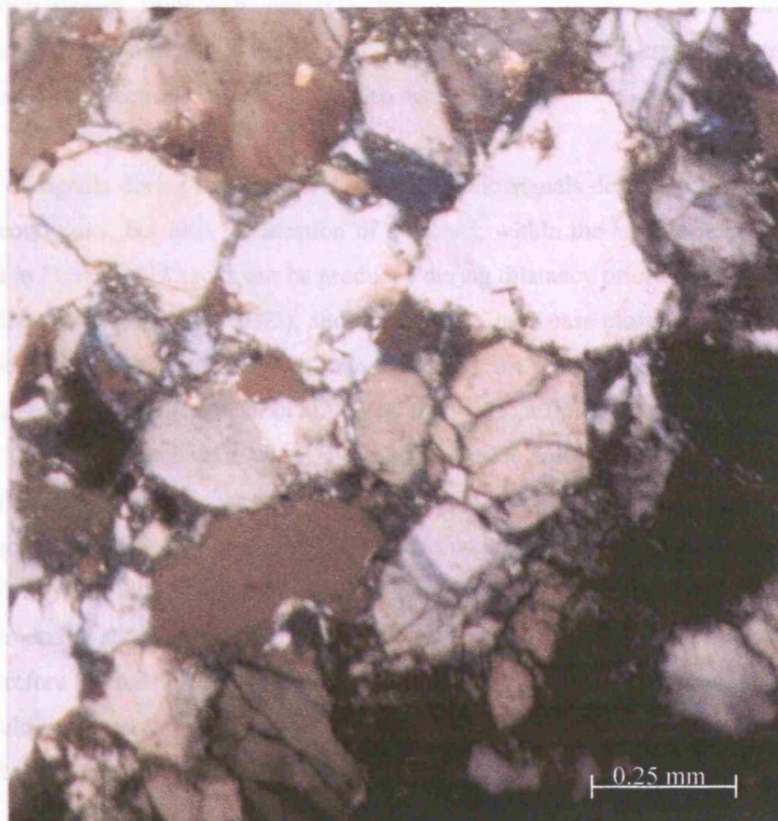


Figure 9.4: Photomicrographs of Clashach sandstone in cross-polarised light after deformation failure showing the presence of grain cracking. [Experiment No.: 14]

The effect of the deformation can be seen by numerous fractured crystals close to the fault. The effects further away from the fault are reduced. The void space of the fault itself represents a major conduit for hydraulic currents. The hydraulic pathway is controlled by a length scale l^4 (David 1993) and is reduced during deformation. However, the electrical current pathway obeys a length scale l^2 , because it is not inhibited as much as the fluid flow during deformation, since the current can travel through the bulk matrix as well as the additional hydraulic pathways. Also, with the presence of clay minerals, surface conductivity can give rise to an additional electrical signal. The enhanced fluid flow and additional electrical pathways carries the increased positive charge under a pressure gradient into the fault, resulting in an instantaneous rise in the electrical potential signal.

After failure, the magnitude of the electrical potential signal decays to a base value as the signal dissipates. Within the fault either slip weakening or slip strengthening takes place depending upon the nature of the asperities on the fault surface. Interlocking asperities give the rock strength. The frictional strength remains approximately constant until the experiment is stopped. Biegel et al. (1992) note that even surfaces with nominally similar surface roughness have significant topographic differences which affect frictional properties. With water-saturated samples, a linear increase in potential signal is observed for strains of about 1.2% after failure for both sandstones and limestones. As this signal is not observed under dry conditions, it rules out the piezoelectric effect as a possible mechanism, suggesting it is related to the electrokinetic phenomenon. The possible mechanisms are: 1) an increase in fault gouge generated with on-going slip, increasing the rocks surface area thereby creating new surfaces for the EDL to form. Particle size analysis of the fault gouge material showed a maximum grain size of 30 μm . This compares with a mean grain size of 1mm, demonstrating that massive accumulation has occurred. 2) With the increase in the amount of fault gouge, fluid flow occurs into the fault zone creating a streaming potential signal. A reaction at the electrode surface would also occur.

The magnitude of signals during dilatancy and pre/co-seismic signals depends not only on the rock and environmental conditions, but also the location of the crack within the sample relative to the electrode location as seen in Figure 9.5. Cracks can be produced during dilatancy prior to dynamic failure, forming weak zones in the rock (Tang et al. 2002), and these cracks may pass close-to or through an electrode. Fluid in these zones can remove the positive charge reducing the potential signal in that region. As faults are not formed instantaneously (Lockner et al. 1991), fluid takes a finite time to enter the fault area. With the presence of these offshoot cracks, water is forced into these areas before the main event. Therefore, with the fluid flow generating a change in potential signal, the pre-seismic signals are observed even earlier. It is concluded that the position of the electrodes could be used for fracture location and give an earlier indication of when failure will occur. In the laboratory setting the pre-seismic signal is of the order of less than a second at strain rates of 10^{-6} s^{-1} , however, on the crustal scale strain rates of 10^{-12} s^{-1} are present, and therefore the pre-seismic signal will appear even earlier. Also, the magnitude of the signal is related to the fluid movement, which in turn, is related to the void space created by the microcracking so that a large fault may generate a larger pre-seismic signal than a smaller fault.

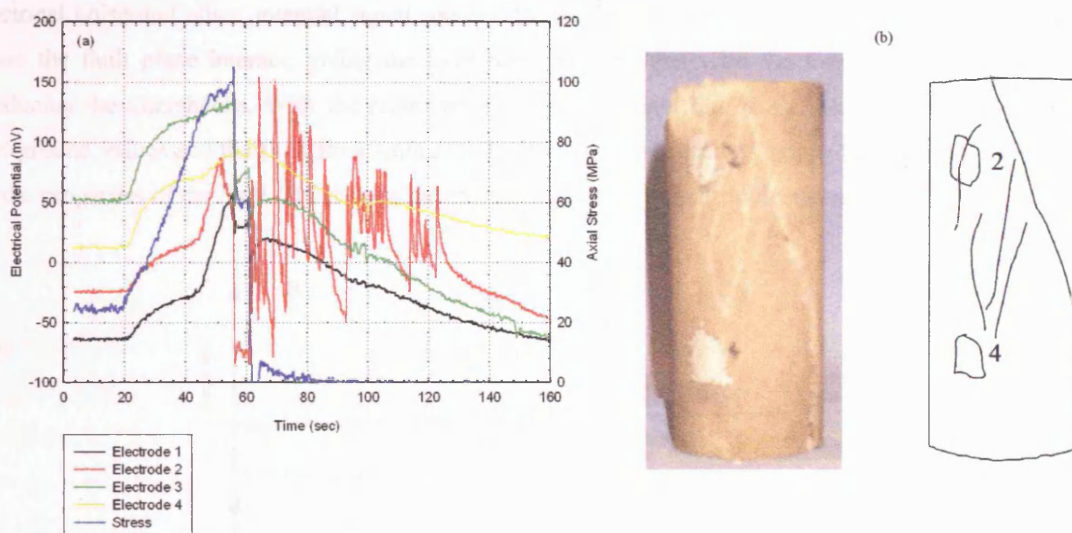


Figure 9.5: Replot of Figure 7.14 showing (a) the deformation of Clashach sandstone showing the effect of a crack fault passing through an electrode and (b) photograph and schematic diagram of the deformed sample showing the position of cracks and fault. $P_e = 20$ MPa and strain rate $1.5 \times 10^{-4} \text{ s}^{-1}$. [Experiment No.: 21]

Based on the results gathered here and on models proposed by Sammonds et al. (1992), Main et al. (2000) and Ohnaka (2004), Figure 9.6 represents a model of what occurs during earthquake faulting, illustrating how the parameters of strain rate, tectonic stress, seismic activity, permeability, the seismic b-value and electrical potential vary with time.

During stage (1) there is little change in the parameters with time and these represent background values. Stage (2) is the premonitory stage when the conditions within the focal region begin to change during long-term tectonic loading. This includes the strain rate increasing slightly which is accompanied by an increase in stress. Crustal deformation generates additional seismic activity which produces a slow decline in the seismic b-value. The increase in fracturing enhances the fluid flow within the focal region as shown in Figure 9.4 which generates a steady increase in the average electrical potential. However, with the electrical noise and other possible sources for the electrical potential this increase may not be detectable. (3) shows the region where foreshocks begin to occur as the stress reaches the maximum before failure. Here, the strain rate accelerates and approaches values which can be reproduced in a laboratory of around 10^{-7} s^{-1} (see below for details). The increase in movement within the fault produces a corresponding increase in seismic activity and a decrease in seismic b-value. The electrical potential also continues to increase slightly. Whether this change can be measured in the crust is at the heart of the VAN debate. As noted in Chapter 1, a severe shortcoming of the VAN method is in providing a correct order of magnitude from electric signals measured away from the source, with the need to assume energy conservation, and with local signals being easily misinterpreted as distant sources, all serving to make the hypothesis less plausible (Gruszow et al. 1996). Stage (4) represents failure of the fault. The slip movement along the fault plane occurs at speeds approaching the shear wave velocity. This rapid movement generates an exponential increase in seismic activity as well as a minimum in seismic b-value. This slip movement also causes rapid fluid flow which generates a peak in the electrical potential signal. This signal may or may not be observed by geophysical methods depending on electrode location,

electrical noise and other potential signal sources. Stage (5) is after the main shock. Here the asperities along the fault plane interact, giving the fault some strength, but with the failure of these asperities, producing the aftershocks. With the reduction in stress the strain rate is significantly reduced towards background values and the fluid flow within the fault region is reduced or stopped completely depending on the properties of the fault. This causes the electrical potential signals to decrease.

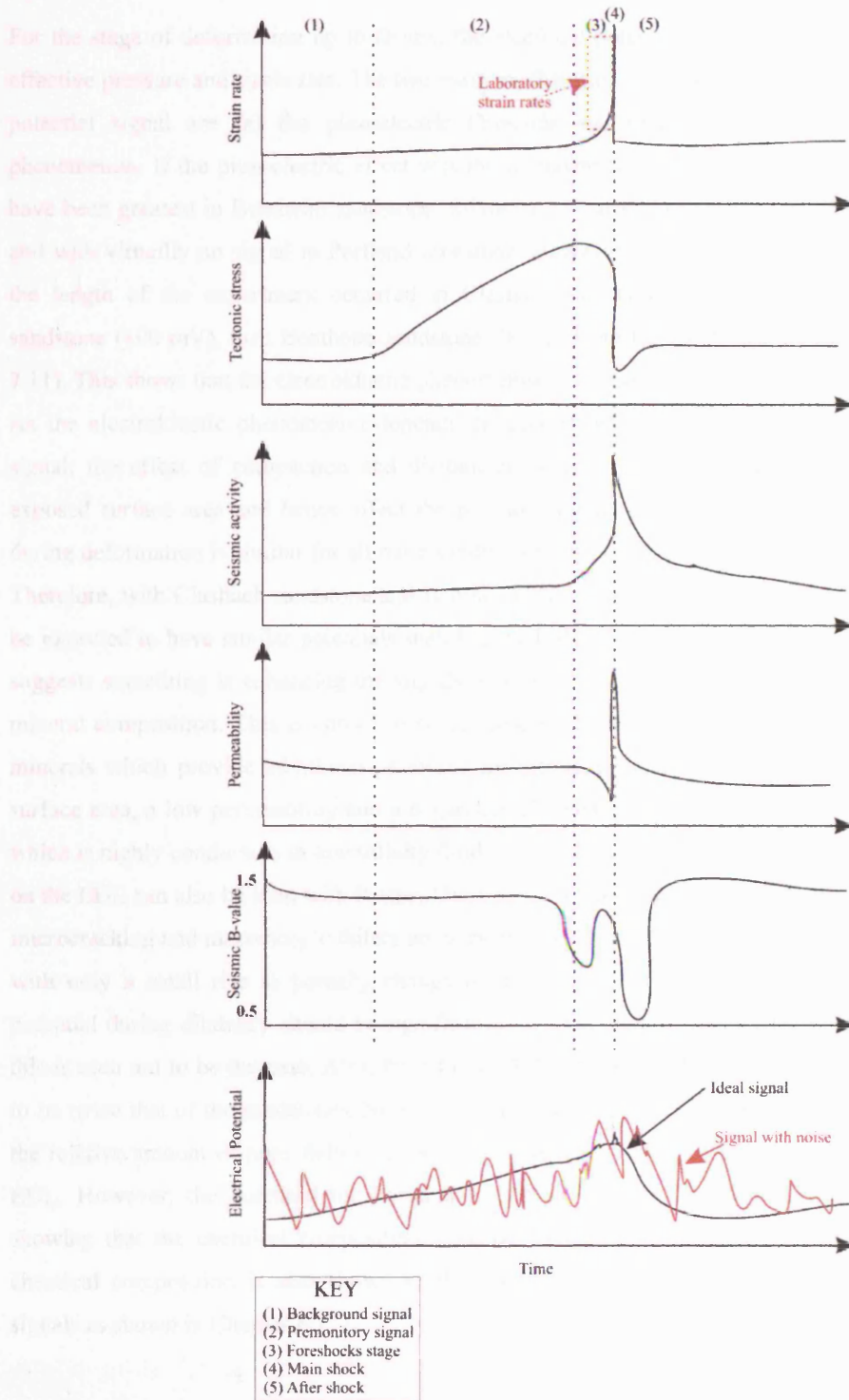


Figure 9.6: A schematic diagram illustrating changes in the electrical parameter in relation to strain rate, tectonic stress, seismic activity, permeability, the seismic b-value and electrical potential during earthquake faulting.

9.1.2 The Difference Between Quartz Rich and Quartz Free Rocks on the Electrical Potential Signal

Regardless of rock type, the microscopic processes occurring within compressively stressed rock materials are similar in being brittle processes following the sequence of initiation, propagation, and coalescence of microcracks, leading to eventual formation of macroscopic fractures.

For the stage of deformation up to failure, the electrical potential signal varies with rock type at given effective pressure and strain rate. The two main mechanisms which exist and could produce the electrical potential signal are (a) the piezoelectric (Yoshida and Ogawa 2004) and (b) the electrokinetic phenomenon. If the piezoelectric effect was the dominant mechanism, then the electrical signals would have been greatest in Bentheim sandstone, followed by Darley Dale sandstone, then Clashach sandstone and with virtually no signal in Portland limestone. However, the greatest electrical potential signal over the length of the experiment occurred in Clashach sandstone (120 mV), followed by Darley Dale sandstone (100 mV), then Bentheim sandstone (90 mV) and finally Portland limestone (80 mV) (Figure 7.11). This shows that the electrokinetic phenomenon is the dominant mechanism in fluid saturated rocks. As the electrokinetic phenomenon depends on surface area within the rock to generate the potential signal; the effect of compaction and dilatant cracking during deformation influences the amount of exposed surface area and hence affect the potential signal. Figure 9.7 shows that the porosity change during deformation is similar for all three sandstones during compaction (-0.15%) and dilatancy (0.15%). Therefore, with Clashach sandstone and Bentheim sandstone having similar initial porosities they would be expected to have similar potentials with Darley Dale having a lower value. As this is not the case it suggests something is enhancing the signals generated in Clashach and Darley Dale sandstone such as mineral composition. This is known to be the case in Darley Dale sandstone which contains some clay minerals which provide additional pathways for electrical conduction. Clay is known to have a large surface area, a low permeability and a negatively charged high surface conductivity (Ruffet et al. 1995) which is highly conductive in low salinity fluids (Revil and Glover 1998). The effect of different minerals on the EDL can also be seen with Portland limestone. A study by Ayling (1991) suggests that the onset of microcracking and macroscopic failure are very close in fine-grained limestone. This is seen in Figure 9.7 with only a small rise in porosity change before failure. This therefore suggests that the change in potential during dilatancy should be significantly less than that of sandstone, however from Figure 7.11 this is seen not to be the case. Also, from Figure 9.7 the porosity decrease for Portland limestone is seen to be twice that of the sandstones. Now the greater the porosity decrease during deformation, the greater the relative amount of pore fluid is moved out of the rock and the less surface area is available for the EDL. However, the potential for Portland Limestone is only 10 mV less than Bentheim sandstone showing that the chemical composition must be the cause of such a small difference. The effect of chemical composition is also shown in the discussion below when dealing with streaming potential signals as shown in Chapter 8.7.

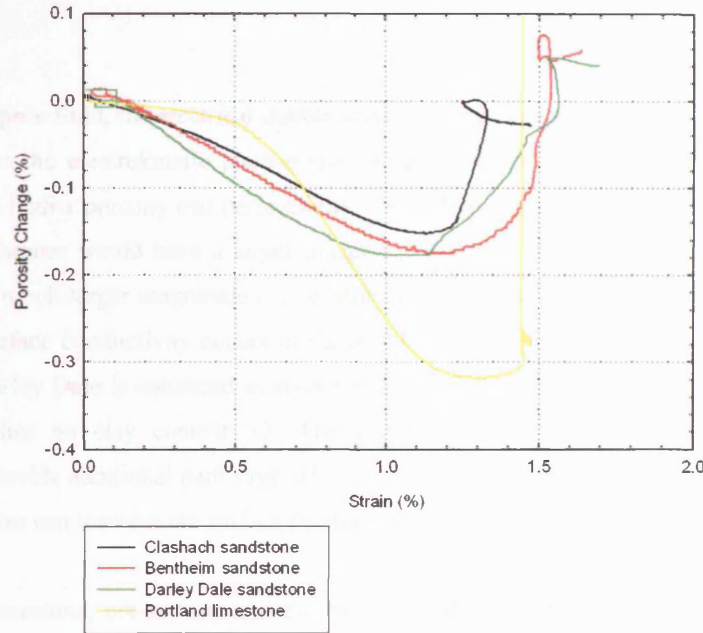


Figure 9.7: The porosity change of Bentheim, Clashach and Darley Dale sandstone and Portland limestone during deformation with an effective pressure of 20 MPa and a strain rate of $1.5 \times 10^{-5} \text{ s}^{-1}$. [Experiment No.: 13, 19, 26, 30]

The typical pre-seismic and co-seismic potentials for all five rock types are shown in Table 9.1. Using equation 3.7, the voltage can be directly related to the proportion of quartz crystals present in the rock.

$$\varphi(t) = \frac{1}{4\pi\epsilon_p} \sum_m \frac{-b^{(m)} r_i^{(m)} c_{ijk}^{(m)} \sigma_{jk}^{(m)}(t) * g(t)}{|r^{(m)}|^3} \quad (3.7)$$

The highest pre-seismic and co-seismic signals for sandstone should be for Bentheim (99%), Darley Dale (75%) and finally Clashach sandstone (70%). However, the electrical potential difference for Darley Dale sandstone is greater than those for Clashach and Bentheim sandstone. The effect of clay immersed in water on electrical signal has been well documented (Ishido and Mizutani 1981, Lorne et al. 1999b). However the effect under dry conditions has not yet been comprehensively studied. The cation movement under dry conditions, caused by the change in stresses may react with the clay surface and become bonded to them, forming a mobile conductive layer. This would explain why the electrical potential difference for Darley Dale is greater than the other sandstones tested under dry conditions.

For the dry quartz-free rocks (limestone and basalt) no piezoelectric effect is present. Therefore no pre-seismic signal is seen, but a co-seismic signal change is observed. A possible explanation for this is electron emissions from crack tips forming at failure (Yamada et al. 1989). Where the stress state is altered sufficiently it can produce mobile electronic charges capable of producing charged surfaces even within insulating materials. This can be used to explain the signal observed in basalt where the signal was found at the lower electrodes located near the fault. However, this does not explain the signal observed in

limestone where the electrode which recorded the co-seismic signal, was some distance away from the main fault.

In the presence of pore fluid, the electrical double layers form at the grain boundary interface in all rock types which makes the electrokinetic phenomena the main source for the electrical potential signals observed. With the higher porosity and permeability, it could be expected that the signals from Bentheim and Clashach sandstones would have a larger magnitude than that of Darley Dale sandstone. However Darley Dale has a much larger magnitude pre-seismic and co-seismic signal. This could be explained in three ways: (1) Surface conductivity occurs in the double layer. With the presence of clays, the surface conductivity of Darley Dale is enhanced as shown in Figure 2.29 having a higher amplitude than Berea sandstone which has no clay content. (2) The presence of clay minerals such as Kaolinite and Montmorillonite provide additional pathways to transport electrical currents (Lorne et al. 1999b) and (3) a decrease in grain size can increase the surface conductivity effects (Revil et al 1999a).

With basalt and limestone, pre-seismic and co-seismic signals are observed. The electrical signals for basalt exceed that of limestone by over one order of magnitude but its permeability is several magnitudes smaller. Around failure, multiple cracks are created, thereby forming additional pathways for electrical current to flow through. This seems to affect basalt more than limestone which is more plastic.

Rock Type	Pre-seismic (dry)	Co-seismic (dry)	Pre-seismic (sat)	Co-seismic (wet)
Clashach	15.4	30.5	25.8	45.0
Darley Dale	20.4	110.3	100.3	115.3
Bentheim	20.8	40.7	30.6	65.8
Portland	0	100.9	3.7	12.3
Seljadur	0	35.8	20.1	232.2

Table 9.1: Variation of electrical potential pre-seismic and co-seismic of different rocks under dry and saturated conditions. Values given to an accuracy of ± 0.1 mV.

9.1.3 Effect of Strain Rate on Rock Type and Electrical Signals

In order to relate laboratory experiments to field scales, experiments have to be done over a sufficiently large range of strain rates so that the results can be extrapolated to the field situation, provided that there is no change in mechanism. If this is possible it would provide useful information on actual faults and perhaps allow models to be formulated. Clashach, Bentheim, Darley Dale sandstone and Portland limestone were used to investigate both the mechanical and electrical properties of the rock with strain rates between $1.5 \times 10^{-4} \text{ s}^{-1}$ and $1.5 \times 10^{-7} \text{ s}^{-1}$ corresponding to experimental times ranging from 200 seconds to over 2 days.

For all rock types, the elastic modulus remains fairly constant and unaffected by strain rate as shown in Figure 9.8 for limestone. Strain hardening occurs up to the peak stress, and is then followed by strain softening just prior to failure at strain rates of $1.5 \times 10^{-5} \text{ s}^{-1}$ or lower. At higher strain rates (e.g. $1.5 \times 10^{-4} \text{ s}^{-1}$) a period of strain softening is not observed because it is caused by the accumulation of microcracks. This takes a finite amount of time and at such high strain rates this accumulation is so rapid

that the fault forms within a few seconds and so no period of softening is seen. At any strain rate, the sample then undergoes dynamic failure, slip strengthening and steady frictional sliding. Under the conditions explored, the strain-rate dependence of the mechanical properties in both sandstone and limestone is negligible over the strain-rate range investigated.

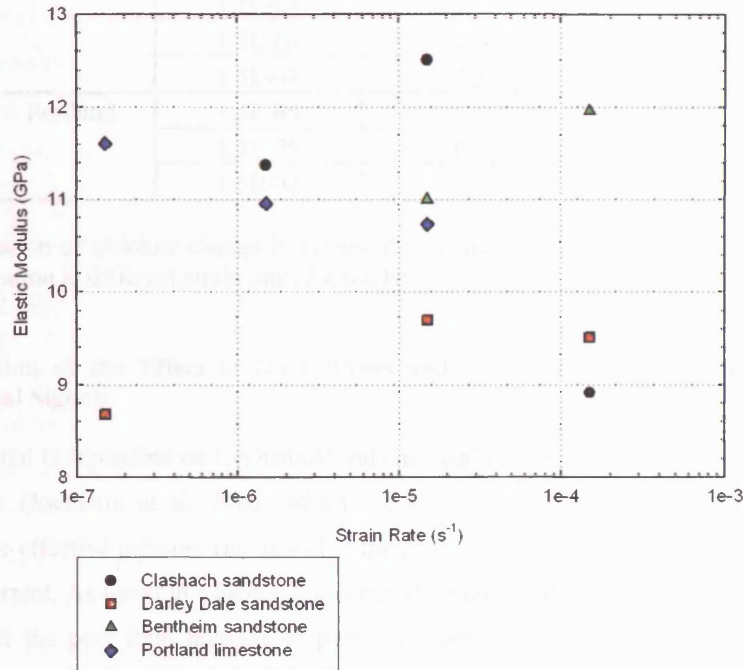


Figure 9.8: The elastic modulus of Clashach, Bentheim and Darley Dale sandstone and Portland limestone from experiments at strain rates ranging from $1.5 \times 10^{-4} \text{ s}^{-1}$ to $1.5 \times 10^{-7} \text{ s}^{-1}$. All values given to an accuracy of $\pm 0.1 \text{ GPa}$ with no apparent link between elastic modulus and strain rate [Experiment No.: 21, 22, 23, 25, 26, 27, 29, 30, 31, 32, 33]

The effect on electrical potential signal of strain rate variation is shown in Figure 7.21. With the slower strain rates the magnitude of the potential change is reduced (with slight differences in potentials between the electrodes probably due to local features). Concentrating on compaction and dilatancy, the absolute changes observed are shown in Table 9.2 for Clashach and Darley Dale sandstone and Portland limestone. All three rocks show a decrease in electrical potential change with strain rate. Applying this to crustal deformation, the electrical potential change would approach zero with strain rates approaching tectonic strain rates: a phenomenon which has been reported by Gross and Williams (1982). With similar peak stresses and absolute volume changes being similar for all strain rates, the increase in charge redistribution can be ruled out as a possible mechanism. This suggests, therefore, that the rate of fluid flow may be responsible for the differences in potentials. The lower the strain rate, the slower the fluid velocity enters and reacts with the crack surfaces to produce the electric potential as investigated by Yoshida (2001). Also at very low strain rates (crustal values), the electrical signal would dissipate before being measured and collectively the electrical potential would not be observed.

Rock Type	Strain Rate (s^{-1})	Compaction (mV)	Dilatancy (mV)
Clashach	1.5E-04	31.4	68.2
	1.5E-05	22.3	46.3
	1.5E-06	13.7	30.4
Darley Dale	1.5E-04	25.1	200.6
	1.5E-05	8.8	73.1
	1.5E-06	2.6	29.0
	1.5E-07	4.5	28.4
Portland	1.5E-05	22.3	37.2
	1.5E-06	10.2	16.7
	1.5E-07	2.0	3.6

Table 9.2: Variation of absolute change in electrical potential signals during compaction and dilatancy stages of deformation at different strain rates for sandstone and limestone samples. The values given to an accuracy of ± 0.2 mV.

9.1.4 Discussion of the Effect of Rock Types and Environmental Conditions on Streaming Potential Signals

Streaming potential is dependent on mechanical and chemical processes. Effects include permeability and formation factor (Jouniaux et al. 2000) which are affected by crack generation (dilatancy) due to deformation. The effective pressure can also alter the pore network (permeability) which transmits fluids and electrical current. As noted in Chapter 7.3, compaction and dilatancy regimes within the rock during deformation alter the pore fluid pressure or pore fluid volume under undrained or drained conditions respectively. Therefore, during deformation the pore fluid pressures may vary locally which changes the behaviour of the streaming potential signal, hence the streaming potential provides useful information about rock deformation. This is shown below in Figure 9.9.

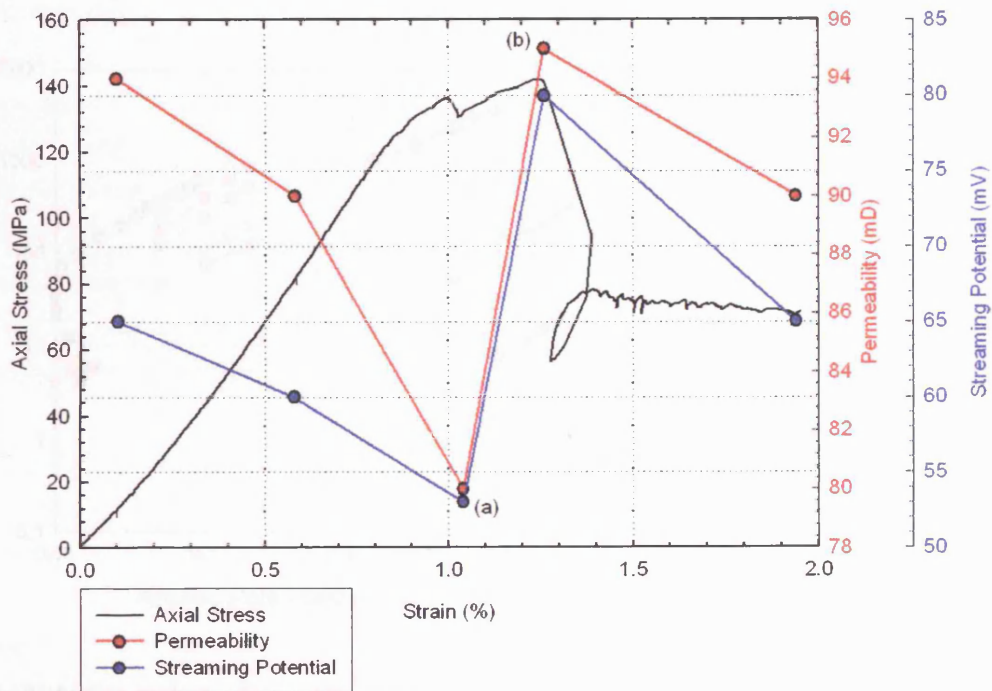


Figure 9.9: Plot of streaming potential and permeability variation during a deformation cycle of Portland Limestone. The stress-strain curve, involving compaction, dilatancy, fracture and stable sliding indicate deformation. A strain rate of $1 \times 10^{-5} s^{-1}$ was used and an effective pressure of 20 MPa with deionised water was maintained. Each point is given to an accuracy of ± 0.5 mD for permeability and 0.1 mV for streaming potential measurements. [Experiment No.: 24]

In Figure 9.9 the permeability and streaming potential are measured at different stages of deformation. In this experiment, deformation is stopped at certain strain intervals and the streaming potential is measured using the steady state flow technique by applying a constant pore pressure gradient of 20 MPa across the sample. The flow rate is also measured and used to compute the hydraulic permeability. In Figure 9.9, point A represents the beginning of dilatancy where compaction and closing of pores and crack networks has occurred. From the initial readings the streaming potential has decreased by 18.5% during this stage. The hydraulic permeability decreases by 15% in the same stage. Therefore, both transport properties show they are sensitive to the closing of the pore network. Point B represents the point of failure of the rock. At this stage the streaming potential increases by a factor of 1.5 while the hydraulic permeability increases by a factor of only 1.2. Continued deformation in the form of stable sliding occurs after dynamic fracture where the streaming potential decreases by 19% with the permeability changing by 5%. These results agree with Clint (1999) and Jouniaux and Pozzi (1995a).

Pore pressure gradients of up to 30 MPa were applied to Clashach, Bentheim and Darley Dale sandstone and Portland limestone in this study. It was found that streaming potential increased linearly with pressure up to 25-30 MPa (depending on rock type) with constantly varying potentials at higher pore pressure gradients. This linear relationship between pore pressure gradient and the streaming potential signal has also been observed in previous studies (Figure 9.10) under hydrostatic pressures in Fontainebleau sandstone (Jouniaux and Pozzi 1995b), crushed Fontainebleau sandstone (Lorne et al. 1999a) and crushed quartz samples (Ishido and Mizutani 1981). A non-linear relationship is present in Berea sandstone without confining pressure (Tuman 1963), with both linear and non-linear behaviour reported for unconfined Triassic sandstone and fractured granites (Middleton 1997).

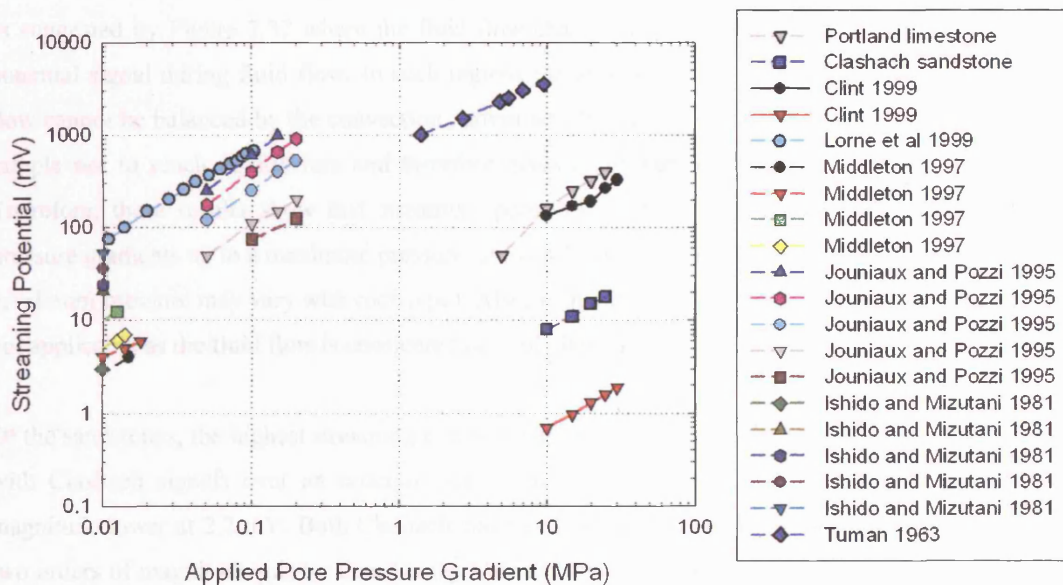


Figure 9.10: Comparison of streaming potentials measured from sandstones and limestone with values from the literature. Sources of data are given in the legend.

Study	Maximum Pressure Gradient (MPa)
Eccles 2005	35
Clint 1999	40
Lorne et al. 1999a	0.25
Middleton 1997	0.0125
Jouniaux and Pozzi. 1995b	0.2
Ishido et al. 1981	0.01

Table 9.3: Maximum pore pressure gradients used to generate streaming potential signals during previous studies.

To investigate why the streaming potential signal could not reach equilibrium with pressure gradients greater than 30 MPa, the Reynolds number (R_e) was used to investigate if the fluid flow was laminar or turbulent. The Reynolds number is given as

$$R_e = \frac{\rho v l}{\eta} \quad (2.42)$$

where ρ is the density (1000 kg m^{-3}), v is the fluid velocity in the matrix, l is the characteristic pore dimension (grain width) and η is the fluid viscosity at $1 \times 10^{-3} \text{ Pa s}$. The fluid velocities are calculated from the flow rate divided by the surface area of the end of the sample through which the fluid flows (e.g. porosity). Using the highest velocities for sandstone (0.159 cm s^{-1}) and limestone (0.0796 cm s^{-1}) at a pore pressure gradient of 30 MPa, the Reynolds number is calculated to be 56 for Clashach sandstone and 8 for Portland limestone. This number shows that the flow within the rock is not truly turbulent ($Re \geq 1000$) or truly laminar ($Re \leq 1$). However, localised areas within the rock matrix will have turbulent flow present as suggested by Figure 7.32 where the fluid flow change is not constant with constant variation in the potential signal during fluid flow. In such regions the ions which are stripped off by the turbulent fluid flow cannot be balanced by the convection current which causes the streaming potential within the whole sample not to reach equilibrium and therefore gives a constantly varying potential during fluid flow. Therefore, these results show that streaming potential signal can be linearly related to applied pore pressure gradients up to a maximum pressure, above which streaming potential cannot be maintained (this maximum pressure may vary with rock type). Also, with a Reynolds number greater than 1 Darcy's law is not applicable as the fluid flow is considered not truly laminar.

Of the sandstones, the highest streaming potential signal is observed in Darley Dale sandstone of 320 mV with Clashach signals over an order of magnitude lower (20 mV) and Bentheim a further order of magnitude lower at 2.2 mV. Both Clashach and Bentheim sandstones have hydraulic permeabilities over two orders of magnitude greater than Darley Dale sandstone and porosities 5-8% larger but have a lower streaming potential. Jouniaux and Pozzi (1995b) found an increase in streaming potential coefficient with increasing permeability under a 10 MPa confining pressure during static tests. However, Lorne et al. (1999b) reports no clear evidence of a link between permeability of crushed Fontainebleau sandstone under zero confining pressure and the streaming potential coefficients. Using equation 3.21, implies the fluid velocity is seen to affect the electric current.

$$I = 2\pi r q u_{\delta} \quad (3.21)$$

Based on the rock types tested here it would be expected that Clashach and Bentheim sandstone would have similar streaming potential signals, however, this is not the case. Therefore, there is another control on the streaming potential signal. Equation 3.27 shows that the streaming potential is affected by the zeta potential.

$$V = \frac{\zeta \epsilon_p}{\eta \sigma_f} P \quad (3.27)$$

The zeta potential varies with minerals such as clays, which are known to be highly conductive and provide additional electrical pathways. This would explain the results obtained here with the clays present in Darley Dale sandstone being responsible for dramatically increasing the potential, Clachach sandstone has minerals other than quartz present which increases the potential slightly and Bentheim sandstone has few or no other minerals to increase the streaming potential signal. The presence of minerals affecting the streaming potential signals is backed up by the results obtained for Portland limestone. The streaming potential signal for Portland limestone was 30 times greater than that of Clashach sandstone with the permeability an order of a magnitude lower. As Portland limestone is made up of CaCO_3 and contains no quartz crystals, the difference in streaming potential signal must be due to the calcium carbonate, because a lower permeability would give a lower potential coefficient which is not the case.

The importance of fluid flow rate during deformation is discussed above in section 9.1.3. Slower fluid flows generate smaller electrical potential changes. Understanding how the streaming potential signal behaves in relation to the heterogeneous nature of the rock would provide useful information on rock permeability. The streaming coupling coefficient can be directly related to the electric current density (3.36) and fluid flow (3.37) given by

$$Q = -\frac{k}{\eta} \nabla P - \frac{\epsilon_p \zeta}{\eta} \nabla \varphi \quad (3.36)$$

$$J = -\frac{\epsilon_p \zeta}{\eta} \nabla P - \sigma_f \nabla \varphi \quad (3.37)$$

Now, if σ_f (electrical conductivity), ϵ (permittivity), ζ (zeta potential), and η (viscosity) can be measured, then rock permeability can be calculated from fluid flow and electrical potential signal changes. Also, with acoustic emission data, using the calculated b-values which are related to the mean crack length (Main 1991), then fault length can be related to fluid flow, through the electrical potential including calculating the tortuosity and connectivity of the crack and pore matrix during crack extension. This relationship between electrical conductivity and crack damage induced by deformation was investigated by Glover et al. (1996) who was able to relate volume change to conductivity measurements. The significance of stress variations can also be identified from electrical potential signals as shown in Figure 7.11 which is a drained test under a constant pore pressure of 20 MPa with a stress pulse applied to the

end of the samples. This produces a small increase in electrical potential which is superimposed on the background signal, with the magnitude of the signal depending on stress change. This relatively small increase in stress may close sub-horizontal cracks, lowering the porosity and increasing the hydraulic tortuosity of the rock as well as forcing fluid out under drained conditions thereby changing the electrical signal. Therefore, this demonstrates that stress changes alter the mechanical properties of the rock which causes the electrical potential signal to change.

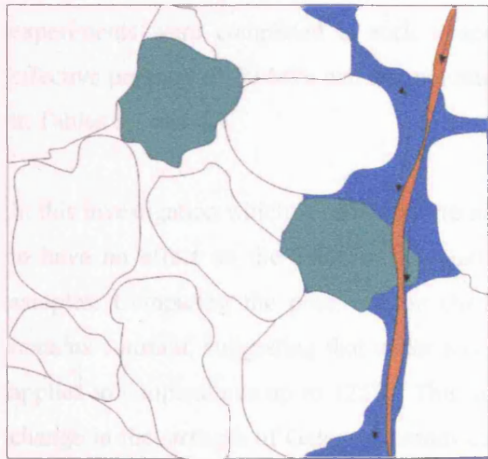
In the past, the fluid and electrical flow have been described by similar equations (e.g. Navier-Stokes). It was therefore assumed that the ions travelled down the same pathways as the fluids under a pressure gradient (Tsang 1984) with the electro-osmosis effect on permeability ignored as it remains very small relative to the fluid flow generated by the pressure gradient. Numerical models however have shown that different pathways exist for electrical and hydraulic permeabilities within the fracture zone (Brown 1989, David 1993). The electrical pathways are affected less than the hydraulic permeability during compaction as the electrical signals can go through both the bulk and fluid whilst the pore fluid can only pass through cracks and open pores. Stesky (1986) puts the main effect on electrical signal due to surface area with rougher surfaces generating greater potential signal. Adding hydrostatic pressure also varies the critical paths for electrical and hydraulic flow controlled by length scales of l^4 for hydraulic flow and l^2 for electrical conductivity (David 1993) and with transport properties significantly varying between samples (David and Darot 1989). Therefore, the pore geometry can be considered important for controlling fluid and electrical flow (Bernabe and Bruderer 1998).

During compaction, sub-horizontal cracks and pores are closed, which increases the hydraulic tortuosity by reducing the connectivity of the pore network. Because the electrical current depends on smaller crack apertures (David 1993) and can take alternative paths through the rock other than that of the fluid (Lorne et al 1999a), the effect on electrical current is lessened so that the streaming potential signal reduction is relatively small. If further compaction occurs to the point that the rock can no longer accommodate the change in strain, dilatant microcracks are formed throughout the rock sample producing measurable AE signals. The closer to failure the more the cracks coalesce creating lower b-values up to failure. In this region the permeability is reduced (Keaney 1998) by increasing the tortuosity of the pathways causing a decrease in the streaming potential. Jouniaux and Pozzi (1995b) reports that the streaming potential decreases up to around 80% of the peak stress for Fontainebleau sandstone while Lorne et al. (1999a) obtained a decreasing potential of up to 79% on the same rock type. At a critical point, the coalescence leads to the formation of the macroscopic fault. This fault represents a large conduit for fluid flow to enter which is shown by the rapid increase in pore volume (e.g. as shown in Figure 7.2) and a spike in electrical potential. After failure frictional sliding occurs where the asperities on both sides of the fault interlock. During steady frictional sliding, the asperities on the fault break creating fault gouge causing an increase in pore volume at the fault but a decrease in permeability (Jouniaux and Pozzi 1995b, Zhu and Wong 1996, Keaney 1998)

Clint (1999) used this idea to produce a model that has been modified into Figure 9.11. This model described the changes in hydraulic and electrical current pathways during various deformation states and is similar to the model proposed by Lorne et al. (1999a). In Figure 9.11a the rock is shown under

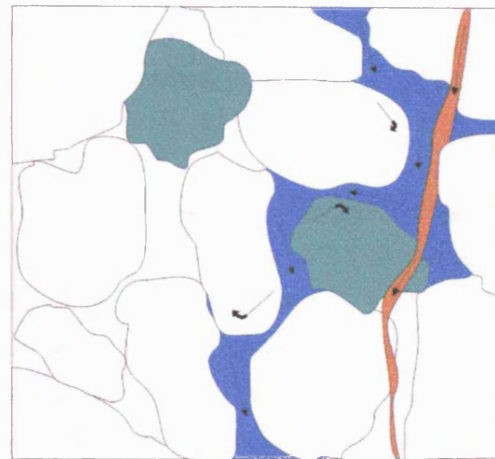
compression, with an example of a fluid pathway, which also carries the convection current. Also shown are the electrical pathways, which can travel through the bulk with the onset of dilatancy. This allows intergranular cracking to take place (Figure 9.11b) as well as some grain rotation. This dilates the pore space, increases the pore volume of the rock, thereby increasing the hydraulic tortuosity and decreasing the permeability. The effect on the streaming potential is small due to the numerous pathways the electrical current can use: i) the current can travel through tighter pore networks; ii) it can pass through the bulk and, iii) with the highly conductive clay minerals the current can be enhanced, increasing the streaming potential. As failure is approached the grains are further reorganised with the coalescence of cracks increasing the pore volume and further reducing the hydraulic permeability. The situation just after failure is shown in Figure 9.11c which represents an area away from the macroscopic fault. The number of electrical pathways is increased as axial cracks are formed which are sufficiently narrow to inhibit fluid flow, but wide enough to allow electrical conduction. These cracks can further reduce the permeability. However, with the coalescing of numerous cracks formed around the time of failure, large aspect ratio cracks may become connected, increasing the permeability, and with grain rotation, additional fluid pathways may be created. After failure, frictional sliding takes place. Asperities will be stripped off due to slip movement and become crushed, creating fault gouge which reduces porosity and permeability further for as long as sliding occurs. Numerical simulations show the complex nature of the fault surface and the different paths taken by electrical current and hydraulic permeability (Brown 1989). Furthermore, this relationship between surface roughness and permeability can cause the fracture permeability to decrease (Olsson 1992), or increase (Olsson and Brown 1993). With the presence of clay minerals, which have a low permeability, but enhanced electrical conduction, the link between the current and hydraulic permeability may be further complicated during frictional sliding.

(a) During Compaction



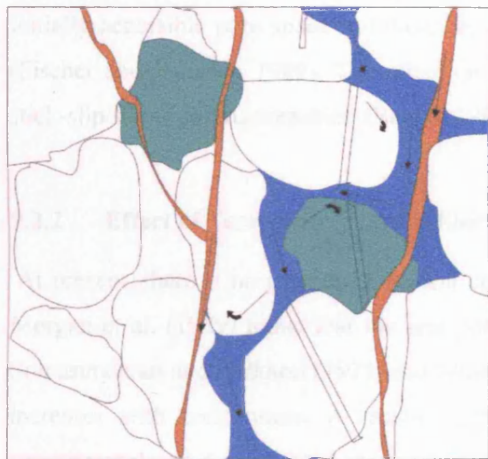
Fluid & Current Flow
 Current Flow
 Clay mineral

(b) During dilatancy with intergranular cracking



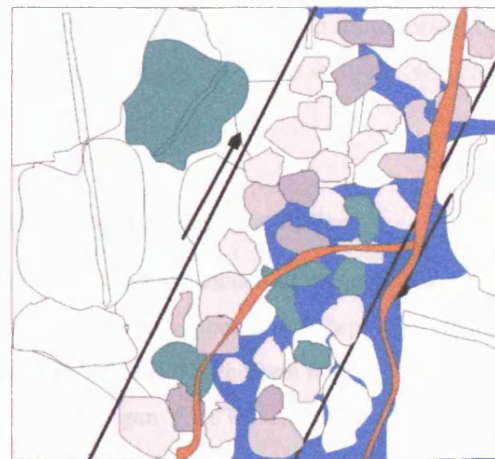
Fluid & Current Flow
 Current Flow
 Clay mineral

(c) Just after dynamic failure with intragranular cracking



Fluid & Current Flow
 Current Flow
 Clay mineral

(d) Fault with frictional sliding



Fluid & Current Flow
 Current Flow
 Clay mineral

Figure 9.11: Evolution of electrical and hydraulic flow paths of impure sandstone during (a) compaction, (b) onset of dilatancy, dominated by intergranular cracking and grain rotation (c) between peak stress and immediately after dynamic fracture, dominated by intragranular cracking and (d) during stable sliding on macroscopic fault plane (Modified from Clint (1999)).

9.2 DISCUSSION OF THE EFFECT OF TEMPERATURE ON THE DEFORMATION OF ROCK SAMPLES

9.2.1 Discussion of the Effect of Temperature on the Mechanical Properties of Sandstone During Shear Failure

The effect of temperature on physical properties was examined using Clashach sandstone. Five experiments were completed at rock temperatures of 25°C, 50°C, 75°C, 100°C and 125°C with an effective pressure of 20 MPa and a strain rate of $1.5 \times 10^{-5} \text{ s}^{-1}$ with a summary of the main results shown in Tables 8.3 and 8.4.

In this investigation which is considered to have been undertaken at low temperatures, temperature seems to have no effect on the peak or frictional stress within the natural variability which exists between samples. Comparing the pore volume change during deformation, the amount of pore fluid change remains constant, suggesting that under a confinement of 20 MPa, the deformation mechanism at 25°C applies to temperatures up to 125°C. This agrees with Blacid et al. (1981) who observed no systematic change in the strength of Galesville sandstone in triaxial compression at temperature between 37°C and 204°C, as did Serdengecti and Boozer (1961) on Berea sandstone and Pala gabbro over a temperature range 26-149°C.

Experiments conducted at higher temperatures have shown that temperature does not become an important factor in the physical properties of rock until it reaches 300°C in the case of granites (Lockner 1998, Odedra 1998). At these high temperatures, the rock strength decreases with increasing ductility (Jaeger and Cook 1979, Cook 1981, Fischer and Paterson 1989) as chemical processes such as stress corrosion are greatly enhanced (Odedra 1998, Ojala 2003). The increase in temperature also decreases the initially accessible pore space and therefore the magnitude of volume change during strain deformation (Fischer and Paterson 1989). The effect on frictional sliding also changes around 200-300°C with the stick-slip/stable sliding transition (Ranalli 1995).

9.2.2 Effect of Temperature on the Electrical Potential Signals During Shear Failure

At present, there is no general agreement concerning the temperature dependence of the zeta potential. Morgan et al. (1989) found that the zeta potential of granite samples is temperature independent while Somasundaran and Kulkarni (1973) and Ishido and Mizutani (1981) found that the zeta potential of quartz increases with temperature. A recent study by Reppert and Morgan (2003a) summaries the main experimental papers conducted at temperature and puts the fact that no agreement is reached down to the different methods used to investigate the electrical and streaming potential signals. This includes an a.c or d.c streaming potential measurement system under various atmospheric conditions on quartz, Fontainebleau and Berea sandstone with different electrolytes such as NaCl or KCl or K₂SO₄ or CaCl₂ and different equilibrium conditions (time).

Initial values

The effect of temperature on confining pressure and the electrical potential signal is demonstrated in Figure 9.12. In the experiment where temperature can be seen to influence the electrical potential signal there are both mechanical and chemical effects. At 200 seconds the furnace is turned on, shortly

afterwards the heat begins to spread out from the heating coils and into the confining medium (silicone oil). The oil thermally conducts the temperature and undergoes thermal expansion. This has the mechanical effect of increasing the confining pressure with temperature. This pressure effect closes pore space which also reduces the surface area for the EDL to form and as a result causes the electrical potential to decrease with increasing confining pressure agreeing with observations by Clint (1999). At 1900 seconds the furnace reaches the desired temperature of 162°C and the power switch is switched on and off to maintain the furnace temperature to an accuracy of ± 5°C. The confining pressure increase tails off and when all the oil is at the same temperature the confining pressure remains constant (as seen at 4000 seconds). At 2300 seconds the chemical effect of the temperature increase is observed with a linear increase in the electrical potential signal at all four electrodes. This temperature effect is observed for up to 30 minutes, at which time the rock has reached thermal equilibrium and the potential signal levels off. This shows that temperature reduced the electrical potential signal indirectly by a mechanical increase in effective pressure and directly through chemical changes to the EDL mechanisms.

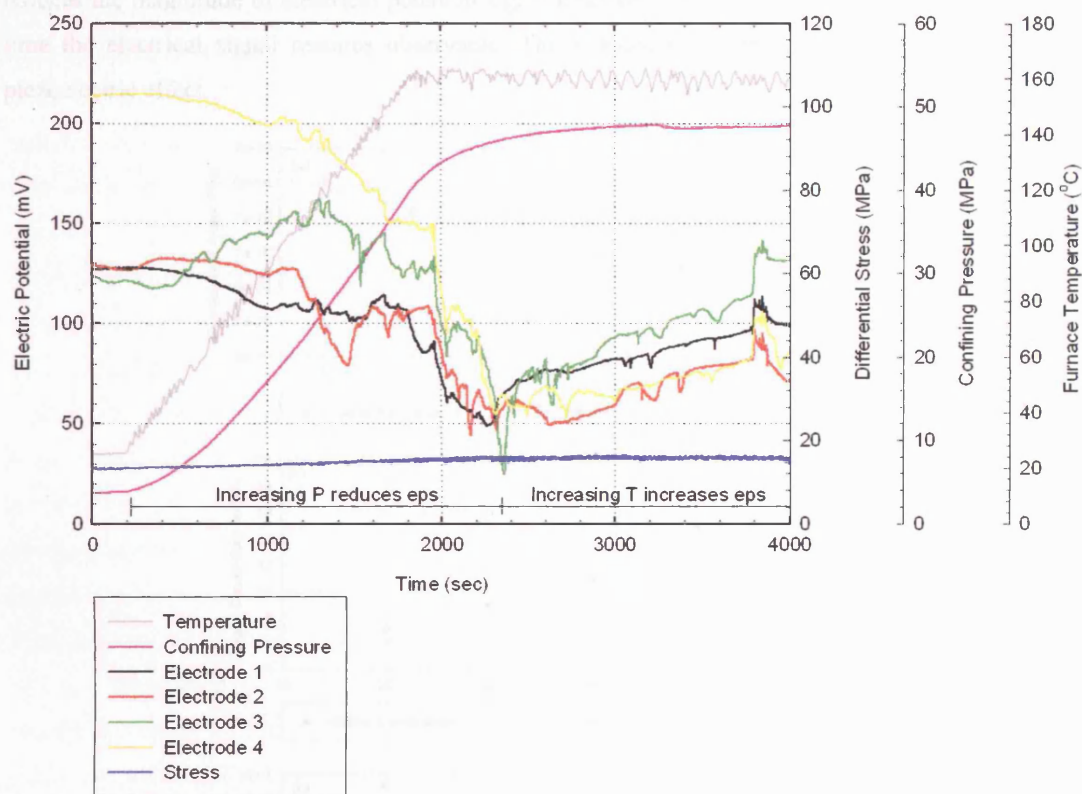


Figure 9.12: Applying a temperature of 160°C to a Clashach sandstone sample and the corresponding effect on the differential stress, confining pressure and electrical potential signals. [Experiment No.: 40]

Wet and Dry Samples

The effect of saturated and air-dried samples at temperature on the electrical signals during deformation can be seen from the results presented in Chapter 8.3 and 8.4 for Portland limestone and Clashach sandstone. As noted in Chapter 7, the piezoelectric effect is the main phenomena responsible for the electrical signal in water-free conditions; which is also the case for rocks heated to 50°C. During deformation at 50°C under air-dried conditions, a maximum potential change of 5 mV is observed compared to nearer 90 mV at 25°C. At failure, a co-seismic signal of 10 mV is observed which is approximately 3 times smaller than the signal observed at 25°C; and then decays rapidly (5 seconds) to

the value just prior to failure and continues to vary slightly until the experiment is stopped. This increase of 25°C significantly reduces the piezoelectric effect. As noted in Chapter 3.4.1 if the stress drop is greater than the electrical relaxation time, then the stress-induced polarization appears as an effective polarization which can be seen outside the rock as an electrical signal with a polarity depending on the electrical axis of the crystal. The relaxation constant is defined as

$$\tau = \epsilon_p / s \tag{3.6}$$

where ϵ_p is the permittivity and s denotes the electric conductivity. This is shown for wet conditions but this also applies under air dried conditions. With increasing temperature the permittivity decreases (Figure 9.13a), but it also increases the atomic activity by increasing the rate of collisions between particles which increases the conductivity of the pore fluid (Figure 9.13b). This reduces the relaxation time (Figure 9.13c) which reduces the ability for polarisation to occur across a crystal grain and therefore reduces the magnitude of electrical potential signal observed for the whole rock as well as the length of time the electrical signal remains observable. The reduced co-seismic signal is probably due to the piezoelectric effect.

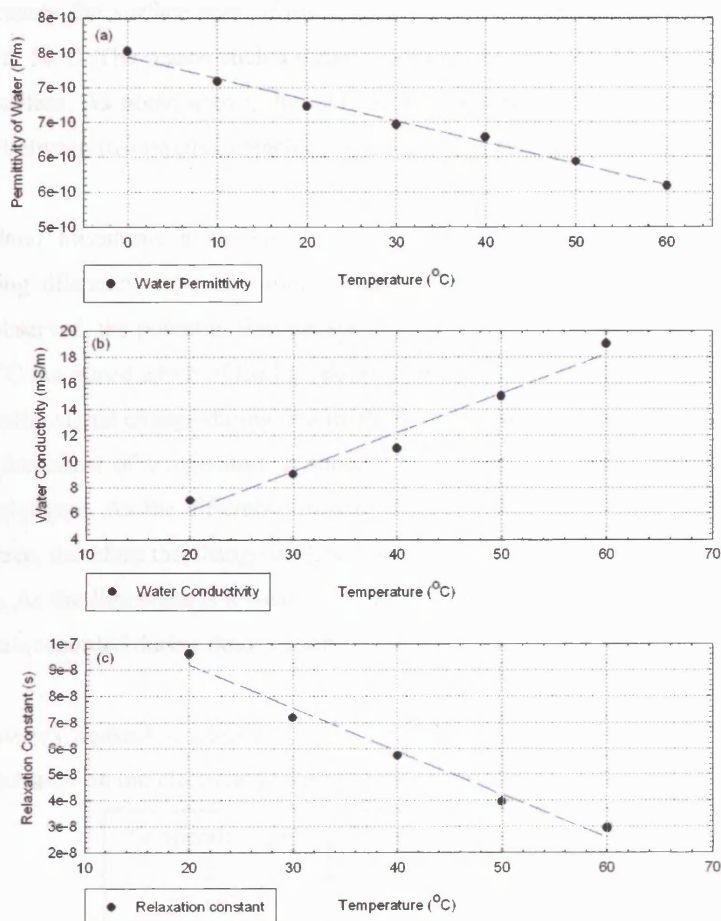


Figure 9.13: The effect of temperature on the (a) water permittivity, (b) water conductivity and (c) electrical relaxation constant. Data on permittivity from Hill (1969) and data on water conductivity from Reppert and Morgan (2003b).

The effect of temperature on Portland limestone was investigated as a side project to identify the differences in electrical and mechanical properties between different rock types. Under water-free conditions, a link between deformation and electrical potential is only observed at failure, which agrees with room temperature experiments. With no pore fluid and no piezoelectric crystals present within the limestone, the electrokinetic and piezoelectric effects can be ruled out as the source mechanisms. Therefore, a different mechanism such as variation in the electromagnetic field through movement of the ram which coincides with rock failure could be responsible for the electrical signal.

Under water-saturated conditions, the electrokinetic mechanism is the main source for the electrical potential signal in rock during deformation as noted earlier in Chapter 9.1.1. With a temperature increase of 25°C in Clashach sandstone, a similar shape in electrical potential is observed during the deformation cycle which shows that the electrokinetic mechanism applies at higher temperatures. With the increase of stress the potential increases by 70 mV up to failure which is equal to that observed at room temperature. At failure a pre-seismic and co-seismic signal are seen which decay away slowly and becomes constant at 2000 seconds. After failure, there is no observable increase in the electrical potential signal as seen at room temperature. If the signal identified at 25°C is due to mechanical changes such as forming fault gouge, which increases the surface area of the crystals exposed, then this same mechanism would be expected to occur at 50°C. The reason such a signal would not be seen can be explained by the electrical relaxation time constant. As noted above, the increase in temperature reduces the time required for the electrical gradient between two points to reach equilibrium. This also applies across the double layer.

In saturated Portland limestone, a similar pattern is present as observed during room temperature experiments. During dilatancy the pore volume change increases up to dynamic failure where a co-seismic signal is observed, the potential then decays away to a background level. However, at an elevated temperature of 50°C the introduction of load produces a decrease in electrical potential signal. As loading continues the potential signal change during deformation is superimposed on a linear increase in potential. From Figure 8.8 the effect of temperature is found to significantly reduce the fluid flow rate and the streaming potential signal. As the difference in temperature is only 25°C, very little thermal expansion will have taken place, therefore the change in fluid flow is related to the chemical interaction of the water and the limestone. As the limestone is a weak rock, some of it will dissolved into the pore fluid and this affects the potentials recorded during deformation.

During deformation of Clashach sandstone

The effect of temperature on the electrical potential signal prior to deformation is shown in Table 9.4.

Temperature (°C)	Electrical Potential (mV)
25	58.1
50	102.0
75	121.2
100	194.8
125	210.6

Table 9.4: The average value of the electrical potential signal prior to deformation of Clashach sandstone between a temperature of 25°C and 125°C under an effective pressure of 20 MPa. Calculated from Figure 8.15. Each value is given to an accuracy of ± 0.1 mV.

These values were obtained by heating the rock samples to the desired temperature and then applying a pore pressure of approximately 20 MPa in order to create an effective pressure of 20 MPa on the sample. The rock was then left under these conditions until the confining pressure and electrical signals became constant which took approximately 30 minutes. Once T, P and electrical potential are constant the experiment was started. From Table 9.4, it can be seen the electrical potential increases with temperature and had an average increase of 38 mV per 25°C. As the electrical potential is related to the zeta potential, it shows indirectly that the zeta potential increases with temperature. This agrees with the observations made by Ishido and Mizutani (1981), Revil et al. (1999a) and Reppert and Morgan (2003b) during static experiments. Ishido and Mizutani (1981) used a water bath and cell assembly with d.c fluid flow to investigate the pH and temperature dependence in relation to the zeta potential. This produced a model which was used by Revil et al. (1999a) to show an increase in zeta potential with temperature. Reppert and Morgan (2003b) used AC streaming potential measurements to investigate the zeta potential showing that the ζ -potential dependence on temperature is primarily controlled by the surface charge density (absorption properties) which affects the Stern layer and hence the properties of the EDL. The use of the Revil and Glover model accounts for much of this change in surface charge density. Revil et al. (1999a) showed that the ζ -potential can be calculated from equation 9.1:

$$\zeta \approx \varphi_d = \frac{2k_b T}{3e} \ln \left(\frac{\sqrt{8 \cdot 10^3 \varepsilon_f k_b T N}}{2e\Gamma_s^0 K_{(-)}} \left(\frac{C_a + C_f + 10^{-pH}}{\sqrt{I}} \right) \times \left(10^{-pH} + C_f K_{Me} \right) \right) \quad (9.1)$$

Where φ_d is the Stern plan potential, k_b and k_{me} are the Boltzmann constant and equilibrium constant, $K_{(-)}$ is the dissociation constant, C_a and C_f is the concentration of the acid and electrolyte respectively, ε_f is the permittivity of electrolyte solution, Γ represents the surface site density, N is the Avogadro's number, I is the ionic strength, T is temperature and e is the charge of an electron. Equation 9.1 is comparable to equation (18) of Ishido and Mizutani (1981) (a Langmuir isotherm-type relationship), which is shown in Figure 9.14. Temperature is also indirectly related to ζ -potential through the temperature dependence of the dielectric constant of the electrolyte solution and the temperature dependence of the surface equilibrium constants, where temperature increases produce more negatively charged surface sites ($>SiO_2^-$).

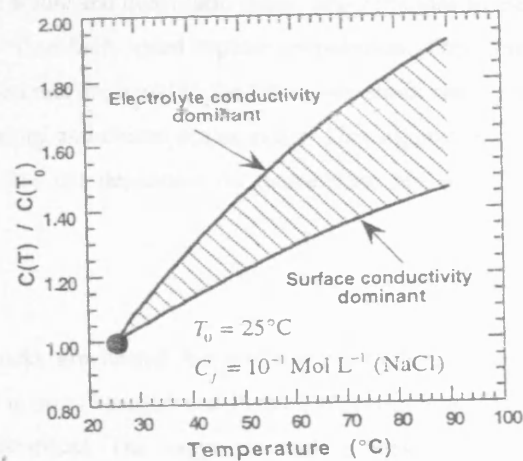


Figure 9.14: Temperature dependence of the streaming potential coupling coefficient ranging between electrolyte conductivity dominant (fluid) and surface conductivity dominant (Taken from Revil et al. (1999a)).

During the deformation of Clashach sandstone at the strain rate of $1.5 \times 10^{-5} \text{ s}^{-1}$, the total potential signal change was found to be independent of temperature, remaining constant at around 75 mV. As this temperature range does not appear to affect the mechanical properties, any changes observed are due to the thermo-chemical reactions. Experiments conducted by Morgan et al. (1989) found no link with temperature, but they allowed only 4 hours for the chemical equilibrium on the silica surface to be reached. However, Somasundaran and Kulkarni (1973) and Ishido and Mizutani (1981) used much longer equilibrium times and found a relationship with temperature thereby suggesting that the reaction at the crystal surface takes several tens of hours. Therefore, with a fast strain rate of 10^{-5} s^{-1} , the reaction between the newly created surface formed during dilatancy and the pore fluid does not reach equilibrium and therefore the temperature does not affect the EDL and the potential change up to failure remains the same.

Pre-seismic and Co-seismic signals

For the signals around failure (pre and co-seismic), no link could be established between temperature and electrical potential signal, with a large variation in potentials between the electrodes. As noted above, it takes over 30 minutes to obtain a steady electrical signal. Therefore with the pre and co-seismic signals occurring over a couple of seconds, the crystals and pore fluid do not reach equilibrium and these signals appear independent of temperature. The fact that thermal equilibrium is not reached agrees with Ishido and Mizutani (1981) who notes that the time to reach equilibrium is much greater at temperature.

At the crustal scale, strain rates of 10^{-14} s^{-1} exist. At these strain rates the crystal surfaces would reach thermal equilibrium as the crystal movement is minimal. Ohnaka et al. (1987) notes that the rupture which leads to failure propagates slowly at first, and then gradually accelerates into a quasistatic phase and finally into an unstable accelerating phase where the rupture velocity can reach a sonic speed. Main (1988) described the maximum fault rupture length of 300 km with ruptures from 100 m – 100 km with growing rates of $10^{-9} - 10^{-5} \text{ m/s}$ to be present at the beginning of the nucleation phase of an earthquake. Basing the calculation on a 100 km fault with 100 m displacement before failure, the laboratory strain rate of 10^{-7} s^{-1} corresponds to a normalised shear velocity (V/V_s) of 10^{-4} . Ohnaka (2004) has normalised shear

velocities of 10^{-5} during the stable and quasistatic phase, and velocities in the unstable accelerating phase ranging from 10^{-4} to 10^0 – then high speed rupture propagation. Therefore, just before an earthquake occurs the strain rates in the crust are equal to the laboratory strain rates and therefore in this region the same trends between laboratory and crustal scales exists. This suggests therefore, that around failure the electrical potential signals are not dependent on temperature but on mineral composition, pH, fluid chemistry and fluid flow.

Healing

Within the Earths crust, rocks are heated for prolonged periods of time. Here the effect of heating increases the dissolution of quartz (Fournier and Potter 1982) which may be transported somewhere else in the rock and then recrystallised. The longer the rock is heated, the less pure the deionised water becomes. As noted by Jouniaux and Pozzi (1997) and Clint (1999), the purer the water the higher the zeta potential and hence the higher the electrical potential becomes. In this study, the water becomes more impure the longer it is heated, however the streaming potential increases whilst the fluid flow remains approximately constant after the first cycle. This indicates that a change at the crystal surface may be occurring such as cleaning, which increases the potential. This could be investigated using glass beads which have been allowed to react with different materials and fluids. By placing the reacted beads in deionised water and by performing fluid flow experiments across the glass surfaces, the streaming potentials could be measured and the pore fluid analysed to identify changes to the glass surface.

9.2.3 Discussion of the Effect of Temperature on the Streaming Potential Signal

The ζ -potential depends on mineral composition, ionic strength, pH and temperature as shown in Figure 9.15 and 9.16 (Ishido and Mizutani 1981).

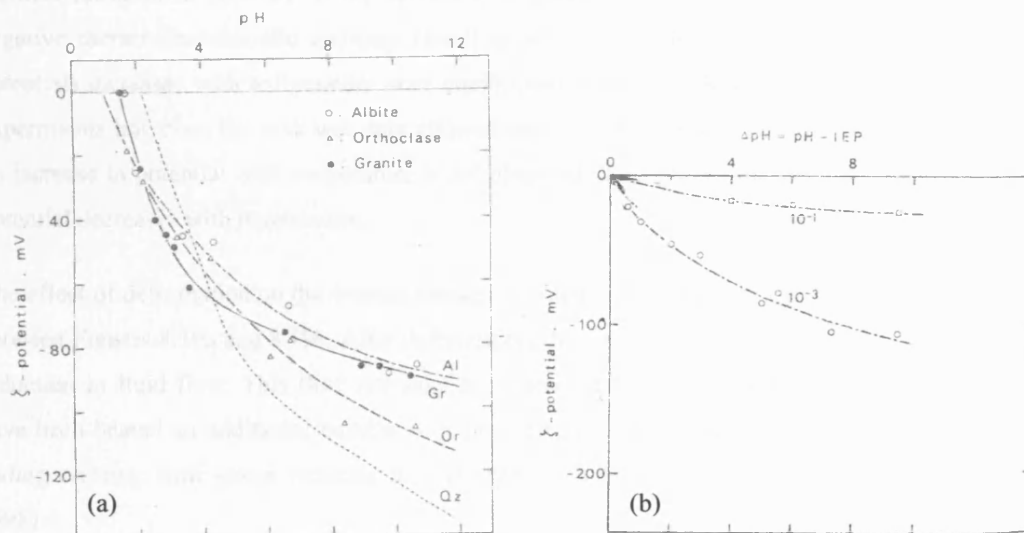


Figure 9.15: (a) Variation of the zeta-potential of (a) orthoclase, albite and granite as a function of pH in aqueous solution of 10^{-3} KNO₃ with Q_z representing the data for the quartz and (b) orthoclase as a function of pH. Temperature is set at 45°C with aqueous solutions of 10^{-3} and 10^{-1} KNO₃. (After Ishido and Mizutani (1981))

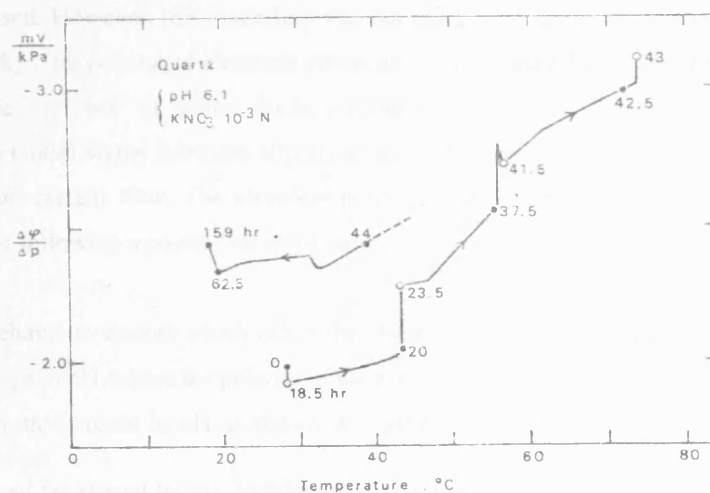


Figure 9.16: Variation of the streaming potential coupling coefficient for quartz as a function of temperature in an aqueous solution of 10^{-3} KNO_3 . The initial value at a temperature is shown by solid circles, and the final value is shown by open circles. The numbers attached to the data points indicate the elapsed time from the beginning of the experiment to each measurement. (After Ishido and Mizutani (1981))

Figures 8.19 and 8.20 show the effect of temperature on the streaming potential signal and fluid flow at high pore pressures, before and after failure. Figure 8.20 shows that the fluid flow decreases with temperature up to 100°C , at 125°C the flow rate has increased above that of 75 and 100°C ; therefore a temperatures increase generally decreases the fluid flow. This trend has been observed by Fischer and Paterson (1989) on Gosford sandstone, Tenthoey et al. (1998) on sand and Ojala (2003) on Clashach sandstone. With the decrease in fluid flow, the streaming potential signal also decreases in magnitude. The link between fluid flow and potential signal can be seen with an up-welling generating a positive thermoelectrokinetic anomaly at the surface of a geothermal field and a down-welling generating a negative thermoelectrokinetic anomaly (Revil et al. 1996b). However, the zeta potential (streaming potential) increases with temperature once equilibrium is reached (Revil et al. 1996b). In this series of experiments however, the rock was only allowed approximately 30 minutes to equilibrate and as a result an increase in potential with temperature is not observed. With the decrease in fluid flow, the streaming potential decreases with temperature.

The effect of deformation on the average streaming potential reading is shown by the potential difference between Figures 8.19a and 8.19b. After deformation, the streaming potential decreases slightly due to the reduction in fluid flow. This flow rate may be affected by thermal expansion because the sample will have been heated an additional number of hours after deformation and/or due to the effect of frictional sliding creating fault gouge reducing the permeability across the fault (Zhu and Wong 1996, Keaney 1998).

9.2.4 Effect of Temperature and Simulated Formation Waters on Electrical Properties of Clashach Sandstone

For all experiments conducted with simulated formation waters (SFW), the electrical potential signals changed during rock deformation. To investigate these results I have initiated some molecular dynamical modelling to investigate the interaction of double layer at the molecular scale. Here I outline a methodology to illustrate how this modelling should be tackled, as it illustrates outstanding questions that

need to be addressed. However, this modelling was not completed due to problems discussed in Chapter 10.2 (Future Work). The amount of electrical potential signal change during deformation is significantly different with the presence of saline fluids compared to deionised water at temperature. During compaction the potential signal increases slightly as pores are closed, expelling fluids and electrical ions through convection current flow. The electrical potential during dilatancy increases around the elastic limit of the sample following a power-law up to failure.

To explain this behaviour, factors which affect the electrokinetic phenomenon must be included in this modelling. A change in pH causes the polarity of the zeta potential to alter from a positive value to a more negative one with an increase in pH as shown in Figure 9.15 (Ishido and Mizutani 1981, Lorne et al. 1999b). The pH can be altered by the addition or subtraction of ions such as SO_4^{2-} or Al^{3-} (Ishido and Mizutani 1981, Lorne et al. 1999b). The electrolyte concentration may also cause a decrease in zeta potential as discussed by Revil et al. (1999a). The effect of temperature must also be included, which at a fixed concentration, the ionic conductivity is approximately one order of magnitude higher at 0°C than at 140°C (Gueguen and Palciauskas 1994). Also a decrease in surface conductivity is observed from 25°C to 125°C for La Peyratte granite (Glover et al. 1995).

The change in electrical potential may therefore be explained by changes to zeta potential by variation in pH of the saturating fluid (see Figure 9.15). During deformation Si, K, Na, Mg and Al increase in ionic concentration (Ojala 2003). The availability of such ions could produce reactions with the quartz cement as suggested by Lorne et al. (1999a) or reactions with the newly formed crack surfaces during dilatancy to increase the potential.

Pre-seismic and Co-seismic signals

The effect of SFW and temperatures of up to 75°C causes the precursory electrical potential signal to decrease below the background electrical noise. During strain softening, subcritical cracks coalesce leading to fluid flow and electrical current flow as discussed above resulting in a difference in electrical potential signal across the sample (e.g. the electrical potential change). With pure water, the conductivity of the water is much less than that of the SFWs. This is because ions such as Cl^- (Table 9.5) are more massive than the OH^- so that the EDL form with the ions such as Cl^- rather than disassociating H_2O . With the higher conductivity of ions present in the pore fluid which is enhanced further by the addition of temperature. This is shown in Figure 2.29 where different salts such as $MgCl_2$ and H_2SO_4 have different conductivities and where temperature increases the conductivity for a given salinity. The effect of concentration has been investigated by Clint (1999) over the range of 0.2 to 4 M for NaCl, who found that the zeta potential decreases non-linearly due to a decreasing Debye length. This relationship between a binary electrolyte and concentration is given by Revil et al. (1999a) who explains the behaviour due to changes in pH. However, the effect of electrolyte over the cycle of deformation varies (compaction and dilatancy) as found by Clint (1999). A reduction in the time constant also occurs which suggests that spontaneous electrical signals such as those around failure decay more rapidly so that precursory signals may not be detected.

Ionic Species	Ionic Radius / pm
O ₂ ⁻	126
Na ⁺	95
Cl ⁻	181
OH ⁻	155
F ⁻	136

Table 9.5: Ionic radii of most common species present in SFWs.

Co-seismic signals are evident during dynamic failure as shown in Figure 8.25 with the values plotted in Figure 8.26 showing that it decreases linearly with increasing temperature over the range investigated here. The linear fits have been extended to the axes to show that with these formation fluids, above 110°C the co-seismic signal will not be observed above the background electrical noise. This is thought to be due to the nature of the co-seismic signal and the effect of elevated temperatures on fluids. The electric signal peak at failure is created almost instantaneously through the rapid coalescing of many cracks leading to macroscopic failure. With the increase in temperature, which excites the pore fluid molecules such as Cl⁻, the pore fluid conductivity will increase, therefore the electrical potential signal will decrease and decay away rapidly as the electrical relaxation time constant gets smaller. Because this process takes place over a very short period of time, the newly formed macro fault will not reach chemical equilibrium with the elevated temperature; therefore the zeta potential will remain constant.

Based on the results described above the effect of temperature and pore fluid chemistry on the pre-seismic and co-seismic electrical potential signals is shown in Figure 9.17. For deionised water, temperature has no effect and remains approximately constant. However, fluid which contains dissolved ions such as NaCl and KCl and at elevated temperature causes the decrease in potential. Depending on the salinity and the temperature, the pre and co-seismic electrical signals will be lower than the background signal and therefore not observed.

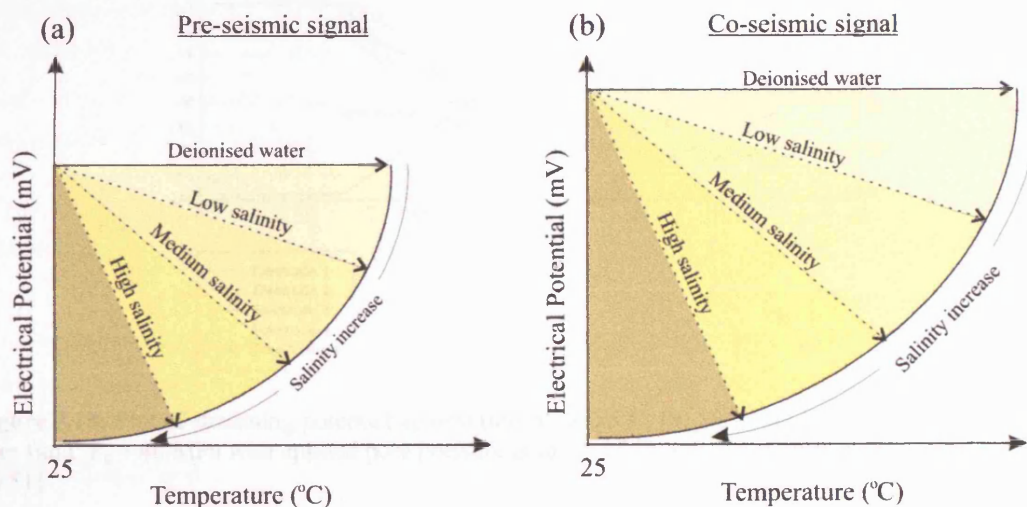


Figure 9.17: Schematic plots showing how the increase in pore fluid salinity causes a decrease in pre-seismic and co-seismic signals in relation to elevated temperatures.

Streaming Potential Signals

The streaming potential signal for the simulated formation fluids is shown in Figure 9.18 for temperatures at 25°C, 50°C and 75°C. At 25°C the typical streaming potential signal is observed with a rapid change in potential following the initiation of fluid flow and remains constant until the fluid flow is stopped and the potential increases or decreases.

At the higher temperatures the streaming potential takes longer to reach the charge difference as the relaxation time constant is shorter as shown in Figure 9.13c. The conduction current dissipates so fast that the change in potential takes longer to build up and therefore longer to produce the convection current. This is shown by the difference in shape of the potential signal shown in Figure 9.18b and 9.18c. At 50°C the decrease in potential with initiation of fluid flow is not as rapid as at 25°C and neither is the increase after fluid flow is stopped. At 75°C, with fluid flow the streaming potential decreases at a set rate until the fluid flow stops. At this point the potential increases slowly up to a value lower than before the fluid flow began.

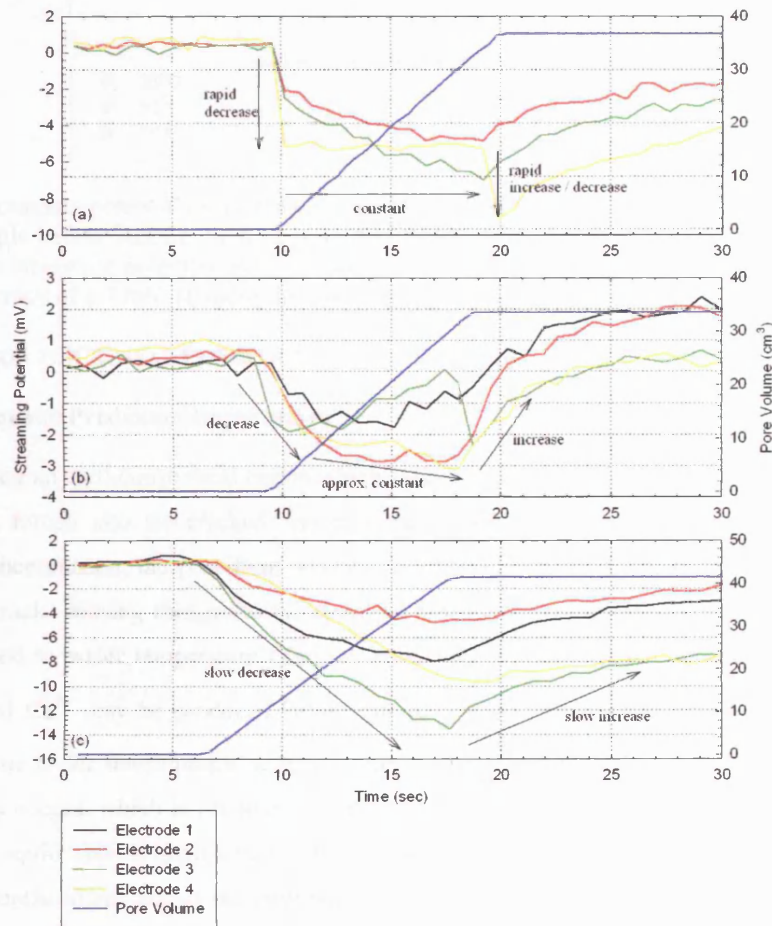


Figure 9.18: Plot of streaming potential against time at (a) 25°C, (b) 50°C and (c) 75°C using SFW#2 as pore fluid; $P_c = 40$ MPa with applied pore pressure gradient of 15 MPa. [Experiment No.: (a) 49, (b) 50, (c) 51]

From Figure 9.19, it can be seen that the increase in applied pore fluid pressure has no effect on the overall change in streaming potential. This is because the SFW and temperature produce a maximum charge difference across the sample. No matter how fast the fluid travels through the rock the maximum

difference between the positive and negative ions remains the same. A link between the magnitude of the streaming potential signals and temperature is not observed, with the lowest potential at 50°C, then 25°C and the highest signals at 75°C. This requires further investigation through both laboratory experiments and molecular dynamical modelling of the EDL to improve our understandings of what is occurring.

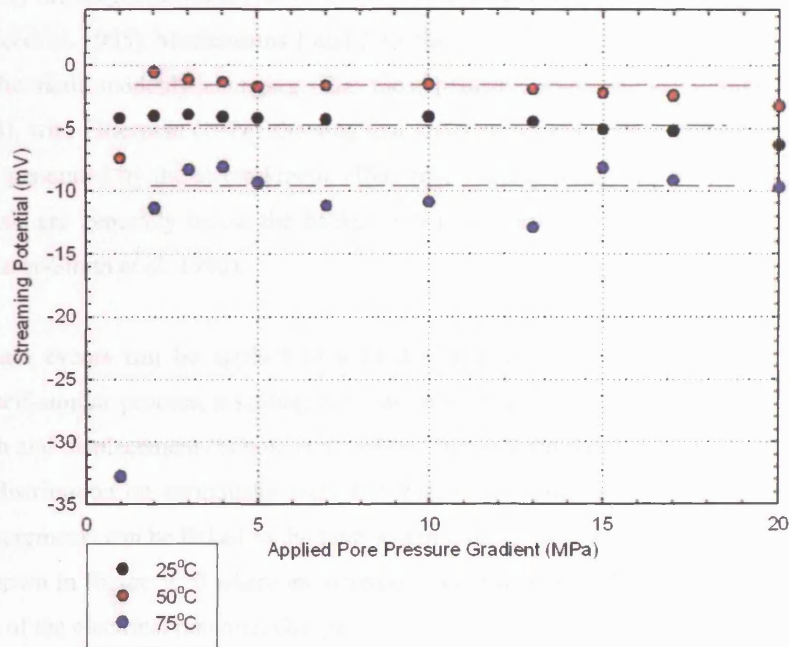


Figure 9.19: Streaming potential measurements generated under increasing pore pressure gradients across a Clashach sample before fracture. SFW#2 is used as the pore fluid, $P_e = 20$ MPa. The broken lines show no link between streaming potential and pore pressure gradients at different temperatures. Each point is given to an accuracy of ± 3 mV. [Experiment No.: 49, 50, 51]

9.3 APPLICATION TO CRUSTAL CONDITIONS

9.3.1 Earthquake Prediction Implications

When considering an earthquake focal region which is undergoing fracture nucleation and coalescence of cracks, fluid is forced into the cracked region under a positive pore pressure gradient. Through the electrokinetic phenomenon, the pore fluid produces a convection current which redistributes the charge into the fluid/cracks causing changes to the electrical potential of the order of mV. This conductivity is closely correlated to water temperature (Zmazek et al. 2002) where various ions such as HCO_3^- , Cl^- , SO_4^{2-} , Na^+ and Ca^{2+} may be produced before failure (Favara et al. 2001) thereby altering it. When failure occurs due to the development of a new fault or movement along an old fault, an instantaneous change in stress occurs, which is accompanied by a peak or trough in electrical potential signal which decays away as equilibrium is approached. If the fault is not sealed, then a pressure gradient will generate a streaming potential signal across the fault which will remain steady until the flow is interrupted. The interaction could include movement of the fault.

If an electrode is located near to or on the fault, then the pore fluid movement, which may occur just prior to fault movement can generate a precursory electrical signal. At failure, the signal received from an electrode close to the fault will show a higher magnitude than those further away. Thereafter the signal is

erratic due to electrical signals leaking from the fault and/or bad contact between the fault and the electrode.

As well as electrokinetic signals, magnetic anomalies have also been observed which have been linked to electrical potential signals. Three mechanisms put forward to generate the ultra low frequency (ULF) emissions are, 1) the magnetohydrodynamic effect, 2) the piezomagnetic effect and, 3) the electrokinetic effect (Fenoglio et al. 1995). Mechanisms 1 and 3 are the result of fluid flow, whilst 2 is produced by high pressures in the fault suddenly changing. The most plausible explanation is fluid flow (Michel and Zlotnicki 1998), with Fitterman (1978) showing that under reasonable pressure gradients the electric and magnetic field generated by the electrokinetic effect reach values which can be detected. Seismic related magnetic signals are generally below the background level and can hardly be detected without special techniques (Fraser-Smith et al. 1990).

Laboratory scale events can be applied to a field situation of the order of km. With fault growth considered a self-similar process, a scaling law can be applied to all locations with a linear dependence between length and displacement (Scholz et al. 1993). This self-similarity can also be recognised through a power-law distribution on earthquake sizes and magnitudes (Sammonds et al., 1992). The electrical potential measurements can be linked to the fault length through the mean crack length described in Main (1991), and shown in Figure 9.20 where an increase in fault length produces a corresponding increase in the magnitude of the electrical potential change

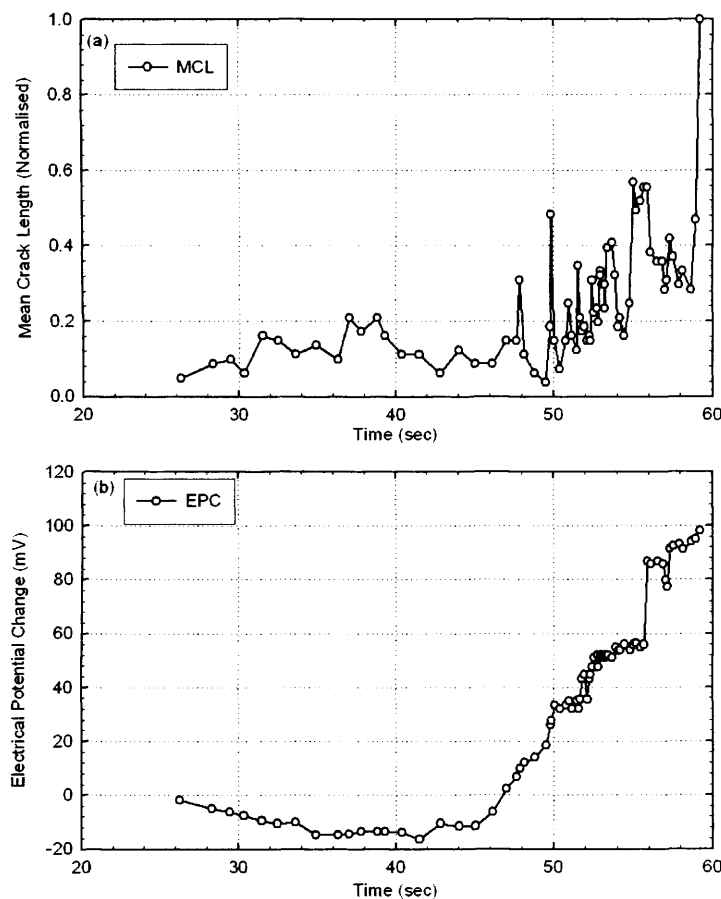


Figure 9.20: The variation of (a) the Mean Crack Length and (b) electrical potential change during the deformation of Clashach; effective pressure of 20 MPa with strain rate of $1.5 \times 10^{-4} \text{ s}^{-1}$. Each point plotted is given to an accuracy of (a) ± 0.01 and (b) $\pm 0.2 \text{ mV}$. [Experiment No.: 21]

The only problem is that there are many potential sources for electrical signals other than a fault, and there is a severe problem providing a correct order of amplitude for electric signals measured hundreds of kilometres away from the fault due to the heterogeneous nature of crustal rocks.

9.3.2 Implications for Shallow Crustal Exploration

Application to hydrocarbon industry

The electrokinetic phenomenon can be used by the hydrocarbon industry to obtain information on the microstructure of the bulk rock in a reservoir. Sprunt et al. (1994) shows that the presence of gas or oil (non-wetting) on the interconnected pore space can significantly affect the streaming potential coupling coefficient (Cs); while steam in porous rocks does not produce a substantial streaming potential signal. In fact, Cs is significantly higher in an oil-rock system than the water-rock system (Rutgers et al. 1959) with the presence of gas within the interconnected pore space enhancing Cs by a factor of 3 or 4 (Morgan et al. 1989). The electroseismic methods which generate a mechanical pulse can be used to generate a streaming potential signal in a borehole down to a depth of 300 m (Thompson and Gist 1993). With this technique, formation boundaries can be identified (Russell et al. 1997) without altering the stress state of the rock by changing the pore pressure or pore volume. As well as using the streaming potential signal to identify the different rock types present, the potential can also be used to identify changes in the rocks permeability as shown in Chapter 9.1.4, where a decrease in permeability has a corresponding decrease in streaming potential signal. As permeability gives some indication of the rock porosity through an empirical relation (Gueguen and Palciauskas 1994), the streaming potential signal can also be used to gauge the amount of pore space present

The presence of electro-magnetic anomalies associated around geologically active areas has been shown by numerous authors including Fitterman (1978), Fenoglio et al. (1995) and Fedorov et al. (2001). As mentioned previously, the most plausible theory to generate the streaming potential signal is due to fluid flow caused by a pore pressure gradient. Numerical simulations have shown that the signal which would be produced by pumping down oil boreholes would only be a few millivolts and would travel a limited distance (Wurmstich and Morgan 1994). This distance would be enhanced if a highly conductive region existed. However, this technique could be used at the well end where a constant pore pressure exists to help identify the appearance of damage zones formed by the drilling process.

For Clashach, Bentheim and Darley Dale sandstone and Portland limestone an upper pore pressure gradient of 30 MPa could be applied across the sample with streaming potential reaching equilibrium; above this value equilibrium was not obtained. As a decrease in streaming potential was observed with a decrease in permeability (Jouniaux and Pozzi 1995a, Clint 1999), the relationship between streaming potential and permeability would be a useful tool for the hydrocarbon industry, at the drill end, to identify how the drilling mud moves into the surrounding rock.

Geothermal Reservoirs

Geothermal areas are known to produce self potential anomalies of the order of a few hundred mV (Corwin and Hoover 1979, Morgan et al. 1989) which in turn can produce magnetic anomalies of tens of

nT. The most important mechanism for the generation of the electric signal is the electrokinetic effect where fluid circulation produces streaming potential signals (Ishido and Mizutani 1981). The SP depends on the surface conductivity, porosity, permeability and fluid chemistry. Analysis of hydrothermal circulation systems by Zlotnicki (1986) shows that thermoelectric currents are present in volcanoes with change in voltage linked to temperature changes ($0.2 \text{ mV}/^\circ\text{C}$). Figure 9.21a represents a model of how the movement of fluid within a volcano would produce positive and negative self potential signals. With the upflow of hot, saline fluids the potential signal would be positive, but with cold fresh water a negative potential signal would be produced. Therefore, the likely self-potential signal observed across the volcano would be as shown in Figure 9.21b.

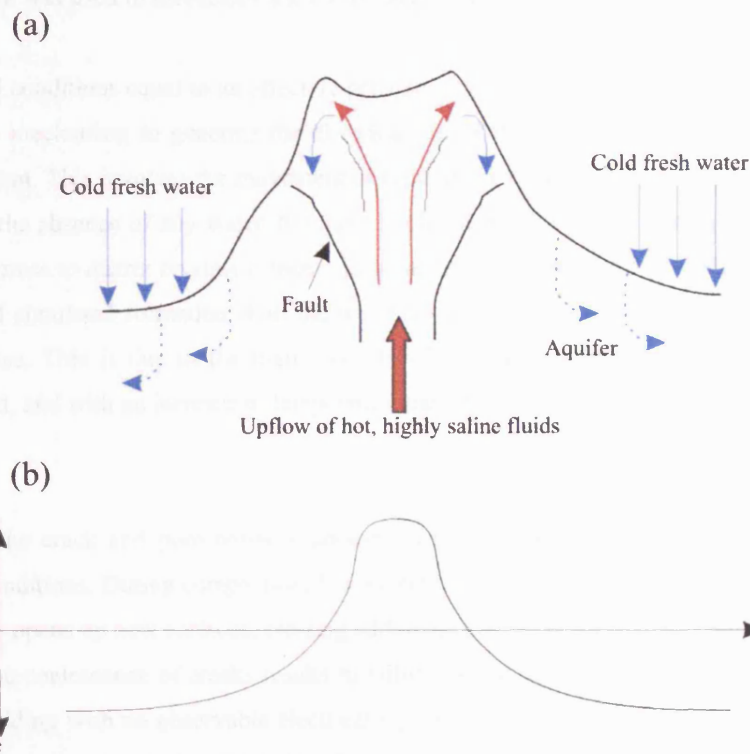


Figure 9.21: The variation of the self-potential signal across an active geothermal area with regions of upflow and downflow.

As noted above, temperature changes the fluid chemistry and conductivity and can change the porosity and permeability if the temperature is high enough. Therefore, SP signals can be used to show the direction of temperature gradients which are related to the movement of fluid in hot springs, solfatara, hydrothermal zones and ground water areas.

10. Conclusions and Future Work

10.1 CONCLUSIONS

Laboratory experiments were conducted on a triaxial rock physics cell to investigate the electrical potential difference, electrical potential change, streaming potential and acoustic emissions at a range of temperatures of up to 125°C, during various stages of deformation on a variety of rock types. The electrical potential difference was measured using an array of electrodes with streaming potential values being determined using a steady-state flow method. An array of four electrodes for the electrical signals and eight transducers were used for the acoustic emission measurements. The effect of rock type, strain rate and temperature was used to investigate the electrical potential generation mechanism.

For shallow crustal conditions equal to an effective pressure of 20 MPa, equivalent to a depth of 1.33 km, the most plausible mechanism to generate the electrical signal is due to the electrokinetic phenomena when water is present. This involves the movement of fluid under a positive pressure gradient into newly formed cracks. In the absence of any water, the most likely mechanism is due to the piezoelectric effect where an applied stress to quartz crystals causes a localised polarization of the crystal. With the addition of temperature and simulated formation fluid the pre-seismic and co-seismic signals are reduced with a temperature increase. This is due to the high mobility of the ions, rapidly equilibrating the electrical potentials produced, and with an increase in temperature the ions are further excited thereby reducing the potential.

The tortuosity of the crack and pore network appears to control electrical current flow through rocks under simulated conditions. During compaction, low aspect ratio cracks are closed reducing the connected network. Dilatancy opens up new surfaces, creating additional pathways for hydraulic and electric current flow. At failure, the coalescence of cracks results in failure, which can cause a reduction in permeability during frictional sliding with no observable electrical signal after dynamic failure. The electrical current has been shown to produce a signal of the order of tens of millivolts from a 1 km reservoir maintaining a near-lithostatic pore pressure (Bernard 1992). Therefore, the electrical signal could be produced through a fluid flow mechanism, which could explain telluric signals occurring prior to earthquakes.

Fluid flow is the principal factor responsible for the electrical current flow during rock deformation. There is a linear relationship between electrical potential change and strain rate. The absolute electrical potential change during compaction and dilatancy decreases with a strain rate reducing to $1.5 \times 10^{-7} \text{ s}^{-1}$. This is the result of a decreasing amount of ionic charge being distributed within the sample. It is therefore possible that the electrical potential signal is not measurable at typical crustal strain rates.

The streaming potential linearly increases up to a pore pressure gradient of 30 MPa for Bentheim, Clashach and Darley Dale sandstone and Portland limestone. Non-linear potential is observed above this pressure gradient because the conduction and convection currents do not equilibrate – possibly due to turbulent fluid flow. The highest streaming potential observed of all the sandstones is Darley Dale which is an order of magnitude greater than Clashach and a further magnitude greater than Bentheim. The

highest permeability is however seen in Clashach and Bentheim sandstone, which have lower streaming potential varying by one order of magnitude; the highest streaming potential recorded is for quartz-free limestone. With a higher permeability, the conduction current will be greater, the convection current will equilibrate with this current leading to a reduction in the streaming potential assuming a constant pressure gradient and zeta potential and no change in the formation factor. The composition of the rock also strongly influences the streaming potential as Bentheim and Clashach have similar permeability but significantly different streaming potentials.

The effect of temperature on all electrical signals depends on the conditions imposed. In water-free conditions, the piezoelectric effect is believed to be the principal mechanism to generate an electrical signal. With a temperature of 50°C, the piezoelectric effect is significantly reduced during deformation, indicating that the heat reduces the ability for the quartz crystal to become polarised. Under water-saturated conditions, the electrokinetic phenomenon represents a plausible mechanism for generating an electrical potential signal at temperatures observed in the shallow upper crust. A temperature increase has been found to increase the zeta-potential if the rock is allowed to reach equilibrium (Revil et al. 1999a) which takes tens of hours. During deformation, the crystal surface does not reach equilibrium, so temperature seems to have no effect on the electrical potential signals during compaction, dilatancy, during failure and frictional sliding. With the addition of simulated formation waters, temperature reduces the potential signal change by exciting the ions present in the water. Around failure, the pre-seismic and co-seismic signals drop in magnitude so that at temperatures in excess of 150°C, no observable signal change would be observed around failure. Therefore, no electrical signal may be observed for an earthquake at depths of 4 km or more. In the case of streaming potential measurements, no direct dependence is found between that and temperature. However, temperature does reduce the permeability of the rock due to thermal expansion; this reduces the fluid flow as well as the streaming potential. The mechanical and chemical processes are believed to be similar with other crystal rocks such as limestone.

10.2 FUTURE WORK

In this investigation, the effect of temperature on the electrical potential signal generated during various stages of deformation with a rock temperature up to a maximum of 125°C is described. Existing work on electrical signals has concentrated on the ζ -potential, calculated from fluid flow experiments (Ishido and Mizutani 1981, Revil et al. 1999). This type of test is static, compared to a dynamic test, which occurs during deformation. Further investigation during deformation is required over a larger temperature range (e.g. 25-300°C) and during deformation; this includes examining the effect of rock type, pore fluid salinity, fluid flow rate, strain rate and pressures on the electrical potential signals generated. This is required to identify if trends present at room temperature (25°C) occur at high temperatures and how the temperature change effects the magnitude of the different types of electrical signals recorded. From this the data can be modelled to actual field situations in order to understand what is taking place. Geochemical analysis should also be investigated to link changes in electrical potential signal to rock and fluid chemistry to aid the understanding of the processes occurring at the EDL boundary.

To understand the electrokinetic phenomena in the laboratory and in the field setting better, further investigation is required to examine streaming potential, during torsion and creep experiments. Additional

experiments on a greater variety of rock types, including volcanic, carbonate and clay rocks are required. Electrical potentials and streaming potential must also be investigated over a wider permeability range such as the range investigated by Brace and Kohlstedt (1980).

From Figure 7.14, the effect of a fault passing through an electrode is shown. This should be examined in detail with a greater array of electrodes around the sample to identify possible applications to the field. These include earthquake prediction and fault location.

Laboratory electrical studies (Ishido and Mizutani 1981, Lorne et al. 1999b, Revil et al. 1999a, Brown and Haupt 2003, Eccles et al. 2004) can be linked to streaming potential signals during deformation (Jouniaux and Pozzi 1995b, Lorne et al. 1999a, Jouniaux et al. 2003) along with changes around failure (Yoshida et al. 1998, Yoshida 2001) and then linked to geophysical field investigations (Bernard 1992, Thompson and Gist 1993, Beamish 1999, Fedorov et al. 2001). This includes studying the different stages of deformation, such as compaction, dilatancy, crack nucleation, fault formation, and frictional sliding in terms of electrical and AE signals. This data can then be used in conjunction with field data to produce appropriate models (Zukoski and Saville 1986, Glover et al. 1996, Revil and Glover 1997, Revil et al. 1999a) that will further the understanding of the electrical potential signal.

Recent work has shown that the ζ -potential is the key parameter to understand the electrokinetic phenomena (Pride 1994). Computational models used to calculate the electrokinetic signal employ factors such as temperature, pressure, flow rate, pore geometry, fluid chemistry (Revil 1999b, Ishido and Pritchett (1999)) and pH and are based on the equations of the zeta-potential given in Ishido and Mizutani (1981). However, these models do not describe the formation of the double layer at the crystal or molecular level, but rather the charge at a given distance from the crystal surface.

Because the experimental data is difficult to interpret, computational modelling at the crystal and molecular level would provide useful information on the variations of the ζ -potential under different temperatures and pressures. The molecular structure and the formation of the double layer can be simulated through classical molecular dynamics (MD) simulations. This information can be used to derive theoretical models to predict the ζ -potential for a system under specific conditions, and applied to interpret the electrical potential signals from the samples investigated experimentally. The experimental data can then in turn be used to understand hydrothermal areas, volcanoes and earthquakes.

Future work is to perform computational model simulations at elevated temperatures and pressures to determine:

- 1) The characteristic of the double-layer and the zeta-potential as a function of temperature and pressure for the clean $\text{H}_2\text{O}/\text{SiO}_2$ interface.
- 2) The partitioning between cations at the interface and in the aqueous solution and to determine the effect on the ζ -potential.
- 3) The effect on the zeta-potential of pH.
- 4) Compare the inter-atomic model (MD) based on de Leeuw et al. (1999) to my experimental data.

References

- ABERCROMBIE, R. 1995. Earthquake source scaling relationship from -1 to 5ML using seismograms recorded at 2.5km depth. *Journal of Geophysical Research* **100**, 24,015 - 24,036.
- AKI, K. 1981. A probabilistic synthesis of precursory phenomena. *In: Earthquake prediction: an international review*. 1 – 16.
- ANTRAYGUES, P. AND AUBERT, M. 1993. Self-potential generated by two-phase flow in a porous medium: Experimental study and volcanological applications. *Journal of Geophysical Research*, **98**, 22,273 - 22,281.
- ARCHIE, G. E. 1942. The electrical resistivity log as an aid to determining some reservoir characteristics. *Trans. American Institute of Mineral Metallurgy and Petroleum Engineering*. **146**, 54 – 62.
- ATKINSON, B. K. 1979. A fracture mechanics study of subcritical tensile cracking of quartz in wet environments. *Pure and Applied Geophysics*, **117**, 1,011 – 1,024.
- ATKINSON, B. K. 1982. Sub-critical crack propagation in rocks: Theory, experimental results and applications. *Journal of Structural Geology*, **4**, 41 – 56.
- ATKINSON, B. K. 1984. Subcritical crack growth in geological materials. *Journal of Geophysical Research*, **89**, 4,077 – 4,114.
- ATKINSON, B. K. 1987. The theory of subcritical crack growth with applications to minerals and rocks. *In: Fracture mechanics of rock*. Atkinson, B., (ed) Academic Press, London. 111 – 166
- AVELLANEDA, M. AND TORQUATO, S. 1991. Rigorous link between fluid permeability, electrical conductivity, and relaxation times for transport in porous media. *Physical Fluids*, 2,529 – 2,540.
- AVES, P. 1995. Mechanics of compaction and dilatancy in triaxially stressed rocks, under simulated crustal conditions studied by pore volumetry. *PhD Thesis*, University College London.
- AYLING, M. R. 1991. An experimental study of physical property changes in crustal rocks undergoing triaxial deformation. *PhD Thesis*, University College London.
- AYLING, M. R., MEREDITH, P. G., AND MURRELL, S. A. F. 1996. Microcracking during triaxial deformation of porous rocks monitored by changes in rock physical properties. I. Elastic-wave propagation measurements on dry rocks. *Tectonophysics*, **245**, 205 – 221.
- BALME, M. R., ROCCHI, V., JONES, C., SAMMONDS, P. R., MEREDITH, P. G. AND BOON, S. A. 2004. Fracture toughness measurements on igneous rocks using a high-pressure, high-temperature rock fracture mechanics cell. *Journal of Volcanology and Geothermal Research*, **132**, 159 – 172.
- BATZLE, M. L., SIMMONS, G., AND SIEGFRIED, R. W. 1980. Microcrack closure in rocks under stress: Direct observation. *Journal of Geophysical Research*, **85**, 7,072 – 7,090.
- BAUD, P. AND MEREDITH, P. G. 1997. Damage accumulation during triaxial creep of Darley Dale Sandstone from pore volumetry and acoustic emission. *International Journal of Rock Mechanics and Mining Sciences*, **34**, 371.
- BEAMISH, D. 1999. Characteristics of near-surface electrokinetic coupling. *Geophysical Journal International*, **137**, 231 – 242.
- BEELER, N. M., TULLIS, T. E., BLANPIED, M. L., AND WEEKS, J. D. 1996. Frictional behaviour of large displacement experimental faults. *Journal of Geophysical Research* , **101**, 8,697 – 8,715.
- BENNETT, P. C. 1991. Quartz dissolution in organic-rich aqueous systems. *Geochimica et Cosmochimica Acta*, **55**, 1,781 – 1,797.

- BERGER, G., CADORE, E., SCHOTT, J., AND DOVE, P. M. 1994. Dissolution rate of quartz in lead and sodium electrolyte solutions between 25 and 300°C: Effect of the nature of surface complexes and reaction affinity. *Geochimica et Cosmochimica Acta*, **58**, 541 – 551.
- BERNABE, Y. AND BRUDERER, C. 1998. Effect of the variance of pore size distribution on the transport properties of heterogeneous networks. *Journal of Geophysical Research*, **103**, 513 – 525.
- BERNARD, P. 1992. Plausibility of long distance electrotelluric precursors to earthquakes. *Journal of Geophysical Research*, **97**, 17,531 – 17,546.
- BERNER, E. K. AND BERNER, R. A. 1996. *Global environments*. Prentice Hall.
- BIEGEL, R. L., WANG, C. H., SCHOLZ, C. H., AND BOITNOTT, G. N. 1992. Micromechanics of rock friction 1. Effect of surface roughness on initial friction and slip hardening in westerly granite. *Journal of Geophysical Research*, **97**, 8,951 – 8,964.
- BLACID, J. D., HALLECK, P. H., D'ONFRO, P., AND RIECKER, R. E. 1981. Thermomechanical properties of Galesville sandstone, Mechanical behaviour of crustal rocks, (ed) Carter, N.L., Friedman, M., Logan, J.M. and Stearns, D.W., *American Geophysical Union*, Washington D.C. **24**, 153 – 159.
- BLANPIED, M. L., LOCKNER, D. A., AND BYERLEE, J. D. 1992. An earthquake mechanism based on rapid sealing of faults. *Nature*, **358**, 574 – 576.
- BLANPIED, M. L., LOCKNER, D. A., AND BYERLEE, J. D. 1995. Frictional slip of granite at hydrothermal conditions. *Journal of Geophysical Research*, **100**, 13,045 – 13,064.
- BRACE, W. F. 1964. Brittle fracture of rocks *In state of stress in the Earth's Crust*. Elsevier, New York.
- BRACE, W. F. 1971. Resistivity of saturated crustal rocks to 40km based upon laboratory measurements, in *Structure and physical properties of the Earth's crust. Geophysical Monograph Series*, **14**, 243 – 255.
- BRACE, W. F. AND KOHLSTEDT, D. L. 1980. Limits on the lithospheric stress imposed by laboratory experiments. *Journal of Geophysical Research*, **85**, 6,248 – 6,252.
- BRACE, W. F. AND ORANGE, A. S. 1966. Electrical resistivity changes in saturated rocks under stress. *Science*, **153**, 1,525 – 1,526.
- BRACE, W. F., PAULDING, B. W., AND SCHOLZ, C. H. 1966. Dilatancy in the fracture of crystalline rocks. *Journal of Geophysical Research*, **71**, 3,939 – 3,953.
- BRADY, P. V. AND WALTHER, J. V. 1990. Kinetics of quartz dissolution at low temperatures. *Chemical Geology*, **82**, 252 – 264.
- BROWN, S. R. 1989. Transport of fluid and electric current through a single fracture. *Journal of Geophysical Research*, **94**, 9,429 – 9,438.
- BROWN, S. R. 1998. Simple mathematical model of a rough fracture. *Physics and Chemistry of The Earth*, **100**, 5,941 – 5,952.
- BROWN, S. R. AND HAUPT, R. W. 2003. Study of electrokinetic effects to quantify groundwater flow. *Sandia Report*.
- BROWN, S. R. AND SCHOLZ, C. H. 1985. Closure of random elastic surfaces in contact. *Journal of Geophysical Research*, **90**, 5,531 – 5,545.
- BROWN, S. R. AND SCHOLZ, C. H. 1986. Closure of rock joints. *Journal of Geophysical Research*, **91**, 4,939 – 4,948.
- BRUNER, W. M. 1976. Comment on 'Seismic velocities in dry and saturated cracked solids'. *Journal of Geophysical Research*, **81**, 2,573 – 2,576.

- BUDD, S. M. 1961. The mechanisms of chemical reactions between silicate glass and attacking agents. *Physics and Chemistry of Glasses*, **2**, 111 – 114.
- BUSSIAN, A. E. 1983. Electrical conductance in a porous medium. *Geophysics*, **48**, 1,258 – 1,268.
- BUTLER, D. B. AND KNIGHT, R. J. 1998. Electrical conductivity of steam-flooded clay-bearing geologic materials. *Geophysics*, **63**, 1,137 – 1,149.
- BYERLEE, J. D. 1978. Friction of rocks. *Pure and Applied Geophysics*, **116**, 615 – 626.
- BYERLEE, J., 1993, Model for Episodic Flow of High Pressure Water in Fault Zones before Earthquakes. *Geology* **21**, 303 – 306.
- BYERLEE, J. D. AND BRACE, W. F. 1968. Stick slip, stable sliding, and earthquakes- effect of rock type, pressure, strain rate, and stiffness. *Journal of Geophysical Research*, **73**, 6,031 – 6,037.
- CARROLL, S. A., MAXWELL, R. S., BOURCIER, W., MARTIN, S., AND HULSEY, S. 2002. Evaluation of silica-water surface chemistry using NMR spectroscopy. *Geochimica et Cosmochimica Acta*, **66**, 913 – 926.
- CARTER, N. L. AND TSENN, M. C. 1987. Flow properties of continental lithosphere. *Tectonophysics*, **136**, 27 – 63.
- CLINT, O. C. 1999. Electrical Potential Changes and Acoustic Emissions Generated by Fracture and Fluid Flow during Experimental Triaxial Rock Deformation. *PhD Thesis*, University College London.
- COOK, N. G. W. 1981. Stiff testing machines, stick slip sliding and the stability of rock deformation, Geophysical monograph series, Mechanical behaviour of crustal rocks, (ed) Carter, N.L., Friedman, M., Logan, J.M. and Stearns, D.W., *American Geophysical Union*, Washington D.C. **24**, 93 – 102.
- CORWIN, R. F. AND D. B. HOOVER. 1979. The self-potential method in geothermal exploration. *Geophysics*, **44**, 226 – 245.
- COSTIN, L. S. 1987. Time-dependent deformation and failure. *In: Fracture mechanics of rocks*. (ed) Atkinson B.K., Academic Press, London, 149 – 160.
- COWIE, P. A. AND SCHOLZ, C. H. 1992a. Growth of faults by accumulation of seismic slip. *Journal of Geophysical Research*, **97**, 11,085 – 11,095.
- COWIE, P. A. AND SCHOLZ, C. H. 1992b. Physical explanation for the displacement-length relationship of faults using a post-yield fracture mechanics model. *Journal of Structural Geology*, **14**, 1,133 – 1,148.
- COX, S. J. D. AND MEREDITH, P. G. 1993. Microcrack formation and material softening on rock measured by monitoring acoustic emissions. *International Journal of Rock Mechanics and Mining Science & Geomechanics Abstracts*, **30**, 11 – 24.
- CRAMPIN, S. AND ZATSEPIN, S. V. 1997. Modelling the compliance of crustal rocks - II. Response to temporal changes before earthquakes. *Geophysical Journal International*, **129**, 495 – 506.
- CRESS, G. O., BRADY, B. T., AND ROWELL, G. A. 1987. Sources of electromagnetic radiation from fracture of rock samples in the laboratory. *Geophysics Research Letters*, **14**, 331 – 334.
- CUOMO, V., LAPENNA, V., MACCHIATO, M., SERIO, C., AND TELESCA, L., 1998, Linear and nonlinear dynamics in electrical precursory time series: implications for earthquake prediction. *Tectonophysics*, **287**, 279-298.
- DAROT, M. AND GUEGUEN, Y. 1986. Slow crack growth in minerals and rocks: Theory and experiments. *Pure and Applied Geophysics*, **124**, 677 – 692.
- DAROT, M., GUEGUEN, Y., AND BARATIN, L. 1992. Permeability of thermally cracked granite. *Geophysics Research Letters*, **19**, 869 – 872.

- DAVID, C. 1993. Geometry of flow paths for fluid transport in rocks. *Journal of Geophysical Research*, **98**, 12,267 – 12,278.
- DAVID, C. AND DAROT, M. 1989. Permeability and conductivity of sandstones. In: *Rocks at great depths*. (ed) Maury, V. Fourmaintraux, D., Balkeme. 203 – 210.
- DE LEEUW, N. H., HIGGINS, F. M., AND PARKER, S. C. 1999. Modelling the surface structure and stability of α -quartz. *Journal of Physical Chemistry (B)* **103**, 1,271 – 1,277.
- DERR, J. S. 1973. Earthquake lights: A review of observations and present theories. *Bulletin of the Seismological Society of America*, **63**, 2,177 – 2,187.
- DEY, T. N. 1986. Permeability and electrical conductivity changes due to hydrostatic stress cycling of Berea and Muddy J Sandstone. *Journal of Geophysical Research*, **91**, 763 – 766.
- DONATH, F. A. AND FRUTH, L. S. JR. 1971. Dependence of strain-rate effects on deformation mechanism and rock type. *Journal of Geology*, **79**, 347 – 371.
- DOVE, P. M. 1999. The dissolution kinetics of quartz in aqueous mixed cation solutions. *Geochimica et Cosmochimica Acta*, **63**, 3,715 – 3,727.
- DOVE, P. M. AND CRERAR, D. A. 1990. Kinetics of quartz dissolution in electrolyte solutions using a hydrothermal mixed flow reactor. *Geochimica et Cosmochimica Acta*, **54**, 955 – 969.
- DOVE, P. M. AND NIX, C. J. 1997. The influence of the alkaline earth cations, magnesium, calcium, and barium on the dissolution kinetics of quartz. *Geochimica et Cosmochimica Acta*, **61**, 3,329 – 3,340.
- DOVE, P. M. AND RIMSTIDT, J. D. 1994. Silica-water interactions. In: *Silica – Physical behaviour, geochemistry and materials applications*. Reviews in Mineralogy, **29**, 259 – 308, (ed) Heaney, P.J. Prewitt, C.T. & Gibbs, C.V., Mineralogical Society of America, Washington D.C.
- DUBA, A. G., HEIKAMP, P., MEURER, W., NOVER, G., AND WILL, G. 1994. Evidence from borehole samples for the role of accessory materials in lower crustal conductivity. *Nature*, **367**, 59 – 61.
- DUNSTAN, D. E. 1994. Temperature-dependence of the electrokinetic properties of two disparate surfaces. *Journal of Colloid and Interface Science*, **166**, 472 – 475.
- ECCLES, D., SAMMONDS, P. R., AND CLINT, O. C. 2004. Laboratory studies of electrical potential during rock failure. Submitted to "*International Journal of Rock Mechanics and Mining*".
- ENOMOTO, Y. AND HASHIMOTO, H., 1992, Transient electrical activity accompanying rock under indentation loading. *Tectonophysics*, **221**, 337 – 344.
- FANG, Z. AND HARRISON, J. P. 2002. Application of a local degradation model to the analysis of brittle fracture of laboratory scale rock specimens under triaxial conditions. *International Journal of Rock Mechanics and Mining Sciences*, **39**, 459 – 476.
- FAVARA, R., ITALIANO, F., AND MARTINELLI, G. 2001. Earthquake induced chemical changes in thermal waters of Umbria region during the 1997-1998 seismic swarm. *Terra Nova*, **13**, 227 – 233.
- FEDOROV, E., PILIPENKO, V., AND UYEDA, S. 2001. Electric and magnetic fields generated by electrokinetic processes in a conductive crust. *Physics and Chemistry of the Earth, Part C: Solar, Terrestrial & Planetary Science*, **26**, 793 – 799.
- FENOGLIO, M. A., JOHNSTON, M. J. S., AND BYERLEE, J. D. 1995. Magnetic and electric fields associated with changes in high pore pressure in fault zones: Application to the Loma Prieta ULF emissions. *Journal of Geophysical Research*, **100**, 12,951 – 12,958.
- FISCHER, G. J. AND PATERSON, M. S. 1989. Dilatancy during rock deformation at high temperatures and pressures. *Journal of Geophysical Research*, **94**, 17,607 – 17,617.

- FITTERMAN, D. V. 1978. Electrokinetic and magnetic anomalies associated with dilatant regions in a layer in a layered earth. *Journal of Geophysical Research*, **83**, 5,923 – 5,928.
- FOURNIER, R. O. 2001. Naturally occurring fluids in rock above 374°C at less than 4-5 km depth. *Proceedings: Workshop on potential thermal extraction from deep-seated rock masses*, 83 – 98.
- FOURNIER, R. O. AND POTTER, R. W. 1982. An equation correlating the solubility of quartz in water from 25 to 900°C at pressures up to 10,000 bars. *Geochimica et Cosmochimica Acta*, **46**, 1,969 – 1,973.
- FOWLER, C. M. R. 2001. 1st edition. *The solid Earth: An introduction to global geophysics*. Cambridge University Press, Cambridge.
- FRANKLIN, S. P., HAJASH, J., DEWERS, T. A., AND TIEH, T. T. 1994. The role of carboxylic acids in albite and quartz dissolution: An experimental study under diagenetic conditions. *Geochimica et Cosmochimica Acta*, **58**, 4,259 – 4,279.
- FRASER-SMITH, A. C., BERNARDI, A., MCGILL, P. R., LADD, M. E., HELLIWELL, R. A., AND VILLARD, J. O. G. 1990. Low-frequency magnetic field measurements near the epicenter of the Ms 7.1 Loma Prieta earthquake. *Geophysics Research Letters*, **17**, 1,465 – 1,468.
- GAUTIER, J. M., OELKERS, E. H. AND SCHOTT, J. 2001. Are quartz dissolution rates proportional to B.E.T. surface areas? *Geochimica et Cosmochimica Acta*, **65**, 1,059 – 1,070.
- GELLER, R. J. 1996. Earthquake prediction: a critical review. *Geophysical Journal International*, **131**, 425 – 450.
- GLOVER, P. W. J., BAUD, P., DAROT, M., MEREDITH, P. G., BOON, S. A., LE RAVALEC, M., AND ZOUSSI, S. 1995. α/β transition in quartz monitored using acoustic emissions. *Geophysical Journal International*, **120**, 775-782.
- GLOVER, P. W. J., GOMEZ, J. G., MEREDITH, P. G., BOON, S. A., SAMMONDS, P. R., AND MURRELL, S. A. F. 1996. Modelling the stress/strain behaviour of saturated rocks undergoing triaxial deformation using complex electrical conductivity measurements. *Survey in Geophysics*, **17**, 307 – 330.
- GLOVER, P. W. J., MATSUKI, K., HIKIMA, R., AND HAYASHI, K. 1997. Fluid flow in fractally rough synthetic fractures. *Geophysics Research Letters*, **24**, 1,803 – 1,806.
- GLOVER, P. W. J., MEREDITH, P. G., SAMMONDS, P. R., AND MURRELL, S. A. F. 1994. Ionic surface electrical conductivity in sandstone. *Journal of Geophysical Research*, **99**, 21,635 – 21,650.
- GLOVER, P. W. J. AND VINE, F. J. 1992. Electrical conductivity of carbon-bearing granulite at raised temperatures and pressures. *Nature*, **360**, 723 – 726.
- GREATHOUSE, J.A., O'BRIEN, R.J., BEMIS, G. AND PABALAN R.T. (2002) Molecular Dynamics Study of Aqueous Uranyl Interactions with Quartz (010) *Journal of Physical Chemistry (b)*. **106**, 1,664 – 1,655.
- GRIFFITH, A. A. 1920. The phenomena of rupture and flow in solids. *Transactions of The Royal Society of London*. A **221**, 163 – 198.
- GRIFFITH, A. A. 1924. The theory of rupture. In *Proceedings. 1st. International. Congress on Applied Mechanical. Techniques.* (ed) Biezeno, C.B. & Burgers, J.M., Boekhanel en Drukkerji, Delft. 53-56
- GROSS, D. AND WILLIAMS, W. 1982. Streaming potential and the electromechanical response of physiologically moist bone. *Journal of Biochemistry*, **15**, 277 – 295.
- GRUSZOW, S., ROSSIGNOL, J. C., TZANIS, A., AND LE MOUËL, J. L. 1996. Identification and analysis of electromagnetic signals in Greece: the case of the Kozani earthquake VAN prediction. *Geophysics Research Letters* **23**, 2,025 – 2,028.
- GUEGUEN, Y. AND PALCIAUSKAS, V. 1994. 1st edition. *Introduction to the Physics of Rocks*. Princeton University Press. Princeton, New Jersey.

- HATTON, C. G., MAIN, I. G., AND MEREDITH, P. G. 1994. Non-universal scaling of fracture length and opening displacement. *Nature*, **367**, 160 – 162.
- HILL, N.E. 1969. The temperature dependence of the dielectric properties of water, University of London, PhD Thesis, 238 – 239.
- ICENHOWER, J. P. AND DOVE, P. M. 2000. The dissolution kinetics of amorphous silica into sodium chloride solutions: effects of temperature and ionic strength. *Geochimica et Cosmochimica Acta*, **64**, 4,193 – 4,203.
- ISHIDO, T. AND MIZUTANI, H. 1980. Relationship between fracture strength of rocks and zeta-potential. *Tectonophysics*, **67**, 13 – 23.
- ISHIDO, T. AND MIZUTANI, H. 1981. Experimental and theoretical basis for electrokinetic phenomena in rockwater systems and its applications to geophysics. *Journal of Geophysical Research*, **86**, 1,763 – 1,775.
- ISHIDO, T. AND PRITCHETT, J. W. 1999. Numerical simulation of electrokinetic potentials associated with subsurface fluid flow. *Journal of Geophysical Research*, **104**, 15,247 – 15,259.
- JAEGER, J. C. AND COOK, N. G. W. 1976. *Fundamental of Rock Mechanics*, 2nd ed. Chapman and Hall, London.
- JAEGER, J. C. AND COOK, N. G. W. 1979. *Fundamental of Rock Mechanics*, 3rd ed. Chapman and Hall, London.
- JONES, C. 1989. An experimental study of the relationship between P-wave velocity, acoustic emission and deformation in rocks under simulated crustal conditions. *PhD Thesis*, University College London.
- JONES, C., KEANEY, G. M., MEREDITH, P. G., AND MURRELL, S. A. F. 1997. Acoustic emission and fluid permeability measurements on thermally cracked rocks. *Physics and Chemistry of The Earth*, **22**, 13 – 17.
- JORGENSEN, J. D. 1978. Compression mechanisms in α -quartz structure-SiO₂ and GeO₂. *Journal of Applied Physics*, **49**, 5,473 – 5,478.
- JOUNIAUX, L. 2000. Streaming potential in volcanic rocks from Mount Pelee. *Journal of Geophysical Research*, **105**, 8,391 – 8,401.
- JOUNIAUX, L., BERNARD, M. L., POZZI, J. P., AND ZAMORA, M. 2000. Electrokinetic in Rocks: Laboratory Measurements in Sandstone and Volcanic Samples. *Physics and Chemistry of The Earth, Part A: Solid Earth Geodesy*, **25**, 329 – 332.
- JOUNIAUX, L., LALLEMANT, S., AND POZZI, J. P. 2003. Changes in the permeability, streaming potential and resistivity of a claystone from the Nankai prism under stress. *Geophysics Research Letters*, **21**, 149 – 152.
- JOUNIAUX, L., MASUDA, K., LEI, X., NISHIZAWA, O., KUSUNOSE, K., LIU, L., AND MA, W. 2001. Comparison of the microfracture localization in granite between fracturation and slip of a preexisting macroscopic healed joint by acoustic emission measurements. *Journal of Geophysical Research*, **106**, 8,687 – 8,698.
- JOUNIAUX, L. AND POZZI, J. P. 1995a. Streaming potential and permeability of saturated sandstones under triaxial stress: consequences for electrotelluric anomalies prior to earthquakes. *Journal of Geophysical Research*, **100**, 10,197 – 10,209.
- JOUNIAUX, L. AND POZZI, J. P. 1995b. Permeability dependence of streaming potential in rocks for various fluid conductivities. *Geophysics Research Letters*, **22**, 485 – 488
- JOUNIAUX, L. AND POZZI, J. P. 1997. Laboratory measurements anomalous 0.1-0.5 Hz streaming potential under geochemical changes: Implications for electrotelluric precursors to earthquakes. *Journal of Geophysical Research*, **102**, 15,335 – 15,343.

- JOUNIAUX, L. AND POZZI, J. P., BROCHOT, M., AND PHILIPPE, C. 1992. Resistivity changes induced by triaxial compression in saturated sandstones from Fontainebleau (France). *Comptes Rendus de l'Académie des Sciences*. Paris **315**, 1,493 – 1,499.
- JOUNIAUX, L. AND POZZI, J. P., BERTHIER, J., AND MASSE, P. 1999. Detection of fluid flow variations at the Nankai Trough by electric and magnetic measurements in boreholes or at the seafloor. *Journal of Geophysical Research*, **104**, 29,293 – 29,309.
- KAGAN, Y. Y. 1997. Are earthquakes predictable? *Geophysical Journal International*, **131**, 505 – 525.
- KAGAN, Y. Y. AND JACKSON, D. D. 1996. Statistical tests of VAN earthquake predictions: comments and reflections. *Geophysics Research Letters*, **23**, 1,433 – 1,436.
- KATO, N., YAMAMOTO, K., YAMAMOTO, H., AND HIRASAWA, T. 1992. Strain-rate effect on frictional strength and the slip nucleation process. *Tectonophysics*, **211**, 269 – 282.
- KATO, N., YAMAMOTO, K., YAMAMOTO, H., AND HIRASAWA, T. 1993. A stress-corrosion model for strain-rate dependence of the frictional strength of rocks. *International Journal of Rock Mechanics and Mining Science & Geomechanics Abstracts*, **30**, 551 – 554.
- KEANEY, G. M. 1998. Experimental study of the evolution of permeability in rocks under simulated crustal stress conditions. *PhD Thesis*, University College London.
- KELLER, G. V. 1987. Rock and mineral properties. *Electromagnetic methods in Applied Geophysics*, **1**, (ed) Namighian, M.N., Series: Investigations in Geophysics, **3**, Society of Exploration Geophysicists Tulsa, Okla. 137 - 156
- KIRBY, S. H. 1984. Introduction and digest to the special issue on chemical effects of water on the deformation and strengths of rocks. *Journal of Geophysical Research*, **89**, 3,991 – 3,995.
- KOHLSTEDT, D. L., EVANS, B., AND MACKWELL, S. J. 1995. Strength of the lithosphere: Constraints imposed by laboratory experiments. *Journal of Geophysical Research*, **100**, 17,587 – 17,602.
- LAWN, B. R. 1993. *Fracture of Brittle Solids*, 2nd edition. Cambridge University Press, Cambridge.
- LAWN, B. R. AND WILSHAW, T. R. 1975. *Fracture of Brittle Solids*, 1st edition. Cambridge University Press, Cambridge.
- LE PICHON, X., KOBAYASHI, K., AND KAIKI-NANKAI SCIENTIFIC CREW. 1992. Fluid venting activity within the eastern Nankai Trough accretionary wedge. *Earth and Planetary Science Letters*, **109**, 303 – 318.
- LEI, X. AND KUSUNOSE, K. 2000. Quasi-static fault growth and cracking in homogeneous brittle rock under triaxial compression using acoustic emission monitoring. *Journal of Geophysical Research*, **105**, 6,127 – 6,139.
- LEI, X., MASUDA, K., NISHIZAWA, O., JOUNIAUX, L., LIU, L., MA, W., SATOH, T., AND KUSUNOSE, K. 2004. Detailed analysis of acoustic emission activity during catastrophic fracture of faults in rock. *Journal of Structural Geology*, **26**, 247 – 258.
- LIQING, R., WEILIN, Q., AND DONGQING, L. 2001. Interfacial electrokinetic effects on liquid flow in microchannels. *International Journal of Heat and Mass Transfer*, **44**, 3,125 – 3,134.
- LOCKNER, D. A. 1993. The role of acoustic emission in the study of rock fracture. *International Journal of Rock Mechanics and Mining Science & Geomechanics Abstracts*, **30**, 883 – 899.
- LOCKNER, D. A. 1998. A generalized law for brittle deformation of Westerly granite. *Journal of Geophysical Research*, **103**, 5,107 – 5,123.
- LOCKNER, D. A., BYERLEE, J. D., KUKSENKO, V., PONOMAREV, A., AND SIDORIN, A. 1991. Quasi-static fault growth and shear fracture energy in granite. *Nature*, **350**, 39 – 42.

- LORNE, B., PERRIER, F., AND AVOUAC, J.-P. 1999a. Streaming potential measurements 1. Properties of the electrical double layer from crushed rock samples. *Journal of Geophysical Research*, **104**, 17,857 – 17,877.
- LORNE, B., PERRIER, F., AND AVOUAC, J.-P. 1999b. Streaming potential measurements 2. Relationship between electrical and hydraulic flow patterns from rock samples during deformation. *Journal of Geophysical Research*, **104**, 17,879 – 17,896.
- LONG, L. T. AND RIVERS, W. K. 1975. Field measurement of the electroseismic response. *Geophysics*, **40**, 233 – 245.
- MAIN, I. G. 1988. Prediction of failure times in the Earth for a time-varying stress. *Geophysical Journal*, **92**, 455 – 464.
- MAIN, I. G. 1990. Influence of fractal flaw distributions on rock deformation in the brittle field. In: *Deformation Mechanisms, Rheology and Tectonics*.
- MAIN, I. G. 1991. A modified Griffith criterion for the evolution of damage with a fractal distribution of crack lengths: application to seismic event rates and b-values. *Geophysical Journal International*, **107**, 353 – 362.
- MAIN, I. G., MEREDITH, P. G., AND JONES, C. 1989. A reinterpretation of the precursory seismic b-value anomaly from fracture mechanics. *Geophysics Journal*, **96**, 131 – 138.
- MAIN, I. G., MEREDITH, P. G., AND SAMMONDS, P. R. 1992. Temporal variations in seismic event rate and b-values from stress corrosion constitutive laws. *Tectonophysics*, **211**, 233 – 246.
- MAIN, I. G., SAMMONDS, P. R., AND MEREDITH, P. G. 1993. Application of a modified Griffith criterion to the evolution of fractal damage during compressional rock failure. *Geophysical Journal International*, **115**, 367 – 380.
- MAIN, I. G., KWON, O., NGWENYA, B. T., AND ELPHICK, S. C., 2000, Fault sealing during deformation-band growth in porous sandstone. *Geology*, **28**, 1131-1134.
- MANDELBROT, B. B. 1982. *The fractal geometry of nature*. New York, Freeman
- MARON, C., BAUBRON, G., HERBRETEAU, L., AND MASSINON, B. 1993. Experimental study of a VAN network in the French Alps. *Tectonophysics*, **224**, 51 – 83.
- MATSUMARA, S. 1993. Overestimates of earthquake prediction efficiency in a 'post-prediction state'. *Journal of Physical Earth*, **51**, 41 – 43.
- MAZUR, P. AND OVERBEEK, J. 1951. On electro-osmosis and streaming-potentials in diaphragms, II, General quantitative relationship between electro-kinetic effects. *Recueil des Travaux Chimiques des Pays-Bas*, 83 – 91.
- MCCLINTOCK, F. A. AND WALSH, J. B. 1962. Friction of Griffith cracks in rock under pressure. In: *Proceedings. 4th US National Congress on Applied Mechanics*. New York. 1015 – 1021.
- MEREDITH, P. G. AND ATKINSON, B. K. 1983. Stress corrosion and acoustic emission during tensile crack propagation on Whin Sill dolerite and other basic rocks. *Geophysical Journal of the Royal Astronomical Society*, **75**, 1 – 21.
- MEREDITH, P. G., AYLING, M. R., MURRELL, S. A. F., AND SAMMONDS, P. R. 1991. Toughening mechanisms in quasi-brittle materials. In: *Cracking, damage and fracture in stresses rock: A holistic approach*. Shah, S.P.(ed), Kluwer Academic Publishers, Netherlands.
- MEREDITH, P. G., MAIN, I. G., AND JONES, C. 1990. Temporal variations in seismicity during quasi-static and dynamic rock failure. *Tectonophysics*, **175**, 249 – 268.
- MICHALSKE, T. A. AND FREIMAN, S. W. 1982. A molecular interpretation of stress corrosion in silica. *Nature*, **295**, 511 – 512.

- MICHEL, S. AND ZLOTNICKI, J. 1998. Self-potential and magnetic surveying of La Fournaikse volcano (Reunion Island): correlation with faulting, fluid circulation, and eruption. *Journal of Geophysical Research*, **103**, 17,845 – 17,857.
- MIDDLETON, P. 1997. Streaming potential measurements of unconfined Triassic sandstone and fractured granites. *Tectonophysics*, **164**, 210 – 218.
- MIKHAILOV, O. V., HAARTSEN, M. W., AND TOKSOZ, M. N. 1997. Electro seismic investigation of the shallow subsurface: Field measurements and numerical modelling. *Geophysics*, **62**, 97 – 105.
- MIKHAILOV, O. V., QUEEN, J., AND TOKSOZ, M. N. 2000. Using borehole electro seismic measurements to detect and characterize fractured (permeable) zones. *Geophysics*, **65**, 1,098 – 1,112.
- MIZUTANI, H., ISHIDO, T., YOKOKURA, T., AND OHNISHI, S. 1976. Electrokinetic phenomena associated with earthquakes. *Geophysics Research Letters*, **38**, 1,015 – 1,030.
- MOGI, K., 1968, Source locations of elastic shocks in the fracturing process in rocks. *Bulletin Earthquake Research Institute*, **46**, 1103 – 1125.
- MOLINA, C., VICTORIA, V., ARENA, A., AND IBANEZ, J. A. 1999. Streaming potential and surface charge density of microporous membranes with pore diameter in the range of thickness. *Journal of Membrane Science*, **163**, 239 – 255.
- MORGAN, F. D., WILLIAMS, E. R., AND MADDEN, T. R. 1989. Streaming potential properties of Westerly granite with application. *Journal of Geophysical Research*, **94**, 12,449 – 12,461.
- MURRELL, S. A. F. 1964a. The theory of the propagation of elliptical Griffith cracks under various conditions of plane strain or plane stress: Part I. *British Journal of Applied Physics*, **15**, 1,195 – 1,210.
- MURRELL, S. A. F. 1964b. The theory of the propagation of elliptical Griffith cracks under various conditions of plane strain or plane stress: Parts II and III. *British Journal of Applied Physics*, **15**, 1,211 – 1,223.
- MURRELL, S. A. F. 1965. The effect of triaxial stress systems on the strength of rocks at atmospheric temperatures. *Geophysics Journal of the Royal Astronomical Society*, **10**, 231 – 281.
- MURRELL, S. A. F. AND DIGBY, P. J. 1970. The theory of brittle fracture initiation under triaxial stress conditions-II. *Geophysics Journal of the Royal Astronomical Society*, **19**, 499 – 512.
- NITSAN, U. 1977. Electromagnetic emissions accompanying fracture of quartz-bearing rocks. *Geophysical Research Letters*, **4**, 333 – 336.
- NUR, A. 1972. Dilatancy, pore fluids, and premonitory variations of τ_s/τ_p . *Bulletin of the Seismological Society of America*, **62**, 1,217 – 1,222.
- NUR, A. AND BYERLEE, J. D. 1971. An exact effective stress law for elastic deformation of rock with fluids. *Journal of Geophysical Research*, **76**, 6,414 – 6,419.
- NUR, A. AND WALDER, J. 1990. Time dependent hydraulics of the earth's crust. In: *The role of fluids in crustal processes*, 113-140. National Research Council.
- OEDRA, A. 1998. Laboratory studies on shear fracture of granite under simulated crustal conditions. *PhD Thesis*. University College London.
- OGAWA, T., OIKE, K., AND MIURA, T. 1985. Electromagnetic radiations from rocks. *Journal of Geophysical Research*, **90**, 6,245 – 6,249.
- OHNAKA, M. 2004. Earthquake cycles & physical modelling of the process to a large earthquake. *Earth and Planetary Science Letters*, **56**, 773 – 793.

- OHNAKA, M. AND MOGI, K. 1982. Frequency characteristics of acoustic emissions in rocks under uniaxial compression and its relation to the fracturing process to failure. *Journal of Geophysical Research*, **87**, 3,873 – 3,884.
- OHNAKA, M., KUWAHARA, Y., AND YAMAMOTO, K. 1987. Constitutive relations between dynamic physical parameters near a tip of the propagating slip zone during stick-slip shear failure. *Tectonophysics*, **144**, 109 – 125.
- OJALA, I. O., 2003. Stress corrosion crack growth in porous sandstones. *PhD Thesis*. University of Edinburgh
- OLHOEFT, G. R. 1981. Electrical properties of granite with implications for the lower crust. *Journal of Geophysical Research*, **86**, 931 – 936.
- OLSSON, W. A. 1992. The effect of slip on the flow of fluid through a fracture. *Geophysics Research Letters*, **19**, 541 – 543.
- OLSSON, W. A. AND BROWN, S. R. 1993. Hydromechanical response of a fracture undergoing compression and shear. *International Journal of Rock Mechanics and Mining Sciences*, **30**, 845 – 851.
- OVERBEEK, J. 1952. Electrochemistry of the double layer, in *Colloid Science. 1, Irreversible Systems*. Elsevier, New York.
- OVERBEEK, J. 1960. *Colloid Science*, (ed) Krupt, H.R., Elsevier, New York.
- PALACKY, G. J. 1987. Resistivity characteristics of geologic targets In: *Electromagnetic methods in applied geophysics*, *Society of Exploration Geophysics*, Tulsa, Okla. 567 – 578.
- PARK, S. K., JOHNSTON, M. J. S., MADDEN, T. R., MORGAN, F. D., AND MORRISON, H. F. 1993. Electromagnetic precursors to earthquakes in the ULF band: A review of observations and mechanisms. *Review of Geophysics*, **31**, 117 – 132.
- PATERSON, M. S. 1978. *Experimental rock deformation: The Brittle Field*. Springer-Verlag, 254.
- PATERSON, M. S. 2000. Rock deformation experimentation. *Geophysical Monograph*, **56**, 187 – 194.
- PHAM, V. N., BOYER, D., CHOULIARAS, G., LE MOUEL, J. L., ROSSIGNOL, J. C., AND STAVRAKAKIS, G. N. 1998. Characteristics of electromagnetic noise in the Ioannina regio (Greece); a possible origin for the so called "Seismic Electric Signal" (SES). *Geophysics Research Letters*, **25**, 2,229 – 2,232.
- PRIDE, S. R. 1994. Governing equations for the coupled electromagnetics and acoustic of porous media. *Physical Review (B)* **50**, 15,679 – 15,696.
- PRIDE, S. R. AND HAARTSEN, M. W. 1996. Electro seismic wave properties. *Journal of the Acoustical Society of America*, **100**, 1,301 – 1,315.
- QU, W. AND LI, D. 2000. A model of overlapped EDL Fields. *Journal of Colloid and Interface Science* **224**, 397 – 407.
- RANALLI, G. 1995. *Rheology of the Earth*, 2nd edition (ed) Ranalli, G., Chapman & Hall
- READ, M. D., AYLING, M. R., MEREDITH, P. G., AND MURRELL, S. A. F. 1995. Microcracking during triaxial deformation of porous rocks monitored by changes in rock physical properties II. Pore volumetry and acoustic emission measurements on water-saturated rocks. *Tectonophysics*, **245**, 223 – 235.
- REPERT, P. M. AND MORGAN, F. D. 2001a. Streaming potential collection and data processing techniques. *Journal of Colloid and Interface Science*, **233**, 348 – 355.
- REPERT, P. M., MORGAN, F. D., Lesmes, D. P., and Jouniaux, L. 2001b. Frequency-dependent streaming potentials. *Journal of Colloid and Interface Science*, **234**, 194 – 203.

- REPPERT, P. M. AND MORGAN, F. D. 2003a. Temperature-dependent streaming potential: 1. Theory. *Journal of Geophysical Research*, **108**, ECV 3-1 – ECV 3-12.
- REPPERT, P. M. AND MORGAN, F. D. 2003b. Temperature-dependent streaming potentials: 2. Laboratory. *Journal of Geophysical Research*, **108**, ECV 4-1 – ECV 4-13.
- Revil, A., 1999, Pervasive press-solution transfer: a poro-visco-plastic model. *Geophysics Research Letters*, **26**, 255 – 258.
- REVIL, A. AND GLOVER, P. W. J. 1997. Theory of ionic-surface electrical conduction in porous media. *Physical Review (B)*, **55**, 1,757 – 1,773.
- REVIL, A. AND GLOVER, P. W. J. 1998. Nature of surface electrical conductivity in natural sands, sandstones and clays. *Geophysics Research Letters*, **25**, 691 – 694.
- REVIL, A., PEZARD, P. A., AND GLOVER, P. W. J. 1999a. Streaming potential in porous media 1. Theory of the zeta potential. *Journal of Geophysical Research*, **104**, 20,021 – 20,031.
- REVIL, A., SCHWAEGER, H., CATHLES, L. M., AND MANHARDT, P. D. 1999b. Streaming potential in porous media 2. Theory and application to geothermal systems. *Journal of Geophysical Research*, **104**, 20,033 – 20,048.
- RIMSTIDT, J. D. AND BARNES, H. L. 1980. The kinetics of silica-water reactions. *Geochimica et Cosmochimica Acta*, **44**, 1,683 – 1,699.
- ROCCHI, V. 2002. Fracture of basalts under simulated volcanic conditions. *PhD Thesis*. University College London.
- ROCCHI, V., SAMMONDS, P. R., AND KILBURN, C. R. J. 2004. Fracturing of Etnean and Vesuvian rocks at high temperatures and low pressures. *Journal of Volcanology and Geothermal Research*, **132**, 137 – 157.
- RUBEY, W. W. AND HUBBERT, M. K. 1959. Role of fluid pressure in mechanics of overthrust faulting. *Bulletin of the Geological Society of America*, **70**, 167 – 206.
- RUFFET, C., DAROT, M., AND GUEGUEN, Y. 1995. Surface conductivity in rocks: a review. *Survey in Geophysics*, **16**, 83 – 105.
- RUSSELL, R. D., BUTLER, K. E., KEPIC, A. W., AND MAXWELL, M. 1997. Seismoelectric exploration. The Leading Edge, *Society of Exploration Geophysics*, **16**, 1,611 – 1,615.
- RUTGERS, A. J., DESMET, M., AND RIGOLE, W. 1959. Streaming current with non-aqueous solutions. *Journal of Colloid and Interface Science*, **14**, 330 – 335.
- SAMMONDS, P. R., AYLING, M. R., MEREDITH, P. G., MURRELL, S. A. F., AND JONES, C. 1989. A laboratory investigation of acoustic emissions and elastic wave velocity changes during rock failure under triaxial stresses. In *Rock at Great Depth – Rock Mechanics and Rock Physics at great Depth*, (ed) Maury and Fourmaintraux, Balkema, Rotterdam, **1**, 233 – 240.
- SAMMONDS, P. R., MEREDITH, P. G., AND MAIN, I. G. 1992. Role of pore fluids in the generation of seismic precursors to shear fracture. *Nature*, **359**, 228 – 230.
- SASAOKA, H., YAMANAKA, C., AND IKEYA, M. 1998. Measurements of electrical potential variation by piezoelectricity of granite. *Geophysics Research Letters*, **25**, 2,225 – 2,228.
- SCHLISCHE, R. W., YOUNG, S. S., AND ACKERMANN, R. V. 1996. Geometry and scaling relations of a population of very small rift-related normal faults. *Geology*, **24**, 683 – 686.
- SCHOLZ, C. H. 1968. Microfracturing and inelastic deformation of rock in compression. *Journal of Geophysical Research*, **77**, 2,104 – 2,114.
- SCHOLZ, C. H. 1972. Static fatigue of quartz. *Journal of Geophysical Research*, **77**, 2,104 – 2,118.

- SCHOLZ, C. H. 2002. *The Mechanics of Earthquakes and Faulting*, 2nd edition. Cambridge University Press.
- SCHOLZ, C. H., DAWERS, N. H., ANDERS, M. H., AND COWIE, P. A. 1993. Fault growth and fault scaling laws: preliminary results. *Journal of Geophysical Research*, **98**, 21,951 – 21,961.
- SCHOLZ, C. H., SYKES, L. R., AND AGGARWAL, Y. P. 1973. Earthquake prediction: a physical basis. *Science*, **181**, 803 – 810.
- SCHWARTZENTRUBER, J., FURST, W., AND RENON, H. 1987. Dissolution of quartz into dilute alkaline solutions at 90°C: a kinetic study. *Geochimica et Cosmochimica Acta*, **51**, 1,867 – 1,874.
- SEIPOLD, U. 1998. Temperature dependence of thermal transport properties of crystalline rocks - a general law. *Tectonophysics*, **291**, 161 – 171.
- SERDENGECTI, S. AND BOOZER, G. D. 1961. *The effects of strain rate and temperature on the behaviour of rocks subjected to triaxial compression*. In proceedings of the fourth symposium on rock mechanics, 83 – 97.
- SHANKLAND, T. J. AND ANDERS, M. E. 1983. Electrical conductivity, temperatures, and fluids in the lower crust. *Journal of Geophysical Research*, **88**, 9,475 – 9,484.
- SHANKLAND, T. J., DUBA, A. G., MATHEZ, E. A., AND PEACH, C. L. 1997. Increase of electrical conductivity with pressure as an indicator of conduction through a solid phase in midcrustal rocks. *Journal of Geophysical Research*, **102**, 14,741 – 14,750.
- SHAW, B. E., CARLSON, J. M., AND LANGER, J. S. 1992. Patterns of seismic activity preceding large earthquakes. *Journal of Geophysical Research*, **97**, 479 – 488.
- SLEEP, N. AND M. BLANPIED. 1992. Creep, compaction and the weak rheology of major faults. *Nature*. **359**. 687 – 692.
- SMITH, W., LESLIE, M. AND FORESTER, T.R. 2003. The DL_POLY_2 User Manual, CCLRC, Daresbury Laboratory, Daresbury, Warrington WA4 4AD, UK, Version 2.14.
- SONDERGELD, C. H., GRANRYD, L. A., AND ESTEY, L. H. 1984. Acoustic emissions during compression testing of rock. In: *Proceeding 3rd Conference on Acoustic Emission/Microseismic Activity in Geologic Structures and Materials*, 45-46.
- SOMASUNDARAN, P. AND KULKARNI, R. D. 1973. A new streaming potential apparatus and study of temperature effects using it. *Journal of Colloid and Interface Science*, **45**, 591 – 600.
- SPRUNT, E. S., MERCER, T. B., AND DJABBARAH, N. F. 1994. Streaming potential from multiphase flow. *Geophysics*, **59**, 707 – 711.
- STERN, O. 1924. Zür theori der elektrolischen doppelschicht. *Z. Elektrochem.* **508**. 27-42
- STESKY, R. M. 1986. Electrical conductivity of brine-saturated fractured rock. *Geophysics*, **51**, 1,585 – 1,593.
- STESKY, R. M., BRACE, W. F., RILEY, D. K., AND ROBIN, P.-Y. F. 1974. Friction in faulted rock at high temperature and pressure. *Tectonophysics*, **23**, 177 – 203.
- TAKEUCHI, A. AND NAGAHAMA, H. 2005. Electric dipoles perpendicular to a stick-slip plane: a possible source of seismo-electromagnetic radiation. Submitted to "*Physics of the Earth and Planetary Interiors*".
- TANG, C. A., THAM, L. G., LEE, P. K. K., YANG, T. H., AND LI, L. C. 2002. Coupled analysis of flow, stress and damage (FSD) in rock failure. *International Journal of Rock Mechanics and Mining Science & Geomechanics Abstracts*, **39**, 477 – 489.
- TENTHOREY, E., SCHOLZ, C. H., AND AHARONOV, E. 1998. Precipitation sealing and diagenesis 1. Experimental results. *Journal of Geophysical Research*, **103**, 23,951 – 23,957.

- THOMPSON, A. H. AND GIST, G. A. 1993. Geophysical applications of electrokinetic conversion. The Leading Edge, *SEG* **12**, 1,169 – 1,173.
- THOMPSON, M. E. AND BROWN, S. R. 1991. The effect of anisotropic surface roughness on flow and transport in fractures. *Journal of Geophysical Research*, **89**, 9,425 – 9,431.
- TSANG, Y. W. 1984. The effect of tortuosity on fluid flow through a single fracture. *Journal of Geophysical Research*, **20**, 1,209 – 1,215.
- TUMAN, V. S. 1963. Streaming potential at very high differential pressures. *Journal of Applied Physics*, **34**, 167 – 189.
- TURCOTTE, D. L. 1989. Fractal in geometry and geophysics. *Pure Applied Geophysics*, **131**, 171 – 196.
- VAROTSOS, P. AND ALEXOPOULOS, K. 1984a. Physical properties of the variations of the electric field of the earth preceding earthquakes, I. *Tectonophysics*, **110**, 73 – 98.
- VAROTSOS, P. AND ALEXOPOULOS, K. 1984b. Physical properties of the variations of the electric field of the earth preceding earthquakes, II, Determination of the epicenter and magnitude. *Tectonophysics*, **110**, 99 – 125.
- WALSH, J. B. 1965. The effect of cracks on the compressibility of rock. *Journal of Geophysical Research*, **70**, 381 – 389.
- WALSH, J. B. AND BRACE, W. F. 1984. The effect of pressure on porosity and the transport properties of rock. *Journal of Geophysical Research*, **89**, 9,425 – 9,431.
- WARWICK, J. W., STOKER, C., AND MEYER, T. R. 1982. Radio emissions associated with rock fracture: possible application to the great Chilean earthquake of May 22, 1960. *Journal of Geophysical Research*, **87**, 2,851 – 2,859.
- WATSON, G.W., KELSEY, E.T., DE LEEUW, N.H., HARRIS, D.J. AND PARKER, S.C. 1996. Atomistic simulation of dislocations, surfaces and interfaces in MgO. *Journal of the Chemical Society Faraday Transactions*, **92**, 433 – 438.
- WIEDERHORN, S. M. 1967. Influence of water vapour on crack propagation in soda-lime glass. *Journal of the American Ceramic Society*, **50**, 407 – 414.
- WOODCOCK, P.R. AND G.V. MIDDLETON. 1994. Mechanics in the earth and environmental sciences. *Cambridge University Press*. p504.
- WURMSTICH, B. AND MORGAN, F. D., 1994, Modelling of streaming potential responses caused by oil well pumping. *Geophysics*. **59** (1), 46 – 56.
- YAMADA, I., MASUDA, K., AND MIZUTANI, H. 1989. *Physics of the Earth and Planetary Interia*, **57**, 157 – 168.
- YAMASHITA, T. AND OHNAKA, M. 1991. Nucleation process of unstable rupture in the brittle regime: a theoretical approach based on experimentally inferred relations. *Journal of Geophysical Research*, **96**, 8,351 – 8,367.
- YOSHIDA, S. 2001. Convection current generated prior to rupture in saturated rocks. *Journal of Geophysical Research*, **106**, 2,103 – 2,120.
- YOSHIDA, S., CLINT, O. C., AND SAMMONDS, P. R. 1998. Electric potential changes prior to shear fracture in dry and saturated rocks. *Geophysics Research Letters*, **25**, 1,577 – 1,580.
- YOSHIDA, S., MANJGALADZE, P., DILPIMIANI, D., OHNAKA, M., AND NAKATANI, M. 1994. Electromagnetic emissions associated with frictional sliding of rocks: *In Electromagnetic Phenomena Related to Earthquake Prediction*. Terrapub, Tokyo. 307 – 322.

- YOSHIDA, S., UYESHIMA, M., AND NAKATANI, M. 1997. Electric potential changes associated with slip failure of granite: Preseismic and coseismic signals. *Journal of Geophysical Research*, **102**, 14,883 – 14,897.
- YOSHIDA, S. AND OGAWA, T. 2004. Electromagnetic emissions from dry and wet granite associated with acoustic emissions. *Journal of Geophysical Research*, **109**, 1 – 11.
- ZATSEPIN, S. V. AND CRAMPIN, S. 1997. Modelling the compliance of crustal rocks - I. Response of shear wave splitting to differential stress. *Geophysics Research Letters*, **22**, 2,333 – 2,336.
- ZHU, W. AND WONG, T. F. 1996. Permeability reduction in a dilating rock: Network modelling of damage and tortuosity. *Geophysics Research Letters*, **23**, 3,099 – 3,102.
- ZHU, W. AND WONG, T. F. 1997. The transition from brittle faulting to cataclastic flow: Permeability evolution. *Journal of Geophysical Research*, **102**, 3,027 – 3,041.
- ZHU, Z. Y., HAARTSEN, M. W., AND TOKSOZ, M. N. 1999. Experimental studies of electrokinetic convections in fluid-saturated borehole models. *Geophysics*, **64**, 1,349 – 1,356.
- ZMAZEK, B., ITALIANO, F., ZIVCIC, M., VAUPOTIC, J., KOBAL, I., AND MARTINELLI, G. 2002. Geochemical monitoring of thermal waters in Slovenia: relationships to seismic activity. *Applied Radiation and Isotopes*. **57**, 919 – 930.
- ZOBACK, M. L. 1989. Global patterns of tectonic stress. *Nature*, **341**, 298.
- ZUKOSKI, C. F. AND SAVILLE, D. A. 1986. The interpretation of electrokinetic measurements using a dynamic model of the Stern layer. I. The dynamic model. *Journal of Colloid and Interface Science*, **114**, 32 – 44.

Appendix 1: Operation Procedure

	<u>Page No:</u>
<u>Clothing</u>	
<u>Rock preparation</u>	267
<i>Coring</i>	267
<i>Cutting</i>	267
<i>Grinding</i>	268
<u>Experimental procedure</u>	269
<i>Porosity measurements</i>	269
<i>Preparing the sample</i>	269
<i>Jacket set-up</i>	269
<i>Sample set-up</i>	269
<i>Locan set-up</i>	270
<i>Labview set-up</i>	270
<i>Turning the machine on</i>	270
<i>Putting the sample in the vessel</i>	271
<i>LVDT set-up</i>	271
<i>Confining pressure set-up</i>	271
<i>Separator set-up</i>	272
<i>Separator A</i>	272
<i>Separator B</i>	272
<i>Pore pressure set-up</i>	273
<i>Furnace and linked equipment set-up</i>	274
<i>Controls</i>	275
<i>Start the test</i>	275
<i>Stopping the test</i>	275
<i>Removing confining fluid</i>	275
<i>Removing pore fluid pressure</i>	276
<i>Remove sample from vessel</i>	276
<i>Remove rock from jacket</i>	276
<u>Other procedures required in the use of the triaxial cell –</u>	
<u>Testing pressure vessel seals</u>	277
<u>Replacing seals and furnace</u>	277
<i>Removing pressure vessel components</i>	277
<i>Bottom closure without furnace (bottom closure with the furnace see section below)</i>	278
<i>Piston</i>	279
<i>Top closure</i>	279
<i>Put the ram, furnace and bottom outer closure back into the pressure vessel</i>	279
<i>Wiring up the furnace (ignore is not used)</i>	280
<i>Putting the rest of the pressure vessel together</i>	280
<u>Pore intensifier</u>	281
<i>Removing intensifier from triaxial machine</i>	281
<i>Replacing seals</i>	282
<i>Putting intensifier back</i>	282
<u>Replace seals in the separator</u>	282
<i>Stripping separator</i>	282
<i>Assembling separator</i>	283
<u>Lead-throughs</u>	283
<i>Stripping lead-throughs</i>	283
<i>Making lead-throughs</i>	283
<u>Checking the furnace for damage</u>	285
<i>Stripping the furnace (store all components together)</i>	285
<i>Assembling the furnace (for more detail see the assembly drawings)</i>	285

Appendix 1: Operational Procedure

Calibration	286
<i>Pressure intensifier calibration</i>	286
<i>Pore volume calibration</i>	287
<i>LVDT calibration</i>	287
<i>Furnace calibration</i>	287
<i>Proving ring (load) calibration</i>	287
Photographs	
<i>Wiring diagram</i>	289
<i>Furnace assembly 2D</i>	290
<i>Furnace</i>	291
<i>Confining pump</i>	292
<i>Coring</i>	293
<i>Coring controls</i>	294
<i>Cutting</i>	295
<i>Experimental set-up</i>	296
<i>Furnace and calibration</i>	297
<i>Furnace assembly</i>	298
<i>Furnace controllers</i>	299
<i>Furnace controls</i>	300
<i>Grinding</i>	301
<i>Grinding controls</i>	302
<i>Hydraulics</i>	303
<i>Intensifier 2</i>	304
<i>Intensifier 2 controls</i>	305
<i>Locan and rack 1, 2 & 3</i>	306
<i>Permeameter & Separator</i>	307
<i>Porosity</i>	308
<i>Power distribution</i>	309
<i>Rack 1, 2 & 3</i>	310
<i>Rack 1</i>	311
<i>Rack 2</i>	312
<i>Rack 3</i>	313

OPERATION PROCEDURE

(MAKE SURE YOU HAVE HAD THE APPROPRIATE TRAINING BEFORE OPERATING THE MACHINERY)

Rock preparation (Always done with 2 people present for safety)

Follow general rock preparation workshop procedure (if in doubt ask)

Coring

- Lab coat, safety shoes, safety glasses and ear defenders
- 10 mm, 16 mm, 20 mm, 25 mm, 38 mm, 40 mm, 60 mm available
- Screw into the drill head by lining up the threads and rotating the drill clockwise – CAREFUL NOT TO CROSS-THREAD THE CORE DRILL [see figure 1 on page 293]
- Gently tighten with spanners - DO NOT OVER TIGHTEN
- Position the rock under the core drill on the flat base in the middle of the board [see figure 4 on page 293]
- Fix the rock sample in place by using the two bars, one on either side of the rock - FIX FIRMLY SO THAT THE ROCK DOESN'T MOVE.
- Make sure the safety sides surrounding the rock are in place and position the front panel in its slot
- Reset the green safety switch on the back of the machine [see figure 2 on page 294]
- Switch the mains power on at the wall panel by rotating the switch to the 1 position [see figure 2 on page 293]
- Choose the appropriate revolution speed depending on the material (approximately 960 RPM), by using the panel on the machine to varying the number to 1,2 and 3 and letters A and B as well as + or - [see figure 4 on page 294]
- Adjust the head position to core at the desired location – (x, y and z). To move the drill to either the left or right and forwards or backwards, use the handle at the side of the machine. In order to lift or lower the whole of the head and core drill, the switch below the RPM switch should be [see figure 4 on page 294]
- Lower the core drill by rotating the central handle clockwise so that the drill touches the flat base where the depth should be marked[see figure 1 on page 294]
- Position the core drill over the rock
- Turn on the water supply from the wall tap so that water comes flowing down the core drill [see figure 6 on page 293]
- Turn on the drill in the appropriate direction (clockwise) as indicated – OPPOSITE TO THE SCREW THREAD DIRECTION [see figure 3 on page 294]
- Slowly lower the drill piece using the two pronged handle located below the drill speed controls – CHOOSE THE APPROPRIATE SPEED FOR THE MATERIAL BEING USED. A MODERATE SPEED IS NEEDED FOR SANDSTONE, WHILST A MUCH SLOWER SPEED IS NECESSARY WHEN USING GRANITE. THIS IS TO AVOID DAMAGE TO THE DRILL AND THE POSSIBILITY OF THE ROCK SAMPLE SPLITTING
- Lift the drill piece occasionally to remove the debris beneath the drill
- Just above the mark indicating where the drill is resting on the flat base move the drill piece down more slowly in order to avoid damage to the end of the rock core
- Lift the core drill piece clear of the core and reposition for the next core
- When finished, turn off the drill and turn off the water supply at the wall tap
- Lift the drill head so that the front safety panel can be removed
- Switch off the mains power by turning the wall switch to the 0 position
- Remove the safety shield at the front
- Remove the core drill by rotating it anticlockwise
- Release the bars securing the rock. Lift it clear and then remove the cored samples
- Clean the machine with water and remove rock fragments
- Take the rock and cores away

Cutting

- Place the rock flat on the base in front of the saw blade and put safety shield in place [see page 295]
- Switch the power on by pressing the green button located on the front of the saw
- Turn on the water supply to the saw
- Cut the sample straight through while rotating it (keep fingers clear)

- If the sawn surface is uneven, use the circular blade to trim where appropriate
- Turn the saw off by pressing the red button
- Remove the pieces of rock from either side of the blade
- Clean the machine with water

Grinding

- Mark the surfaces to be ground with perpendicular lines using a permanent pen
- Position the v-block in the centre of the magnetic plate while the magnet is off (lever is pulled down to the left) [see figure 2 and 3 on page 301]
- Turn the magnet on by pulling the handle over through 180 degrees so that the lever is to the right
- Put the clamp onto the v-block
- Position the rock core against the v-block leaving a small clearance between the core and the base
- Fix the core in position by clamping it to the v-block - **DON'T OVERTIGHTEN AS IT WILL DAMAGE THE SIDE OF THE CORE**
- Make sure the grinding wheel is not obstructed in any way
- Switch on the mains power by turning the switch on the wall to the 1 position [see figure 5 on page 301]
- Release the red emergency stop button by pulling it out
- Turn on the grinding wheel, lubrication fluid and rack by pressing the 3 green buttons located to the lower left of the machine [see figure 2 on page 302]
- Make sure the grinding wheel is rotating correctly and that the lubricant is pouring out
- Position the grinding wheel at the desired location by rotating the 2 wheels on the front of the machine
- Reset the LCD indicators for both the x and y axis [see figure 4 on page 301]
- Using either manual or automatic controls grind off the rock surface — **MAKE SURE LESS THAN 0.1mm IS TAKEN OFF AT ANY ONE TIME FOR SANDSTONE, FOR OTHER ROCKS SUCH AS GRANITE TAKE OFF LESS THAN 0.01mm AT ANY ONE TIME. To use the automatic forward and backward control, pull out the manual handle, push the switch marked (->) and then press either side of the (0) [see figure 1 on page 302]**
- Turn off the machine by pressing the red emergency [see figure 2 on page 302]
- Remove the core sample by releasing the clamp
- Turn the sample upside down repeating the procedure to fix in position and then grind the sample flat
- Remove the core and measure it's length twice. These measurements should be perpendicular to one another. Use an average of the readings
- Replace the sample in the v-block and follow the above procedure until the core is at the desired length
- Make sure the surface parallism varies by less than 0.01 mm for a 40 mm rock core by using a clock gauge
- Turn the machine off by turning the wall switch to the 0 position [see figure 5 on page 301]
- Undo the magnetic base by moving the lever to the left position
- Remove the sample and v-block
- Clean down with water and wipe with WD-40

Experimental Procedure – USING THE TRIAXIAL CELL

- Clothing – e.g. lab coat, safety shoes, safety glasses, hair net

Porosity measurements

- Measure the length and width of the rock core sample in 3 different places and average the results using digital callipers. This is done by measuring the width at the top (95% of height), middle (50%) and bottom (5%). The length should be measured twice, perpendicular to each other
- Put the cored rock sample in the oven at a temperature ranging from 70^oC -90^oC for at least 2 days depending on the rock type (sandstone 2 days, granite 7 days) [see figure 3 on page 302]
- Remove the rock and weigh to an accuracy of 0.01 g
- Place the sample back in the oven for another day or so
- Remove the rock again and re-weigh. If no change occurs (less than 0.01g) from the previous weight then the rock is dry. Repeat the above steps if necessary
- Place distilled water or appropriate fluid inside the vacuum chamber and place the rock so that it is fully submerged [see figure 1 on page 302]
- Using the vacuum pump, pump out the air and saturate the sample with a vacuum of 10² Tors. Depending on the rock this may take hours (sandstone) to weeks (granite) [see figure 2 on page marked 302]
- Remove and weigh the sample to an accuracy of 0.01 g
- Place the sample back in the vacuum for some period of time (depending on the type of rock used) to make sure that it is saturated
- Remove the rock again and re-weigh. If no change occurs then the sample is saturated. If not then repeat the above steps until no change occurs
- Calculate porosity

Preparing the sample

- Put the rock sample approximately in the middle of a STET jacket
- Mark off the positions of the electrodes to be used for electrical measurements. This can be done by passing silver paint through the jacket holes in the jacket to mark their positions
- Remove the sample from the jacket and place a 1 cm diameter circle for each electrode position using the conductive paint
- Place the conductive paint on both ends of the rock sample in a criss-cross pattern. This should be a thin evenly distributed layer

Jacket set-up

- Obtain the appropriate concave inserts with a spike present
- Cover the 2mm diameter copper disc with solder
- For Electric Potential (EP) use the silver conductive glue to fix the copper disc to the insert
- For Acoustic Emissions (AE) glue the copper disc to one end of the AE transducer using the silver conductive glue. The other side of the transducer should be fixed to the insert with the same glue. – Make sure the glue doesn't touch the spike or cover the transducer because this would cause a short circuit and ruin the transducer
- Put the inserts in the 12 jacket holes, usually 8 AE inserts and 4 EP inserts - MAKE SURE THE CONCAVE SURFACE MATCHES THE SURFACE OF THE ROCK TO GIVE A GOOD SURFACE CONTACT
- Place the metal collars over the inserts and rubber area
- Put the holding pieces, used for sealing the jacket, on both ends of the jacket

Sample set-up

- Put the prepared sample in the middle of the jacket which has the appropriate inserts (AE and/or EP)
- Put the distribution plates on both ends of the rock sample. They have to be placed correctly with the spreading pattern touching the rock sample
- Position the jacket on the lower end-cap leaving a small gap between the end of the jacket and end-cap
- Push the holding piece down to the edge of the jacket to seal it
- Repeat the above procedure for the upper end-cap

- Make sure the yoke holes on the end-caps line up
- Fix the upper and lower end-caps by using the tiebars and 10 mm bolts [see figure 6 on page 296]
- Place the yoke in the centre of the bottom inner closer in between the lead-throughs and within the 3 dowel pins to hold it in place [see figure 5 on page 296]
- Make sure the coaxial wires aren't broken by doing a continuity test on each and mark up
- Connected to the appropriate software such as LOCAN and/or Labview
- Fix the pore pressure connections to the two end-caps using the 12mm spanner. Make sure the collar is sufficiently forward so that when the gland nut is tightened up the cone is held firmly in
- Attach the lead-throughs to the appropriate inserts. For EP, the inner core wire needs to be attached to the spike and for AE the inner core wire is attached to the copper disc on the AE transducer with the outer ground wire attached to the spike
- Use rubber bands to tidy up the wiring
- Test the AE transducers with the LOCAN (see below)

Note: Start Locan and Labview simultaneously so the data logging is synchronised

Locan AE analyser set-up [see figure 1 on page 306]

- Make sure the locan console is powered up
- Start the computer in DOS mode
- Load the locan program via DOS commands
 - cd ../..
 - cd locan
 - laqlau.exe
- Load the -ini file found under the file sub-menu to be used for the experiment. They are generally located under users such as david, parick, phil b.
- Check the AE channels are not a creating signal by electrical noise. (if noise is present, adjust the channel setting)
- Check the channel setting located under the test setup sub-menu
- Create a new data file under the file sub-menu and check the channels are working by running the program found under acquire sub-menu

Labview data logging set-up

- Make sure the NI-cards (PCI-6025) have been found and are working correctly using the automation and measurements software
- Make sure all the appropriate BNC-cables are connected to the correct labview board and are in the correct position (all inputs should be via differential input to avoid the electrical noise present in this lab)
- Check all the wiring for breakages and mend as required. Replace with another connector if necessary. They should be protected by metal foil to reduce electrical noise
- Start the computer and load the precision data and acquisition program shortcut
- Load the configuration file located under triaxial users of the F:\ drive – there may be several depending on the experiment - MAKE SURE THE CORRECT CALIBRATION DATA HAS BEEN PUT INTO THE PRECISION DATA AND ACQUISITION PROGRAM, INCLUDING THE TIME
- Check calibrations present in LabView are correct with known values
- Create a new data file and start recording all data
- Reset the time to zero using the reset button
- Check to make sure it is working correctly by comparing the labview readings with the appropriate panel readings

Turning the machine on

- Turn on the hydraulic ring main by pressing the green button on the far wall of the lab located beneath the Emergency Stop button [see figure 3 on page 303]
- Make sure the controls are in displacement control [see figure 1 and 2 on page 310 and page 311]
- Press the zero reset button located on the ramp generator found on the 2nd rack [see figure 1 and 3 on page 310 and page 312]
- Then press the stop button on rack No.2 [see page 312]

Appendix 1: Operational Procedure

- Balance the drive lights so that both are illuminated by rotating the displacement dial on rack No.1[see page 311]
- Switch on the machine by pressing the “pump on”, then the button marked “machine on”

Putting the sample in the vessel

- Go to the actuator/cross-head lever on the far side of the rig
- Make sure a reading of 50 bars is present on one of the pressure dials – IF NOT MAKE SURE THE HYDRAULIC RING MAIN IS OPERATING CORRECTLY
- Move the lever down into crosshead control
- Make sure nothing is obstructing the crosshead and actuator before moving them
- Raise the vessel so that the sample assembly can be pushed beneath it without causing damage
- Slide the bottom inner closer underneath the vessel and fix in position by using the 2 holes at either end of the metal base – MAKE SURE NO WIRES ARE CAUGHT BENEATH THE METAL BASE PLATE BECAUSE THEY WILL GET DAMAGED IF THE VESSEL IS LOWERED ONTO THEM
- Using the black mark on the pressure vessel, line up the vessel and the closure so that the screw threads don't catch on each other (generally line up with the groove for pore pressure from the second intensifier)
- Lift the crosshead slightly so that the weight is just being taken by the ball bearings
- Rotate clockwise until the locking pin is engaged
- Lower the cross-head until the vessel is resting on the metal base plate
- Switch between actuator and cross-head controls to lower the cross-head down to the mark indicated 16+ on the side of the pillars
- Slowly lower the actuator until it touches the hemi-spherical seat which sits on top of the ram. DO NOT LOAD THE SAMPLE BECAUSE IT COULD BE DAMAGED

LVDT set-up(displacement transducers)

- Put the LVDT transducers in the three available holes at the top of the ram and tighten so that they are just touching the pressure vessel [see figure 4 on page 296]
- Make sure the controls on the rack No.2 are set to the AB
- Depress transducer with your finger and check to make sure a reading change occurs on panel No 2

Confining pressure set-up

- Attach the confining pressure piping to the metal base in the middle of the three connectors using 2 adjustable spanners [see figure 1 on page 296]
- Open the relief valve located 7/8th of the way up the side of the pressure vessel and place a jug beneath it to catch the oil
- Open the valve which is located below the 10 cm³ pore pressure handle on the far side of the rig in an anti-clockwise direction
- Turn on the power to the confining pump using the lever on the wall next to the hydraulics so that it shows red and “on” [see figure 5 on page 292]
- Switch on the two green light buttons located on the far wall of the lab next to the control rack [see figure 1 on page 292]
- On the confining pressure panel, set a pressure of approximately 20 MPa [see figure 2 on page 291 / figure 4 also give a pressure reading and figure 2 on page 309]
- The pump should begin (if not, with the assistance of a technician, check the air supply, conical spring, electrical fuse). Eventually oil should begin to flow out of the relief valve. Wait at least one minute until a steady flow is present and then close the relief valve [see figure 3 and 6 on page 291]
- Set the desired confining pressure for the experiment – REMEMBER, PUMPING THE OIL HEATS IT, SO ALLOW FOR IT
- Check for oil leaks at the base plate
- Once the pressure is reached, isolate the confining pressure pump by closing the valve clockwise. This is located below the 10 cm³ pore pressure handle
- Immediately afterwards turn off the power to the confining pump by turning the handle to the green and ‘off’ position the wall switch

- Check to see if oil is coming out of the pore pressure piping top/bottom. If so, stop the test, remove the sample (described elsewhere) and replace with another one, check the connections carefully and the positions of the holding pieces
- If no leaks are present close the plastic doors for safety reasons

Separator set-up (used in conjunction with 50 cm³ permeameter)

Separator A

- Make sure the permeameter is switched off [see figure 1 on page 307]
- Open bleed valve on sample side [see figure 2 on page 307]
- Open isolation valve on separator A [see figure 2 on page 307]
- Open priming valve on separator A [see figure 2 on page 307]
- Open priming valve on the pump A [see figure 2 on page 307]
- Make sure the B priming valve is shut [see figure 2 on page 307]
- Pump fluid until it comes out of the bleed valve as all air has been removed
- Close the bleed valve [see figure 2 on page 307]
- Pump fluid until it comes out of the end of the pip which is connected to the base plate
- Close the isolation valve on separator A [see figure 2 on page 307]
- Open the bleed valve on the intensifier side of separator A [see figure 2 on page 307]
- Pump fluid until it comes out of the bleed valve
- Close the bleed valve on the intensifier side of separator A [see figure 2 on page 307]
- Pump fluid to force the shuttle to one end and until a pressure of 30 bars is present. When the reading stays at 30 bars it implies that the shuttle is all the way to one end of the separator; in this case it is fully backwards and 50 cm³ full of the pore fluid
- Close the priming valve on separator A [see figure 2 on page 307]
- Close the priming valve on the pump [see figure 2 on page 307]
- Release the excess pressure from the pump by rotating the release mechanisms anticlockwise and then closing it clockwise once the pressure has dissipated [see figure 2 on page 307]
- Open the priming valve on the permeameter by switching the lever to the open position (located next to the permeameter pressure vessel)
- Open the isolation valve to intensifier A on the permeameter [see figure 2 on page 307]
- Open bleed valve on intensifier side of separator A [see figure 2 on page 307]
- Pump fluid through to remove all the air from the system
- Close the bleed valve on the intensifier side of separator A [see figure 2 on page 307]
- Close the isolation valve between the permeameter and separator A [see figure 2 on page 307]
- Pump fluid through to move intensifier A piston fully backwards which can be seen by the displacement reading on the permeameter controls reaching zero
- Close the priming valve on intensifier A [see figure 2 on page 307]
- Turn on the permeameter and put in pressure control
 - Make sure the pressure dial is below 0.3
 - Press the “p” button the appropriate rack
- Open the isolation valve between intensifier A and separator A [see figure 2 on page 307]

Separator B

- Make sure the permeameter is switched off
- Open bleed valve on sample side [see figure 2 on page 307]
- Open isolation valve on separator B [see figure 2 on page 307]
- Open priming valve on separator B [see figure 2 on page 307]
- Open priming valve on the pump (B) [see figure 2 on page 307]
- Make sure the A priming valve is shut [see figure 2 on page 307]
- Pump fluid until it comes out of the bleed valve as all air has been removed
- Close the bleed valve [see figure 2 on page 307]
- Pump fluid until it comes out of the end of the pip which is connected to the base plate
- Close the isolation valve on separator B [see figure 2 on page 307]
- Open the bleed valve on the intensifier side of separator B [see figure 2 on page 307]
- Pump fluid until it comes out of the bleed valve
- Close the bleed valve on the intensifier side of separator B [see figure 2 on page 307]
- Pump fluid to force the shuttle to one end and until a pressure of 30 bars is present. When the reading stays at 30 bars it implies that the shuttle is all the way to one end of the separator; in this case it is fully backwards and 50 cm³ full of the pore fluid

- Close the priming valve on separator B [see figure 2 on page 307]
- Close the priming valve on the pump [see figure 2 on page 307]
- Release the excess pressure from the pump by rotating the release mechanisms anticlockwise and then closing it clockwise once the pressure has dissipated
- Open the priming valve on the permeameter by switching the lever to the open position (located next to the permeameter pressure vessel) [see figure 2 on page 307]
- Open the isolation valve to intensifier B on the permeameter [see figure 2 on page 307]
- Open bleed valve on intensifier side of separator B [see figure 2 on page 307]
- Pump fluid through to remove all the air from the system
- Close the bleed valve on the intensifier side of separator B [see figure 2 on page 307]
- Close the isolation valve between the permeameter and separator B [see figure 2 on page 307]
- Pump fluid through to move intensifier B piston fully backwards which can be seen by the displacement reading on the permeameter controls reaching zero
- Close the priming valve on intensifier B [see figure 2 on page 307]
- Turn on the permeameter and put in pressure control
 - Make sure the pressure dial is below 0.3
 - Press the “p” button the appropriate rack
- Open the isolation valve between intensifier B and separator B [see figure 2 on page 307]
- Decide which intensifier you wish to be fully primed with the other intensifier being empty
- For the intensifier you wish to be empty, open the isolation valve on the appropriate separator and collect the fluid that comes out
- Once the fluid ceases, close the isolation valve you have just opened

Pore pressure set-up

- Isolate the 10 cm³ intensifiers from the pressure vessel by turning the isolation valve clockwise, located behind the intensifier [see figure 3 on page 296]
- Turn on the 10 cm³ pore pressure intensifier using the controls located beneath the actuator controls on rack No 3 [see page marked 313]
 - This is achieved by placing the control button located on the rack No 3 into the displacement mode (D) which is located beneath the 5 dials to the left of the LCD display which should then be highlighted
 - On the panel located beneath the LCD display press the error button “E”
 - Rotate the mean displacement dial located to the left of the display until the LCD display ranges 0-10
 - Change the display select panel into Change Over (CO) control
 - Rotate the mean pressure dial located to the left of the display until the LCD display ranges 0-10
 - Check the error reading to make sure it hasn't changed. If it has then repeat the above steps until both the (E) and (CO) displays lie between 0-10
 - Switch on the intensifier by pressing the ‘on’ button to the far right of rack No 3
- Change from displacement control into pressure control
 - To achieve this, set the CO to zero by rotating the mean pressure dial
- Change the display to displacement so the position of the piston can be determined (0=fully backwards, 10 = fully forwards. This is normally set to 4 for tests)
- Open the inlet valve marked inlet P2 located behind the intensifier to draw in the pore fluid
- Lift the hose above the intensifier in order to remove any air that may be present. To fill the hose place it into a container which is $\frac{3}{4}$ full of the pore fluid. The hose must be placed under the surface of the liquid quickly to avoid any air entering the system
- Turn the machine off
- Open the isolation valve
- Pump pore fluid through the intensifier until water comes out of the pore piping which is to be connected to the metal base plate (this process removes all the air from the system)
- Close the isolation valve
- Turn the machine back on
- Pump the pore fluid into the intensifier to the desired level, watching to make sure water is drawn into the intensifier rather than air by looking at the hose
- Close the inlet valve and set the desired experimental pore pressure.
- Slowly open the isolation valve until fluid comes out from the end of the pipe

- Close the isolation valve and connect the pipe to the lower pore pressure connector fitting marked with a “B” with 2 adjustable spanners
- Repeat the above procedure for the 22 cm³ intensifier located next to the pressure vessel which is connected to the T connector [see figure 7 on page marked 296 and page 304]
- Close the isolation valve between the two intensifiers [see figure 1 on page 296]
- Set the pore pressure for both intensifiers and open the isolation valves (ideally neither pistons should move)

Furnace and linked equipment set-up

- **MAKE SURE THE VESSEL IS SEALING ABOVE THE DESIRED PRESSURE YOU WISH TO USE FOR THR TEST. IF NOT, DON'T USE THE FURNACE UNTIL THIS CAN BE ACHIEVED**
- Lower the pressure to a level which allows for thermal expansion which is caused by the furnace
- Turn the furnace controller on at the mains switch (13 Amp plug)
- Make sure the ramp generator is turned off (see below for info) [see pages 299 and 300]
- Check all 3 thermocouples are giving similar readings [see figure 2 on page 300 and figure 2 on page 299]
- Check the thermocouple and heating elements are connected correctly to the back of the furnace controller located above rack No.1 (No obvious broken or loose wires)
- Set the desired temperature and the length of the time at that particular temperature on the left hand controller (model 815) (see book for full instructions and operation) [see figure 1 on page 299]
 - Press (P) to enter the configuration mode until “Pr1” appears, press the up arrow and then set the desired temperature ramp rate by pressing the up and down arrows (maximum of 5⁰C/min is recommended)
 - Press (P) until “P11” appears, press the up arrow and set the desired furnace temperature (remember to allow for cooling related to convection)
 - Press (P) until “Pd1” appears, press the up arrow and set the desired length of time to stay at “P11”
 - Press (P) until “Pr2” appears, press the up arrow and set the desired temperature gradient decrease for after the test (maximum of 10⁰C/min recommended)
 - Press (P) until “Pd2” appears press the up arrow and set this to show the time required before beginning another cycle. Normally this is set to “end” but during healing experiments this should be changed
 - Press (P) until “Sp1” appears, press the up arrow and set this to 0
 - Press (P) until the configuration mode is exited
- On the Omega controller, set the emergency cut off for the furnace wall to 200⁰C (see book for full instructions and operation) [see figure 2 on page 299]
 - Press (menu) to go into the configuration mode until “set pt” appears, press “enter”
 - Press (max) and (min) to set “SP1” and then “enter” to store the change and return to the run mode, “strd”. The new reading should appear if done correctly
 - Press (max) and (min) to set “set pt2” set this to the same value as “SP1”. Then press “enter” and “strd”. The new reading should now appear if it has been set correctly
 - Press “enter” once more to exit “set pt”
 - Keep pressing (menu) until the configuration mode is exited with saved changes and the original screen is present showing room temperature
- To begin heating the furnace, oil, metal, rubber jacket and rock, press the “run” button on the left furnace controller (model 815) - “ramp” SHOULD APPEAR BENEATH THE TEMPERATURE READING [see figure 1 on page 299]
- At all stages now, constantly monitor and record the heating elements temperatures, the thermocouples from the rock and the pressures in order to spot any possible problems - **IF A PRESSURE LEAK IS SPOTTED STOP THE TEST IMMEDIATELY AND WAIT UNTIL THE FURNACE IS COOLED BEFORE FIXING**
- During the ramp process the temperature should increase and occasionally “r1” will flash up for 2 seconds on the controller
- During the stage where the temperature is constant “d1” will flash up for 2 seconds and the temperature should only vary by 10⁰C caused by convection currents
- During the temperature decrease stage “c1” will flash up for 2 seconds occasionally
- To suspend or pause the heating elements, press the “run” button causing the “ramp” indicator to flash . Pressing this again will re-start the heating cycle and “ramp” will be highlighted

Appendix 1: Operational Procedure

- To turn off the heating cycle prematurely press the up and down arrows together and the “ramp” indicator should disappear
- After the experiment is completed, monitor the oil temperature. Only when it is back at room temperature (25°C) can any valves be opened and the sample removed

Controls

- Lower the actuator slowly under displacement control until a reading of zero appears on the top LCD panel. Marked as stress this should remain constant. This may take some time due to friction of the seals and the ram, which means that this may need to be repeated several times
- Make sure the ramp regulator is set to “stop” located on rack No.2 beneath the LCD [see page 312]
- Once settled, change the controls into LVDT displacement by balancing the controls
- This is achieved by pressing the displacement control button on rack No.2 and rotating the dial marked mean level until both drive lights present on rack No.1 next to the LCD flash alternately. At this stage the control should switch into displacement, but may need slight adjustment so move the dials slowly in either direction
- Set the desired ramp rate using calibration data, then press the ramp generation button to the right of the LCD on rack No.2 and rotate the rate dial until set. – MAKE SURE THE MOVEMENT ARROW PRESENT UNDERNEATH THE DIALS IS SET FOR DOWNWARD MOTION [see page 312]

Start the test

- Press the “str” button on the ramp generator located underneath the dials and LCD on rack No.2 [see page 312]
- Record data using computers – see elsewhere for details)
- Alter the pore pressure and confining pressure depending on the test procedure, e.g. streaming potential, pore pressure will need to be change

Stopping the test

- Turn the ramp generator off by pressing “STP” located on rack No.2 next to the LCD display [see page 312]
- Put the controls back into actuator displacement control via the balance and crossover method described earlier
- Stop recording data via Labview and LOCAN
- If the situation gets out of control and is becoming an emergency press the emergency button

Removing confining fluid

- Open the isolation valve located below the pore pressure handle behind the pore pressure 10 cm³ intensifier. The panel reading below rack No.3 should decrease to around 2 MPa when at atmospheric pressure
- Attach the nitrogen supply via the reinforced hose to the closed relief valve located on the side of the pressure vessel
- Remove the middle screw located on the metal base plate to allow for oil drainage
- Attach the blue pipe with the screw thread fitting to the hole created by the removal of the middle screw. The other end of the pipe goes into the confining pump
- Turn on the nitrogen supply to a maximum 6 bar,
 - Using a square spanner rotate SLOWLY anticlockwise until the pressure in the regulator on top of the nitrogen cylinder gives a constant readings, e.g. 100 bars
 - Turn the round dial clockwise until the desired pressure reading is shown
- Open the relief valve to allow nitrogen gas to force out the oil
- Make sure that all the oil is removed. This can be confirmed by the presence of nitrogen escaping from the pipe and a resultant change in the noise emitted from the pipe
- Turn off the nitrogen gas by turning the square spanner clockwise on the regulator and letting the readings return to zero
- Unscrew the hose attached to the relief valve
- Detach the blue tube connected at the base of the vessel and tidy it away
- Check the level of oil in the confining pump because it may occasionally need topping up (check the gauge on the side to see when this is necessary) [see figure 6 on page 292]

Removing pore fluid pressure

- Isolate the two intensifiers/separators by closing the valve located between them
- Turn the pore pressure intensifiers (10 cm³ and 22 cm³) off by pressing the off buttons [see page 304 and page 312]
- Undo the pipe at the base of the vessel using 2 adjustable spanners but after the confining pressure has been removed. Begin by cracking the sealed system to allow any pore fluid still under pressure to escape

Remove sample from vessel

- The machine is assumed to be turned on. If this is not the case, read the appropriate instructions to accomplish this before continuing
- Make sure the controls are in actuator displacement control and all the pressures have been removed e.g. confining pressure and pore pressure
- Remove the LVDT's located on the ram and store next to the side walls
- Lift up the actuator so that it is clear of the ram by at least 4 cm
- Go to the actuator/crosshead controls located on the far side of the vessel
- Move the lever down into crosshead control
- Lift the vessel until all the weight is resting on the ball bearings
- Rotate the vessel counter-clockwise until the black mark at its base is in-line with the groove for the pore pressure pipe
- Lift the vessel slowly all the way up making sure nothing gets caught
- Remove the 2 bolts stopping the bottom inner closure from rotating
- Remove the bottom inner closure assembly from the vessel onto it's carriage by sliding it along the base
- Using a flashlight and WITHOUT PUTTING YOUR HEAD UNDER THE VESSEL, have a quick look with a mirror to inspect and make sure no damage has occurred to the inner surface of the pressure vessel and furnace
- Lower the vessel until it is resting on the base
- Change the actuator/crosshead lever into the actuator position
- Move the actuator to the bottom of its range if not already there
- Turn the machine off by pressing the hydraulics and power button on the right side of rack No. 1
- Reset the ramp generator located below the LCD on rack No.2 by pressing the "zero" button
- Then press the "stp" button next to the "zero" button
- Turn off the hydraulic ring main by pressing the unlock (red button) on the far wall

Remove rock from jacket

- Remove the rubber bands holding the coaxial wires together with the sample
- Detach the lead-through wires from the AE and EP transducers by de-soldering them avoiding damage to the transducers and the coaxial wires and then put the wires from the same lead-through together
- Check the wires are intact following the test results and do a continuity test
- Undo the pore pressure piping from the two end-caps using a 12 mm spanner
- Move the yoke assembly onto a bench
- Take the top and bottom end-caps off the jacket by removing the 10 mm bolts holding the yoke together
- Inspect the jacket for any visible damage and note if present – (It may need to be replaced if the damage is extensive)
- Put one of the 40 mm diameter metal dummy samples into the lower end of the jacket and push the rock out of the top. Once the electrical contacts used for EP are visible mark them with the same number as the channel used, so a comparison can be done later. A rubber band may help in holding the sample together after being removed from the jacket
- Clean the distribution plate, jacket and bottom inner closure of oil by using an air hose, and check for any visible damage, and if present replace where required
- Take a photograph of the rock specimen and mark on it the type of experiment done, e.g. creep, load, strain, length, conditions

CLEAN UP THE LAB AND LOCK UP WHEN YOU GO !!!

Other procedures required in the use of the triaxial cell –

- Follow general ob15b procedure
- See above section for the exact detail on how to use the equipment

Testing pressure vessel seals

- Remove the electrical lead-throughs used during deformation experiments by pulling them out from the bottom inner closure – MAKE SURE ALL WIRES ARE DISCONNECTED FIRST
- Check the plug holes for damage by cleaning with a high pressure air line
- Clean the heat resistance plate
- Replace the O-rings and PTFE backing rings on the 5 blank lead-through plugs
- Check these and the PTFE backing rings for damage on all surfaces – if any is found then replace them immediately
- Place the 5 blank lead-throughs into the bottom inner closure gently to avoid damage to the O-rings and backing rings
- Put the bottom inner closure into the pressure vessel and test to 200 MPa for several hours
- If the pressure becomes constant, the seals are working and the pressure vessel is sealed. If there is a leak, then the remaining seals need to be removed and replaced. A further pressure test is required to identify if the pressure vessel are working correctly. Following this procedure, replace the seals as necessary until a satisfactory result is obtained

Replacing seals and furnace

Removing pressure vessel components

- Make sure the sample assembly, LVDT's, bottom closure, pore pressure and confining pressure piping are disconnected
- Unscrew the Hex 16 screws attached from the load cell to the top of the pressure vessel
- Lift the vessel under crosshead control until the screws are clear
- Remove the hemispherical seat from the top of the ram and unscrew the ram plate placing it on a side bench
- Put two M12 x 100 screws into the top breech nut, rotate the nut anticlockwise until becomes loose
- Lift the nut clear of the screw threads and put on the side bench
- Attach the other ram plate and screw down tightly
- Using the actuator and crosshead controls wrap some strong wire around the ram plate and slowly lift the ram out. Once fully lifted out, remove the wire and place the ram on the side bench
- Using the black bar and two M12 x 70 screws attach this to the top retaining nut and rotate it anticlockwise until it is resting on the top thread only
- With **TWO** people, lift the top retaining nut on the floor next to the work bench
- Remove the relief valve by unscrewing the 16AF attached on the inside of the pressure vessel
- Lift out the top assembly. This is achieved by connection the "I" bar. The smaller end connects to the top of the top closure on the 85 PCD, the upper rests on the top of the vessel. By rotating the bolt on the screw thread, the assembly is slowly raised out
- To stop the bottom outer closure falling out the nylon pieces and screw thread bar must be used. Place the screw thread bar down the centre of the vessel avoiding damage to the seals and surface e.g. furnace
- Lower the crosshead and screw the Hex 16 screws back into the pressure vessel linking it to the actuator – MAKE SURE THEY ARE TIGHT
- Under crosshead control lift the pressure vessel above the support frame
- Put the bars across the frame to support the pressure vessel and then tighten up the M16 x 40 screws so that it becomes secure
- Slowly lower the pressure vessel down until it is almost touching the supporting frame
- Rotate the vessel until the holes in the frame and the hole on the bottom of the vessel line-up
- Put screws up through the support frame and slightly tighten into the vessel.
- Lower the vessel onto the support frame
- Fully tighten the screws holding the pressure vessel and support frame together
- Change the controls over to actuator
- Place the wood plank shaped like an "I" under the frame and vessel

- Remove the wire protector which covers the thermocouple and heating element wires
- Put the round 82.5mm nylon disc up into the bottom outer closure with the bolt on the lower side and screw into the threaded bar until 20mm of metal is remains exposed
- Put the large circular nylon disc with a hole in the centre, on the top of the vessel so that the threaded bar goes through it
- Put the rectangular nylon bar, with the bolt facing upwards onto the threaded bar and rotate clockwise until it become tight – check to make sure it isn't catching on anything (when tight the bottom outer closure is being held in place)
- Remove the wooden plank
- Put the nylon jack alignment tool on the hole beneath the pressure vessel so that it can slide in and out
- Put the jack on the alignment piece underneath the pressure vessel
- Place the circular metal piece with two M12 x 30 screws pointing upwards onto the jack
- Raise the jack using a ½ inch socket wrench until the plate is nearly flat against the bottom retaining nut whilst avoiding trapping the screw and damaging the pressure vessel
- Rotate the metal disc until the screws can be tightened slightly
- Lower the jack
- Replace the two M12 x 30 screws with the black bar, two spacers and two M12 x 70 screws so that the screws point up through the bar with the spacers on top
- Rotate the bottom retaining nut anticlockwise three complete revolutions
- Replace the black bar, two spacers and two M12 x 70 screws with the two M12 x 30 screws
- Undo the wires on the side of the pressure vessel connected from the furnace controller to the furnace e.g. heating elements and thermocouples
- Pull the heating element and thermocouple wires through the vessel wall so that they wont be broken when the bottom outer closure is removed
- Raise the jack so that it is almost supporting the bottom retaining nut
- Using the holes in the side of the plate continue to rotate the nut anticlockwise whilst keeping the jack just underneath. Once the nut is no longer engaged by the screw threads the jack will supports it
- Lower the jack completely
- Attach the black bar and two M12 x 50 screws to the top of the bottom retaining nut
- With **TWO** people, lower the bottom retaining nut onto the floor next to the bench
- Reach under the pressure vessel and put two M3 x 100 screws into the bottom outer closure
- Remove the stopper bar located on the far side of the pressure vessel marked with a red knob
- Loosen the rectangular nylon block 1 cm so that the bottom outer closure can fall slightly without causing damage
- Attach the "I" bar to the base of the bottom outer closure. The smaller end connects to the closure on the 85 PCD, the wider part rests on the bottom of the vessel. By rotating the bolt on the screw thread, the assembly is slowly raised out
- Put the jack under the pressure vessel
- Raise the jack and place two nylon blocks lengthways to support the bottom outer closure
- Rotate the rectangular nylon block on the top end of the vessel to the end of the screw thread
- Lower the jack slowly to avoid causing damage
- Once the bottom outer closure is held by the final screw thread, reposition the nylon block by putting them on their flat side
- Once the blocks are supporting the weight, remove the rectangular block at the top of the pressure vessel
- Take the bottom outer closure (furnace) out of the pressure vessel
- Remove all nylon pieces and screw thread to a side bench

Replacing seals

Bottom closure without furnace (See section below for the bottom closure with the furnace)

- Clean the bottom outer closure by removing the oil with the use of a dry cloth
- Check for any visible damage – if present request the help of a technician
- Unscrew the four M4 x 15 screws which hold down the bottom seal retainer
- Remove this seal retainer, inner and outer mitre rings and the O-rings
- Check the mitre rings and O-rings for surface damage – replace where appropriate
- Use existing mitre rings if not damaged e.g. neither bent or have surface marks

Appendix 1: Operational Procedure

- Clean the O-ring surface grooves and check for damage
- Cover the O-ring grooves with a light coating of graphite anti-scuffing paste
- Replace the mitre rings and O-rings – THE VESSEL WILL NOT SEAL IF THE MITRE RINGS ARE NOT CORRECTLY PLACED
- Place the bottom seal retainer on the bottom outer closure
- Fix the retainer in place using four M4 x 15 screws

Piston

- Take off the end piece used for lifting the piston out of the pressure vessel
- Slide off the ram collar
- Remove the M2 x 20 screws holding the ram collar together
- Check the O-rings and mitre rings for damage replacing the O-rings if necessary but use the mitre rings if possible
- Cover the O-rings and mitre rings with anti-scuffing paste
- Place the O-rings and mitre rings correctly
- Replace the top piece on
- Tighten up the M2 x 20 screws
- Slide the ram collar correctly into place

Top closure

- Unscrew the four M4 x 15 screws holding the top ceramic spacer and the top plate to the top plug
- Place the pieces on the side bench
- Remove the inner and outer mitre rings and O-rings, checking for surface marks
- Unscrew the top plate anticlockwise
- Remove the spacer ring from the inner and outer surfaces so that the O-rings and mitre rings can be removed and checked for damage
- Unscrew the top seal retainer anticlockwise
- Clean the different components
- Get replacements for all the O-rings and mitre rings where required, cover them all with anti-scuffing paste
- Replace the appropriate mitre ring, O-ring and spacer onto the top outer closure
- Screw down clockwise the top seal retainer
- Put the appropriate mitre rings, O-rings and spacers onto the top plug
- Screw the top plug down clockwise
- Place the top plate onto the top plug with the four holes lined up
- Place the top ceramic spacer on top of the top plate and fix in position using four M4 x 15 screws – if the furnace is not being used don't use the ceramic spacer on top of the bottom seal retainer

Put the ram, furnace and bottom outer closure back into the pressure vessel

- Under crosshead control lift the pressure vessel above the support frame
- Put the two bars across the frame to support the pressure vessel and then tighten up the M16 x 40 screws slightly
- Slowly lower the pressure vessel until it is almost touching the supporting frame
- Rotate the vessel until the holes in the frame and the holes in the bottom of the vessel line-up. Put screws up through the support frame and slightly tighten into the vessel.
- Lower the vessel onto the support frame
- Change the controls over to actuator
- Fully tighten the screws holding the pressure vessel and support frame together

IF THE FURNACE IS ABSENT, MISS OUT THE APPROPRIATE STEPS

- Make sure the lower length screw thread is down the centre of the pressure vessel because it is used with the nylon disc's to hold the furnace in position
- Lay the two nylon block on their thinnest side and place onto the jack
- Put the 82.5mm nylon disc under the bottom outer closure with the bolt facing downwards
- Put the bottom outer closure and furnace onto the jack
- Raise the jack slowly with the ½ inch socket wrench

Appendix 1: Operational Procedure

- Slowly guide the furnace into the inner pressure vessel wall – IF THE JACK BECOMES STIFF THE FURNACE IS NOT LINED UP CORRECTLY, LOWER SLIGHTLY AND REPOSITION BEFORE RAISING IT AGAIN (HAVING 2 PEOPLE FOR THIS HELPS)
- Continue to raise the furnace until the jack cannot go any higher with the nylon blocks in their current orientation
- Holding the 82.5 mm nylon disc under the closure, rotate the screw thread to engage the bolt until 20 mm of the screw thread sticks out of the bottom of the nylon piece
- Put the large circular plate over the screw thread at the top of the vessel together with the rectangular block with the bolt facing upwards
- Rotate the rectangular block until the bottom outer closure begins to be raised by the screw thread
- Lower the jack and rotate the nylon blocks so that the new position has them on the centre of the jack and on the narrow side
- Raise the jack to support the bottom outer closure
- Continue to raise the jack until the 5 threads used for the bottom retaining nut can be seen
- Very slowly raise the bottom outer closure to avoid damage to the bottom outer ceramic spacer – ALTERNATIVELY THIS CAN BE DONE WITH THE RECTANGULAR BLOCK AND SCREW THREAD BUT IT TAKES LONGER
- Tighten up the rectangular nylon block by rotating it clockwise so that it takes the weight of the bottom outer closure
- Lower the jack
- Put two M3 x 100 screws in the holes on the bottom closure and rotate the closure until the holes in the side of the closure approximately match up with the holes in the side of the pressure vessel
- Slowly raise the bottom closure with the jack until the seals have gone into the vessel and the groove present on the side of the bottom outer closure can be seen through any of the 4 holes in the pressure vessel wall (use a light to help here)
- Tighten up the rectangular nylon block so that it is taking the weight of the bottom outer closure
- Rotate the closure until the holes in the pressure vessel match exactly with the holes in the pressure vessel wall – IF THIS IS DONE CORRECTLY YOU SHOULD BE ABLE TO SEE THE 82.5 NYLON DISC FROM ANY OF THE 4 HOLES IN THE PRESSURE VESSEL
- Put the stopper bar in the marked hole, this stops the bottom closure rotating
- Remove the jack, nylon pieces, M3 x100 screws and the jack alignment piece

Wiring up the furnace (ignore is not used)

- See the wiring diagram on page 289 for more details
- Place the wooden plank underneath the vessel and the support frame
- Mark up the thermocouples and the heating elements for use in the furnace controller
- Put the largest diameter heat shrink which fits through the pressure vessel walls into the vessel so that the wires can be guided through the bottom closure and vessel wall
- Use one of the remaining three holes for two wires from the same heating element and the thermocouple furthest away from that hole so that the thermocouple connection remains on the inner surface of the closure and doesn't get caught and broken in the pressure vessel wall
- Use one of the remaining two holes for two wires from the same heating element, the furthest away thermocouple and one of the heating element wires nearest the hole used for the stopper bar
- With the final hole, put the remaining two wires from the same heating element, the remaining thermocouple and the remain heating element wire through it
- Connect the heating element wires with their labelled partners on the outside of the pressure vessel
- Connect all the wires to the two plugs which go into the back of the furnace controller, 1) Heating elements and 2) Thermocouples
- Check the wiring with a continuity test – IF BROKEN IDENTIFY THE PROBLEM AREA AND TRY TO FIX WITHOUT REMOVING THE FURNACE, IF NOT POSSIBLE THEN REMOVE THE FURNACE (SEE ABOVE)

Putting the rest of the pressure vessel together

- Remove the "I" shaped wooden plank
- Put the jack alignment piece and the jack under the vessel

- Use two M12 x 30 screws to fit the metal plate to the base of the bottom retaining nut
- Use two M12 x 70 screws to fix the black bar to the top of the bottom retaining nut
- With **TWO** people, place the bottom retaining nut onto the jack
- Remove the M12 x 70 screws and the black bar from the top of the retaining nut
- Line up the screw threads of the retaining nut and the pressure vessel
- Lift the retaining nut into the vessel until the screw threads engaged by using a clockwise motion
- Rotate the nut all the way into the pressure vessel
- Remove the jack and alignment piece
- Replace the two M12 x 30 screws with M12 x 70 screws, the black bar and spacers
- Continue to rotate the retaining nut until it locks in place
- Remove the M12 x 70 screws, black bar, spacers and the metal plate
- Put the retainer plate in the groove in the base of the bottom retaining nut and screw up tightly with a Hex 5/32 key to connect the nut to the vessel
- Remove the hexagonal nylon block and 82.5 mm nylon piece
- Fix the wire retaining screen onto the inner surface of the bottom outer closure to ensure all the wires are protected from damage
- Undo the M16 x 40 bolts holding the pressure vessel to the support frame
- Lift the pressure vessel off the support frame and lower to the ground
- Unscrew the Hex 16 x 180 screws attaching the load cell to the pressure vessel
- Raise the crosshead so that the screws are at least 50 cm clear
- Remove the screw and the nylon pieces
- Put in the dummy furnace if the actual furnace is not being used to fill up some of the void space
- Lift the top closure and associated bits onto the pressure vessel
- Gently lower the top closure (top plate first) into the top of the vessel. Make sure the hole in the outer closure and the piping used for the relief valve match up
- Screw up the 16AF screw used for the relief valve
- Use two M12 x 70 screws to fix the black bar to the top of the top retaining nut
- With **TWO** people, put the top retaining nut onto the pressure vessel
- Rotate the retaining nut clockwise until the nut locks
- Put the ram down the centre of the pressure vessel, making sure the inner part of the ram is fully depressed – generally achieved with gentle pressure
- Remove the ram end piece
- Put two M3 x 100 screws into the top breach nut
- Lower the breech nut into the top of the vessel so the screw threads do not lock
- Once fully down rotate clockwise until the breech nut rests against the retaining plate – this will involve lifting the nut slightly
- Put the ram top piece and the hemispherical seat back onto the ram
- Lower the crosshead until the two Hex 16 x 180 screws can be tightened up
- Tighten up the Hex 16 x 180 screws

Pore intensifier

Removing intensifier from triaxial machine

- Turn off the hydraulic ring main when no-one is running a test by pressing the red emergency stop button located on the far wall of the laboratory
- Isolate the hydraulic inlet by pulling the lever so that it is perpendicular to the piping
- Remove the L-shaped pieces of piping connecting the base of the 10cc fluid intensifier to the ring main
- Use two blanking plugs to blank off the pipes
- Release the red emergency stop button
- Remove the horizontal bars located at the top and bottom of the intensifier rig using a 5 hex key
- Undo the 16AF screw attached to the end of the pore pressure piping which is connected to the bottom inner closure
- Undo the confining pressure transducer using a 16 spanner and position it so that it won't get caught when the intensifier is removed
- Pull out all the electrical connectors including P1, P2, disp and main appt located next to the priming valve handle

Appendix 1: Operational Procedure

- Pull out the pore intensifier unit and put it back on the floor – MAKE SURE IT DOESN'T CATCH ON ANYTHING

Replacing seals

- Rotate the 22AF screw, located at the end of the intensifier, in an anti-clockwise direction
- Unscrew the three 16AF screws on the left hand side of the intensifier so that the piping can be removed in one piece
- Remove the piping and store in a safe place
- Unscrew with a 17 spanner the two bolts which hold the intensifier down to the base plate
- With **TWO** people lift the intensifier onto a bench
- Remove the three Hex 4 screws holding the displacement transducer to the potentiometer adapter
- Remove the four Hex 4 screws holding the potentiometer adapter to the intensifier
- Undo the eight Hex 4 screws, which hold the front and back part of the intensifier together
- With one person supporting the displacement transducer, gently pull the intensifier apart and support on the bench – REMEMBER TO UNSCREW THE FITTING HOLDING THE DISPLACEMENT TRANSDUCER TO THE PISTON, OTHERWISE IT WILL BE BROKEN
- Replace the O-ring with a new one into the correct groove and cover with anti-scuffing paste
- Reconnect the piston and displacement transducer
- Push the front and back halves of the intensifier together – MAKE SURE THE O-RINGS DOESN'T MOVE OUT OF IT'S GROOVE BECAUSE IT MAY GET BADLY DAMAGED
- Place the eight Hex 4 screws into their holes without tightening
- Gently tighten the 8 screws in a cross pattern to produce a good fit
- Tighten the four Hex 4 screws holding the potentiometer adapter to the intensifier
- Tighten the three Hex 4 screws holding the displacement transducer to the potentiometer adapter
- With **TWO** people lift the intensifier off the bench and position it on the pore pressure unit in the correct orientation so that the holes and pipes match up
- Tighten the two bolts which hold the intensifier to the unit with a 17 spanner
- Position the removed piping back over the intensifier
- Tighten up the three 16AF screws located on the left hand side of the intensifier
- Tighten firmly the 22AF screw located at the end of the intensifier
- Check all connectors for loose fittings, if present tighten firmly

Putting intensifier back

- Put the intensifier unit back into the side next to the pressure vessel
- Connect the electrical connectors which include P1, P2, disp and the mains appt located next to the priming handle
- Connect the confining pressure gauge using a 16 spanner
- Replace the horizontal bars to fix the unit in position so that it cant be removed by using hex 5 screws
- Turn off the hydraulic ring main when no-one is running a test by pressing the red emergency stop button located on the far wall
- Remove the blanking plugs from the ring mains
- Put the L-shape pieces of piping back into their correct position and tighten with adjustable spanners – MAKE SURE THEY ARE TIGHT
- Open the hydraulic inlet by pulling the lever parallel to the piping
- Release the emergency stop button located on the far wall of the laboratory

Replace seals in the separator

Stripping separator

- Mark the ends of the separator as “saline” and “no saline” to correspond with the piping which is labelled in the same way
- Undo the AF16 screws at either ends of the separator
- Unscrew the two M6 x 15 screws holding the separator to the base plate
- With **TWO** people, lift the separator onto the bench
- Using Hex 16, unscrew anticlockwise the eight screws at both ends of the separator
- Pull out the end pieces
- Using a soft material (MUST BE SOFT OR YOU RISK DAMAGE TO THE INNER SEPARATOR WALL), push the piston out of end of the separator using a soft mallet

Appendix 1: Operational Procedure

- Remove the two mitre rings, three O-rings and the scrapper from the piston
- Check the mitre rings, O-rings, scraper and inner bore of the separator for damage

Assembling separator

- Put new O-rings, mitre rings and a scraper on the piston
- Using a soft material (MUST BE SOFT OR YOU RISK DAMAGE TO THE INNER SEPARATOR WALL), push the piston gently into one end of the separator using a soft mallet until the piston is roughly in the middle of the separator
- Put an end piece on both ends of the separator
- Line up the eight holes on the separator and the end pieces
- Using the Hex 16, screw clockwise the eight screws at both ends of the separator – DO THIS IN A CRISS CROSS PATTERN TO AVOID PROBLEMS
- With **TWO** people, lift the separator back into the separator unit with the saline fluid end connecting to the saline pipe work and vice versa
- Screw down the M6 x 15 screws which hold the separator to the base unit
- Connect the AF16 screws to both ends of the separator
- Check everything is tightened correctly

Lead-throughs

Stripping lead-throughs

- Using a soldering iron (at least 300°C) and de-solder the three ground wires connected to the brass pins on the top and bottom of the lead-through
- Unscrew the brass pins and put in a glass dish
- Unscrew the Hex 5.5 x 8, Hex 5.5 x 10 and Hex 5.5 x 12 screws
- Pull on each of the three coaxial wires at the base of the lead-throughs to break the connection with the metal conductors
- Separate the three wires and check for surface damage and do a continuity check
- Place the lead-through in a vice with the bottom pointing upwards
- Put a 1.5 mm drill piece into each of the three holes and gently knock out the metal connectors with a soft mallet
- Check the O-rings and PTFE rings on the side of the lead-though for damage and replace as necessary
- Make sure all the ULTEM cones in the lead-throughs and on the metal conductors are removed and accounted for (3 in total)
- Check the ULTEM cones and insulators for damage and if so replace if necessary
- De-solder the metal conductors from the wires and check for surface damage followed by a continuity test

Making lead-throughs

- You will need
 - 1 x lead-through
 - 1 x Hex 5.5 x 8, 1 x Hex 5.5 x 10 and 1 x Hex 5.5 x 12
 - 1 x O-ring
 - 1 x PTFE ring
 - 3 x insulators
 - 3 x metal conductors
 - 3 x ULTEM cones
 - 3 x short coaxial wires (approximately 20 cm)
 - 3 x long coaxial wires (approximately 200 cm)
- With a piece of 20 cm coaxial wire make sure the ground wire is 20 mm long and peeled away from the inner core which has had the plastic coating removed to reveal less than 3 mm of exposed wire
- Repeat the above step for the other end of the wire
- Put a light covering of solder onto the ends of the exposed wires to tidy them up
- Place the Hex 5.5 x 8 screws onto the wire head first and push onto the peeled back ground wire
- Put an insulator onto the wire so that the bulge is nearest the end of the wire
- Put a metal conductor into a vice with the cone facing downwards – DO NOT OVER TIGHTEN OR YOU RISK DAMAGE TO THE CONES

- Using plenty of solder on the soldering iron, place the tip on top of the connector and leave in place for several minutes while the conductor is heated to above 200°C
- Once the conductor is hot, slide the 3 mm central wire core down into the hole on the conductor
- Remove the soldering iron while keeping the coaxial wire still – IF SUCCESSFUL THE WIRE AND THE CONDUCTOR WILL BE CONNECTED WITH LITTLE APPARENT SOLDER PRESENT (this may take several attempts)
- Gently slide the insulator and the Hex 5.5 x 8 screw over the end of the conductor down as far as they will go
- Remove the metal conductor from the vice
- Check the connection between the coaxial wire and the conductor by gently pulling on both ends –BUT UNDER GENTLE TENSION THEY SHOULD REMAINS SOLID, DON'T PULL TOO HARD BECAUSE THIS MAY BREAK THE CONNECTION
- Repeat the above procedure using the hex 5.5 x 10 and hex 5.5 x 12 screws
- With a piece of 200 cm coaxial wire make sure the ground wire is at least 60 mm long and peeled away from the inner core which has had the plastic coating removed to reveal less than 3 mm of exposed wire
- Repeat the above step for the other end of the wire
- Put a light covering of solder onto the ends of the exposed wires
- Place the lead-through face up in a vice
- Push one of the 60 mm central core wires through one of the three holes so that it comes out of the other end
- Put an ULTEM cone over the wire, point first and let it drop into the lead-through
- Hold the 60mm wire in place with a crocodile clip and some cloth to stop it from moving and to avoid damage to the wire itself
- Remove the lead-through from the vice
- Put the coaxial wire with the metal conductor back into the vice with the cone pointing upwards
- With the soldering iron, place it at the base of the metal conductor and heat for a short period of time
- Lower the 200 cm coaxial cable onto the conductor so that all 3 mm of exposed wire goes into the hole
- Remove the soldering iron while keeping the coaxial wire still – IF SUCCESSFUL THE WIRE AND THE CONDUCTOR WILL BE CONNECTED WITH LITTLE APPARENT SOLDER PRESENT (This may take several attempts)
- Replace the lead-through back into the vice
- Lower the metal connector, insulator and hex 5.5 x 8 screw into the lead-through and screw down until seated
- Do a conductivity test to make sure the wires aren't broken or short circuiting – IF SO TAKE IT APART AND TRY AGAIN
- Repeat the above procedure for the other two coaxial cables and the hex 5.5 x 10 and hex 5.5 x 12 screws
- Place a thin piece of wire around the coaxial cables and tie off around the screw so that damage to the coaxial wires is avoided
- Place the brass screws in both ends of the lead-through
- Solder the ground wires to both brass screws so that any tension is taken on these wires rather than the inner core wires i.e. the ground wire breaks before the inner core takes the strain
- Put a piece of 0.7 mm heat shrink on the 200 cm long coaxial cable and shrink it over the wires just beneath the lead-through. This will encase the brass screw and wires firmly in place further reducing the risk of pulling damage
- Put the top of the lead-through and coaxial wires into the end of the nitrogen tube and fix in position with a jubilee clip
- Pressure test the lead-through for leaks – IF IT IS LEAKING A HISS WILL BE HEARD AND THE LEAD-THROUGH NEEDS TO BE TAKEN APART AND REPAIRED
- Tighten up the screws on the lead-throughs and do a continuity test to make sure the wires are connected and not short circuiting – Sometimes a wire will break so you may want to take that particular channel apart and fix it
- Mark up the three wires so they can be identified easily e.g. 1,2 and 3 or a, b and c or I, II and III
- Put the O-ring and PTFE ring onto the lead-through
- Store the lead-through in a safe place where it wont get knocked

Checking the furnace for damage

Stripping the furnace (store all components together)- detail on how to remove the furnace from the pressure vessel see above

- Check for any potential damage at all stages – if present repair as necessary before reusing
- Separate all wires into individual bundles
- Remove the four M4 x 25 screws anticlockwise from the top of the outer furnace wall
- Take out the upper holding piece and top ceramic piece
- Empty out the ceramic beads into a plastic container
- Remove four M4 x 25 screws anticlockwise from the bottom of the outer furnace wall
- Lift off the outer furnace shell, remembering to catch the remaining beads
- Remove the thermocouples between the inner furnace wall and the heating elements
- Lift out the inner furnace wall
- Take off the metal ring which holds the heating elements in position
- Remove the L-shape holding pieces located behind the heating elements
- Lift the bottom furnace piece 20 cm and slide the three thermocouple out of the 2mm holes
- Lift out the bottom furnace piece and the lower holding copper piece
- Remove the three thermocouples from the bottom closure and check the O-rings and PTFE rings
- Remove the blank plug from the bottom closure and check the O-rings and PTFE rings
- Remove the four heating elements from the bottom closure and check the O-rings and PTFE rings
- Unscrew the four M4 x 15 screws holding the bottom ceramic spacer, bottom seal retainer and bottom outer closure together
- Remove the bottom ceramic spacer
- Remove the bottom seal retainer
- Remove the O-rings and mitre rings from the closure and check for damage
- Clean all components of the furnace except the ceramic beads

Assembling the furnace (for more detail see the assembly drawings)

- See page 290 and 291 for a schematic diagram showing the furnace and where the yoke is positioned
- Place the high temperature bottom outer closure on the centre of the bench [see figure 1 page 298]
- Wipe down and check for any damage such as burs present
- Put anti-scuffing paste on the O-rings and mitre rings and place onto the closure
- Place down the bottom seal retainer and rotate until the four holes used by the M4 x 15 screws match up
- Place the bottom outer ceramic spacer on top of the seal retainer [see figure 2 page 298]
- Screw up four M4 x 15 screws clockwise evenly into the bottom closure –LEAVE SLIGHTLY LOOSE TO ALLOW MOVEMENT OF THE CERAMIC SPACER FOR WHEN THE FURNACE IS BEING PUT INSIDE THE PRESSURE VESSEL
- On the lead-throughs put the O-rings and PTFE rings using a light smearing of anti-scuffing paste
- Put a blank lead-through plug in any of the eight holes present in the ceramic spacer
- Using holes which are 90° rotation from the hole with the blank plug in, place the three thermocouples and mark them as 1 (lower), 2 (upper) and 3 (wall) on the lower surface of the bottom closure where the wires come out [see figure 3 and 4 page 298 and page 293 for further details]
- In two of the remaining four holes, place two lower heating elements in opposite holes so that the elements can intertwine
- In the remaining two holes, place two upper heating elements so that the elements can intertwine and rest above the lower heating elements
- Mark the heating elements on the lower surface of the bottom closure using the notation L1, L2, U1, and U2
- Keep all the thermocouples and heating element wires tidy and together using some copper wire
- In the 8 holes filled with heating elements and thermocouples, place a collar to stop them lifting during an experiment
- Place the bottom furnace piece and furnace holding piece in the middle with the heating elements on the outer surface

- Slide down the middle of the coiled heating elements the inner furnace wall (copper tube) so that it rests flat between the furnace holding piece and the bottom furnace piece
- Poke the thermocouple through the nearest 2mm hole present in the bottom furnace piece and mark
- Place the heating elements into the nearest of the four grooves present in the bottom furnace piece
- Put the L-shaped holding piece behind the heating elements to leave a small ridge all the way around the bottom furnace piece
- Place the metal ring down onto this ridge to stop the elements moving [see figure 5 page 298]
- Position thermocouples 1 and 2
 - 1) between the lower heating elements and the inner furnace wall
 - 2) between the upper heating elements and the inner furnace wall
- Lower the outer furnace shell down over the furnace bottom piece to rest on the bottom ceramic spacer
- Rotate the outer furnace shell until the holes in the shell and bottom furnace piece match up
- Countersink four M4 x 25 screws clockwise into the shell until they are below the surface – THEY MUST BE BELOW THE SURFACE OR THE FURNACE WILL NOT FIT INTO THE PRESSURE VESSEL
- Position the remaining thermocouple against the outer furnace shell near the top
- Fill the space evenly between the inner and outer furnace walls with ceramic beads – OCCASIONALLY PACK DOWN THE BEADS
- Fill until only 10 mm of the inner and outer shell furnace are exposed above the level of the beads [see figure 6 page 298]
- Reposition the wall thermocouple if required
- Place the top ceramic piece between the inner and outer furnace walls
- Rotate the top ceramic spacer until the holes match up
- Place the upper holding piece on the inner surface of the top ceramic piece
- Countersink four M4 x 25 screws clockwise into the shell until they are below the surface – THEY MUST BE BELOW THE SURFACE OR THE FURNACE WILL NOT FIT INTO THE PRESSURE VESSEL
- Check everything is tightened up correctly

Calibrations: -

Pressure intensifier calibration

- This is to be applied to pore pressure and confining pressure transducers on the triaxial cell, also to the pressure transducers in the separators, and the transducers in the permeameter
- Unscrew the pressure transducers connected to the piping containing the fluid to be pressurised. For the pore pressure this is usually deionised water, for confining pressure it is silicone oil
- Take out the Buddenberg pressure calibration machine
- Place the instrument on a flat bench with the rotating handle resting over one side
- Check the instrument is level using the in-built levelling device
- Rotate the four legs to adjust the level of the instrument – this is when the air bubble is in the centre of panel
- Using the appropriate connections (found inside Buddenberg box) connect the pressure transducer to the top of the instrument with two adjustable spanners
- On top of the piston used for calibration, place the 20 bar weight
- Make sure the transducer is connected to its control panel and a volt meter
- Identify whether the calibration will be done in the lower range (blue) of 0-200 bar or higher range (red) +200 bar
- Using the two small black handles on the top of the Buddenberg marked “A” and “B”, rotate the dials into the calibration range using the labels present
- Dial the four pronged handle all the way anticlockwise to the end of its range
- Place a 30 bar weight on to the piston (totalling 50 bar (20 + 30))
- Gently spin the weight during the calibration
- Rotate the four pronged handle clockwise until the piston lifts and becomes stable in the lower range (blue)
- In a table format, write down the load, panel and voltage readings
- Rotate the handle anticlockwise until the piston is fully down
- Place on the next weight and repeat the above procedure up to 1000 bar (100 MPa)
- Dismantle the weights and put back into their carrying case

Appendix 1: Operational Procedure

- Unscrew the pressure transducer from the Buddenberg and reconnect to the pressure piping
- Put the calibration instrument back into its case

Pore volume calibration

- Turn on the pore intensifiers using the procedure mentioned previously
- Move the piston fully back by priming it
- Mark off the panel and voltage readings
- Open all the valves which are connected to the pore piping
- Place a 30 mm measuring cylinder at the end of the pore piping
- Under pressure control, move the piston fully forwards until water comes out of the pipe
- If no water comes out, then re-prime the intensifier and repeat until it does
- Re-prime the intensifier and empty the 30 mm measuring cylinder
- Move the piston fully forward and measure the amount of water collected
- Repeat the above procedure five times and calculate the average the volume of water collected
- For the calibration, calculate the change in panel and voltage readings relative to volume change and put the calibration into the appropriate software e.g. Labview
- Turn the machine off

LVDT calibration

- Take the modified v-block located on the side bench and move next to the LVDT
- Place the LVDT along the v-block with the ball touching the dial gauge located at one end of the v-block
- Tighten the LVDT in position using two bolts – DON'T OVERTIGHTEN BECAUSE AS YOU RISK DAMAGE TO THE TRANSDUCER
- On the appropriate panel and using a voltage meter record the initial readings
- Rotate the dial two full revolutions equal to 1 mm and record the panel and voltage readings into a table format
- Repeat every mm until the transducer is fully depressed
- Follow the same procedure until the transducer is fully out
- Do this a further three times and average the results
- Plot the results of displacement Vs panel reading and displacement Vs voltage and calculate the calibration and r^2 value which should be greater than 0.99. Then put the calibration into the appropriate software e.g. Labview
- Detach the transducer from the v-block and store in it's usual place

Furnace calibration

- Replace the four electrical lead-throughs with four thermocouple lead-throughs – check for damage to the O-ring, PTFE ring, bottom inner closure and lead-through surfaces – IF DAMAGE IS PRESENT REPLACE WHERE NECESSARY
- Put a dummy rock sample containing a central hole into a high temperature rubber jacket
- Use the specially modified end-cap, which contains the thermocouple, assemble the sample (see above) on the bottom inner closure with the thermocouple end being in the middle of the rock
- Put the other end of the thermocouple, which is in the modified lead-through into the spare hole in the bottom inner closure which normally contains a blank plug
- Identify the thermocouples and record their positions on the lead-through
- Wrap the thermocouple around the jacket at different heights, ideally place them at equal distance
- Record the relative position of the thermocouples
- Put the bottom inner closure into the pressure vessel and pressurise using the procedure mentioned previously
- In Labview set up a calibration file which contains the thermocouples and confining pressure
- Heat the furnace up to 50, 75, 100, 125 and 150°C. Leave the furnace at each temperature level for several hours until the oil and rock temperatures becomes constant
- Remove the sample assembly and change back to the standard yoke for use of electrical measurements at temperature
- From the recorded data, plot a profile of furnace temperature Vs oil temperature, furnace temperature Vs rock temperature and oil temperature Vs rock temperature

Appendix 1: Operational Procedure

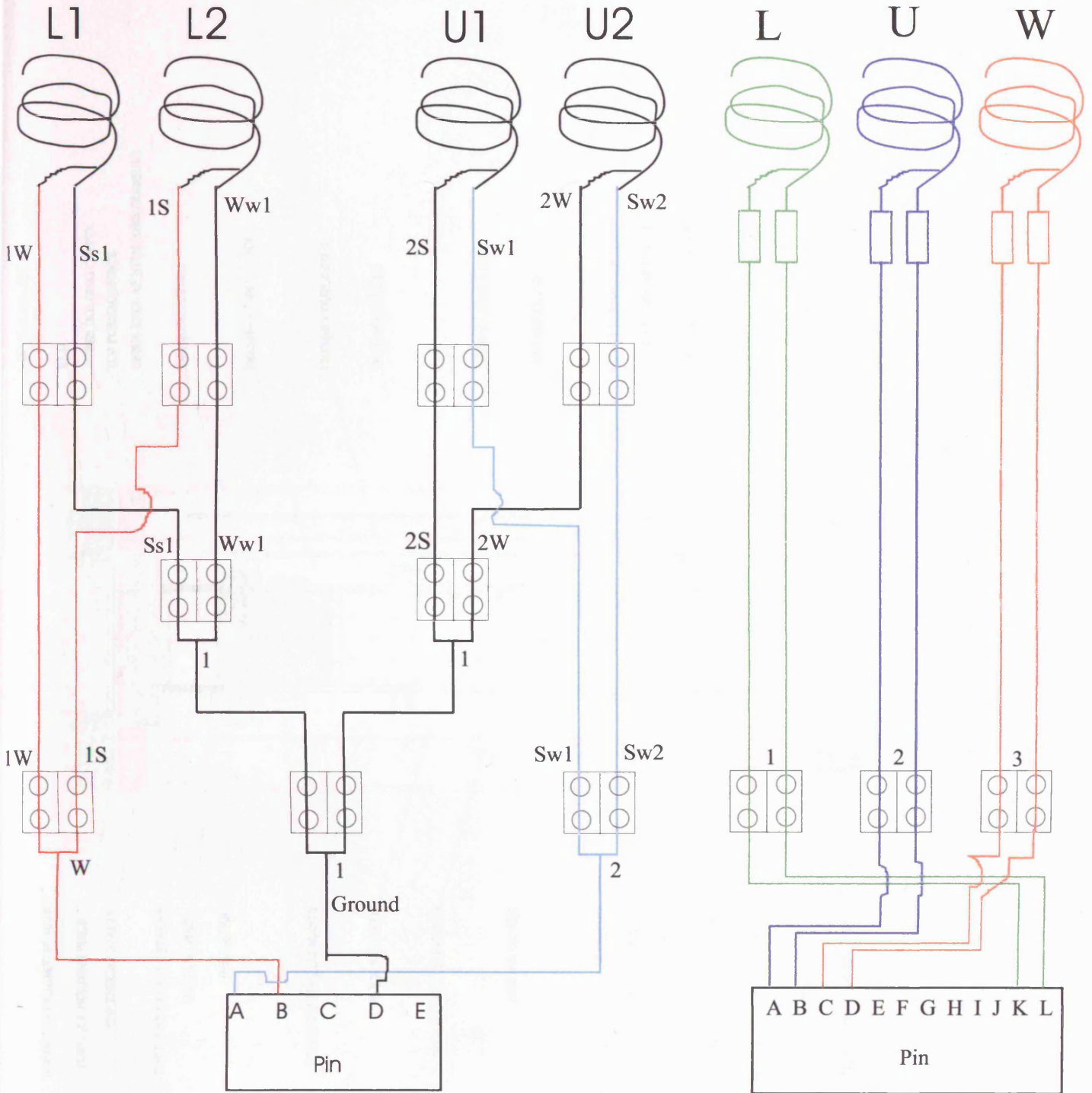
- Using the table collated, display pressure Vs panel reading and pressure Vs voltage and calculate the calibration (the data should have an r^2 value of 0.99)
- Put the calibration data into the appropriate software e.g. Labview

FOR ANY OTHER CONCERNS – SEE A TECHNICAL MEMBER OF STAFF !!!!

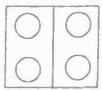


FURNACE WIRING DIAGRAM

Heating elements

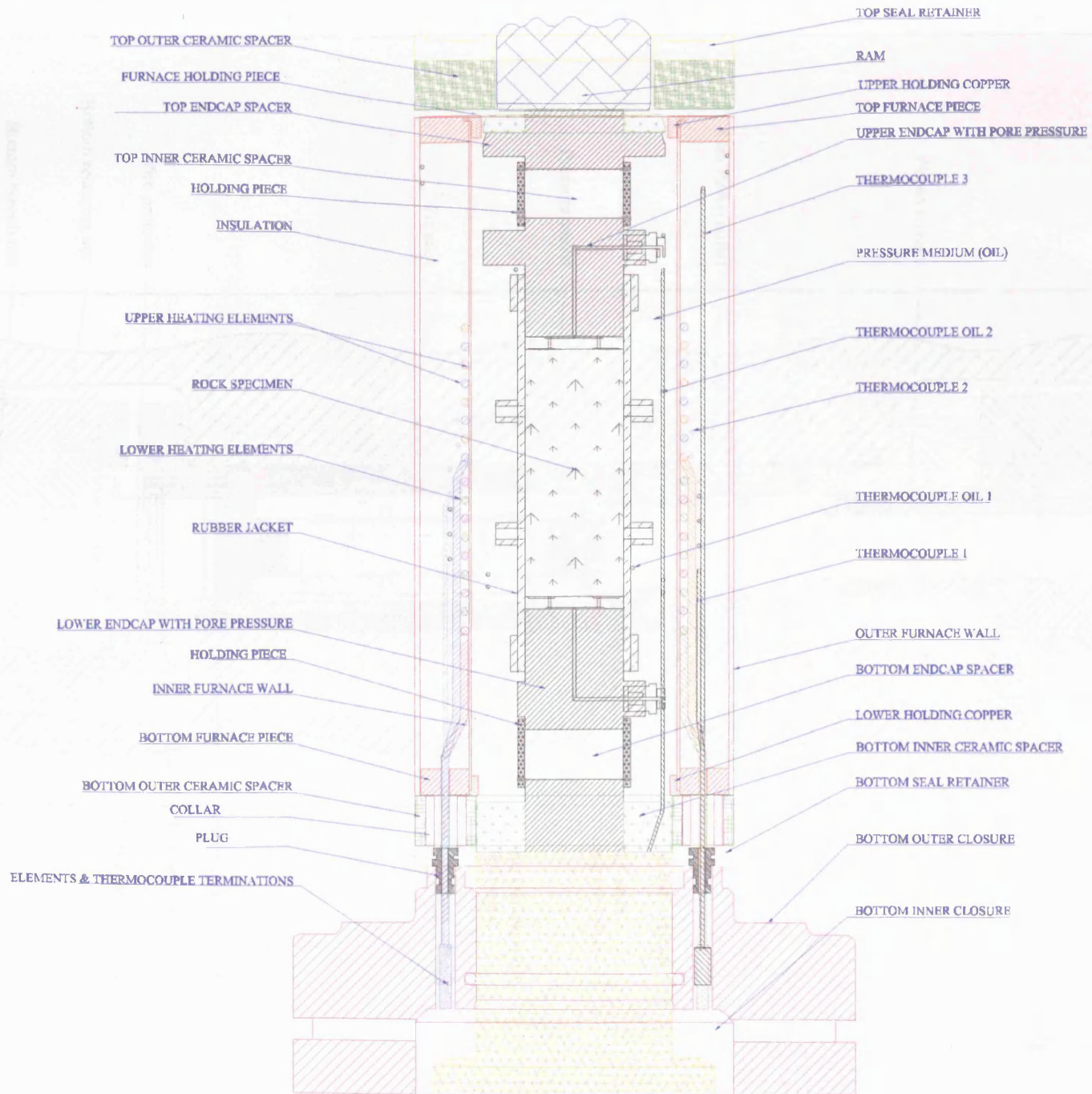
Thermocouples

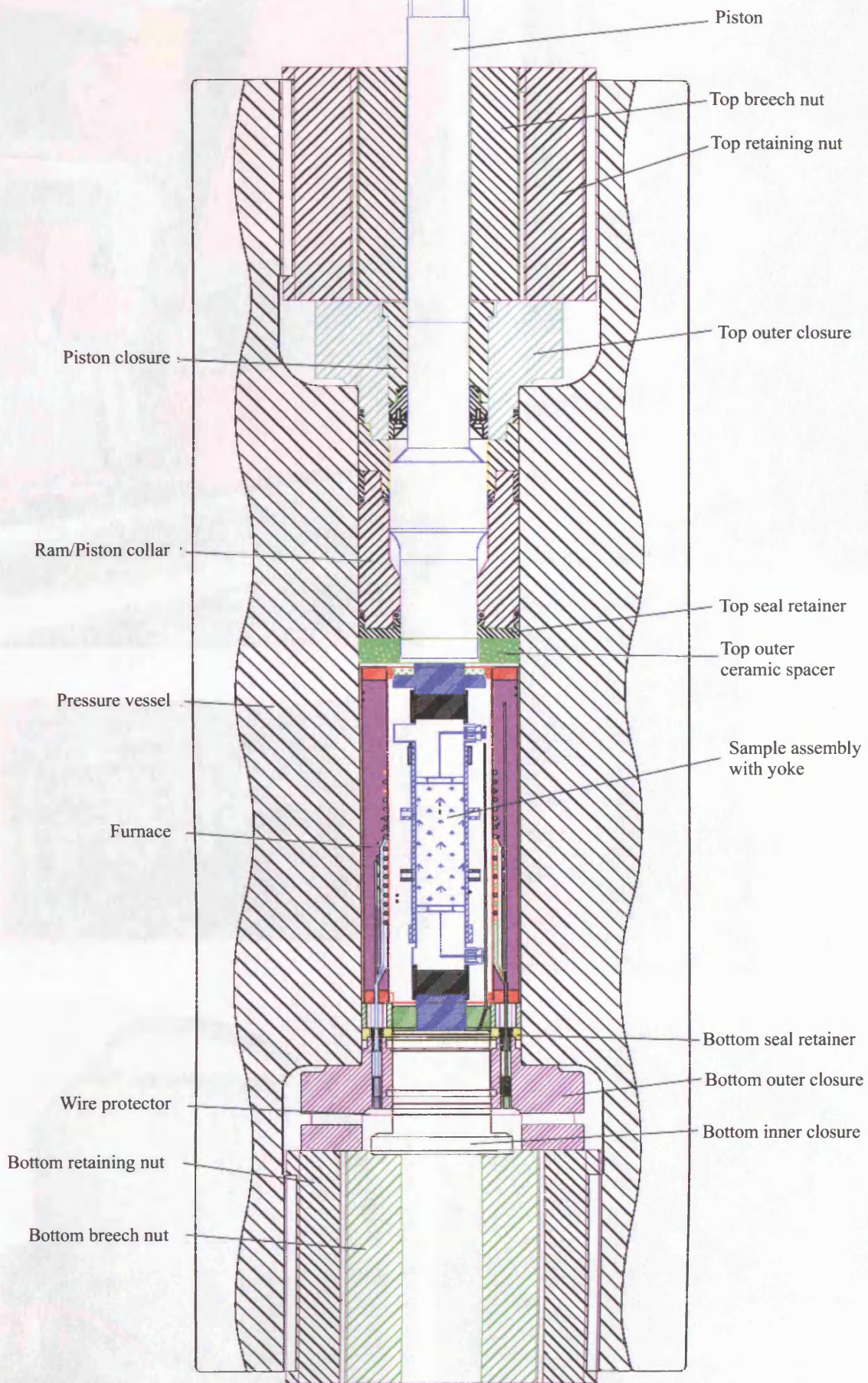


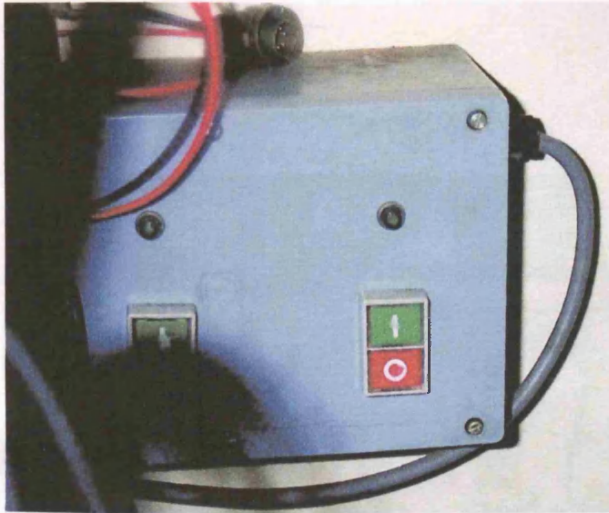
KEY

-  = terminal block
-  = connector
-  = wire

Make sure + heat results in + Volts



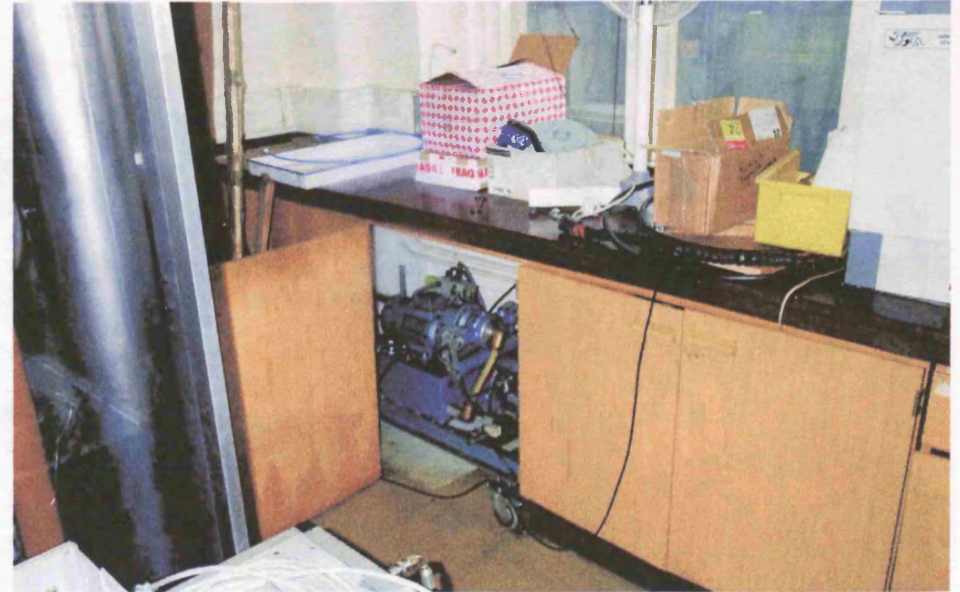




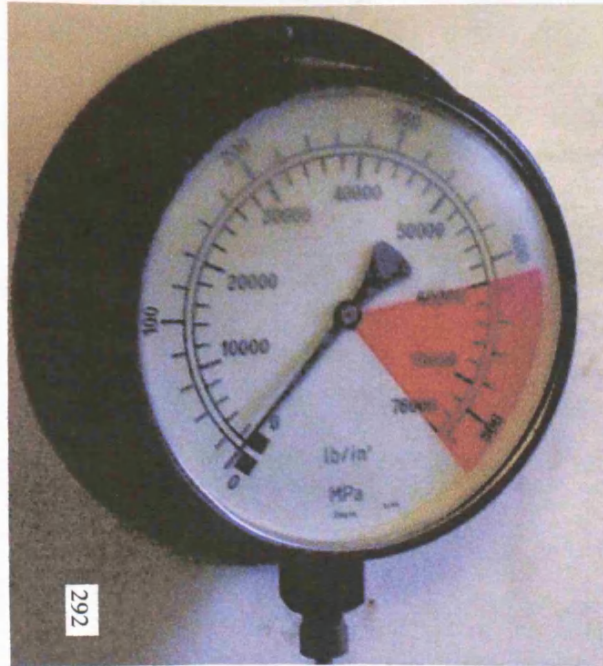
1) Above: Confining pump pressure switches



2) Above: Confining pressure controls



3) Above: Confining pressure pump cupboard



4) Above: Confining pressure gauge



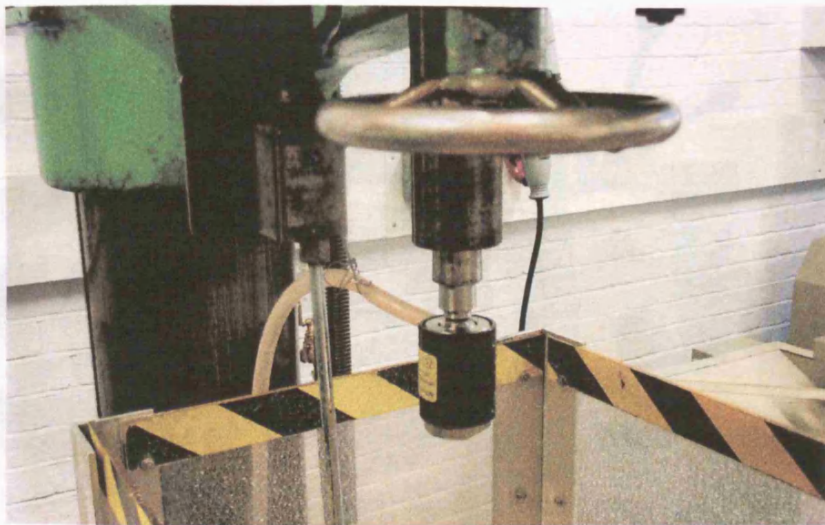
5) Above: Confining pump mains switch

Confining pressure equipment



6) Above: Confining pump

Coring



1) Above: Core drill with emergency stop button above safety cage



2) Left: Mains power for drill

3) Right: Core drill looking from the front



6) Right: Water supply for the core drill

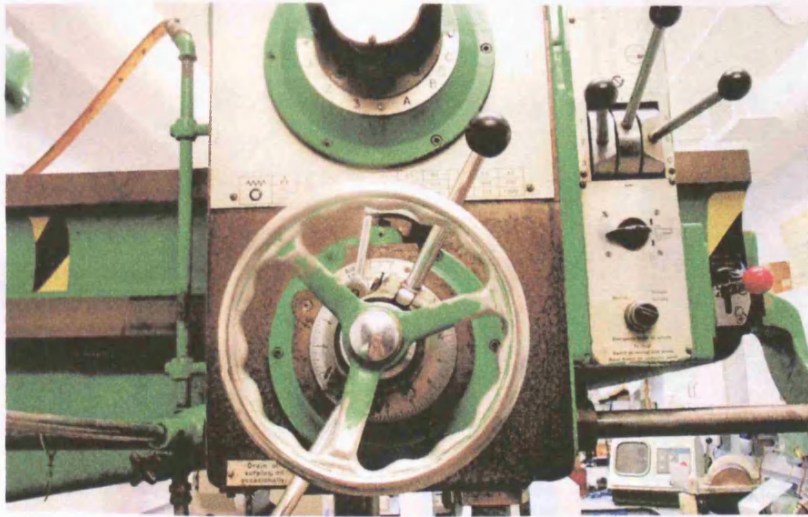


5) Left: Core drill looking from the back

4) Right: Where the rock is fixed in position



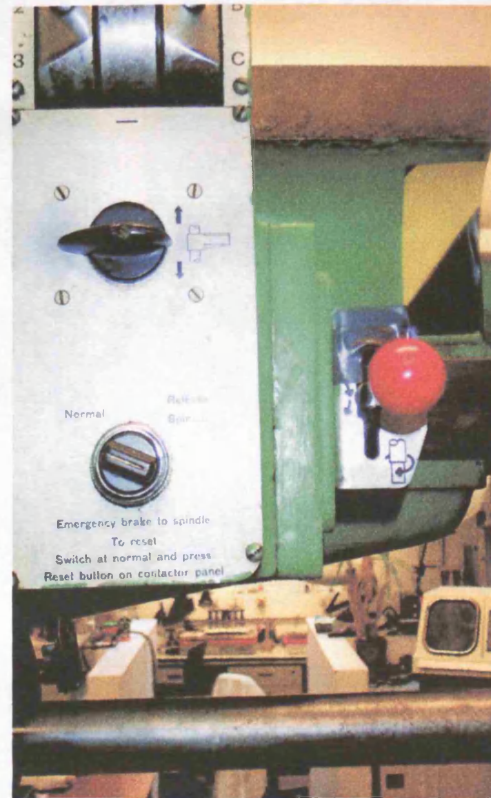
Coring controls



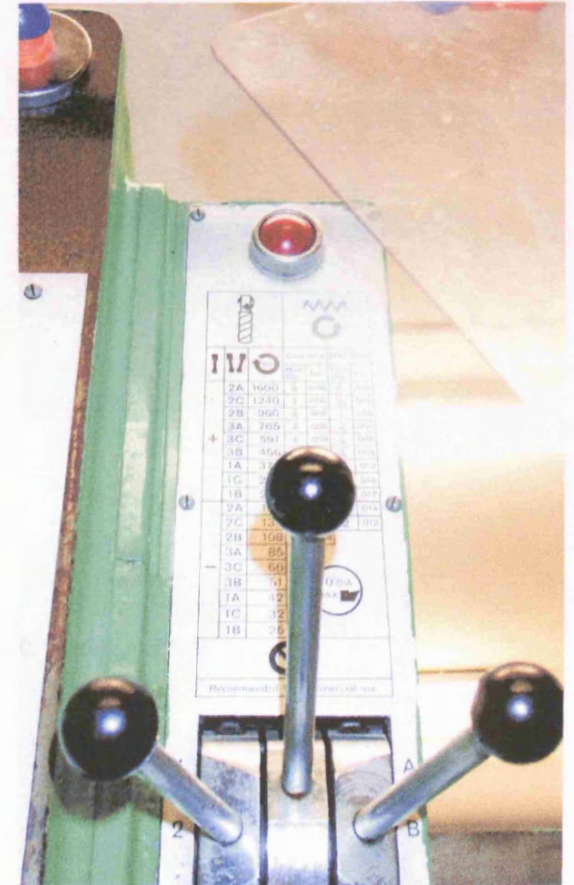
1) Above: Controls for the core drill



2) Above: Emergency reset button located on the back of the coring machine

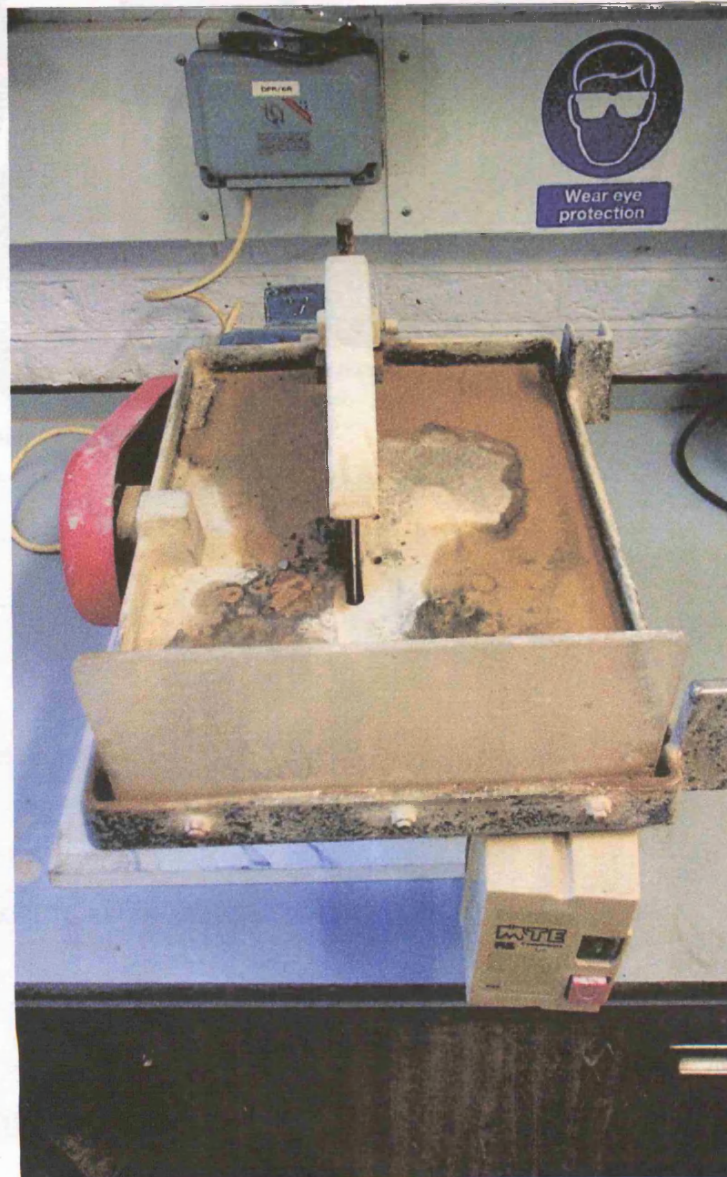


3) Above: Controls for raising the coring machine and rotating the drill

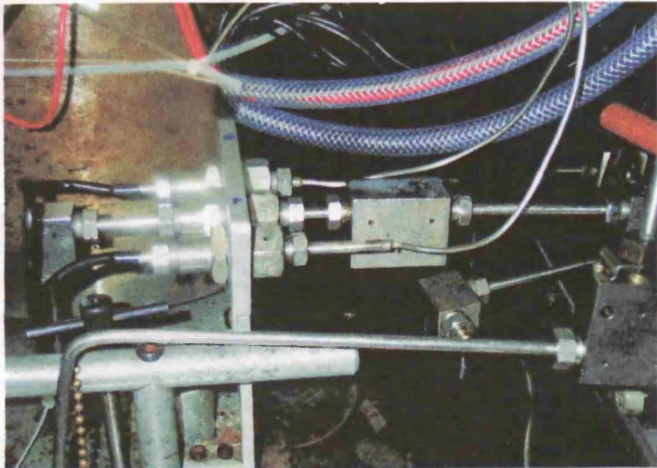


4) Above: Controls to set RPM of the core drill

Cutting



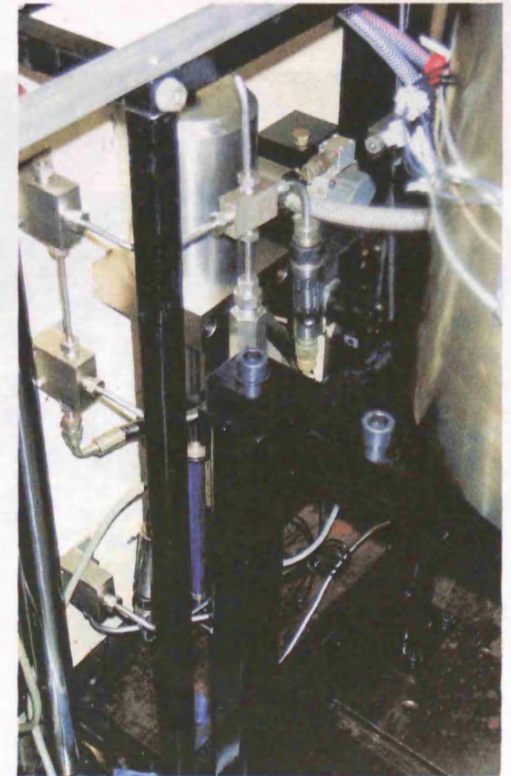
Left: Cutting machine



1) Above: Connections for the confining & pore pressure piping



2) Above: Confining pump

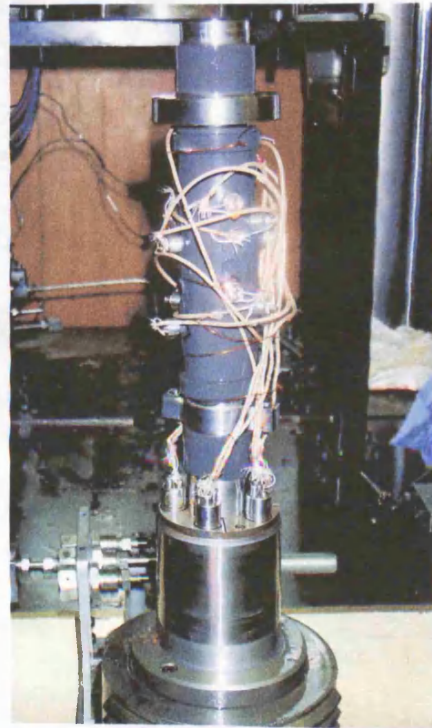


3) Above: Intensifier 1 (10cc)
7) Below: Intensifier 2 (22cc)

Experimental set-up

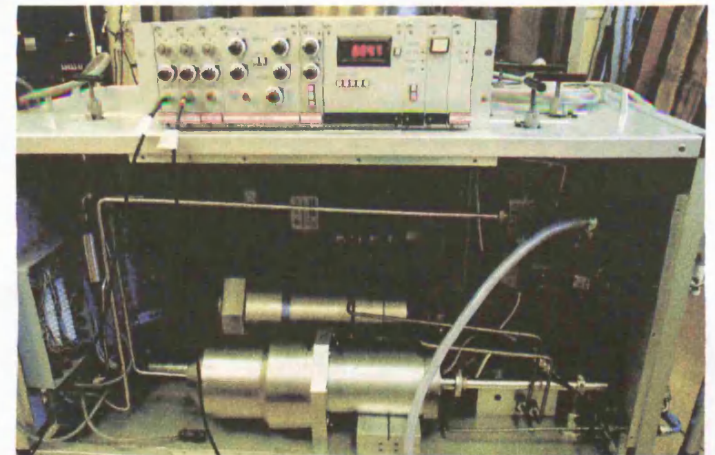


4) Above: Triaxial rig



5) Above: Sample set-up for high temperature on bottom closure

6) Below: Yoke set-up

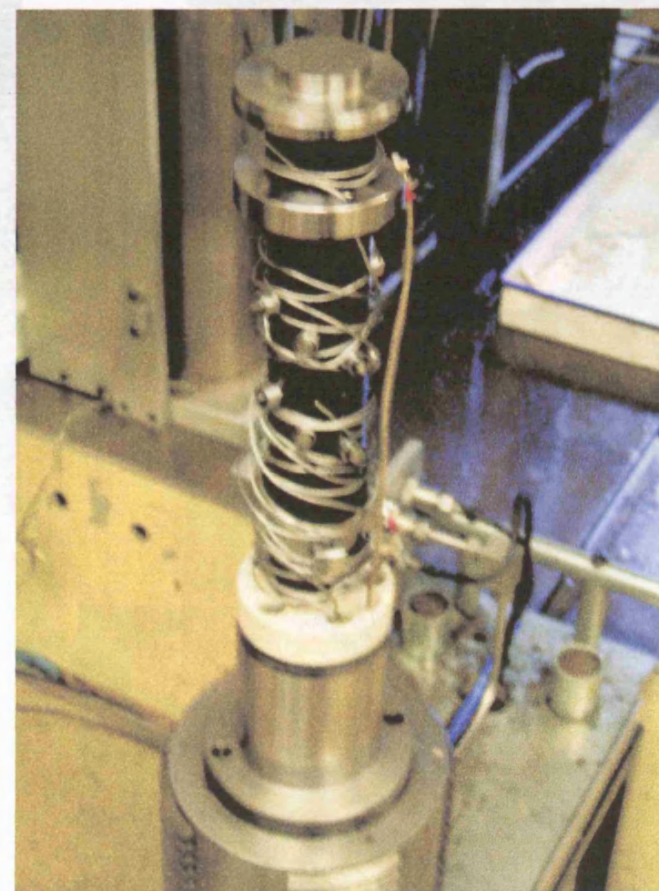
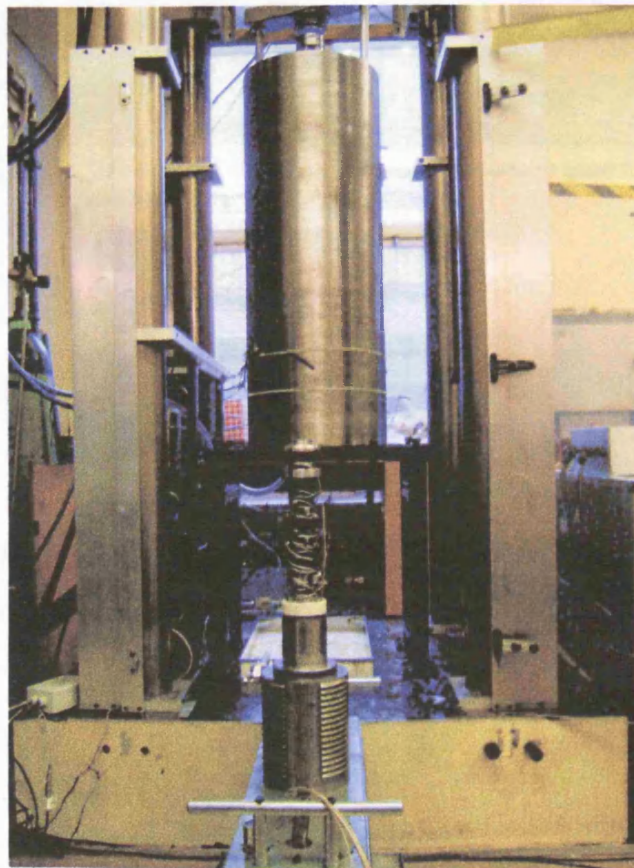


Furnace and calibraion



1) Above: Putting the furnace into the pressure vessel using the jack and support frame

2) Below: Furnace calibration sample ready to be tested

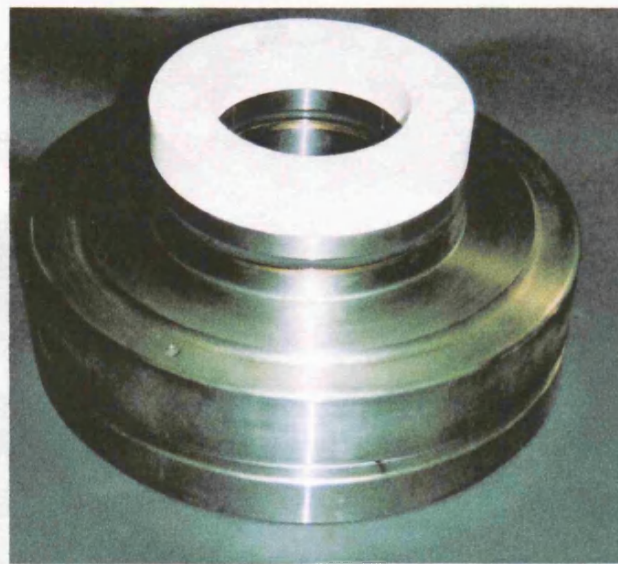


3) Above: Close-up of furnace calibration set-up involving several thermocouples

Furnace assembly



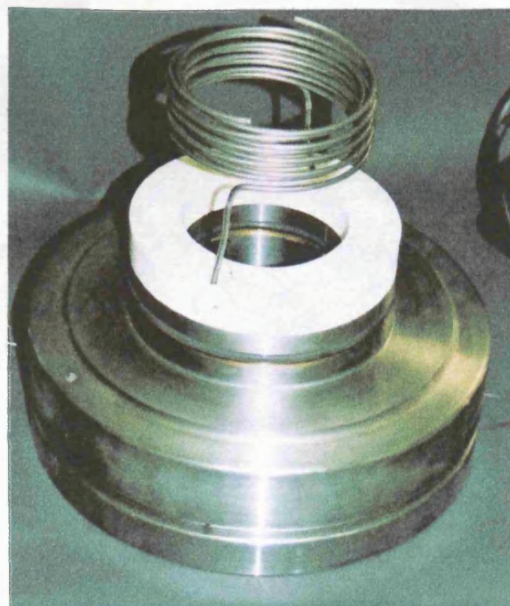
1) Above: Bottom closure, seal retainer and ceramic spacer



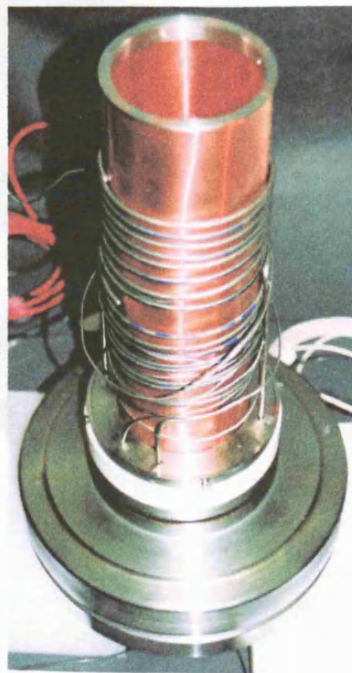
2) Above: Mitre rings, O-rings, seal retainer and ceramic spacer fixed to the bottom outer closure



3) Above: Lower heating elements placed into bottom closure



4) Above: Linking of lower heating elements

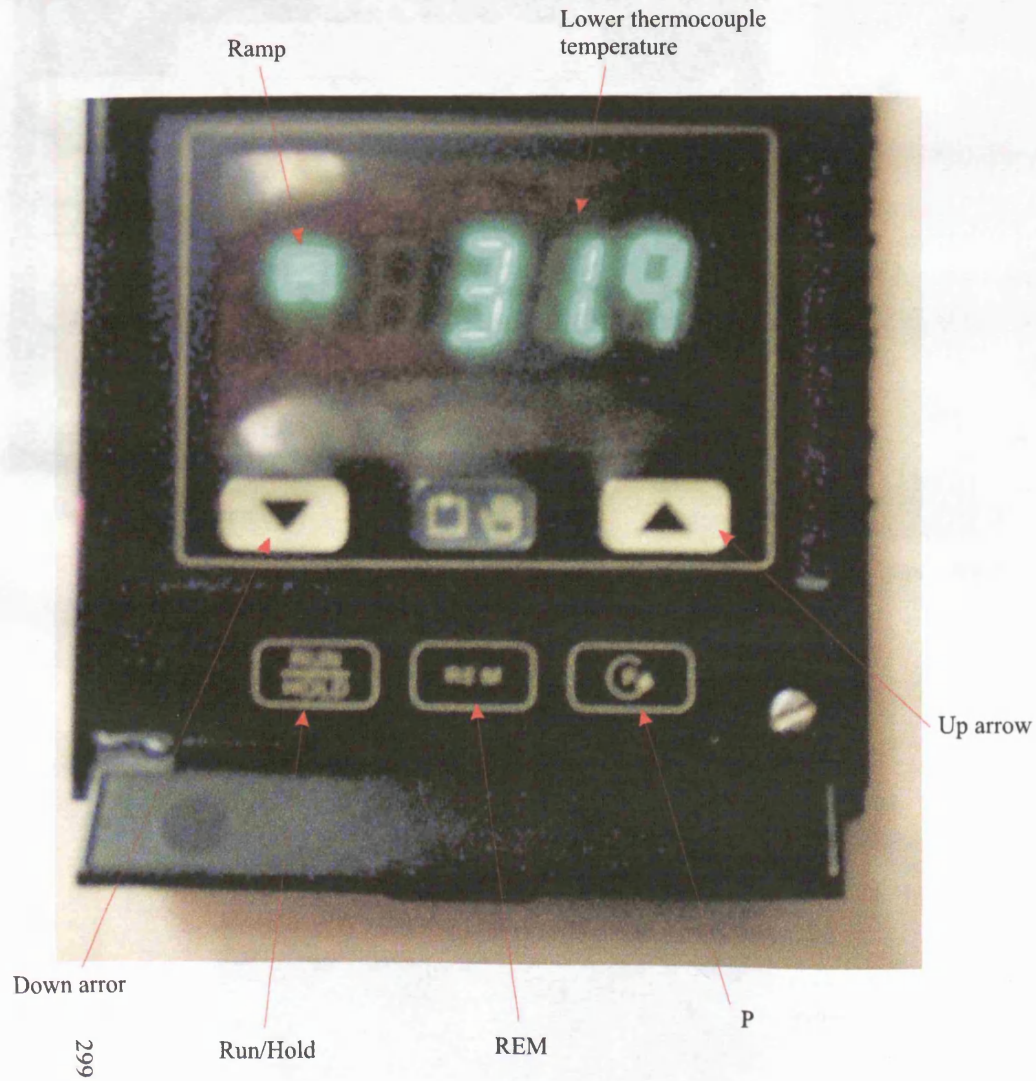


5) Left: Heating elements and copper tube

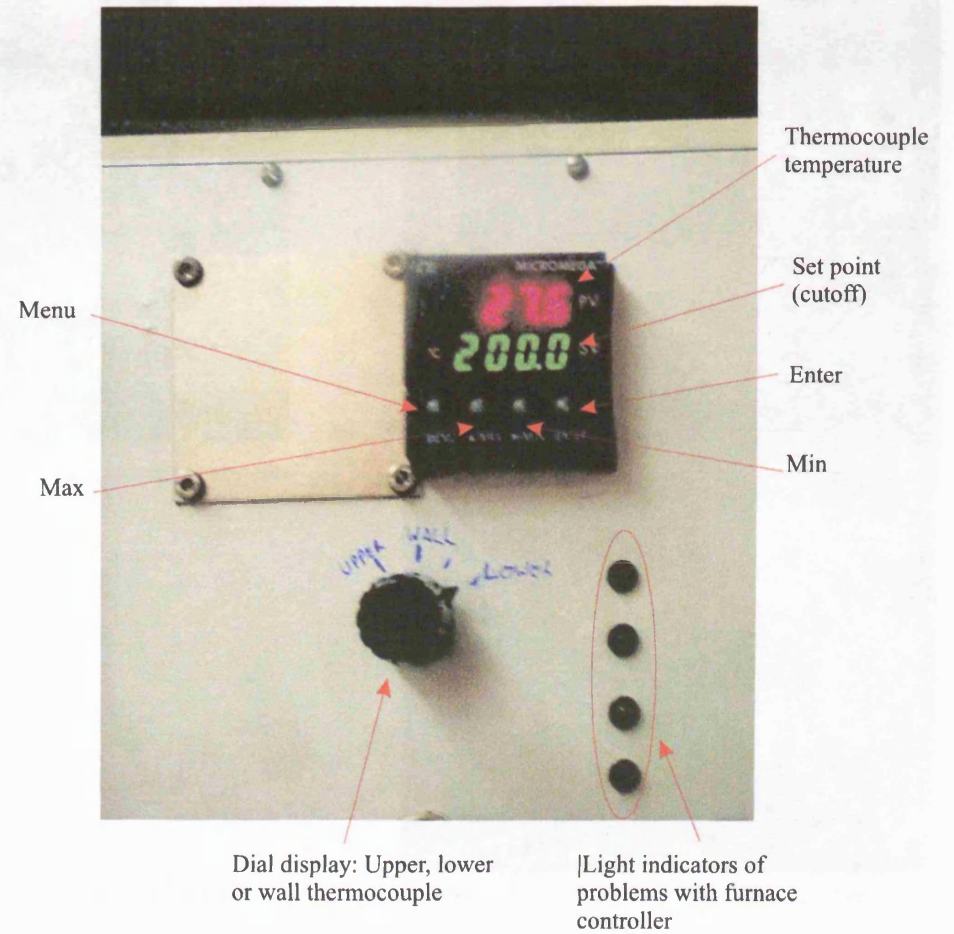


6) Left: Ceramic beads in the space between the copper tube and outer wall. Top piece missing

Furnace controllers



1) Model 815



2) Omega model

Appendix 3: Furnace Calculations

In order to calculate the power required to heat a rock to 320⁰C several steps need to be followed.

- 1) Heat required to heat the oil to 320⁰C. This pressure medium used is oil and it accompanies the rock. In order to heat the rock to the desired temperature the oil must be heated to 320⁰C or greater
- 2) Heat required to heat the steel to 320⁰C. A steel end piece is attached to both ends of the rock sample which also needs to be heated to 320⁰C or greater
- 3) Heat required to heat the rock to 320⁰C at which tests will be conducted.
- 4) Total heat required to the heat oil, steel and rock to 320⁰C.
- 5) Heat loss from the ends of the rock sample into the pistons.
- 6) Heat loss from the side of the rock sample into the furnace itself.
- 7) Surface area of a single coil.
- 8) Heat radiated from the electric coils at a desired temperature.
- 9) Power required for the elements to determine if enough power is present to heat the rock, oil and steel to 320⁰C.
- 10) Determining the temperature of the inner steel pressure vessel wall to find if it gets too hot.

On the next page a simplified diagram (Figure 1) is shown which contains the major values required to heat the rock to 320⁰C.

1) HEAT REQUIRED TO THE HEAT OIL TO 320°C

(Q) Heat required = Mass of oil x Heat capacity x 320°C (Watts)

(i) (ii)

i) Mass of oil (g) = Density (g/cm³) x Volume (cm³)

Volume of oil is total volume minus rock and steel $\Rightarrow V_{oil} = V_{tot} - V_{rock} - V_{steel}$

V_{tot} = Total volume of oil, rock and steel (cm³)

V_{rock} = Rock volume (cm³)

V_{steel} = Steel volume (cm³)

PV_{dia} = Pressure vessel diameter = 130mm = 13cm

PV_{len} = Pressure vessel length = 274mm = 27.4cm

$$V_{tot} = \pi \cdot \left(\frac{PV_{dia}}{2} \right)^2 \cdot PV_{len}$$

$$V_{tot} = 3.14 \times \left(\frac{13}{2} \right)^2 \times 27.4$$

$$V_{tot} \approx 3687 \text{cm}^3$$

R_{dia} = Rock diameter = 40mm = 4cm

R_{len} = Rock length = 100mm = 10cm

$$V_{rock} = \pi \cdot \left(\frac{R_{dia}}{2} \right)^2 \cdot R_{len}$$

$$V_{rock} = 3.14 \times \left(\frac{4}{2} \right)^2 \times 10$$

$$V_{rock} \approx 126 \text{cm}^3$$

ST_{dia} = Steel diameter = 40mm = 4cm

ST_{len} = Steel length = 91.5mm = 9.15cm

2 steel ends

$$V_{steel} = \left(\pi \cdot \left(\frac{ST_{dia}}{2} \right)^2 \cdot ST_{len} \right) \cdot 2$$

$$V_{steel} = (3.14 \times \left(\frac{4}{2} \right)^2 \times 9.15) \times 2$$

$$V_{steel} \approx 230 \text{cm}^3$$

Appendix 3: Furnace Calibrations

$$V_{oil} = V_{tot} - V_{rock} - V_{steel}$$

$$V_{oil} = 4035\text{cm}^3 - 126\text{cm}^3 - 230\text{cm}^3$$

$$V_{oil} \approx 3331\text{cm}^3$$

$$\text{Density of oil} = 0.00036 \text{ kg/cm}^3$$

$$\text{Mass of oil (g)} = \text{Density (g/cm}^3) \times \text{Volume (cm}^3)$$

$$M_{oil} = 0.00036\text{kg/cm}^3 \times 3331\text{cm}^3$$

$$M_{oil} \approx 1.2\text{kg}$$

ii) Specific heat capacity of oil is 2.25kJ/kg K

iii) Heat required (W)= Mass of oil (kg) x Heat capacity (kJ/kg) x 320°C

$$Q_{oil} = M_{oil} \times H_{cap} \times 320^\circ\text{C} \quad (\text{kJ})$$

$$Q_{oil} = 1.2\text{kg} \times 2.25\text{kJ/kg} \times 320^\circ\text{C} \quad (\text{kJ})$$

$$Q_{oil} \approx 864 \text{ kJ}$$

2) HEAT REQUIRED TO THE HEAT STEEL TO 320°C

(Q) Heat required (W) = Mass of oil (kg) x Heat capacity (kJ/kg) x 320°C

(i) (ii)

i) Mass of steel (g)= Density (g/cm³) x Volume (cm³)

$$ST_{dia} = \text{Steel diameter} = 40\text{mm} = 4\text{cm}$$

$$ST_{len} = \text{Steel length} = 91.5\text{mm} = 9.15\text{cm}$$

$$V_{steel} = \left(\pi \cdot \left(\frac{ST_{dia}}{2} \right)^2 \cdot ST_{len} \right) \quad (\text{cm}^3)$$

$$V_{steel} = (3.14 \times \left(\frac{4}{2} \right)^2 \times 9.15) \quad (\text{cm}^3)$$

$$V_{steel} \approx 115\text{cm}^3$$

$$\text{Mass of steel (g)} = \text{Density (g/cm}^3) \times \text{Volume (cm}^3)$$

$$M_{steel} = 7.8\text{g/cm}^3 \times 115\text{cm}^3$$

$$M_{steel} \approx 897\text{g} = 0.897\text{kg}$$

ii) Heat capacity from notes = 0.55kJ/kg K

Appendix 3: Furnace Calibrations

iii) Heat required (W) = Mass of oil (kg) x Heat capacity (kJ/kg) x 320°C (2 steel ends)

$$Q_{\text{steel}} = M_{\text{steel}} \times H_{\text{cap}} \times 320^{\circ}\text{C} \times 2 \quad (\text{kJ})$$

$$Q_{\text{steel}} = 0.897\text{kg} \times 0.55\text{kJ/kg} \times 320^{\circ}\text{C} \times 2 \quad (\text{kJ})$$

$$Q_{\text{steel}} \approx 315\text{kJ}$$

3) HEAT REQUIRED TO HEAT ROCK TO 320°C

(Q) Heat required (W) = Mass of oil (kg) x Heat capacity (kJ/kg) x 320°C

(i) (ii)

i) Mass of rock (g) = Density (g/cm³) x Volume (cm³)

$$R_{\text{dia}} = \text{Rock diameter} = 40\text{mm} = 4\text{cm}$$

$$R_{\text{len}} = \text{Rock length} = 100\text{mm} = 10\text{cm}$$

$$V_{\text{rock}} = \pi \cdot \left(\frac{R_{\text{dia}}}{2} \right)^2 \cdot R_{\text{len}} \quad (\text{cm}^3)$$

$$V_{\text{rock}} = 3.14 \times \left(\frac{4}{2} \right)^2 \times 10 \quad (\text{cm}^3)$$

$$V_{\text{rock}} \approx 126\text{cm}^3$$

Mass of rock (g) = Density (g/cm³) x Volume (cm³)

$$M_{\text{rock}} = 2.65\text{g/cm}^3 \times 126\text{cm}^3$$

$$M_{\text{rock}} \approx 334\text{g} = 0.334\text{kg}$$

ii) Heat capacity of rock is generally 0.2kJ/kg K

iii) Heat required (W) = Mass of oil (kg) x Heat capacity (kJ/kg) x 320°C

$$Q_{\text{rock}} = M_{\text{rock}} \times H_{\text{cap}} \times 320^{\circ}\text{C} \quad (\text{kJ})$$

$$Q_{\text{rock}} = 0.334\text{kg} \times 0.2\text{kJ/kg} \times 320^{\circ}\text{C} \quad (\text{kJ})$$

$$Q_{\text{rock}} \approx 22\text{kJ}$$

4) HEAT REQUIRED TO HEAT OIL, STEEL & ROCK TO 320°C

$$Q_{\text{total}} = Q_{\text{oil}} + Q_{\text{steel}} + Q_{\text{rock}} \quad (\text{kJ})$$

$$Q_{\text{total}} = 864\text{kJ} + 315\text{kJ} + 22\text{kJ}$$

$$Q_{\text{total}} = 1201\text{kJ} = (1287 \times 10^3)\text{J}$$

Heat mediums up in 1 hour

$$1 \text{ hour} = 60 \text{ minutes} \times 60 \text{ seconds}$$

$$q_2 = \frac{Ak(T_1 - T_2)}{l} \quad (\text{W})$$

$$q_2 = \frac{1.26 \times 10^{-2} \times 15 \times (593 - 373)}{20 \times 10^{-3}} \quad (\text{W})$$

$$q_2 \approx 2079\text{W}$$

Total heat rate (Q) = Heat required to heat the rock + Heat flow through rock ends + Heat through rock walls

$$\text{Total heat rate (Q)} = Q_{\text{total}} + q_1 + q_2 \quad (\text{W})$$

$$Q = 334\text{W} + 416\text{W} + 2079\text{W}$$

$$Q = 2829\text{W}$$

Therefore $\approx 2900\text{W}$ is required to heat and maintain the rock at a temperature of 320°C .

Therefore 3 elements of 1000W each are required to heat the rock to 320°C .

7) CALCULATE THE AREA OF A SINGLE COIL

$$\text{Coil diameter} = C_{\text{dia}} = 0.125'' = 3.2 \times 10^{-3}\text{m}$$

$$\text{Coil length} = C_{\text{len}} = 50'' = 1.27\text{m}$$

Surface area of coil (m^2)

$$SA_{\text{coil}} = \pi \cdot C_{\text{dia}} \cdot C_{\text{len}} \quad (\text{m}^2)$$

$$SA_{\text{coil}} = 3.14 \times 3.2 \times 10^{-3} \times 1.27 \quad (\text{m}^2)$$

$$SA_{\text{coil}} \approx 0.013\text{m}^2$$

8) Heat radiated from coils

a) At 320°C

This is calculated using a black body radiation solution

$$E = \epsilon \sigma T^4 \quad (\text{Wm}^{-2})$$

E = Watts required to heat element (Wm^{-2})

ϵ = Emissivity

σ = Stefan Boltzman constant = 5.67×10^{-8}

Appendix 3: Furnace Calibrations

T = Temperature (K)

$$E = \epsilon\sigma T^4 \quad (\text{Wm}^{-2})$$

$$E = 1 \times 5.67 \times 10^{-8} \times (320 + 273)^4 \quad (\text{Wm}^{-2})$$

$$E \approx 7012 \text{Wm}^{-2}$$

Area of coil needed to reach 320°C

$$A_{\text{coil}} = \frac{Q \text{ (W)}}{E \text{ (Wm}^{-2}\text{)}} \quad (\text{m}^2)$$

$$A_{\text{coil}} = \frac{2829 \text{W}}{7012 \text{Wm}^{-2}}$$

$$A_{\text{coil}} = 0.40 \text{m}^2$$

Number of elements required to occupy a surface area of 0.41m²

$$El = \frac{A_{\text{coil}}}{SA_{\text{coil}}}$$

$$\frac{0.40 \text{m}^2}{0.013 \text{m}^2} \approx 31.5 \text{ elements}$$

$$0.013 \text{m}^2$$

Therefore 31.5 elements are required which can't do!!

But: If you heat the elements up to 750°C.

Heat elements to 750°C

$$E = \epsilon\sigma T^4 \quad (\text{Wm}^{-2})$$

$$E = 1 \times 5.67 \times 10^{-8} \times (750 + 273)^4 \quad (\text{Wm}^{-2})$$

$$E \approx 62100 \text{Wm}^{-2}$$

Area of coil needed to reach 750°C

$$A_{\text{coil}} = \frac{Q \text{ (W)}}{E \text{ (Wm}^{-2}\text{)}} \quad (\text{m}^2)$$

$$A_{\text{coil}} = \frac{2829 \text{W}}{62100 \text{Wm}^{-2}}$$

$$A_{\text{coil}} \approx 0.046 \text{m}^2$$

$$EI = \frac{A_{\text{coil}}}{SA_{\text{coil}}}$$

$$\frac{0.046\text{m}^2}{0.013\text{m}^2} \approx 3.5 \text{ elements}$$

$$0.013\text{m}^2$$

Using this arrangement the temperature can be achieved

What this means is if

$$T \Rightarrow \infty \quad \text{then} \quad E \Rightarrow \infty \quad \text{then} \quad A_{\text{coil}} \Rightarrow 0$$

If the temperature goes to infinity, then a lesser surface area is required to get to a given wattage

9) POWER OF EACH ELEMENT

$$\text{Power} = \text{Volt} \times \text{Amp}$$

$$P = 115\text{Volts} \times 9\text{Amps} = 1035\text{W}$$

$$3 \text{ elements will give you} = 3 \times 1035\text{W} = 3105\text{W}$$

This value is greater than the power required to heat the rock to 320°C therefore only 3 elements are needed.

10) TEMPERATURE OF INNER WALL

$$\text{Heat gradient} = Q = \frac{A \cdot DT \cdot K}{DX}$$

$$\text{Insulation diameter} = 130\text{mm} = 0.130\text{m}$$

$$\text{Insulation height} = 274\text{mm} = 0.274\text{m}$$

$$\text{Insulation thickness} = 20\text{mm} = 0.02\text{m} \text{ (assume coils are absent)}$$

$$Q = \text{Heat (W)} = 4140\text{W}$$

$$A = \text{External surfaces (m}^2\text{)} = \pi \times 0.130 \times 0.274\text{m}$$

$$DT = \text{Temp difference (in K)}$$

$$K = \text{Thermal conductivity (W/m K)} = 2 \text{ W/m K}$$

$$DX = \text{Insulation thickness (m)} = 0.02\text{m}$$

Heat dissipation is extremely high in the coils. As a result, heating the coils to 750°C will locally be nearer 320°C. Assuming this, then there is a re-arranged heat gradient equation :-

Rearranged heat gradient equation

$$\frac{Q.DX}{A.K} = DT$$

$$\frac{4140 \times 0.02}{\pi \times 0.13 \times 0.274 \times 2} = 370^{\circ} K$$

$$\therefore DT = 370 K$$

The coils are at 320°C which is 593°K

The inner cell wall = 593°K – 370°K = 223°K

Therefore heat of inside of pressure vessel wall < 0°C

Therefore 20mm thick insulation is enough to lower the inner pressure wall to a temperature below 100°C. This value, in practise, will be greater than zero because the insulation isn't solid (ceramic beads), oil is present (holes in beads) and the outside temperature will affect actual temperature.

Appendix 4: Stress Analysis

As the pressure vessel is capable of 400 MPa confining pressure, certain parts of the furnace must be able to withstand these forces. Therefore, before I could finish the designs required to use the electric furnace, the designs needed to be tested to determine if the stresses imposed on them during an experiment would lead them to failure. If so, the design of the furnace would need to be modified to improve its strength.

The calculations were done in two parts. Firstly, a Finite Element Analysis (FEA) of the 3D autoCAD drawings was done using a program called Design Space 6.1. This program analyses the whole of the 3D structure and determines where the stress concentrations will be along with the maximum and minimum stresses. Secondly, the calculations were checked by hand in order to compare with the model. The results of both forms of analysis are given below.

1) FEA ANALYSIS OF BOTTOM OUTER CLOSURE

1. Summary

This report documents design and analysis information created and maintained using the DesignSpace® engineering software program.

Scenario 1

- Based on the Autodesk® Mechanical Desktop® part "*C:\Documents and Settings\ucfbdec\My Documents\Davids plug\Bottom closure FEA.dwg*" <>.
- Considered the effect of structural loads <> and structural supports <>.
- Calculated safety factors and margins based on the Mohr-Coulomb theory <> and maximum tensile stress <> along with structural <> results.
- **All results passed the defined convergence criteria <>.**
- No alert criteria <> defined.
- See Scenario 1 <> below for supporting details and Appendix A1 <> for corresponding figures.

2. Introduction

The DesignSpace CAE (Computer-Aided Engineering) software program was used in conjunction with 3D CAD (Computer-Aided Design) solid geometry to simulate the behaviour of mechanical parts under thermal/structural loading conditions. DesignSpace automated FEA (Finite Element Analysis) technologies from ANSYS, Inc. <<http://www.ansys.com>> to generate the results listed in this report.

Each scenario presented below represents one complete engineering simulation. The definition of a simulation includes known factors about a design such as material properties per part, contact behaviour between parts (in an assembly), and types and magnitudes of loading conditions. The results of a simulation provide insight into how the parts may perform and how the design might be improved.

Multiple scenarios allow comparison of results given different loading conditions, materials or geometric configurations.

Convergence and alert criteria may be defined for any of the results and can serve as guides for evaluating the quality of calculated results and the acceptability of values in the context of known design requirements.

- *Solution history* provides a means of assessing the quality of results by examining how values change during successive iterations of solution refinement. *Convergence criteria* sets a specific limit on the allowable change in a result between iterations. A result meeting this criteria is said to be "converged".
- *Alert criteria* define "allowable" ranges for result values. Alert ranges typically represent known aspects of the design specification.

The discussions below follow the organization of information in the DesignSpace "Explorer" user interface. Each scenario corresponds to a unique branch in the Explorer "Outline". Names emphasized in "double quotes" match preferences set in the user interface.

All values are presented in the "SI Metric (m, kg, Pa, °C, s)" unit system.

Notice

Do not accept or reject a design based solely on the data presented in this report. Evaluate designs by considering this information in conjunction with experimental test data and the practical experience of design engineers and analysts. A quality approach to engineering design usually mandates physical testing as the final means of validating structural integrity to a measured precision.

3. Scenario 1

3.1. "Model"

"Model" obtains geometry from the Autodesk® Mechanical Desktop® part "C:\Documents and Settings\ucfbdec\My Documents\Davids plug\Bottom closure FEA.dwg".

- The **bounding box** \diamond for the model measures 93.0 by 230.21 by 230.21 m along the global x, y and z axes, respectively.
- The model weighs a total of 1.79×10^{10} kg.

Table 3.1.1. Parts

Name	Material	Nodes	Elements
"PART1_1"	"Structural Steel" $\langle \rangle$	47593	30796

3.1.1. Mesh

- "Mesh", associated with "Model", has an overall relevance of 0.
- "Mesh" contains 47593 nodes and 30796 elements.

No mesh controls specified.

3.2. "Environment"

"Environment" contains all loading conditions defined for "Model" in this scenario.

The following tables list local loads and supports applied to specific geometry.

3.2.1. Structural Loading

Table 3.2.1.1. Structural Loads

Name	Type	Magnitude	Vector
"Pressure"	Surface Pressure	400.0 Pa	N/A
"Pressure 2"	Surface Pressure	400.0 Pa	N/A
"Pressure 3"	Surface Pressure	400.0 Pa	N/A

3.2.2. Structural Supports

Table 3.2.2.1. Structural Supports

Name	Type	Reaction Force	Reaction Vector
"Fixed Support"	Fixed Surface	3.14×10^6 N	$[3.14 \times 10^6$ N x, -4.36×10^{-3} N y, -3.3×10^{-3} N z]

3.3. "Solution"

"Solution" contains the calculated response for "Model" given loading conditions defined in "Environment".

3.3.1. Structural Results

Table 3.3.1.1. Values

Name	Scope \triangleleft	Orientation	Minimum	Maximum	Alert Criteria
"Maximum Principal Stress"	"Model"	Global	-502.53 Pa	498.91 Pa	None
"Minimum Principal Stress"	"Model"	Global	-1,364.6 Pa	41.82 Pa	None
"Total Deformation"	"Model"	Global	0.0 m	2.51×10^{-7} m	None
"Maximum Shear Stress"	"Model"	Global	5.66 Pa	482.98 Pa	None
"Directional Deformation X"	"Model"	World X Axis	-2.22×10^{-7} m	1.24×10^{-8} m	None
"Directional Deformation Y"	"Model"	World Y Axis	-1.33×10^{-7} m	1.34×10^{-7} m	None
"Directional Deformation Z"	"Model"	World Z Axis	-1.33×10^{-7} m	1.33×10^{-7} m	None

Table 3.3.1.2. Convergence Tracking

Name	Type	Allowable Change	Last Change	Status
"Maximum Principal Stress"	Maximum	$\pm 20.0\%$	+11.81%	Converged

Table 3.3.1.3. Solution History

Name	Base Solution	Refinement 1
"Maximum Principal Stress"	443.3 Pa	498.91 Pa [+11.81%]

Mesh properties	Nodes: 47593	Nodes: 94747
	Elements: 30796	Elements: 64211

3.3.2. Tensile Stress Safety

Table 3.3.2.1. Definition

Name	Tensile Limit
"Stress Tool"	Yield strength per material.

Table 3.3.2.2. Results

Name	Scope \diamond	Type	Minimum	Alert Criteria
"Stress Tool"	"Model"	Safety Factor	15.0	None
"Stress Tool"	"Model"	Safety Margin	14.0	None

3.3.3. Mohr-Coulomb Stress Safety

Table 3.3.3.1. Definition

Name	Compressive Limit	Tensile Limit
"Stress Tool 2"	Yield strength per material.	Yield strength per material.

Table 3.3.3.2. Results

Name	Scope \diamond	Type	Minimum	Alert Criteria
"Stress Tool 2"	"Model"	Safety Factor	15.0	None
"Stress Tool 2"	"Model"	Safety Margin	14.0	None

Appendixes

A1. Scenario 1 Figures

No figures to display.

A2. Definition of "Structural Steel"

Table A2.1. "Structural Steel" Properties

Name	Type	Value
Modulus of Elasticity	Temperature-Independent	2.0×10^{11} Pa
Poisson's Ratio	Temperature-Independent	0.3
Mass Density	Temperature-Independent	7,850.0 kg/m ³
Coefficient of Thermal Expansion	Temperature-Independent	1.2×10^{-5} 1/°C
Thermal Conductivity	Temperature-Independent	60.5 W/m·°C

Table A2.2. "Structural Steel" Stress Limits

Name	Type	Value
Tensile Yield Strength	Temperature-Independent	2.5×10^8 Pa
Tensile Ultimate Strength	Temperature-Independent	4.6×10^8 Pa
Compressive Yield Strength	Temperature-Independent	2.5×10^8 Pa
Compressive Ultimate Strength	Temperature-Independent	0.0 Pa

2) FEA ANALYSIS OF HEATING ELEMENT PLUG

1. Summary

This report documents design and analysis information created and maintained using the DesignSpace® engineering software program. Each scenario listed below represents one complete engineering simulation.

Scenario 1

- Based on the Autodesk® Mechanical Desktop® part "C:\Documents and Settings\ucfbdec\My Documents\Davids plug\3.2mm plug revised FEA.dwg" <>.
- Considered the effect of structural loads <> and structural supports <>.
- Calculated safety factors and margins based on the Mohr-Coulomb theory <> and maximum tensile stress <> along with structural <> results.
- No convergence criteria <> defined.
- No alert criteria <> defined.
- See Scenario 1 <> below for supporting details and Appendix A1 <> for corresponding figures.

2. Introduction

The DesignSpace CAE (Computer-Aided Engineering) software program was used in conjunction with 3D CAD (Computer-Aided Design) solid geometry to simulate the behavior of mechanical parts under thermal/structural loading conditions. DesignSpace automated FEA (Finite Element Analysis) technologies from ANSYS, Inc. <<http://www.ansys.com>> to generate the results listed in this report.

Each scenario presented below represents one complete engineering simulation. The definition of a simulation includes known factors about a design such as material properties per part, contact behavior between parts (in an assembly), and types and magnitudes of loading conditions. The results of a simulation provide insight into how the parts may perform and how the design might be improved. Multiple scenarios allow comparison of results given different loading conditions, materials or geometric configurations.

Convergence and alert criteria may be defined for any of the results and can serve as guides for evaluating the quality of calculated results and the acceptability of values in the context of known design requirements.

- *Solution history* provides a means of assessing the quality of results by examining how values change during successive iterations of solution refinement. *Convergence criteria* sets a specific limit on the allowable change in a result between iterations. A result meeting this criteria is said to be "converged".
- *Alert criteria* define "allowable" ranges for result values. Alert ranges typically represent known aspects of the design specification.

The discussions below follow the organization of information in the DesignSpace "Explorer" user interface. Each scenario corresponds to a unique branch in the Explorer "Outline". Names emphasized in "double quotes" match preferences set in the user interface.

All values are presented in the "SI Metric (m, kg, Pa, °C, s)" unit system.

Notice

Do not accept or reject a design based solely on the data presented in this report. Evaluate designs by considering this information in conjunction with experimental test data and the practical experience of design engineers and analysts. A quality approach to engineering design usually mandates physical testing as the final means of validating structural integrity to a measured precision.

3. Scenario 1

3.1. "Model"

"Model" obtains geometry from the Autodesk® Mechanical Desktop® part "C:\Documents and Settings\ucfbdec\My Documents\Davids plug\3.2mm plug revised FEA.dwg".

- The **bounding box** $\langle \rangle$ for the model measures 12.0 by 21.0 by 12.0 m along the global x, y and z axes, respectively.
- The model weighs a total of 9.2×10^6 kg.

Table 3.1.1. Parts

Name	Material	Nodes	Elements
"PART1_1"	"Structural Steel" $\langle \rangle$	5610	3240

3.1.1. Mesh

- "Mesh", associated with "Model", has an overall relevance of 0.
- "Mesh" contains 5610 nodes and 3240 elements.

No mesh controls specified.

3.2. "Environment"

"Environment" contains all loading conditions defined for "Model" in this scenario.

The following tables list local loads and supports applied to specific geometry.

3.2.1. Structural Loading

Table 3.2.1.1. Structural Loads

Name	Type	Magnitude	Vector
"Pressure"	Surface Pressure	400.0 Pa	N/A

"Pressure 2"	Surface Pressure	400.0 Pa	N/A
--------------	------------------	----------	-----

3.2.2. Structural Supports

Table 3.2.2.1. Structural Supports

Name	Type	Reaction Force	Reaction Vector
"Fixed Support"	Fixed Surface	29,771.31 N	$[-7.19 \times 10^{-6} \text{ N x}, 29,771.31 \text{ N y}, -6.44 \times 10^{-5} \text{ N z}]$

3.3. "Solution"

"Solution" contains the calculated response for "Model" given loading conditions defined in "Environment".

It was selected that the program would choose the solver used in this solution.

3.3.1. Structural Results

Table 3.3.1.1. Values

Name	Scope \triangleleft	Orientation	Minimum	Maximum	Alert Criteria
"Maximum Principal Stress"	"Model"	Global	-406.48 Pa	440.23 Pa	None
"Minimum Principal Stress"	"Model"	Global	-1,177.79 Pa	9.19 Pa	None
"Total Deformation"	"Model"	Global	0.0 m	$1.07 \times 10^{-8} \text{ m}$	None
"Total Deformation 2"	"Model"	Global	0.0 m	$1.07 \times 10^{-8} \text{ m}$	None
"Directional Deformation X"	"Model"	World X Axis	$-9.43 \times 10^{-9} \text{ m}$	$9.46 \times 10^{-9} \text{ m}$	None
"Directional Deformation Y"	"Model"	World Y Axis	$-8.42 \times 10^{-9} \text{ m}$	$1.29 \times 10^{-9} \text{ m}$	None
"Directional Deformation Z"	"Model"	World Z Axis	$-9.09 \times 10^{-9} \text{ m}$	$9.25 \times 10^{-9} \text{ m}$	None
"Maximum Shear Stress"	"Model"	Global	2.18 Pa	734.69 Pa	None

3.3.2. Tensile Stress Safety

Table 3.3.2.1. Definition

Name	Tensile Limit
"Stress Tool"	Yield strength per material.

Table 3.3.2.2. Results

Name	Scope \triangleleft	Type	Minimum	Alert Criteria
"Stress Tool"	"Model"	Safety Factor	15.0	None
"Stress Tool"	"Model"	Safety Margin	14.0	None

3.3.3. Mohr-Coulomb Stress Safety

Table 3.3.3.1. Definition

Name	Compressive Limit	Tensile Limit
"Stress Tool 2"	Yield strength per material.	Yield strength per material.

Table 3.3.3.2. Results

Name	Scope \diamond	Type	Minimum	Alert Criteria
"Stress Tool 2"	"Model"	Safety Factor	15.0	None
"Stress Tool 2"	"Model"	Safety Margin	14.0	None

Appendixes

A1. Scenario 1 Figures

No figures to display.

A2. Definition of "Structural Steel"

Table A2.1. "Structural Steel" Properties

Name	Type	Value
Modulus of Elasticity	Temperature-Independent	2.0×10^{11} Pa
Poisson's Ratio	Temperature-Independent	0.3
Mass Density	Temperature-Independent	7,850.0 kg/m ³
Coefficient of Thermal Expansion	Temperature-Independent	1.2×10^{-5} 1/°C
Thermal Conductivity	Temperature-Independent	60.5 W/m·°C

Table A2.2. "Structural Steel" Stress Limits

Name	Type	Value
Tensile Yield Strength	Temperature-Independent	2.5×10^8 Pa
Tensile Ultimate Strength	Temperature-Independent	4.6×10^8 Pa
Compressive Yield Strength	Temperature-Independent	2.5×10^8 Pa
Compressive Ultimate Strength	Temperature-Independent	0.0 Pa

3) FEA ANALYSIS OF LEAD-THROUGH PLUG

1. Summary

This report documents design and analysis information created and maintained using the DesignSpace® engineering software program. Each scenario listed below represents one complete engineering simulation.

Scenario 1

- Based on the Autodesk® Mechanical Desktop® part "C:\Documents and Settings\ucfbdec\My Documents\Davids plug\Leadthrough plug FEA.dwg" <>.
- Considered the effect of structural loads <> and structural supports <>.
- Calculated safety factors and margins based on maximum equivalent stress <> along with structural <> results.
- **One or more results failed to meet defined convergence criteria** <>.
- No alert criteria <> defined.
- See Scenario 1 <> below for supporting details and Appendix A1 <> for corresponding figures.

2. Introduction

The DesignSpace CAE (Computer-Aided Engineering) software program was used in conjunction with 3D CAD (Computer-Aided Design) solid geometry to simulate the behavior of mechanical parts under thermal/structural loading conditions. DesignSpace automated FEA (Finite Element Analysis) technologies from ANSYS, Inc. <<http://www.ansys.com>> to generate the results listed in this report.

Each scenario presented below represents one complete engineering simulation. The definition of a simulation includes known factors about a design such as material properties per part, contact behavior between parts (in an assembly), and types and magnitudes of loading conditions. The results of a simulation provide insight into how the parts may perform and how the design might be improved. Multiple scenarios allow comparison of results given different loading conditions, materials or geometric configurations.

Convergence and alert criteria may be defined for any of the results and can serve as guides for evaluating the quality of calculated results and the acceptability of values in the context of known design requirements.

- *Solution history* provides a means of assessing the quality of results by examining how values change during successive iterations of solution refinement. *Convergence criteria* sets a specific limit on the allowable change in a result between iterations. A result meeting this criteria is said to be "converged".
- *Alert criteria* define "allowable" ranges for result values. Alert ranges typically represent known aspects of the design specification.

The discussions below follow the organization of information in the DesignSpace "Explorer" user interface. Each scenario corresponds to a unique branch in the Explorer "Outline". Names emphasized in "double quotes" match preferences set in the user interface.

All values are presented in the "SI Metric (m, kg, Pa, °C, s)" unit system.

Notice

Do not accept or reject a design based solely on the data presented in this report. Evaluate designs by considering this information in conjunction with experimental test data and the practical experience of design engineers and analysts. A quality approach to engineering design usually mandates physical testing as the final means of validating structural integrity to a measured precision.

3. Scenario 1

3.1. "Model"

"Model" obtains geometry from the Autodesk® Mechanical Desktop® part "C:\Documents and Settings\ucfbdec\My Documents\Davids plug\Leadthrough plug FEA.dwg".

- The bounding box <> for the model measures 16.0 by 38.0 by 16.0 m along the global x, y and z axes, respectively.
- The model weighs a total of 4.35×10^7 kg.

Table 3.1.1. Parts

Name	Material	Nodes	Elements
"PART1_1"	"Structural Steel" <>	26112	17555

3.1.1. Mesh

- "Mesh", associated with "Model", has an overall relevance of 0.
- "Mesh" contains 26112 nodes and 17555 elements.

No mesh controls specified.

3.2. "Environment"

"Environment" contains all loading conditions defined for "Model" in this scenario.

The following tables list local loads and supports applied to specific geometry.

3.2.1. Structural Loading

Table 3.2.1.1. Structural Loads

Name	Type	Magnitude	Vector
"Pressure"	Surface Pressure	400.0 Pa	N/A

3.2.2. Structural Supports

Table 3.2.2.1. Structural Supports

Name	Type	Reaction Force	Reaction Vector
"Fixed Support"	Fixed Surface	50,656.25 N (not updated)	[1.23×10^{-5} N x, 50,656.25 N y, 1.44×10^{-5} N z] (not updated)

3.3. "Solution"

"Solution" contains the calculated response for "Model" given loading conditions defined in "Environment".

It was selected that the program would choose the solver used in this solution.

3.3.1. Structural Results

Table 3.3.1.1. Values

Name	Scope \diamond	Orientation	Minimum	Maximum	Alert Criteria
"Equivalent Stress"	"Model"	Global	0.3 Pa	1,525.66 Pa	None
"Maximum Principal Stress"	"Model"	Global	-433.27 Pa	1,303.3 Pa	None
"Shear Stress"	"Model"	World XY Plane	-690.33 Pa	802.32 Pa	None
"Total Deformation"	"Model"	Global	0.0 m	2.11×10^{-8} m	None
"Directional Deformation X"	"Model"	World X Axis	-8.08×10^{-9} m	8.02×10^{-9} m	None
"Directional Deformation Y"	"Model"	World Y Axis	-2.0×10^{-8} m	1.62×10^{-10} m	None
"Directional Deformation Z"	"Model"	World Z Axis	-8.27×10^{-9} m	7.85×10^{-9} m	None

Table 3.3.1.2. Convergence Tracking

Name	Type	Allowable Change	Last Change	Status
"Equivalent Stress"	Maximum	$\pm 20.0\%$	+60.95%	Unconverged

Table 3.3.1.3. Solution History

Name	Base Solution	Refinement 1
"Equivalent Stress"	813.01 Pa	1,525.66 Pa [+60.95%]
Mesh properties	Nodes: 26112 Elements: 17555	Nodes: 75900 Elements: 52341

3.3.2. Equivalent Stress Safety

Table 3.3.2.1. Definition

Name	Stress Limit
"Stress Tool"	Yield strength per material.

Table 3.3.2.2. Results

Name	Scope \diamond	Type	Minimum	Alert Criteria
"Stress Tool"	"Model"	Safety Factor	15.0	None

Appendixes

A1. Scenario 1 Figures

No figures to display.

A2. Definition of "Structural Steel"

Table A2.1. "Structural Steel" Properties

Name	Type	Value
Modulus of Elasticity	Temperature-Independent	2.0×10^{11} Pa
Poisson's Ratio	Temperature-Independent	0.3
Mass Density	Temperature-Independent	7,850.0 kg/m ³

Appendix 4: Stress Analysis

Coefficient of Thermal Expansion	Temperature-Independent	$1.2 \times 10^{-5} \text{ 1/}^\circ\text{C}$
Thermal Conductivity	Temperature-Independent	$60.5 \text{ W/m}\cdot^\circ\text{C}$

Table A2.2. "Structural Steel" Stress Limits

Name	Type	Value
Tensile Yield Strength	Temperature-Independent	$2.5 \times 10^8 \text{ Pa}$
Tensile Ultimate Strength	Temperature-Independent	$4.6 \times 10^8 \text{ Pa}$
Compressive Yield Strength	Temperature-Independent	$2.5 \times 10^8 \text{ Pa}$
Compressive Ultimate Strength	Temperature-Independent	0.0 Pa

4) HAND CALCULATION OF STRESSES APPLIED ON THE BOTTOM OUTER CLOSURE

The maximum stress applied to the closure would be at the around the holes to which the thermocouples and heating elements will go through with the use of a plug. If the stresses here are less than the yield stress, then the stresses elsewhere will be lower than the yield stress and of no consequence to damage caused to the bottom outer closure during an experiment.

Yield strength of 3.5% Nickel chrome alloy is 50 tonnes per sq inch.

Yield force equals

50 tonnes per sq inch
 “ “ “ 645.16mm²
 “ “ “ 6.4516cm²
 “ “ “ 6.4516 x 10⁻⁴m²

Yield stress equals

Force (N) = Stress (MPa) * Area (m²) ∴

Force (N) / Area (m²) = Stress (MPa)

50 tonnes per sq inch

1 tonne ≈ 10,000 N ∴

1 tonne ≈ 10 KN

50 tonnes = 50 x 10KN ∴

50 tonnes = 500,000 N

Stress =
$$\frac{500,000N}{6.45 \times 10^{-4}m^2}$$

Yield stress = 775MPa

Ultimate Tensile Strength (UTS) = 1080MPa

The triaxial rock deformation cell is capable of having confining pressure up to 400MPa. Therefore the maximum stress applied onto the surface area of a plug is 400 MPa, however the plug rests on a surface area of the total surface area end minus what would be the hole surface area.

Stress plug edge places on bottom closure

$$\text{Stress} = \text{Force (N)} / \text{Area (m}^2\text{)}$$

$$\text{Stress} = \frac{45000\text{N}}{6.27 \times 10^{-5}\text{m}^2}$$

$$\text{Stress} \approx 720\text{MPa}$$

∴ Using the maximum confining pressure of 400MPa results in a stress on the bottom outer closure of 720MPa.

$$\text{Yield stress} = 775\text{MPa}$$

$$\text{Max stress applied by plug} = 720\text{MPa}$$

$$\therefore 720\text{MPa} < 775\text{MPa}$$

$$\therefore \text{applied stress} < \text{yield stress}$$

∴ Vessel with confining pressure of up to 400MPa can be used during an experiment.

5) HAND CALCULATION OF STRESSES APPLIED ON THE ELEMENT PLUG

In part (4) the stresses the plug applied on the bottom outer closure was calculated at 720MPa. The yield stress of the FV520 to which the plug will be made has a value of is 1030MPa.

$$720\text{MPa} < 1030\text{MPa}$$

$$\therefore \text{applied stress} < \text{yield stress}$$

∴ The plug can go to the confining pressure of 400MPa.

6) HAND CALCULATION OF STRESSES APPLIED ON THE LEAD-THROUGH

Like part (5) the maximum stress is applied to the end of the plug, the forces were calculated in the same manner as shown in part (4)

Appendix 4: Stress Analysis

Stress plug edge places on bottom closure

Stress = Force (N) / Area (m²)

$$\text{Stress} = \frac{80000\text{N}}{8.7 \times 10^{-45}\text{m}^2}$$

Stress \approx 920MPa

\therefore Using the maximum confining pressure of 400MPa results in a stress on the bottom outer closure of 920MPa.

Yield stress = 1030MPa

\therefore 920MPa < 1030MPa

\therefore applied stress < yield stress

\therefore Lead-through plugs with confining pressure of up to 400MPa can be used during an experiment.

In conclusion all parts can be used up to a confining pressure of 400MPa \therefore no changes in experimental practises was required and no damage would occur to the furnace and triaxial rock deformation cell.

Appendix 5: Auto-CAD Drawings for the Furnace, Separator, Yoke etc.

The Appendix contains a list of all the drawings for the furnace, separator and yoke of components created by me with assistance from Neil Hughes in order to accomplish my PhD. All drawings were checked by John Bowles, Neil Hughes & Prof. Peter Sammonds.

Furnace

- 400MPa Leadthrough Plug.dwg
- Bottom closure outer seal retainer.dwg
- Bottom inner closure.dwg
- Bottom outer ceramic spacer.dwg
- Ceramic 10mm piece.dwg
- Collar.dwg
- Endcap B modified.dwg
- Endcap C modified.dwg
- Furnace assembly 2d.dwg
- Furnace assembly.dwg
- Furnace holding pieces.dwg
- Furnace thermocouple 1.dwg
- Furnace thermocouple 2.dwg
- Furnace thermocouple 3.dwg
- Holding piece.dwg
- Holding pieces.dwg
- Inner shell furnace.dwg
- Leadthrough thermocouple 1.dwg
- Leadthrough thermocouple 2.dwg
- Leadthrough thermocouple plug.dwg
- Lower furnace end.dwg
- Lower heating element.dwg
- Lower yoke ceramic piece.dwg
- Metal ring.dwg
- Outer shell furnace.dwg
- Revised blank plug.dwg
- Revised Plug 2mm hole.dwg
- Revised Plug 3.2mm hole.dwg
- Top outer ceramic spacer.dwg
- Top retaining seal.dwg
- Transducer fitting.dwg
- Upper ceramic end.dwg
- Upper heating element.dwg
- Upper yoke ceramic piece.dwg

Separator

- Flange.dwg
- Mitre.dwg
- Plug.dwg
- Sealret.dwg
- Sep.dwg

Yoke

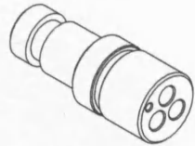
- 40mm Disc.dwg
- Alignment ring.dwg
- Distribution plate.dwg
- Insul.dwg
- New endcap A.dwg
- New endcap assembly.dwg
- New endcap B.dwg
- New endcap C.dwg
- New endcap D.dwg
- Pore pressure collar.dwg
- Pore pressure cone.dwg
- Pore pressure gland nut.dwg
- Tie bar 2.dwg

SPECIAL NOTE

**ITEM SCANNED AS SUPPLIED
PAGINATION IS AS SEEN**

USED ON

DRAWING No.
RP\400MPA\LEAD\003

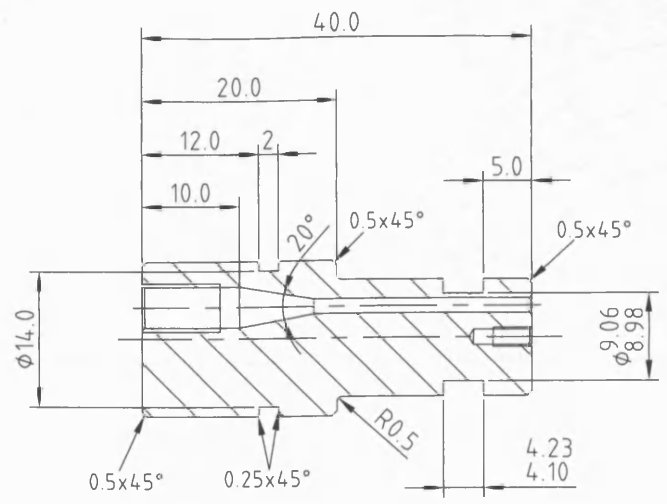
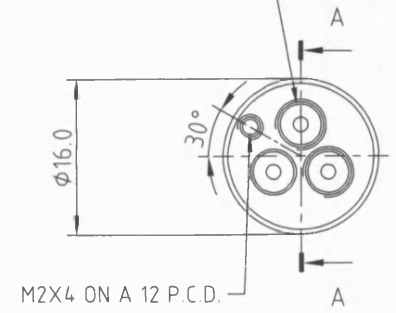


THIRD ANGLE PROJECTION

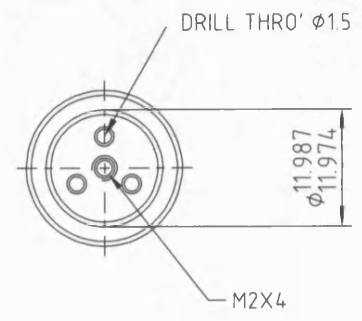
DO NOT SCALE

REMOVE ALL BURRS & SHARP EDGES

3 HOLES M5X8
EQUISPACED ON A 6.5 P.C.D.
AS SHOWN




SECTION A-A



NOTE

- 1) All Internal Corners to R0.2
- 2) Surface Finish 0.4µm Ra
- 3) Polish 20° cone
- 4) Chamfer Hole Edges 0.25x45°
- 5) 3 Holes on 6.5 P.C.D Are Identical


CHECKED				PROTECTIVE FINISH	MATERIAL & SPECN. FV520B (DBL AGE HARDENED)	TOLERANCES DECIMAL DIMENSIONS ± 0.1 NON DECIMAL DIMENSIONS ± 0.5 SURFACE FINISH - 0.8 Ra
TRACED						UNLESS OTHERWISE STATED
DRAWN NJH	ISSUE	DATE	AMENDMENT	DIMENSIONS IN MILLIMETRES UNLESS OTHERWISE STATED		SCALE
		OCT 97	CERTIFIED			



ROCK & ICE PHYSICS LABORATORY

DEPARTMENT OF GEOLOGICAL SCIENCES

UNIVERSITY COLLEGE LONDON



TITLE 400MPA LEADTHROUGH PLUG	DRAWING No. RP\400MPA\LEAD\003
----------------------------------	-----------------------------------

DRAWING No.

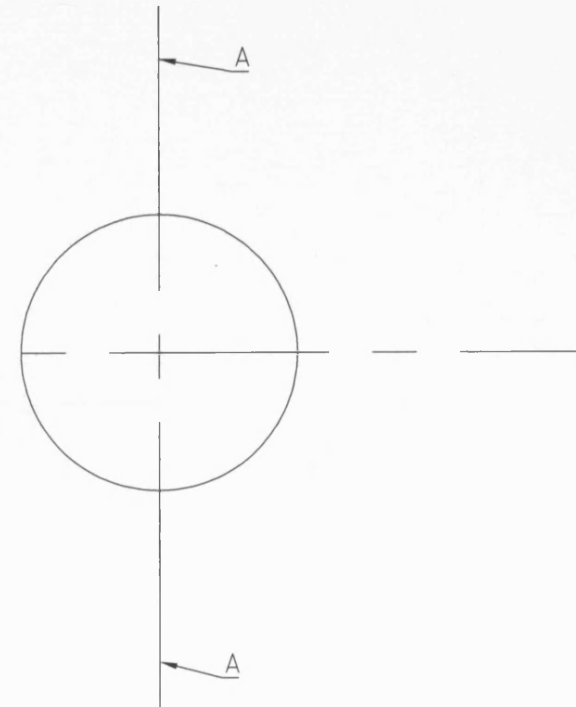
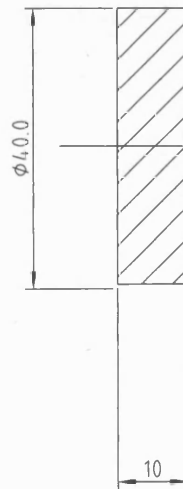
THIRD ANGLE PROJECTION

DO NOT SCALE

REMOVE ALL BURRS & SHARP EDGES

USED ON

SECTION A-A



NOTE
4 PER SET

CHECKED				PROTECTIVE FINISH	MATERIAL & SPECN.	TOLERANCES
PRS				BUBBLE WRAP	ALUMINIA	DECIMAL DIMENSIONS ± 0.1 NON DECIMAL DIMENSIONS ± 0.5 SURFACE FINISH - 0.8 Ra
TRACED						UNLESS OTHERWISE STATED
DRAWN	ISSUE	DATE	AMENDMENT	DIMENSIONS IN MILLIMETRES UNLESS OTHERWISE STATED		SCALE
DE		0/01/03	CERTIFIED			



MINERAL, ICE & ROCK PHYSICS LABORATORY
 DEPARTMENT OF GEOLOGICAL SCIENCES
 UNIVERSITY COLLEGE LONDON



TITLE	DRAWING No.
UPPER & LOWER CERAMIC 10MM PIECE	MIRP/400MPA/ENDCAP2002A\003\B

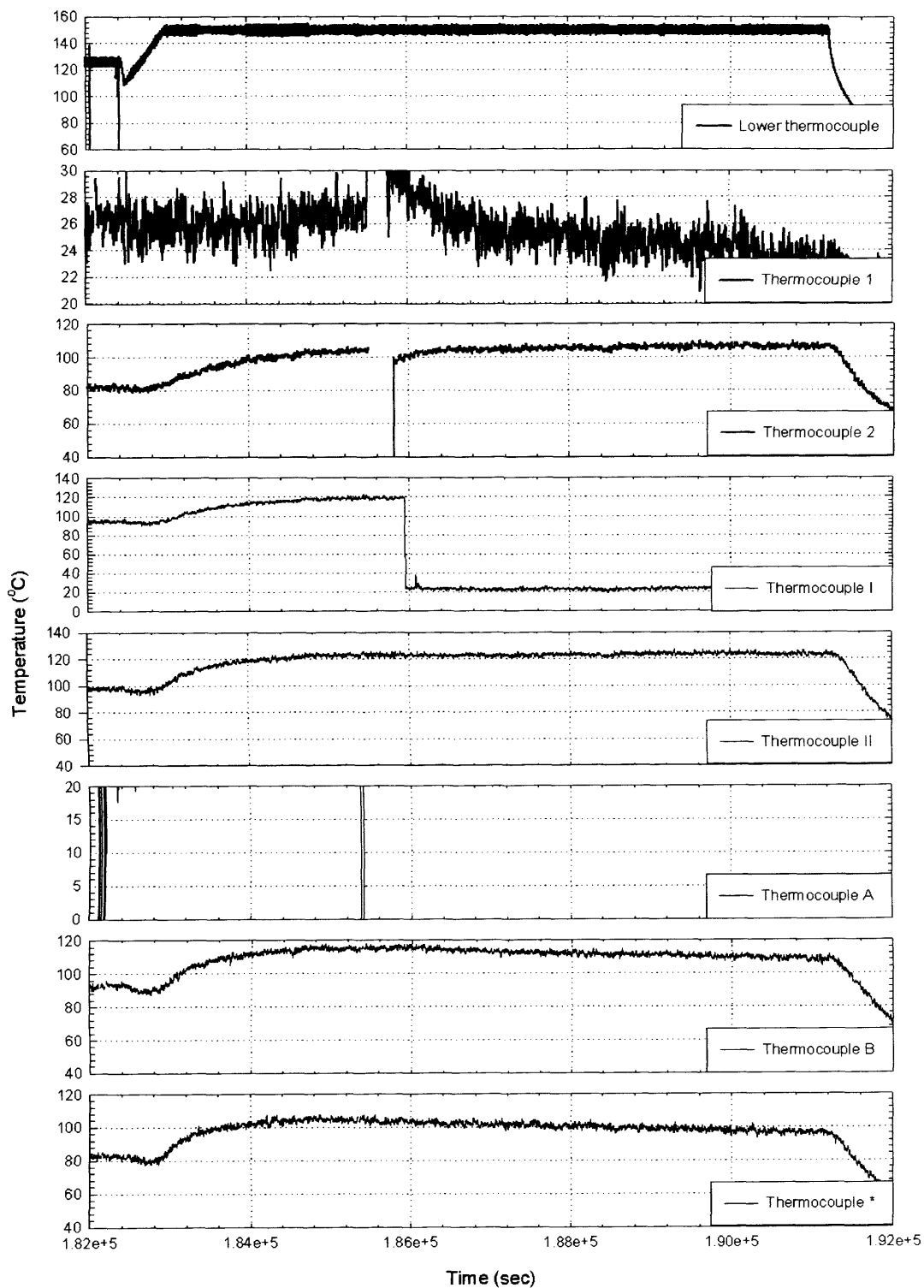


Figure 6: Furnace calibration at 150°C.

Appendix 8: Mobility and Electrical Time Constant

Ionic Mobility

The mobility μ_m of a particular ionic species is equal to

$$\mu_m = \frac{q\lambda}{2mv} \quad (\text{A-1})$$

where q is charge carrier charge, λ is average length of the free path of electrons, m is electron mass, v is the average speed of the thermal speed of electron in conductor and

Electrical Time Constant

Electrical signals decay according to the electrical time constant (11-5), which is inversely proportional to conductivity of the bulk medium and is the time required to attain electrical equilibrium in a medium

$$\tau_0 = \frac{\epsilon}{\sigma_b} \quad (\text{A-2})$$

Appendix 9: Programs to Aid Study

```
/******  
/*  
/*      Program which calculates b-value using AKI's weighting method      */  
/*      Written David Eccles, June 2001: hit or time interval              */  
/*  
/******  
  
#include<stdio.h>  
#include <stdlib.h>  
#include<fstream.h>  
#include<math.h>  
  
int main()                /* Main program */  
{  
    float amp[100];  
    int check, channel;  
    int i, j, low_amp=0, high_amp=0;  
    int amp_temp=0, cum_hits=0, hits=0, no=1, hitint;  
    float time, para, para2, ch, rise, count, energy, amplitude, duration, freq;  
    float tot_amp=0.0, tot_dur=0.0, tot_time=0.0, calc_time=0.0;  
    float U=0, levents, tamp, average, b_amp, b_value=0.0, temp_time=0.0;  
        char locan_file[50], b_file[50];  
    FILE *fp, *fpp;  
  
    /****** Loads the file with the data in it *****/  
  
    while(no==1)  
    {  
        printf("Enter Locan ASCII Filename : ");  
        scanf("%s",locan_file);  
  
        fp = fopen(locan_file,"r+");  
  
        no=0;  
        if((fp = fopen(locan_file,"r+")) == NULL)  
        {  
            printf("\nFile does not exist\n");  
            no=1;  
        }  
    }  
  
    /****** Output file where the calculations are put *****/  
  
    printf("\nEnter Output Filename : ");  
    scanf("%s",b_file);  
    fpp = fopen(b_file,"w+");  
  
    /*** Above this point the amplitude (col 4) the calculations are done ***/  
    /***** E.g. This acts as a filter to remove noise below a given value *****/  
  
    printf("\nEnter Threshold Amplitude : ");  
    scanf("%d",&b_amp);  
  
    /****** Interval duration to calculating b-values *****/  
    printf("\nEnter Interval Spacing : ");  
    scanf("%d",&hitint);  
  
    high_amp = 100;  
    low_amp= 0;  
    //hitint = 100;
```

Appendix 9: Programs to Aid Study

```
        check = 1;
        for(j=0;j<100;j++)amp[j]=0;

/***** To show it works print message on screen *****/

        while(!feof(fp))
        {
            //      printf("\n\nCalculating AE statistics for David Eccles");

            fscanf(fp,"%f%f%f%f%f%f%f%f%f",&time,&para,&para2,&ch,&rise,&count,&energy,&duration,&amplitude,&freq);
            printf("%f\n\n\n\t\t\t",time);
            if(check==1)
            {
                temp_time = time;
                check=0;
            }

            time = time * 1;
            para = para * 1;
            duration = duration * 1;
            amplitude = amplitude * 1;

/***** Set the values using the below equations *****/

            if(amplitude > low_amp && amplitude < high_amp)
            {
                tot_amp = tot_amp + amplitude;
                tot_dur = tot_dur + duration;
                tot_time = tot_time + time;
                amp_temp = amplitude;
                amp[amp_temp] = amp[amp_temp] + 1;
                cum_hits+=1;
                hits+=1;
                calc_time = time;

/***** Calculates b-values when limit reach and writes in program *****/

                if(hits == hitint)
                //if (calc_time > 30.5 && calc_time < 31.5)
                {
                    average = 0, levents = 0, tamp = 0;

                    for(i=b_amp;i<high_amp;i++)
                    {
                        levents = levents + amp[i];
                        tamp = (amp[i] * (i+0.5)) + tamp;
                    }
                    average = tamp/levents;
                    b_value = 8.6859 / (average - b_amp);

                    if(cum_hits<0)cum_hits*=-1;
                    printf("\n\nWriting!");

                    fprintf(fpp,"%7.3ft%7.3ft%d\t%7.3ft%7.3ft%7.3fn",tot_time/hits, hits/(time - U), cum_hits,
tot_amp/hits, tot_dur/hits, b_value);

                    U = time, tot_amp=0, tot_dur=0;
                    tot_time=0; hits=0, amp_temp=0;
                    channel=0;
```

Appendix 9: Programs to Aid Study

```
        for(j=0;j<100;j++)amp[j]=0;
        }
        check=1;
    }
}

/***** Closes file after running program *****/

    fclose(fp);
    fclose(fpp);
    return 0;
}
```

Appendix 9: Programs to Aid Study

```

/*****
/*
/*      Program which calculates Mean Crack Length and relates it to EP      */
/*      Written by Oswald Clint, September 1998                          */
/*      Modified by David Eccles, October 2003                            */
/*
*****/

#include<stdio.h>
#include<stdlib.h>
#include<dos.h>
#include<conio.h>
#include<math.h>

// Program to calculate mean crack density

void main(void)                /* Main program */
{

    int no=1;
    float bval=0;
    float frac_dim=0;
    float time=0;
    float nt=0, ck_len1=0;
    float ck_len2=0, pwr=0, pwr2=0, pwr3=0, a=0, b=0, c=0;
    int pwr4=0, pwr5=0, pwr6=0, pwr7=0;
    float time_lab=0, diff_stress=0, extension=0;

    float eptime=0, diffstress=0, exten=0, confp=0;
    float pp1=0, pv1=0, pp2=0, pv2=0;
    float el1=0, el2=0, el3=0, el4=0;
    float curr=0, stre=0, stra=0, ave1=0, ave2=0, ave3=0, ave4=0, avecurr=0;

    float variable=0;
    int i;                        //iterator
    int gottime=0; //boolean
    int epfilelinecount=0, epfilecurrentline=1;

    float vol=0, cubed=0;
    float mean_ck_len=0, mean_energy=0, crack_den=0;
    char loc_file[50], res_file[50], ep_file[50];

    FILE *floc, *fres, *fep;

    while(no==1)
    {

        printf("Enter B-Value Filename: ");
        scanf("%s",loc_file);

        floc = fopen(loc_file,"r+");
        no=0;
        if((floc = fopen(loc_file,"r+")) == NULL)
        {
            printf("File does not exist\n");
            no=1;
        }
    }

    no=1;
    while(no==1)

```

```
{

printf("Enter EP Filename: ");
scanf("%s",ep_file);

fep = fopen(ep_file,"r+");
no=0;
if((fep = fopen(ep_file,"r+")) == NULL)
{
printf("File does not exist\n");
no=1;
}
}

printf("Enter Output Filename: ");
scanf("%s",res_file);
fres = fopen(res_file,"w+");

printf("Enter no of lines in epfile: ");
scanf("%d",&epfilelinecount);

while(!feof(floc))
{
fscanf(floc,"%f%f%f%f%f%f",&time,&a,&nt,&b,&c,&bval);
printf("%f\t%f\t%f\t%f\n",time,nt,bval);

frac_dim = bval;

pwr = 1/(frac_dim+1);

pwr2 = 1-frac_dim;

pwr3 = frac_dim/(frac_dim - 1);

pwr4 = pwr2/(frac_dim+1);

ck_len1 = (1 - (frac_dim*nt));

pwr5 = pow(ck_len1,pwr4);

ck_len2 = (1 - frac_dim*nt);

pwr6 = (-1) * (frac_dim/(frac_dim+1));

pwr7 = pow(ck_len2,pwr6);
mean_ck_len = 0.000112 * pwr3 * (pwr5/pwr7);

cubed = pow(mean_ck_len,3);

vol = 3.14159265 * 0.04 * 0.04 * 0.1;

crack_den = (nt * cubed) / vol;

gottime = 0;
epfilecurrentline = 1;
while (gottime == 0)
{

fscanf(fep,"%f\t",&etime);

for (i=0; i<18; i++)
```



```
{
    fscanf(fep,"%f\t",&variable);
    if (i==0)
    {
        diffstress = variable;
    }
    if (i==1)
    {
        exten = variable;
    }
    if (i==2)
    {
        confp = variable;
    }
    if (i==3)
    {
        pp1 = variable;
    }
    if (i==4)
    {
        pv1 = variable;
    }
    if (i==5)
    {
        pp2 = variable;
    }
    if (i==6)
    {
        pv2 = variable;
    }
    if (i==7)
    {
        el1 = variable;
    }
    if (i==8)
    {
        el2 = variable;
    }
    if (i==9)
    {
        el3 = variable;
    }
    if (i==10)
    {
        el4 = variable;
    }
    if (i==11)
    {
        curr = variable;
    }
    if (i==12)
    {
        stre = variable;
    }
    if (i==13)
    {
        stra = variable;
    }
    if (i==14)
    {
        ave1 = variable;
    }
    if (i==15)
```


SPECIAL NOTE

**ITEM SCANNED AS SUPPLIED
PAGINATION IS AS SEEN**